

This item is held in Loughborough University's Institutional Repository (<https://dspace.lboro.ac.uk/>) and was harvested from the British Library's EThOS service (<http://www.ethos.bl.uk/>). It is made available under the following Creative Commons Licence conditions.



For the full text of this licence, please go to:  
<http://creativecommons.org/licenses/by-nc-nd/2.5/>

# Molecular Dynamics Modelling of Nanoindentation

David Christopher

A DOCTORAL THESIS

SUBMITTED IN PARTIAL FULFILMENT OF THE REQUIREMENTS  
FOR THE AWARD OF  
DOCTOR OF PHILOSOPHY OF LOUGHBOROUGH UNIVERSITY  
OCTOBER 2002

Supervisor: R Smith Ph.D, Loughborough University

© D CHRISTOPHER 2002



# Acknowledgements

I would like to thank my supervisor Prof. Roger Smith for his help and enthusiasm over the last three years. Thanks must also go to Dr. Steven Kenny, particularly for many helpful discussions on parallel programming. I would also like to express my gratitude to Prof. Asta Richter for providing the experimental results that are presented in this thesis, and to Dr. Keith Watling for assistance with numerous computing technicalities. Finally I wish to acknowledge EPSRC for studentship, award number 99802401.

# Abstract

This thesis presents an atomic-scale study of nanoindentation, with carbon materials and both bcc and fcc metals as test specimens. Classical molecular dynamics (MD) simulations using Newtonian mechanics and many-body potentials, are employed to investigate the elastic-plastic deformation behaviour of the work materials during nanometre-sized indentations. In a preliminary model, the indenter is represented solely by a non-deformable interface with pyramidal and axisymmetric geometries. An atomistic description of a blunted  $90^\circ$  pyramidal indenter is also used to study deformation of the tip, adhesive tip-substrate interactions and atom transfer, together with damage after adhesive rupture and mechanisms of tip-induced structural transformations and surface nanotopography. To alleviate finite-size effects and to facilitate the simulation of over one million atoms, a parallel MD code using the MPI paradigm has also been developed to run on multiple processor machines. The work materials show a diverse range of deformation behaviour, ranging from purely elastic deformation with graphite, to appreciable plastic deformation with metals. Some qualitative comparisons are made to experiment, but available computer power constrains feasible indentation depths to an order of magnitude smaller than experiment, and over indentation times several orders of magnitude smaller. The simulations give a good description of nanoindentation and support many of the experimental features.

# Contents

<b>1</b>	<b>Introduction</b>	<b>8</b>
1.1	Simulation and Techniques . . . . .	8
1.2	Indentation of Materials . . . . .	11
1.2.1	Background . . . . .	11
1.2.2	Indentation at the Nanometre Scale . . . . .	13
	Experimental Review . . . . .	13
	Theoretical Review . . . . .	15
1.3	Overview of Thesis . . . . .	16
<b>2</b>	<b>Simulation Methodology</b>	<b>18</b>
2.1	Introduction . . . . .	18
2.2	Molecular Dynamics . . . . .	18
2.2.1	Interatomic Potentials . . . . .	19
2.2.2	Integration Algorithms . . . . .	22
2.2.3	Boundary Conditions . . . . .	23
2.2.4	Neighbour Lists . . . . .	25
2.2.5	Molecular Dynamics Profile . . . . .	27
2.3	Molecular Dynamics Simulation of Nanoindentation . . . . .	29
<b>3</b>	<b>Nanoindentation of Carbon Materials Implementing the Interface Indenter Model</b>	<b>31</b>
3.1	Introduction . . . . .	31
3.2	Interface Indenter Model . . . . .	34
3.3	Simulation Results and Discussion . . . . .	37
3.3.1	Graphite {0001} Substrate . . . . .	37
	Indentation with 5 ps Period . . . . .	38

Indentation with 50 ps Period . . . . .	43
3.3.2 Diamond {100} Substrate . . . . .	48
3.4 Determining Mechanical Properties . . . . .	54
3.4.1 Nanohardness . . . . .	54
3.4.2 Young's Modulus . . . . .	55
3.5 Mechanical Properties of Graphite and Diamond . . . . .	56
3.6 Summary . . . . .	58
<b>4 Nanoindentation of Carbon Materials Implementing the Atomistic Indenter Model</b>	<b>60</b>
4.1 Introduction . . . . .	60
4.2 Atomistic Indenter Model . . . . .	61
4.3 Simulation Results and Discussion . . . . .	63
4.3.1 Graphite {0001} Substrate . . . . .	63
4.3.2 Diamond {100} Substrate . . . . .	66
4.3.3 C <sub>60</sub> Fullerene Substrate . . . . .	75
4.4 Hydrogen Surface Termination . . . . .	78
4.4.1 Diamond {100} Substrate . . . . .	79
4.4.2 Amorphous Carbon Substrates . . . . .	81
4.5 Experimental Results and Discussion . . . . .	89
4.5.1 Graphite {0001} . . . . .	90
4.5.2 Diamond {111} . . . . .	91
4.5.3 C <sub>60</sub> Fullerene Film . . . . .	92
4.6 Summary . . . . .	93
<b>5 Nanoindentation of bcc and fcc Metals Implementing the Atomistic Indenter Model</b>	<b>95</b>
5.1 Introduction . . . . .	95
5.2 Simulation Details . . . . .	99
5.3 Simulation Results and Discussion . . . . .	101
5.3.1 Body-centred-cubic Iron . . . . .	101
Fe {100} Substrate . . . . .	101
Fe {100}{111} Grain Boundary Substrate . . . . .	111
5.3.2 Face-centred-cubic Silver . . . . .	114



5.4	Modification of Ackland's Ag Potential . . . . .	121
5.5	Experimental Results and Discussion . . . . .	126
5.5.1	Body-centred-cubic Iron . . . . .	126
5.5.2	Face-centred-cubic Silver . . . . .	128
5.6	Summary . . . . .	132
<b>6</b>	<b>Parallel Molecular Dynamics</b>	<b>135</b>
6.1	Introduction . . . . .	135
6.2	Program Development . . . . .	138
6.2.1	Revision to Fortran 90 . . . . .	139
6.2.2	Profile of Serial MD Code . . . . .	140
6.2.3	Functional Decomposition . . . . .	141
	Energy and Force Evaluation . . . . .	141
	Neighbour List Construction . . . . .	145
6.3	General MPI Programs and Basic Concepts . . . . .	148
6.4	Message-Passing Operations . . . . .	149
6.4.1	Send and Receive Operations . . . . .	149
6.4.2	Data Movement . . . . .	150
6.4.3	Reduction Operations . . . . .	152
6.5	Decomposition Methods . . . . .	153
6.6	Parallelisation Scheme . . . . .	154
6.6.1	Adaptive Load Balancing . . . . .	154
6.6.2	Energy and Force Evaluation . . . . .	158
6.6.3	Neighbour List Construction . . . . .	159
6.7	Performance Evaluation . . . . .	161
6.8	Performance Tuning . . . . .	163
6.9	Summary . . . . .	170
<b>7</b>	<b>Million Atom Simulations of Fe Nanoindentation</b>	<b>172</b>
7.1	Introduction . . . . .	172
7.2	Adding Curvature to the Indenter Tip . . . . .	173
7.3	Simulation Details . . . . .	174
7.4	Simulation Results and Discussion . . . . .	177
7.4.1	Fe {110} Substrate . . . . .	177

7.4.2	Fe {100} Substrate . . . . .	184
7.4.3	Fe {111} Substrate . . . . .	186
7.4.4	Force-depth Curve Analysis . . . . .	189
7.5	Experimental Results and Discussion . . . . .	190
7.5.1	Fe {110} Substrate . . . . .	190
7.5.2	Fe {100} Substrate . . . . .	193
7.5.3	Fe {111} Substrate . . . . .	194
7.5.4	Force-depth Curve Analysis . . . . .	195
7.6	Summary . . . . .	196
8	Conclusions and Future Work	199
A	Animated Movies	204
	Bibliography	205

# Chapter 1

## Introduction

### 1.1 Simulation and Techniques

Understanding the fundamental behaviour of some real system is best facilitated by constructing a model of the system. The term ‘system’ essentially refers to an assembly of interrelated entities within some notional boundary. Models are usually governed by mathematical equations that describe the behaviour of the system at a simplified level, by making assumptions about how it operates. In many engineering and scientific disciplines, observed phenomena can stem from very complicated mechanisms. Hence, execution of a model which mimics such complex behaviour can involve considerably large numerical calculations. After the Second World War, engineers and scientists started employing computing machines to execute the large scale numerics that previously were not feasible. This quickly led to the utilisation of computer simulation [1] as a research tool. The term ‘simulation’ can be simply defined as a numerical technique which executes a mathematical model to yield a description of system behaviour over a specified period of time.

Computer simulation has had a dramatic influence in scientific research and industry over the last fifty years or so, and has become a widely established and practiced discipline [2]. It allowed existing theories to be tested, which inevitably led to the revision of many models and therefore an improvement in our understanding. After initial scepticism, computer simulation has evolved into a standard method whereby theoretical models can be validated against experimental observations, and subsequently modified by analysing any discrepancies. Thus, the role of computer simulation lies somewhere between theory and experiment. One of the principal qualities of computer simulations



is that they do not incur the complexity or expense of experiments. They are amenable to manipulations and so allow the exploration of science under conditions where experiments may not be physically viable. For example, while it may be impossible to perform experiments under extremes of temperature or pressure, a computer simulation would be feasible. Furthermore, simulations permit better control over experimental conditions that can be achieved realistically. However, simulations are not without drawbacks since they are often very time-consuming, both to develop and implement.

One of the most widespread uses of computer simulation is in materials science [3]. With increases in computer power and the development of better interatomic potentials, computer simulations are proving to be an essential integrated tool in materials research. There exists several different types of numerical simulations to study material phenomena, which can be divided up into atomistic models and continuum models. In continua, the material is often treated as a continuous medium, where the finite element method [4] is usually employed to solve the partial differential continuum equations that describe the material. In atomistic methods [5], the material is described at the atomic scale as an aggregate of individual atoms. This allows the dynamics of each atom to be studied, therefore allowing a detailed insight into atomic processes and mechanisms behind material phenomena. It has long been recognised that continuum models are less applicable when the scale of the material under investigation is reduced towards atomic dimensions.

There are a wide range of atomistic modelling methods available. Routinely utilised techniques are Monte Carlo (MC) [5], the binary collision approximation (BC) [6] and molecular dynamics (MD) [6]-[7]. With the emergence of more powerful computers, material phenomena are also being calculated from first principles. Quantum mechanical methods, like *ab initio* [8] and tight-binding [9], describe the material at the electronic level by solving approximations to Schrödinger's equation. They are becoming increasingly important in predicting elementary physical material properties. However, they are somewhat restricted in the size of systems that can be studied by the complexity of the calculations. Currently, feasible systems described by *ab initio* involve up to a maximum of about 1000 atoms, although larger systems can be computed using tight-binding, but at the expense of further approximations. While the MC, BC and MD approaches allow employment of larger system sizes compared with first principles calculations, they are more restricted with accuracy.



MC simulations are typically applied to problems having a probabilistic basis. In materials science applications, MC simulations employ importance sampling to generate low states of energy. The first MC computer simulations were applied to the study of dense liquids in 1953 by Metropolis *et al* [10]. BC computer simulations model the atomic collisions by assuming that the particles interact in a pairwise fashion. Such a pairwise interaction is known as a binary collision. BC simulations were developed by authors such as Robinson [11] and implemented to examine radiation effects in crystalline materials. The application of the BC method is best suited to the simulation of high energy ion bombardment. The first reported MD computer simulations were performed in 1956 by Alder and Wainright [12] to study the dynamics of hard spheres. In essence, MD simulations employ Newtonian mechanics to describe the dynamics for a system of atoms. Interaction forces are derived from classical many-body potentials, which are purely functions of the atomic positions. The classical equations of motion cannot be solved analytically, and so a finite difference scheme is implemented to integrate the differential equations at discretised timesteps, where the dynamics of the system is then allowed to evolve to the next time interval. The primary MD simulation of a ‘real’ material was published in 1960 by Vineyard *et al* [13] which reported on the simulation of radiation damage in crystalline Cu. In 1964 Rahman reported the initial MD simulation of a real liquid [14]. MD simulations were later developed by many authors, such as Beeler [15] and Harrison [16]. The first MD simulations were restricted to modelling a very small number of atoms, in the order of hundreds. However, with modern parallel architectures, systems involving millions of atoms can now be studied.

Computer visualisation and animation [17] have become an essential integrated part of simulations. The role of computer graphics has greatly assisted many research areas, such as the design of new molecules [18]. Our understanding of material phenomena can be considerably enhanced by graphical representation, since the human eye cannot be relied upon to accurately perceive the information contained in large numerical data. Thus, computer visualisation provides a method to reveal processes and mechanisms in material phenomena that could otherwise go unseen by examining mass numerics. Informative visualisation is generally achieved by effective employment of colour, form and animation. The latter can be crucial in the exploration of data from simulations where minor kinetic processes (like small vibrations) have occurred. With modern day computer power, interactive visualisation software is increasingly used to provide an

excellent method for detailed examination of simulation data.

## 1.2 Indentation of Materials

### 1.2.1 Background

The suitability of a material for employment in a given process, can be determined from knowledge of its mechanical properties. The science of tribology has matured over the last few hundred years as a variety of methods to probe material attributes, such as hardness, Young's modulus and elastic-plastic deformation behaviour, have been developed. The deformation behaviour of materials is characterised by *elastic* and *plastic* deformation. If a force is applied to a material then constituent atoms will displace towards an equilibrium state, deforming the initial bonds in the process. If the bonds return to the original state as the applied load is reversed, then the deformation is said to be *elastic*. If bonds stay deformed then the deformation is defined as *plastic*. In plastic deformation the bonding between atoms can be considered to rupture and then reform, but in a different configuration. Thus, plastic deformation is characterised by permanent displacements of atoms. However, if broken bonds are not reformed then fracture can occur. The bulk material deformation behaviour is a function of the individual deformations of the bonds and can therefore be elastic and/or plastic. A simple way to examine the deformation behaviour of a material is through hardness testing.

Hardness can be defined as the resistance to deformation. The first hardness calculations were based on scratch tests [19], which depend on the ability of one solid body to scratch the surface of another. Some of the first scratch tests were performed by Reaumur in 1722. Mohs introduced a hardness scale in 1822 that was calibrated by selecting ten minerals as standards [20], ranging from talc to diamond. The modern scratch test has developed from the Mohs scale, where the hardness is evaluated from the dimensions of a diamond stylus scratch in the material [21]. This method has been shown to be successful at determining the variation in hardness across a grain boundary [22]. Mechanical properties of materials have also been studied by abrasion and erosion testing, where the hardness is determined from the rate of wear and loss of the material. However, these methods are generally less accurate compared with conventional techniques and are not typically utilised.



Indentation is the most preferred technique to characterise the mechanical properties of materials. A commonly used procedure is dynamic indentation or ‘rebound testing’. Here, an indenter is dropped onto the surface of a material, where the rebound height gives a measure of the hardness [23]. There are several variations of this method, such as damping or pendulum tests, which is generally used for large scale work materials. The most extensively used method is ‘static’ indentation, which forms the basis of this thesis. In this procedure, a hard indenter is forced into the surface of a solid body and the force is measured as a function of the indentation depth. The force-depth information allows the mechanical properties of the sample to be readily evaluated.

Towards the end of the 19th century, the Swedish engineer Brinell introduced a method known as the ‘Brinell test’ [24]. This procedure uses a spherical indenter, which is generally made from steel or even tungsten carbide for indentation of hard materials. The technique was developed further in 1908 by Meyer [25]. However, very hard materials constrain feasible implementation of the Brinell test. In 1908, Ludwik implemented the first conical diamond indenters for hardness measurements [26]. These were later employed by Rockwell in 1919 for indentation of very hard materials [19]. Rockwell further implemented conical indenters with hemispherical tips. The first diamond pyramidal indenters were introduced in 1922 by Smith and Sandland [27]. These square pyramidal indenters were later developed into the familiar Vickers hardness technique [28]. The introduction of the Knoop indenter in 1939 [29], allowed adequate indentations in materials which had not been viable with the Vickers or Brinell indentations. This was because the Knoop indenter, which has a cross-sectional contact area in the shape of a parallelogram, allows a satisfactory contact area at relatively small penetration depths. The introduction of the Berkovich indenter [30] in 1951 produced a sharper tip compared with the Vickers and Knoop indenters and soon became commonly used. With Berkovich geometry, three non-adjacent planes intersect at a single point, forming a three-sided pyramid.

The underlined methods above have been extensively used to probe the micromechanical behaviour of materials. However, the exploration of science on the nanometre scale ( $10^{-9}\text{m}$ ) has continued the miniaturisation of technology [31]-[32]. Materials beyond submicrometre dimensions are now readily employed in many applications. For example, thin films have found numerous uses from protective coatings to functional layers with special electrical and magnetic properties. The mechanical behaviour of



nanosize materials may differ from the bulk material, due to the comparatively high surface area to volume ratio. Furthermore, mechanical properties may vary locally for a material if it is measured over nanoscale dimensions, due to the density of local defects and surface asperities. The mechanical behaviour of nanoscale materials is not only physically interesting, but it is also of significant technological importance as science and technology develops on the nanometre scale. Knowledge of mechanical behaviour and mechanisms at the nanometre scale is crucial for the design of nanosize materials with tailor-made properties. However, indentation into materials with nanosize dimensions is difficult. Indentation of thin films for example, needs to be only a few nanometres deep to avoid any influence from the underlying substrate.

## 1.2.2 Indentation at the Nanometre Scale

### Experimental Review

The development of new techniques to measure mechanical properties, friction, adhesion and surface topography on the nanometre scale, has given rise to the new research field of nanotribology. Proximal probe tips, such as the scanning force microscope (SFM) and the atomic force microscope (AFM), and related methods, have allowed investigations of materials on the nanometre scale. A widely expanding area of nanotribology is nanoindentation, which is a new technique designed to measure the mechanical properties of materials on the nanoscale [32]. The experimental nanoindentation procedure involves applying very small forces from a few  $\mu\text{N}$  up to tens of  $\text{mN}$ , to press a nanosize tip into the surface of a material, where the force is measured as a function of the indentation depth. The experimental procedure usually incorporates the SFM so that topographic images can be obtained using the same tip. Impressions only a few nanometres deep can be made to generate the force-depth information from which the mechanical behaviour of the sample can be evaluated. Therefore, this method allows the properties of materials like thin films to be readily investigated.

The experimental development of small-scale indentations has generated considerable interest in the detailed mechanisms governing deformation. Over the last ten years or so, there has been an outbreak of activity in the study of tip-surface interactions. In the literature there is no shortage of papers encompassing the application of nanoindentation. Initial experimental work involved the indentation of materials of known



hardness so to calibrate the indenting instrument. A review of nanoindentation is given in the article by Nix [33]. Nanoindentation has been successfully implemented in experimental work to investigate the mechanical behaviour of a wide range of materials, including covalent materials [34]-[35], semiconductor materials [36]-[37], metallic films [38]-[39], quasi-crystals [40]-[41], ceramics [42]-[43], thin films [44]-[45], biological materials [46], ionic materials [47], and soft samples such as polymers [48]. In addition to these materials, more atypical specimens have also been probed experimentally, such as glass [49], ice [50], automotive brake pads [51], human dental enamel and dental restorative [52]-[53] and human bone [54]. The experimental investigations report a wide range of interesting phenomena during nanoindentation testing. Over the range of materials studied experimentally, contrasting deformation behaviour from purely elastic to severe inelastic has been observed.

The general criteria for an indenter is for it to have a high mechanical hardness and a sharp protruding tip (or small radius of curvature), whose geometry should be precisely known when evaluating the mechanical properties of the substrate. In reality the tip blunts with continued operation and so the curvature of the apex is modified with repeated use. It should be emphasised that in reality, the apex of every indenter is paraboloidal in shape. A variety of indenter configurations have been reported in the literature for experimental nanoindentation studies. These include the commercially used three-sided Berkovich [55]-[56], cube-cornered [57]-[58] and four-sided Vickers indenters [59]-[60] as well as axisymmetric configurations like spherical [61]-[62] and conical [63]-[64] indenters. The most preferable indenter shape will depend on the kind of measurement required. A comparison between indentations made with different indenter geometries is given by Breder *et al* [65]. Generally the tip is made from diamond, the hardest material known to date, although other hard materials have also been implemented experimentally. Examples include Si [66],  $\text{Si}_3\text{Ni}_4$  [67], Si with metal coatings [68], metals [69] and carbon nanotubes [70]. Axially symmetric indenters are not generally used since they are difficult to manufacture with the precision required in nanoindentation experiments. Furthermore, spherical indenters are not self symmetric and therefore the contact area is a more complicated function of depth. Cube-cornered diamond indenters are generally preferred for nanoindentation testing since they are less susceptible to blunting and are comparatively easy to fabricate from cut crystals.

Usually the experiments are performed at room temperature and ambient pressure.



Although, in some cases there has been an attempt to control the surface chemistry and environment during nanoindentation testing. For example, experiments have been performed in ultrahigh vacuum (UHV) to maintain a specimen surface free from adsorbates [71] and in a liquid environment [72] to relieve surface tension. Other indentation parameters have also been investigated experimentally. For example, the effect of tip momentum has been considered by Beake and Leggett [73] during nanoindentation of polymer films. They found that nanohardness exhibited different trends with a change in loading rate. Baltá Calleja [74] studied the influence of the holding time at peak load on polymeric materials and reported time-dependent mechanical behaviour.

## Theoretical Review

Determining the mechanical properties of materials using modern nanoindentation equipment is relatively simple. However, understanding the mechanisms and nature of plastic deformation is difficult. Concurrent to experimental investigations, comprehensive computational studies have also been undertaken to elucidate material deformation behaviour. Recent developments in interatomic potentials coupled with advances in computer power and improved theoretical techniques, have enabled realistic nanoscale behaviour of materials to be studied. Computer simulations offer an ideal approach to investigating numerous questions which cannot be fully answered from experimental nanoindentation measurements. Furthermore, the simulated force-depth curve is advantageous since the shape can be related to specific atomic-scale events.

One of the first finite element simulations of nanoindentation was performed by Bhattacharya and Nix [75] to study the indentation of silicon, nickel and aluminium using a 2D axisymmetric model. Subsequent finite element simulations have been performed by authors such as Vlachos *et al* [76] and Smith *et al* [77]. Such simulations have allowed qualitative information regarding mechanical properties of different materials to be extracted. However, since the very nature of nanoindentation involves the deformation and rupture of bonds, the process is best studied atomistically to elucidate mechanisms of structural transformation during deformation. The atomistic model approach is generally preferred to the finite element model because it allows a more detailed understanding of the transition from elastic to plastic behaviour and also the way in which defects and dislocations are created by the indentation process.

Quantum mechanical techniques have allowed a thorough study of tip-surface in-

teractions [78]-[79]. The first principles calculations give a description of the quantum mechanical nature of interfacial bonding, and have therefore allowed detailed investigations into the rupture and formation of bonds during plasticity. However, the complexity of the calculations involved, heavily constrain the number of atoms in a feasible simulation. For example, in one *ab initio* quantum mechanical investigation by Ke *et al* [78], a Si tip was configured from only 4 atoms and a GaAs (110) substrate consisted of just under 100 atoms. Primarily, the materials studied from first principles are covalent materials such as Si and diamond. Apart from having large practical applications, such materials are computationally easier to study using quantum mechanics since the number of electrons used in the calculations is relatively small. Typically, nanoindentation studies do not implement quantum mechanical methods since most related phenomena of interest stem from large scale dynamics. Hence, the most favourable approach to investigate the nanoindentation of materials is by the mature field of MD simulation.

The limiting factor in modest sized MD simulations of nanoindentation is system size and feasible simulation time, which are constrained by the available computing power. The use of parallel computers with multiple processors relax these constraints, and allow systems involving potentially millions of atoms to be routinely employed [80]. A wealth of literature exists reporting MD simulations of nanoindentation for a wide range of materials, complementary to many of the experimental specimens. For a brief review of MD simulations of nanoindentation the reader is referred to the excellent review by Stuart *et al* [81]. In addition to nanoindentation, MD simulations have also been applied in other studies of nanotribology. Authors such as Harrison *et al* [82] and Komanduri *et al* [83] have reported, respectively, on the nanoscratching of diamond and metal surfaces. Nanometric cutting of metal crystals has been examined by Fang *et al* [84] and Komanduri *et al* [85]. Recent studies by Landman *et al* [86] and Shimizu *et al* [87], reported on simulations of nanofriction for Si-Si and diamond-Cu interfaces observing the stick-slip phenomenon (the transition from static to dynamic motion).

### 1.3 Overview of Thesis

Motivated by the aforementioned experimental and theoretical work, this thesis presents an atomic scale study of nanoindentation, employing carbon materials and both bcc and fcc metals as test specimens. Classical MD using Newtonian mechanics are im-



plemented to simulate the indentation process. The principal intent of this work is to gain insight into the nanomechanical behaviour of materials, together with the tip-induced mechanisms that impart irreversible change in atomic structure. Qualitative comparisons between experimental measurements and the simulations are made where possible. While the experimental length scales have been reducing, with improved computer power those of simulations have been increasing. However, the available computing power and the timely execution of MD simulations constrain feasible investigations to systems comparatively smaller than those utilised in experimental work. Consequently, viable simulations performed here comprise of indentation depths an order of magnitude smaller than experimental values, and over indentation times several orders of magnitude smaller. In addition to nanoindentation simulations, this thesis also discusses the development of a parallel MD code using the MPI paradigm to facilitate the simulation of more atoms and to alleviate finite-size effects.

The fundamental principles of MD simulations are introduced in Chapter 2, together with the pertinent details of the application to simulating nanoindentation. Numerous methods to increase computational efficiency are also discussed. A preliminary model of the indenter is introduced in Chapter 3, where the atomic structure is ignored and represented solely by a non-deformable interface. Simulation results implementing this indenter model with graphite and diamond substrates are presented. The influence of indentation speed and tip geometry on the deformation behaviour of the carbon materials is also discussed. In Chapter 4, an atomistic pyramidal indenter model is introduced together with simulation results for different carbon materials, namely graphite, diamond, a  $C_{60}$  fullerene film and amorphous carbon. The physical behaviour of the indenter during indentation is examined together with the role of surface termination on adhesion. The deformation behaviour of bcc Fe and fcc Ag metals is investigated in Chapter 5. The nature of the deformed material under the indenter and the induced surface topography is examined. The development of the parallel MD code is reviewed in Chapter 6. The performance of the parallel code is evaluated and opportunities for efficiency tuning are discussed. Parallel MD simulations of Fe indentation are presented in Chapter 7. Three different surfaces of Fe are examined with over one million atoms to study indentation-induced dislocations, together with the preferred crystallographic directions for pile-up. Finally, general conclusions and ongoing work are discussed in Chapter 8, together with suggestions for future work.



# Chapter 2

## Simulation Methodology

### 2.1 Introduction

This chapter discusses the pertinent details of the MD technique and its application to simulating the nanoindentation process. The MD simulation method is introduced in the next section. The discussion is not intended to be an exhaustive attempt to cover the MD field, but only a review on the most fundamental principles. In addition, some ‘tricks of the trade’ that are commonly used to improve the computational efficiency, such as bookkeeping techniques, are also introduced. The discussion is necessarily short and so for a more detailed discussion on the vast subject of MD, the reader is referred to Smith [6] or Allen and Tildesley [7]. The final section details the application of MD to the simulation of nanoindentation.

### 2.2 Molecular Dynamics

In this thesis the nanoindentation process is simulated at the atomic scale by MD [6]-[7]. In essence, the MD technique is used to model the motion of a system of atoms, interacting with each other by the means of Newton’s law. The atoms evolve by the independent variables of space and time. The dynamics are described by assuming multiple interactions, where the forces the atoms exert on each other govern the rate and direction of motion. Hence, the basic feature of MD simulations is the calculation of the force on each atom and therefore the position of each atom throughout a specified period of time. In classical MD it is assumed that the motion of atoms can be modelled

using Newtonian mechanics. Thus, the equation of motion for the  $i$ th atom is

$$\frac{d^2 \mathbf{r}_i}{dt^2} m_i = \mathbf{F}_i \quad (2.2.2.1)$$

where  $\mathbf{F}_i$  denotes the force acting on the  $i$ th atom, with mass  $m_i$  and position vector  $\mathbf{r}_i$ .

Atoms are modelled as point masses with positions defined by Cartesian coordinates. The maximum number of atoms used in a simulation is determined by both the available computer resources and the complexity of the interatomic potential. Simulations typically involve between  $10^3$  and  $10^7$  atoms, with a time scale in the order of ps. The phenomena under investigation is usually simulated in a three-dimensional computational box. This is merely a simplistic approach; there is no constraint imposed on the form of the computational box. Although two-dimensional simulations are seldom used, some have been reported on for studying nanoindentation [88]-[90].

### 2.2.1 Interatomic Potentials

Atoms interact with other atoms through many-body interactions from chemical bonds, van der Waals forces or electrostatic forces. Given all the atomic positions and velocities, mechanical quantities such as potential and kinetic energy can be evaluated. It is assumed that the interaction forces can be obtained from the gradient of the interatomic potential  $V$ , with respect to the atomic positions. Hence, for a system of  $N$  atoms, the force acting on the  $i$ th atom is given by the expression

$$\mathbf{F}_i = - \frac{\partial V(\mathbf{r}_1, \mathbf{r}_2, \dots, \mathbf{r}_N)}{\partial \mathbf{r}_i} \quad (2.2.2.2)$$

where  $\mathbf{F}_i$  denotes the force vector for atom  $i$ , with position vector  $\mathbf{r}_i$ .

The quantum aspects of the problem are contained in the interatomic potential. The function  $V$  generally contains a number of free parameters which are chosen to model the phenomena of interest. The interatomic potential is principally fitted to specific material properties such as the lattice constant, elastic constants and vacancy formation energy from experimental data or *ab initio* calculations. The detailed calculations necessary in MD simulations are timely to execute, making simulations lengthy, particularly for systems involving a large number of atoms. Force evaluations can be very time consuming, taking up to 90% of the total CPU time. For interaction between atoms where the energy rapidly decreases with increased separation, it can be assumed to be zero after a specific distance. Hence, the computational efficiency can be increased by truncating



the potential at a certain cut-off distance. However, the potential energy function must be continuous to prevent instabilities from occurring. This issue is usually overcome by introducing a ‘switching’ function so that the potential energy is smoothly cut-off to zero at a specified cut-off distance. The only constraints on the potential  $V$  are that it must allow a broad range of simulations to be accurately performed and permit a physically meaningful interpretation from the results. Furthermore, the calculation of the interatomic potential must be computationally feasible. Hence, the form of the potential is crucial for efficient evaluation of the interaction forces and for the simulation to have sound predictive power.

A simple approach to determine the energy of an atom is to sum over all pairwise interactions. Thus, for an atom  $i$  with neighbour(s)  $j$ , the energy  $U_i$  can be written as

$$U_i = \frac{1}{2} \sum_j V(r_{ij}) \quad (2.2.2.3)$$

where  $V$  is a pair potential and  $r_{ij} = |r_{ij}|$  is the separation between atoms  $i$  and  $j$ . The factor  $\frac{1}{2}$  ensures that the energy of the  $ij$  bond is shared equally among atoms  $i$  and  $j$ . For a system of  $N$  atoms, the total energy of the system can be written as

$$U = \sum_i \sum_{j>i}^N V(r_{ij}) \quad (2.2.2.4)$$

The pair potential  $V$  is usually constructed as an ‘effective’ pair potential to represent the true many-body effects.

Short-ranged pair potentials, like the screened Coulomb potential [6] and the Born-Mayer potential [91], are used to describe interactions between atoms at close separation, typically less than 1 Å. Generally they are very computationally efficient to implement and have been used extensively in high energy collision cascades where atomic cores come into close separation. Two commonly used intermediate and long-range pair potentials are the Lennard-Jones ‘12-6’ potential [92] and the Morse potential [93]. Both contain attractive and repulsive parts and have been successfully applied to simulations involving many-body dynamics. Most pair potentials are generally computationally inexpensive to perform and were typically used in MD simulations between the 1950’s and the 1980’s. However, two-body potential energy functions are limited since they fail to describe accurately large numbers of material properties. This problem can be overcome by extending the pair potential to describe the energy by a many-body expression.

In a many-body potential, the energy can be described by summations over interactions between pairs, triplets,..etc. of atoms. It is assumed that such a potential will

converge quickly and hence only three-body terms are usually considered. Furthermore, the force evaluations are desired to be as efficient as possible and the inclusion of higher order terms would obviously be more time-consuming. Numerous many-body potentials have been developed over the years and received widespread use in MD simulations. One example is bond order potentials, such as the Tersoff potential [94],[95] and the Brenner potential [96],[97].

Bond order potentials, and related methods, were developed for application where directional bonding is important, like in covalent materials. In the basic formulation, the energy of an atom is given as the following sum over nearest neighbours  $j$  of  $i$

$$U_i = \frac{1}{2} \sum_{j \neq i} [V_R(r_{ij}) - B_{ij} V_A(r_{ij})] \quad (2.2.2.5)$$

where  $V_R$  and  $V_A$  are pair-additive repulsive and attractive potential parts respectively, dependent only upon the atomic separation  $r_{ij}$ . The function  $B_{ij}$  is a many-body one, related to bond order and is dependent on bond angles and the positions of atoms  $i, j$  and the local environment of  $i$ . This approach is more complex compared with the pair potentials, but it is still significantly simpler than first principles methods.

Another example of many-body potentials is the embedded atom method (EAM), which was developed by Daw and Baskes [98] for application to metals. The EAM method is based on the Hohenberg-Kohn theorem [99] which states: *the energy contribution of an atom in an array of interacting atoms is a function of the local electron density, due to all other atoms, at the position of the atom concerned.* The energy of an atom  $U_i$  is described by both a pair potential and a many-body function which are dependent only on the short range atomic separations. The energy  $U_i$  can be written as

$$U_i = \frac{1}{2} \sum_j V(r_{ij}) - F(\rho_i) \quad (2.2.2.6)$$

where  $V(r_{ij})$  is a pair potential and  $F$  is a many-body embedding function which takes the form  $F(\rho_i) = \rho_i^{\frac{1}{2}}$ . The function  $\rho_i$  serves as a measure of the local electron density and is given as

$$\rho_i = \sum_j \phi_{ij} \quad (2.2.2.7)$$

where  $\phi_{ij}$  is purely a function of the atomic separation. For a given atomic site  $i$ , the function  $\rho_i$  determines the contribution to the electron density from atom  $j$ . The exact form of the potential  $V(r_{ij})$  and the function  $\rho_i$  are specific to bcc and fcc metals.



The EAM has been successfully applied to simulations of phenomena in metals and has proved to give better results compared with pair potential energy functions. Consequently, the EAM has received widespread use for indentation of metals. Short ranged nearest-neighbour approximations of the EAM have also been developed for fcc metals by authors such as Johnson [100]. The simulations presented in this thesis employ both pair potentials and many-body potentials, and can all be analytically differentiated for force evaluations.

## 2.2.2 Integration Algorithms

For a computational cell consisting of  $N$  atoms, the dynamics are described by  $3N$  simultaneous differential equations. The simulated phenomena is discretised into timesteps, where the  $3N$  Newtonian equations of motion are integrated numerically by means of a suitable integration algorithm. In the keV to sub eV energy range, timesteps are typically of the length one tenth to a few femtoseconds. This ensures that atoms (particularly high energy atoms) do not displace a large distance in a single timestep. Most MD simulations routinely employ between one thousand and one million timesteps for a period of a few picoseconds to a few nanoseconds. Clearly, there will be an error in the calculations because of the transition from continuous to discrete variables. No integration algorithm provides an exact solution over a long duration of time, however, there are essential needs the algorithm must satisfy. Primarily the algorithm should be simple to implement and allow speedy execution, yielding accurate dynamical behaviour in the computational cell. However, for simulations utilising many-body potentials, the integration speed becomes less significant compared with the lengthy interaction calculations.

A range of algorithms have been suggested to integrate the equations of motion based on finite difference methods [101]. The most widely used method for integrating the equations of motion is the Verlet algorithm [7], which is derivable from a Taylor series expansion. The Verlet algorithm is also a low order algorithm which is symplectic. There are a variety of algorithms derived from Verlet, such as the leap-frog algorithm [102] and the velocity Verlet algorithm [103]. Another widely used algorithm is the Beeman algorithm [104], which employs more accurate terms to describe the velocity at the expense of increased computation, but which is not symplectic.

The time evolution of the position of atom  $i$  in the velocity Verlet algorithm is

described by

$$\mathbf{r}_i(t + \Delta t) = \mathbf{r}_i(t) + \Delta t \mathbf{v}_i(t) + \frac{1}{2} \Delta t^2 \mathbf{a}_i(t) \quad (2.2.2.8)$$

where  $\mathbf{r}_i$ ,  $\mathbf{v}_i$  and  $\mathbf{a}_i$  are the position, velocity and acceleration vectors respectively for atom  $i$  and  $\Delta t$  denotes the timestep. The velocity evolution of atom  $i$  is determined by

$$\mathbf{v}_i(t + \Delta t) = \mathbf{v}_i(t) + \frac{1}{2} \Delta t [\mathbf{a}_i(t) + \mathbf{a}_i(t + \Delta t)] \quad (2.2.2.9)$$

The integration algorithm thus serves to predict the positions and velocities of  $N$  interacting atoms at a later point in time ( $t + \Delta t$ ), given the dynamical data at time  $t$ . Hence, MD is a deterministic method which generates a trajectory that yields a description of the time evolution of the system dynamics. The Verlet algorithm only permits small timesteps. There are higher order integration algorithms, such as the predictor-corrector algorithm, that allow the use of long timesteps. However, these require storage of higher-order derivatives of the atomic position and suffer from larger neighbour lists or more frequent updates. The Verlet algorithm and its numerous equivalents are suitable in most cases for employment in MD simulations. Most MD simulations generally use constant timesteps, although variable timesteps are also implemented, typically where there is a significant variation in kinetic energy.

### 2.2.3 Boundary Conditions

For crystalline materials, the computational box is usually generated by an algorithm which executes repetitions of the unit crystal cell along each dimension until the required system size is obtained. The constraints of computer power force MD simulations to employ small systems of atoms and hence it is important to choose a computational cell large enough to minimise any finite-size effects. Boundary conditions [8] are employed to maintain as accurately as possible the realistic physical behaviour of the simulated material. Hence, boundary conditions serve to mimic the influence of bulk material surrounding the computational cell. This ensures that physically meaningful properties of the material can be obtained from simulations employing a small number of atoms.

There are typically four different types of boundary conditions imposed on atoms in the computational cell and are specific to the kind of phenomena under investigation. When there are no restrictions on the dynamics of an atom (typically atoms central to the simulated phenomena) then free boundary conditions are usually applied. Fixed



or rigid conditions can be applied to edge atoms to constrain the vertical or horizontal motion of the computational cell. An atom is simply made rigid by not integrating the equations of motion for that particular atom. However, although the fixed atoms are sited away from the centre of interest, they can be a problem by creating an artificial interface between the rigid atoms and the dynamic atoms.

Another important use of boundary conditions is to control the temperature of the system. In classical MD simulations, the temperature of the system is proportional to the total kinetic energy of the atoms. In reality, energy imparted to material is allowed to dissipate through the bulk. However, due to the small number of atoms employed in typical MD studies, this cannot occur and therefore surplus energy is ‘trapped’ in the computational box. In simulations of nanoindentation, the tip-substrate interactions produce heat which will be conducted through the substrate by atomic-vibrations. This will lead to heating of the system which may ensue in unrealistic behaviour of the material under investigation or even melting within the system. Hence, boundary conditions can be used to simulate effectively the dissipation of energy in the computational cell. There are numerous thermostats available, but the most straightforward approach is to damp the motion of selected atoms. Here, the dynamics of the atoms evolve in accordance with Newtonian mechanics, but the velocities are periodically rescaled in accordance with some energy loss model. More sophisticated thermostats are achieved by Langevin dynamics, where additional friction and force terms are added to the equations of motion. For a thorough discussion of thermostats typically used in MD simulations the reader is referred to Hoover [105].

Edge effects can also stem from atoms at the edges of the computational cell, which behave differently than those in the bulk. This can sometimes be minimised by employing periodic boundary conditions (PBCs) which allow edge atoms to interact with those on the opposite side of the computational cell. Therefore, atoms on the left side of the computational box can interact with those on the right side and so forth. If an atom leaves the computational cell, it reappears on the opposite side with unchanged velocity, ensuring that a constant number of atoms is maintained. Hence, PBCs can be employed to model infinite or semi-infinite system of atoms. When PBCs are utilised, the dimensions of the computational box must be calculated appropriately with respect to the material structure to ensure continuity in the atomic structure. PBCs can be disadvantageous when simulating inhomogenous systems or polycrystalline materials.

## 2.2.4 Neighbour Lists

The timely execution of MD simulations is chiefly governed by force and energy evaluations. Hence, the efficiency of the code depends critically on how the force is calculated. Two atoms do not interact if their separation is larger than a certain cut-off distance, hence interactions are typically short. This does not imply that the interactions should be pairwise. There can be many-body terms. Therefore, the computational efficiency for force evaluations can be greatly improved by only calculating the interaction between atoms within a small distance of each other. This can be achieved by bookkeeping methods which exploit temporal locality. A common bookkeeping method used in MD simulations is the neighbour list [106].

In Fig. 2.2.1 the neighbour list for atom  $a_0$  contains all atoms within a radius  $r_c$  from  $a_0$ , where  $r_c$  is equal to the cut-off distance of the interaction potential for atom  $a_0$ . Hence, only atoms within a radius  $r_c$  from atom  $a_0$  contribute to the force acting on atom  $a_0$ . The neighbour list also contains atoms that are sited outside the interaction range  $r_c$  and within a radius  $r_s$  from atom  $a_0$ , where  $r_s > r_c$ . These atoms are contained within the so-called ‘skin’ radius, which is implemented to improve further

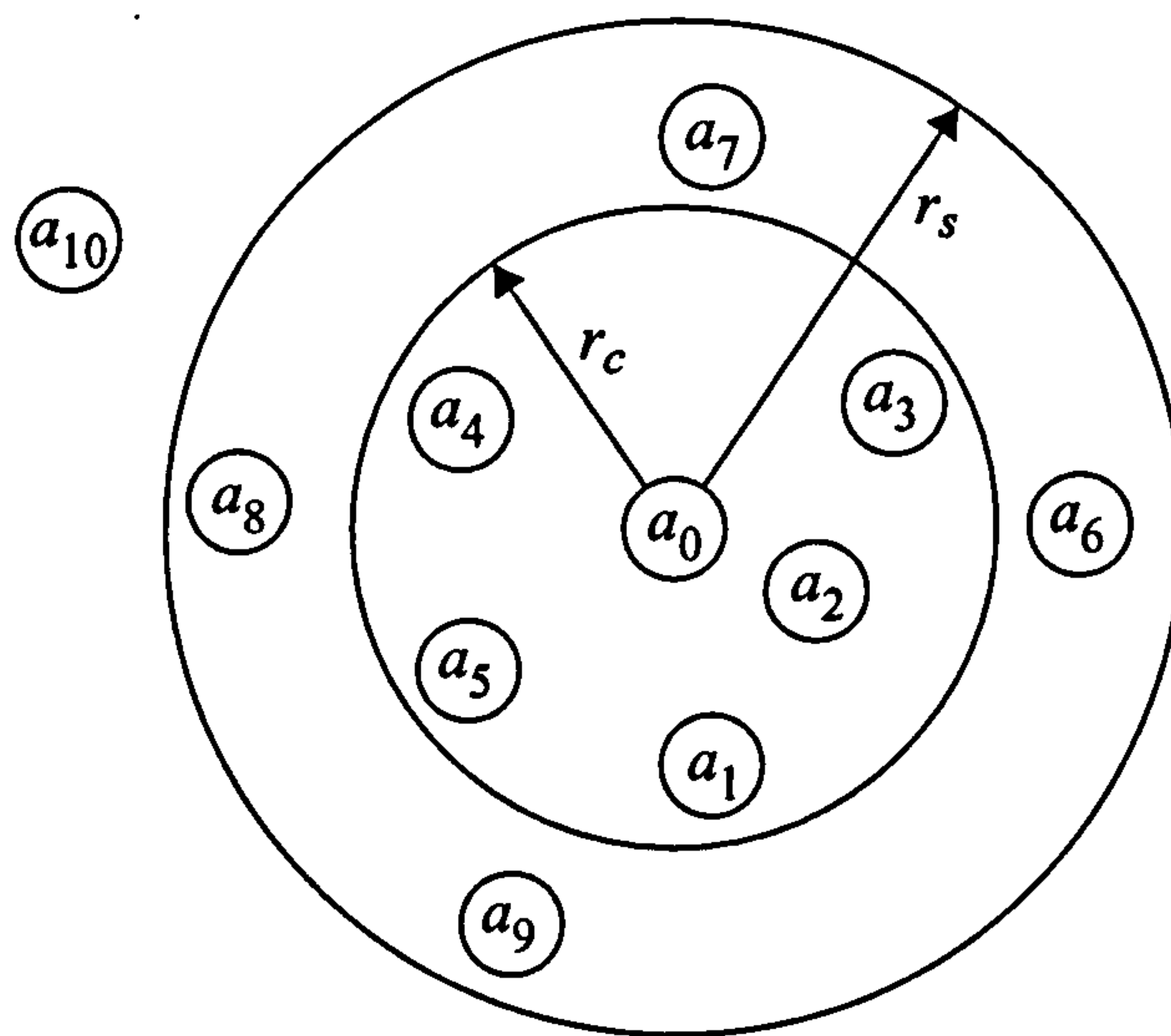


Fig. 2.2.1. Two-dimensional representation of a spherical neighbour list for atom  $a_0$ . Atoms  $a_1$  to  $a_9$  are sited within a distance  $r_s$  from atom  $a_0$  and are included on the neighbour list. Only atoms  $a_1$  to  $a_5$  contribute to the force acting on atom  $a_0$  since they are within the potential cut-off distance  $r_c$ . Atoms  $a_6$  to  $a_9$  are sited outside the interaction range in the skin radius ( $r_s - r_c$ ). Atom  $a_{10}$  lies outside radius  $r_s$  and therefore is not included on the neighbour list.



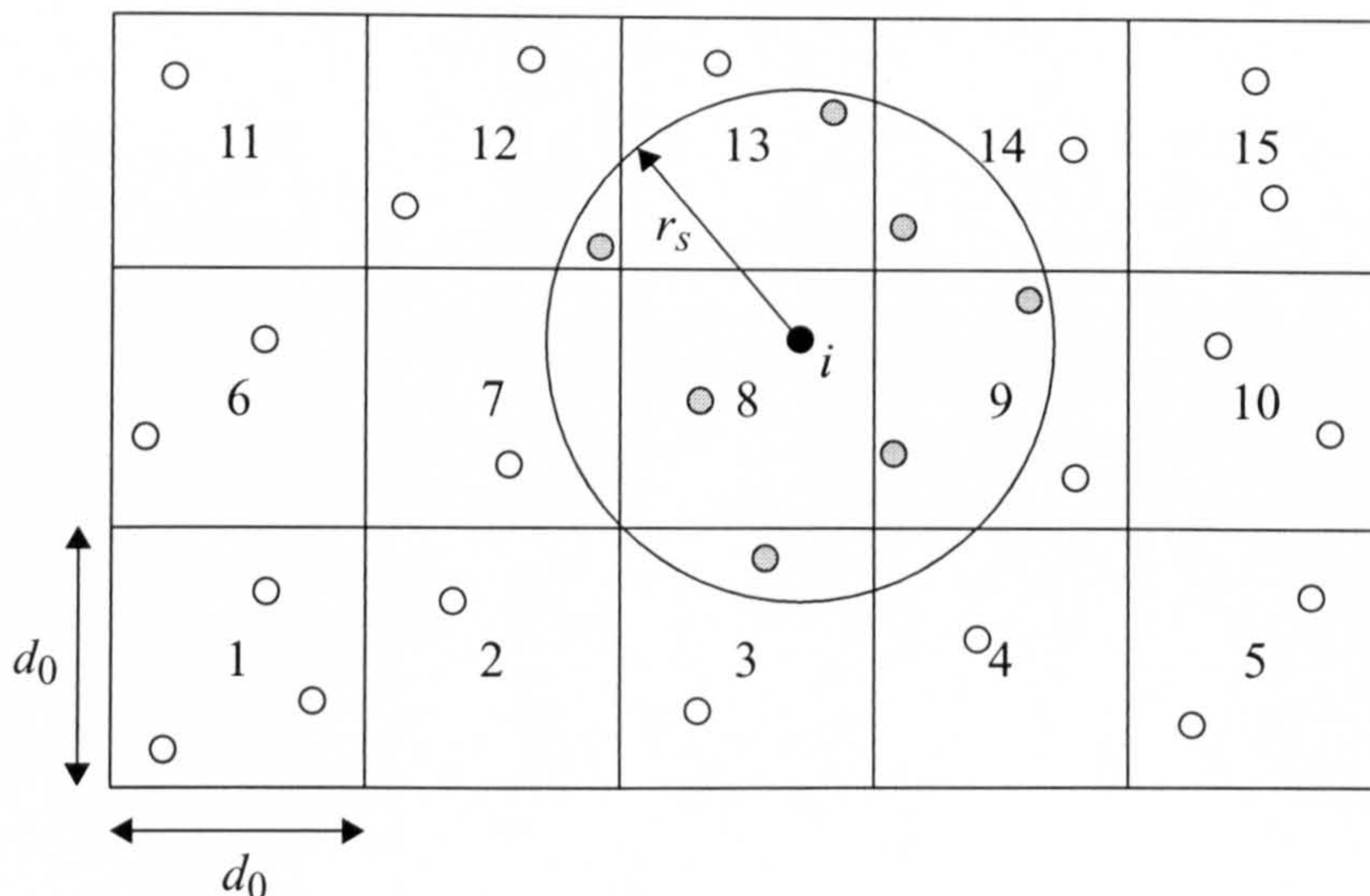


Fig. 2.2.2. Two-dimensional representation of the cell index method where the computational box is split into cells. The radial distance  $r_s$  is equal to the cut-off distance of the interatomic potential and the skin thickness. The dimension of the cells  $d_0$  is equal to  $r_s$ . Only the shaded atoms are contained on the neighbour list for atom  $i$ .

computational efficiency. The skin radius is chosen to be of sufficient thickness so that an atom outside the radius  $r_s$ , such as atom  $a_{10}$  in Fig. 2.2.1, cannot displace into the interaction range  $r_c$  after a single integration of the Newtonian equations. Therefore, the neighbour lists do not have to be updated every timestep, but only if the displacement of an atom outside  $r_s$  exceeds the skin thickness,  $r_s - r_c$ . Atoms in the skin can displace within the interaction range  $r_c$  without the need for updating the neighbour lists since they have already been included. The thickness of the skin is a question of efficiency. A smaller skin thickness will reduce the size of the neighbour list for each atom and therefore memory usage. However, in this scenario the neighbour lists will need to be updated more frequently. In contrast, if a large skin thickness is used, the updates of the neighbour list will be less frequent but the size of the lists will increase together with memory consumption. Hence, the skin thickness is generally chosen to balance the time computing the surplus atoms on the neighbour lists against the time taken to update them. Since atoms do not move very far during a single timestep, a neighbour list can be typically valid for up to 50 timesteps before the requirement to update.

For a large system of atoms, the generation of neighbour lists itself can be computationally expensive if loops over all atoms are used to determine those atoms within interaction range and within the skin radius. There are several methods that have been



proposed to avoid this inefficient approach, such as the cell index method [107]. Here, the computational box is divided into cubic cells, as illustrated in Fig. 2.2.2. The dimension of each cell ( $d_0$ ) is equal to the summation of the cut-off distance of the interatomic potential and the skin thickness of the neighbour lists. For each cell, linked lists of inhabitant atoms and cell identification numbers are constructed. For any atom  $i$ , all neighbours within a radius  $r_s$  of  $i$  will be located within the host and primary neighbouring cells. Therefore, the neighbour lists can be generated for each atom by rapidly looping over the list of atoms contained in the host and the primary neighbouring cells, instead of looping over all atoms in the computational box.

## 2.2.5 Molecular Dynamics Profile

The basic profile of the MD simulation method is briefly summarised in Fig. 2.2.3. For details on how to construct a MD simulation code the reader is referred to Eckstein [108]. Firstly, the initial configuration of the computational cell must be defined together with the relevant atomic data. Crystal structures generated from an algorithm are usually constructed close to the equilibrium state. However, materials which have reconstructed or terminated surfaces must be allowed to relax to the minimum energy configuration before employment in the simulated phenomena. Once the initial configuration of the computational box has been defined, the boundary conditions and primary velocities must be declared for all atoms. The neighbour lists are then constructed and the initial energies and forces evaluated. From the force evaluations of each atom, the initial acceleration of the atoms can then be determined.

The MD simulation then enters the core loop where the dynamics of the system are allowed to evolve to the next period in the discretised time scale by incrementing  $t$  to  $t + \Delta t$ . The force is assumed to remain constant during the integration timestep. The acceleration of the atoms is implemented together with the positions and velocities at time  $t$  to calculate the positions at time  $t + \Delta t$ . After the positions have been advanced, the validity of the neighbour lists at time  $t + \Delta t$  is checked and, if necessary, the neighbour lists are reconstructed. The force is then evaluated at the new time of  $t + \Delta t$  and the acceleration of the atoms is subsequently calculated. The velocities are then integrated to the time  $t + \Delta t$  using the accelerations from both the current timestep and the previous timestep. If the motion of atoms is damped then the positions and velocities are adjusted, in accordance with some energy loss model. The process is then

repeated to evolve the dynamics of the system to  $t + 2\Delta t$  and so forth until the required simulation time has been executed. Integration timesteps are also usually coupled with periodic data output.

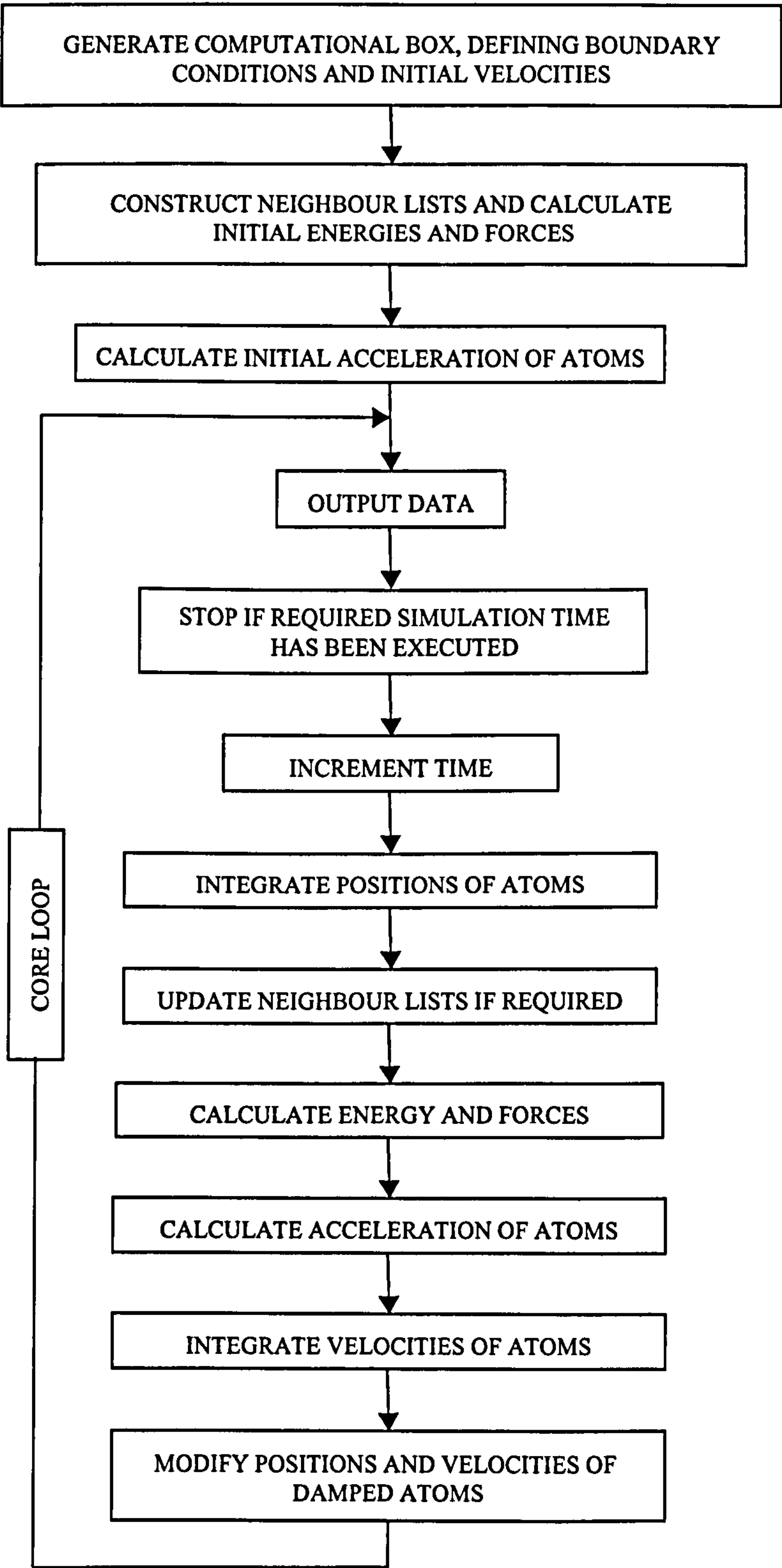


Fig. 2.2.3. Flowchart representing the basic framework of the MD simulation method.



## 2.3 Molecular Dynamics Simulation of Nanoindentation

The MD code used for simulating the indentation process has been developed from an existing standard MD code [109]. The original MD code is written in Fortran 77 and the MD simulations reported on here have been performed on SUN workstations under the UNIX environment. In the MD simulations, time is measured in femtoseconds ( $10^{-15}$ s) and distance is measured in angstroms ( $1 \text{ \AA} = 10^{-10}\text{m}$ ). The angstrom is an ideal unit to use since most bond lengths are of the order of a few  $\text{\AA}$ . The equations of motion for all non-rigid atoms are integrated using the robust velocity Verlet algorithm with a constant integration timestep, between 0.5 - 1.0 fs depending on the speed of the indentation. Forces are measured in eV/ $\text{\AA}$ , where  $1 \text{ eV}/\text{\AA} \approx 1.602 \text{ nN}$ . Preliminary simulations are performed with systems containing up to  $10^5$  atoms over maximum time scales of 150 ps. All of the simulation snapshot pictures presented in this thesis were produced using the public domain software *Rayshade*, which is designed for creating ray-traced images [110]. In the snapshots of the indentation process, atoms are represented as spheres and substrate atoms are coloured according to their vertical position, displacement or energy, so that deformation is more discernible to the eye. In addition to these images, the indentation process is elucidated by making numerous animated movies of the simulations using animation software to study the atomic scale mechanisms and processes that may not be evident from the static snapshot images. Such movies were generated from a few hundred still images rendered using the Rayshade software package. A selection of movies are on the CD in the appendix.

All the substrates considered in this study take the form of a rectangular crystal lattice, with the indenting surface being approximately square and described by the corresponding miller indices [111]. The substrates are modelled as ideal solids, with atomically flat surfaces. Each substrate atom is initially assigned zero velocity and the simulations are started from zero temperature. The surface of the work material is located at  $y = 0$  and the indentation depth is measured positively into the material. The force acting on the indenter is measured during both indentation and retraction, where the repulsive force is measured as positive and attractive force is taken as negative. For plotting convenience the load-displacement curves are produced by averaging out the force every 10 - 100 timesteps, depending on the length of the simulation.



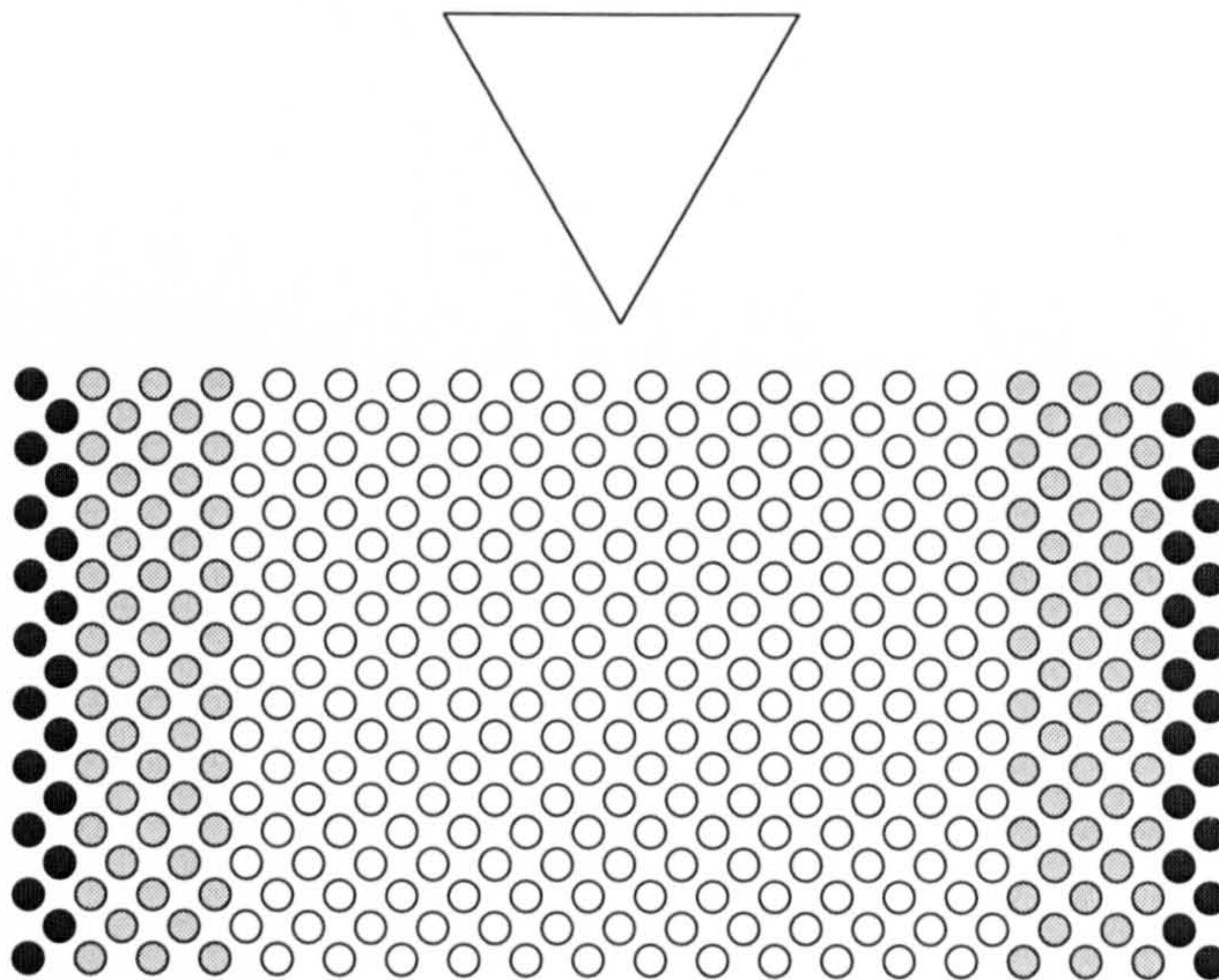


Fig. 2.2.4. Schematic diagram of typical substrate boundary conditions utilised in the nanoindentation simulations. The dark and grey shaded atoms denote rigid and damped atoms respectively. No constraints are applied to the remaining atoms, which are described solely by Newtonian mechanics.

The strategy for substrate boundary conditions implemented in the simulations presented in this thesis varies depending on the material. However, as a visual aid a typical set of employed substrate boundary conditions is shown schematically in Fig. 2.2.4. The dark shaded atoms on the horizontal edges are fixed to prevent the work material from moving horizontally or vertically during the indentation process. This emulates reality where the substrate would be fixed to a sample holder. The grey shaded atoms are damped and free boundary conditions are applied to all the remaining atoms in the substrate. This scheme ensures that no significant variation in temperature occurs since the surplus imparted energy dissipates through the work material and is removed by the damped atoms at the horizontal boundaries. The damping model is not based on any concept of temperature control but for simplicity the Lindhard-Scharff inelastic loss model [112] is used, where the velocities of the dynamic atoms are rescaled intermittently at the end of each timestep. Periodic boundary conditions are applied to side atoms of the substrates in the horizontal plane. No periodic boundary condition is imposed in the direction normal to the surface of the work material. Interestingly, some simulations of the nanoindentation procedure have reported use of periodic boundary conditions in the direction of indentation [113].



# Chapter 3

## Nanoindentation of Carbon Materials Implementing the Interface Indenter Model

### 3.1 Introduction

Few elements have the ability to compose their atoms into such diverse crystalline forms as carbon [114]. The most familiar polymorphs of carbon include diamond, graphite and the recently discovered fullerenes. Carbon materials are finding widespread use in many advanced tribological applications [115]. For example, graphite is utilised to provide high wear resistance and low friction. Diamond coatings have been applied to machining purposes and to microelectromechanical systems. Amorphous carbon (*a*-C) films, or more specifically diamond-like-carbon (DLC) films, are used extensively in the computer industry to provide protective coatings on magnetic storage disks. The numerous attractive qualities offered by polymorphs of carbon to the field of nanotribology have motivated the exploration of their mechanical properties at the nanoscale. The ability of carbon to constitute a variety of configurations, together with the fact that the indenter is also commonly composed of the same material, also make it an ideal specimen for study. A number of groups have performed both MD simulations and experimental investigations to examine the mechanical behaviour of carbon materials by nanoindentation.

One of the first groups to simulate the nanoindentation of graphite and diamond by

MD was Harrison *et al* [116]-[117]. Using a hydrogen terminated diamond pyramidal tip, Harrison *et al* [116] indented the basal plane of graphite and also hydrogen terminated diamond {111} and {100} surfaces. The simulation results showed the indentations to be purely elastic with no irreparable damage to any of the work materials. Another study by Harrison *et al* [117] reported on the indentation of diamond {111} using a hydrogen terminated  $sp^3$ -bonded tip. On reversal of the tip from the work specimen, adhesion between the tip-substrate interface was marked by connective strings of atoms. Rupture of the connective atomic strings was observed with increasing the tip retraction. This resulted in small plastic deformation to the tip and the local indentation area of the work material. However, these simulations were somewhat limited since only a very small number of atoms were used to simulate the indentation process. In [116] the tip was configured from 325 atoms and the substrates contained between 600 and 1200 atoms. Peak indentation depths were in the range of 1 - 3 Å and consequently only the mechanical behaviour of the near surface region was probed.

Using MD, Garg *et al* [118]-[119] reported on the indentation of diamond and graphite using single-walled capped carbon nanotubes as proximal probe tips. During indentation of hydrogen-terminated diamond and a graphite sheet, Garg *et al* [118] observed buckling of the carbon nanotube tip followed by ‘slip’ such that the tube was sharply bent with the end pointing upwards. On tip retraction, the nanotube indenter returned to its original configuration, and the diamond substrate deformed purely elastically. However, indentation of adsorbate free diamond resulted in interfacial bonding which destroyed the capped indenter on tip reversal. Another study by Garg *et al* [119], examined indentation of diamond and graphite substrates using multiwalled capped carbon nanotubes as tips. They found the multiwalled tubes deformed in a similar fashion to the single-walled tubes, but were much stiffer than comparably sized single-walled tubes, due to the shell-shell interactions within the tip. Garg *et al* concluded that short carbon nanotubes make excellent proximal probe tips since they do not plastically deform during tip crashes on inert surfaces, as conventional tips sometimes do. Indentation with carbon nanotubes by MD has also been applied to other materials, such as silicon [120].

In addition to diamond and graphite, MD simulations have also been performed to examine the nanoindentation of amorphous carbon ( $a$ -C) films by authors such as Glosli *et al* [121] and Sinnott *et al* [122]. Glosli *et al* [121] observed appreciable plastic de-



formation during indentation of a 4 nm thick  $a$ -C film using a hard diamond indenter. The more recent study by Sinnott *et al* [122] reported on indentation of an  $a$ -C:H film on a diamond {111} substrate. After full extraction of the tip they found no depression left in the surface. The composition of the film was subsequently analysed and they found an almost exact bonding distribution as prior to indentation. This suggested that no significant structural rearrangement took place and therefore the indentation was considered primarily elastic.

Experimental investigations have also been performed on diamond and graphite [123]-[124], reflecting purely elastic deformations. There has also been extensive experimental studies of disordered carbon. Martinez *et al* [125] performed nanoindentation of tetrahedral  $a$ -C films deposited on Si substrates with a diamond Berkovich indenter and reported primarily elastic behaviour. Li *et al* [126] investigated nanoindentation of  $a$ -C films deposited on Si substrates and observed fractured surfaces at different loads. Also reported in the experimental literature, is the indentation of polycarbonate using a carbon nanotube tip by Akita *et al* [127]. They observed plastic deformation of the capped tip, though the body of the nanotube maintained its initial configuration.

This chapter presents MD simulations of nanoindentation of graphite and diamond. The atomic structure of the indenter is ignored and is instead described entirely as a non-deformable interface. The influence of indenter geometry is considered, where nanoindentations are performed using both pyramidal and axisymmetric interfaces. Furthermore, the influence of indentation speed is also examined for graphite by varying the period of indentation. For each substrate, the interaction forces between the atoms are derived from the many-body Brenner bond order potential for hydrocarbons [96]-[97]. The simulations with graphite implement an additional Van der Waals potential to describe the long-range interactions [128]. This is necessary to correctly describe the elastic properties of the work material. The interaction between the interface and the substrate is assumed to be purely repulsive and is described by the pairwise Biersack-Ziegler potential (ZBL) [129] for C-C interactions, smoothly cut-off at 4.0 Å. For all substrates, the atoms neighbouring the fixed vertical borders are damped, while free boundary conditions are applied to all remaining atoms. In each simulation, the equations of motion are integrated using a fixed timestep of 0.5 fs. Unless otherwise stated, all indentations are performed to a depth of 8 Å and substrate atoms are coloured according to their vertical displacement. For graphite, indentation periods of 5 ps and



50 ps are employed, reflecting average indentation speeds of  $480 \text{ ms}^{-1}$  and  $48 \text{ ms}^{-1}$ , respectively. An indentation period of 50 ps is used for diamond. Each simulation is run for the duration of the indentation period. All of the simulations in this Chapter (and the next two) are run in serial on small systems containing up to a maximum of around 100,000 atoms.

## 3.2 Interface Indenter Model

In this preliminary model, the indenter is represented as an interface which cannot deform and is therefore modelled as infinitely hard. This is an extension of the work by Henkel [130]. Three different apex forms are considered for the indenter. The first indenter geometry has the configuration of a  $90^\circ$  pyramid, as shown in Fig. 3.3.1. The three faces ABC, ACD and BCD constitute the total contact area of the indenter and meet at the vertex C. At the beginning of each simulation, the tip is positioned such that the line CH, which denotes the direction of motion, is normal to the substrate surface. The penetration depth of the indenter is denoted by  $h$  and the length of the sides of the cross-sectional triangular plane ABD is given by  $a$ , which is related to  $h$  by  $a = \sqrt{6}h$ . The total contact area of the indenter is given by  $A_t = 4.5h^2$  and the cross-sectional area is given by  $A_c = 1.5\sqrt{3}h^2$ .

In addition to the pyramidal representation of the indenter, smooth indenters formed by hyperbolae and parabolae of revolution are also investigated. Thus, these axisym-

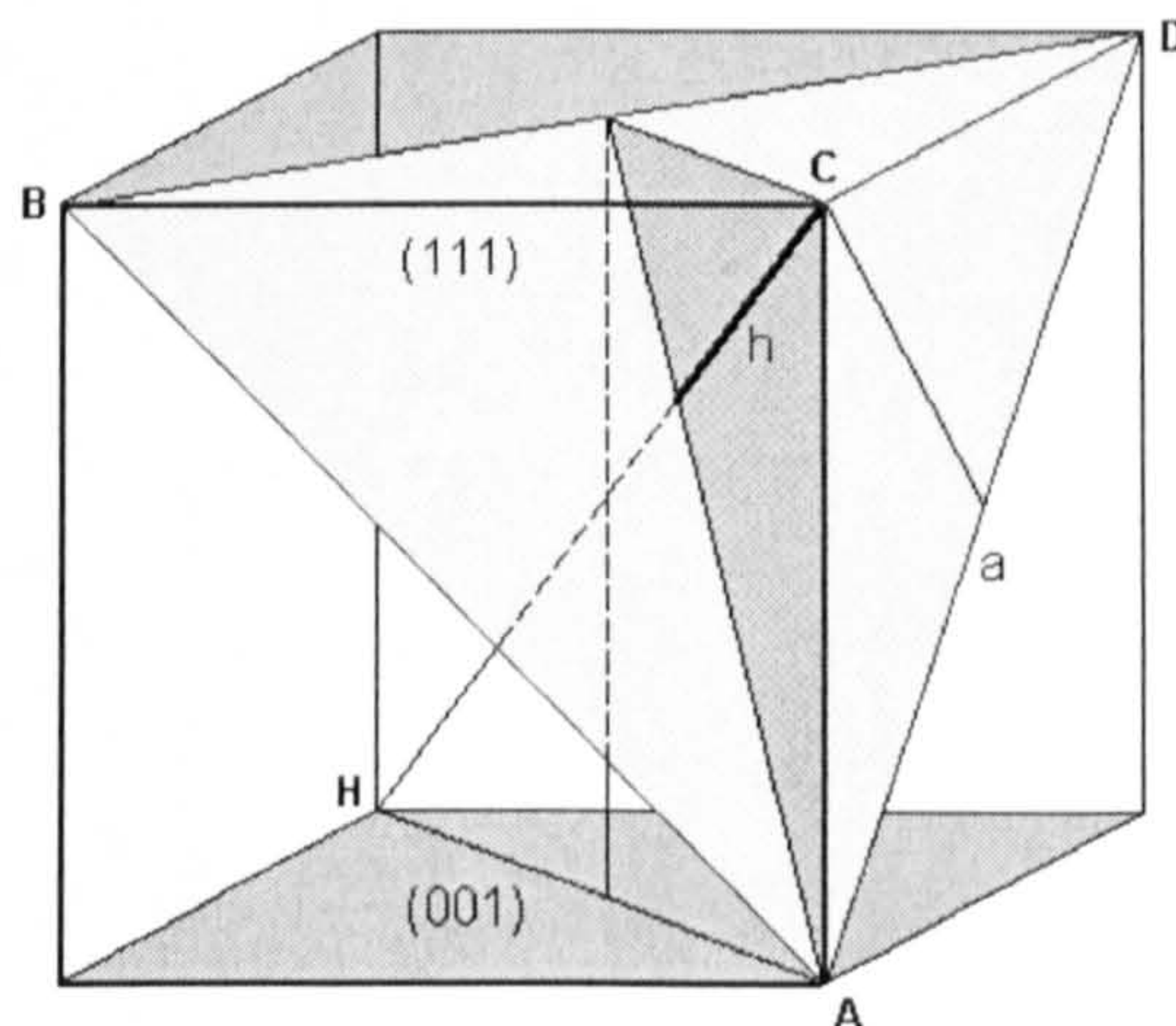


Fig. 3.3.1. Schematic crystal geometry of the  $90^\circ$  pyramidal indentation tip.



metric indenters will result in circular cross-sectional contact rather than triangular with the pyramidal indenter. The hyperboloid is described by  $z^2 = z_0^2 + k^2 r^2$ , where  $r^2 = x^2 + y^2$ ,  $z_0$  is the distance from the vertex to the origin and  $k$  is the gradient of the corresponding asymptotes. The paraboloid takes the form  $z = z_0 + r^2/2R$ , where  $R$  is the radius of curvature. The apex of the hyperboloid can therefore be approximated to that of the paraboloid by the relationship

$$R = z_0/k^2. \quad (3.2.3.1)$$

At the start of each simulation, the apex of the interface is positioned at a height above the centre of the substrate surface equal to the cut-off radius of the tip-substrate interaction potential. Thus, in the description of the axisymmetric interfaces,  $z_0$  is equated to 4 Å. The radius of curvature of the paraboloid indenter,  $R$ , is chosen to be 25 Å. The apex of the hyperboloid is chosen to approximate that of the paraboloid and therefore, from Eqn. 3.2.3.1,  $k$  is assigned the value 0.4.

Fig. 3.3.2 shows the vertical cross-section of the paraboloid and hyperboloid interfaces, sited 4 Å above the centre of the substrate surface. The axisymmetric interfaces are positioned such that the bold dashed line AB, is normal to the substrate surface. The contact area of the pyramidal interface together with the axisymmetric interfaces is shown in Fig. 3.3.3, as a function of indentation depth. Clearly, the axisymmetric interfaces have a much greater contact area than the pyramidal indenter. At an indentation

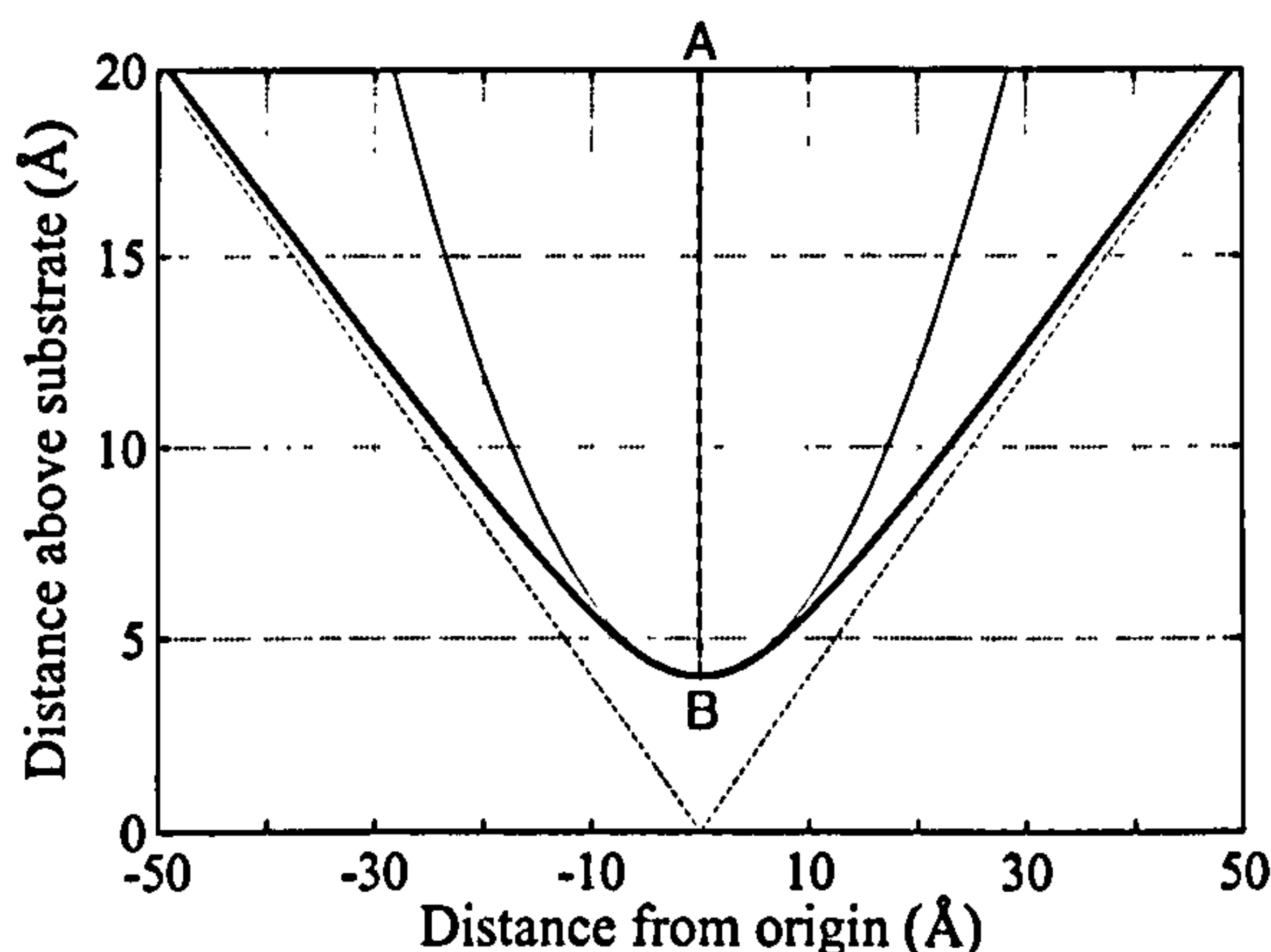


Fig. 3.3.2. Cross-sections of the hyperboloid and paraboloid interface configurations with  $z_0$  equal to 4 Å. The bold solid line denotes the hyperboloid interface with  $k = 0.4$  and the light dashed lines represent the corresponding asymptotes. The remaining solid line represents the paraboloid interface with a radius of curvature  $R = 25$  Å. The bold dashed line AB represents the direction of motion.



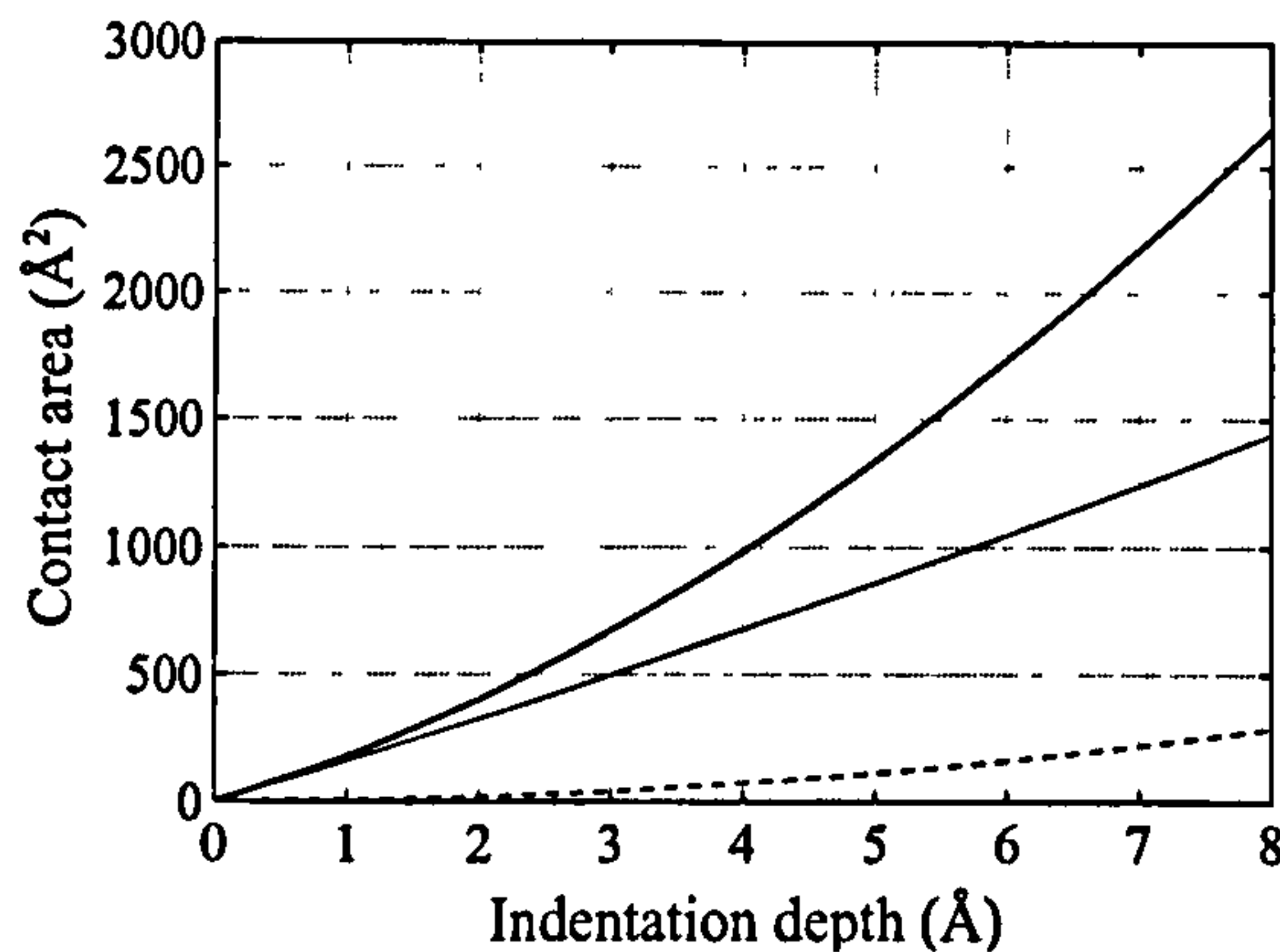


Fig. 3.3.3. Contact area of the interface as a function of the indentation depth. The solid bold line represents the hyperboloid interface and the dashed line denotes the pyramidal interface. The thin solid line denotes the paraboloid model of the interface.

depth  $< 1 \text{ Å}$  the hyperboloid and paraboloid interfaces have comparable contact areas. However, as the indentation depth of the hyperboloid increases, i.e. the hyperboloid tends towards its asymptotes, the respective contact area increases considerably compared with the paraboloid interface. At an indentation depth of  $8 \text{ Å}$ , the total contact area of the hyperboloid interface is almost twice that of the paraboloid. At the same penetration depth, the cube-cornered interface has a total contact area approximately one ninth and one fifth that of the hyperboloid and paraboloid interfaces, respectively.

The height of each interface is equal to the maximum indentation depth, plus the cut-off radius of the tip-substrate interaction potential. Thus, the calculated height accounts for interaction between the substrate and the interface above the surface throughout the indentation. The pyramid interface is defined by four vectors, corresponding to the position of the four vertices. A single vector corresponding to the position of the apex is defined for the paraboloid and hyperboloid interface. For each interface, the indentation depth is measured by calculating the distance between the apex and the undisturbed substrate surface. The movement of the tip is simulated in a stepwise, quasistatic fashion by imparting small increments to the interface. For each timestep during the simulation, a sinusoidal displacement,  $r(t)$ , is imparted on the vector(s) defining the position of the interface to incrementally lower the apex towards the surface. The displacement  $r(t)$  is described by

$$r(t) = r_{\max} \sin\left(\frac{\pi t}{T}\right) \quad (3.2.3.2)$$

where  $r_{\max}$  is the maximum displacement of the tip from its initial position above the substrate surface,  $T$  is the indentation period (i.e. equal to half of the sine period) and  $t$  is the time elapsed. As the indentation period  $T$  increases, the slower the indenter will displace. To simulate an even slower indentation speed, the system could also be allowed to relax for an extended period of time after each displacement of the indenter [131]. For simulations of time  $T$ , the time schedule for the loading and unloading of the indenter is  $T/2$ . The manner in which the interface displaces in the simulations differs from experimental methods. In reality, a specified force is applied to the tip which displaces into the substrate until the repulsive force from the work material equates to the force applied the indenter. Thus, in experiment the applied force to the indenter results in the penetration depth being the dependent variable. However, in the MD computer simulations employed here, the depth and velocity of approach is pre-specified and hence the force becomes the dependent variable.

From the simple harmonic motion of the indenter given in Eqn. 3.2.3.2, the indenter will therefore be decelerating during the loading stage and accelerating during the unloading stage. The average speed of the interface during the indentation process is described by  $2r_{\max}/T$ . The constraints on feasible computer simulations yield average indentation speeds typically between tens of  $\text{ms}^{-1}$  and a few hundred  $\text{ms}^{-1}$ . Even at the slower displacement, the average indentation speed is still several orders of magnitude faster compared with experimental values, where the indentation speed is typically of the order  $10^{-6}$  -  $10^{-9}$   $\text{ms}^{-1}$ . Indentation speeds as slow as experimental values are beyond present day capabilities of MD simulations. Although simulated indentation speeds are very fast, they are still several times slower than the speed of sound.

### 3.3 Simulation Results and Discussion

#### 3.3.1 Graphite {0001} Substrate

The structure of graphite [132] is illustrated in Fig. 3.3.4. The crystal is configured from hexagonal arrays of atoms, which are situated on a series of equally spaced parallel planes stacked in an alternating sequence A B A B. The distance between the parallel planes is 3.35 Å, where the bonding is by Van der Waals forces [133]. The nearest neighbours in the hexagonal arrays are sited 1.42 Å away. Each atom in the plane is



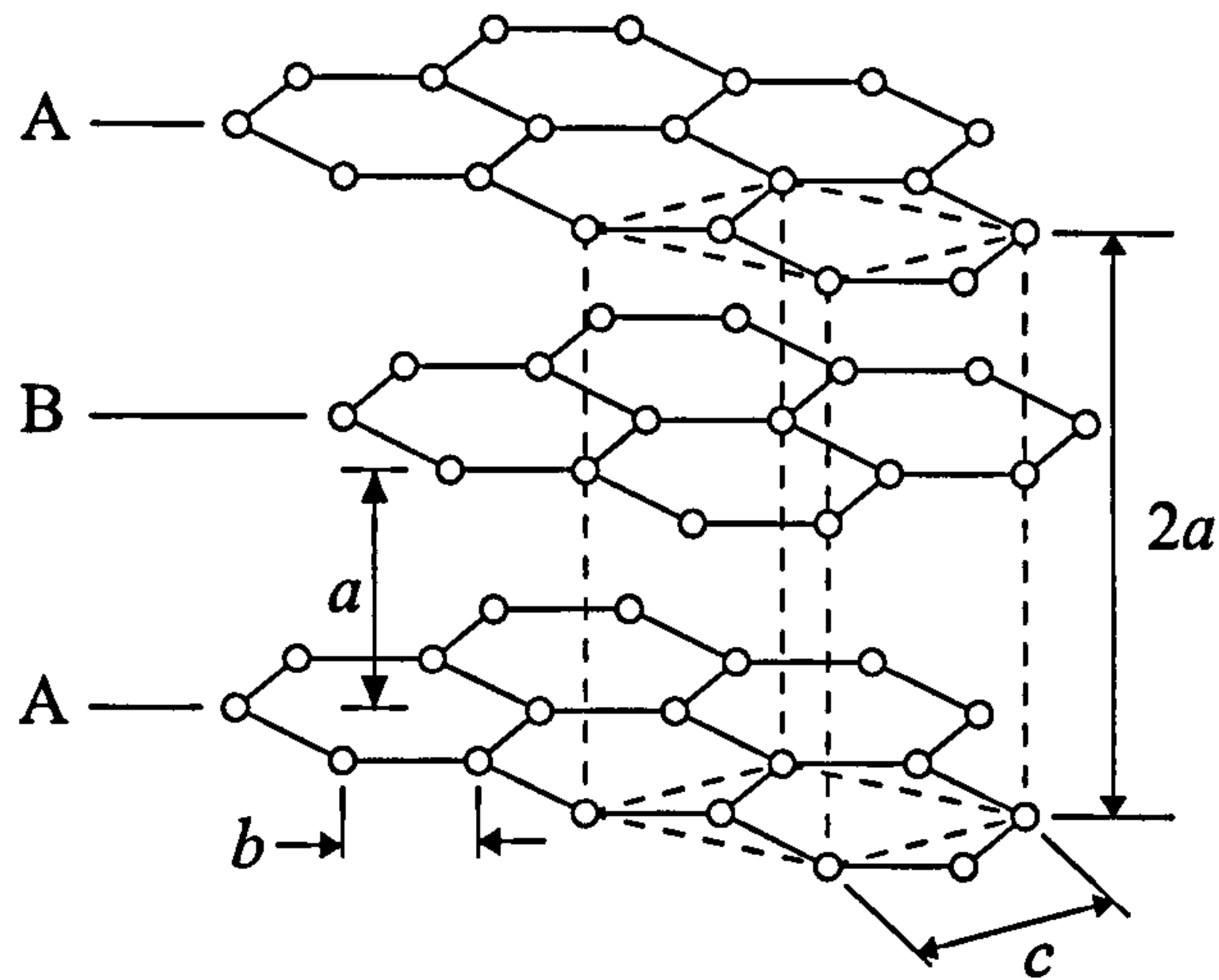


Fig. 3.3.4. The graphite crystal structure. The interplanar distance,  $a$ , is equal to 3.35 Å. The distance between the nearest neighbours,  $b$ , is 1.42 Å. The planes A and B denote the stacking formation of the graphite crystal. The hexagonal elementary unit cell has a base of length  $c = 2.46$  Å. The carbon atoms exist in  $sp^2$  hybridization.

symmetrically related to the three nearest neighbours. The covalent bonding in the layers is very strong, however the weak Van der Waals forces between the planes allows relatively easy displacement in a direction parallel to the layers. As a result, graphite is a material which is very soft and easily deformed. For simulations with graphite, the basal plane is indented. A crystal with approximate dimensions  $102 \text{ Å} \times 102 \text{ Å} \times 20 \text{ Å}$ , configured from 7 atomic layers, is utilised. The work material is composed from 28,244 atoms with 2,464 atoms constituting the fixed boundary and 4,004 atoms forming the neighbouring damped region.

### Indentation with 5 ps Period

Fig. 3.3.5 presents the force-depth curves from the  $T = 5$  ps simulations of indentation into the graphite  $\{0001\}$  lattice. The graphite specimen shows purely elastic behaviour towards indentation. However, for each different interface, the loading and unloading curves do not overlap. This feature arises from the unphysically fast speed of the indentation process. The interlayer atomic forces are quite weak and, in each case, the interface is extracted from the substrate at a speed which is quicker than the relaxation process in the graphite crystal. This gives rise to the unloading curve falling sharply during tip retraction, a feature normally associated with plastic deformation. In each force-depth curve, the peak force occurs just before maximum penetration and

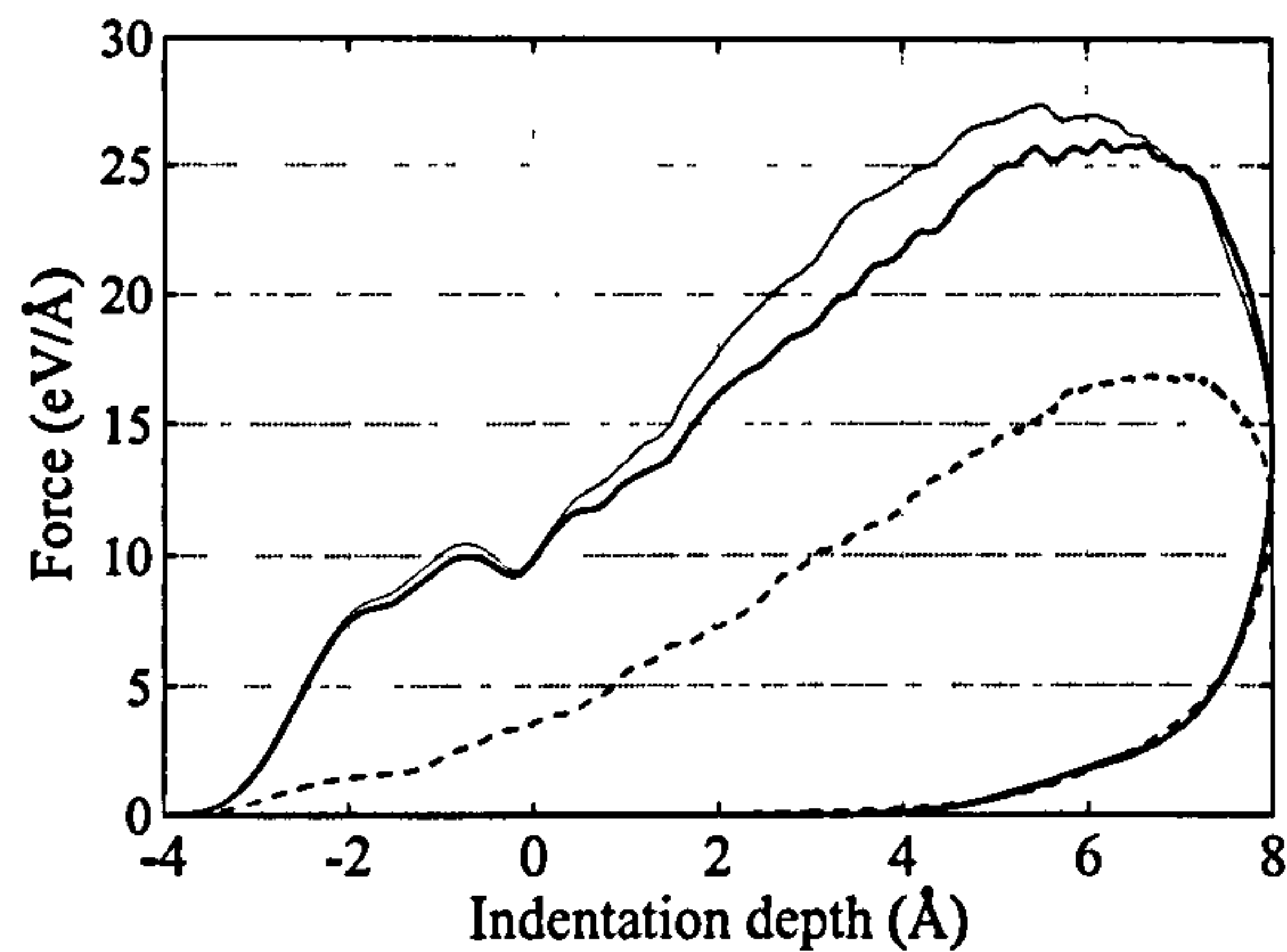


Fig. 3.3.5. Force-depth curves from the  $T = 5$  ps simulations with the graphite  $\{0001\}$  crystal. The dashed line denotes the pyramid model of the interface. The bold solid line and thin solid line correspond to the hyperboloid and paraboloid models of the interface respectively. The loading and unloading curves do not overlap since the indenter is extracted quicker than the surface can relax.

furthermore, the peak force for the axisymmetric interfaces occurs at a slightly lower penetration depth compared with the pyramidal interface. This attribute is further due to the high speed at which the interface penetrates and extracts from the substrate. As the interface makes mechanical contact with the first graphite layer it causes a quick displacement towards the second layer and so forth. This effect continues deep into the material such that several graphite layers have undergone a large displacement before the apex reaches the peak depth. This ensues in the peak force occurring before the

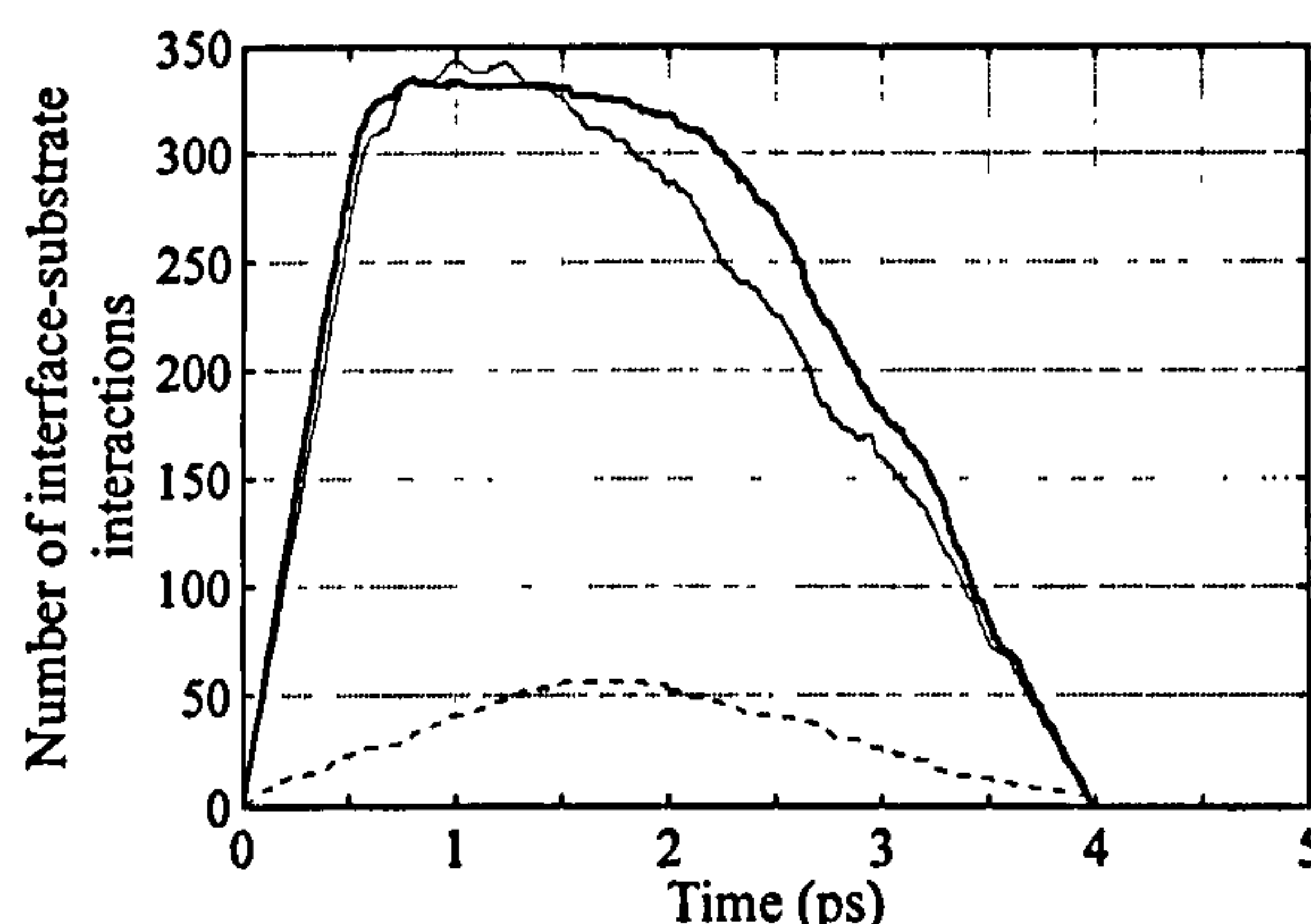


Fig. 3.3.6. The total number of interface-substrate atom interactions during the  $T = 5$  ps simulations on the graphite  $\{0001\}$  crystal. The dashed line denotes the pyramid model of the interface. The bold solid line and thin solid line correspond to the hyperboloid and paraboloid models of the interface respectively.



maximum depth. For indentation speeds slower than the relaxation process in the substrate, the force acting on the interface should decrease with the peak value occurring near to maximum penetration.

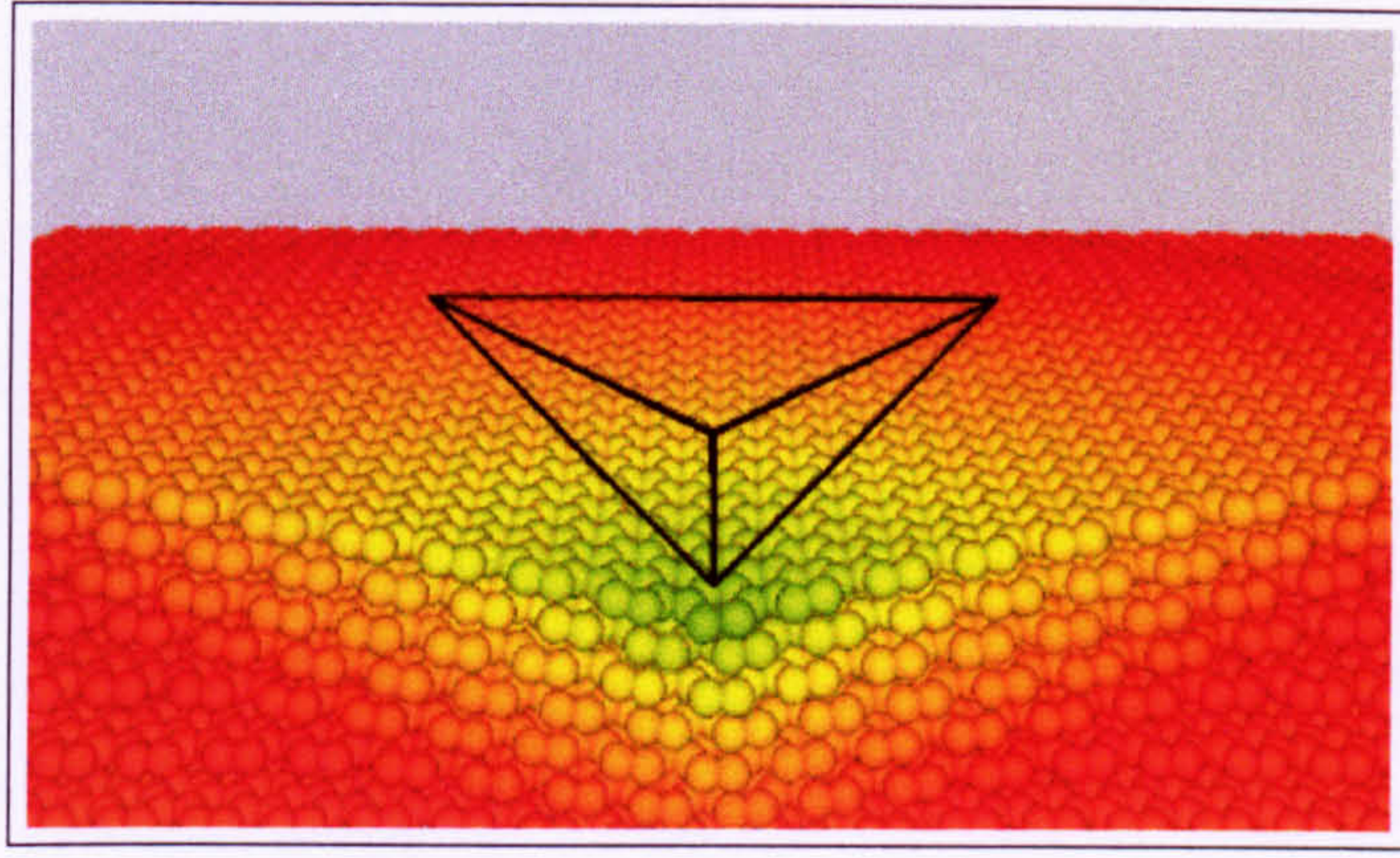
The graphite work material shows greater resistance to the impinging axisymmetric interfaces, compared with the pyramidal structure. For the cube-cornered interface, the maximum force is  $17 \text{ eV/\AA}$  which occurs at a penetration depth of approximately  $7 \text{ \AA}$ . The work piece shows a very similar response as the hyperboloid and paraboloid interfaces approach the surface, where both load-displacement curves show a characteristic dip in the force. The peak force acting on the axisymmetric interfaces was roughly  $27 \text{ eV/\AA}$  occurring at an approximate penetration depth of  $5.5 \text{ \AA}$ .

The number of atoms interacting with the interface during the  $T = 5 \text{ ps}$  simulations is shown in Fig. 3.3.6. The axisymmetric interfaces interact with approximately six times as many atoms compared with the pyramidal interface, which explains the higher indentation forces. For each of the curves in Fig. 3.3.6, the peak number of interface-substrate interactions occurs before the maximum indentation depth has been reached at  $t = 2.5 \text{ ps}$ . The number of atoms interacting with the axisymmetric interfaces increases in a very rapid fashion during the first  $0.5 \text{ ps}$  of the indentation process. This is because of the relatively large bulky tip compared with the pyramidal apex. The maximum for each curve corresponds roughly to the peak indentation force in Fig. 3.3.5. As each interface is rapidly extracted from the work sample, the number of interface-substrate interactions approaches zero at  $4 \text{ ps}$ , corresponding to an indentation depth of approximately  $3 \text{ \AA}$ .

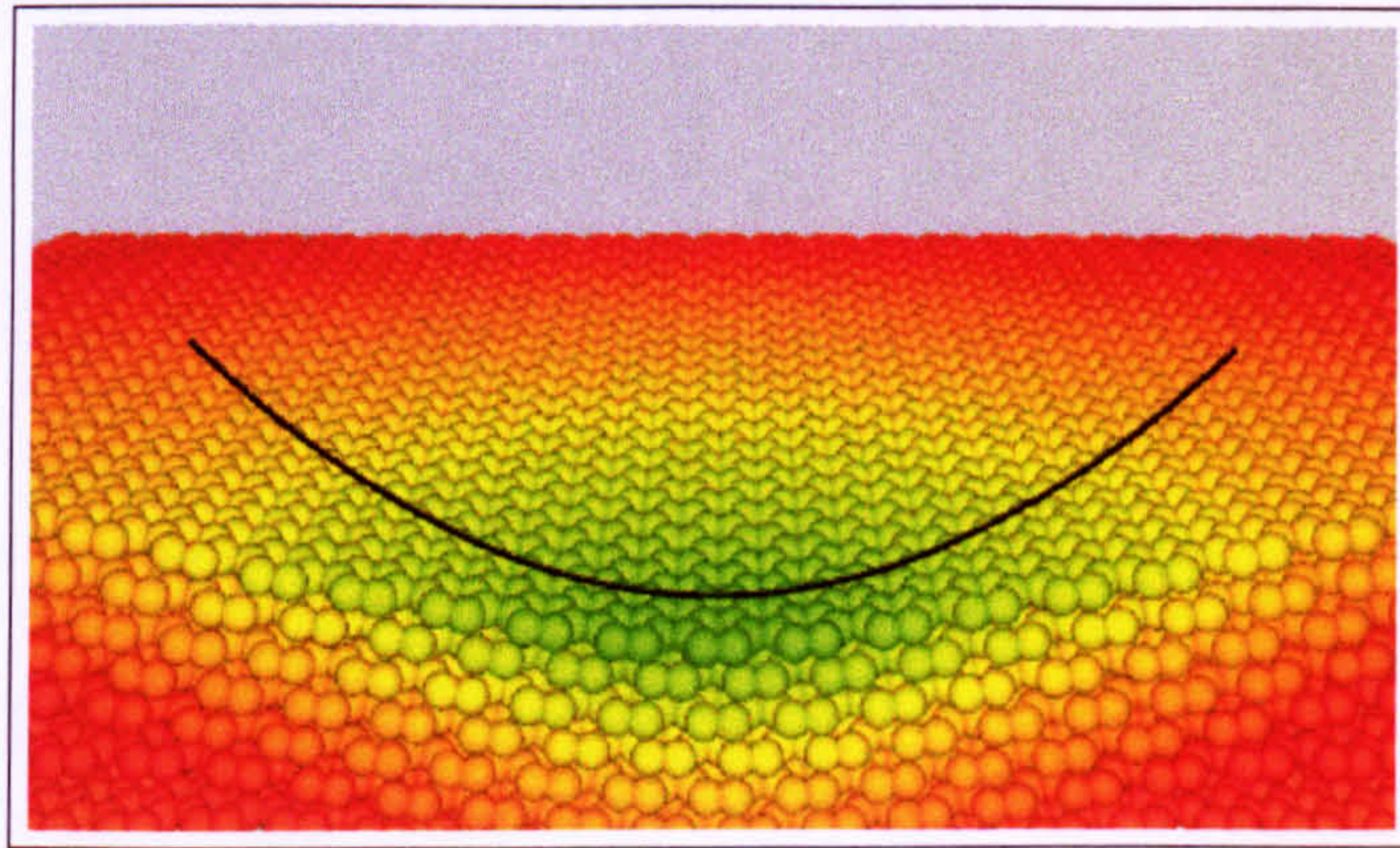
The halfway stage of the indentation process is shown in Fig. 3.3.7 for each of the interface descriptions. Each snapshot shows the individual graphite layers bend under the influence of the impinging indenter. Clearly, the axisymmetric interfaces impart greater elastic deformation in the work material, compared with the pyramidal interface. At the completion of the indentation, Fig. 3.3.8 shows the distortion left in the work material. The distortion is more significant for indentation with the axisymmetric interfaces. This is not a permanent deformation of the substrate, as the graphite layers are oscillating after extraction of the apex. Simulations run for longer time, but with the same indentation period, show the damping of the system drives the system towards equilibrium and there is no remaining distortion in the substrate.

Fig. 3.3.9 shows how the total energy of the graphite crystal changes during the

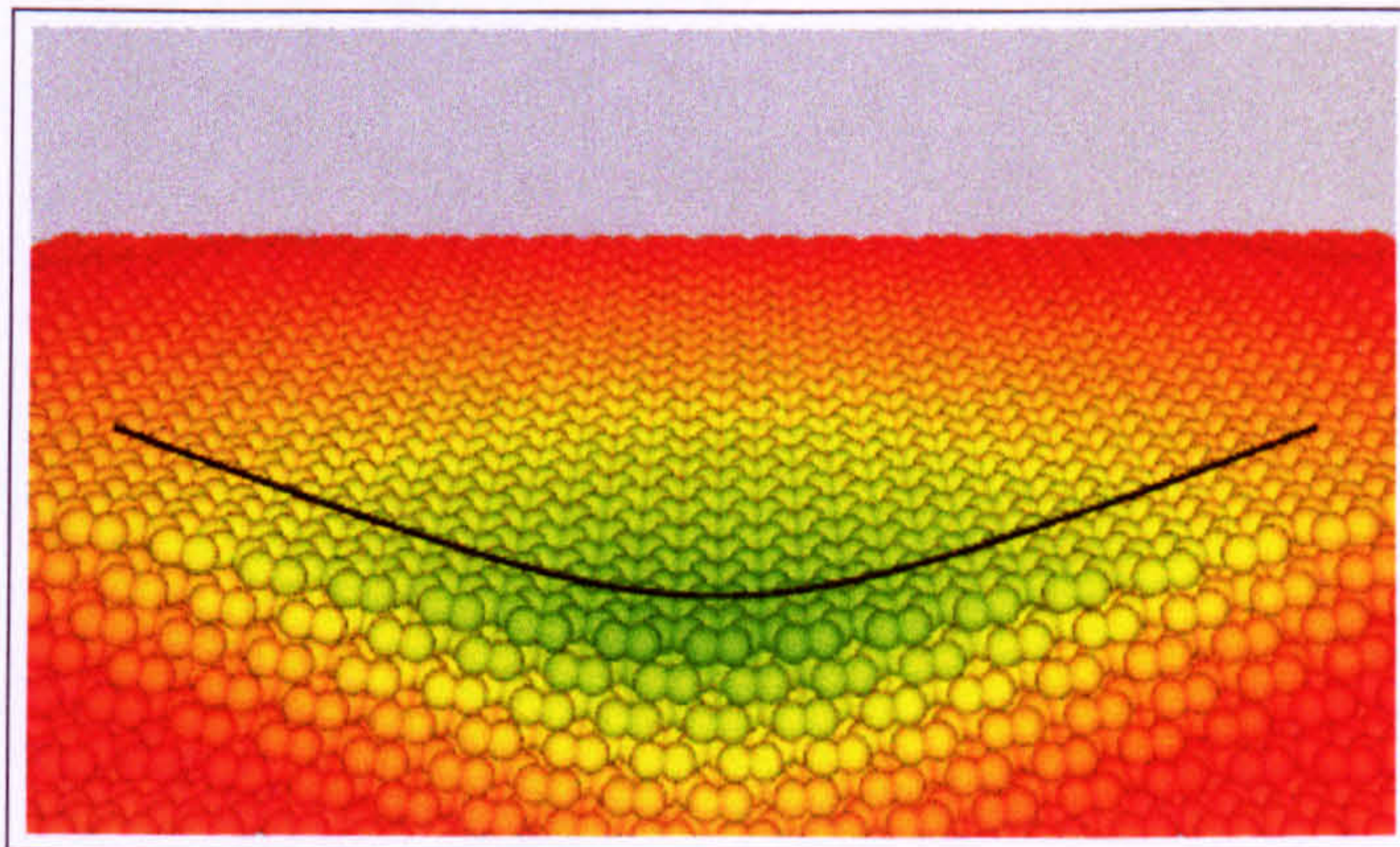




(a)



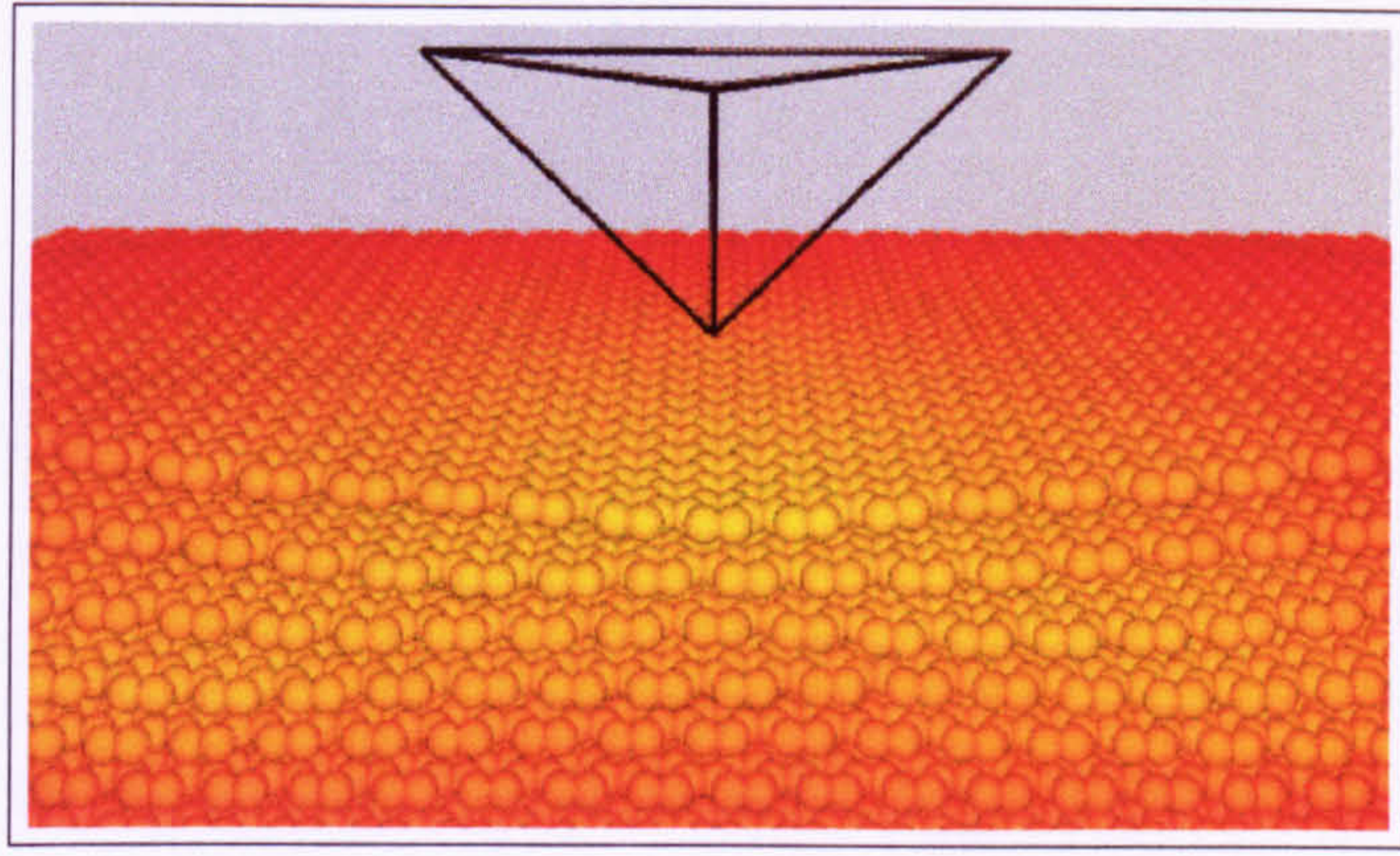
(b)



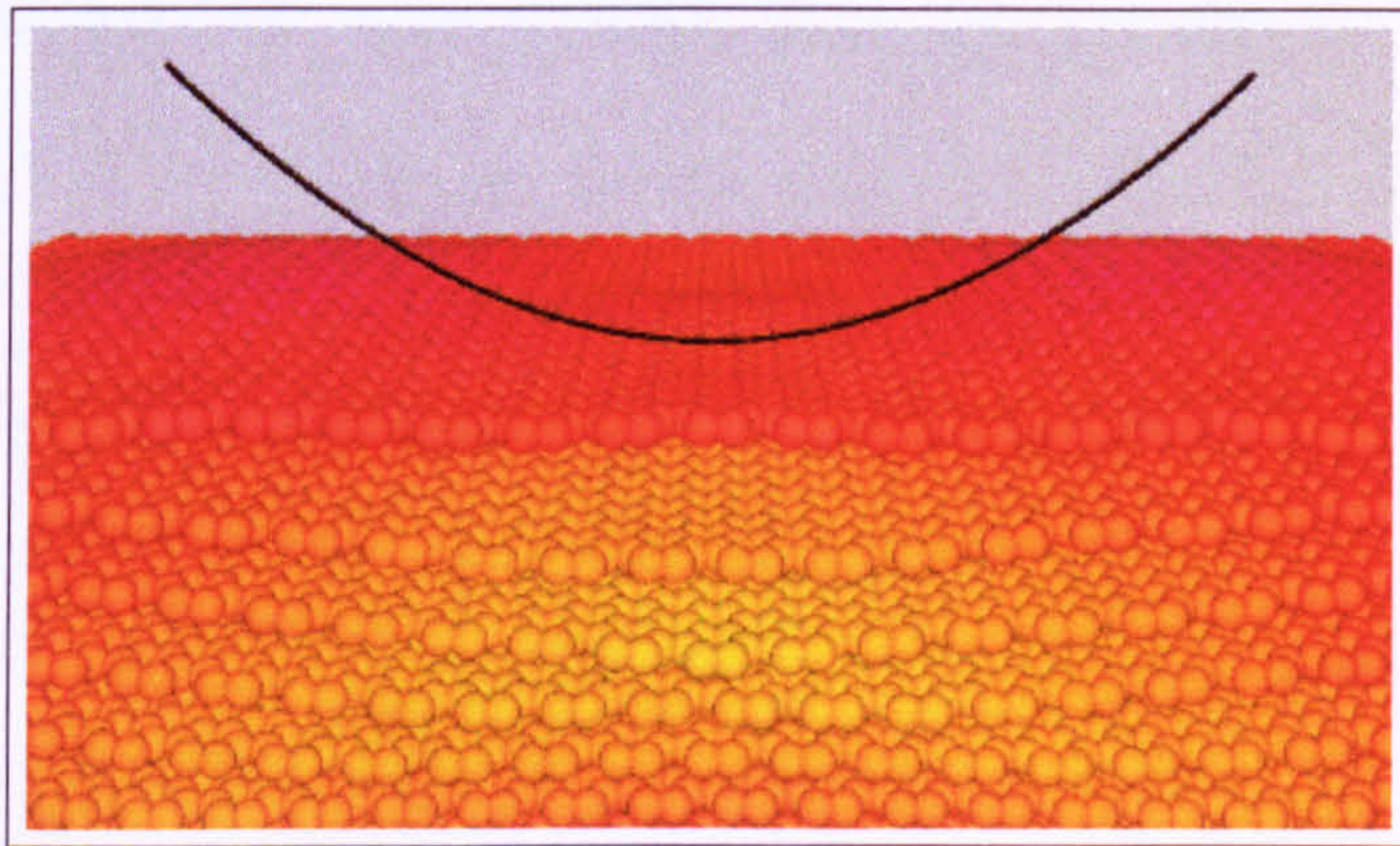
(c)

Fig. 3.3.7. Cross-sectional snapshot from the  $T = 5$  ps simulations with the graphite  $\{0001\}$  crystal at  $t = 2.5$  ps with the interface profile for: (a) pyramid; (b) paraboloid; (c) hyperboloid. In these images, half of the atoms have been removed.

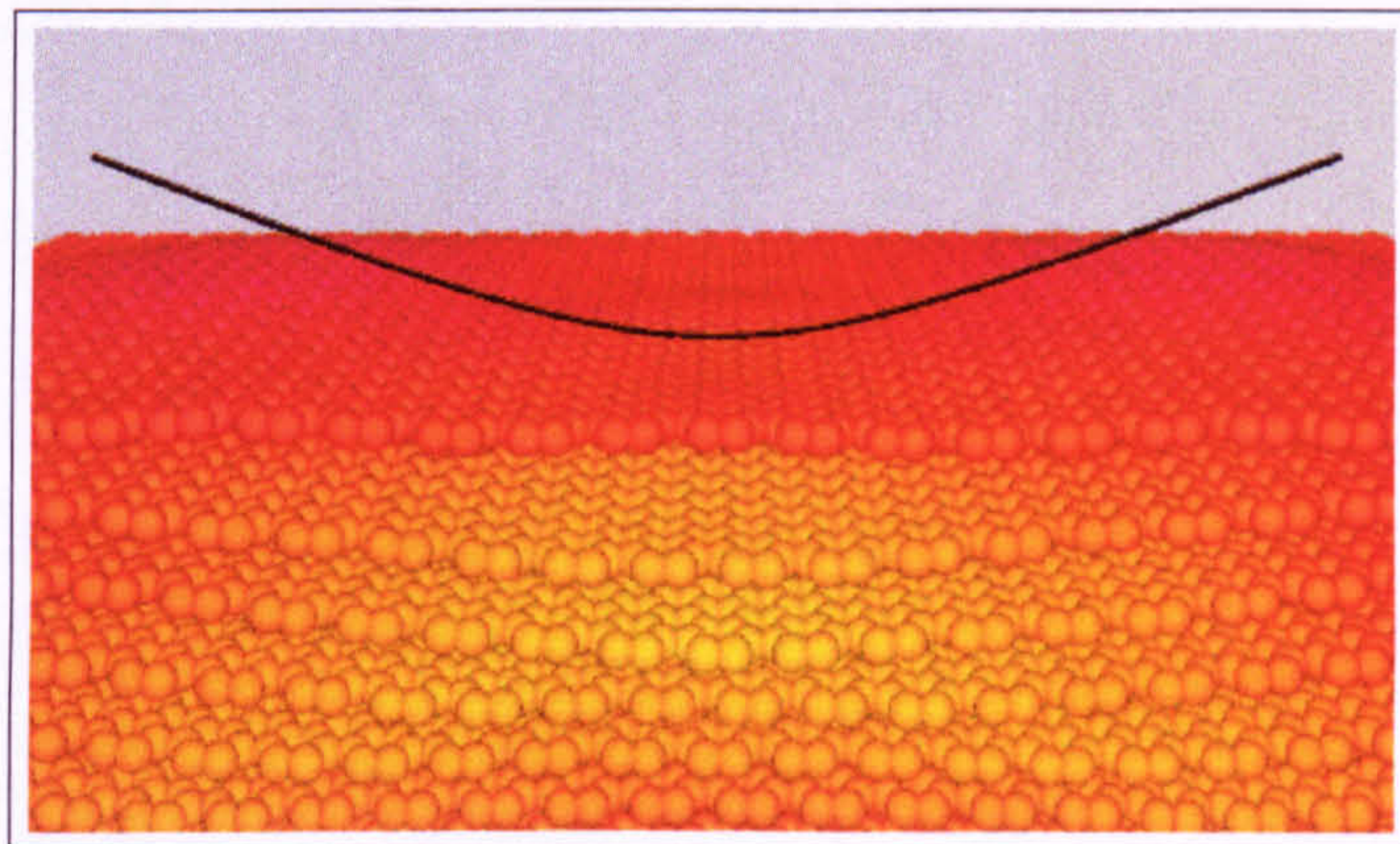




(a)



(b)



(c)

Fig. 3.3.8. Cross-sectional snapshot from the  $T = 5$  ps simulations with the graphite  $\{0001\}$  crystal at  $t = 5$  ps with the interface profile for: (a) pyramid; (b) paraboloid; (c) hyperboloid. In these images, half of the atoms have been removed.



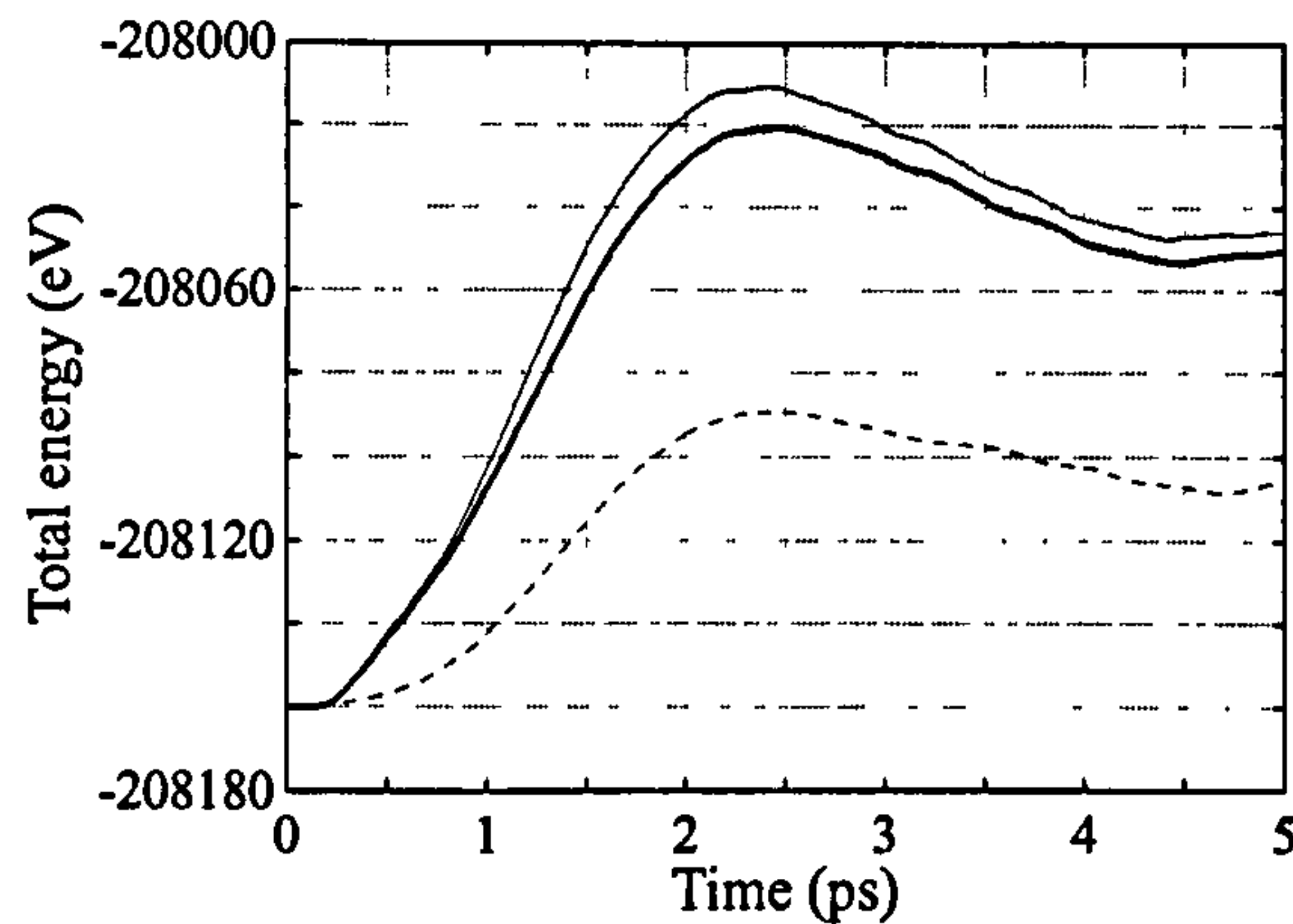


Fig. 3.3.9. Total energy of the graphite {0001} crystal during the  $T = 5$  ps simulations. The dashed line denotes the pyramid model of the interface. The bold solid line and thin solid line correspond to the hyperboloid and paraboloid models of the interface respectively.

indentation process. As the interfaces penetrate the surface, energy is added to the substrate as the atomic layers are compressed. In each case the energy added is greatest at approximately the halfway stage of the indentation process. The axisymmetric interfaces add the energy to the graphite substrate at a quicker rate compared to the pyramid interface. The hyperboloid and paraboloid interfaces added approximately 140 eV and 150 eV to the small graphite substrate respectively, while the pyramid interface added roughly 70 eV. These low energy values verify that the damped graphite atoms allow the surplus energy induced by the interface to effectively dissipate through the crystal. As each interface is extracted from the graphite crystal, the total energy decreases more slowly compared with the loading stage due to the rapid unloading speed of the interface. It can be inferred from Fig. 3.3.9 that at the completion of the indentation, the graphite substrate has not fully recovered as there is still energy stored in the crystal.

### Indentation with 50 ps Period

Shown in Fig. 3.3.10 are the load-displacement curves for the  $T = 50$  ps simulations with the graphite substrate. The slower displacement of the interfaces has resulted in the loading and unloading curves overlapping, clearly reflecting the purely elastic response from the graphite substrate. This shows that the employed indentation speed is more akin to the relaxation process in the work material. This is further supported since, in each case, the peak force now occurs at the maximum penetration depth. Also, the force



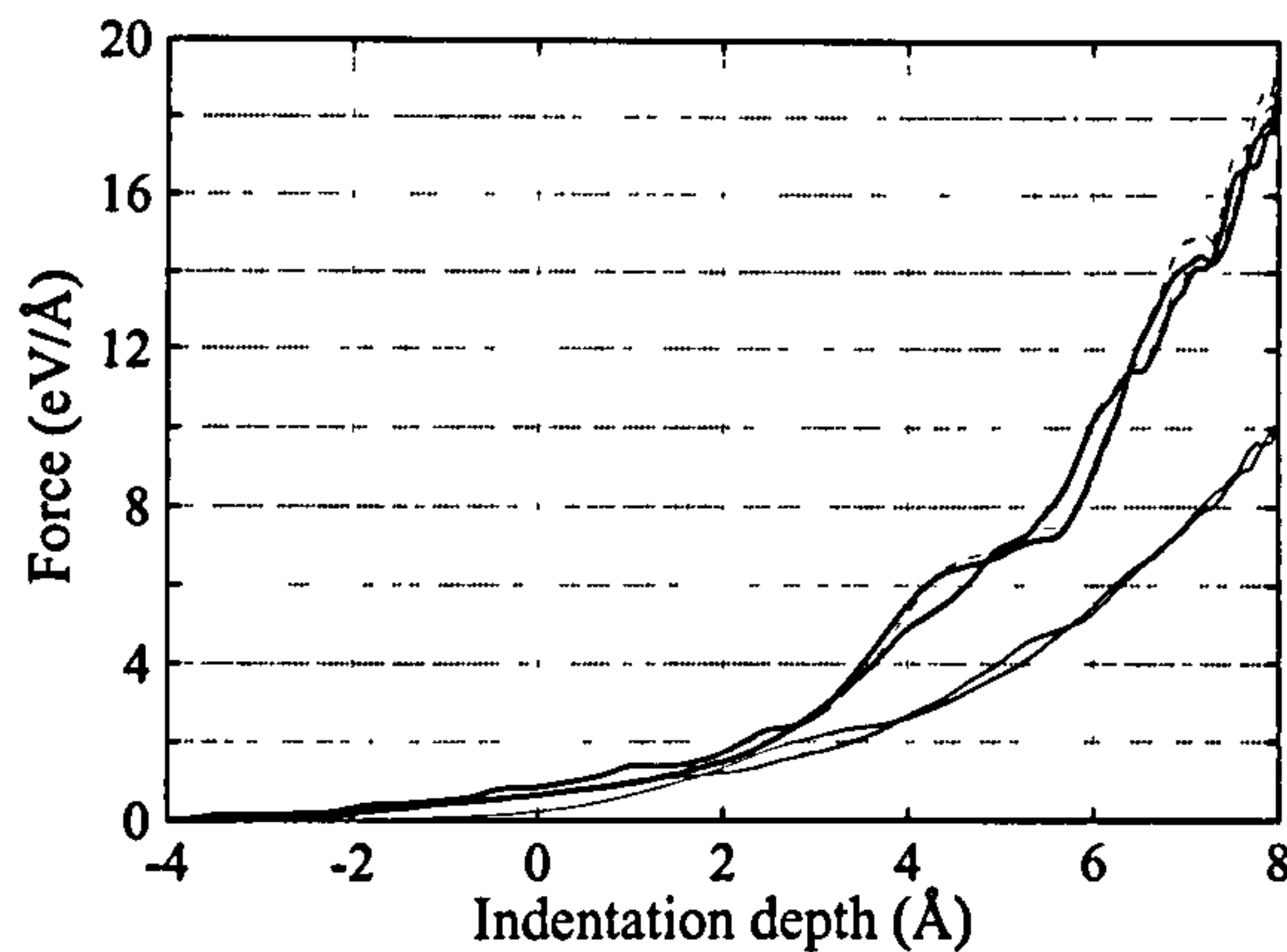


Fig. 3.3.10. Force-depth curves from the  $T = 50$  ps simulations of 8 Å indentation into the graphite {0001} crystal. The thin solid line denotes the pyramid model of the interface. The bold solid line and dashed solid line correspond to the hyperboloid and paraboloid models of the interface respectively.

acting on each interface approaches zero *after* the apex is extracted from the substrate surface. Comparisons with the force-depth curves in Fig. 3.3.5 show that the slower indentation speed has reduced the force acting on each of the interfaces. The maximum force acting on the cube-cornered interface has decreased by about 40% to 10 eV/Å, while the hyperboloid and paraboloid interfaces show an approximate reduction of 30% in the maximum force to 18 eV/Å and 19 eV/Å respectively. The force-depth curves corresponding to the axisymmetric interfaces are more analogous than in the faster  $T = 5$  ps simulations.

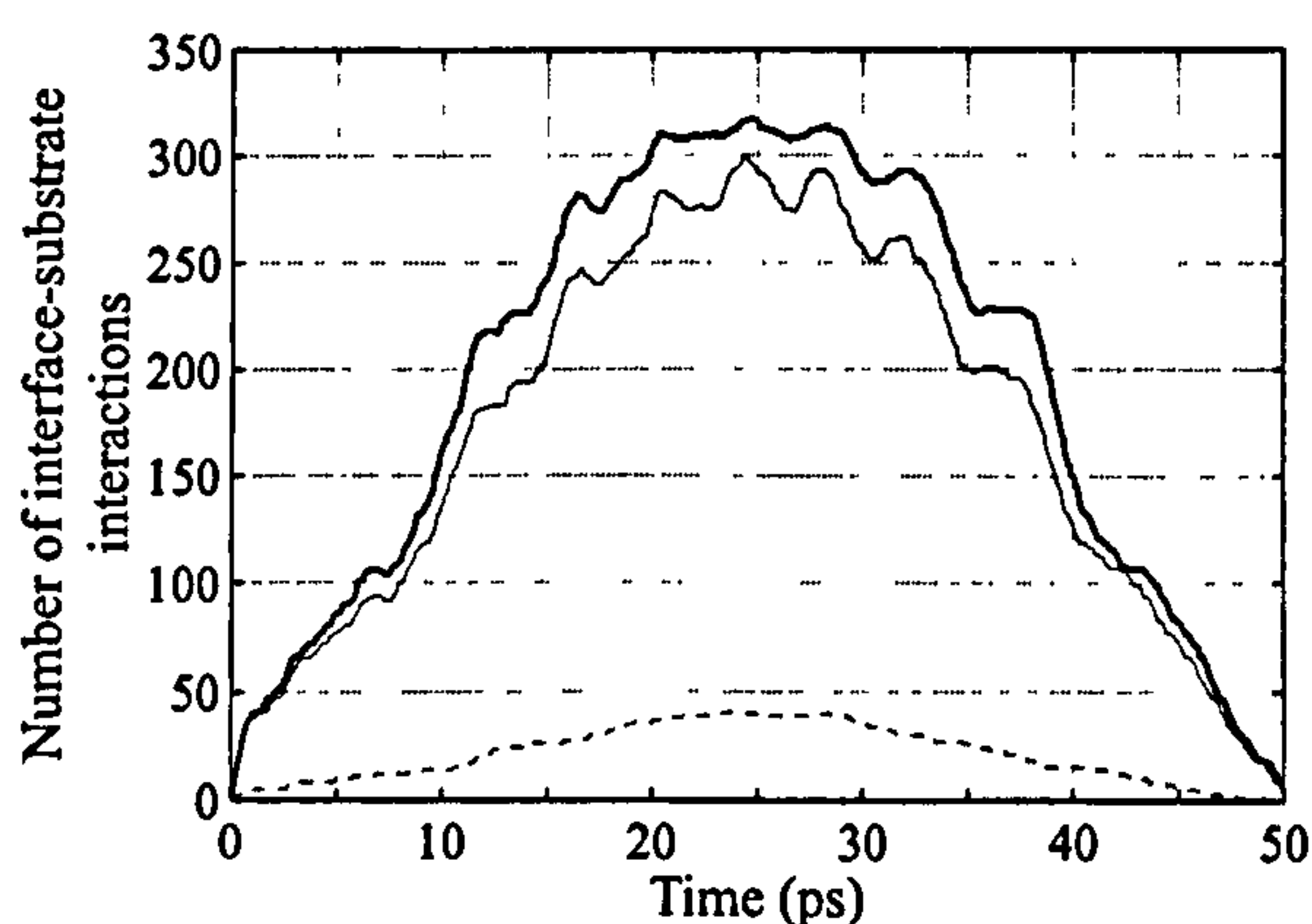


Fig. 3.3.11. The total number of interface-substrate atom interactions during the  $T = 50$  ps simulations with the graphite {0001} crystal. The dashed line denotes the pyramid model of the interface. The bold solid line and thin solid line correspond to the hyperboloid and paraboloid models of the interface respectively.

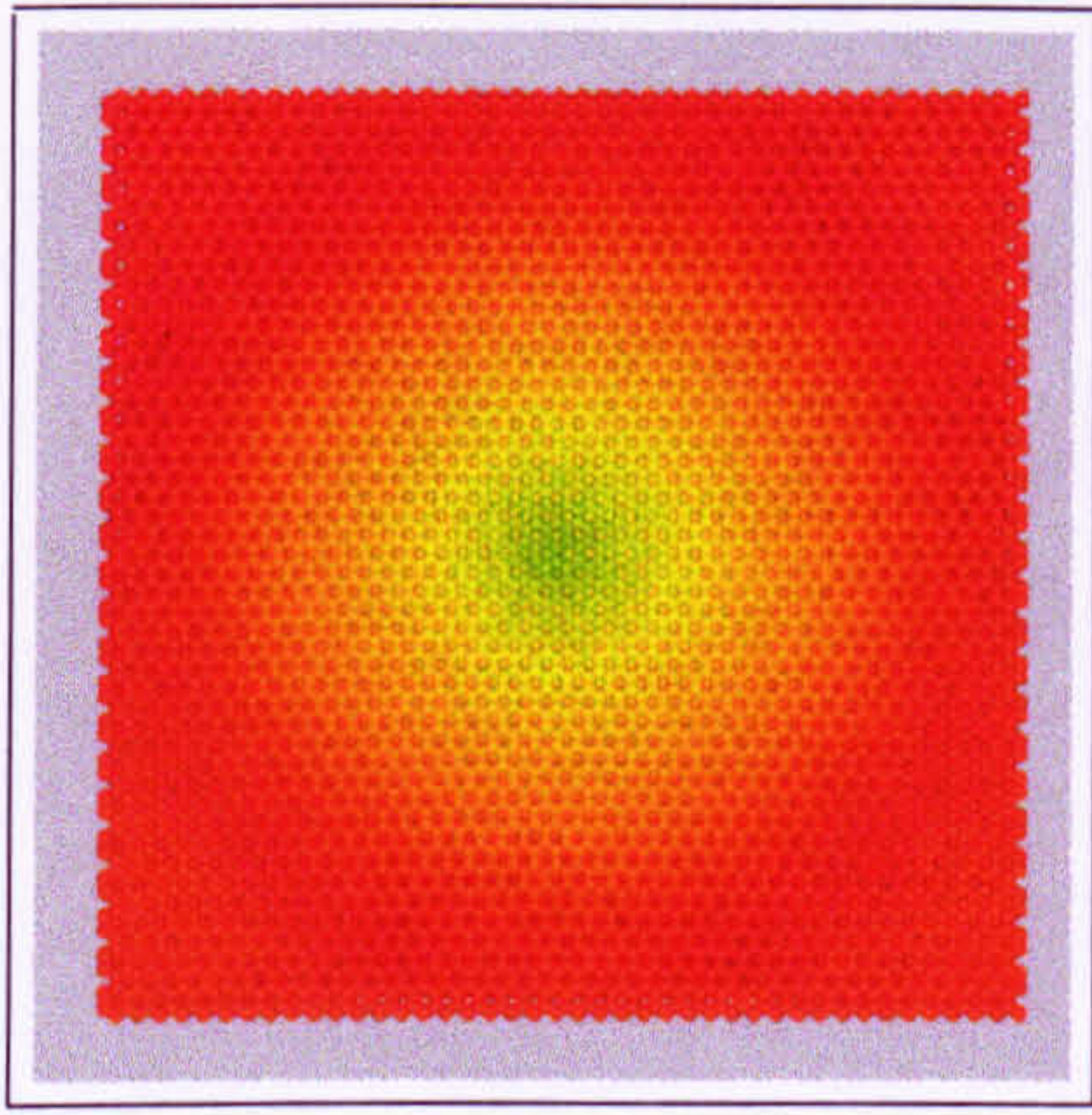


Fig. 3.3.11 illustrates how the three interfaces interact with the graphite crystal during the  $T = 50$  ps simulations. Comparisons with Fig. 3.3.6 show a similar number of atoms interact with each of the interfaces during the slower indentation. The maximum number of interface-substrate interactions occurs at the halfway stage of the indentation process. The slower penetration of the interface into the work material has resulted in a similar number of atoms interacting during the loading and unloading stages. The axisymmetric interfaces exhibit very similar interaction behaviour with the substrate throughout the indentation.

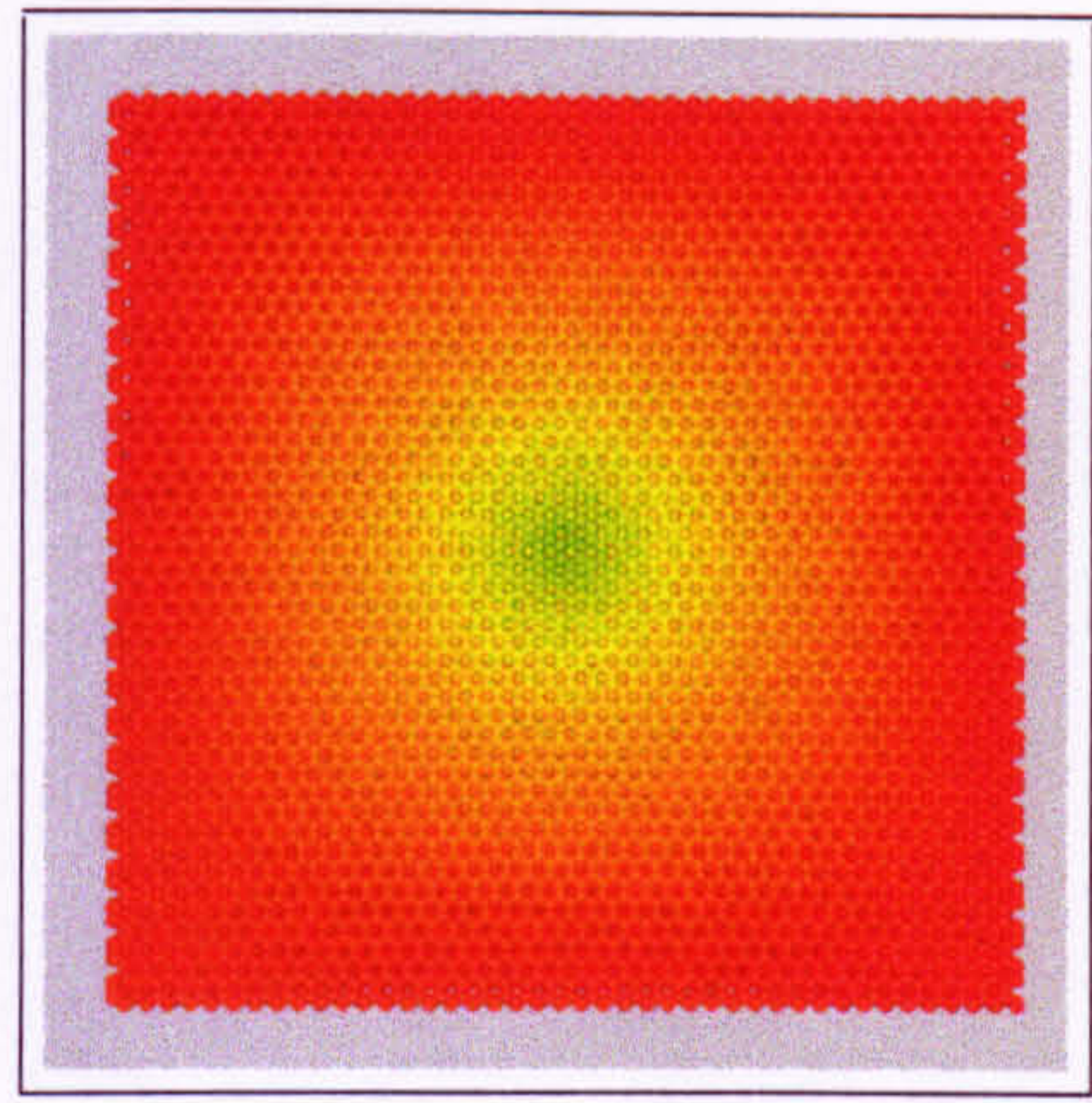
Plan views of the graphite work material are presented in Fig. 3.3.12 at the halfway stage of the indentation process for both the  $T = 5$  ps and  $T = 50$  ps simulations. The slower indentation speed of the pyramidal interface in Fig. 3.3.12(b) has allowed a greater displacement of atoms away from the tip, compared with Fig. 3.3.12(a). The same effect is observed with indentation utilising the axisymmetric interfaces. At the halfway stage of the indentation process, the images in Fig. 3.3.12(c) and (e) show the axisymmetric interfaces impart displacements up to the constrained boundaries of the work material. However, in Fig. 3.3.12(d) and (f) the slower indentation speed has allowed time for the displacements near the edges of the substrate to be reflected back. Hence, the elastic deformation was semi-restricted, rather like the bending of a beam with fixed abutments. This indicates that the force acting on the interface will be influenced by the size of the substrate and hence, a larger graphite sample is needed for indentation. The conclusion of the  $T = 50$  ps simulations is shown in Fig. 3.3.13. Comparison with Fig. 3.3.8 shows there is less distortion in the substrate when the indentation speed is reduced. However, even longer indentation periods are required to preclude the distortion in the graphite work material by the end of the indentation process.

Shown in Fig. 3.3.14 is the total energy of the graphite crystal during the  $T = 50$  ps simulations. Comparisons with Fig. 3.3.9 show that the slower displacement of the interfaces adds less energy to the graphite lattice, since the longer indentation time has allowed greater dissipation. In the  $T = 50$  ps simulations the hyperboloid and paraboloid interfaces added approximately 29 eV and 30 eV respectively to the substrate while the pyramidal interface added roughly 16 eV. The greatest quantity of energy added to the substrate in the  $T = 50$  ps simulations occurs approximately at the maximum penetration depth, as observed with the faster indentation speeds.

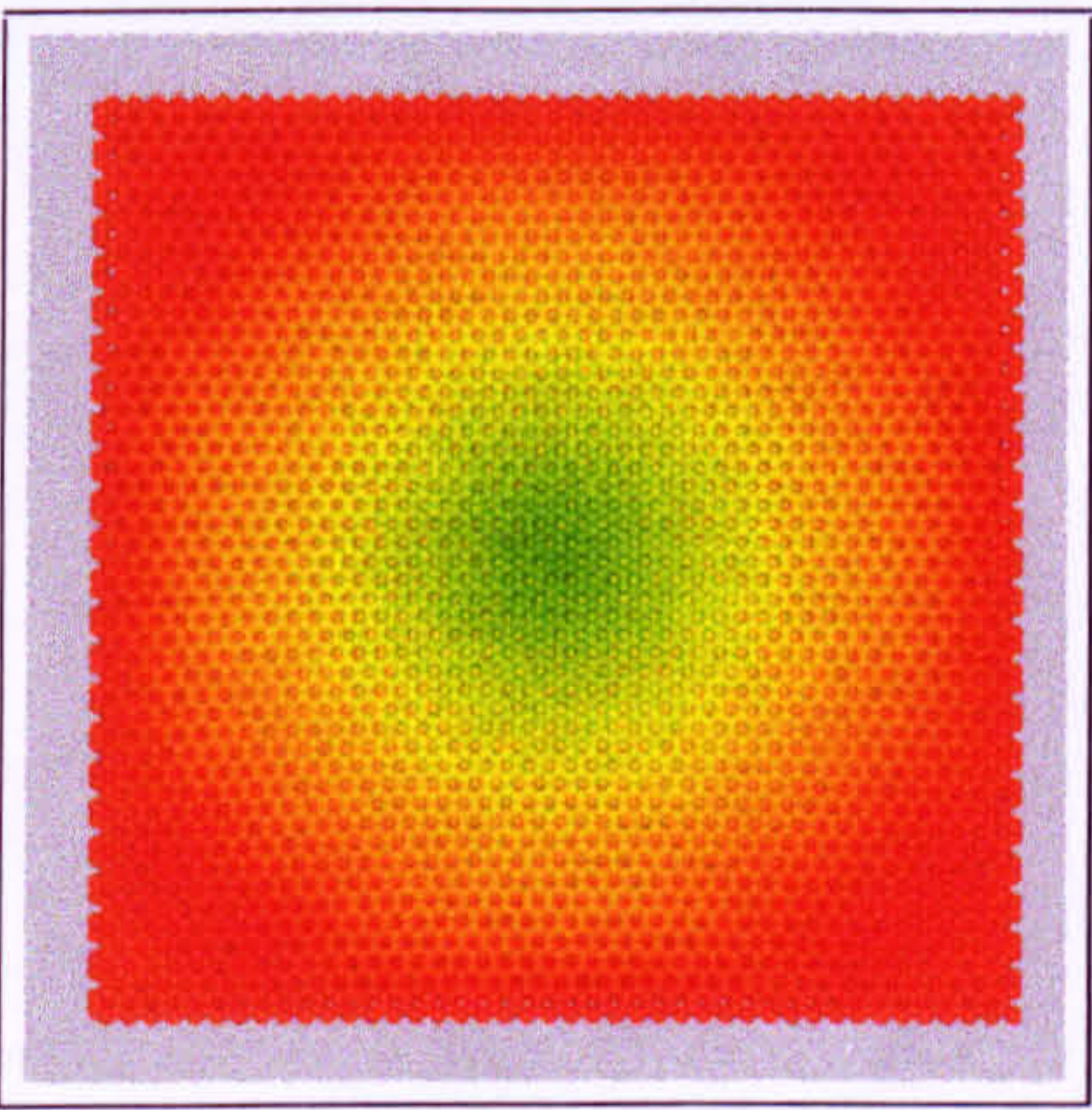




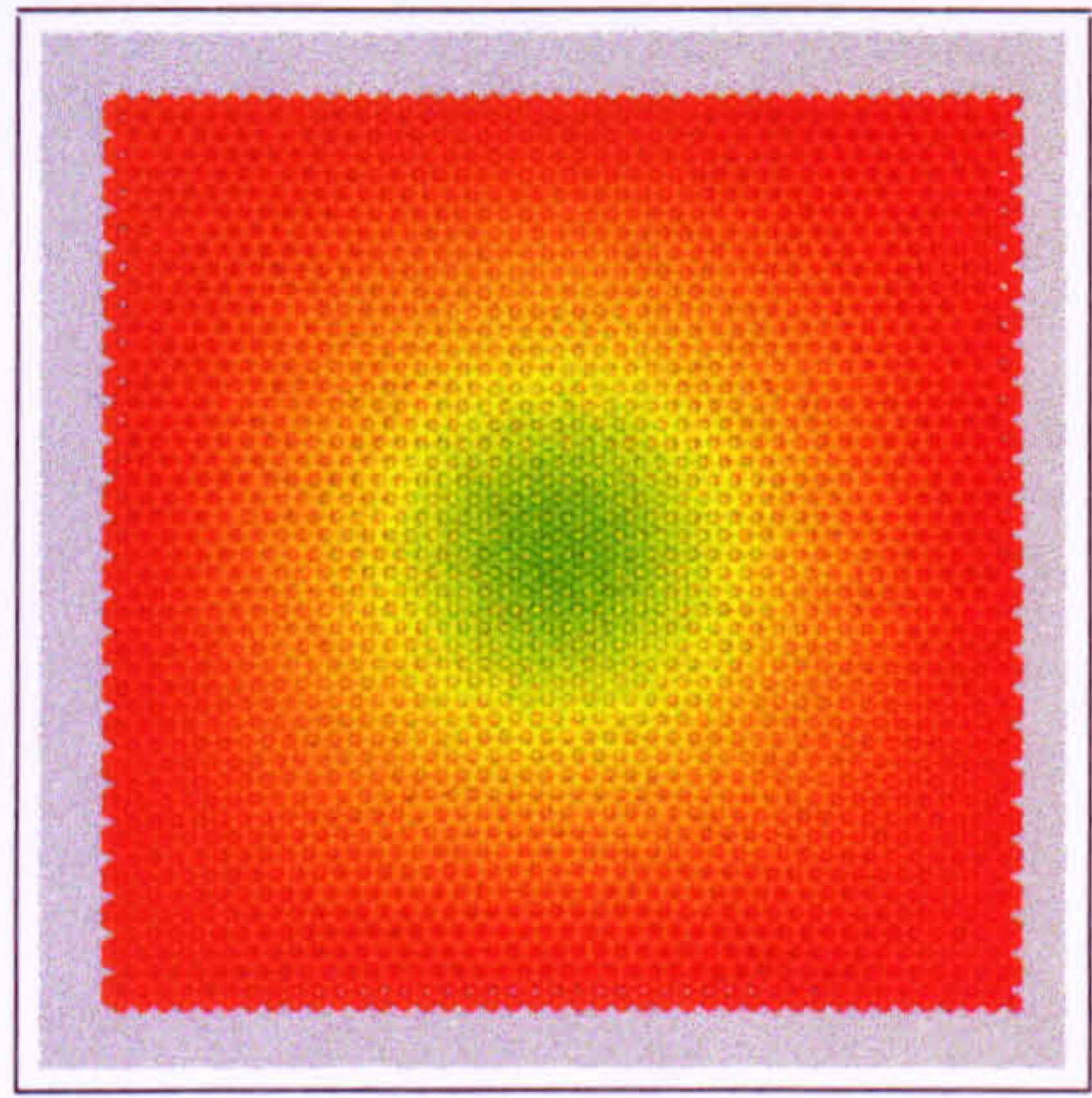
(a)



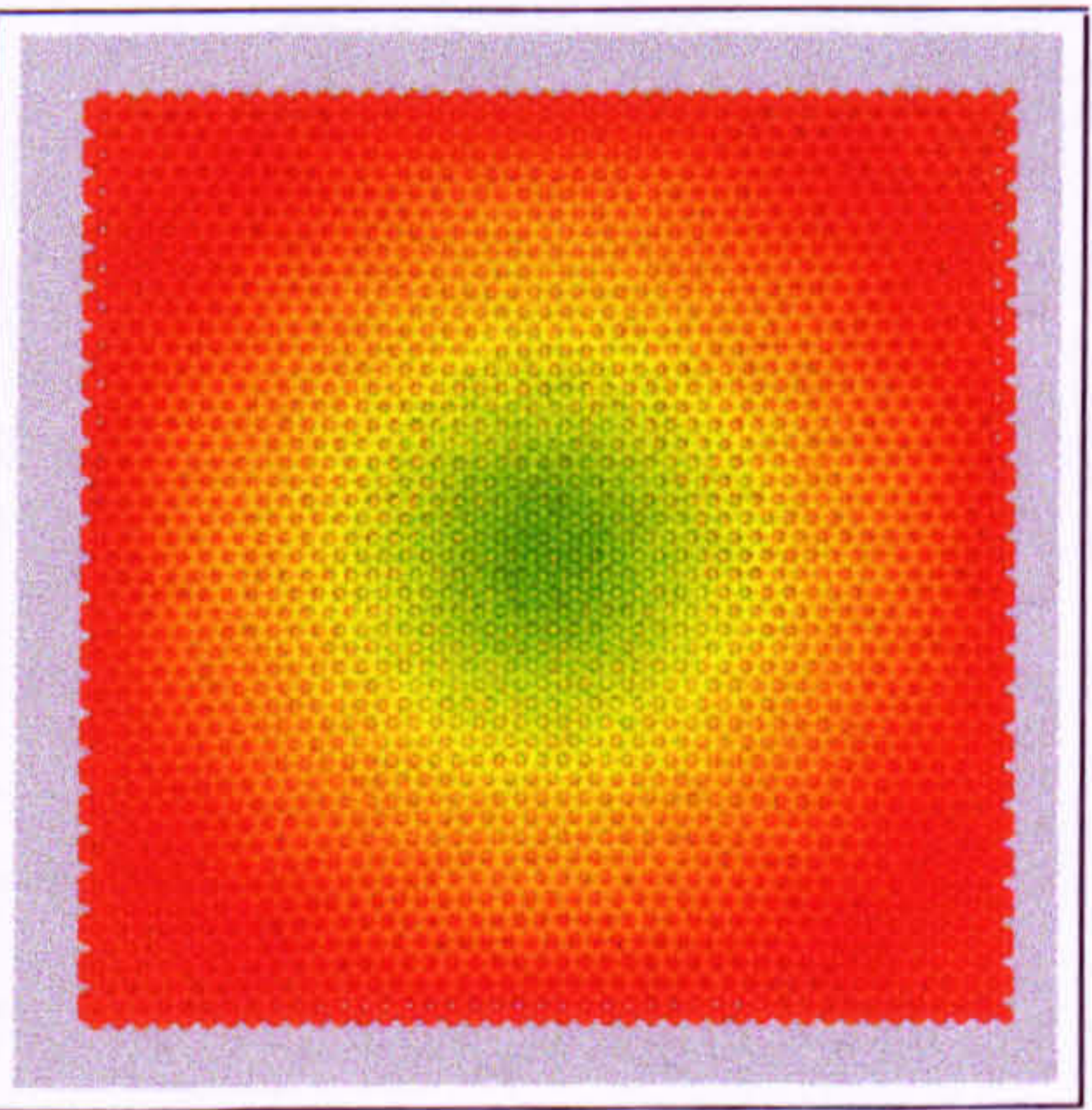
(b)



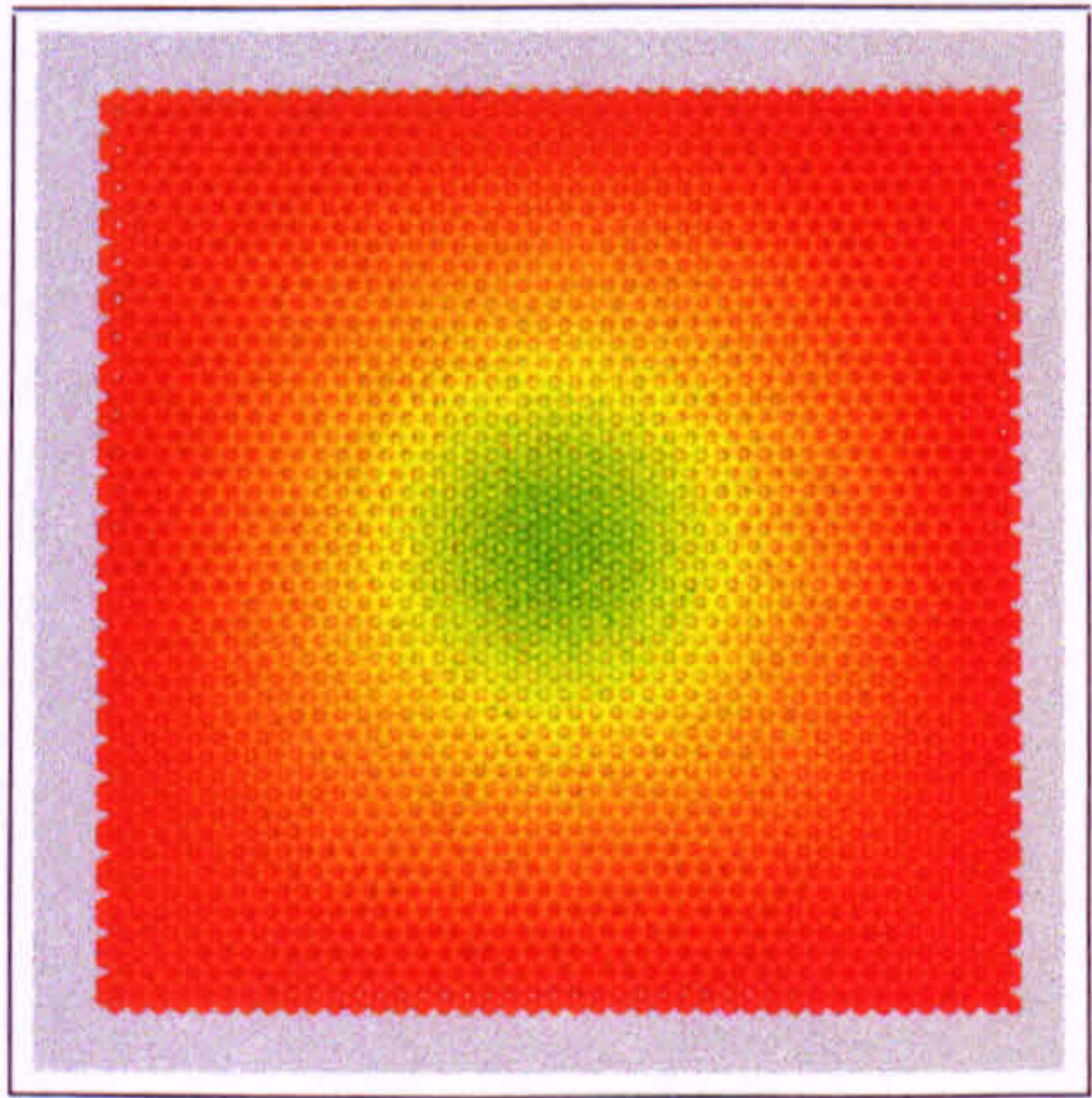
(c)



(d)



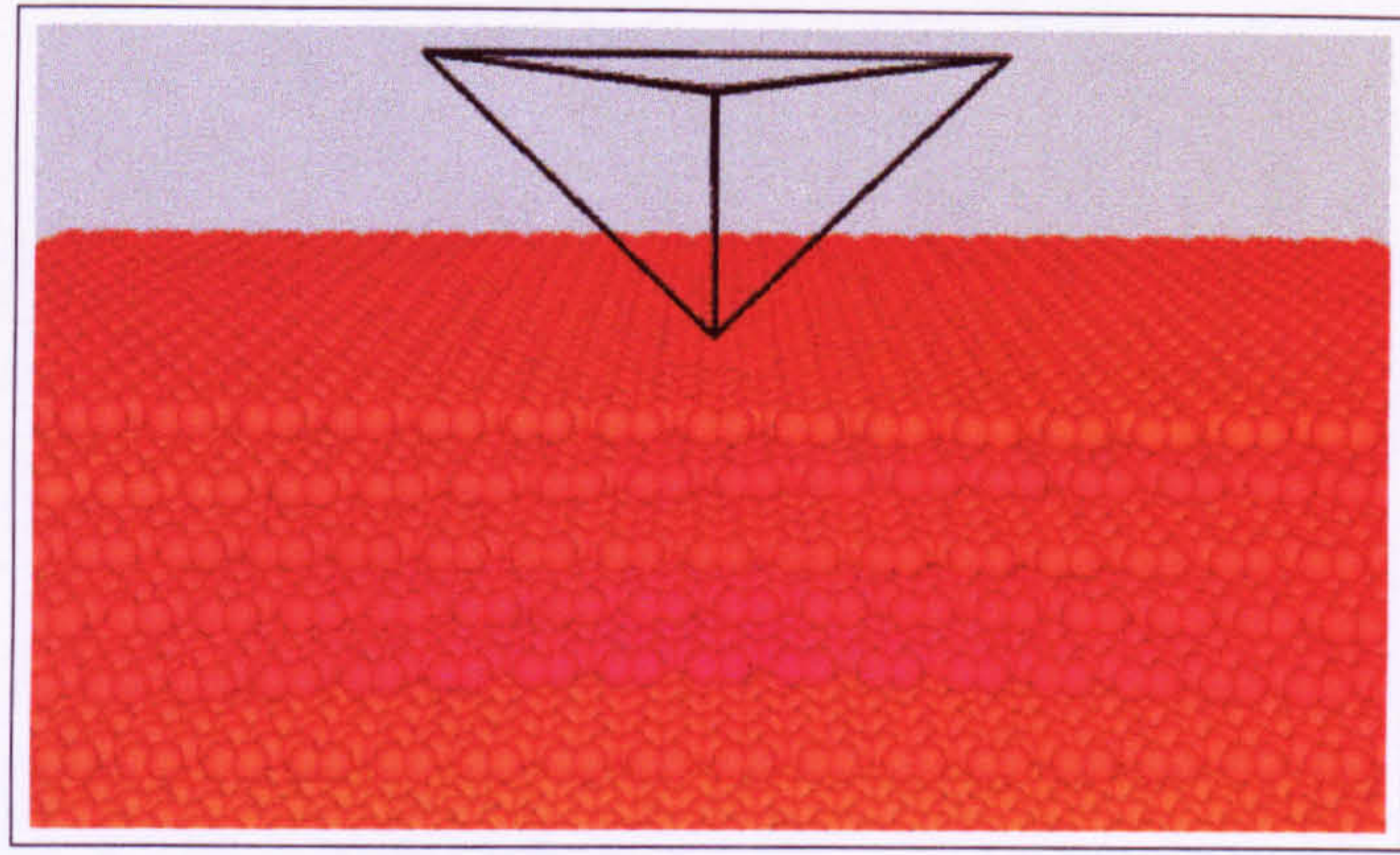
(e)



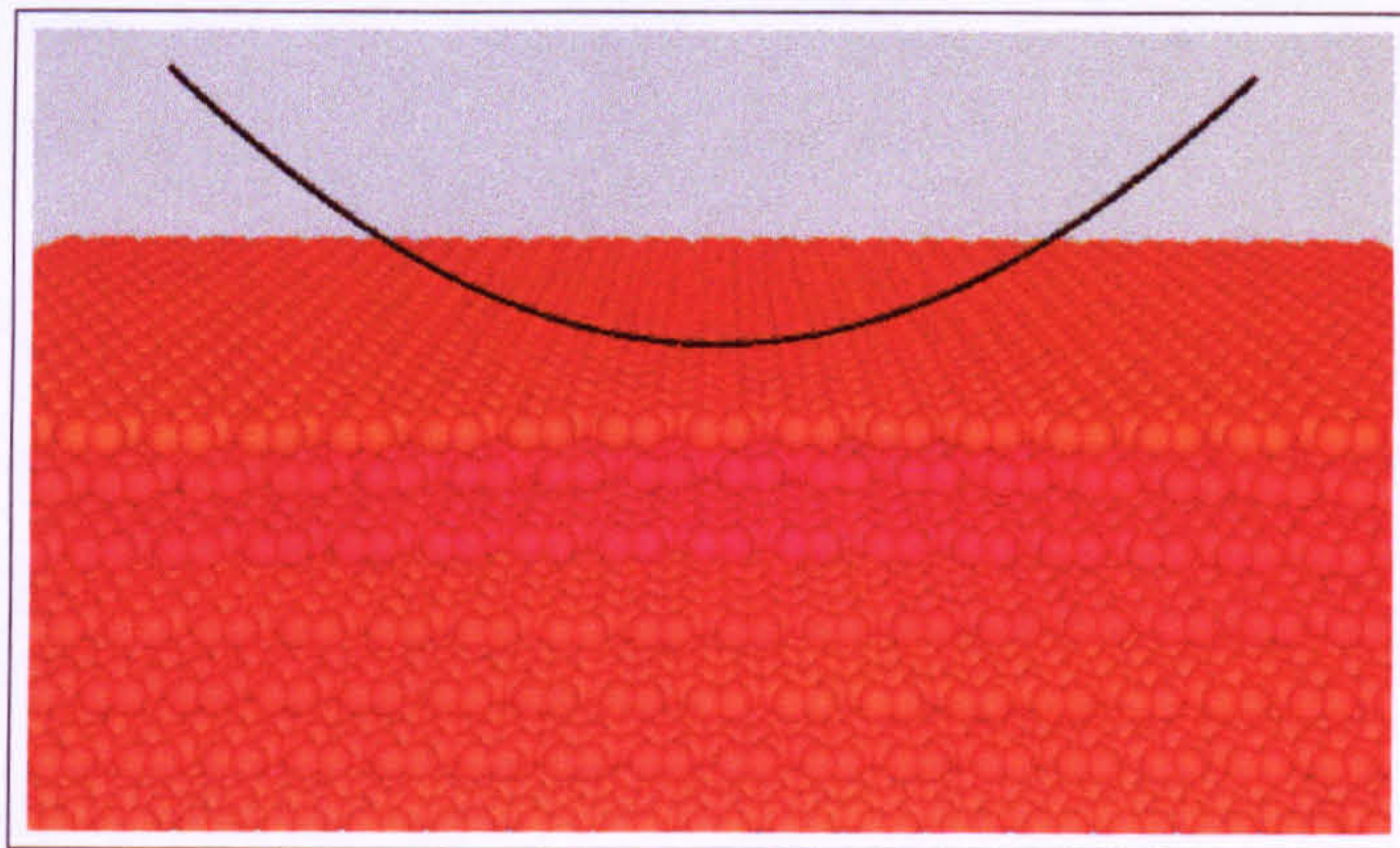
(f)

Fig. 3.3.12. Plan view of the graphite  $\{0001\}$  substrate at the halfway stage for indentation with: (a) pyramid ( $T = 5$  ps); (b) pyramid ( $T = 50$  ps); (c) paraboloid ( $T = 5$  ps); (d) paraboloid ( $T = 50$  ps); (e) hyperboloid ( $T = 5$  ps); (f) hyperboloid ( $T = 50$  ps).

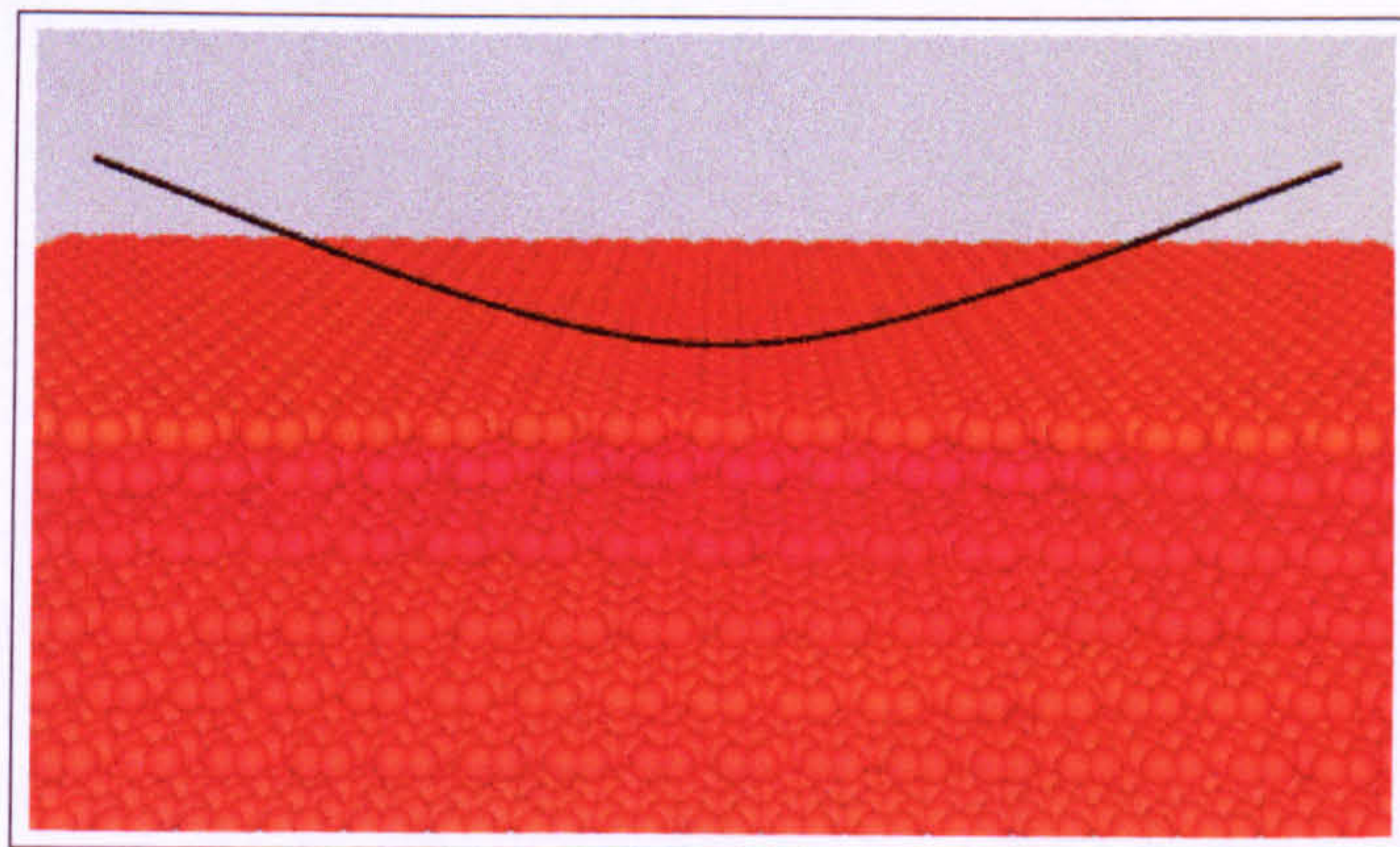




(a)



(b)



(c)

Fig. 3.3.13. Cross-sectional snapshot from the  $T = 50$  ps simulations with the graphite  $\{0001\}$  crystal at  $t = 50$  ps with the interface profile for: (a) pyramid; (b) paraboloid; (c) hyperboloid. In these images, half of the atoms have been removed.



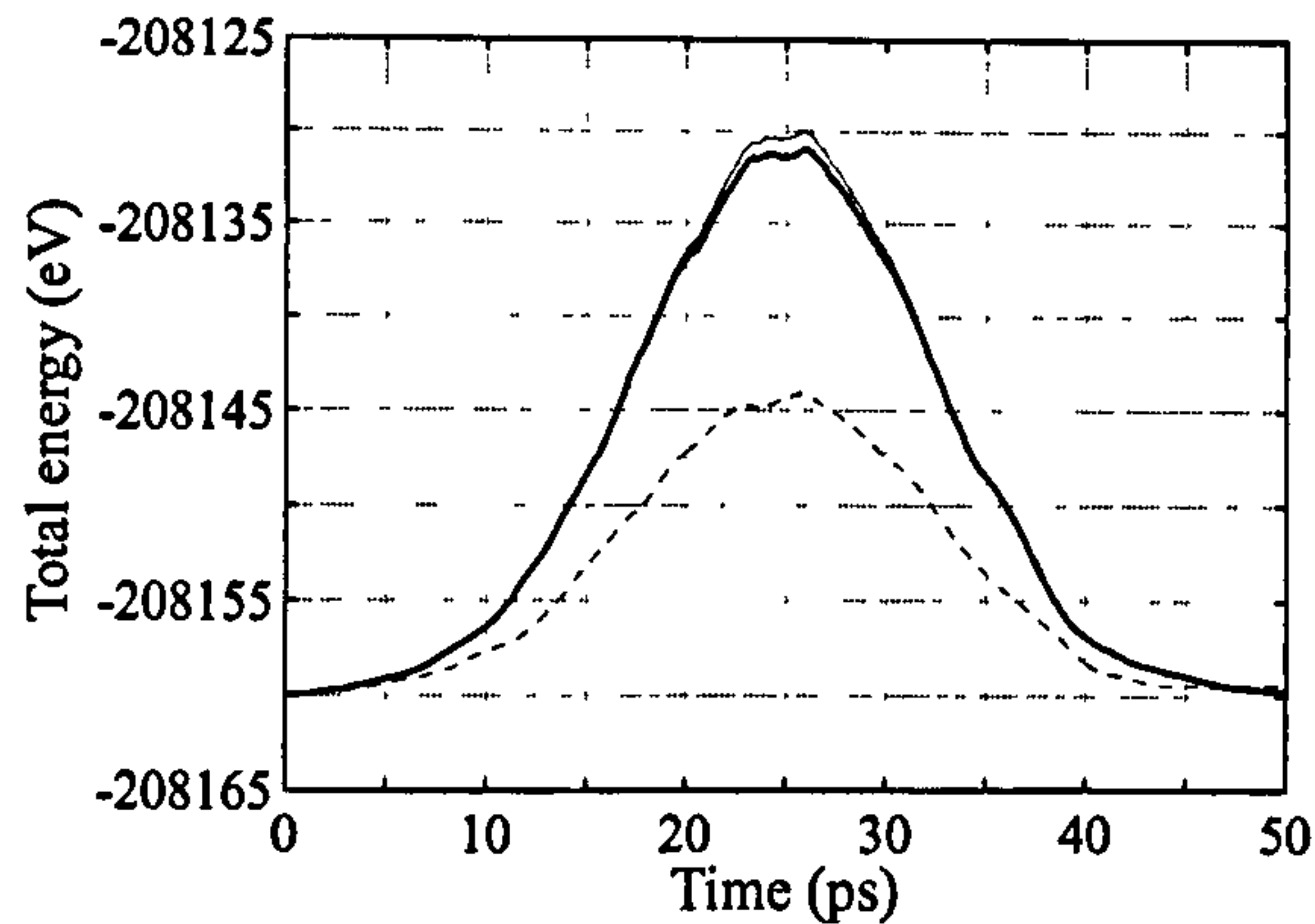


Fig. 3.3.14. Total energy of the graphite  $\{0001\}$  crystal during the  $T = 50$  ps simulations. The dashed line denotes the pyramid model of the interface. The bold solid line and thin solid line correspond to the hyperboloid and paraboloid models of the interface respectively.

The total energy of the graphite lattice in the  $T = 50$  ps simulations decreases at a similar rate to the increase in the loading stage, since the slower indentation speed has allowed the substrate more time to relax. At the completion of the simulations, the total energy of the work material is almost equal to its initial value, further verifying that the indentation period  $T = 50$  ps is more analogous to the relaxation process in the graphite substrate.

### 3.3.2 Diamond $\{100\}$ Substrate

Shown in Fig. 3.3.15 is the elementary cell of a diamond crystal. In diamond [134] each carbon atom bonds to its four nearest neighbours, which are sited  $1.544 \text{ \AA}$  away at the vertices of a regular tetrahedron. This particular arrangement results in the high atomic density of the material, which is the hardest known to date. In this investigation, a diamond crystal is utilised with the  $\{100\}$  surface orientation. The crystal has approximate dimensions  $103 \text{ \AA} \times 103 \text{ \AA} \times 21 \text{ \AA}$  and is composed from 24 atomic layers. The work piece is configured from 40,368 atoms where 5,727 atoms constitute the fixed boundary and 9,329 atoms compose the damped adjoining region.

The load-displacement curves from the indentation into the diamond crystal are presented in Fig. 3.3.16. The loading and unloading curves corresponding to each model of the interface overlap, reflecting a purely elastic response from the work material. Comparisons between Fig. 3.3.10 and Fig. 3.3.16 clearly reflect the greater nanohardness



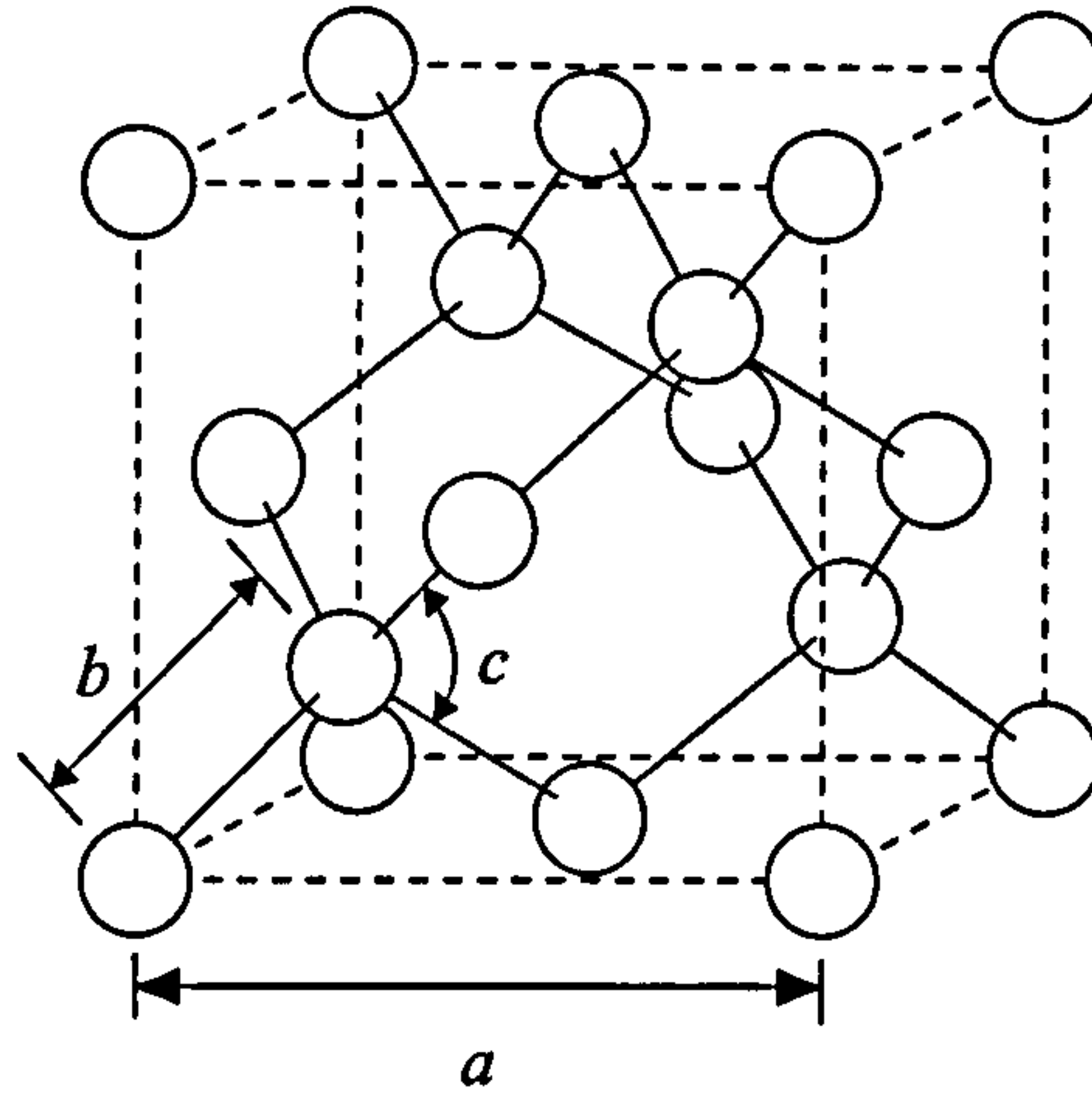


Fig. 3.3.15. The elementary unit cell of a diamond crystal. The length of the cell,  $a$ , is equal to  $3.58 \text{ \AA}$  and the distance between the nearest neighbours,  $b$ , is equal to  $1.54 \text{ \AA}$ . The angle  $c$  is equal to  $109^\circ$ . The carbon atoms exist in  $sp^3$  hybridization. The tetrahedral arrangement of the bonds is clearly seen.

of diamond compared with graphite. The overlapping loading and unloading curves suggest that the speed of indentation is akin to the relaxation process in the diamond substrate. For indentation with the axisymmetric interfaces the loading curve exhibits a sizeable oscillatory nature, whereas the unloading part of the force-depth curves is relatively smooth. As the pyramidal interface reaches the indentation limit, it experiences a force of about  $89 \text{ eV/\AA}$  from the substrate. At the maximum indentation depth, the force acting on the hyperboloid and paraboloid interfaces is approximately  $123 \text{ eV/\AA}$  and  $178 \text{ eV/\AA}$  respectively.

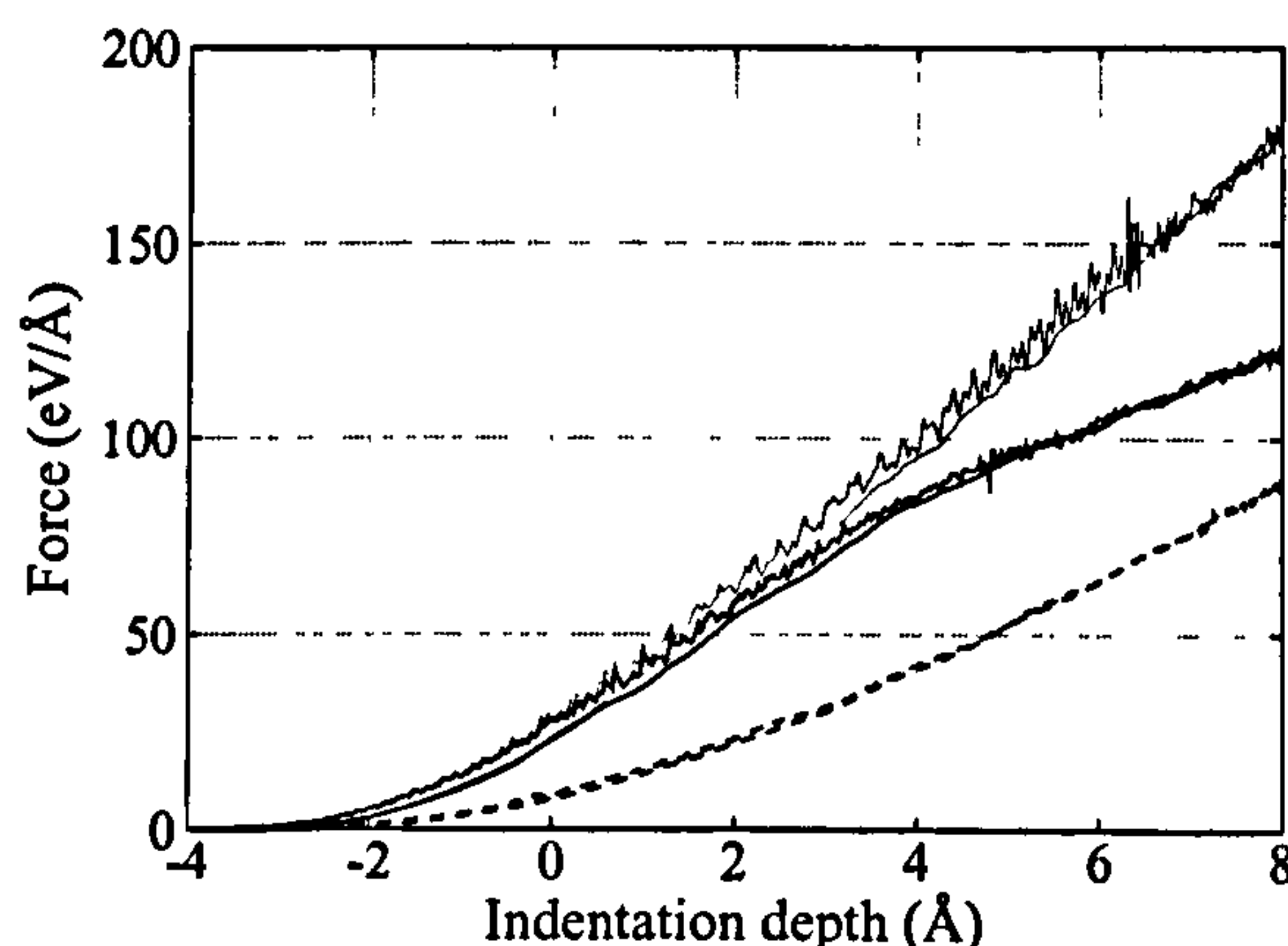


Fig. 3.3.16. Force-depth curves from indentation into the diamond  $\{100\}$  crystal. The dashed line denotes the pyramid model of the interface. The bold solid line and thin solid line correspond to the hyperboloid and paraboloid models of the interface respectively.



Shown in Fig. 3.3.17 is the number of interface-substrate interactions for each of the three interfaces during the simulations with the diamond crystal. Comparisons with Fig. 3.3.11 show a larger number of atoms in the diamond lattice interact with the interfaces compared with atoms in the graphite substrate, clearly reflecting the greater atom-density of diamond. Hence, the interaction with more atoms in the diamond crystal ensues in greater repulsive forces exerted on the interfaces. Indentation into the diamond crystal has resulted in alike numbers of interface-substrate interactions during both the loading and unloading stages. The hyperboloid interface interacts with more atoms than the paraboloid interface, and the work material offers greater repulsive force to the paraboloid interface. Interestingly, the peak number of interacting atoms with the hyperboloid interface occurs in the region  $t = 18$  ps to  $t = 32$  ps, i.e. 7 ps either side of the halfway stage which corresponds to a penetration depth of approximately 6.8 Å. Within this region the number of interface-substrate interactions is very consistent, yet in the corresponding load-displacement curve in Fig. 3.3.16 the force continues to increase up to the indentation limit and decrease in a similar fashion during the unloading stage.

Snapshots from the simulations with the diamond {100} crystal at the halfway stage are presented in Fig. 3.3.18. The images clearly show the diamond work piece deforms far less compared with graphite. Furthermore, the greater rigidity of the structure prevents the wave-like motion that occurs in the graphite substrate. Indentation with the

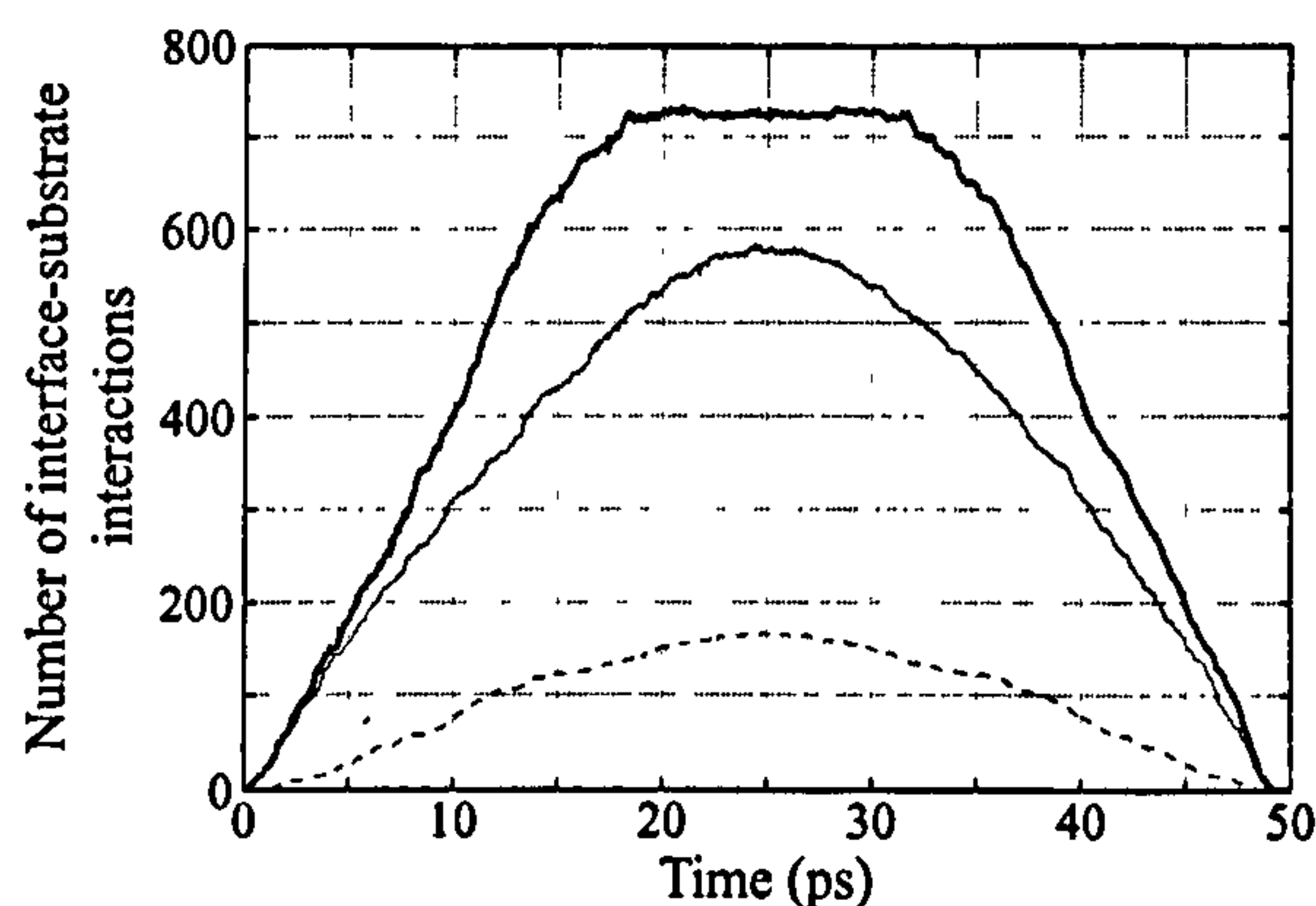
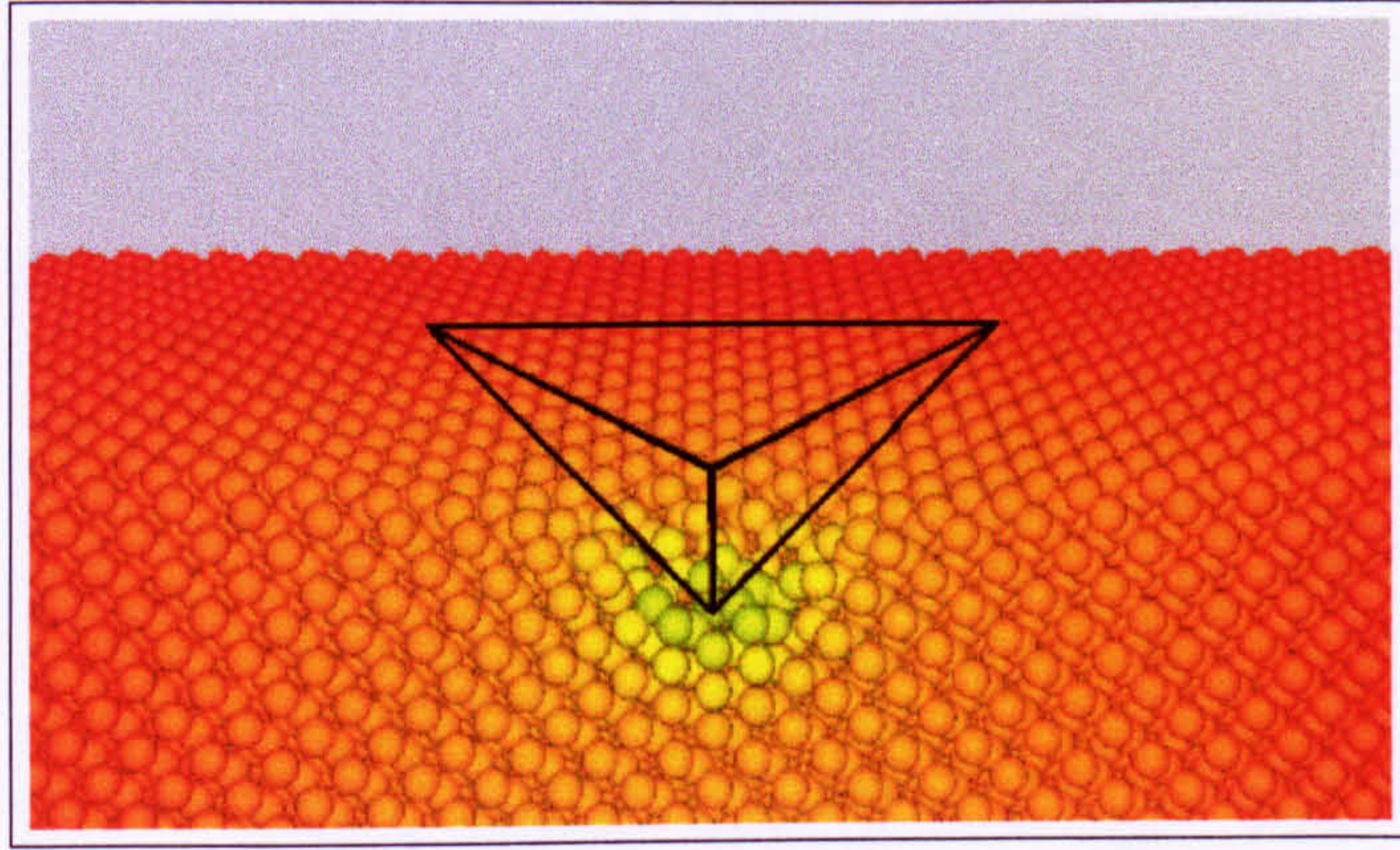
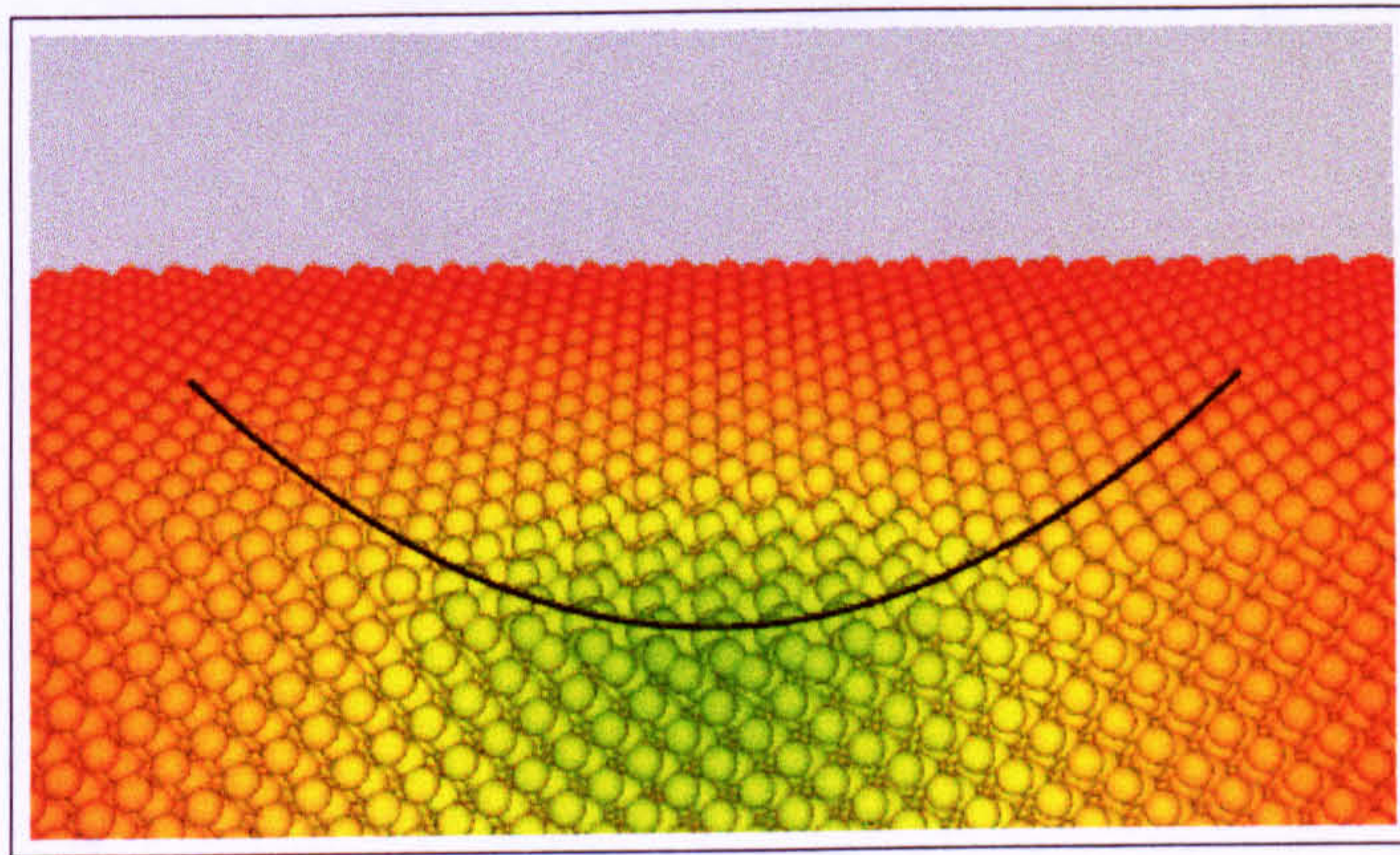


Fig. 3.3.17. The total number of interface-substrate atom interactions during the simulations with the diamond {100} crystal. The dashed line denotes the pyramid model of the interface. The bold solid line and thin solid line correspond to the hyperboloid and paraboloid models of the interface respectively.

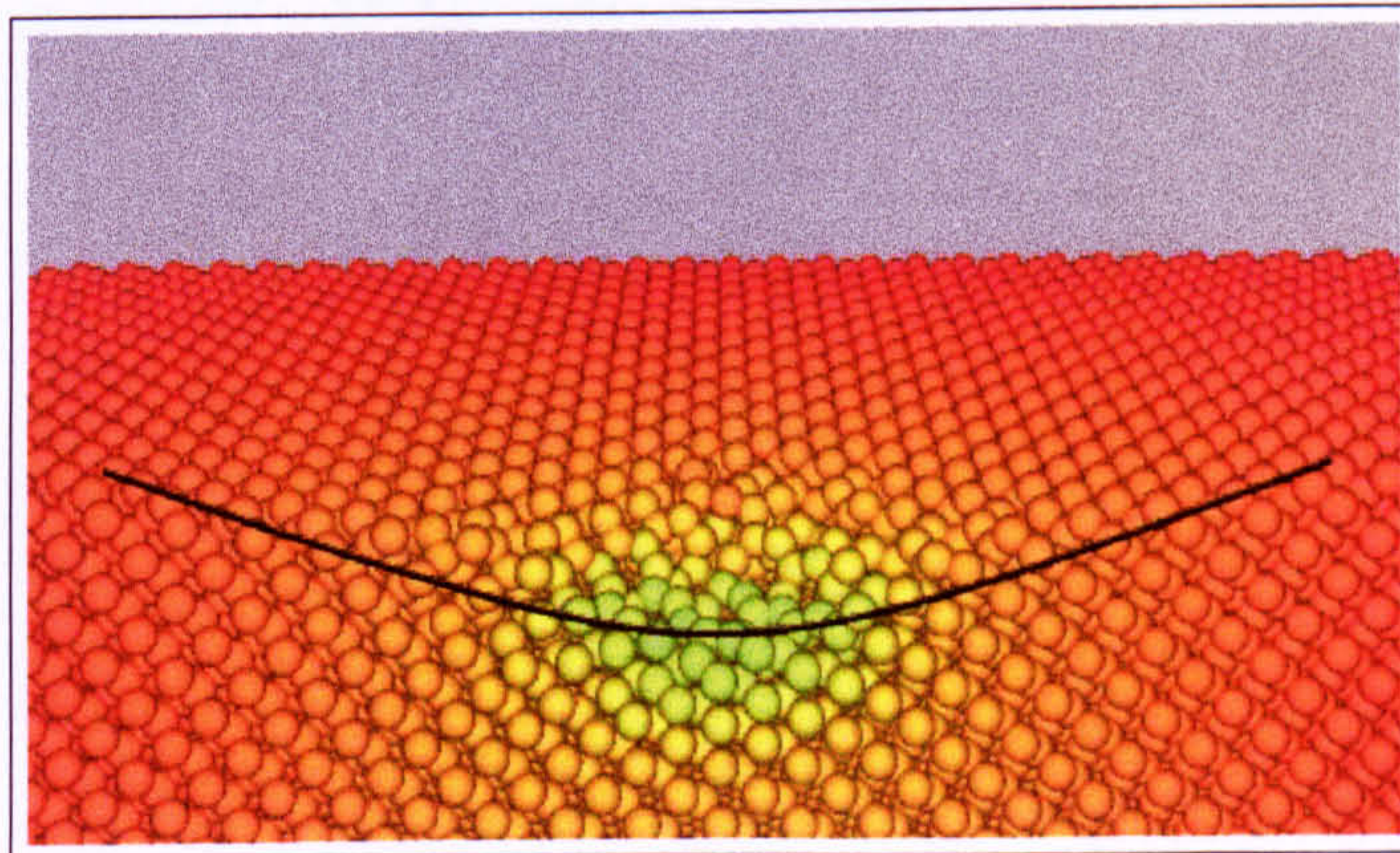




(a)



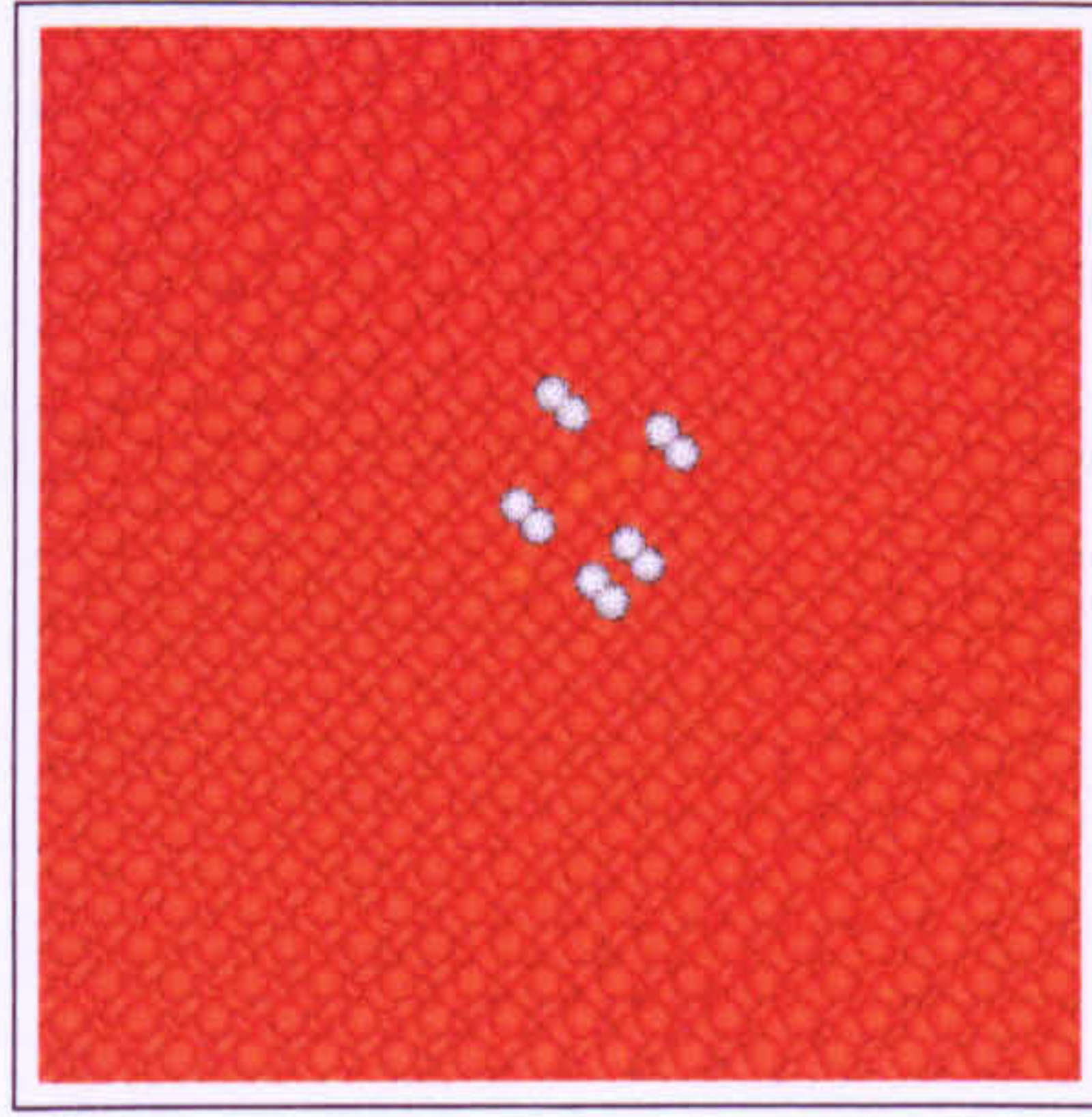
(b)



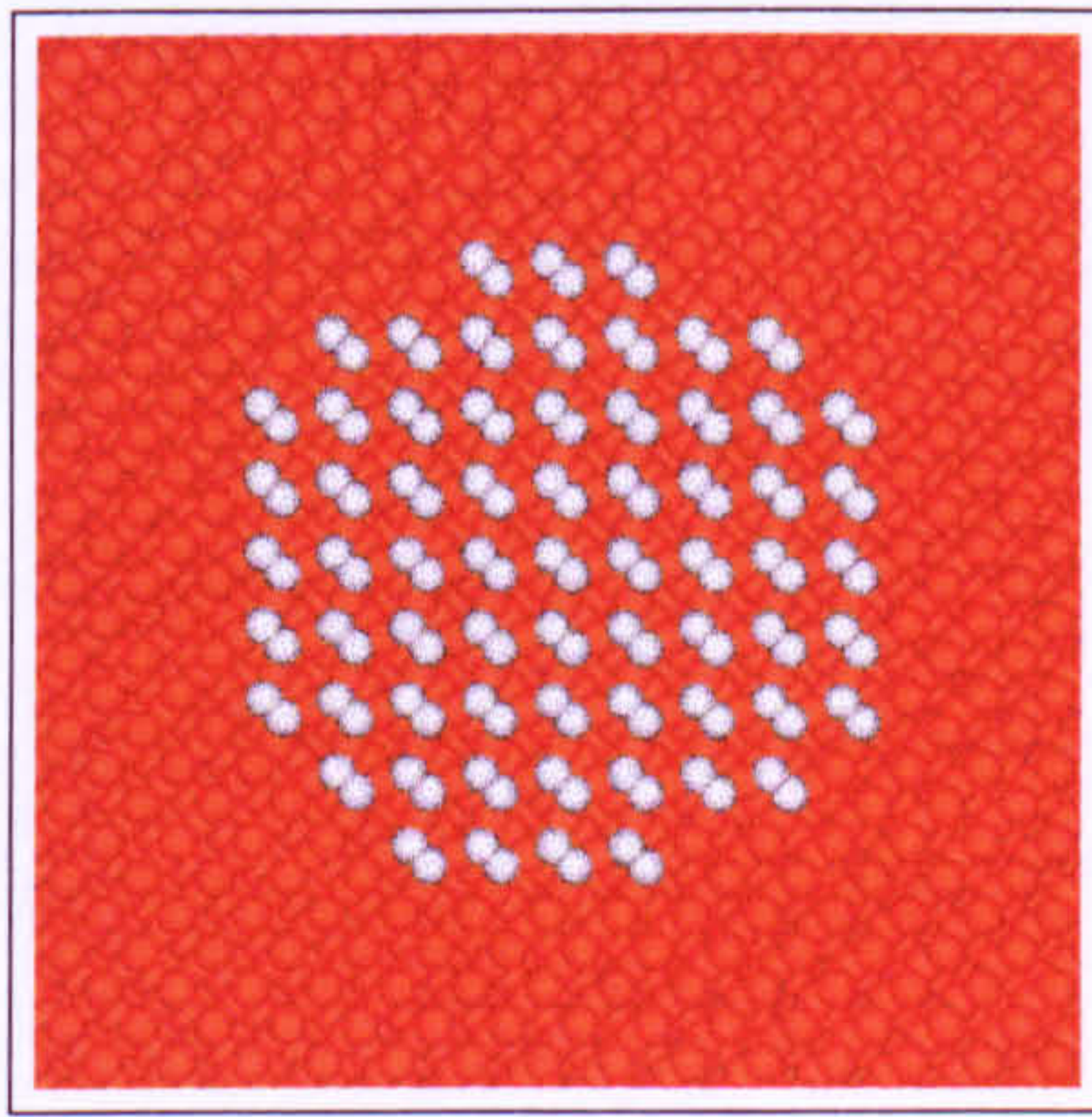
(c)

Fig. 3.3.18. Cross-sectional snapshot from the simulations with the diamond  $\{100\}$  crystal at  $t = 25$  ps with the interface profile for: (a) pyramid; (b) paraboloid; (c) hyperboloid. In these images, half of the atoms have been removed.

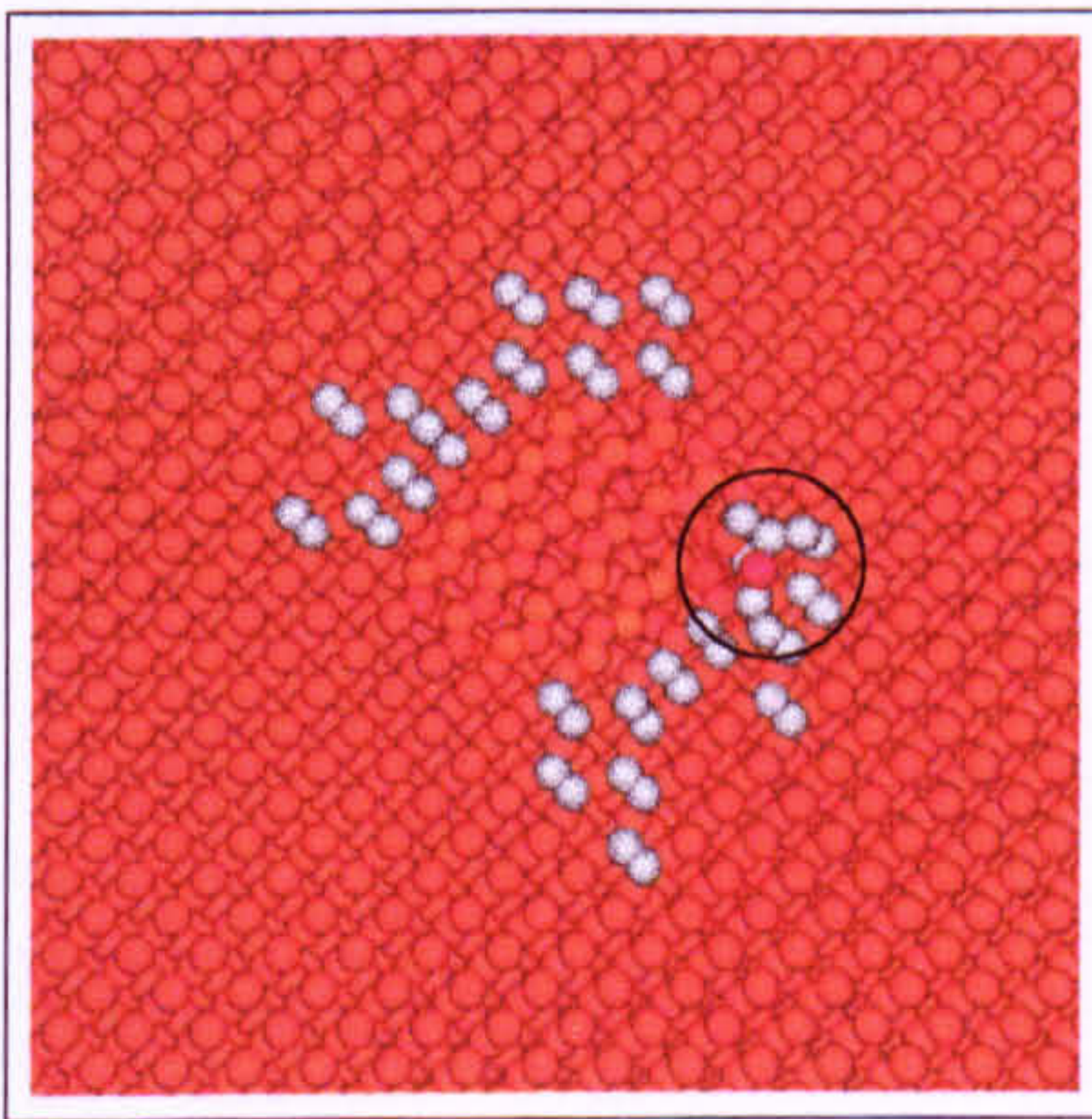




(a)



(b)



(c)

Fig. 3.3.19. Plan view of the indented area in the diamond  $\{100\}$  crystal at  $t = 50$  ps. Interface corresponds to: (a) pyramid; (b) paraboloid; (c) hyperboloid. The white atoms show the reconstruction between 1<sup>st</sup> layer atoms. Note the damage to the surface in (c) inside the marked circle.



pyramidal interface in Fig. 3.3.18(a) shows that only atoms very close to the tip undergo a significant displacement. Penetration with the axisymmetric interfaces results in the reconstruction of surface atoms local to the indent. Plan views of the indentation region are presented in Fig. 3.3.19 at the conclusion of the simulation. Each image shows reconstruction of the surface atoms, mainly in the form dimers. The sharp apex of the impinging pyramidal indenter induces little surface reconstruction. By comparison, both the axisymmetric interfaces generate a comparatively large reconstruction of the surface, but show some dissimilar characteristics. The paraboloid interface induces a broadly symmetric dimer surface reconstruction encompassing the local indentation region. However, with the blunter hyperboloid indenter the reconstruction occurs in a more distorted manner and non-symmetric fashion. The hyperboloid interface has actually caused the subsurface atoms sited directly underneath the apex to reconstruct. The surface dimer reconstruction imparted by the hyperboloid indenter surrounds the reconstructed subsurface. Clearly indentation with the hyperboloid interface has ensued in fractional tip-induced plastic deformation, as marked by the circle in Fig. 3.3.19(c).

Fig. 3.3.20 presents the total energy of the diamond crystal during the indentations. At the beginning of each simulation the diamond surface begins to reconstruct under its own potential and the energy decreases to some minimum configuration. The pyramidal interface added a maximum of roughly 200 eV to the substrate, occurring at approximately the halfway stage. The total energy decreases during the unloading process of each of the interfaces and approaches a minimum energy configuration at

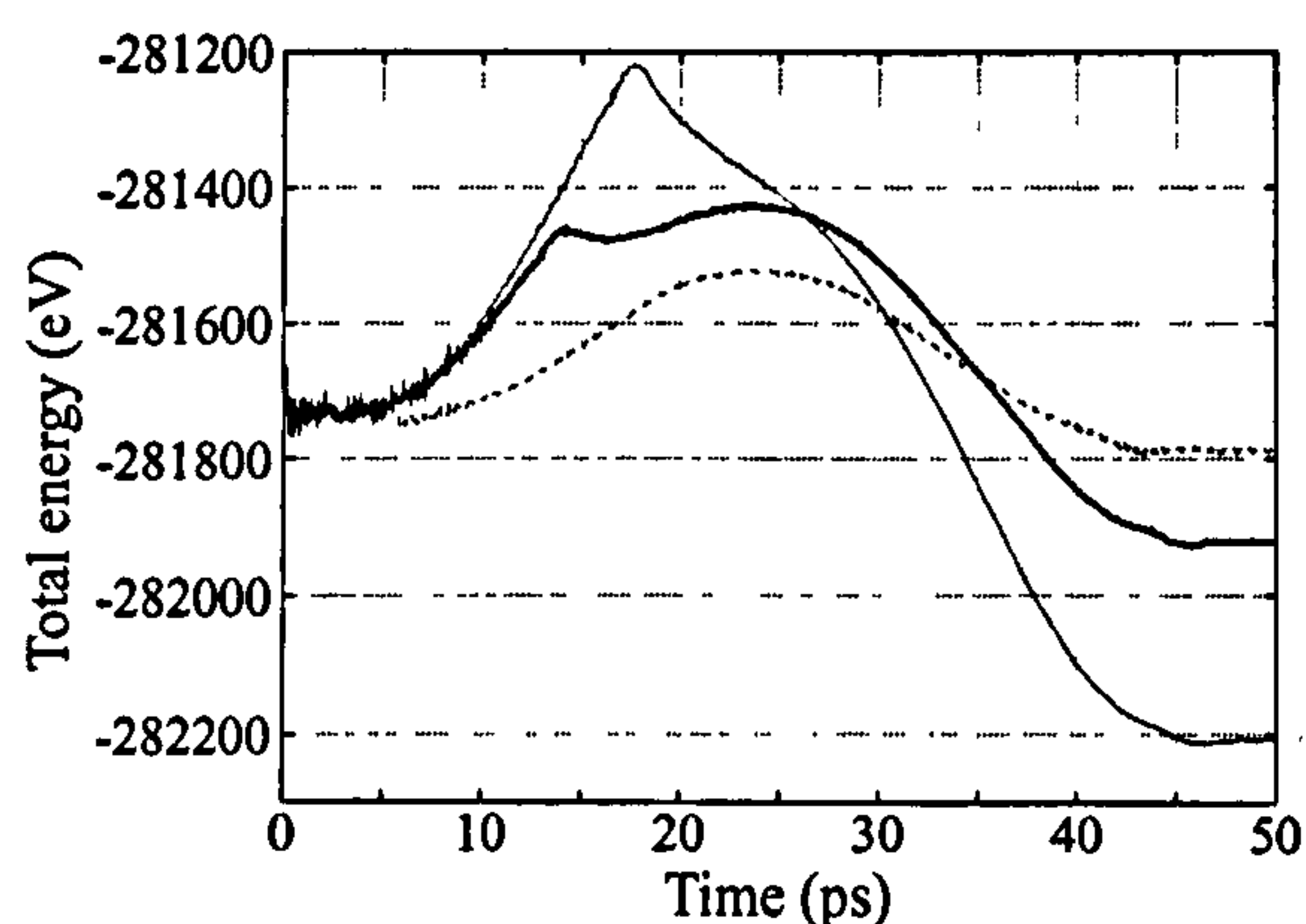


Fig. 3.3.20. Total energy of the diamond {100} crystal during the indentation. The dashed line denotes the pyramid model of the interface. The bold solid line and thin solid line correspond to the hyperboloid and paraboloid models of the interface respectively.



approximately  $t = 45$  ps, which corresponds to the apex of the interface at the surface of the work material. At the completion of the simulation with the cube-cornered interface, the total energy of the substrate is approximately equal to its minimum value after relaxation of the surface. Fig. 3.3.20 shows that the paraboloid indenter induces comparatively more energy into the diamond substrate than the hyperboloid interface. The maximum energy added by the hyperboloid interface was approximately 300 eV, occurring at the halfway stage of the indentation process. Interestingly, the total energy curve corresponding to the hyperboloid interface exhibits an unusual peak at  $t = 14$  ps, conforming to an indentation depth of approximately 5.3 Å. At the conclusion of the simulation implementing the hyperboloid interface, the total energy of the diamond substrate has decreased by approximately 200 eV from its initial value. The paraboloid interface added a maximum of 500 eV to the diamond crystal. However, unlike the cube-cornered and paraboloid interface, this occurs not at the halfway stage of the indentation process as would be expected, but at  $t = 17.5$  ps which corresponds to an indentation depth of approximately 6.7 Å. Hereafter, the total energy starts to decrease, even though the paraboloid interface is continuing to penetrate deeper into the work piece and interacting with more atoms. At the completion of the simulation with the paraboloid interface, the total energy of the substrate has decreased by just over 500 eV from the initial value. The lower energy configuration of the diamond substrate following indentation with the axisymmetric interfaces arises from greater tip-induced structural re-arrangements. The peak in the curves for the axisymmetric interfaces probably stems from reconstruction within the bulk. As the interface is pressed into the diamond the atoms are compressed which increases the energy within the system. However, bulk reconstruction will lower the energy and so the total energy curve can decrease during the loading stage. Ideally, a reconstructed diamond surface should be used before the indentation is made.

## 3.4 Determining Mechanical Properties

### 3.4.1 Nanohardness

Traditionally, hardness is determined from the maximum force on the indenter divided by the cross-sectional area of the indent. However, on the nanometre scale this concept



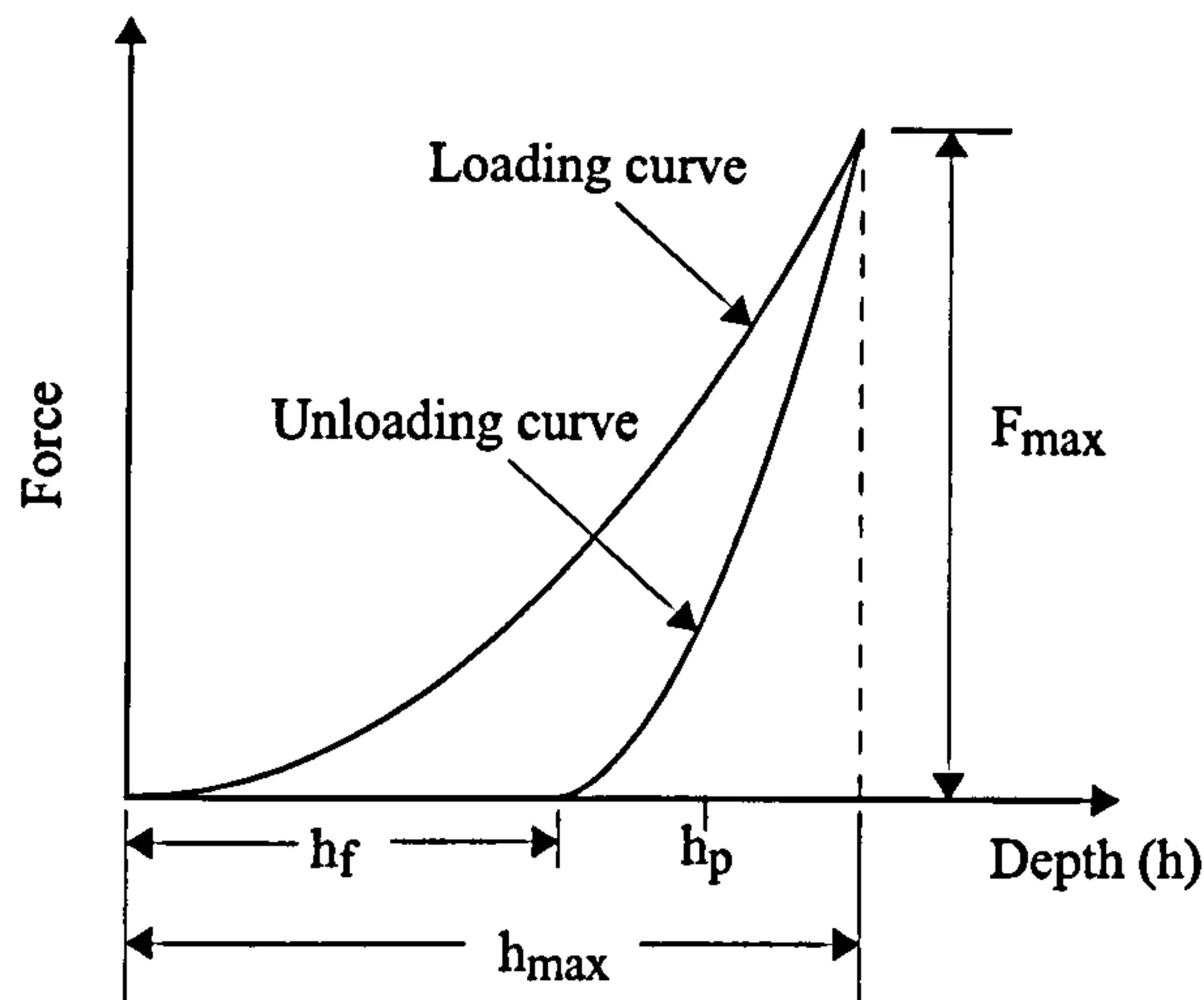


Fig. 3.3.21. Force-depth indentation curve showing the key quantities used to determine the mechanical properties of the substrates.

is inadequate since if the indentation is purely elastic the calculated hardness would be infinite. In the definition of nanohardness, the subsequent quantities are used. The maximum penetration depth of the indenter is denoted by  $h_{\max}$  and on extraction, the depth where the force equates to zero is defined by  $h_f$ , as illustrated in Fig. 3.3.21. The nanohardness  $H$  of the substrate is calculated from the formula

$$H = \frac{F_{\max}}{A_c} \quad (3.4.3.1)$$

where  $F_{\max}$  is the exerted force at depth  $h_{\max}$  and  $A_c$  is the cross-sectional area at the penetration depth  $h_p$ , as shown in Fig. 3.3.21. The depth  $h_p$  is taken to be half of the elastic recovery plus  $h_f$ . Thus, even for purely elastic indentations, the concept of nanohardness is valid. The nanohardness technique eliminates the need to visualise indentations for extracting mechanical properties. Experimentally, the cross-sectional area  $A_c$  can be determined using a calibration grid [124].

### 3.4.2 Young's Modulus

The Young's modulus  $E$  of the work material is a measure of the elastic properties. This is calculated from the formula

$$E = 0.5(dF/dh)/\sqrt{A_c/\pi} \quad (3.4.3.2)$$

where  $dF/dh$  is the slope of the force-depth curve at the maximum penetration depth of the indenter. The simple macroscopic theory of contact theory by Hertz [135] states



that the applied load  $F$  is proportional to  $h^m$  where  $m$  is a constant to be determined from the force-depth data. Typically  $m$  is in the range 1.4 to 1.6 (1.5 is characteristic for spherical indentation). For a detailed discussion on Hertzian mechanics, the reader is referred to Johnson [136].

### 3.5 Mechanical Properties of Graphite and Diamond

The mechanical properties of the carbon materials were evaluated using force-depth data yielded from simulations employing larger substrates with the pyramidal indenter. Here, indentations were performed to a maximum penetration depth of 20 Å with an indentation period of  $T = 100$  ps. The nanohardness of the graphite and diamond substrates were evaluated using the formula given in Eqn. 3.4.3.1. The extracted nanohardness values for graphite and diamond were 3.5 GPa and 45 GPa respectively. These are much less than typical values in the literature [124], of approximately 10.5 GPa and 117 GPa respectively. To determine the Young's modulus of the carbon specimens, the index  $m$  was determined from a log-log plot of the loading force-depth curve shown in Fig. 3.3.22. An analysis of the plots in Fig. 3.3.22 clearly shows that the force-depth curve for graphite does not follow a power law dependency. Even so, the index  $m$  was extracted using the slope of the curve at maximum indentation which gave a value of approximately 3.0. The log-log plot of the load-displacement curve for diamond broadly suggests a power law dependency. Here, the index  $m$  is determined to be 1.2. The values extracted for the index  $m$  are clearly outside the range assumed in Hertzian theory and hence the Young's modulus cannot be evaluated. Most likely, the problem here is two-fold. Firstly, larger indentation depths are required to produce results more comparable with experiment and the continuum model. Secondly, the Brenner potential used to describe the C-C interactions in the carbon materials was principally developed to model chemical vapour deposition of diamond films and so little attention was paid to fitting the elastic constants. Thus, the Young's modulus determined from the simulations presented here would obviously differ from experimentally determined values. While this work was in progress, an improved version of the Brenner potential, with correct fitting to the elastic constants, has been published [137].

To determine the extent of the limitation in the Brenner potential, nanoindentation was repeated on graphite using the Tersoff potential for C-C interactions, [94]-[95].



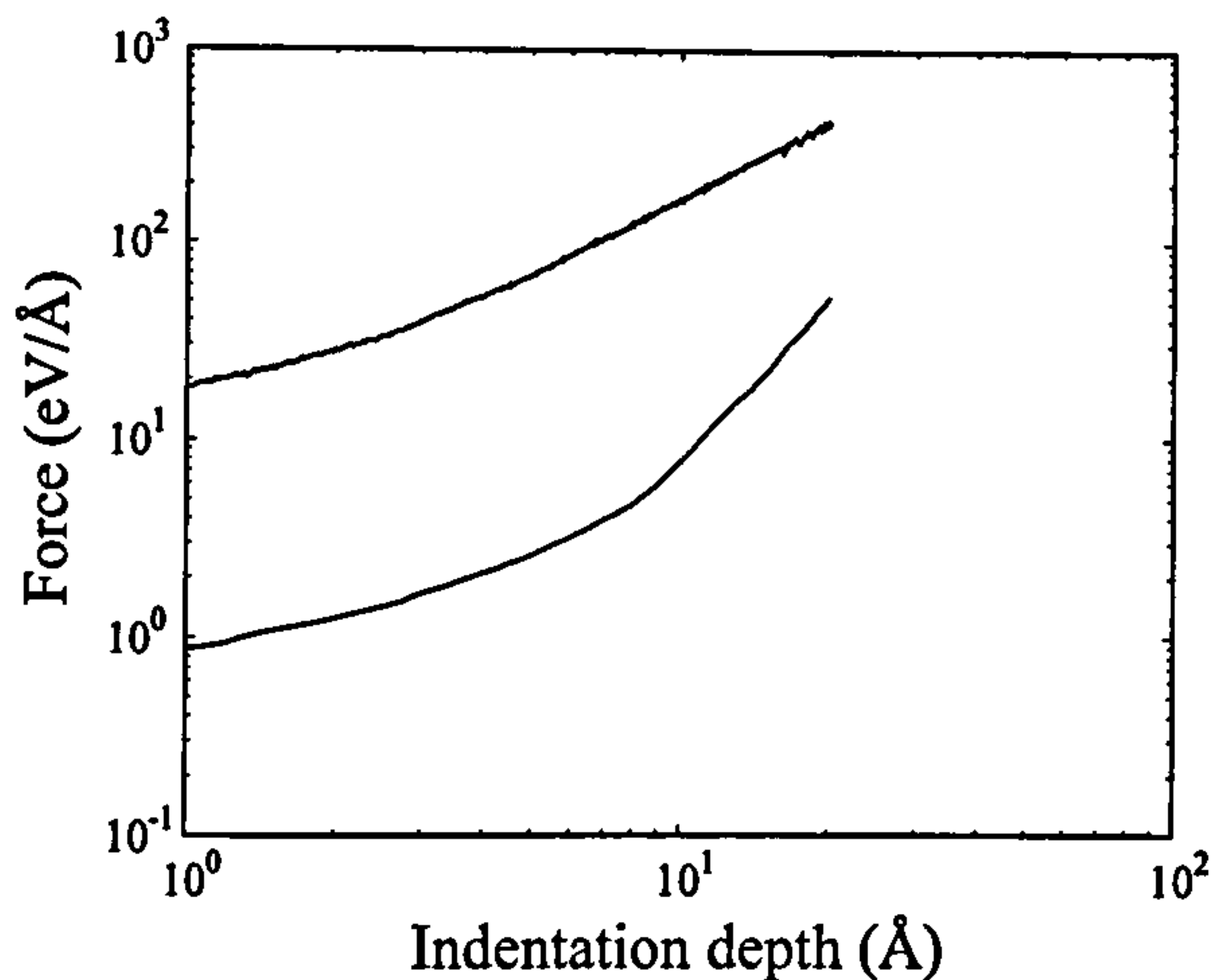


Fig. 3.3.22. A log-log plot of the loading force-depth indentation curves for the  $T = 100$  ps simulations on the graphite  $\{0001\}$  crystal (lower plot) and diamond  $\{100\}$  crystal (upper plot) with the pyramidal interface.

The corresponding force-depth curve is presented in Fig. 3.3.23 together with the load-displacement curve from indentation employing the Brenner potential. Firstly, both potentials show the same qualitative behaviour of the carbon specimen. For shallow indentation depths around 2 Å both potentials yield a similar description of the deformation. However, as the indentation progresses there is a significant difference in the elastic behaviour of the material described by the two potentials. Indentation using the Brenner potential ensues in a peak force of approximately 10 eV/Å compared with 17 eV/Å (i.e. 70% more than Brenner) using the Tersoff potential. Evaluation of the nanohardness using the Tersoff potential yields approximately 7 GPa. This value is closer to experiment than that determined from Brenner, but is still lower. Hence, even with the Tersoff potential, larger indentation depths are required to determine mechanical properties that agree better with experiment. The mechanical properties were also evaluated using the axisymmetric interfaces, which also ensued in values significantly different from experiment.

It has been argued that the nanohardness of a material is actually a function of depth for small indentations. Both increases [138] and decreases [139] in nanohardness have been reported as the indentation depth increases. This is known as the *indentation size effect*. However, it is not known if such observations are real material effects. It may indeed be possible that mechanisms of deformation behaviour change in small volumes. It has also been argued that the apparent change in nanohardness at low indentation



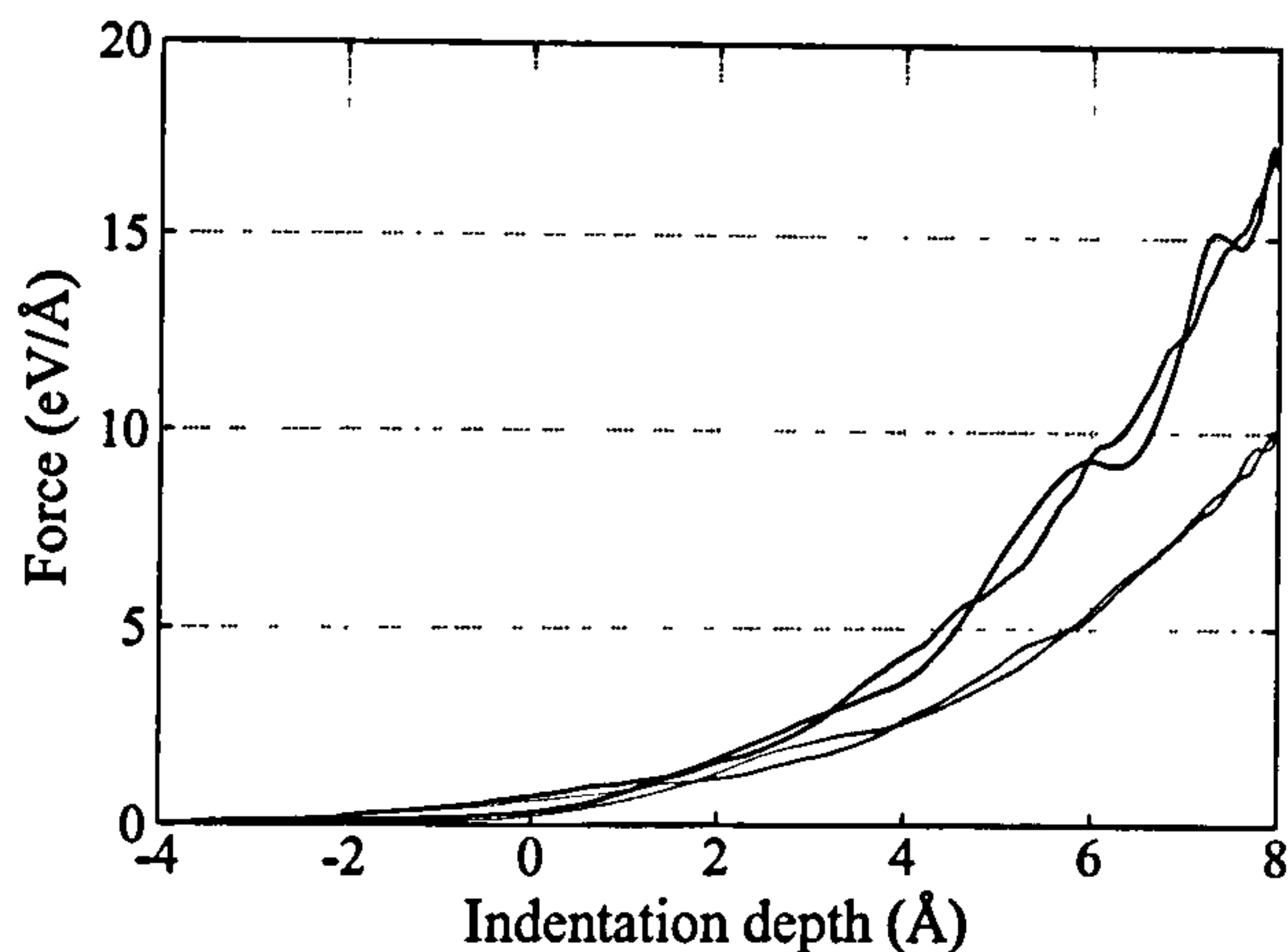


Fig. 3.3.23. Force-depth curve from the indentation of graphite  $\{0001\}$  with the pyramidal interface and  $T = 50$  ps. The upper curve (bold) corresponds to indentation using the Tersoff potential and the lower curve to the Brenner potential.

depths stems from the experimental testing procedure [140]. Since the simulations presented in this thesis involve indentation depths an order of magnitude smaller than in experiment, one can speculate how realistic any comparable discrepancies are.

### 3.6 Summary

The elastic deformation of the basal graphite plane and diamond  $\{100\}$  has been probed by nanoindentation, implementing an interface description of the indenter where the atomic structure was neglected. The influence of indenter geometry was investigated utilising pyramidal and axisymmetric interface configurations. The simulations showed that tip geometry has a significant influence on the deformation around the indent. Both materials under investigation offered greater resistance to the axisymmetric interfaces than the pyramidal interface due to the significantly greater contact area. Simulations with diamond showed that indentation of the  $\{100\}$  surface can ensue in dimer reconstruction of surface atoms local to the indent. Reconstruction was least significant for indentation with the pyramidal interface and more pronounced for the axisymmetric interfaces. The paraboloid interface yielded greater dimer reconstruction than the hyperboloid, and was distributed in a axisymmetric fashion encompassing the local indentation region. Penetration with the blunter hyperboloid tip revealed reconstruction of the subsurface atoms, accompanied with fractional tip-induced plastic deformation. The damage imparted to the diamond substrate was highly localised, with no long-range



displacements of the perturbed atoms observed. The fractional plastic deformation of the diamond work piece was not reflected in the load-displacement curves and was only evidenced by visual inspection of the surfaces after the indentation.

The influence of loading rate was also examined in the MD simulations with graphite by performing both ‘fast’ and ‘slow’ tip displacements. Indentation with the unphysically fast indentation speed during the  $T = 5$  ps simulations left the substrates in a highly non-equilibrium state as surface waves oscillated about the undisturbed surface. This was attributed to the indentation speed surpassing the relaxation process in the indented specimen. The fast indentation speed ensued in unusual features in the corresponding force-depth curves. The quick extraction of the tip resulted in the unloading curve decreasing rapidly, exhibiting features usually associated with plastic deformation. However, the simulations employing the quick indentation times still described the qualitative deformation behaviour. As the indentation speed was reduced, the force acting on the interfaces generally decreased, since the more leisurely displacement of the tip allowed the substrate more time to relax to the minimum energy configuration. With the slower loading rate, the force-depth curves now reflected the elastic response of the sample, since the loading and unloading curves overlapped. This suggested that the speed of indentation was more akin to the relaxation process in the substrate.

Since the utilised Brenner potential was not correctly fitted to the elastic constants, simulations were also performed on graphite using the Tersoff potential for comparison. The corresponding force-depth curves showed the discrepancy between the two potentials affected only the quantitative results, with the qualitative behaviour of the specimen being maintained. The nanohardness of the graphite and diamond specimens was considerably less than experimental values due to the small length scales involved. With this in mind, immediate future work was aimed at extracting qualitative information about the deformation behaviour of the indented specimens. Comparisons between the MD simulation results implementing the interface indenter description with experiment [124] are made in the subsequent chapter.

Representing the indenter by a non-deformable interface is a simplistic approach. It suffers from not being able to allow the substrates to make a physical impact on the indenter. This limitation prohibits many tip-surface interaction phenomena, like tip deformation and adhesion for example, from being studied. Therefore the indenter is best described atomistically.



# Chapter 4

## Nanoindentation of Carbon Materials Implementing the Atomistic Indenter Model

### 4.1 Introduction

This chapter presents MD simulations of nanoindentation into various carbon materials, where the indenter is described atomistically. The atomistic model will allow the interaction with the substrate to have some physical impact on the indenter [141]. Thus, deformation of the tip, adhesive tip-substrate interactions and atom transfer can be studied. The simulations with the atomistic indenter model probe the indentation behaviour of graphite, adsorbate-free diamond and a crystalline film configured from C<sub>60</sub> molecules. Simulations with diamond examine indenter apex deformation by compression and adhesion, for both ‘sharp’ and ‘blunt’ tips. Termination of the indenter surfaces with an adsorbate is also considered. Indentations implementing the saturated indenter are performed on both hydrogen terminated diamond and *a*-C substrates. Simulations with the *a*-C:H substrates also investigate the hybridisation status following indentation, to ascertain tip-induced rearrangements in substrate bonding structure. In all simulations, the C-C, C-H and H-H interactions are described by Brenner’s potential for hydrocarbons [96]-[97]. Unless otherwise stated, all substrate atoms are coloured according to their vertical displacement. For simulations with graphite and the C<sub>60</sub> film, an additional Van der Waals potential is implemented to describe the long-range inter-



actions [128]. The interaction between the tip and the  $C_{60}$  film is also described by the Van der Waals potential. The MD simulations using both the interface and atomistic indenter model are also compared to the experimental results of Richter *et al* [124] for nanoindentation of highly oriented pyrolytic graphite (HOPG), synthetic diamond and a  $C_{60}$  fullerene film.

## 4.2 Atomistic Indenter Model

In the atomistic model, only one configuration for the indenter is considered. The indenter takes the form of a  $90^\circ$  pyramid, as shown in Fig. 3.3.1 (Chapter 3), and is formed by taking a cubic diamond  $\{100\}$  crystal and cutting along the  $\{111\}$  plane. The indenter is positioned such that the line  $CH$ , which denotes the direction of motion, is normal to the substrate surface. Therefore, the tip manoeuvres with the  $\{111\}$  planes parallel to the face of the sample. This particular orientation is chosen since a diamond crystal is more rigid when compressing perpendicular to the  $\{111\}$  planes, compared with the  $\{100\}$  planes. Furthermore, this is the same orientation used experimentally. However, at the atomic scale a perfect  $90^\circ$  diamond pyramid is unstable and the atoms on the three  $\{100\}$  surfaces will reconstruct. Furthermore, the tip will also develop a certain curvature at the apex.

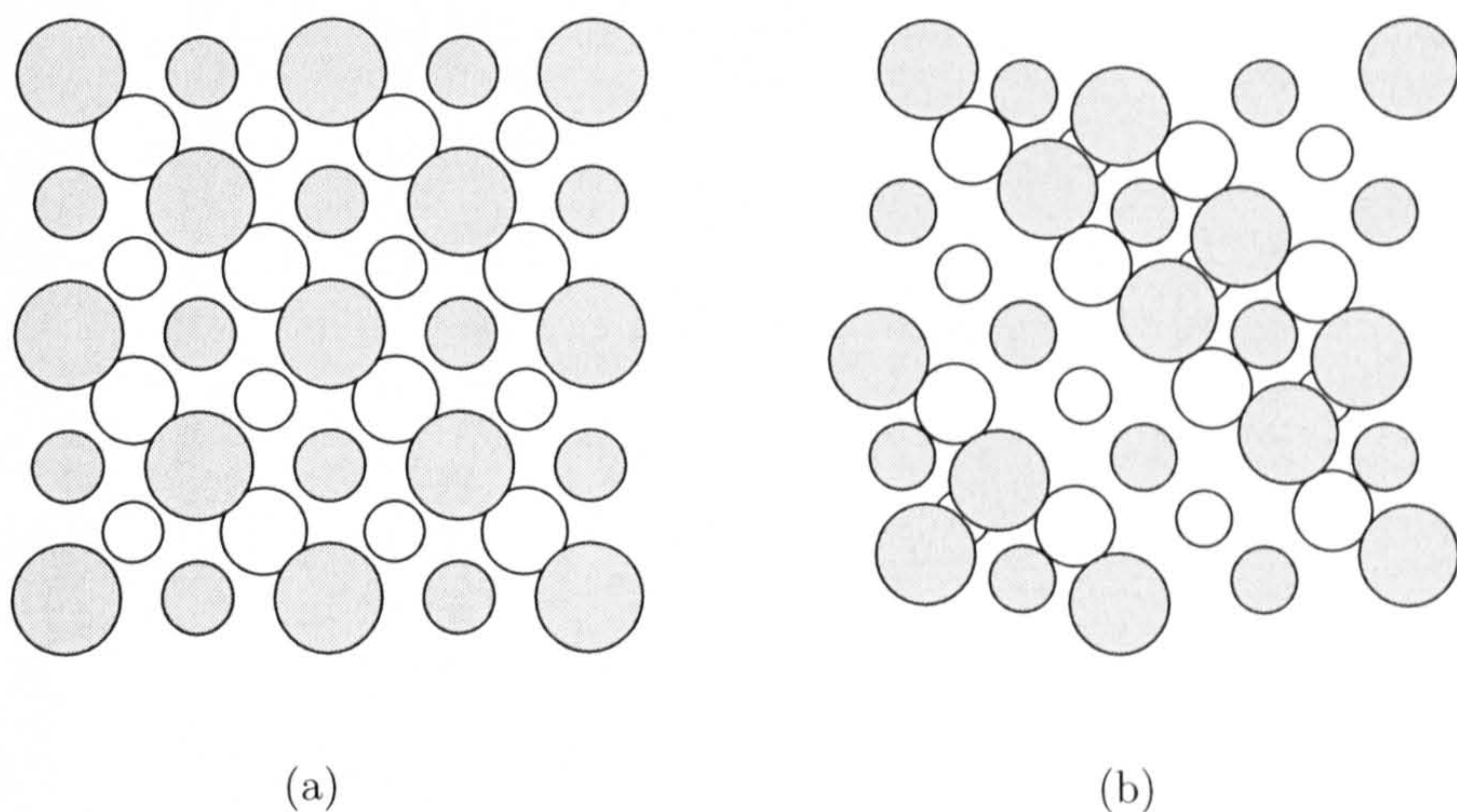


Fig. 4.4.1. Atom configuration for; (a) diamond  $\{100\}$  surface (b) reconstructed  $\{100\}(2 \times 1)$  diamond surface. Large and small shaded circles represent the first and third layer atoms respectively. The remaining large and small circles denote the second and fourth layer atoms respectively.



The atoms on the three adjacent  $\{100\}$  surfaces expose two dangling bonds. Hence, to employ the most stable indenter in the simulations, the surface atoms are dimer  $\{100\}(2\times 1)$  reconstructed as imaged in Fig. 4.4.1. The reconstruction is achieved by imparting small displacements of the  $\{100\}$  surface atoms prior to relaxation under the interatomic potential. An alternative method to dimer reconstruct the adjacent  $\{100\}$  surfaces would be to apply heat to the indenter. The dimerisation results in one of the pair of dangling bonds becoming saturated and therefore lowering the energy of the indenter. Inelastic energy loss is applied to all atoms and the indenter is allowed to equilibrate. Following relaxation, the atomic coordinates are written out to a data file. Hence, at the start of an indentation simulation, the atomic data is simply read in from the data file and appropriate positioning and dynamical data is assigned.

The diamond indenter tip is positioned at an appropriate height above the centre of the substrate surface, where the impression is to be made, outside the range of the tip-substrate interaction potential. The top two layers (i.e. the  $\{111\}$  planes) of the indenter have a prescribed motion, therefore mimicking the cantilever in the experimental procedure. The remainder of the indenter atoms are damped. The displacement of the indenter is simulated in the same quasistatic fashion as in the interface model. For each timestep, a sinusoidal displacement,  $r(t)$  (as described by Eqn. 3.2.3.2, Chapter 3), is imparted on the constrained atoms of the indenter. Hence, by displacing the rigid

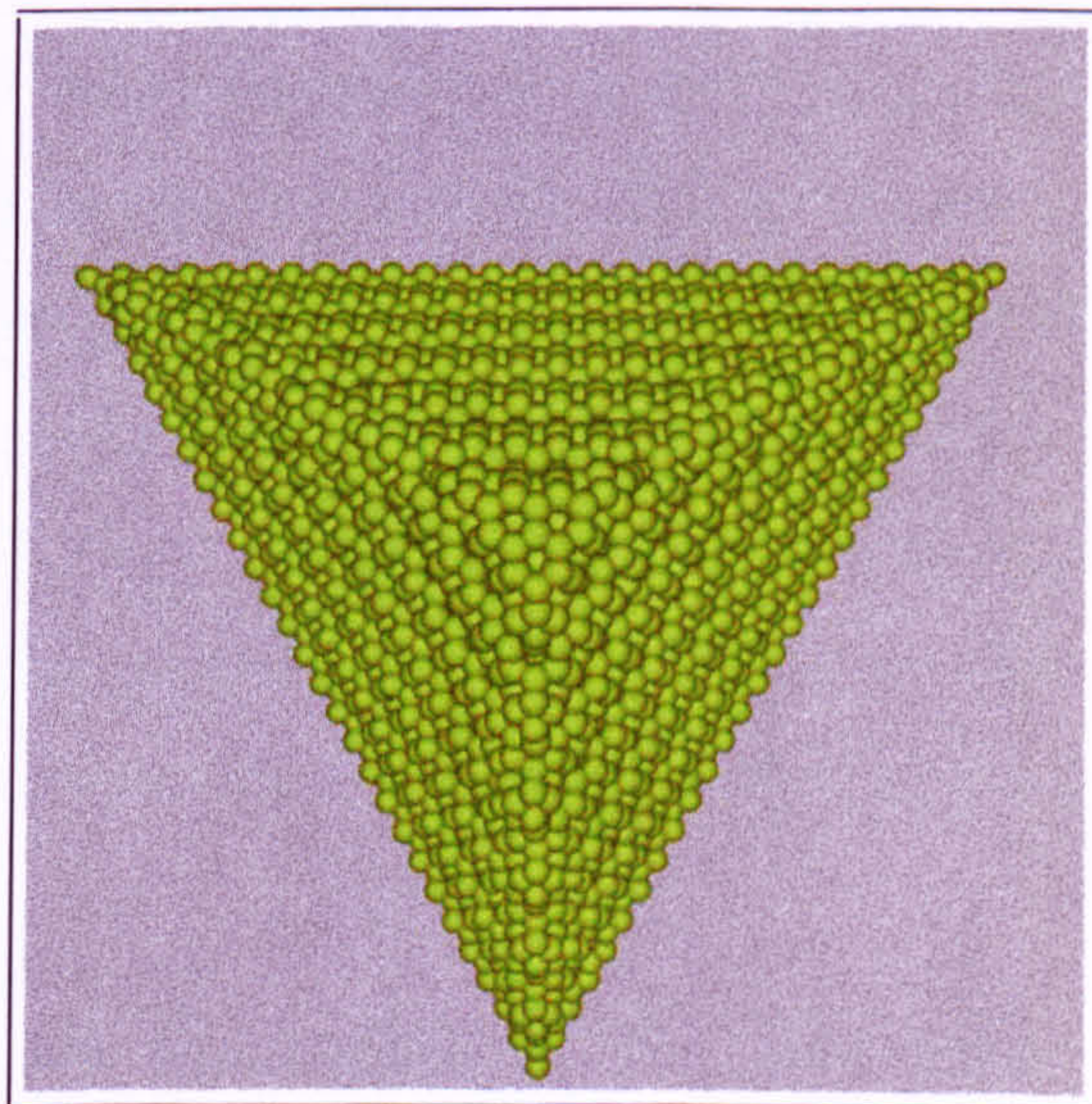


Fig. 4.4.2. Plan view of the preliminary  $90^\circ$  diamond pyramidal indenter used in the simulations. The dimer reconstruction of the three  $\{100\}$  faces is clearly seen together with the rounded apex.



atoms in the indenter, the tip will be forced to move relative to the substrate. The displacement of the constrained top layer atoms thus governs the motion of the indenter. The non-rigid atoms are displaced by integrating the equations of motion. The velocity of the fixed indenter atoms at time  $t$  is given as

$$v(t) = \frac{\pi}{T} r_{\max} \cos\left(\frac{\pi t}{T}\right) \quad (4.2.4.1)$$

At time  $t = 0$ , all the atoms constituting the indenter have an assigned velocity of  $r_{\max}\pi/T$ . The indentation depth is measured by calculating the distance between the lowermost central carbon atom in the indenter tip and the undisturbed substrate surface. Mechanical contact is made when the tip-substrate separation is comparable to inter-atomic separation. The force acting on the indenter is simply determined by summing all the vertical force components on each constituent atom of the indenter, thus

$$F_{y_{total}} = \sum_{tip} F_{y_i} \quad (4.2.4.2)$$

In the preliminary simulations with the atomistic indenter model, a diamond pyramid is implemented with an approximate maximum depth  $h = 26 \text{ \AA}$ , as illustrated in Fig. 4.4.2. The structure is composed from 4,056 atoms with 784 atoms fixed in the top  $\{111\}$  plane, which has a side of approximate length  $a = 68 \text{ \AA}$ . The simulated indenter is about 100 times smaller in size than some of the finest tips used in experiments. The first two layers of the diamond apex in the  $\{111\}$  plane were truncated prior to relaxation under the many-body potential. The truncation of the  $\{111\}$  layers in the tip produces a blunt apex which, after relaxing to the minimum energy configuration, produces a small degree of curvature. Clearly this is still an approximation to the true experimental situation, where measurements have shown that a tip can have a radius of curvature up to several tens of nanometres, especially after continued use [124],[142]. Although curvature has been added to the apex, the tip is still atomically sharp.

## 4.3 Simulation Results and Discussion

### 4.3.1 Graphite $\{0001\}$ Substrate

Simulations with graphite are performed employing the small substrate implemented with the interface indenter model in the preceding chapter. The indentation period is



$T = 50$  ps and the maximum displacement of the constrained indenter atoms,  $r_{\max}$ , is set to 12 Å with the indenter apex sited 4 Å above the graphite surface. This yields a maximum indentation depth of 8 Å and an average indentation speed of 48 ms<sup>-1</sup>. The simulation is run for a duration of 50 ps with a fixed timestep of 0.5 fs. The overlapping loading and unloading curves in Fig. 4.4.3(a) reflect a purely elastic deformation in response to indentation. The apex has compressed during the loading stage of the indentation process, since the maximum penetration depth of the indenter is 6.5 Å and not 8 Å as specified at the start of the simulation. Fig. 4.4.3(b) shows the diamond tip begins to constrain as it penetrates the graphite surface and continues to compress by a maximum of 1.5 Å, occurring at the halfway stage of the indentation process. The maximum compression of 1.5 Å corresponds to approximately 19 % of the specified 8 Å indentation distance into the graphite substrate. As the indenter is extracted from the substrate, the compression begins to relax and the indenter returns to its initial configuration at a depth of approximately 2 Å. Hence, the indenter only deforms elastically and maintains its structural integrity.

Fig. 4.4.3(a) shows that the peak force acting on the indenter was approximately 7 eV/Å, which occurred when the tip reached its peak indentation depth of 6.5 Å. The  $T = 50$  ps simulation with the pyramidal interface showed a peak repulsive force from

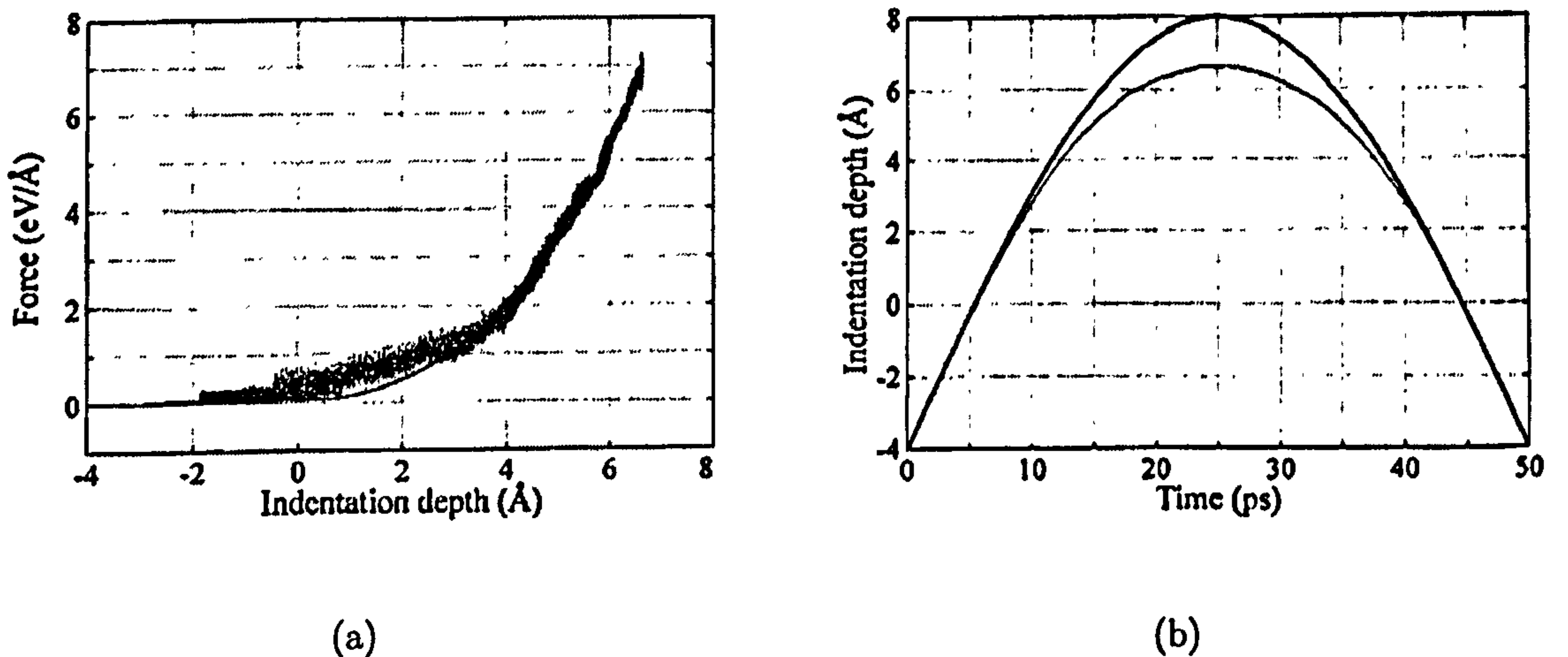


Fig. 4.4.3. (a) Force-depth curve from the simulation of indentation into the graphite {0001} crystal. (b) The displacement of the apex during the simulation. The thin line represents the tip position during the simulation and the bold line denotes how the tip would displace in the absence of the substrate.



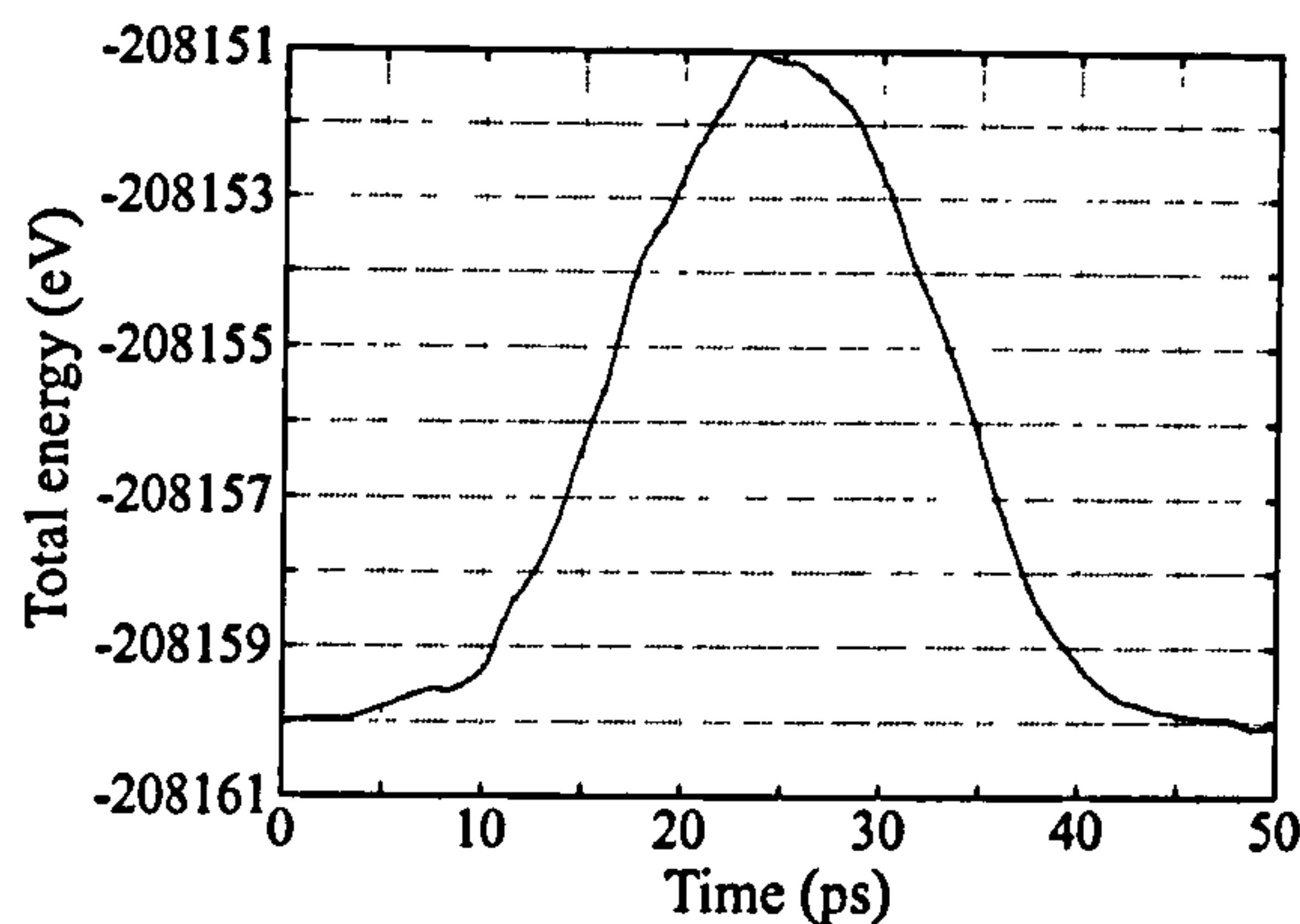


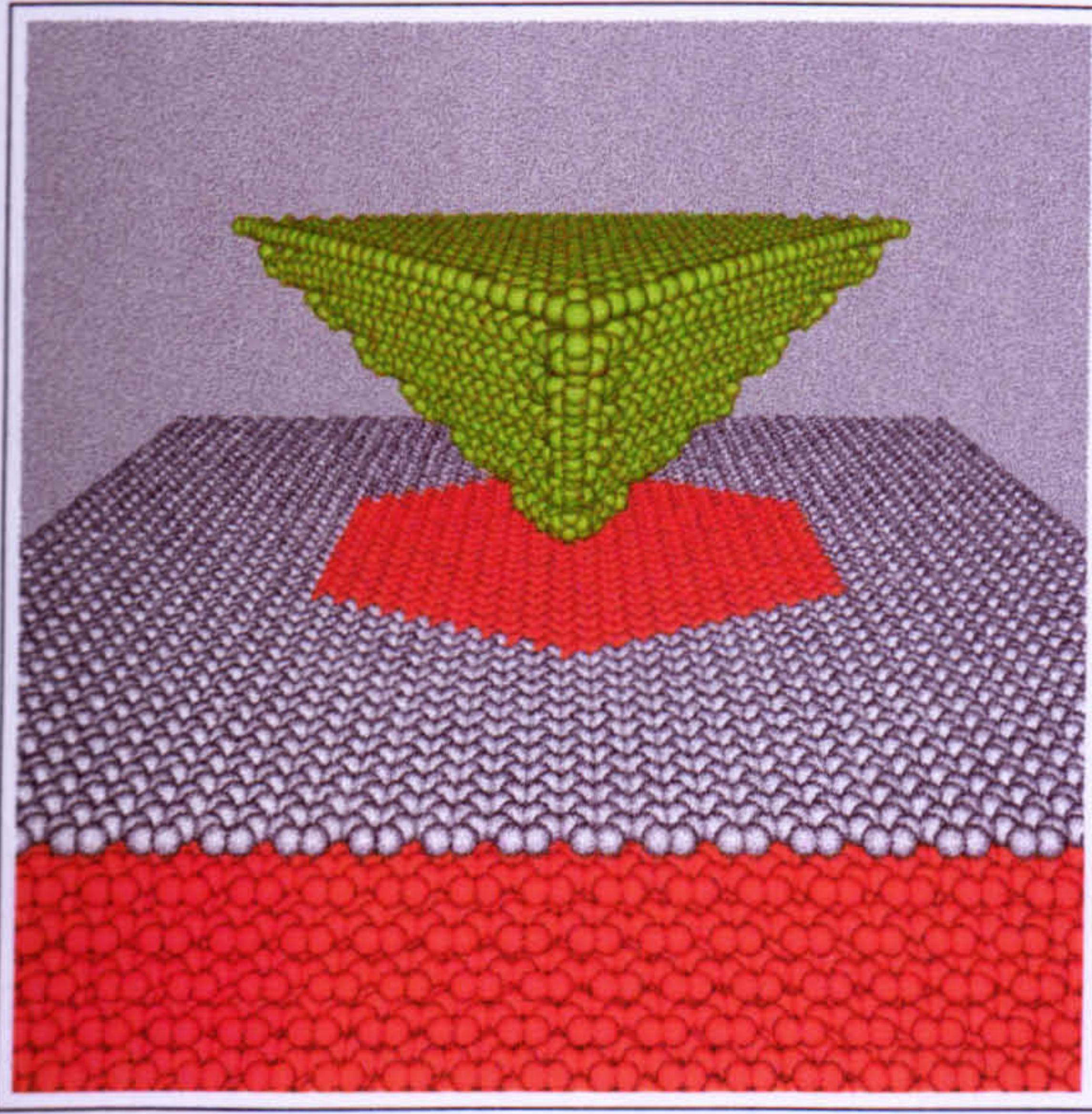
Fig. 4.4.4. Total energy of the graphite {0001} crystal during the indentation process.

the graphite of approximately  $10 \text{ eV/\AA}$  at maximum penetration (Fig. 3.3.10, Chapter 3), which is in good agreement with peak force obtained with the atomistic model of the indenter. Fig. 4.4.3(a) exhibits an oscillatory nature of the force during the loading stage of the indentation process. The largest oscillations occur during the first  $4 \text{ \AA}$  of indentation. As the apex advances towards the indentation limit the oscillations decrease. The unloading component of the curve shows a comparatively smooth decrease in force. The speed at which the indenter penetrates and extracts from the graphite surface, causing quick displacement of atoms, gives rise to these oscillatory features. Simulations utilising the same depth of indentation carried out over longer periods of time, show the oscillations in force decrease.

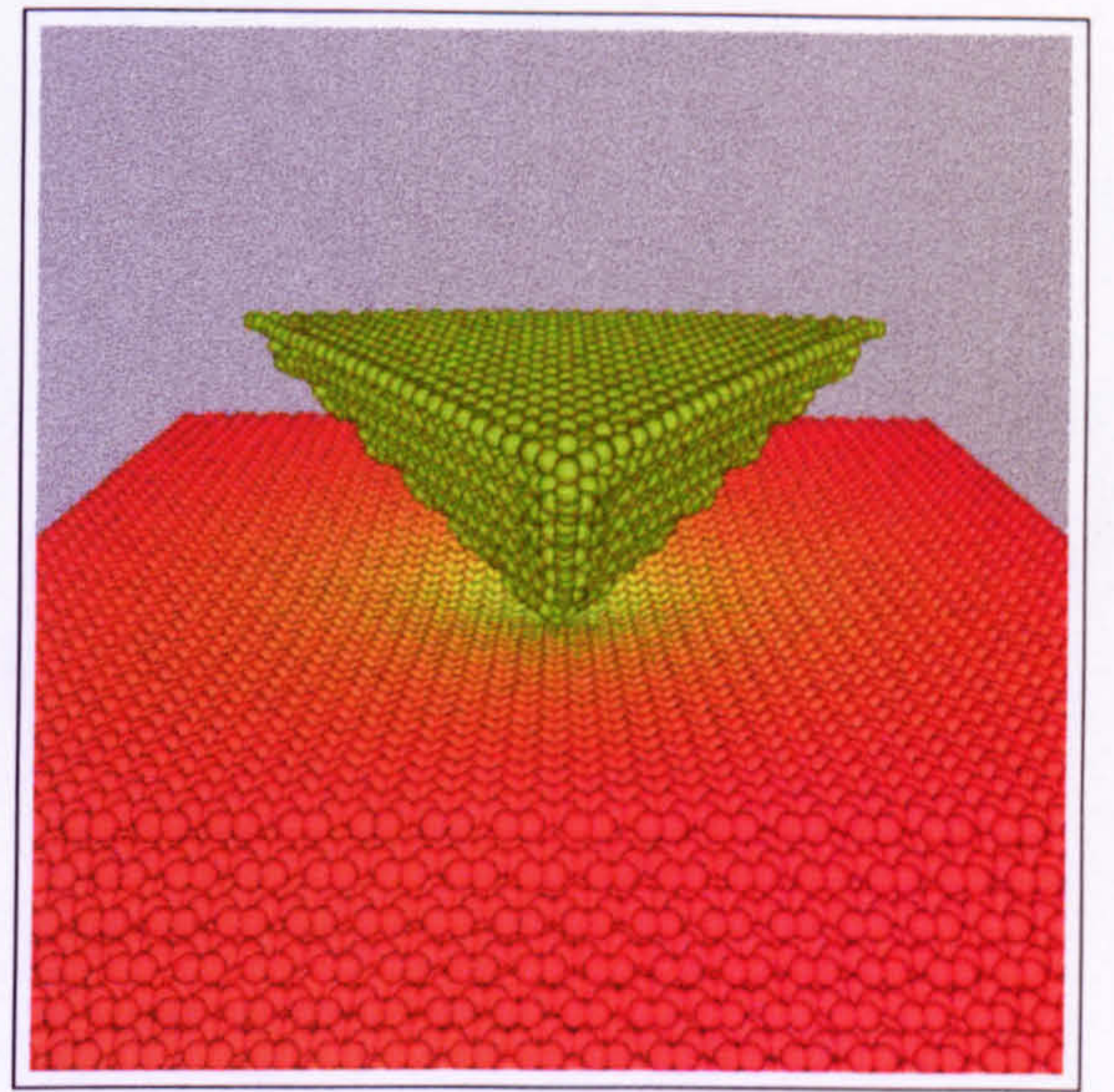
Shown in Fig. 4.4.4 is the total energy of the graphite substrate during the indentation. The maximum energy added to the graphite substrate is about  $9 \text{ eV}$ , which occurs approximately just before the halfway stage of the indentation process, at  $t = 23.5 \text{ ps}$ . Comparison with Fig. 3.3.14 (Chapter 3) shows this is lower than the maximum energy added to the graphite by the cube-cornered interface, in the  $T = 50 \text{ ps}$  simulation. This is because the atomistic indenter penetrates less into the work material, due to compression of the apex.

Two snapshots during indentation of the graphite crystal are presented in Fig. 4.4.5. A hexagonal wave of displacing graphite atoms propagating across the substrate surface is shown in Fig. 4.4.5(a) at  $t = 2.8 \text{ ps}$ . The form of the wave clearly reflects the hexagonal structure of the graphite substrate. The halfway stage of the indentation process, at  $t = 25 \text{ ps}$ , is shown in Fig. 4.4.5(b). After extraction of the diamond tip, oscillatory hexagonal surface and subsurface waves were observed, which continued to oscillate for an extended period of time. There is no adhesion between the tip and the substrate





(a)



(b)

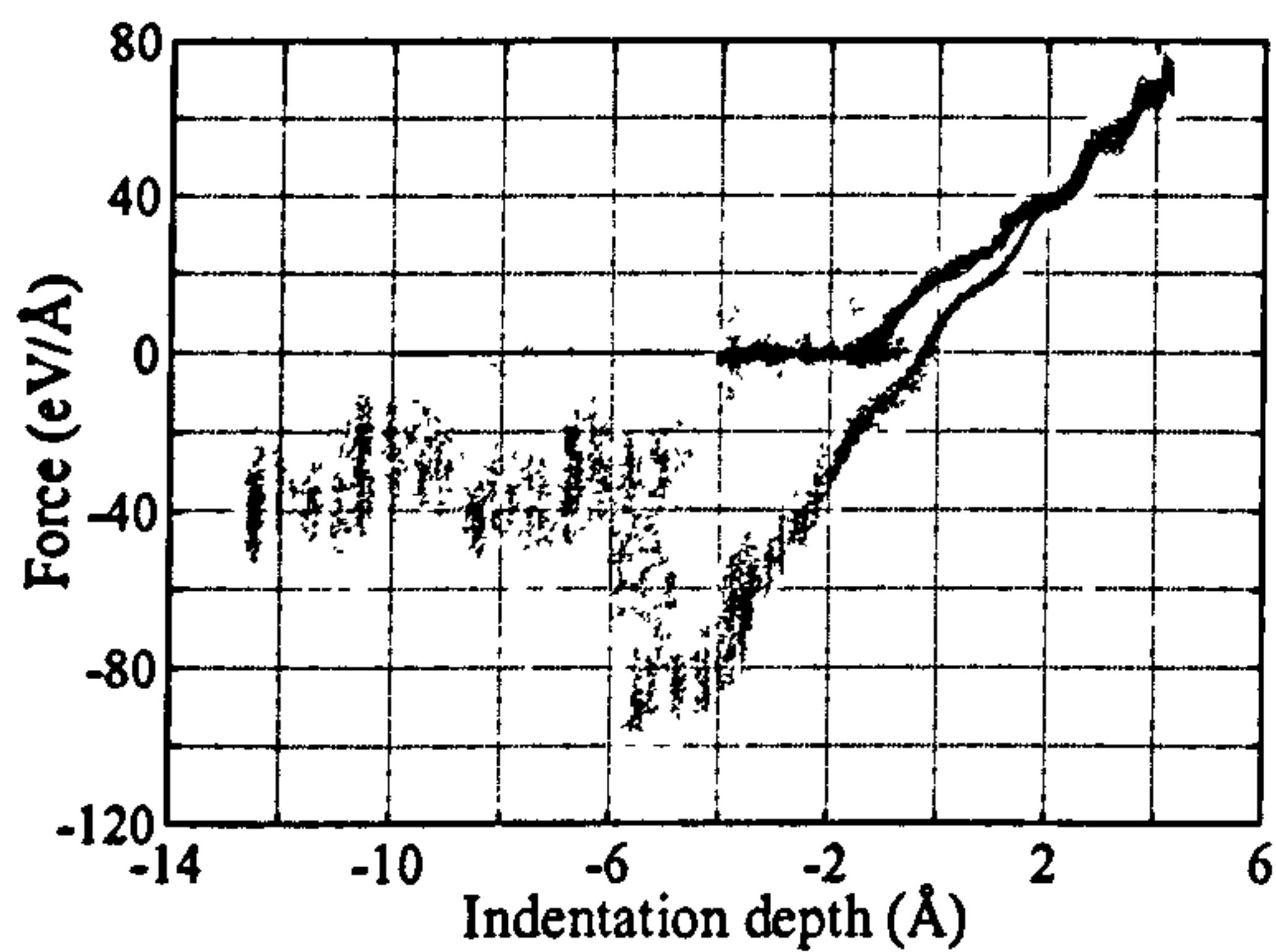
Fig. 4.4.5. Snapshots from the simulation of indentation into the graphite  $\{0001\}$  crystal. (a) The indentation process at  $t = 2.8$  ps. Note the hexagonal wave propagating across the graphite surface. The white shaded atoms represent the undisturbed surface. (b) Halfway point of the indentation process at  $t = 25$  ps.

since the graphite surface is rather inert towards the diamond indenter. The *ab-initio* analysis by Ciraci *et al* [143] reported on the indentation between an Al tip and graphite  $\{0001\}$  and observed significant tip-sample interaction with bond formation.

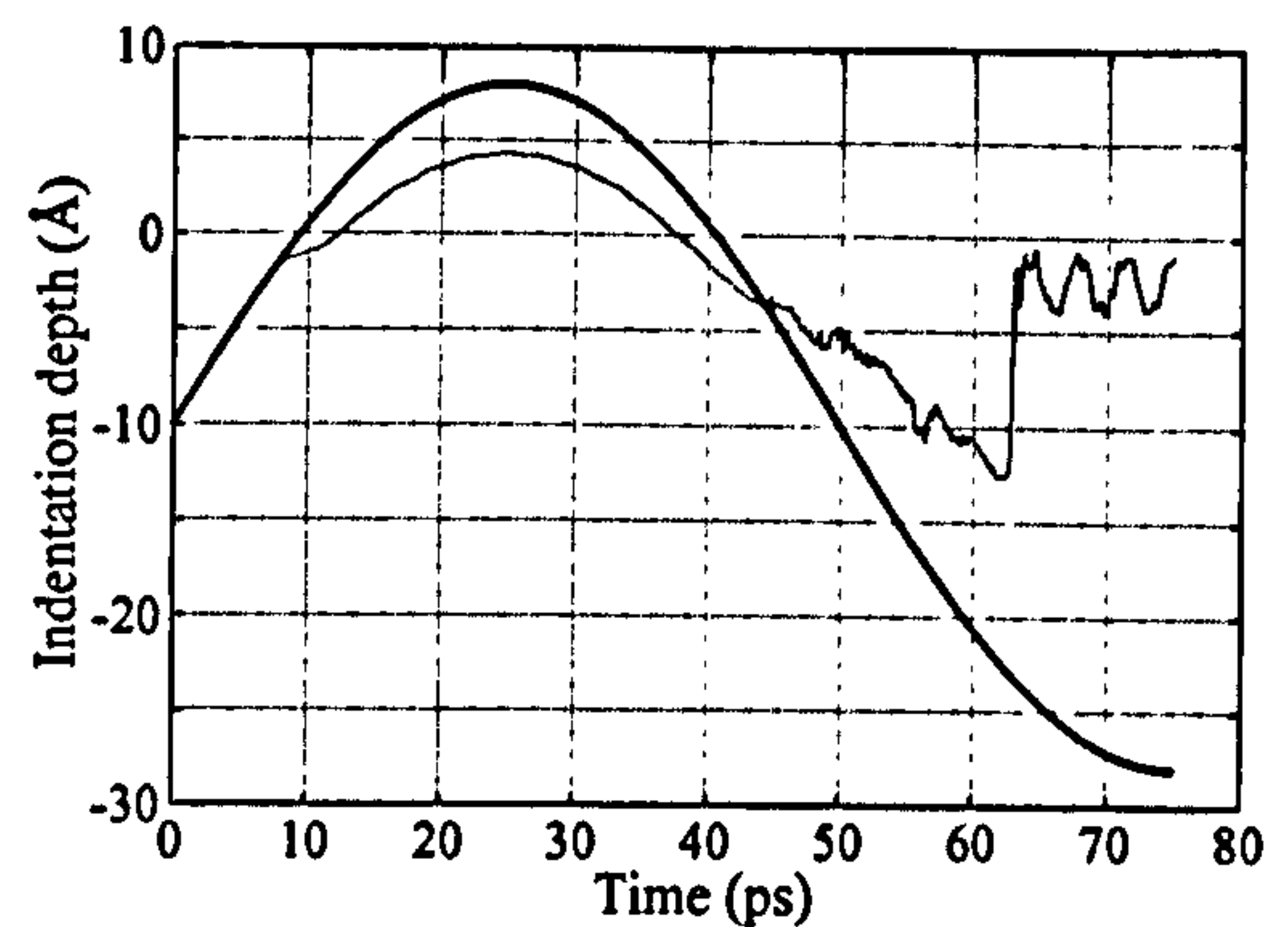
### 4.3.2 Diamond $\{100\}$ Substrate

Unless otherwise stated, simulations with pure diamond are performed employing the same small crystal implemented with the interface indenter model in the preceding chapter. The surface atoms of all diamond  $\{100\}$  substrates are dimer reconstructed, as illustrated in Fig. 4.4.1, and allowed to relax fully to the minimum energy configuration before commencing the indentation. The indentation period is  $T = 50$  ps and the maximum displacement of the fixed indenter atoms,  $r_{\max}$ , is set to  $18 \text{ \AA}$  with the indenter apex sited  $10 \text{ \AA}$  above the diamond surface. This gives a maximum indentation depth of  $8 \text{ \AA}$  and an average indentation speed of  $72 \text{ ms}^{-1}$ . The simulations with diamond substrates are run with a fixed timestep of  $0.5 \text{ fs}$  for a duration of  $75 \text{ ps}$  to allow further retraction of the tip to study interfacial adhesion. The load-displacement curve in





(a)



(b)

Fig. 4.4.6. (a) Force-depth curve from the simulation of indentation into the diamond {100} crystal. The upper curve corresponds to the loading stage. (b) The displacement of the apex during the simulation. The thin line represents the tip position during the simulation and the bold line denotes the how the tip would displace in the absence of the substrate.

Fig. 4.4.6(a) exhibits various atomic-scale events during the indentation. As with the graphite substrate, the force-depth curve for the diamond crystal also shows oscillations in the force. The loading and unloading curves in Fig. 4.4.6(a) overlap in the region from 2 Å to 6 Å, showing the deformation to be elastic over this range. The diamond tip indented to a maximum depth of 4.5 Å, where the reacting force was approximately 80 eV/Å. The  $T = 50$  ps simulation with the cube-cornered interface showed a peak repulsive force of approximately 89 eV/Å from the diamond crystal (see Fig. 3.3.16, Chapter 3) when the tip reached the maximum indentation depth.

Fig. 4.4.6(b) shows the compression of the indenter apex during the indentation. Comparing Fig. 4.4.3(b) with Fig. 4.4.6(b) shows the indenter apex begins to compress only when it has reached the small graphite surface, whereas the compression of the tip initiates just above the the surface of the diamond work material. Furthermore, the indenter tip has compressed by approximately 3.5 Å at maximum penetration, i.e. by about 44 % of the specified 8 Å indentation distance into the diamond substrate, compared to the value of about 17 % for the graphite work piece. The greater nanohardness of diamond compared with graphite is clearly reflected by the greater compression of the tip and the greater force exerted on the indenter. The compression of the indenter tip at the maximum penetration depth in the diamond {100} substrate is shown in Fig. 4.4.7.



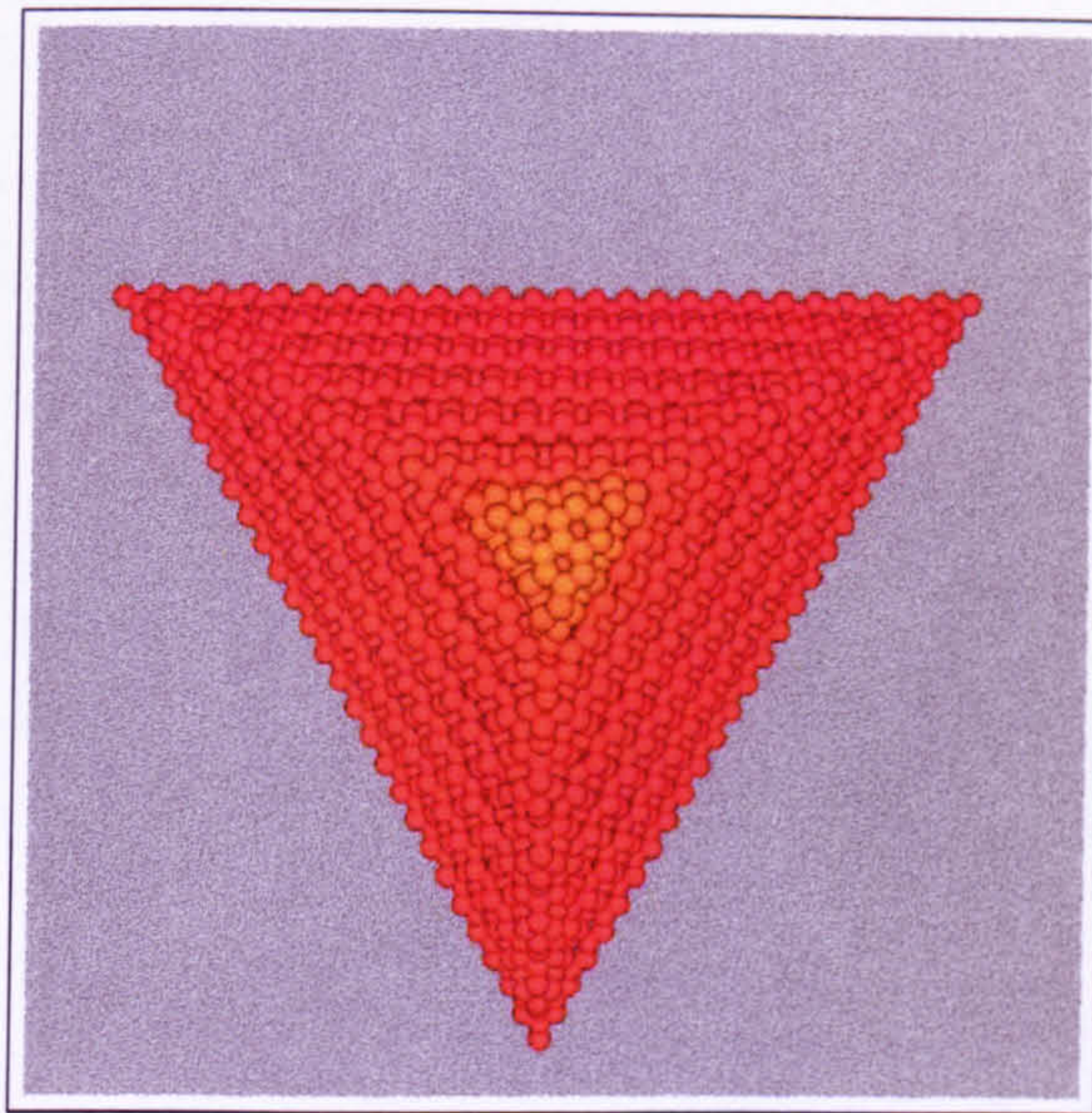


Fig. 4.4.7. A plan view of the diamond indenter at the maximum indentation depth into the diamond  $\{100\}$  substrate. The atoms are shaded according to their vertical compression during the indentation. The red shaded atoms denote those atoms that have not compressed.

The tip compression is highly localised around the apex within a few atomic layers. This is because the tip is atomically sharp and hence, the tip atoms have low coordination. Since the network structure of diamond is not sufficiently formed in the apex, the mechanical strength of the acute tip is less compared with bulk diamond and hence, it compresses more easily. Both Fig. 4.4.3(b) and Fig. 4.4.6(b) show the tip compresses rapidly during initial mechanical contact. After several atomic layers in the apex, the diamond network structure is sufficiently developed such that indentation then ensues primarily in deformation imparted to the substrate rather than further compression of the tip. As the indenter penetrates the surface of the work piece the tip is slightly twisted, which is clearly seen in Fig. 4.4.7.

The negative force in Fig. 4.4.6(a) arises from interfacial bonding between the indenter apex and the surface atoms of the diamond lattice. This occurs because the carbon atoms on the diamond surface only have three covalent bonds with the nearest neighbours, leaving a fourth unsaturated bond dangling on the surface. The force of adhesion, which is the force required to pull-off the tip from the substrate, is approximately  $100 \text{ eV}/\text{\AA}$ . Fig. 4.4.6(b) shows the indenter is still compressed as the tip is pulled out from the surface but at approximately  $4 \text{ \AA}$  above the diamond face, the indenter tip begins to elongate due to the bonding with the work material. At approximately



13 Å above the substrate, the force exerted by the surface atoms becomes sufficient to break the bonding with the apex. A number of the atoms constituting the indenter tip become permanently displaced and are bonded to the substrate surface. However, none of the diamond substrate atoms are found bonded to the indenter after rupture of the interfacial bonding.

Snapshots of the simulation indenting the diamond work material are presented in Fig. 4.4.8<sup>1</sup>. The halfway stage of the indentation process is shown in Fig. 4.4.8(a) at  $t = 25$  ps. Fig. 4.4.8(b)-(d) reveal the process whereby blunting of the indenter apex can occur. As the indenter is extracted from work material, Fig. 4.4.8(b) shows the bonding of the indenter tip with the substrate produces connective 'threads' of atoms, as marked by the arrows. This causes the surface of the diamond substrate to rise up towards the indenter. The connective strands of atoms form from the indenter apex where the atoms have low coordination. The threads of atoms measured up to a maximum of approximately 9 Å and are formed almost entirely from indenter atoms. The indenter tip becomes highly disordered as the connective threads of atoms form. Fig. 4.4.8(c) shows the connective skeins of atoms break as the indenter displaces further away from the work piece. The threads of connective atoms do not break near the substrate surface or near the indenter apex, but approximately halfway between. The blunted apex then reconstructs and Fig. 4.4.8(d) shows a ring of carbon atoms formed during the recrystallisation process, as marked by the arrow. After rupture of the connective threads, the atoms around the apex vibrated vigorously and the surface of the work piece was observed oscillating about the undisturbed surface. Fig. 4.4.8(d) also shows the 53 atoms composing the indenter tip that have been permanently displaced and remain bonded to the substrate surface in an amorphous arrangement. This is shown in detail in Fig. 4.4.9(a), while Fig. 4.4.9(b) shows that some of the substrate surface atoms have been permanently displaced above the dimer rows, as marked by the arrows. However, the subsurface layers remain intact so the recovery of the substrate is highly elastic, although the displacement of a few local surface atoms suggests fractional adhesion-induced plastic deformation.

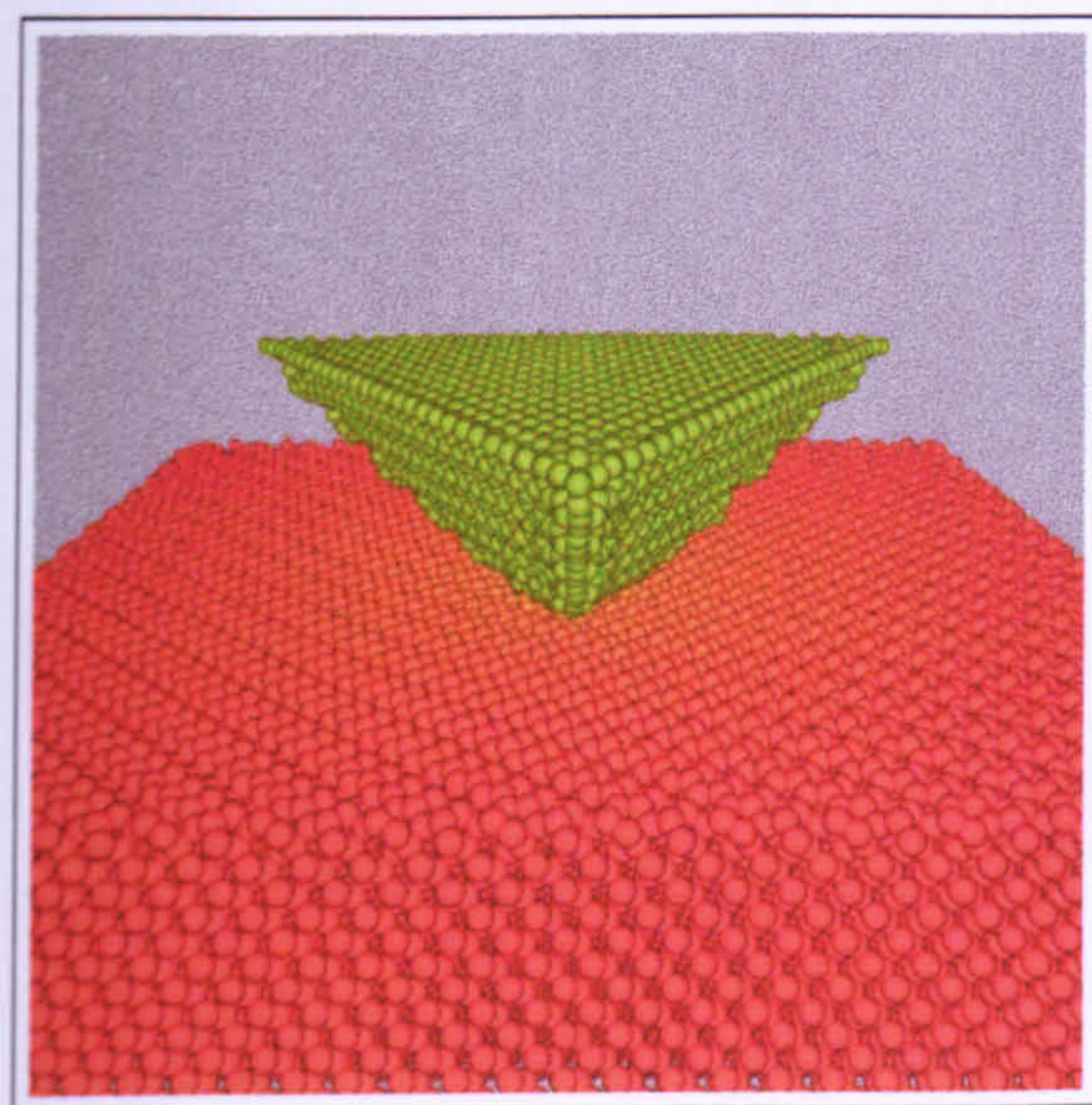
The total energy of the diamond work material during the indentation process is shown in Fig. 4.4.10. The peak energy added to the work piece during the indentation was approximately 140 eV, compared with 200 eV using the interface description of the

---

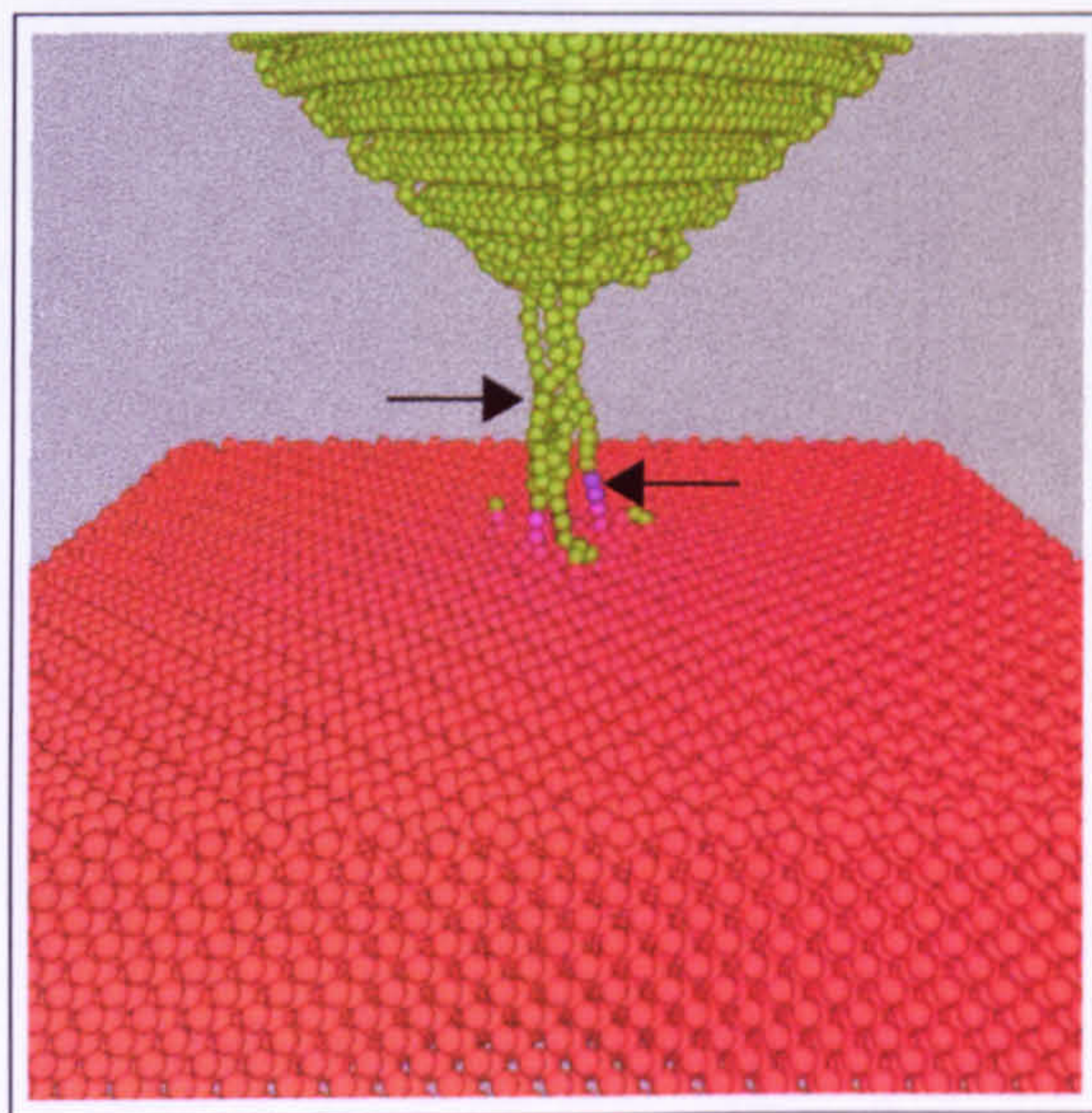
<sup>1</sup>An animated movie of this is on the CD in the Appendix



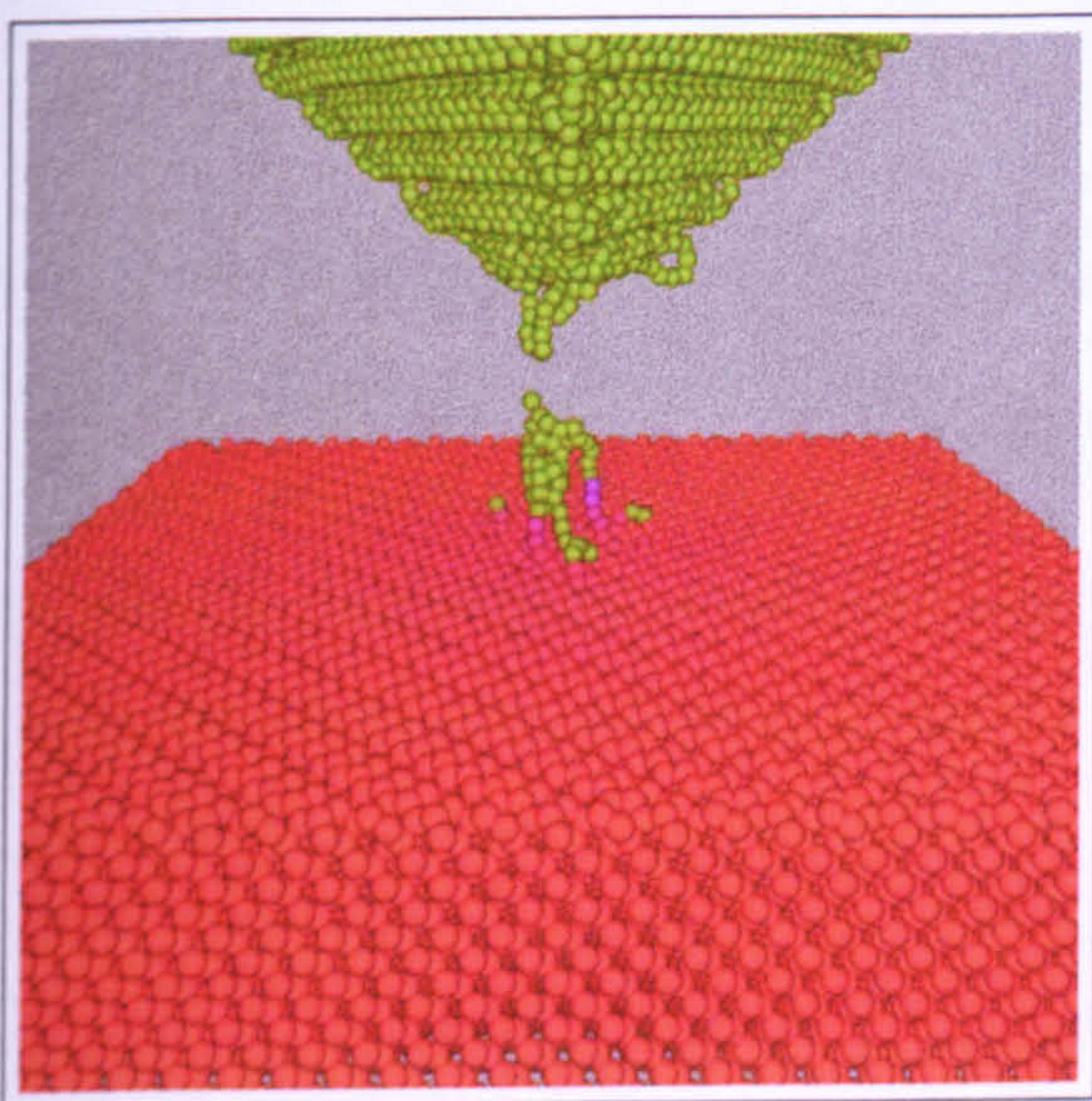
pyramidal indenter. As the apex is extracted from the surface, the substrate energy increases as interfacial bonding exerts a pulling force on the substrate surface. The energy peaks just before  $t = 50$  ps where a few ‘strands’ of indenter atoms are broken and then



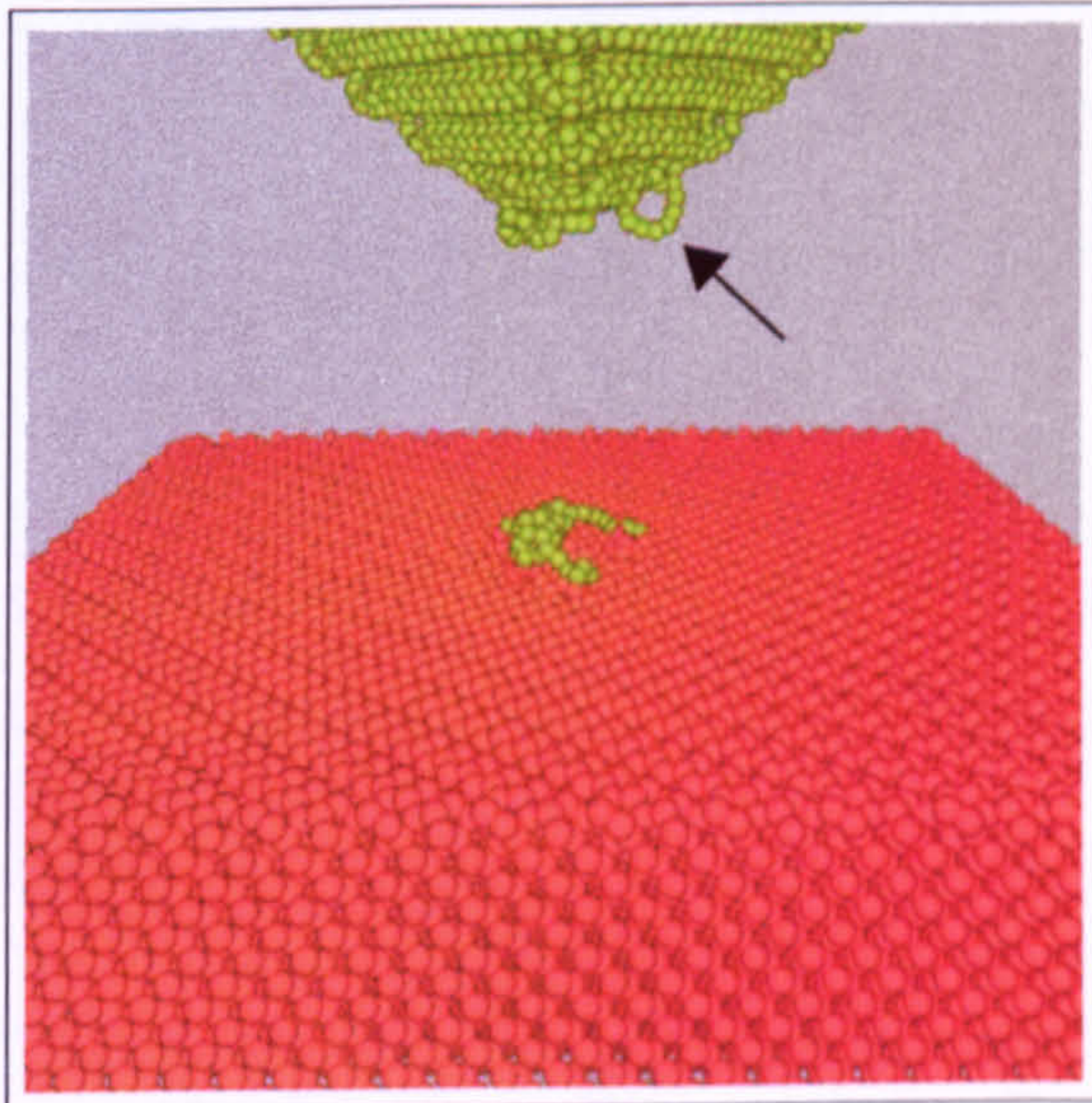
(a)



(b)



(c)



(d)

Fig. 4.4.8. Snapshots from the simulation of indentation into the diamond  $\{100\}$  crystal. The indentation process at: (a)  $t = 25.0$  ps; (b)  $t = 60.9$  ps; (c)  $t = 62.8$  ps; (d)  $t = 75.0$  ps. Note the connective ‘threads’ of indenter atoms and the ring of atoms formed as the apex reconstructs, as marked by the arrows.



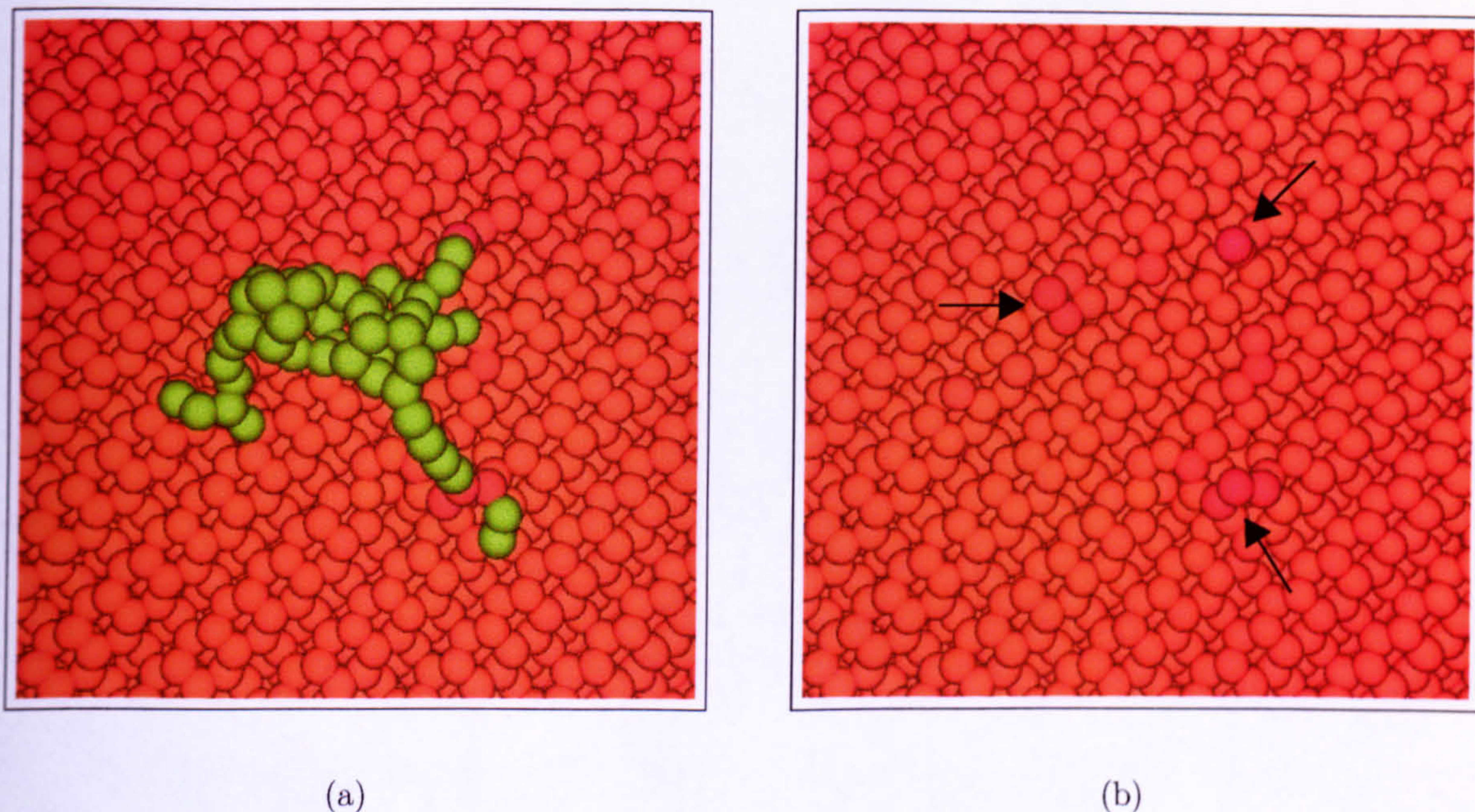


Fig. 4.4.9. The indentation region of the diamond  $\{100\}$  crystal surface at completion of the simulation showing the adhesion-induced plastic deformation. (a) The indenter atoms bonded to the diamond surface in an amorphous arrangement. (b) The primarily elastically recovered surface together with the permanent displacement of some surface atoms, as marked by the arrows.

starts to decrease. As the final ‘threads’ of atoms are ruptured at approximately  $t = 62.8$  ps, the energy decreases further.

Since the indenter tip compresses easily due to low atom coordination, indentation on the diamond substrate has also been performed with a blunt tip indenter. The diamond indenter is blunted by truncating the lowermost eight atomic layers of the tip in

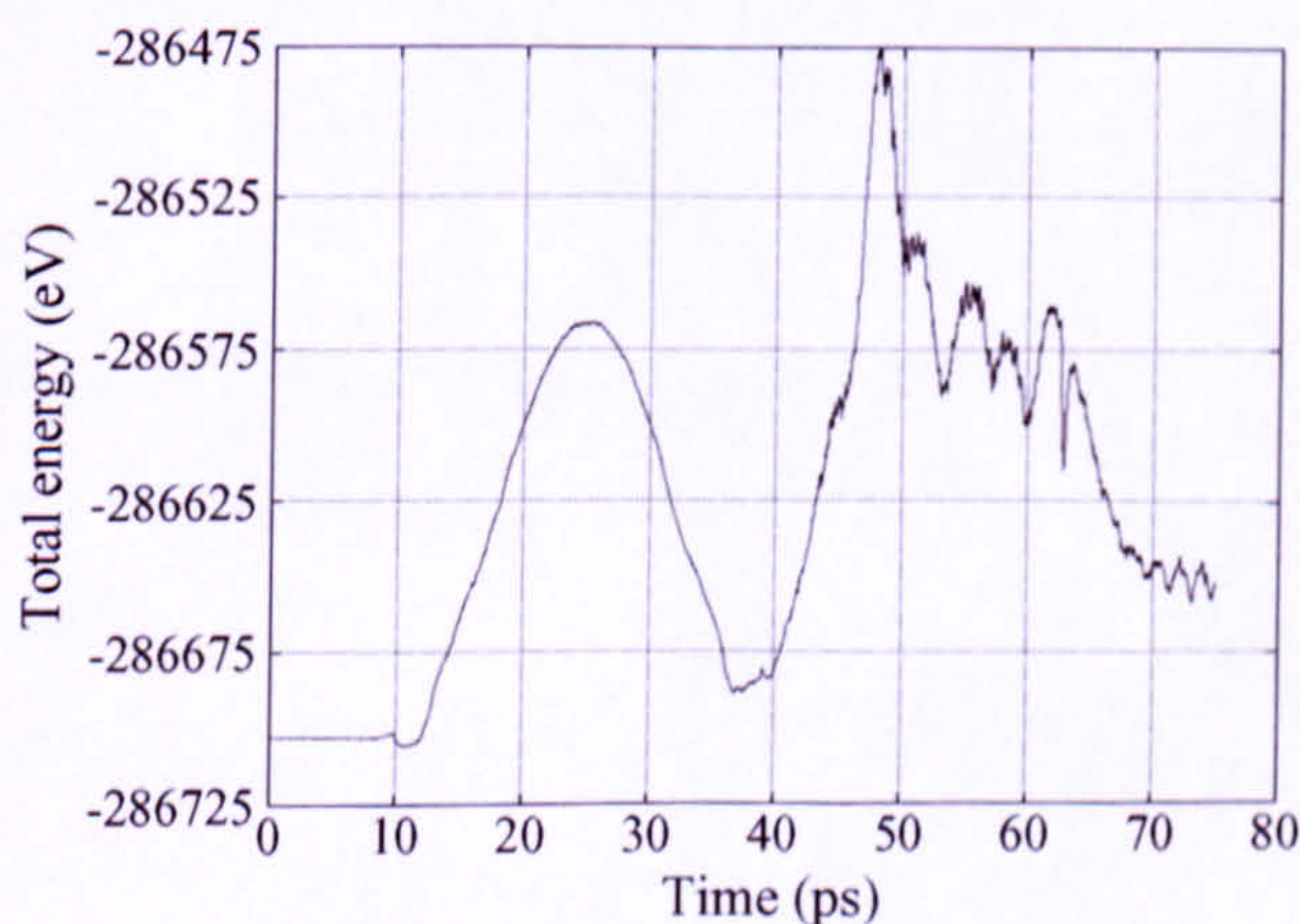


Fig. 4.4.10. Total energy of the diamond  $\{100\}$  crystal during the indentation process.



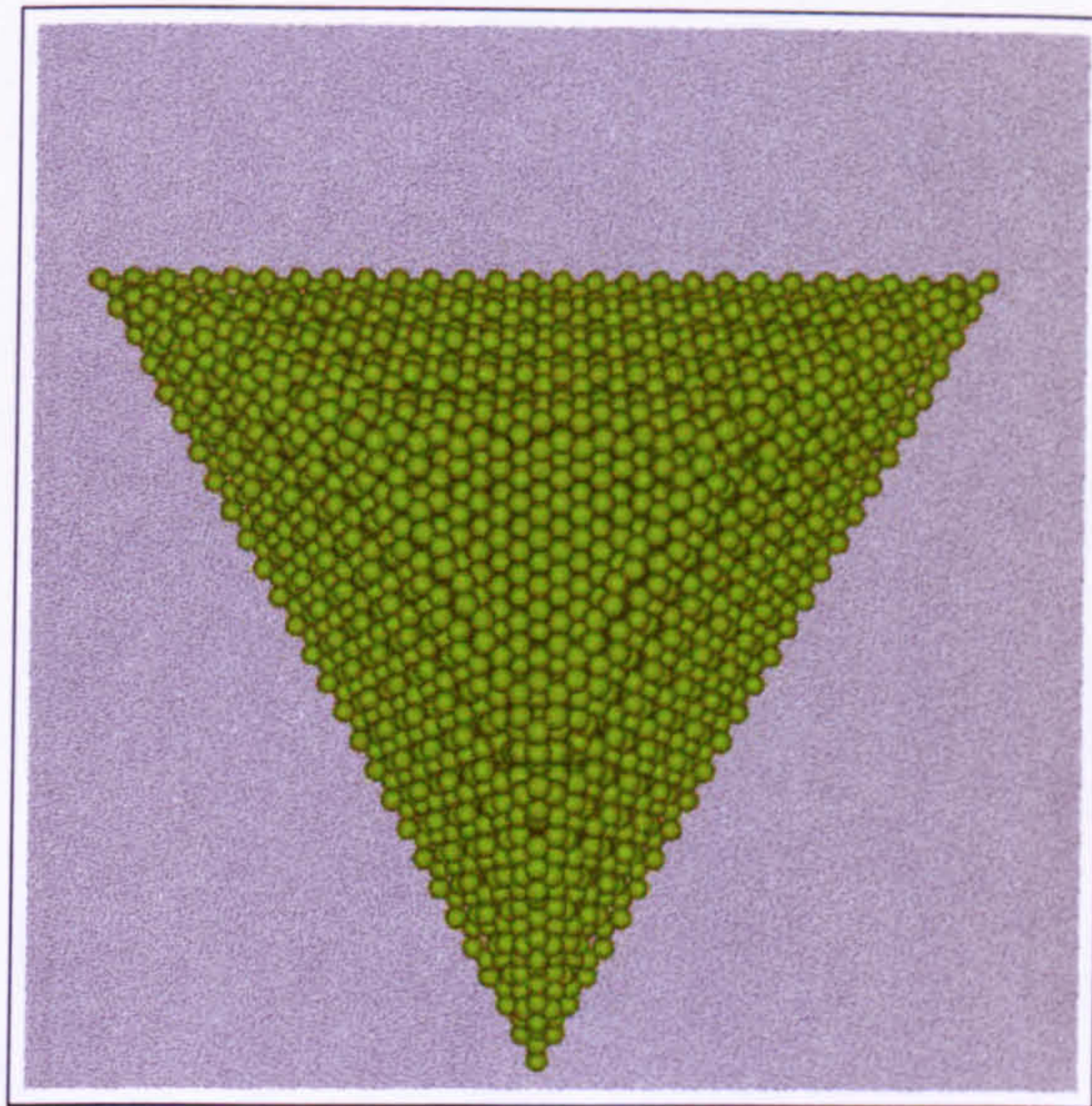
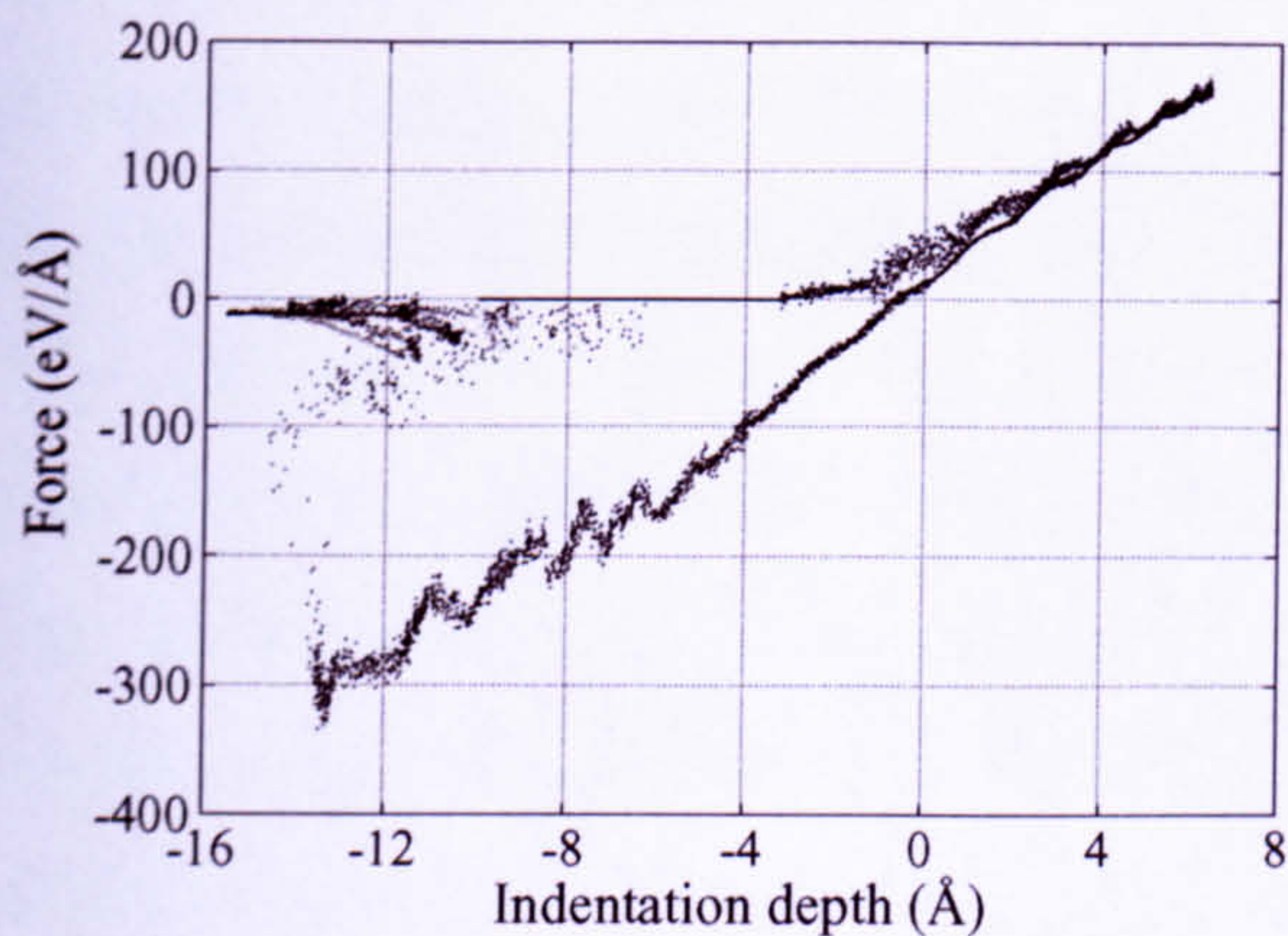


Fig. 4.4.11. Plan view of the blunt ‘flat’ tip diamond pyramidal indenter.

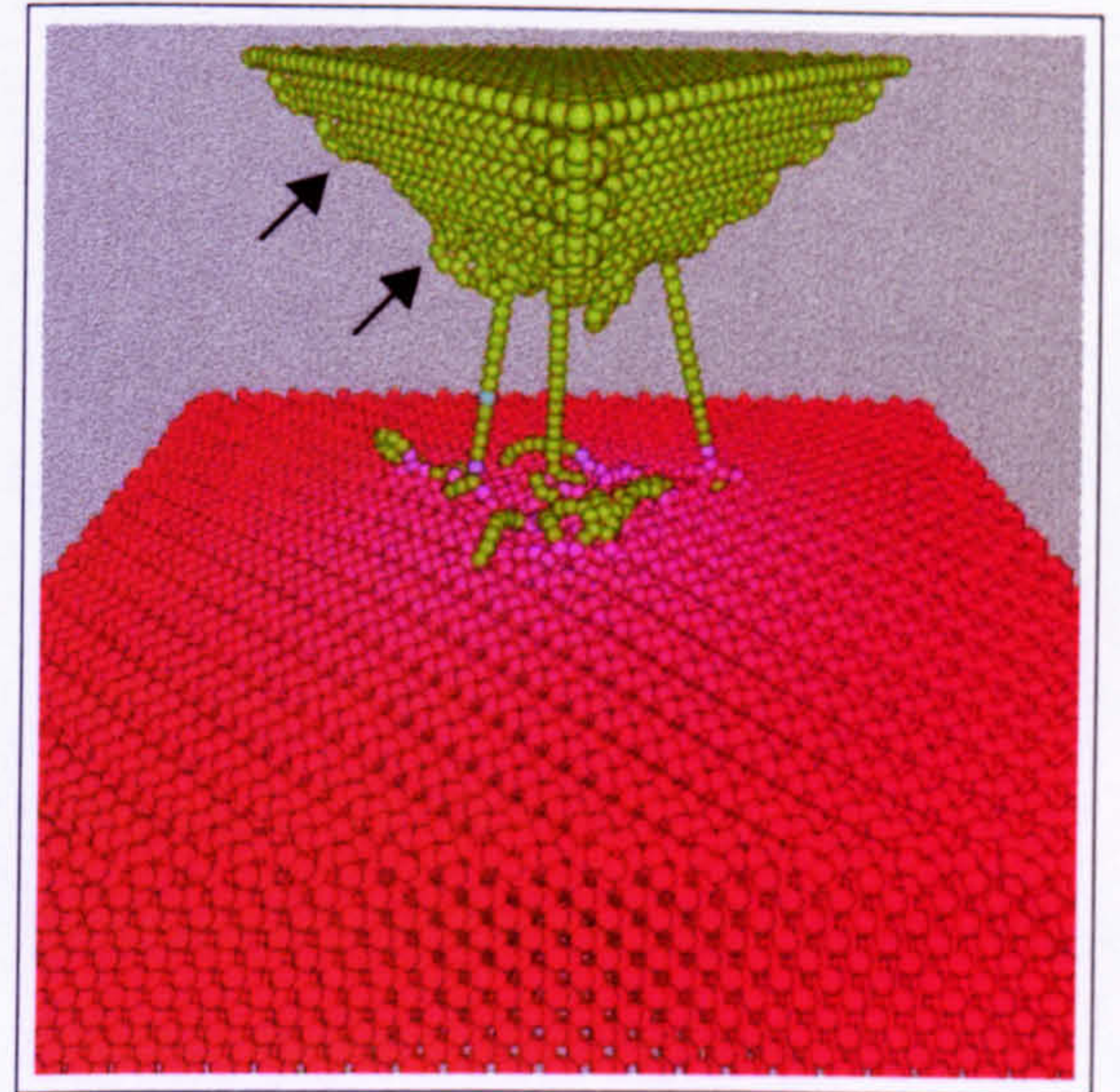
the  $\{111\}$  plane. The indenter tip is therefore ‘flat’ and not rounded as in experiment. The small indentation depth constrains the size of the indenter such that the apex is too small to blunt by rounding to give a well defined radius of curvature. Larger substrates will permit greater indentation depths, where blunting of the indenter tip by rounding will be feasible. The diamond indenter, as illustrated in Fig. 4.4.11, is configured from 3,940 atoms with a height  $h \approx 21 \text{ \AA}$  and side length  $a = 68 \text{ \AA}$ .

The force-depth curve for indentation of the diamond work material with the blunt ‘flat’ tip indenter is shown in Fig. 4.4.12(a). The indenter tip reached a maximum indentation depth of approximately  $6.5 \text{ \AA}$ , thus compressing by  $1.5 \text{ \AA}$ . As would be expected the compression is much less compared with the indenter having a single atom apex. A snapshot of the conclusion of the simulation is shown in Fig. 4.4.12(b). The tip-substrate adhesion has clearly imparted more damage to the substrate surface compared with Fig. 4.4.8 because the tip compressed less and indented further. However, the adhesion does not occur primarily with the apex atoms, since they are more highly coordinated than in the previous simulation. Instead, the adhesion predominantly develops with indenter atoms sited along the edges where the adjacent  $\{100\}$  planes intersect since atom coordination is low. This is clearly illustrated in Fig. 4.4.12(b) by the three connective threads protruding from the indenter edges. The apex-substrate adhesion has resulted in considerable damage along one edge of the indenter, as marked by the arrows in Fig. 4.4.12(b). At the conclusion of the indentation, the indenter and the substrate are still bonded by connective threads of atoms. The influence of ‘sharp’ and





(a)



(b)

Fig. 4.4.12. (a) Force-depth curve from the indentation of the diamond  $\{100\}$  substrate with the blunted indenter tip. (b) Snapshot of the conclusion of the simulation at  $t = 75$  ps. The arrows show the damage along one edge of the indenter caused by rupture of the tip-substrate adhesion.

‘flat’ tips has also been examined by Astala *et al* [144] using tight-binding MD simulations with a diamond indenter and Si substrate.

Indentation has also been performed on a larger diamond substrate in an attempt

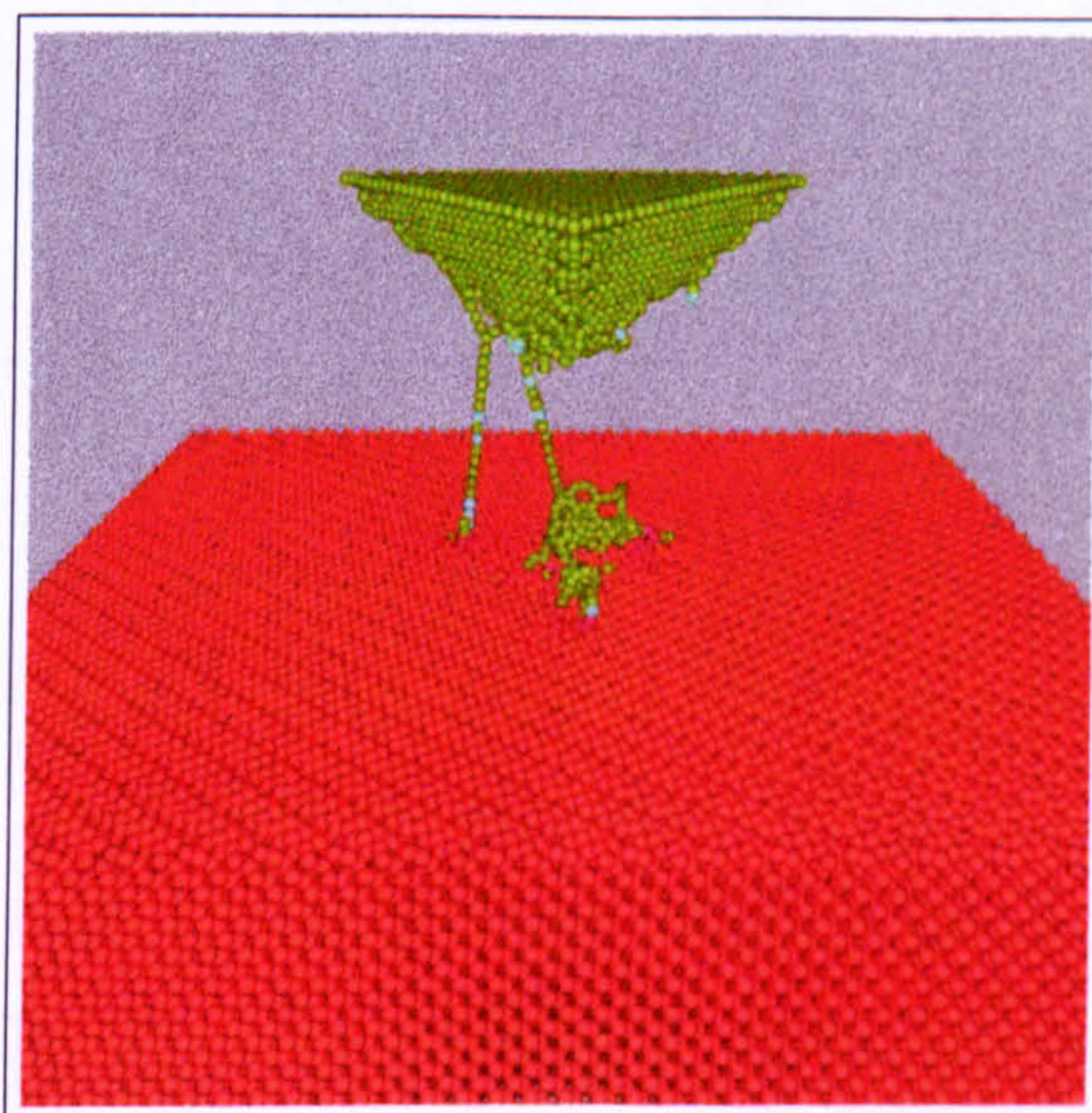


Fig. 4.4.13. Snapshot of the simulation with the large diamond  $\{100\}$  substrate at  $t = 100$  ps. Note the transfer of substrate atoms to the indenter and vice versa.



to study the impact of a deeper indentation depth on the interfacial adhesion. The larger crystal has approximate dimensions  $150 \text{ \AA} \times 150 \text{ \AA} \times 35 \text{ \AA}$  and is composed from 40 atomic layers. The work material contains 141,120 atoms and the fixed boundary is constructed from 9,915 atoms and 24,660 atoms configure the neighbouring damped region. A simulation was performed for indentation to  $20 \text{ \AA}$ , with an indentation period  $T = 100 \text{ ps}$ . The indenter apex was sited  $10 \text{ \AA}$  above the specimen at the start of the simulation, yielding an average indentation speed of  $60 \text{ ms}^{-1}$ . The simulation was run for a duration of  $100 \text{ ps}$  with a fixed timestep of  $1.0 \text{ fs}$ . The greater indentation depth ensues in a higher degree of interfacial bonding since there is more interaction with the dangling bonds emanating from the substrate surface. This results in a larger pull-off force compared with indentation of the smaller diamond substrate. A similar fate occurs with the indenter tip and substrate atoms as interfacial bonding produces strands of connective atoms, which reached a peak length of approximately  $15 \text{ \AA}$ . Fig. 4.4.13 shows that in addition to apex atoms, the connective threads of atoms are also composed from several substrate atoms. As the connective strands of atoms rupture, 8 substrate atoms become permanently bonded to the indenter as the tip reconstructs.

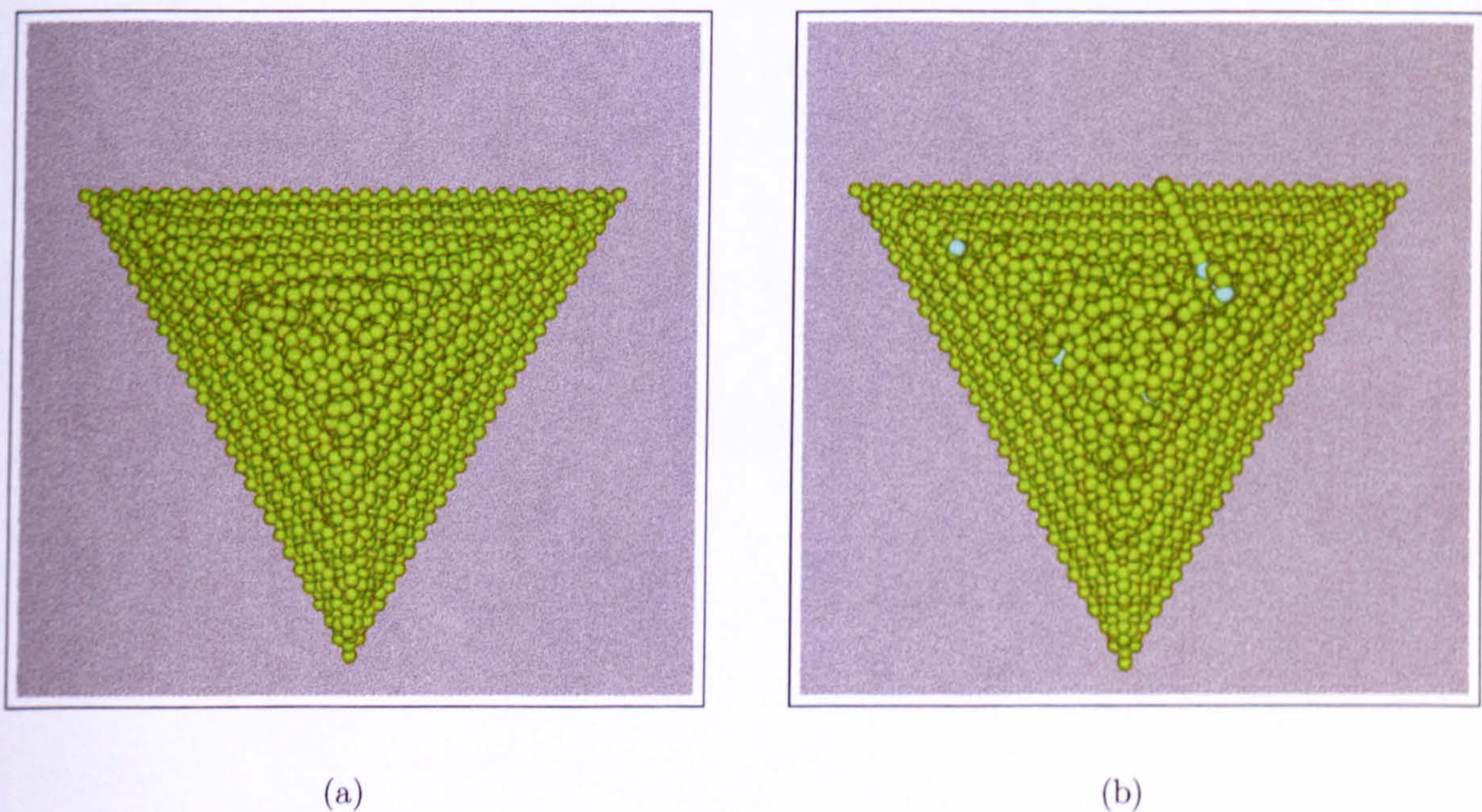


Fig. 4.4.14. Plan view of the indenter following indentation of diamond for: (a)  $T = 50\text{ps}$  simulation; (b)  $T = 100 \text{ ps}$  simulation. Note the structural disorder around the apex and edges. Also note the permanently displaced substrate atoms in (b) (shaded blue) that have become bonded to the indenter and those embedded in the tip.



The greater interaction between the substrate and the indenter has resulted in a larger transfer of tip atoms (approximately 150) to the surface of the work material. The simulations therefore suggest that the extraction of an indenting tip may constitute towards blunting effects by the *addition* and/or *dispossession* of atoms.

The damage imparted to the indenter from the interfacial bonding is shown in Fig. 4.4.14(a) and (b) following indentation of diamond with the  $T = 50$  ps and  $T = 100$  ps simulations, respectively. The structural arrangement of the indenter has been impaired locally around the tip and along the edges. Clearly, the larger indentation depth ensues in greater damage to the apex. Fig. 4.4.14(b) shows that some of the substrate atoms bonded to the indenter become embedded in the tip as the apex reconstructs following rupture of the interfacial adhesion.

### 4.3.3 $C_{60}$ Fullerene Substrate

The fullerenes [145], also known as ‘Buckminsterfullerenes’ or ‘Buckyballs’, are a family of spherical molecules configured from fused atoms arranged as pentagons and hexagons. The pentagonal arrangement of a number of the atoms provides the curvature of the molecule. To close into a spheroid these molecules must have 12 pentagons, giving a general composition  $C_{20+2n}$ , where  $n$  is the variable number of hexagons. The  $C_{60}$  fullerene is a soccer ball shaped molecule configured from 60 C atoms, as illustrated in Fig. 4.4.15, and is formed from 12 pentagons and 20 hexagons. The form of the  $C_{60}$  fullerene resembles a rolled up graphene sheet. The most abundant of the fullerenes, the

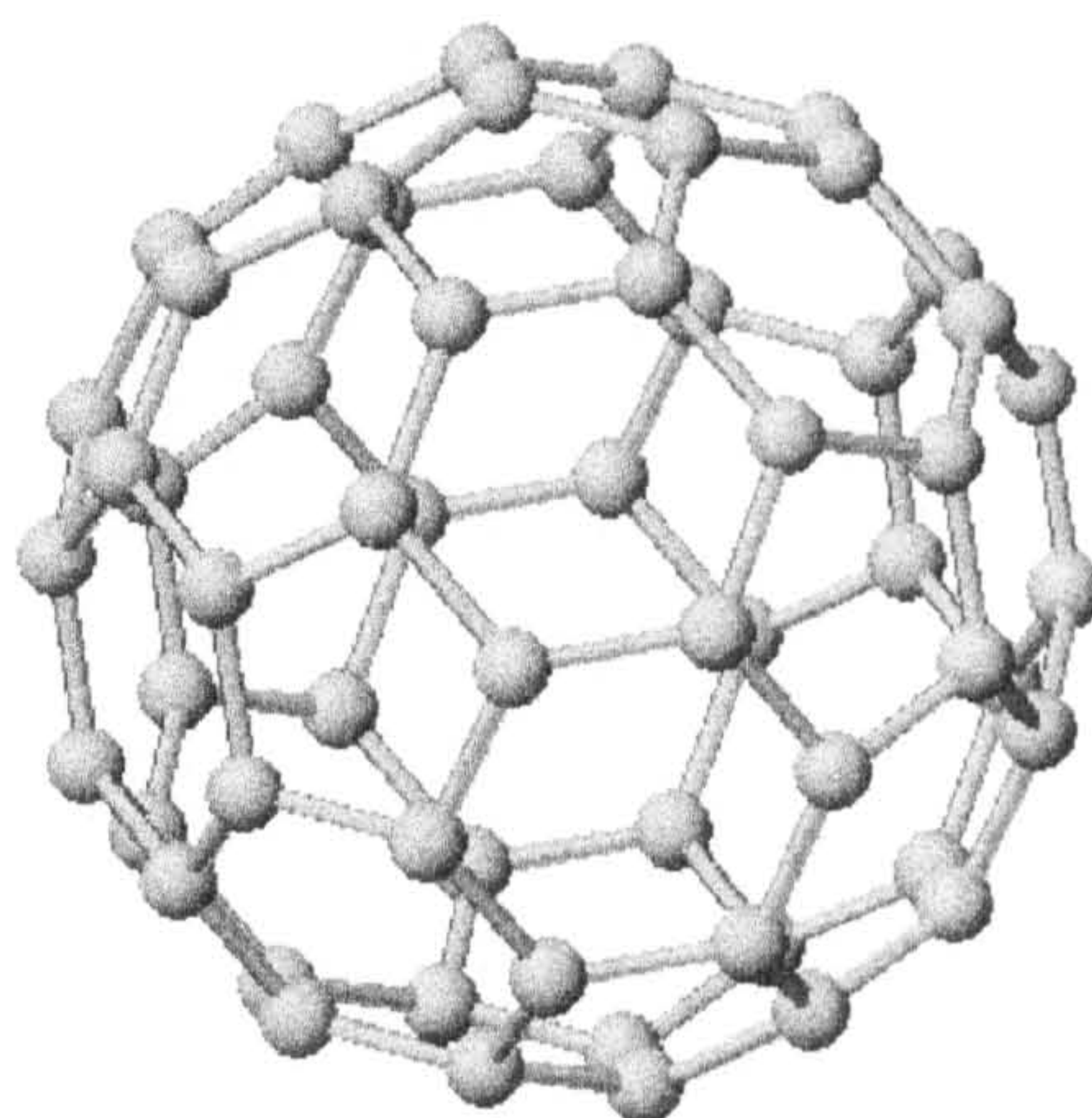


Fig. 4.4.15. The  $C_{60}$  fullerene molecule. The hexagonal and pentagonal arrangement of the atoms is clearly seen.



$C_{60}$  molecule is also the smallest stable member of the family, and hence it is the most difficult to compress. In molecular solids configured from  $C_{60}$  fullerenes, the molecules are bound by weak Van der Waals forces in all planes. This property therefore allows the individual  $C_{60}$  molecules to readily slip over each other in a similar fashion to the **AB** planes in graphite (see Fig. 3.3.4, Chapter 3). Hence, although a  $C_{60}$  molecule is very strong, a crystalline  $C_{60}$  substrate is comparatively easy to compress.

For simulations of indentation into a  $C_{60}$  substrate, a lattice with approximate dimensions  $154 \text{ \AA} \times 154 \text{ \AA} \times 61 \text{ \AA}$ , composed from 8 layers of  $C_{60}$  molecules is implemented. Crystalline molecular solids composed from  $C_{60}$  molecules are generally employed as thin films. Therefore, in addition to the vertical borders, the underside layer of the  $C_{60}$  work material is fixed to emulate the physical presence of a hard underlying substrate. The substrate consists of 129,600 atoms and the fixed boundary is constructed from 28,499 atoms and the damped neighbouring region is configured from 13,519 atoms. The indentation period is  $T = 50 \text{ ps}$  and the maximum displacement of the constrained indenter atoms,  $r_{\text{max}}$ , is set to  $24 \text{ \AA}$  with the apex sited  $4 \text{ \AA}$  above the substrate surface. This yields a maximum indentation depth of  $20 \text{ \AA}$  and an average indentation speed of  $96 \text{ ms}^{-1}$ . The simulation is run with a constant timestep of  $0.5 \text{ fs}$  for a duration of  $75 \text{ ps}$  to allow further retraction of the tip.

Fig. 4.4.16 presents the force-depth curve for indentation into the  $C_{60}$  work material. Because of the oscillations, the loading and unloading curves are shown separately in

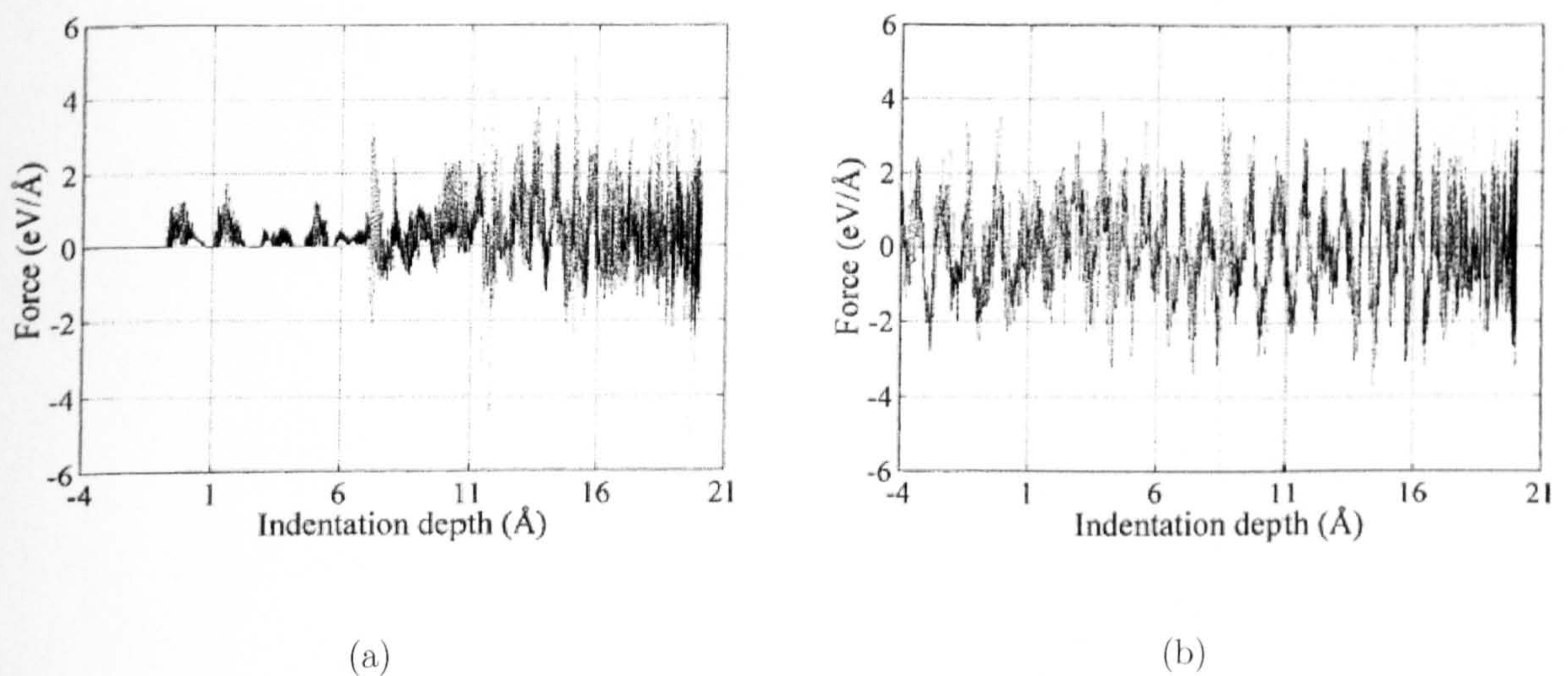


Fig. 4.4.16. Force-depth curve from the simulation of indentation into the  $C_{60}$  substrate for: (a) Loading process; (b) Unloading process.



Fig. 4.4.16(a) and Fig. 4.4.16(b) respectively. Both figures show very different features compared to the graphite and diamond force-depth curves. The loading curve shows small peaks of repulsive force for the approach of the indenter until a penetration depth of approximately 7 Å. Hereafter, the load-displacement curve shows a rapid oscillation of both repulsive and attractive forces. As the indenter penetrates the first layer of the substrate the attraction is very small. However, after the first layer the bulk of the tip interacts with the substrate and the attractive interactions become significant, as shown in Fig. 4.4.16(a). The unloading curve shows the similar oscillatory features present in the loading curve. These characteristics are still present even when the indenter has been extracted from the surface of the  $C_{60}$  substrate. The oscillations reflect only the small attractive and repulsive forces between the tip and individual  $C_{60}$  molecules. Since the  $C_{60}$  molecules are bound by very small intermolecular forces, any initial repulsive force from the indenter becomes sufficient to displace the weakly bound molecules and so the force then decreases until the indenter reaches the next molecule. Thus, for the small indentation depths implemented here, the force-depth curve would not be expected

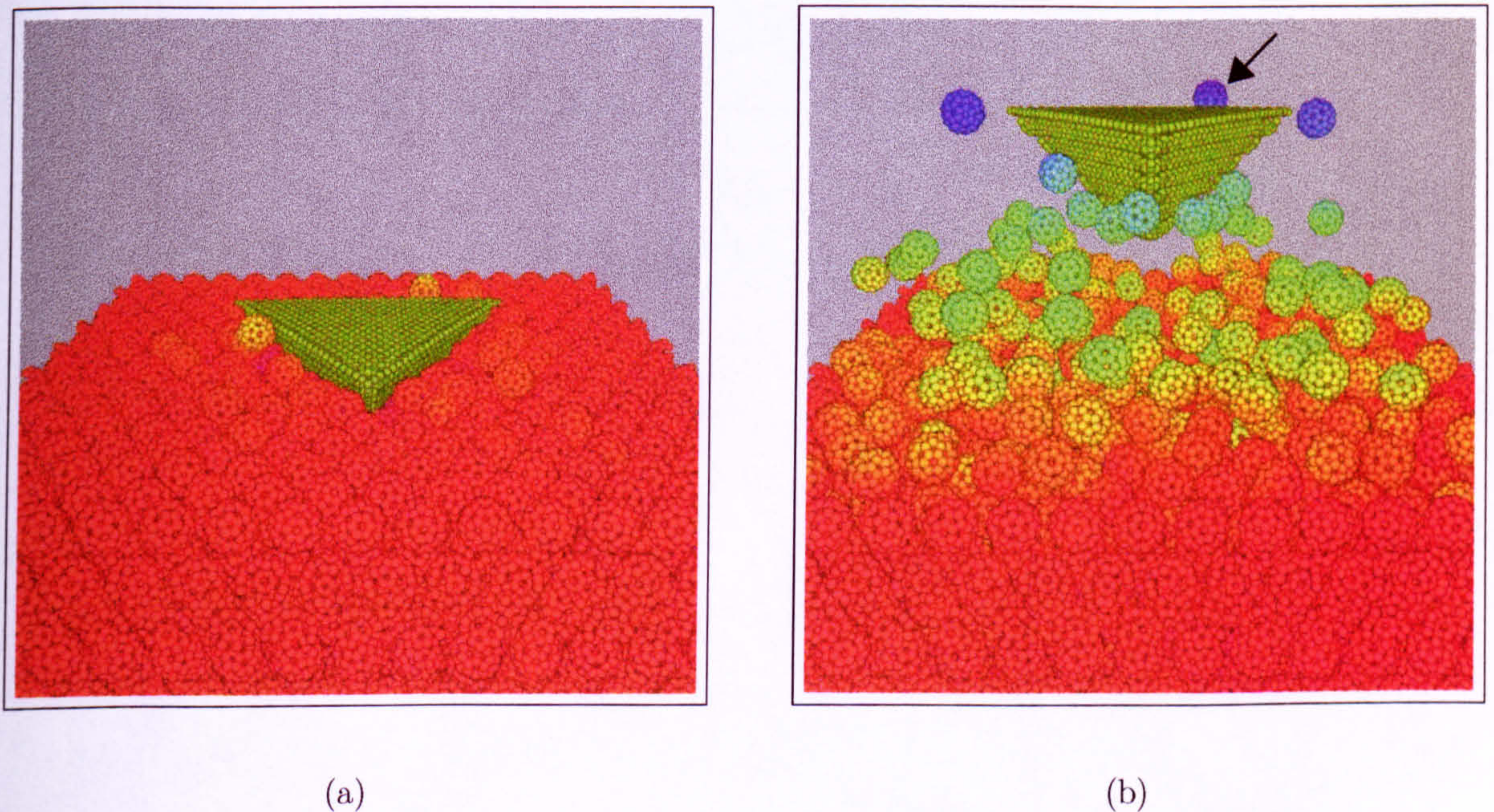


Fig. 4.4.17. Snapshots from the simulation of indentation into the  $C_{60}$  substrate. (a) Halfway point in the indentation process at  $t = 25$  ps. Note the emission of a few  $C_{60}$  molecules. (b) Completion of the simulation at  $t = 75$  ps. Note the emission of a multitude of  $C_{60}$  molecules and the bonding of a  $C_{60}$  molecule to the indenter (marked by the arrow).



to exhibit a general increase/decrease to and from maximum penetration, as with the graphite and diamond simulations. The easy displacement of these molecules results in very low forces exerted on the tip, which showed only a very small compression.

Shown in Fig. 4.4.17 are snapshots of the simulation of indentation into the  $C_{60}$  structure. In Fig. 4.4.17(a) the indentation process is shown at the halfway point,  $t = 25$  ps. The displacement of the indenter to the maximum penetration depth has caused the emission of a few  $C_{60}$  molecules from the surface. In Fig. 4.4.17(b) the conclusion of the simulation is shown at  $t = 75$  ps. It is evident that the indentation has induced sufficient energy into the  $C_{60}$  substrate to cause the ejection of a multitude of  $C_{60}$  molecules. Considering only those atoms displaced by more than 5 Å above the substrate surface reveals an approximate total of 117  $C_{60}$  molecules emitted from the work material. However, the final positions of the atoms in the surface show no identifiable 'hole' as molecules from other parts of the surface have moved to fill the gap left by the extracted tip. This permanent displacement of individual molecules clearly shows the indentation into the  $C_{60}$  structure to be plastic. Fig. 4.4.17(b) also shows evidence of interfacial adhesion, where the arrow marks a  $C_{60}$  molecule bonded to the indenter. The transfer of  $C_{60}$  molecules to the indenter tip has been detected experimentally by Ruan and Bhushan during indentation of  $C_{60}$ -rich fullerene films [146].

## 4.4 Hydrogen Surface Termination

Adsorbate-free diamond is extremely reactive since it exposes a mass of dangling bonds. The simulations presented in the preceding section show how easily an impinging diamond tip can bond with a substrate. However, in reality a diamond surface contains a layer of some adsorbate, such as hydrogen. Hydrogen-coated diamond, or hydrogen terminated diamond is very unreactive since the adsorbate saturates the dangling bonds. Therefore, the bonding between the work materials can be minimised by terminating the three adjacent {100} surfaces of the indenter with hydrogen to satisfy the valency requirements of the C atoms [147]. However, covering the indenter surface with a layer of some adsorbate will reduce tip-substrate adhesion, but not necessarily prohibit it from occurring, since tip-induced reactions make break some C-H bonds creating a dangling bond. The very nature of the indentation process causes bonds between atoms to be broken and reformed. A diamond indenter terminated with hydrogen is shown in Fig.



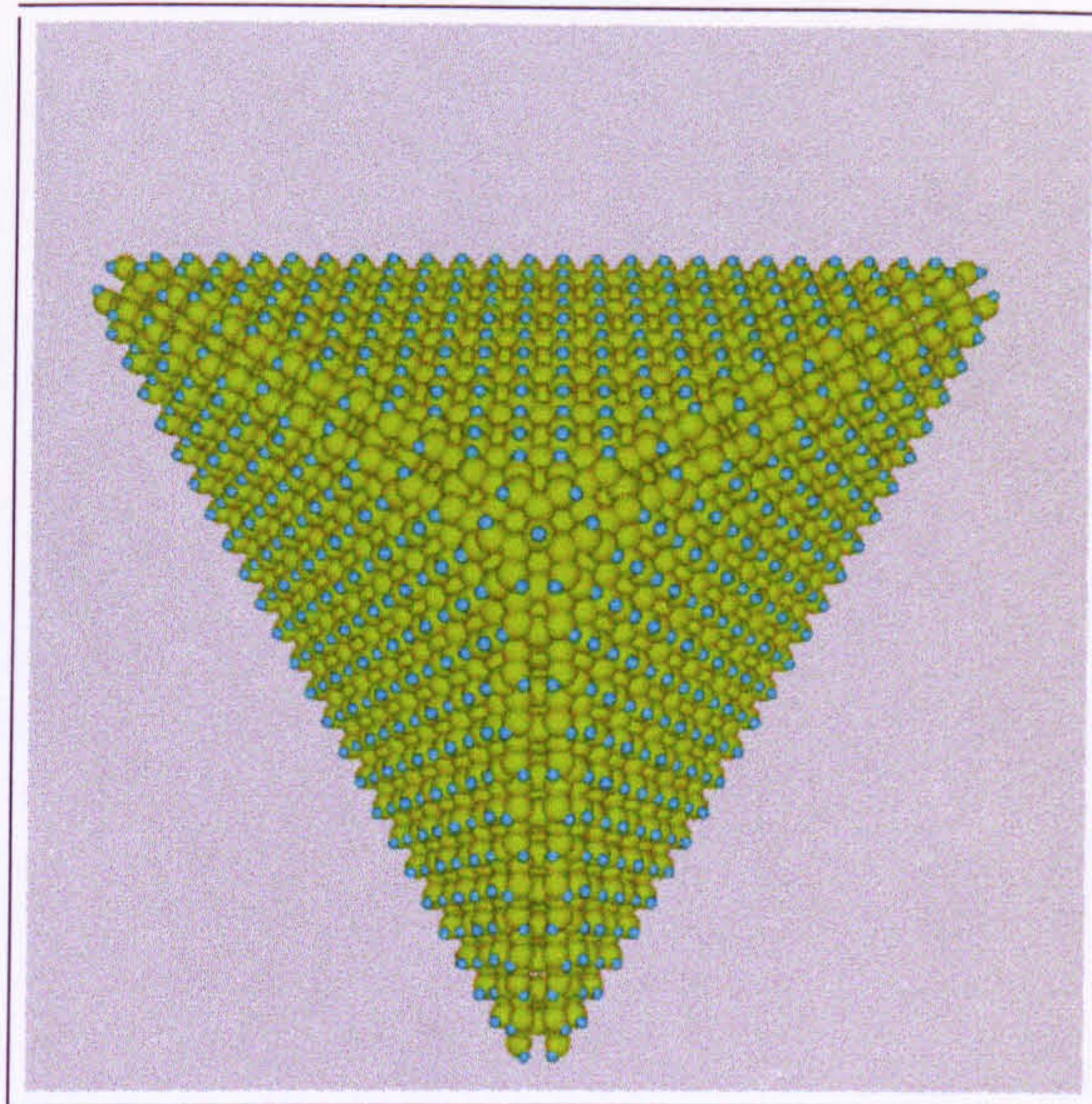


Fig. 4.4.18. Plan view of the hydrogen terminated indenter used in the simulations. The green atoms denote carbon and the blue atoms represent hydrogen.

4.4.18 after relaxation to the minimal energy configuration. It was generated by placing a hydrogen atom directly above each atom in the dimer rows at a distance equal to the C-H bond length of  $1.078 \text{ \AA}$ . In addition to the  $\{100\}$  surfaces, an adsorbate H atom is also allowed to bond with the apex atom. The indenter is configured from 3,996 C atoms and 547 H atoms with a height  $h \approx 25 \text{ \AA}$  and side length  $a = 68 \text{ \AA}$ .

#### 4.4.1 Diamond $\{100\}$ Substrate

For simulations with the diamond  $\{100\}$  substrate, the indenting surface is hydrogen terminated and dimer reconstructed. The diamond crystal has approximate dimensions

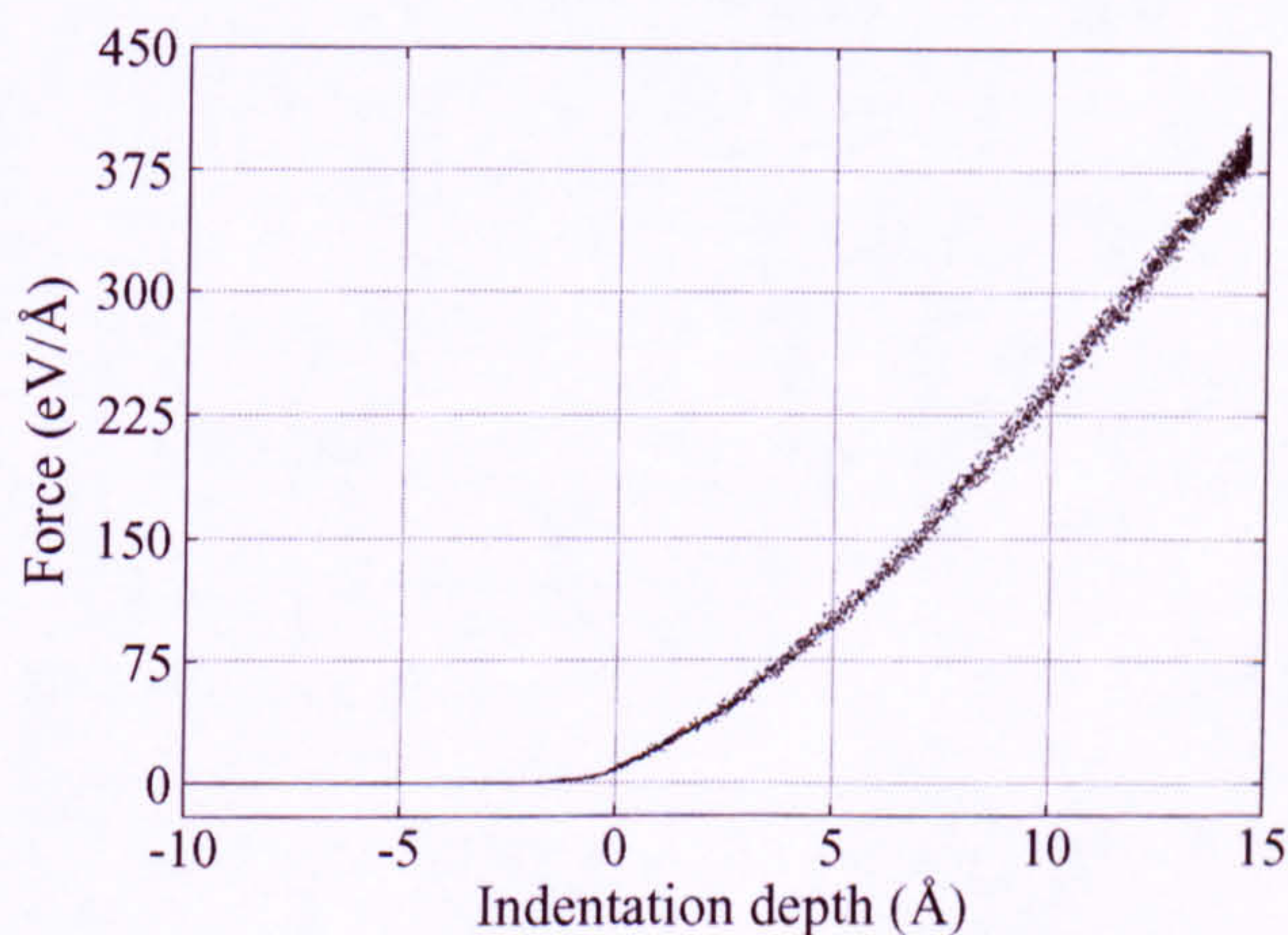


Fig. 4.4.19. Force-depth curve from the simulation of indentation into the large diamond  $\{100\}$ :H substrate with the hydrogen terminated indenter.



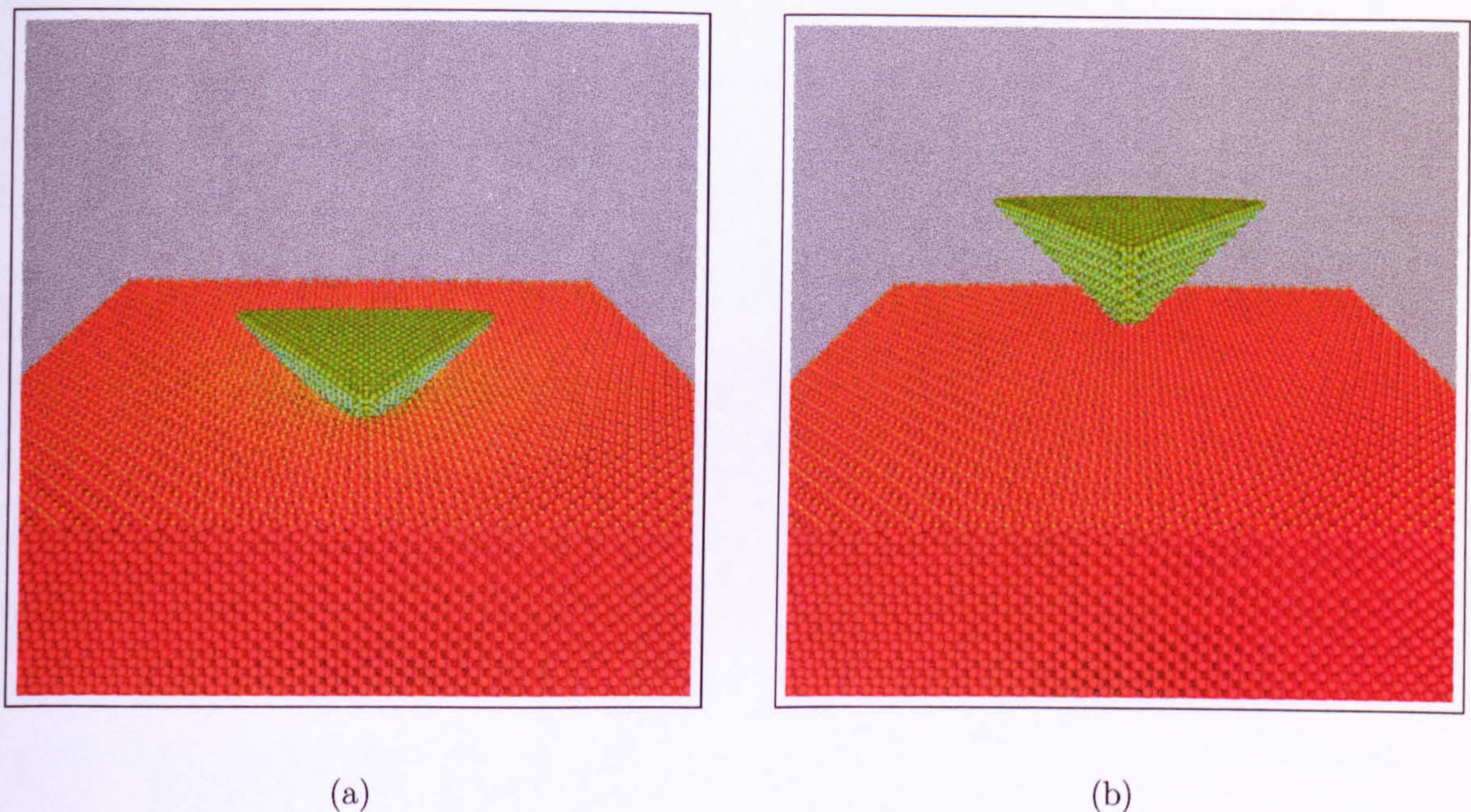


Fig. 4.4.20. Snapshots from indentation of diamond  $\{100\}$ :H. (a) Halfway stage of the indentation at  $t = 75$  ps. Note the bending of the atomic layers. (b) Conclusion of the indentation process at  $t = 150$  ps.

$150 \text{ \AA} \times 150 \text{ \AA} \times 35 \text{ \AA}$ , containing 144,648 atoms where 3,528 hydrogen atoms terminate the indenting surface. The fixed vertical boundary is composed from 10,167 atoms with 25,272 atoms forming the damped neighbouring terms. The indentation period is  $T = 150$  ps and the maximum displacement of the fixed indenter atoms,  $r_{\text{max}}$ , is set to  $30 \text{ \AA}$  with the tip sited  $10 \text{ \AA}$  above the substrate surface. This renders a maximum displacement of  $20 \text{ \AA}$  with an average indentation speed of  $40 \text{ ms}^{-1}$ . The simulation is run for a duration of 150 ps with a constant timestep of 1.0 fs.

Fig. 4.4.19 presents the force-depth curve from the simulation of indentation into the diamond  $\{100\}$  substrate. The overlapping loading and unloading curves show the work material undergoes a completely elastic deformation with no evidence of interfacial adhesion. The peak force acting on the indenter was approximately  $410 \text{ eV/\AA}$  which occurred during the loading stage at an indentation depth of approximately  $14.5 \text{ \AA}$ . The apex compressed by a maximum of  $5.5 \text{ \AA}$  at the peak penetration depth. Snapshots from the simulation of indentation into the diamond  $\{100\}$  substrate are shown in Fig. 4.4.20<sup>2</sup>. At the halfway stage of the indentation process, Fig. 4.4.20(a) shows the diamond layers bending under the influence of the indenter. Fig. 4.4.20(b) shows the

<sup>2</sup>An animated movie of this is on the CD in the Appendix



completely elastic recovery of the work material at the conclusion of the simulation. Visual inspection of the local indentation surface shows that there is no disruption to the original ordering of the hydrogen monolayer or the diamond surface atoms.

#### 4.4.2 Amorphous Carbon Substrates

Since carbon has the ability to have two-fold, three-fold and four-fold coordination, there is a degree of freedom in the hybridisation status of atoms in *a*-C. The films are therefore characterised by determining both the mass density and nature of the chemical bonding. In theoretical work, the composition of the substrate can be derived from the carbon coordination number. For example, an atom with either four-fold, three-fold or two-fold coordination is described as an  $sp^3$ -,  $sp^2$ - or  $sp$ -like atom, respectively. A large fraction of tetrahedral coordinated atoms ( $sp^3$ -like) imparts a greater diamond-like character into the film and hence a high mechanical hardness. Films with a high  $sp^3$  content are usually called tetrahedral amorphous carbon or diamond-like-carbon (DLC). The fraction of  $sp^2$  and  $sp^3$  bonds is influenced by the formation process of the film. Experimentally, *a*-C films produced by sputtering graphite are primarily  $sp^2$  hybridised. Alternatively, deposition of *a*-C films by low-energy ion beams ensues in a high  $sp^3$  content.

Two *a*-C substrates are used here, with comparatively high and low densities. The *a*-C substrates are formed from tessellation of a 128-atom bulk supercell, which is derived from an annealing regime using tight-binding [148]. Following repetitions of the supercell, the surface of the work material is hydrogen terminated and allowed to relax to a minimal energy configuration by applying inelastic energy loss. Both substrates have approximate dimensions  $150 \text{ \AA} \times 150 \text{ \AA} \times 40 \text{ \AA}$ . The low-density *a*-C:H work material is configured from 100,352 C atoms and 2,777 H adsorbate atoms. The rigid vertical boundary is formed from 12,061 atoms and the neighbouring damping region is configured from 33,970 atoms. The high-density *a*-C:H work piece is composed of 131,072 C atoms and 4,194 H adsorbate atoms. The fixed vertical boundary is configured from 13,089 atoms and the adjacent damping region is configured from 46,151 atoms. Simulations were performed on the *a*-C substrates with an indentation period  $T = 150 \text{ ps}$  with the maximum displacement of the constrained indenter atoms,  $r_{\text{max}}$ , set to  $30 \text{ \AA}$  with the tip sited  $10 \text{ \AA}$  above the substrate surface. This yields a maximum indentation depth of  $20 \text{ \AA}$  with an average indentation speed of  $40 \text{ ms}^{-1}$ . The simula-



Table 4.1. Structure and bonding data for the  $a$ -C:H substrates at equilibrium prior to indentation.

$a$ -C:H substrate	$\rho$ (g cm <sup>-3</sup> )	Mean C-C	Mean C-C-C	Hybridization status <sup>a</sup>		
		bond length (Å)	bond angle (degrees)	$sp$ (%)	$sp^2$ (%)	$sp^3$ (%)
Low-density	2.2	1.47	116.3	10.3	68.8	19.4
High-density	2.9	1.53	110.9	4.5	30.5	63.5

<sup>a</sup>For the low-density substrate the remaining percentage are outermost atoms with a coordination number of 1. For the high density substrate the remaining percentage are primarily outermost atoms with a coordination number of 1, together with some five-fold coordinated atoms.

tions are run for a duration of 150 ps with a fixed timestep of 1.0 fs.

Structure and bonding data for the two  $a$ -C:H substrates at equilibrium is given in Table 4.1. The structural composition of the  $a$ -C:H substrates is evaluated by assessing the hybridisation status of each atom. The carbon coordination number for each atom is determined by summing all the nearest neighbours, defined by the interaction cut-off radius of 2 Å in the Brenner potential. The composition of the low-density  $a$ -C:H substrate is largely dominated by  $sp^2$ -like atoms. Hence, the mean C-C bond length and C-C-C bond angle is close to that of graphite. The high-density  $a$ -C:H substrate is composed chiefly from  $sp^3$ -like atoms and so has a larger mean bond length and smaller mean bond angle (similar to diamond) compared with the low-density  $a$ -C:H work material. The high-density  $a$ -C:H film also contains a small fraction of atoms with five-fold coordination.

The force-depth curve from indentation into the low- and high-density  $a$ -C:H substrates is shown in Fig. 4.4.22(a) and (b) respectively. Both curves show a large elastic recovery of the work material and also adhesion between the tip and the substrate. Only the surface atoms have been hydrogen terminated and since the surface of the work material is not atomically flat, there are void regions where carbon bonds remain unsaturated. Such voids are shown in Fig. 4.4.21 for both the low- and high-density  $a$ -C:H substrates. Clearly, the void regions are larger for the low-density material. Hence,



the unconcealed void regions imply that the *a*-C substrates employed here are only partially hydrogen terminated. The adhesion with the tip occurs primarily with unsaturated subsurface atoms which are exposed in the void regions. However, adhesion may also occur from rupture of the C-H bonds in the tip which will create dangling bonds. The interfacial adhesion was investigated further by attempting to terminate the unsaturated bonds that exist in the subsurface. However, when the substrate was allowed to relax to the minimum energy configuration, the surface was found to be unstable. In another attempt to improve the surface valency, a thicker film of hydrogen was deposited on the substrate surface. This still did not prevent the tip from adhering to subsurface atoms. In reality, an *a*-C:H film would have a multitude of surface impurities concealing the subsurface.

Indentation with the low-density material results in a peak force of just over 100 eV/Å at the maximum indentation depth of approximately 17.5 Å. Thus, the indenter tip has deformed by about 2.5 Å. As the indenter is extracted from the work material,

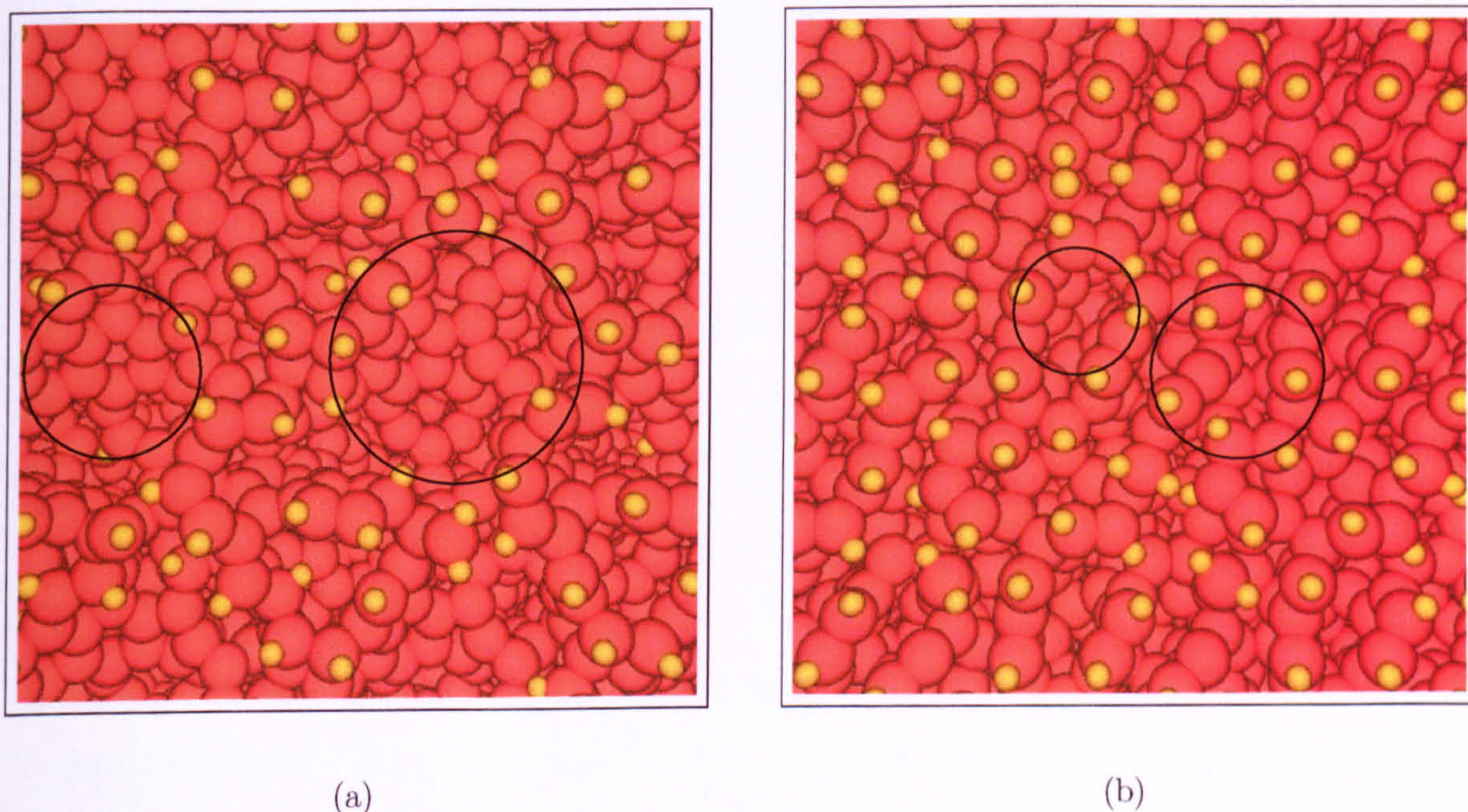


Fig. 4.4.21. Surface of the work material for: (a) low-density *a*-C:H; (b) high-density *a*-C:H. The circles encompass void regions of unsaturated subsurface atoms. The yellow atoms represent hydrogen and the red atoms denote carbon. (Note the formation of small rings of carbon atoms in the subsurface. This effect is less pronounced on the surface since the hydrogen atoms terminate the network paths.)



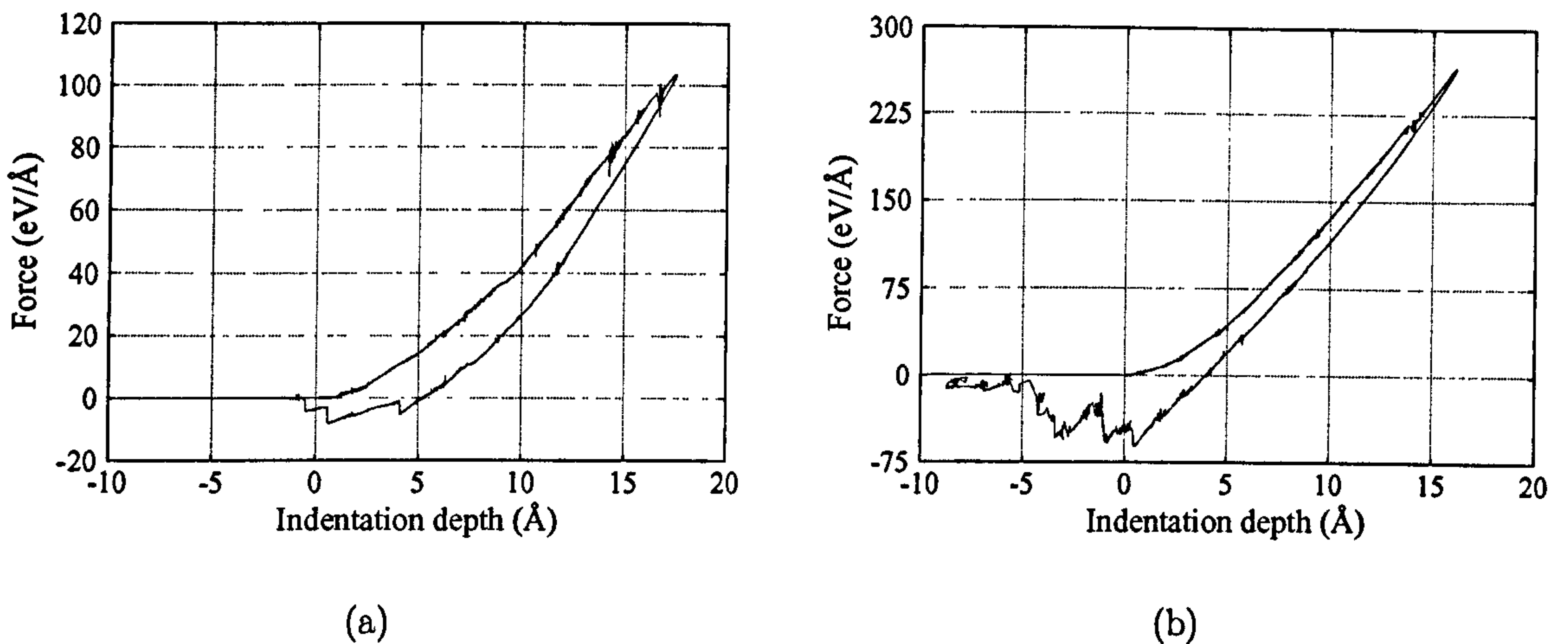


Fig. 4.4.22. Force-distance curve for: (a) low-density  $a$ -C:H and (b) high-density  $a$ -C:H.

the pull-off force required to rupture the interfacial bonding is just under 10 eV/Å. Snapshots from the indentation of the low-density  $a$ -C:H substrate are shown at both the halfway stage and the conclusion in Fig. 4.4.23(a) and (b) respectively<sup>3</sup>. As the indenter is extracted from the work material, no threads of connective atoms are produced, as were observed with the adsorbate-free diamond substrate. Since most of the dangling bonds in the surface of the work piece have been saturated, the tip-substrate adhesion is minimal. The interfacial bonding is ruptured with relative ease and by the conclusion of the simulation no indenter atoms have been displaced to the work material, although 3 H atoms and 1 C atom from the substrate remain bonded to the indenter. The small plastic deformation stemming from rupture of tip-induced interfacial adhesion could be further reduced with increased H saturation on the surface of the  $a$ -C:H substrates.

At the maximum penetration depth of approximately 17 Å into the high-density  $a$ -C:H substrate, the tip had compressed by 3 Å and the indenter experienced a peak force of about 265 eV/Å. At the conclusion of the indentation process the interfacial bonding has not ruptured and the force of adhesion is greater than the pull-off force with the low-density  $a$ -C:H substrate at just under 70 eV/Å. Snapshots of the indentation process are presented in Fig. 4.4.23(c) and (d). The two atoms marked by the arrows in Fig. 4.4.23(c) are surplus hydrogen atoms from the termination of the surface. These atoms are immobile throughout the simulation and remain above the undisturbed surface unbonded to any other atoms. As the tip is withdrawn from the work material, a small connective thread of atoms is produced. Even though the void regions

<sup>3</sup>An animated movie of this is on the CD in the Appendix



of unsaturated subsurface atoms are smaller compared with the low-density material, indentation of the high-density material ensues in slightly larger adhesion. This stems

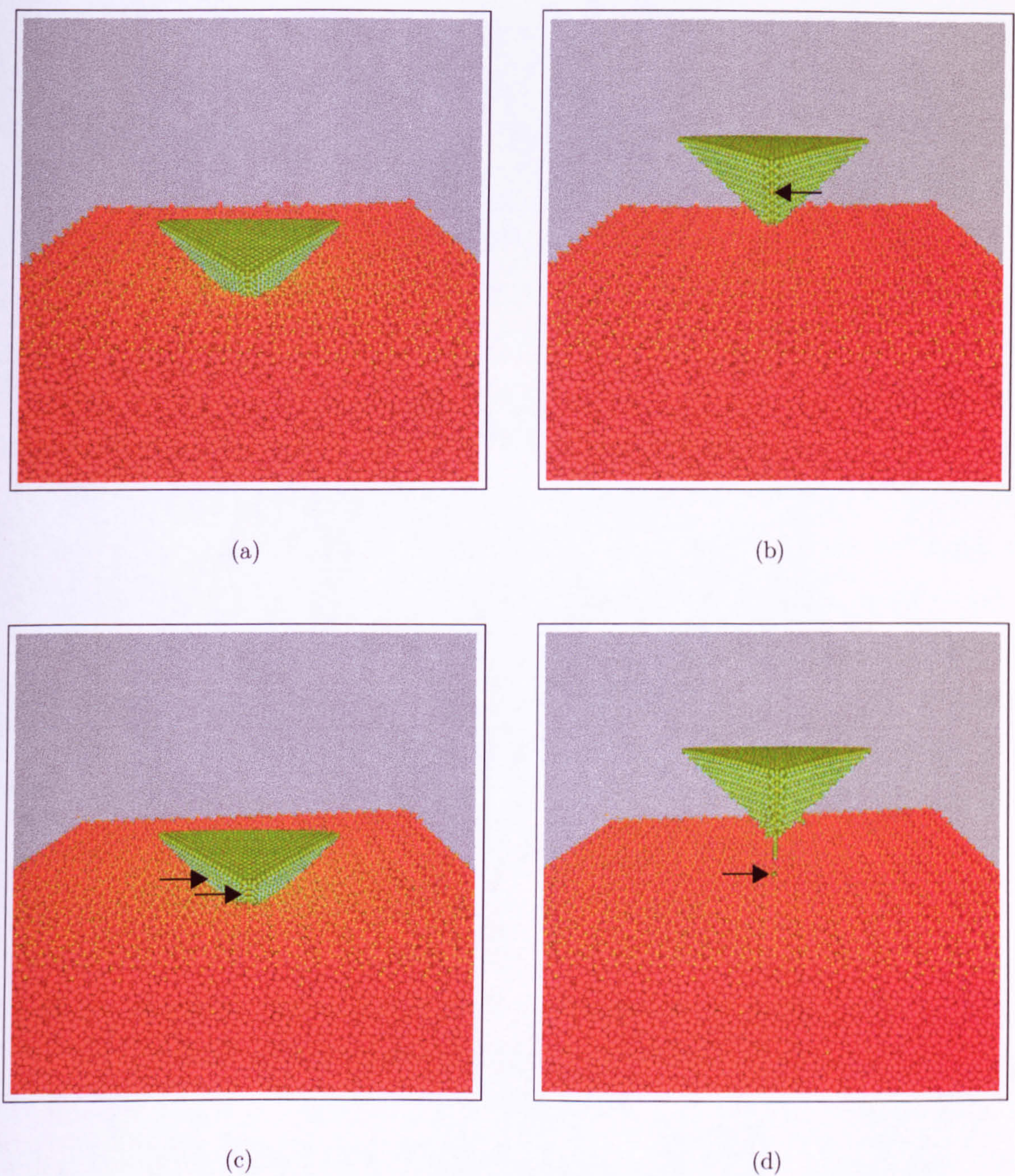


Fig. 4.4.23. Snapshots from the simulation of indentation into: (a) low-density  $a$ -C:H at  $t = 75$  ps; (b) low-density  $a$ -C:H at  $t = 150$  ps; (c) high-density  $a$ -C:H at  $t = 75$  ps; (d) high-density  $a$ -C:H at  $t = 150$  ps. Note the transfer of atoms between tip and substrate as marked by the arrows in (b) and (d). The atoms marked by the arrows in (c) are immobile hydrogen atoms above the undisturbed surface and are not bonded to any other atoms.



from the greater density of the material. With the low-density  $\alpha$ -C:H work piece, only substrate atoms were transferred between the tip and the sample. However, with the high-density work piece, the greater interfacial bonding ensues in a small quantity of both tip and substrate atoms being transferred. Only 3 C tip atoms were permanently displaced to the surface of the work material, while 3 C atoms and 1 H atom were transferred from the substrate to the indenter apex. Although hydrogen termination of both the indenter and the  $\alpha$ -C substrates has not prohibited interfacial bonding, the quantity of atom transfer is minimal compared with the simulations of adsorbate-free diamond indentation. The images in Fig. 4.4.23(b) and (d) show that there is no depression left in the substrate surface following full extraction of the indenter tip. Further structural analysis reveals no cracks in the  $\alpha$ -C:H substrates since the indentation depth is too small.

To determine the extent of rearrangement in the  $\alpha$ -C:H substrates, the bonding in the work materials was examined subsequent to indentation. The bond length and bond angle statistics are presented in Fig. 4.4.24. The shortest C-C bond length in both materials is approximately 1.18 Å, which probably conforms to a triple bond. The histograms show that there is a marginal change in bonding structure at the halfway stage of the indentation process as bonds local to the indent are distorted. Some of the C-H bonds sited around the indentation region are ruptured and reformed during penetration by the tip. The breakage of some C-H bonds creates defect states (i.e., dangling bonds), and leads to reconstruction locally which may therefore aid adhesion between tip and sample. The temporary fractional change in bonding structure at the halfway is reflected by the small variation in the carbon coordination numbers in Table 4.2. As the indenter reaches the maximum indentation depth at  $t = 75$  ps, neighbouring substrate atoms are compressed and so the number of lower coordinated atoms is reduced and higher-coordinated atoms are formed. Clearly, more atoms with a large coordination number are formed for the high-density material compared with the low-density material. The increased coordination numbers of the compressed atoms thus ensues in a temporary distortion to the bond length and bond angles. This permutation is only a transitory change in the bonding structure since the distributions of bond length and bond angles in Fig. 4.4.24 at the conclusion of the simulation are approximately the same as prior to indentation.

At the end of the indentation process, Table 4.2 shows a reduction in higher coor-



minated atoms as the compression around the indent has relaxed. However, there are a small fraction of atoms that remain with higher coordination numbers. The results presented in Fig. 4.4.24 and Table 4.2 indicate that no significant permanent structural rearrangement takes place, suggesting that the indentation is primarily elastic for both materials. The fractional plastic deformation stems from tip-induced adhesion and rup-

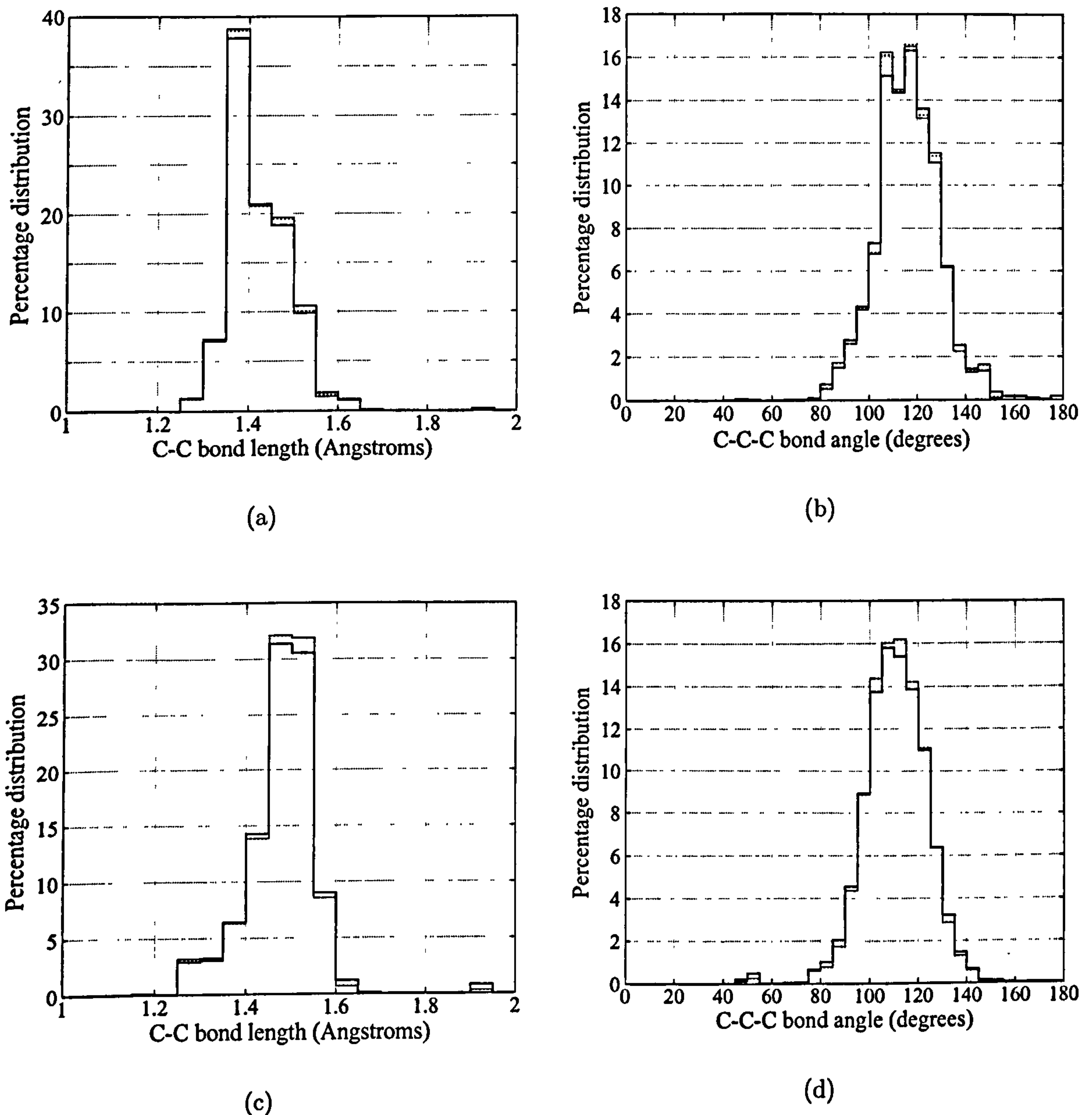


Fig. 4.4.24. Histograms of: (a) low-density  $a$ -C:H bond lengths; (b) low-density  $a$ -C:H bond angles; (c) high-density  $a$ -C:H bond lengths; (d) high-density  $a$ -C:H bond angles. The distribution of bond lengths and bond angles are calculated in bins of  $\frac{1}{20}$  of an Å and  $5^\circ$  respectively. The thin solid line and bold solid line correspond to  $t = 0$  ps and  $t = 75$  ps respectively. The remaining dashed line corresponds to  $t = 150$  ps.



ture together with deformation around the subsurface. In addition to the simulations presented here, indentations were also performed at different locations on the surface of the  $a$ -C:H substrates. The shape of the indentation curves was highly reproducible and the simulations yielded similar results for structural rearrangement. However, the degree of interfacial bonding was influenced by the the position of the tip with respect to the void regions of unsaturated subsurface atoms.

The study by Sinnott *et al* [122] reported on indentation of diamond {111} covered by an  $a$ -C:H film. The  $a$ -C:H film was produced by heating central layers of a diamond slab to 8000K and then quenching the disordered section to room temperature. Preceding indentation, the amorphous film was composed of 21%  $sp^3$ -like atoms and 58%  $sp^2$ -like atoms. Less than 2% had a coordination number of 2 and approximately 0.1% of atoms had five-fold coordination. Thus, the film is analogous to the low-density material used in our simulations. The flat-ended  $sp^3$  tip penetrated to about 4 Å,  $\approx$  20% of the film thickness. After full extraction of the tip they found no depression left in the surface. The composition of the film was subsequently analysed and they found an almost exact bonding distribution as prior to indentation. This suggested that no significant structural rearrangement took place and therefore the indentation was con-

Table 4.2. Carbon coordination numbers for the  $a$ -C:H substrates at different stages during the indentation process.

$a$ -C:H substrate	$t$	Coordination number							
		2	3	4	5	6	7	8	9
	(ps)	(Number of atoms)							
Low-density	0	10337	69081	19441	0	0	0	0	0
	75	10314	68813	19604	142	36	6	1	1
	150	10350	69043	19517	7	1	0	0	0
High-density	0	5857	40007	83180	1233	0	0	0	0
	75	5840	39604	82449	2204	152	48	7	5
	150	5874	40023	83284	1116	4	1	0	0



sidered elastic. They obtained a modulus of 157 GPa for the  $a$ -C:H, which compared well with experimental values of 100 - 260 GPa for films with 0% - 16%  $sp^3$ -like atoms [149]. With the larger indentation depths used in the simulations presented here for  $a$ -C:H, the qualitative results are similar to the smaller indentation simulations by Sinnott *et al* [122].

The use of Brenner's potential in modelling the  $sp^3$  content in  $a$ -C films has been investigated in a recent report by Jäger *et al* [150]. They employed MD simulations to study ion beam deposition of diamond-like carbon (DLC) films. Using Brenner's potential in the original form, where the covalent bonding of nearest neighbours is cut-off between 1.7 Å and 2.0 Å, they found the potential yielded  $a$ -C films with a very low  $sp^3$  content. However, the films had a high density despite having a significant composition of  $sp^2$  hybridised atoms. This discrepancy was attributed to the short range cut-off radius between nearest neighbours in the potential. By increasing the nearest neighbour interaction radius, in accordance with the bond-order concept and so not altering the originally fitted potential properties, they discovered an improvement in modelling the  $sp^3$  content in the films. Their results now compared more favourably with experimental data, showing similar calculated densities and  $sp^3$  content. In addition to the study by Jäger *et al* [150], other authors have also reported on the implementation of extended cut-off interactions. Nordlund *et al* [151] recently reported on an extended cut-off radius for the Tersoff potential [94]-[95], in a study of small-scale defects on graphite surfaces.

## 4.5 Experimental Results and Discussion

This section discusses the experimental load-displacement curves by Richter *et al* [124] for nanoindentation into HOPG {0001}, the {111} face of synthetic diamond and a C<sub>60</sub> fullerene film, grown on glass. The experiments by Richter *et al* were performed using the Hysitron Nanoindenter Triboscope [152], based on a conventional SFM [153]. The preparation of the carbon samples is discussed in detail by Richter *et al* [124]. The indenter is made from diamond and has the configuration of a three-sided 90° pyramid, as in Fig. 3.3.1 (Chapter 3). Knowledge of the tip geometry is important since the apex curvature changes with use, so the actual contact area of the diamond indenter is determined by the SFM instrument. The tip, as shown in the scanning electron microscopy picture in Fig. 4.4.25, is attached to the end of a cantilever and aligned such that the



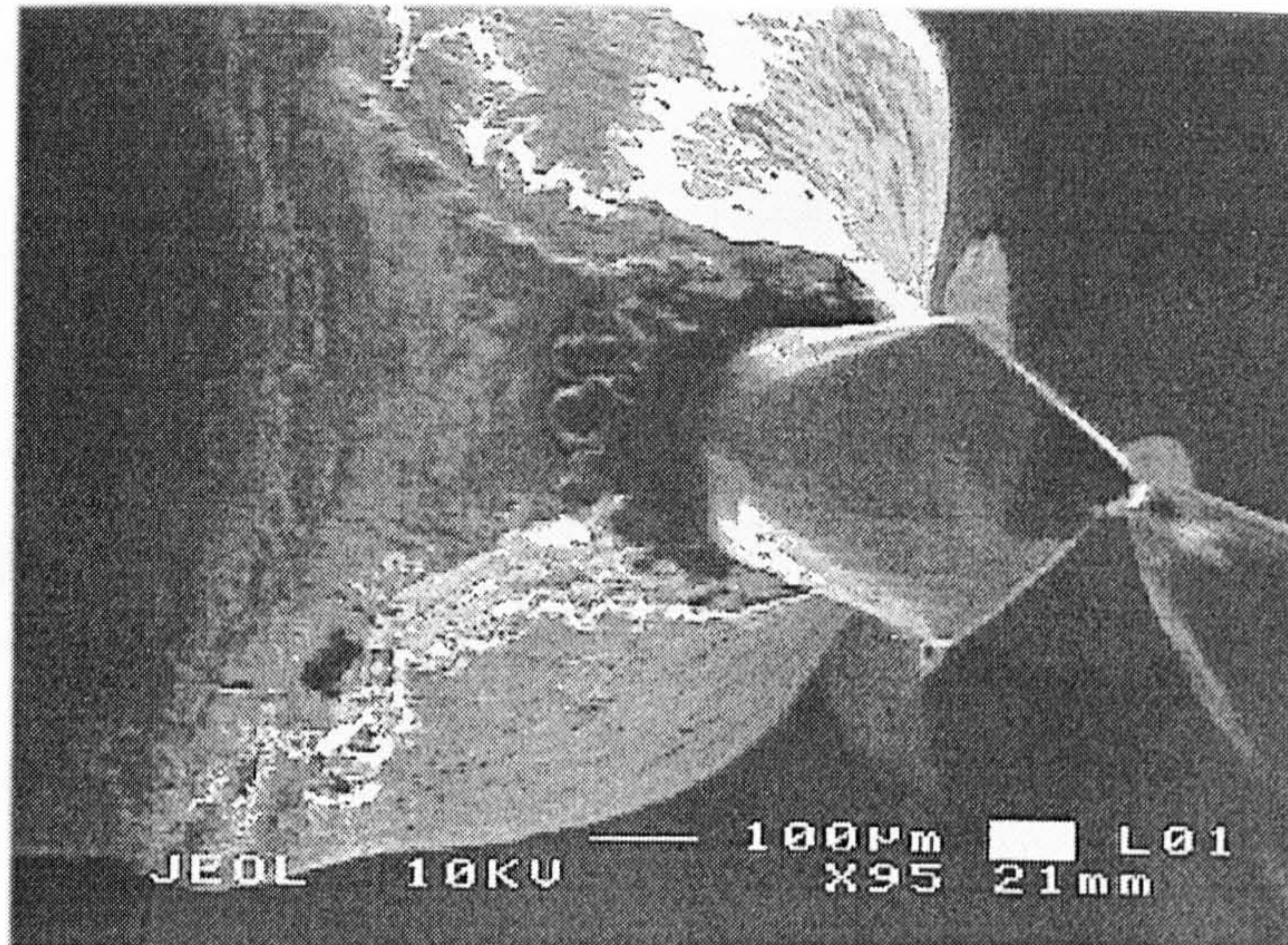


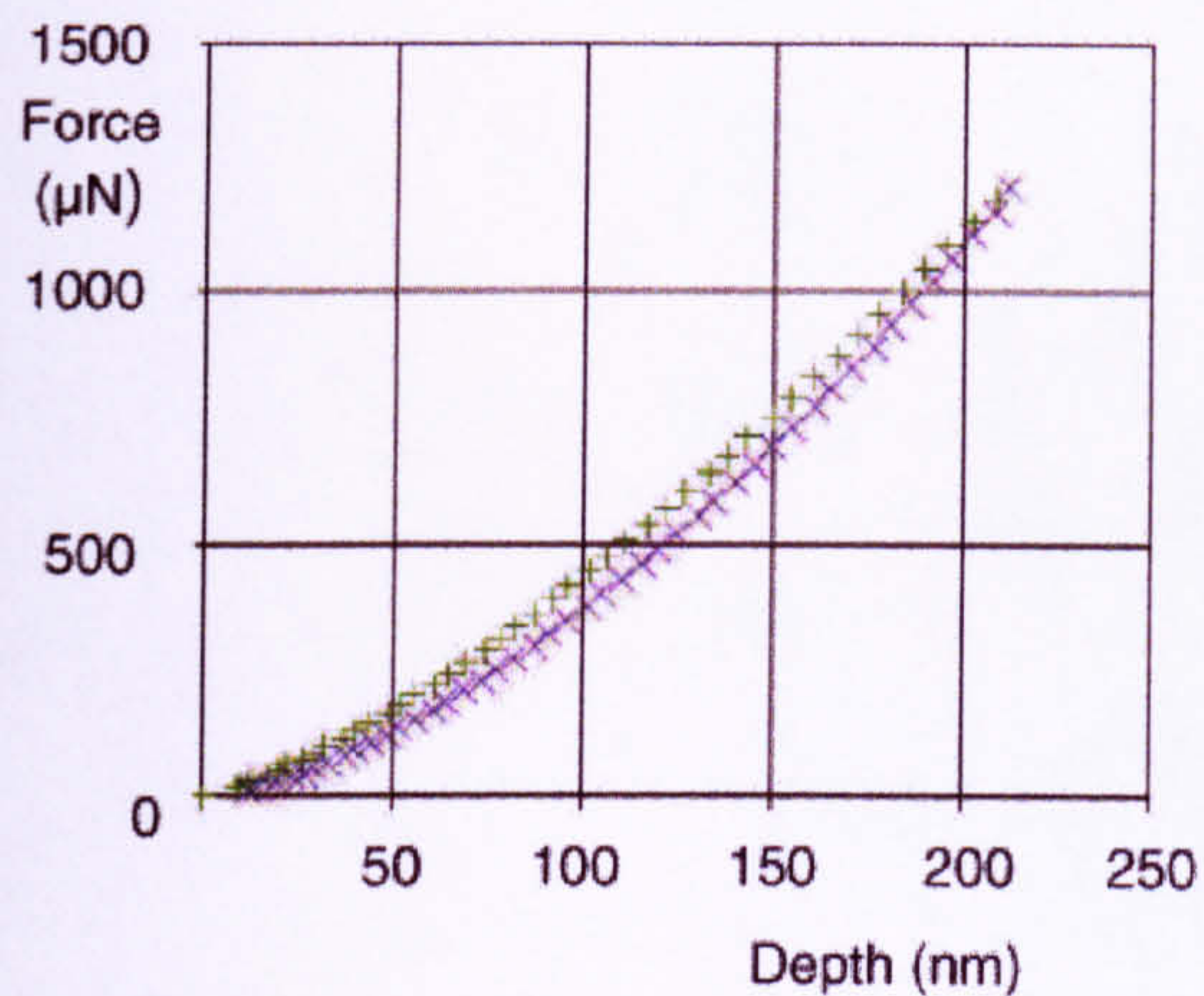
Fig. 4.4.25. SEM image, showing the geometry of the diamond indenter tip.

$\{111\}$  planes lie parallel to the face of the substrate. The cantilever is generally made from Si or  $\text{Si}_3\text{Ni}_4$  and is desired to have a low spring constant so forces can be determined from very small deflections. The nanoindentation procedure involves advancing the indenter towards the surface of the sample material by the application of a dc voltage to generate an electrostatic force. The resulting force acting on the indenter will elastically deform the cantilever and the deflection is measured by a displacement sensor. Hence, the force can be measured as a function of the indentation depth. The indentation region of the sample can also be imaged using the same tip, but in the scanning force microscopy mode. In this mode, the tip is brought to within a few nanometres of the sample and the surface topography is subsequently obtained by scanning the tip over the surface of the sample and measuring the small atomic forces between the apex and the substrate.

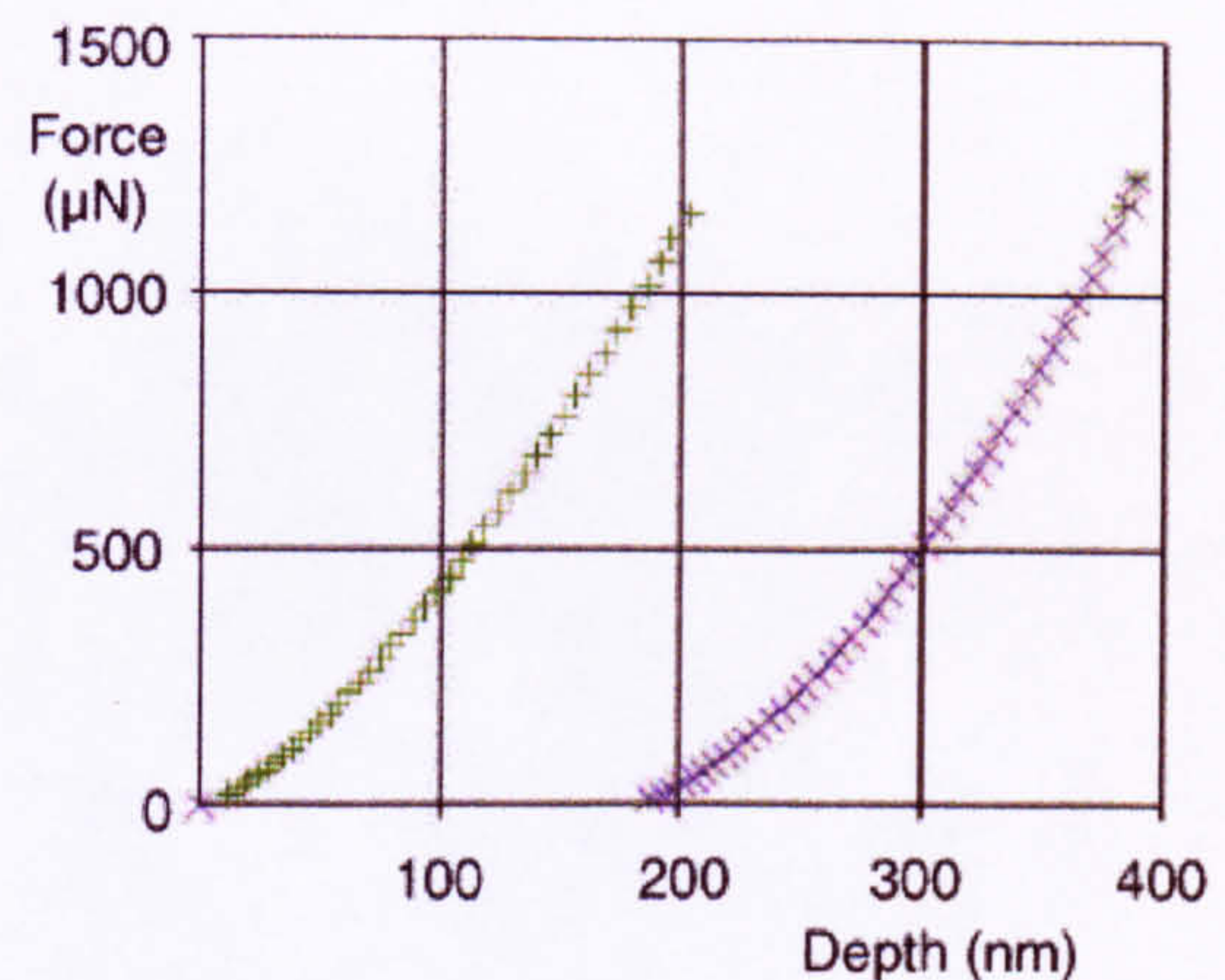
#### 4.5.1 Graphite $\{0001\}$

Nanoindentation was performed on the graphite substrate for varying loads from 350  $\mu\text{N}$  to 1500  $\mu\text{N}$ . Fig. 4.4.26 presents the experimental load-displacement curves for indentation into the  $\{0001\}$  face of the HOPG substrate for loads of 1240  $\mu\text{N}$  and 1450  $\mu\text{N}$ . Fig. 4.4.26(a) shows the loading and unloading curves to overlap, which gives a purely elastic response from the graphite substrate. As the load is increased to about 1240  $\mu\text{N}$ , the experimental load-displacement curve in Fig. 4.4.26(b) shows that a dis-





(a)



(b)

Fig. 4.4.26. Experimental force-depth curves for indentation into the  $\{0001\}$  face of HOPG graphite: (a) complete elastic behaviour; and (b) increasing force causing break-through of the layers: (+) increasing load curve; (x) decreasing load curve.

continuity occurs in the value of the indentation depth. This attribute arises from the increased load, which has become sufficient to break through a number of the graphite layers, in this case about 130. This number of layers is dependent on the local defect structure in the graphite material. The breakthrough of graphite layers could not be verified in the MD simulations, primarily due to the low penetration depths. Considerably larger substrates would be required to observe a breakthrough of an atomically layered material such as graphite. Despite the breakage of a number of the substrate layers, the unloading curve in Fig. 4.4.26(b) lies parallel to the loading curve, and so shows an elastic recovery of the sample. The experimental curves show a power law dependency of the form  $F = kh^m$ , as discussed in Section 3.4, Chapter 3. An analysis of the force-depth curve in Fig. 4.4.26(a) shows the index  $m$  to be approximately 1.4 for the HOPG substrate. The nanohardness for graphite calculated from Eqn. 3.4.3.1 (Chapter 3) is 2.35 GPa for an elastic deformation depth of 202 nm. From Eqn. 3.4.3.2 (Chapter 3) the Young's modulus is determined to be  $E = 10.5$  GPa.

### 4.5.2 Diamond $\{111\}$

Varying loads from 2000  $\mu\text{N}$  up to 3350  $\mu\text{N}$  were applied to the indenter to penetrate the  $\{111\}$  surface of the synthetic diamond substrate. The corresponding experimental



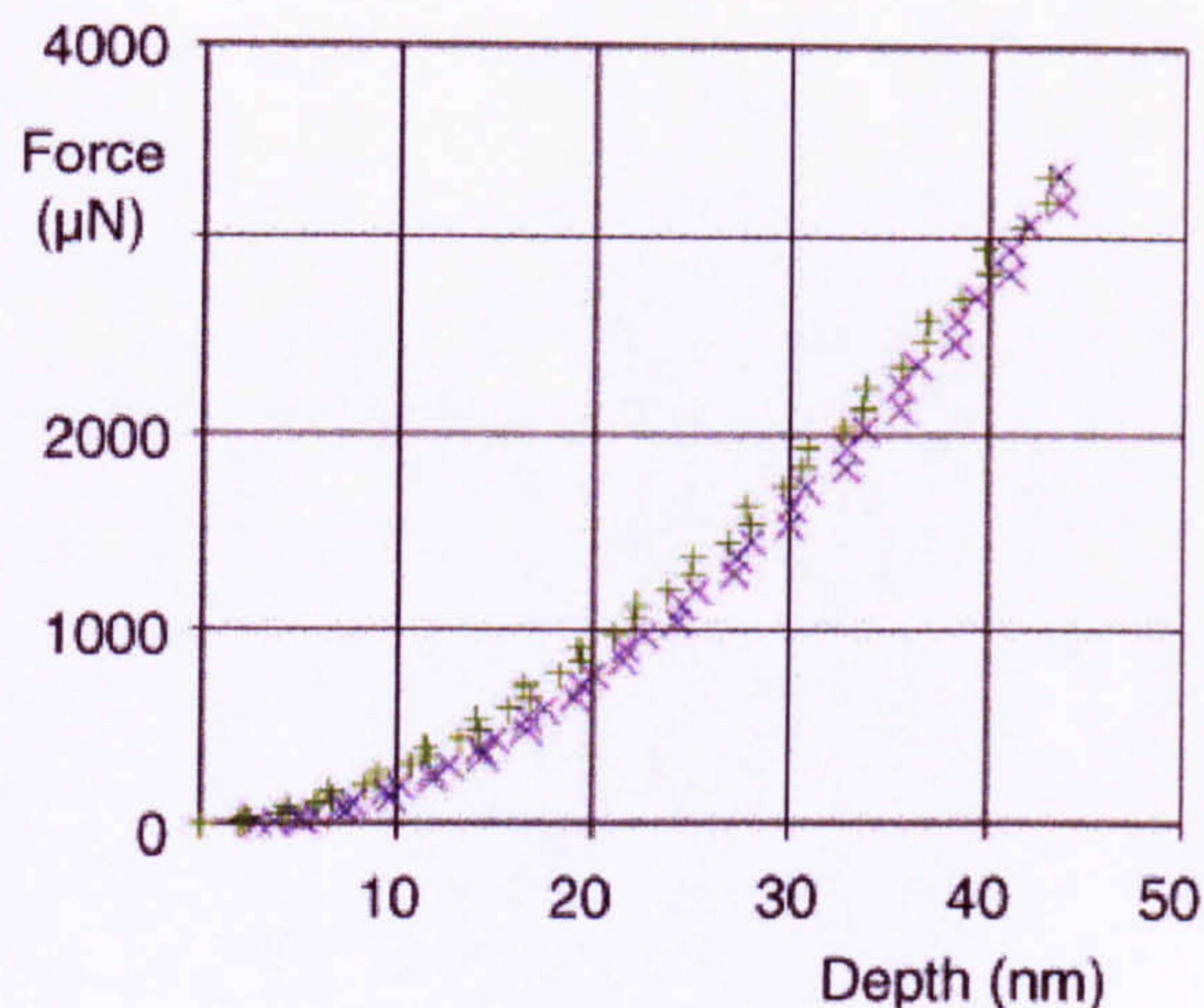


Fig. 4.4.27. Force-depth curve for indentation into the  $\{111\}$  face of diamond at the maximum applied load of  $3350 \mu\text{N}$ : (+) increasing load curve; (x) decreasing load curve.

load-displacement curve is illustrated in Fig. 4.4.27, reflecting a purely elastic response from the material. It is interesting to note from Fig. 4.4.27, the small indentation depth achieved from the high force that was applied to the tip, clearly reflecting the nanohardness of diamond. An examination of the force-depth curve in Fig. 4.4.27 shows that the index  $m$  takes a value of approximately 1.6 for diamond, giving a Young's modulus of  $E = 1137 \text{ GPa}$  for an elastic recovery of  $36 \text{ nm}$ . The respective nanohardness is calculated to be  $117 \text{ GPa}$ . These values correspond well to those published in the literature [154]-[156].

### 4.5.3 $\text{C}_{60}$ Fullerene Film

A maximum load of  $150 \mu\text{N}$  was used to indent the surface of a  $\text{C}_{60}$  substrate of  $1 \mu\text{m}$  thickness grown on glass. The corresponding load-displacement curve is presented in Fig. 4.4.28. Despite a small elastic response during the unloading stage, primarily a large plastic deformation of the  $\text{C}_{60}$  substrate takes place. The response from the substrate to the small applied load clearly reflects a very weakly bound material where the individual  $\text{C}_{60}$  molecules are readily displaced. From an analysis of the force-depth curve in Fig. 4.4.28 the index  $m$  is calculated to be approximately 1.5 giving a Young's modulus for the fullerene substrate of  $E = 13.0 \text{ GPa}$ . The nanohardness of the  $\text{C}_{60}$  substrate is calculated to be  $0.21 \text{ GPa}$ . These values are lower than those published in the literature [157]-[160].



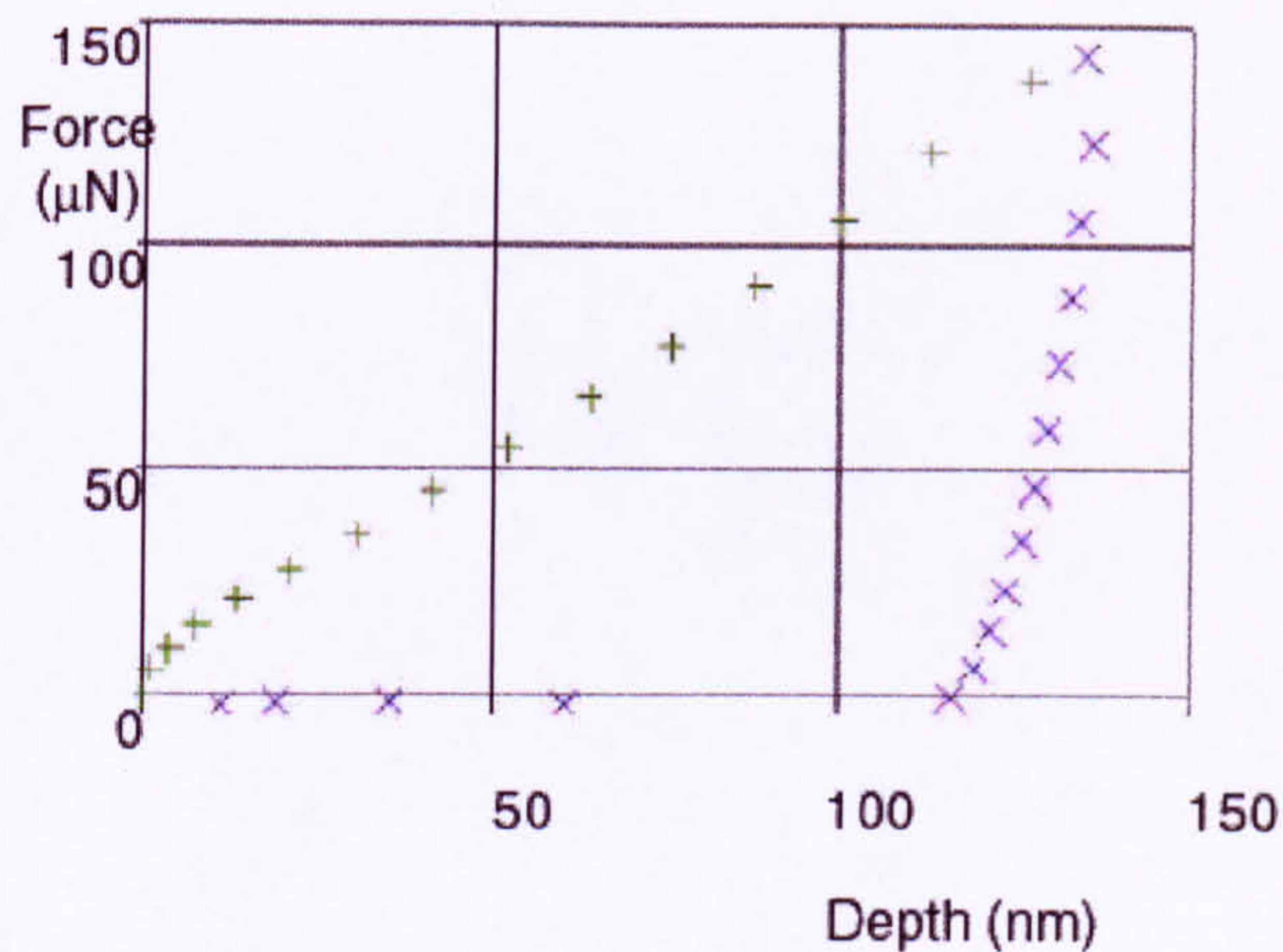


Fig. 4.4.28. Force-depth curve for indentation into the  $C_{60}$  substrate on glass at the maximum applied load of  $150 \mu\text{N}$ : (+) increasing load curve; (x) decreasing load curve.

## 4.6 Summary

Nanoindentation of various carbon materials has been probed by MD simulations implementing an atomistic description of the indenter. The simulations yield the same qualitative behaviour for graphite and diamond as the interface indenter description in the previous chapter. For both indenter models, qualitative agreement was found between the MD simulations and the experimental results of Richter *et al* [124]. The experimental results extracted mechanical properties that compared well with other studies in the literature. Simulations with graphite reflected a chemically inert material, deforming purely elastically towards indentation, accompanied with hexagonal surface waves propagating from the point of indentation. The experimental observations also suggested that the elastic behaviour of graphite can be accompanied with catastrophic breaking of atomic layers. Indentation of the  $C_{60}$  film by MD revealed the permanent displacement molecules, reflecting a weakly bound material. The plastic deformation of the work piece resulted in adhesion between the tip and some individual  $C_{60}$  molecules. Experimental verification of the weakly bonded  $C_{60}$  film also suggested the predominately plastic response was also accompanied with small elastic behaviour.

Simulations implementing the atomistic indenter representation have allowed the indentation to have some physical impact on the tip. Elastic deformation of the apex was observed as the tip compressed during penetration of the substrates. The hardest of the samples, diamond, compressed the tip the most, while indentation of the much softer



C<sub>60</sub> film resulted in virtually no compression. Since the tip is atomically sharp, the apex atoms have low coordination. This leads to different mechanical properties compared with bulk diamond, and the tip is much softer and compresses more easily. Indentation of diamond with a blunted ‘flat’ tip indenter showed less compression since the network structure in the apex was significantly more developed.

The simulations show that when contacting surfaces are clean, i.e. free from adsorbates, then strong interfacial adhesion can occur. The tip-substrate adhesion stems from the large number of dangling bonds in the indenter and substrate. In the case of adsorbate-free diamond, interfacial adhesion was characterised by connective threads of atoms between the substrate and the tip. Connective strands measuring up to 15 Å were observed, and were composed chiefly from indenter atoms, although some substrate atoms were also constituents. Rupture of the connective threads ensued in atom transfer to and from both the indenter and work piece, in a predominantly amorphous arrangement. The addition and dispossession of atoms showed how the initial stages of tip blunting can occur. The tip-substrate adhesion imparted a small degree of plastic deformation in the surface local to the indentation. However, the fractional plastic deformation was not reflected in the force-depth curves and only determined by visual inspection of the indentation region. Despite interfacial adhesion, the diamond material reflected a predominantly elastic response towards indentation.

Saturation of the indenter and substrate surfaces with an adsorbate show that a layer of impurities can significantly reduce, or even completely prevent, adhesion between tip and sample. Indentation of hydrogen terminated diamond {100} ensued in a purely elastic deformation of the work piece, with no observable interfacial adhesion and the tip retaining its structural integrity. Simulations performed on *a*-C:H substrates with comparatively high and low densities showed minimal tip-substrate adhesion occurred, with a very small transfer of atoms across the contacting interface. The adhesion with *a*-C:H occurred primarily because the substrate surface is only partially terminated and there are void regions where subsurface atoms expose dangling bonds. No significant rearrangement in the bonding structure of the *a*-C:H work materials was found subsequent to indentation and the therefore the deformation was considered primarily elastic.



# Chapter 5

## Nanoindentation of bcc and fcc Metals Implementing the Atomistic Indenter Model

### 5.1 Introduction

There has long been considerable motivation to probe the mechanical properties of metals because of their widespread applications. The bulk deformation behaviour of metals towards indentation has been widely studied and documented [20]. It is well known that metals undergo appreciable plastic deformation in response to indentation, which can be partially recovered by annealing. It has been shown for macroindentations of metals that the material around the indenting tool can be extruded upwards in a process known as ‘piling-up’, forming a collected heap on the surface [161] (the pile-up is also called a hillock). The opposite trend in metal indentation is called ‘sinking-in’ where the material around the indent is depressed. In 1968 a pioneering study by Gane and Bowden [162] reported different metallic behaviour during hardness testing at different depth scales. Subsequent work has also suggested that the bulk behaviour of metals differs as the scale of indentation depth is reduced. Hence, as the present day importance of device miniaturisation continues, probing the mechanical properties of metals at the nanoscale is becoming ever more crucial. To explore the nanoscale behaviour of metals, experimental and complementary theoretical studies have recently been undertaken.

Extensive MD simulations of metal indentation have been performed by Landman



and co-workers [163]-[165] in the early part of the last decade. They reported on indentation of several different metals, including Au and Ni, using sharp metallic pyramidal tips. During the simulations an interesting asperity-substrate phenomena was observed in the loading stage. When the tip-substrate separation distance surpassed a critical value, some of the atoms in the tip and those sited directly underneath in the substrate surface jumped towards each other in a relatively short time span. This phenomenon, called a 'jump-to-contact' (JC) or 'avalanche in adhesion', stems from mechanical instability in the tip-substrate system and ensues in 'wetting' of the tip by substrate atoms (or vice versa). In the JC phenomena Landman *et al* observed that the material with the lowest modulus tended to bulge out towards the other. On reversal of the tip, the adhesive interface stretched and a 'connective neck' was formed which proceeded to elongate leading to significant structural rearrangement and ultimately breakage. The formation and rupture of the connective neck allowed substantial atom transfer between the tip and the work piece. A recent study by Buldum *et al* [166] reported on the indentation of Cu {110} and Cu {100} using both sharp and blunt Ni tips. The sharp tip had a single atom asperity and produced multiple sequential JC phenomena on approach to the surface. The behaviour of the blunt hemispherical Ni tip was considerably different since only a single JC was observed.

Landman *et al* [165] researched the tip-substrate bonding further by coating the tip with an epitaxial monolayer. During indentation with the coated tip the JC phenomena was again observed, but the asperity-substrate adhesion was significantly reduced. Although a connective neck was formed, atom transfer between the work material and the tip also decreased. This behaviour was attributed to the expitaxial monolayer preventing a multitude of interfacial bonds. The force of adhesion for Ir and Pb substrates was examined by Sutton *et al* [113] for indentation with Ir and Pb tips. They introduced a monolayer on the surface of the work material. Although 'soft' and 'hard' monolayers were considered, in both cases a JC phenomena was observed and a connective neck formed during reversal of the indenter. The only difference between the soft and hard monolayer was a dominance in which of the surface or tip atoms stimulated the JC. Independent of the soft or hard monolayer, Sutton *et al* found the layer of impurities prevented a multitude of tip-substrate bonds forming, even when the apex penetrated through the surface impurities. Consequently the force of adhesion was less compared with indention with the clean surface. In conclusion, they found that interfacial adhe-



sion could be minimised by a monolayer of impurities on the sample surface.

More recent MD studies of Pb indentation were reported by Tomagnini *et al* [167]. Using a pyramidal Au tip they simulated the indentation of Pb {110} at a temperature of 600 K. The high temperature caused the substrate surface and subsurface to melt forming a liquid surface region. Subsequent to an observed JC phenomena as the indenter approached the work material, the tip of the impinging indenter dissolved in the liquid region of the work piece. During tip retraction a liquid-like connective neck was formed and increased in length as the indenter displaced further away from the substrate. In a study by Belak *et al* [168] the indentation of Cu {111} with a diamond indenter was explored. At an indentation depth of seven atomic layers almost the entire volume of the probing tip had been consumed. The range of the plastic deformation was limited to within a few lattice spacings about the indenter. Furthermore, little pile-up of atoms around the indent was observed. A minor dislocation loop was marked by the presence of a small step in the surface local to the indentation region. Further tip-induced phenomena occurring in metals have also been investigated. The induced surface topography in the form of pile-up has been studied by Bolshakov *et al* [169]. In a finite element study they found evidence that the piled-up material around an indented aluminium alloy material supported the load of the indenter.

On the experimental front, numerous investigations of asperity contact with metals have also been reported. Kuipers and Frenken [170] investigated the indentation of Pb {110} with a W tip. At elevated temperatures the JC phenomena was observed, followed by the formation of a connective neck. Using STM Brandbyge *et al* [171] measured a nanowire up to 20 Å in length when a connective neck between the tip and Au {110} substrate was elongated. Experimental indentation of metals has also been performed with a covalently bonded tip. For example, Pharr and Oliver [172] investigated the indentation of Ag {111} with a diamond pyramidal indenter. They observed a depth dependency of nanohardness, in two distinct stages. For indentation depths of about 100 nm a gradual increase in nanohardness was found. However, when the indentation depth was reduced to 50 nm or less, the nanohardness increased sharply. The influence of specimen preparation methods on nanohardness was investigated by Liu *et al* [173] for indentation of high purity Cu {111} crystals. At indentation depths lower than 400 nm they observed significant differences in nanohardness of the same sample polished by two different methods. The work by Corcoran *et al* [174] reported on diamond Berkovich



indentation of single Au crystals with different grain orientations. They found a series of ‘pop-ins’ in the force-depth curves, which is a displacement discontinuity where increased indentation depth results in a stationary force value. Experimental studies have also been extended to investigate the nanomechanical behaviour of alloys [175]-[176].

This chapter presents MD simulations of nanoindentation into body-centred-cubic (bcc) Fe and face-centred-cubic (fcc) Ag using the atomistic indenter model. The two specific metals are chosen simply to investigate the behaviour of both bcc and fcc metals in response to indentation and to compare with available experimental results. The crystal configuration of Fe and Ag is presented in Fig. 5.5.1. Hillock growth phenomenon has been observed for indentation in quasi-crystals [40]-[41], showing a definite orientation and crystallographic dependence. The nature of the deformed material under the indenter and the induced surface topography in the form of hillocks, together with defects and the reconstruction of material after penetration is studied. In reality, metals occur as an assembly of small crystals randomly orientated with respect to each other. The boundaries between them are commonly referred to as grain boundaries [177]-[179] and are typically areas of low atomic density. Hence, indentation along grain boundaries is also studied by simulation, since they play an important role in the adhesion and deformation of polycrystalline materials. Furthermore, different surface orientations are chosen for simulated indentation near a grain boundary so that the influence of surface

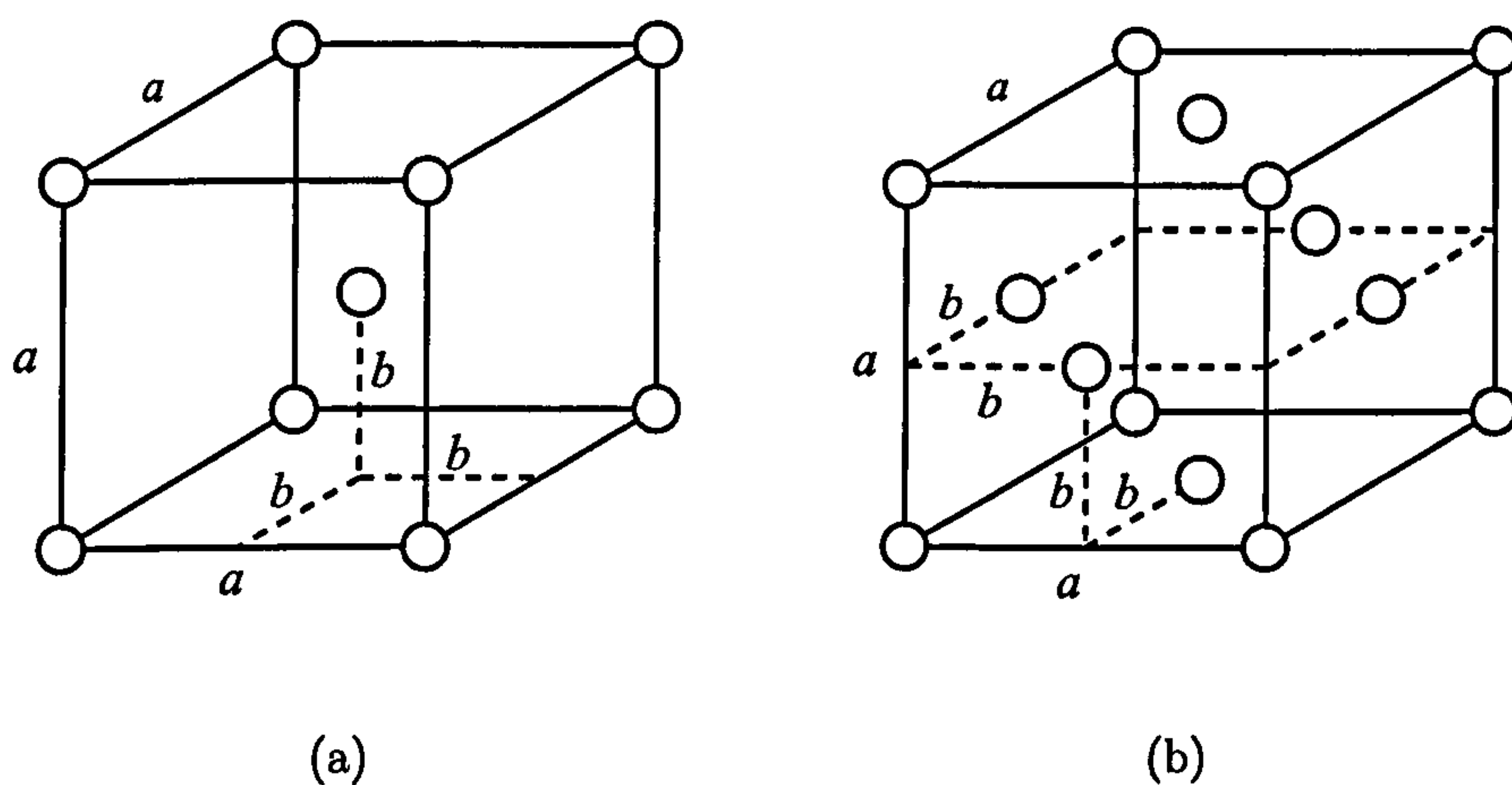


Fig. 5.5.1. (a) The unit bcc cell of a Fe crystal, where  $a$  denotes the lattice constant equal to  $2.866 \text{ \AA}$  and  $b$  denotes half the lattice constant. (b) The unit fcc cell of a Ag crystal, where  $a$  denotes the lattice constant equal to  $4.086 \text{ \AA}$  and  $b$  denotes half the lattice constant.



grain on mechanical behaviour can be studied. The simulation results are compared with experimental results for polycrystalline Fe and Ag in a companion paper [180], where nanoindentations were performed using the Hysitron Nanoindenter Triboscope [152] as detailed in the preceding chapter. The preparation of the polycrystalline samples is described in the companion paper. Also discussed in this chapter is the computational efficiency of Ackland's potential used to describe the Ag-Ag interactions.

## 5.2 Simulation Details

Indentations are performed on the bcc and fcc  $\{100\}$  crystal surfaces. For the investigation near a grain boundary, Fe  $\{100\}\{111\}$  crystal grains are employed. Atoms on the vertical edges of the substrate are held fixed and all remaining substrate atoms are damped. Adhesion between the indenter and the work material is not permitted since the tip-substrate interactions are modelled in a purely repulsive way by the ZBL potential [129], which is smoothly cut-off at 3.59 Å. Since the indenter and substrate interactions are modelled in an entirely repulsive way, the atomistic indenter without hydrogen termination is implemented here.

For simulations with Fe  $\{100\}$ , a crystal with approximate dimensions  $115 \text{ Å} \times 115 \text{ Å} \times 40 \text{ Å}$  is employed. The  $\{100\}$  work piece is composed of 28 atomic layers and is configured from 44,800 atoms, where 4,368 atoms form the constrained boundary. The Fe  $\{100\}\{111\}$  grain boundary substrate has approximately the same dimensions as the  $\{100\}$  substrate and is composed from 46,216 atoms, where 6,658 atoms form the fixed vertical border. The  $\{100\}$  grain and  $\{111\}$  grain are composed from 28 and 49 atomic layers respectively. The grain boundary in the substrate is aligned vertically along the centre of the work material, where the indentation is made. The work material is formed by combining a Fe  $\{100\}$  and  $\{111\}$  crystal where the atoms at the boundary reconstruct. This process is repeated by translational motion between the two different crystal orientations and relaxing to find the minimum energy configuration. The Fe-Fe interactions are described by a potential with the Finnis-Sinclair form [181], which is smoothly cut-off at 3.62 Å. Simulations with Ag are performed on a crystal with approximate dimensions  $130 \text{ Å} \times 130 \text{ Å} \times 40 \text{ Å}$ . The  $\{100\}$  work material is composed of 20 atomic layers and contains 40,960 atoms, where 4,960 atoms compose the fixed vertical border. The Ag-Ag interactions are described by Ackland's EAM potential [182], which



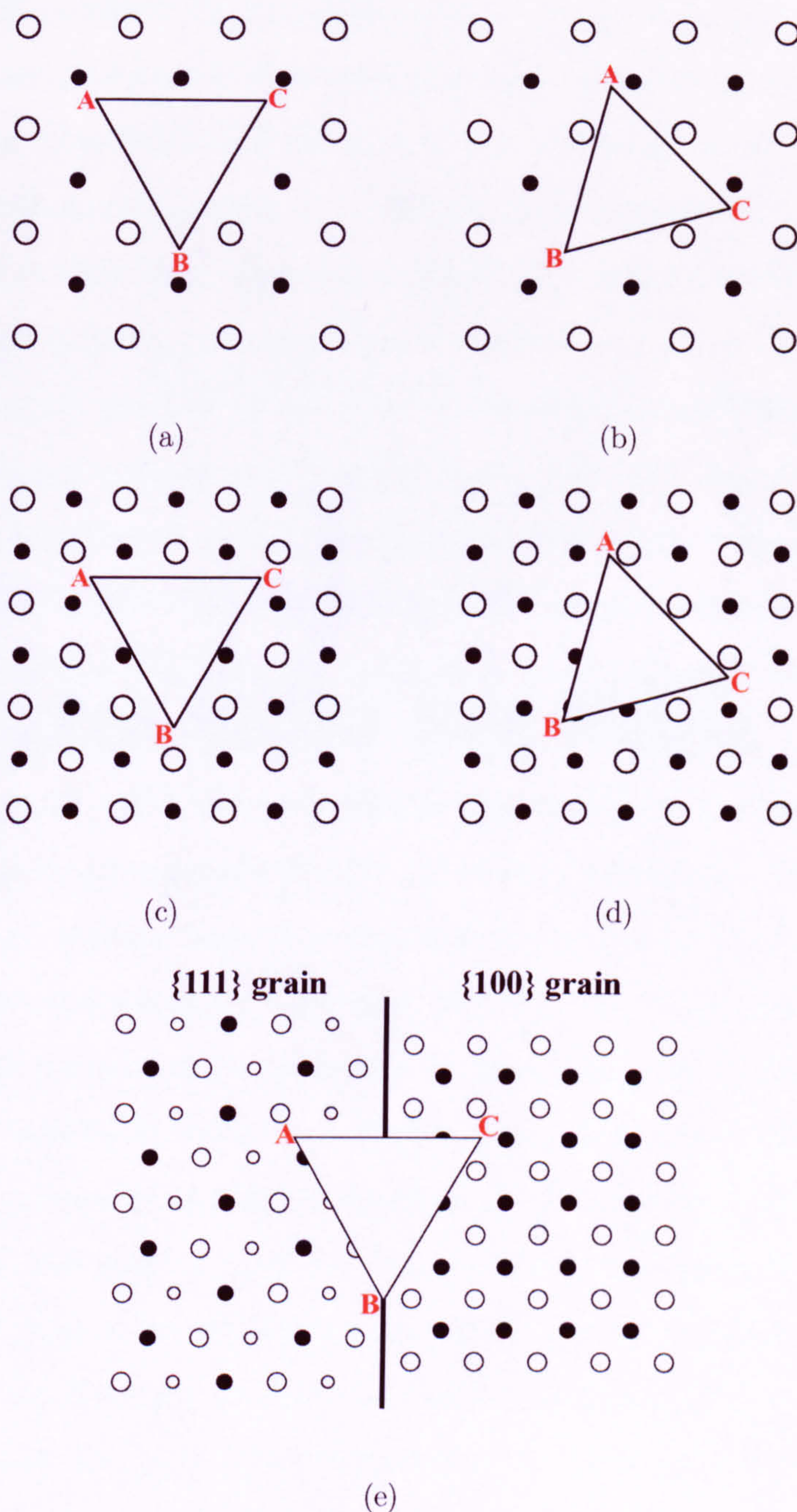


Fig. 5.5.2. Plan views of the indenter rotation with respect to the atomic structure of the substrate for: (a) Fe  $\{100\}$  with  $\phi = 0^\circ$ ; (b) Fe  $\{100\}$  with  $\phi = 45^\circ$ ; (c) Ag  $\{100\}$  with  $\phi = 0^\circ$ ; (d) Ag  $\{100\}$  with  $\phi = 45^\circ$ ; (e) Fe  $\{100\}\{111\}$  grain boundary with  $\phi = 0^\circ$ . Large and small unshaded circles denote 1<sup>st</sup> and 3<sup>rd</sup> layer atoms respectively, while shaded circles represent 2<sup>nd</sup> layer atoms. In (a) and (c) the indenter side AC is parallel to  $\langle 100 \rangle$  with remaining sides sited  $15^\circ$  from  $\langle 110 \rangle$ . In (b) and (d) the indenter side AC is parallel to  $\langle 110 \rangle$ , with remaining sides aligned  $15^\circ$  from  $\langle 100 \rangle$ . In (e) the central bold line denotes the grain boundary.



is smoothly cut-off at 5.0044 Å. The elastic constants and stacking fault energy for the metal potentials are given in the references and are found to be in good agreement with experimental data. Simulations of duration 150 ps are exercised here for all work materials, with an indentation period,  $T = 150$  ps. At the beginning of each simulation, the indenter apex is sited 10 Å above the middle of the substrate surface and the maximum displacement of the constrained indenter atoms,  $r_{\max}$ , is set to 30 Å. This gives an average indentation speed of 40 ms<sup>-1</sup> and a maximum possible penetration depth of 20 Å. The equations of motion are integrated with a constant timestep of 1.0 fs. Unless otherwise stated all substrate atoms are shaded on their vertical displacement.

The distribution of piled-up material reflects the crystal structure of the substrate. With axially symmetric indenters like spheres or cones, the tip-induced deformation should reflect only the crystal symmetry of the substrate. However, spherical indenters are not generally used since they are difficult to manufacture with the precision required in nanoindentation experiments and are not self symmetric. With cube-cornered indenters there is an overlap between crystal and indenter symmetry, which complicates the analysis of pile-up formation. Therefore, the rotation of the indenter with respect to the atomic configuration of the substrate is examined. Pile-up will be a maximum if one side of the pyramidal indenter is aligned along a preferred direction for hillock formation. The rotation of the tip (defined by  $\phi$ ) is considered only for indentation of the single {100} bcc and fcc crystals. Two indenter orientations are studied where one cross-sectional edge of the pyramid is parallel to either the  $\langle 100 \rangle$  or  $\langle 110 \rangle$  direction. These alignments are chosen to reflect the surface symmetry of the crystals. For the grain boundary substrate, only one orientation of the indenter is considered. The rotation of the indenter with respect to the work material is shown schematically in Fig. 5.5.2.

## 5.3 Simulation Results and Discussion

### 5.3.1 Body-centred-cubic Iron

#### Fe {100} Substrate

The force-depth curves for indentation of Fe {100} are shown in Fig. 5.5.3 where the upper portion of the curves corresponds to the loading stage and the lower portion is



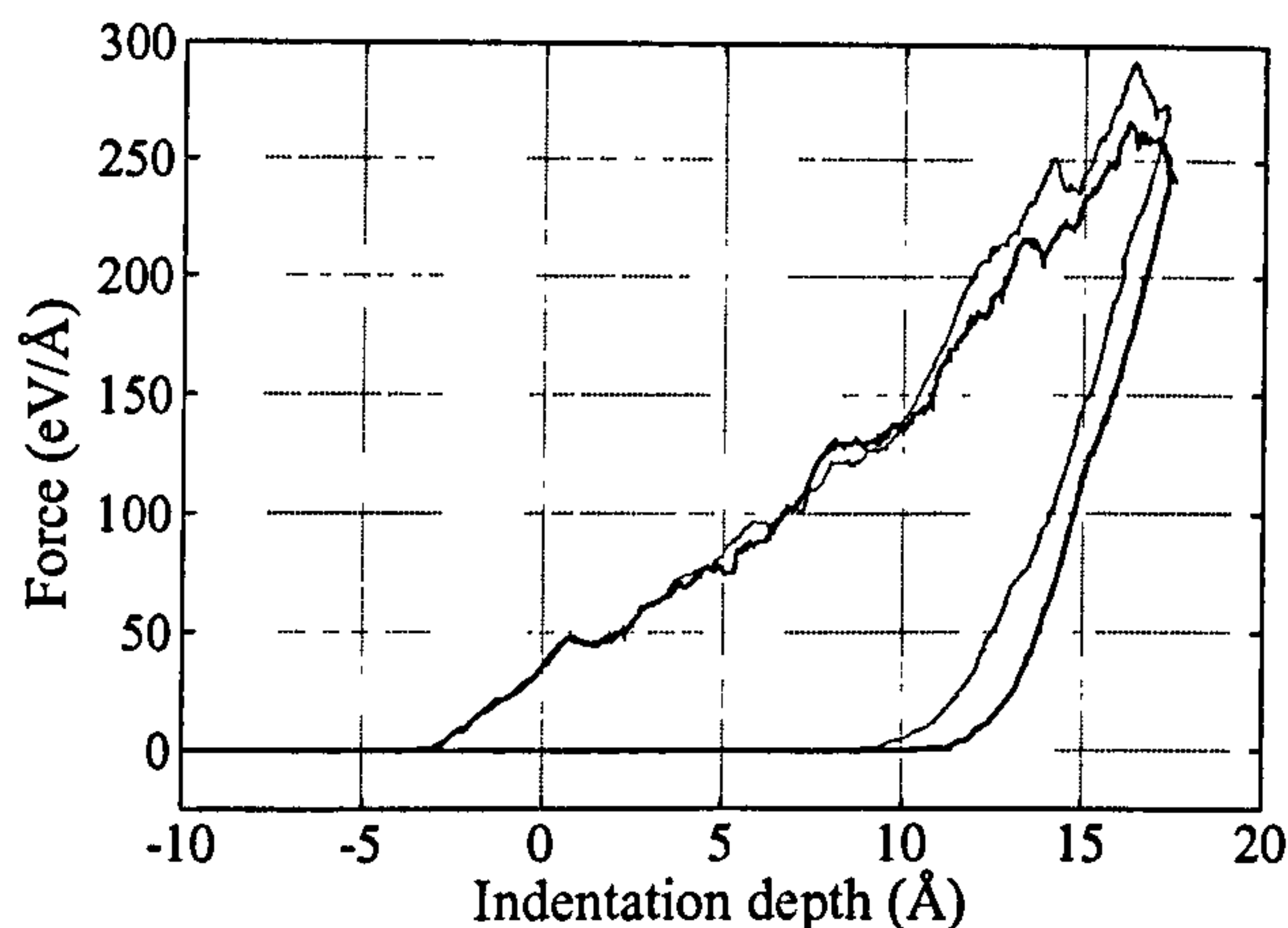


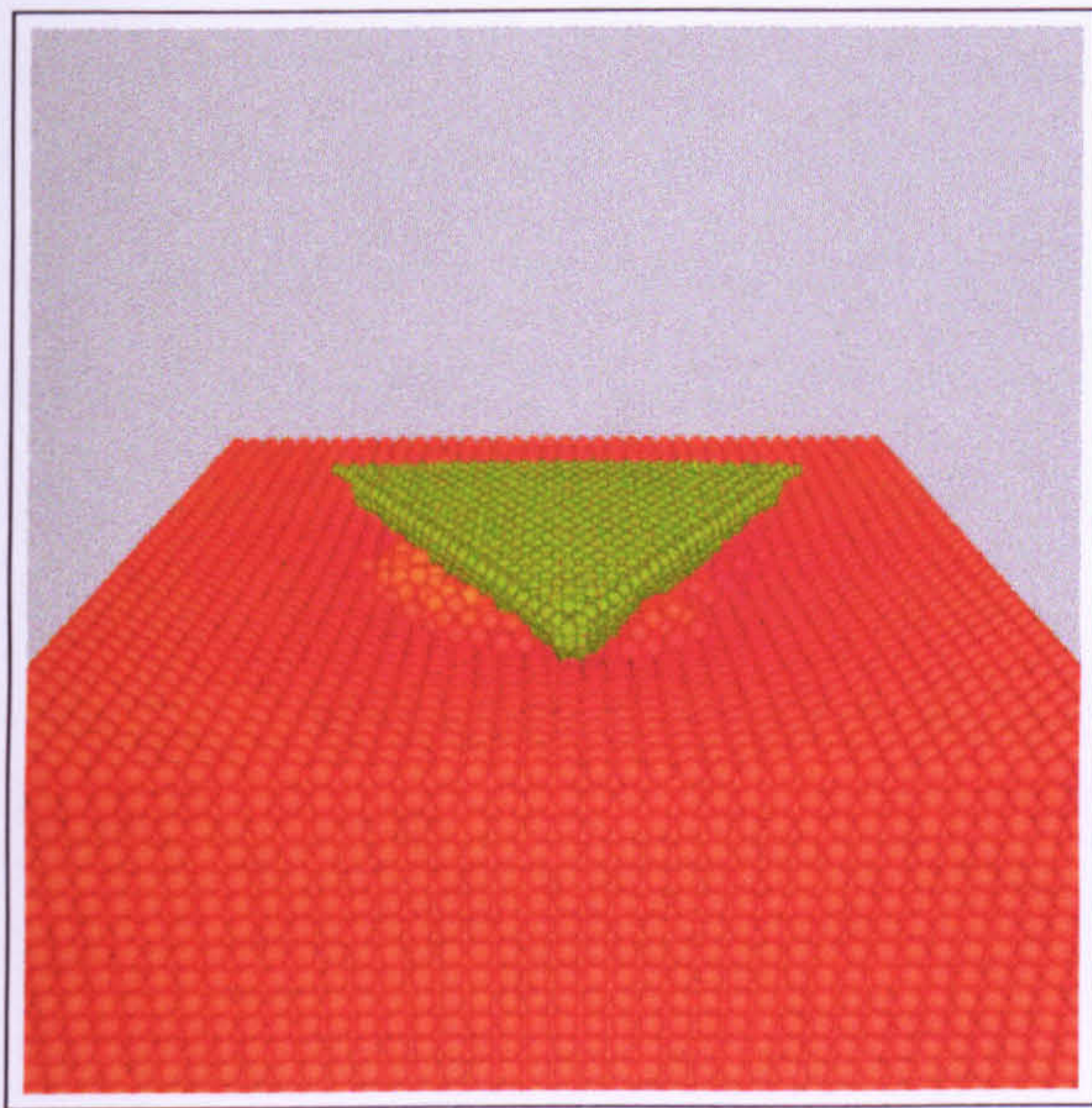
Fig. 5.5.3. Force-depth curves from the simulations of indentation into the Fe {100} crystal. The bold solid line corresponds to indentation with  $\phi = 0^\circ$  and the remaining line denotes indentation with  $\phi = 45^\circ$ .

the load during extraction. The different orientations of the indenter with respect to the substrate surface result in very similar force-depth curves. In both simulations the indenter reached a maximum penetration depth of approximately 17 Å. The peak force acting on the diamond tip was 265 eV/Å and 290 eV/Å for indentation with  $\phi = 0^\circ$  and  $\phi = 45^\circ$  respectively, which occurred during the loading stage just before the maximum penetration depth at roughly 16 Å. On tip retraction the force acting on the indenter quickly declines because appreciable plastic deformation has occurred. The elastic recovery of the substrate during the unloading stage takes place over approximately 7 Å depth. From Fig. 5.5.3 the load-displacement curves show the low coordinated tip compressed by roughly 3 Å during the indentation. Snapshots from the halfway stage of the simulations in Fig. 5.5.4(a) and (c) reveal the piling-up of work material along the indenter sides. At the conclusion of the simulations, Fig. 5.5.4(b) and (d) show the plastic deformation is characterised by a permanent impression in the Fe sample, which corresponds to the geometry of the indenter. Note the difference in the distribution of the material pile-up along the sides of the plastically deformed triangular region. This will be discussed in more detail in Chapter 7.

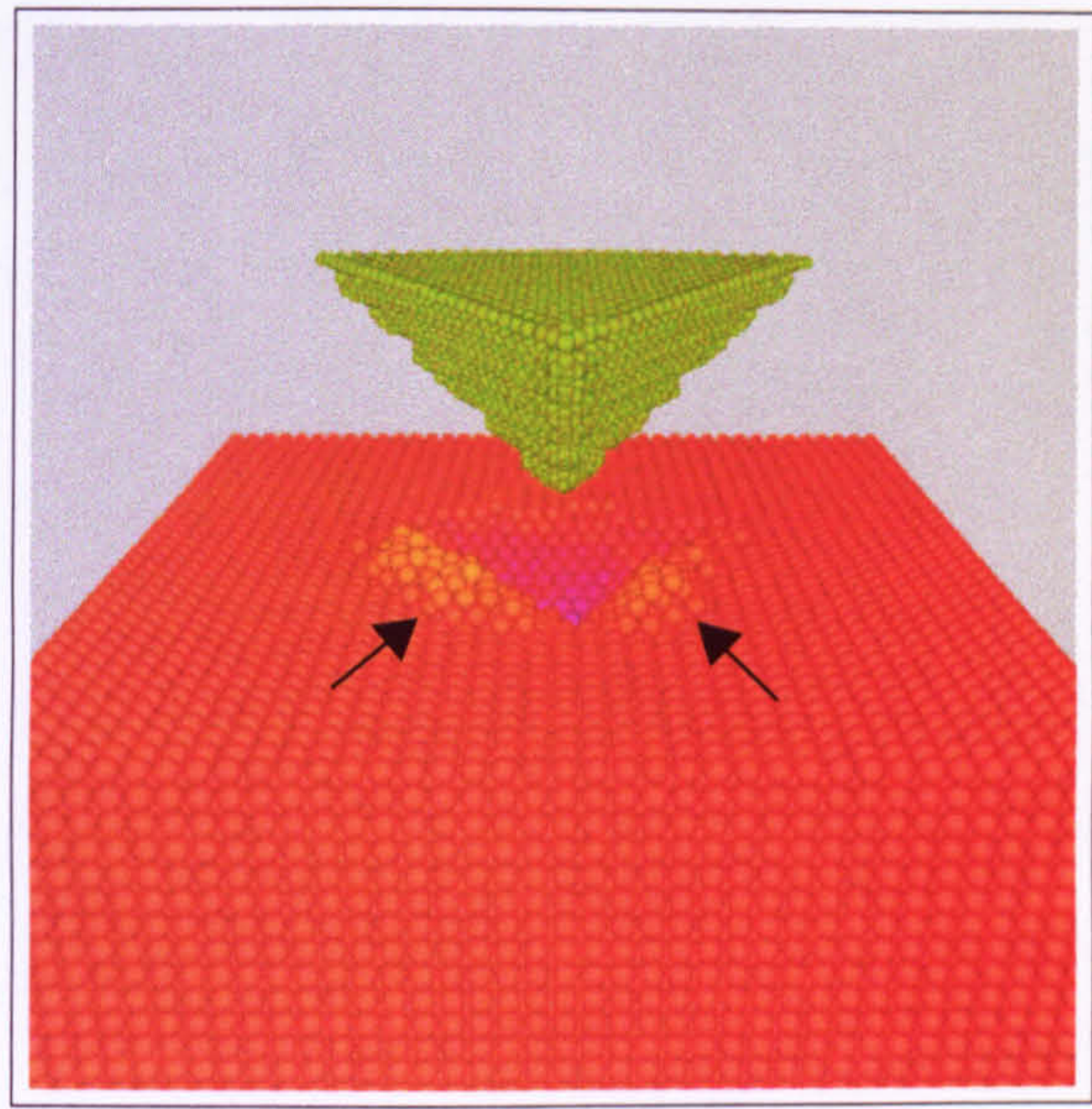
As the impinging indenter makes mechanical contact with the substrate, some of the atoms sited directly below the tip are forced to release their stored elastic energy. A number of the Fe atoms close to the apex are displaced further into the substrate, while those Fe atoms that lie along the sides of the indenter are displaced outwards towards their neighbours. The displacement of these atoms introduces a series of point



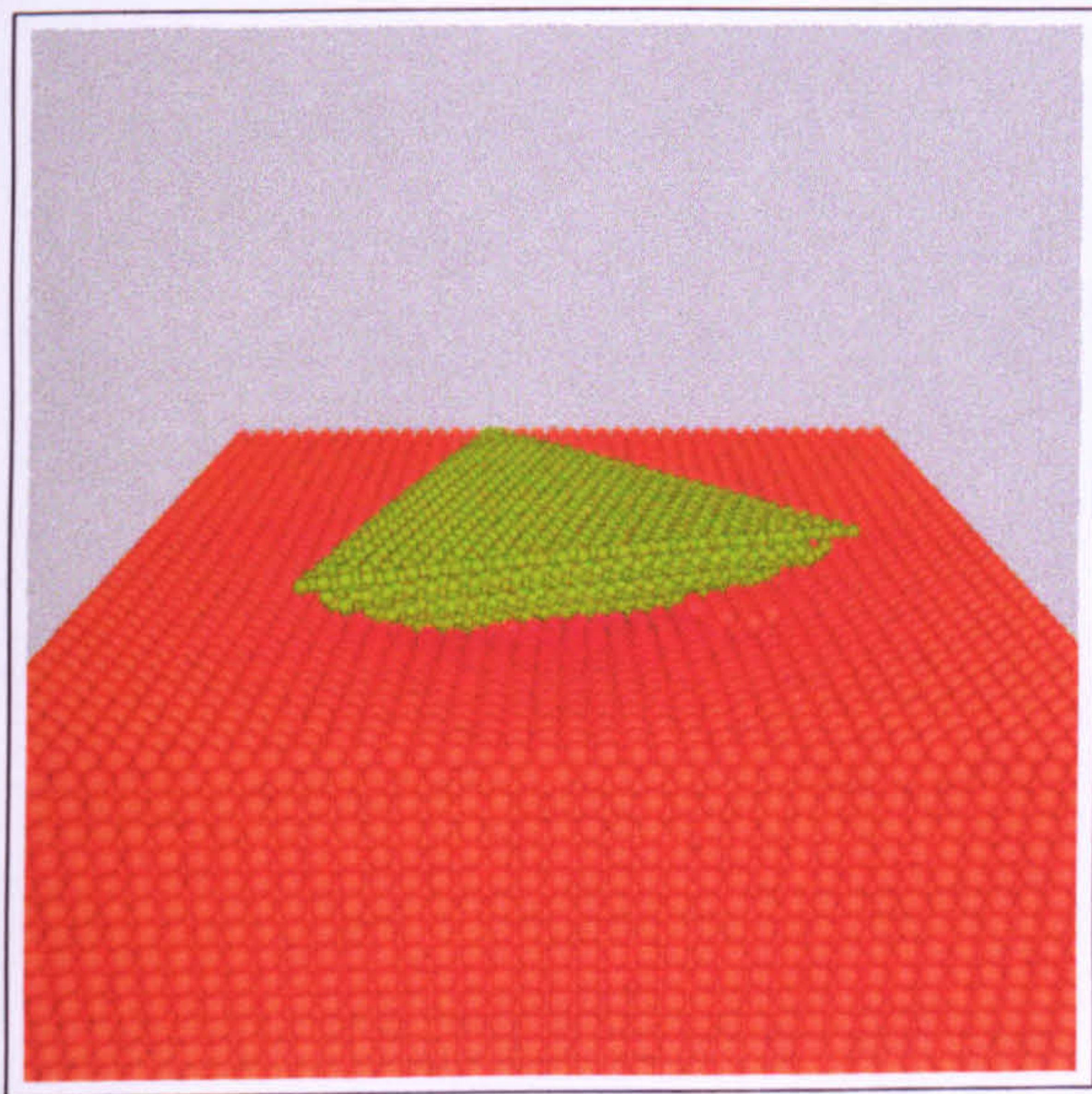
defects (i.e. atomic irregularities in the lattice) in the substrate which evolve through the material during the indentation process. Hence, the plastic deformation develops by rapid rearrangement of bonding in the network structure. For more information on



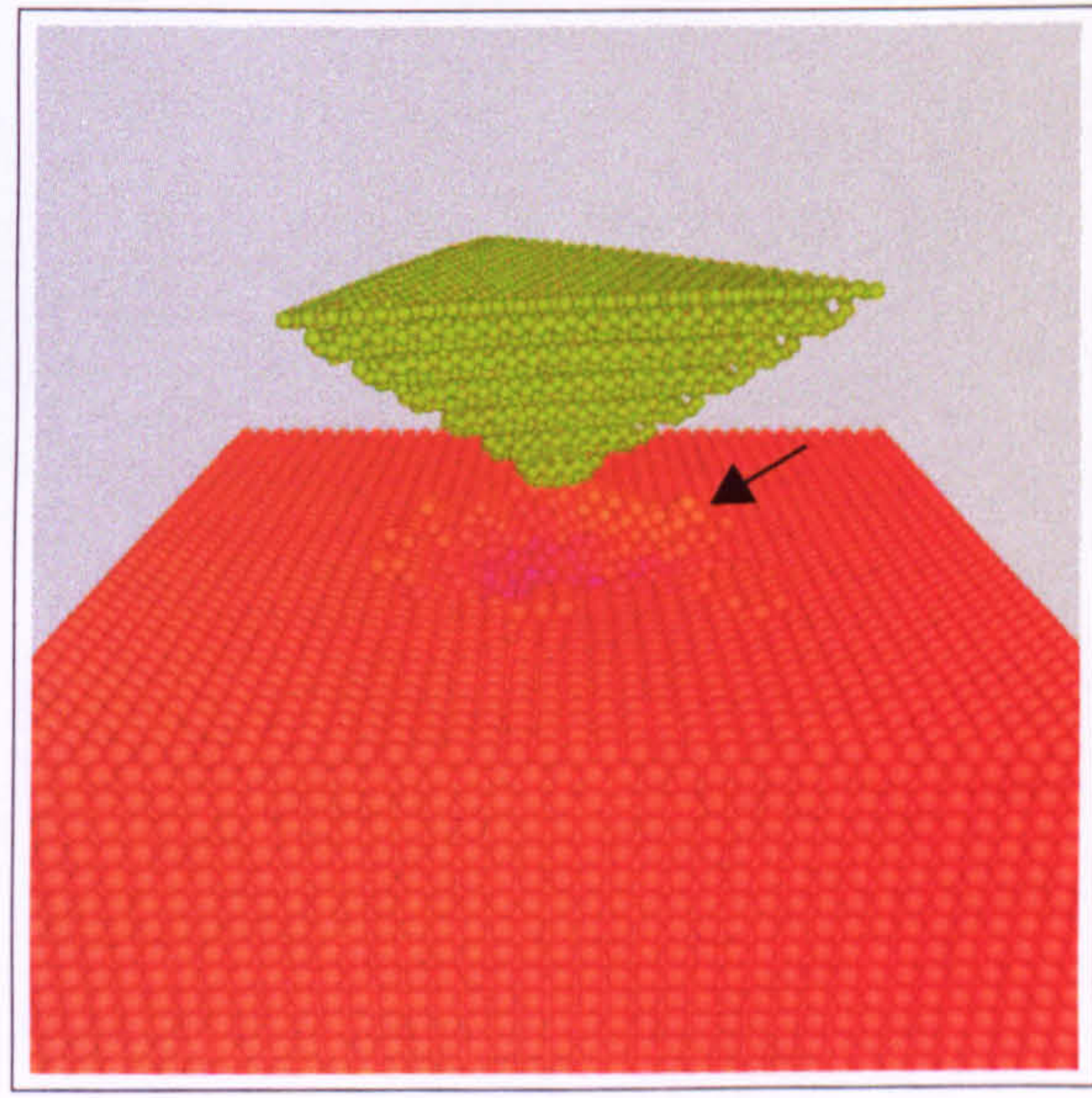
(a)



(b)



(c)



(d)

Fig. 5.5.4. Snapshots from the simulation of indentation into the Fe {100} crystal with: (a)  $\phi = 0^\circ$  at  $t = 75$  ps; (b)  $\phi = 0^\circ$  at  $t = 150$  ps; (c)  $\phi = 45^\circ$  at  $t = 75$  ps; (d)  $\phi = 45^\circ$  at  $t = 150$  ps. Note the large plastic deformation of the substrate and the pile-up along the sides of the plastically deformed triangular region, as marked by the arrows.



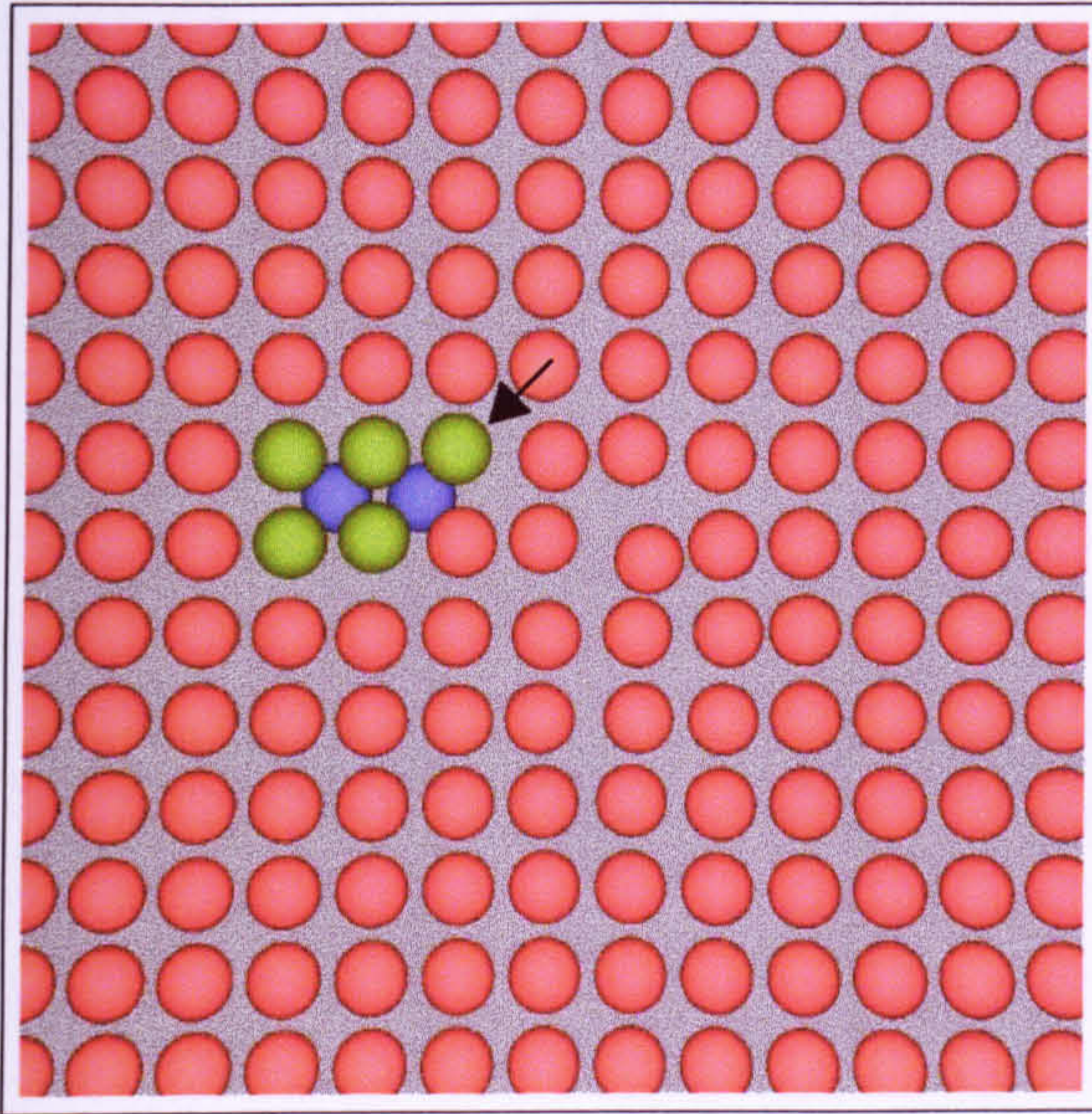
crystalline irregularities in metals the reader may proceed to Damask and Dienes [183]. Some of the surface atoms that displace outwards move towards interstitial sites which ensues in the atom ‘popping’ up on top of the surface. As a by product, vacant lattice sites are introduced which can become occupied by subsurface atoms as the indentation progresses. This process also occurs in subsurface layers and therefore produces a plastic flow of atoms from the near surface region towards the crystal surface as they are sequentially displaced to and from lattice sites in consecutive atomic layers. As the indentation depth increases the atoms displaced above the surface accumulate and a well defined ‘pile-up’ is formed. The atoms displaced further into the substrate do so sequentially through the motion of the point defects. At the halfway stage of the indentation process with  $\phi = 0^\circ$ , 135 Fe atoms have been displaced vertically by more than 10 Å into the substrate compared with 113 Fe atoms for indentation with  $\phi = 45^\circ$ . At the end of the indentation process, the maximum vertical displacement of a Fe atom into the material is 15.7 Å and 14.2 Å for indentation with  $\phi = 0^\circ$  and  $\phi = 45^\circ$  respectively.

A mechanism responsible for pile-up and plastic flow is captured in the snapshots shown in Fig. 5.5.5. The series of images show the transition of 2 4<sup>th</sup> layer atoms displacing to the 3<sup>rd</sup> layer. The impinging indenter causes a green 3<sup>rd</sup> layer atom in Fig. 5.5.5(a) to displace towards an interstitial site in Fig. 5.5.5(b), as marked by the arrows. However, Fig. 5.5.5(c) shows the atom does not occupy the interstitial site and that it is energetically more favourable for the atom to be displaced up to a vacant lattice site in the 2<sup>nd</sup> layer. Similar behaviour is also observed with the blue 4<sup>th</sup> layer atoms as Fig. 5.5.5(d) show they eventually occupy the vacant lattice sites inhabited by the displaced 3<sup>rd</sup> layer atoms. Hence, the plastic flow of atoms is not of interstitial character since atoms are displaced to and from lattice sites during the transition to pile-up. Inspection of numerous other atom trajectories during the transition stage revealed this mechanism to be responsible for plastic flow and pile-up. However, other mechanisms ensuing in plastic flow and pile-up may also be active.

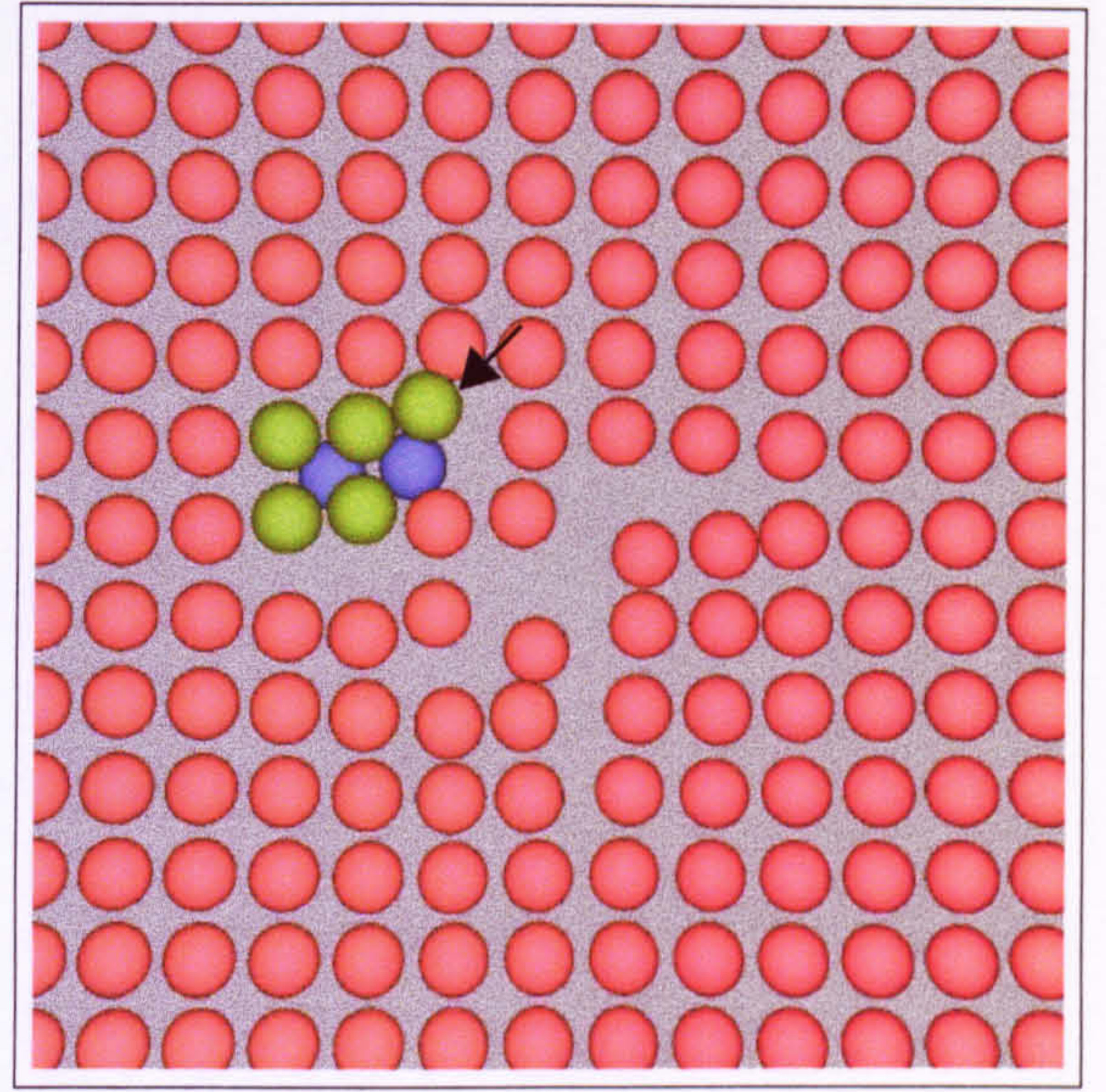
Fig. 5.5.6 shows the displacement path of a 3<sup>rd</sup> layer Fe atom illustrating the transition to pile-up via sequential jumps to preceding atomic layers. As the indentation progresses the atom is displaced towards the 4<sup>th</sup> layer. At point (A) the atom jumps upwards to a vacant site in the 2<sup>nd</sup> atomic layer at (B). The jumping time between the two atomic layers is very small, with a speed of approximately 80 ms<sup>-1</sup>. The jumping speed is faster than the average indentation speed of 40 ms<sup>-1</sup> yet considerably slower than the



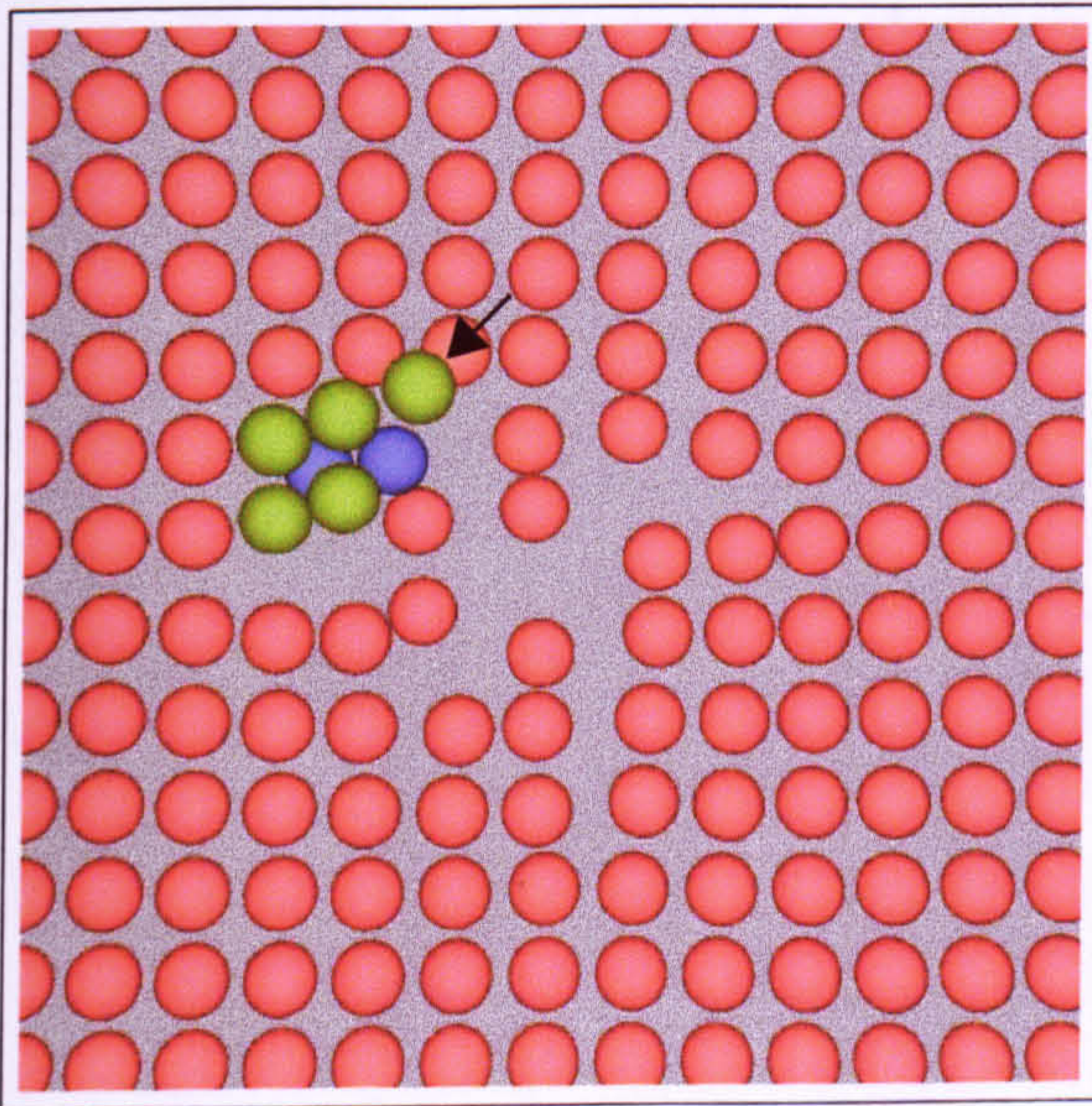
speed of sound. After (B), the atom continues to displace further into the substrate as the indenter penetrates further until at point (C) where another jump occurs to a vacant lattice site. However, this jump occurs over two atomic layers such that at point



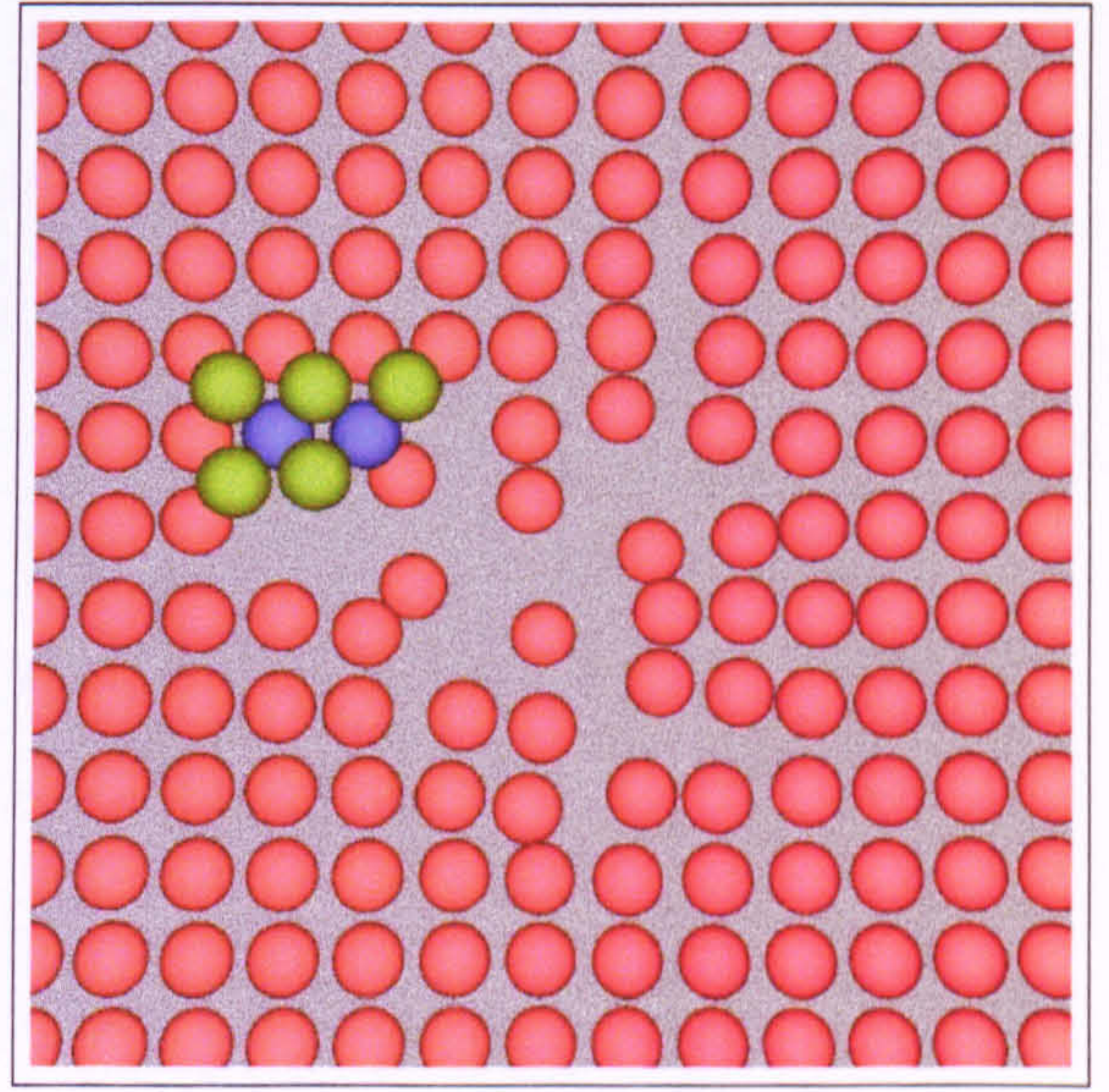
(a)



(b)



(c)



(d)

Fig. 5.5.5. Snapshots of the indentation area for the 3<sup>rd</sup> Fe {100} layer illustrating the mechanisms of pile-up and plastic flow. The green and red atoms represent the 3<sup>rd</sup> layer and the blue atoms are 4<sup>th</sup> layer atoms. The snapshots correspond to  $\phi = 0^\circ$  at: (a)  $t = 23.4$  ps; (b)  $t = 24.0$  ps; (c)  $t = 24.6$  ps; (d)  $t = 25.2$  ps.



(D) the atom is effectively above the surface of the work piece. The jumping speed is approximately the same as that during the transition from (A) to (B). Even though the atom is above the surface, the vertical position is still positive due to the small elastic deformation surrounding the indent. After the halfway stage there is a small elastic recovery of the surface as the tip is extracted and by the conclusion of the simulation the atom is displaced by half a lattice constant above the undisturbed surface.

As the indenter reaches maximum penetration, Fig. 5.5.7(a) and (b) show the plastically deformed triangular region of the work material is surrounded by an area of axially symmetric elastic deformation. Thus, the elastically deformed area does not reflect the symmetry of either the tip or the substrate. The minicracks marked by the black arrows in Fig. 5.5.7(a) arise from the boundary conditions imposed on the work material. These characteristics are also present in the substrate during indentation with  $\phi = 45^\circ$ , but both Fig. 5.5.7(c) and (d) show the edges of the substrates have fully relaxed at the end of the simulation. Another interesting feature in all of the images in Fig. 5.5.7 is the minicracks near the edges of the central plastically deformed region where the stress concentration is high, as marked by the white arrows. For indentations with both  $\phi = 0^\circ$  and  $\phi = 45^\circ$  the minicracks are only observed propagating along the  $\langle 100 \rangle$  directions up to a maximum of approximately 12 Å in length. They are most significant at the halfway stage of the simulation, but at the conclusion of the indentation process, Fig. 5.5.7(c) and (d) show that the surface has partially reconstructed.

The piling-up of work material along the indenter sides occurs during the loading

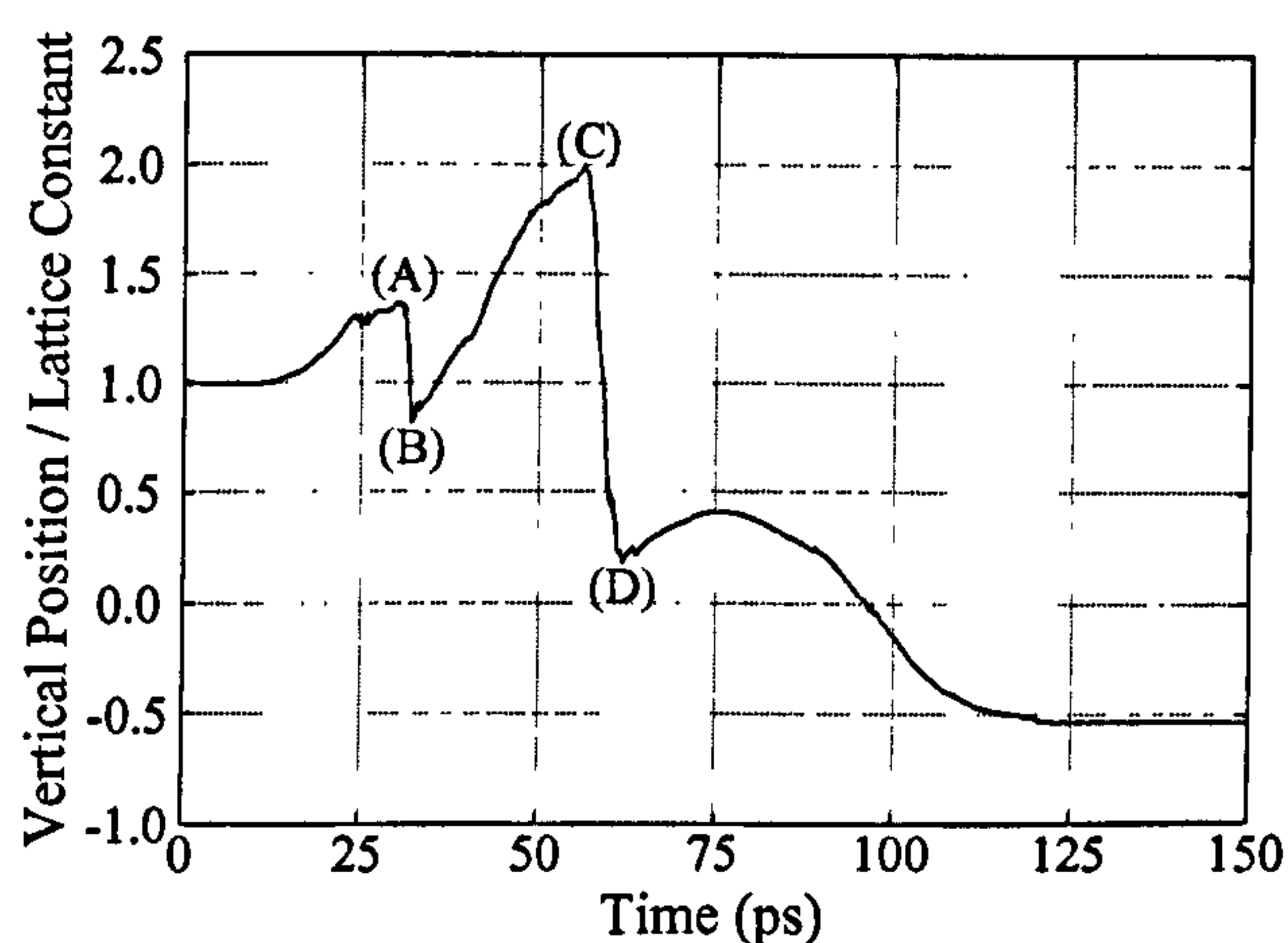
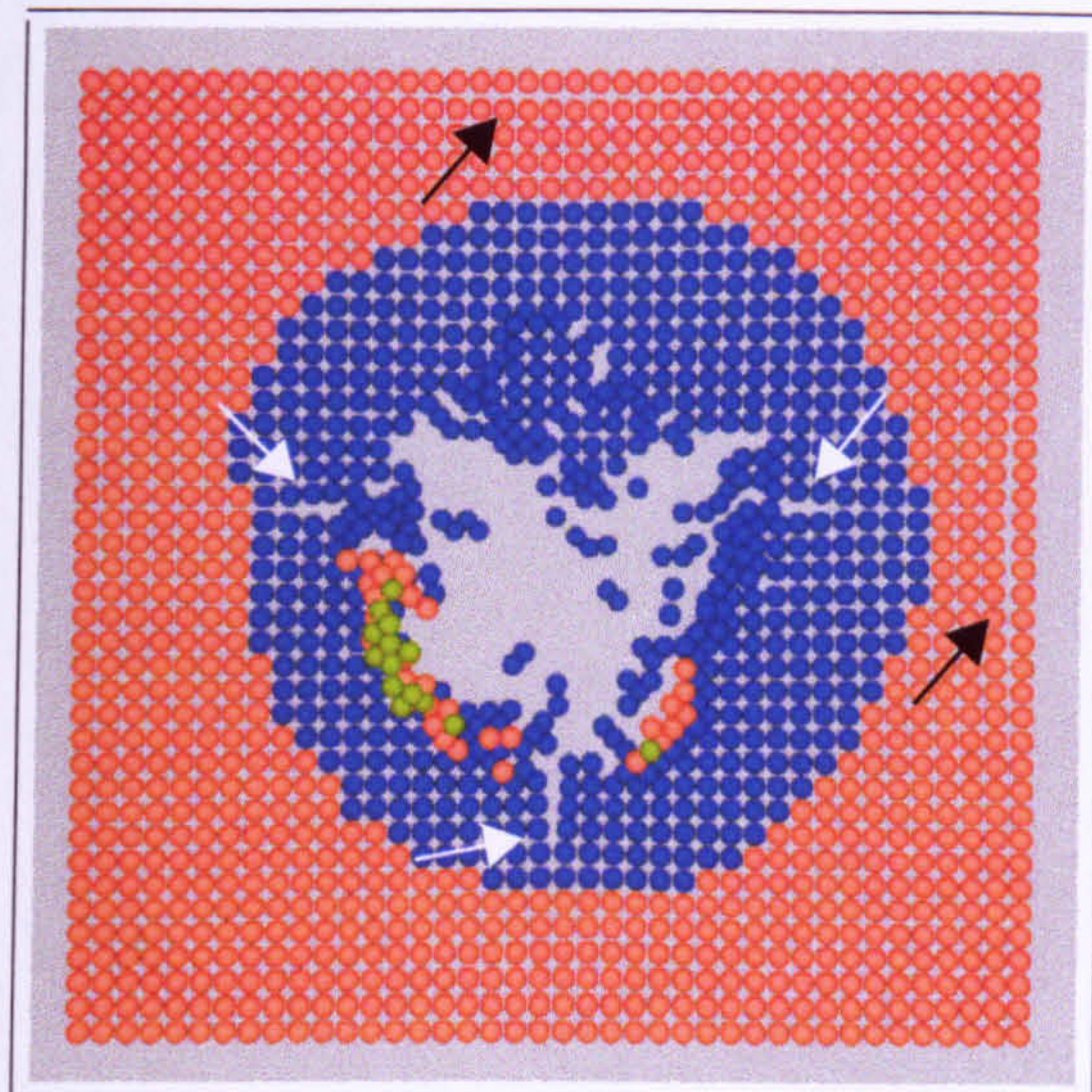
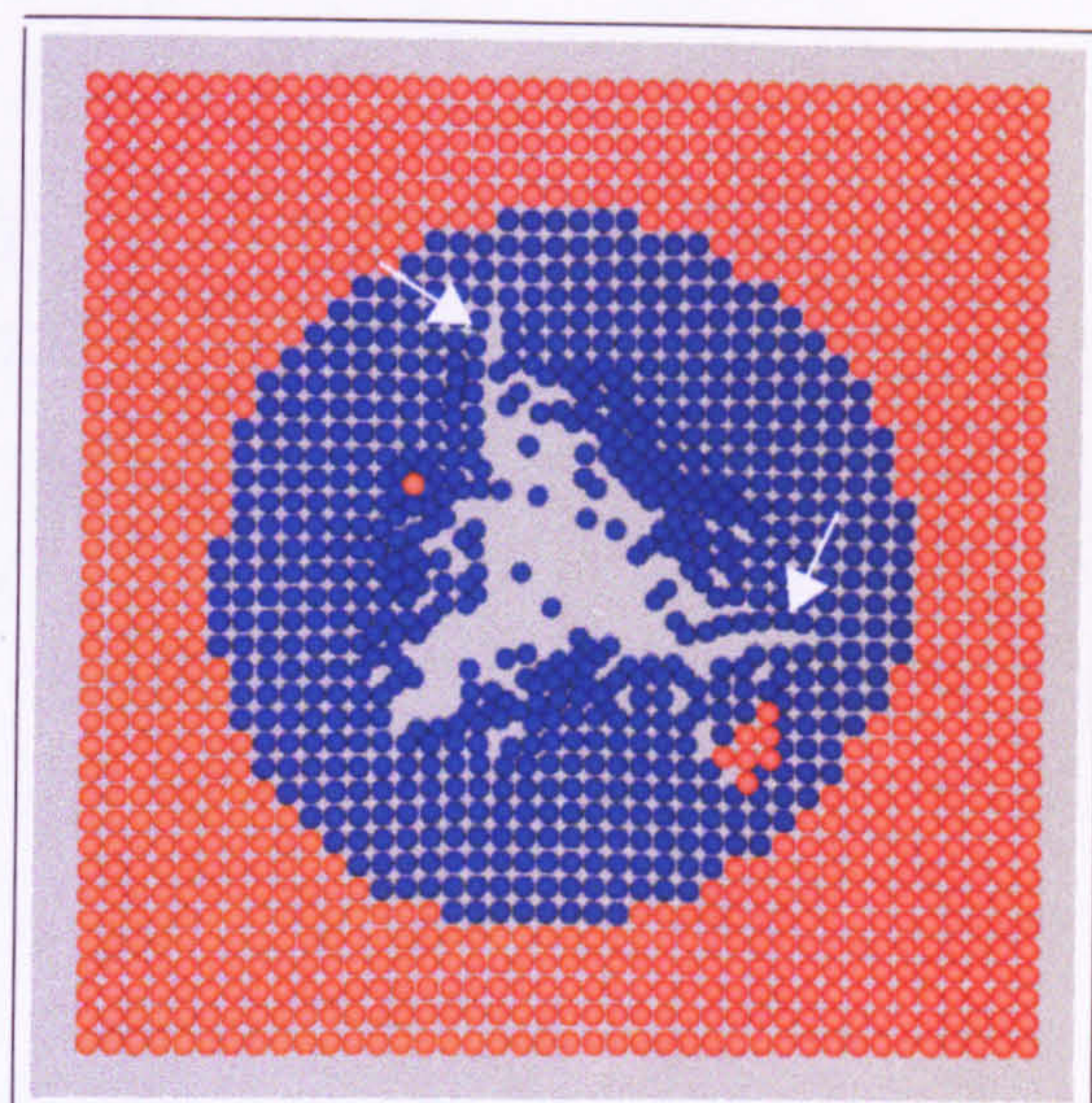


Fig. 5.5.6. The vertical displacement path of a 3<sup>rd</sup> layer Fe atom showing the transition to pile-up during indentation with  $\phi = 0^\circ$ . The capital letters indicate where the atom jumps to vacant atomic sites in preceding layers during the transition stage.





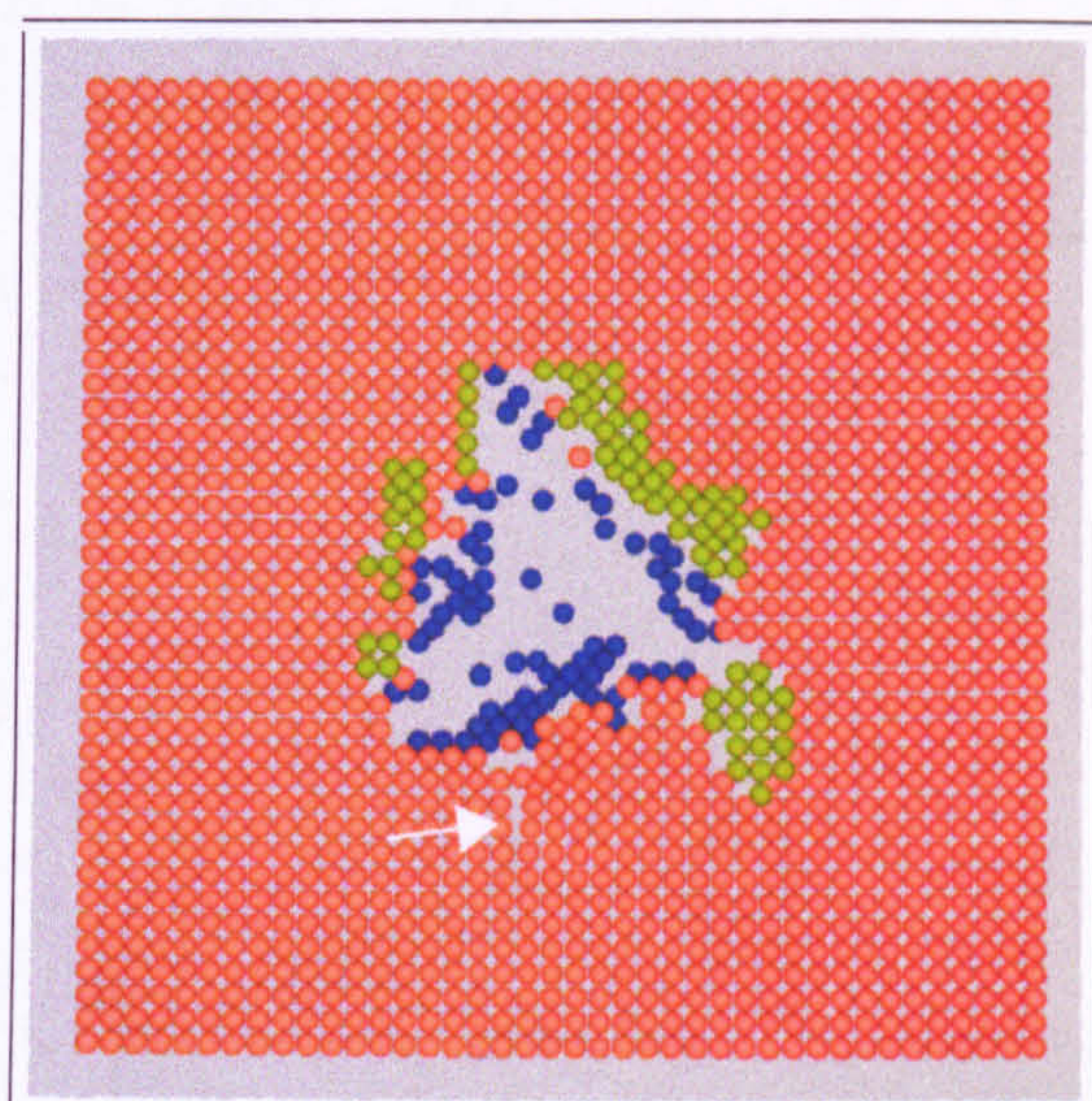
(a)



(b)



(c)



(d)

Fig. 5.5.7. Plan view of 1<sup>st</sup> layer atoms in the Fe {100} substrate showing the plastically deformed triangular region with: (a)  $\phi = 0^\circ$  at  $t = 75$  ps; (b)  $\phi = 45^\circ$  at  $t = 75$  ps; (c)  $\phi = 0^\circ$  at  $t = 150$  ps; (d)  $\phi = 45^\circ$  at  $t = 150$  ps. Green shaded atoms denote those atoms displaced above the surface by more than 1 Å and blue shaded atoms represent those atoms displaced by more than 1 Å below the surface. The red atoms have not been displaced by more than 1 Å either above or below the surface. Note the minicracks near the edges of the plastically deformed region as marked by the white arrows. Also note the edge effects of the substrate marked by the black arrows in (a).

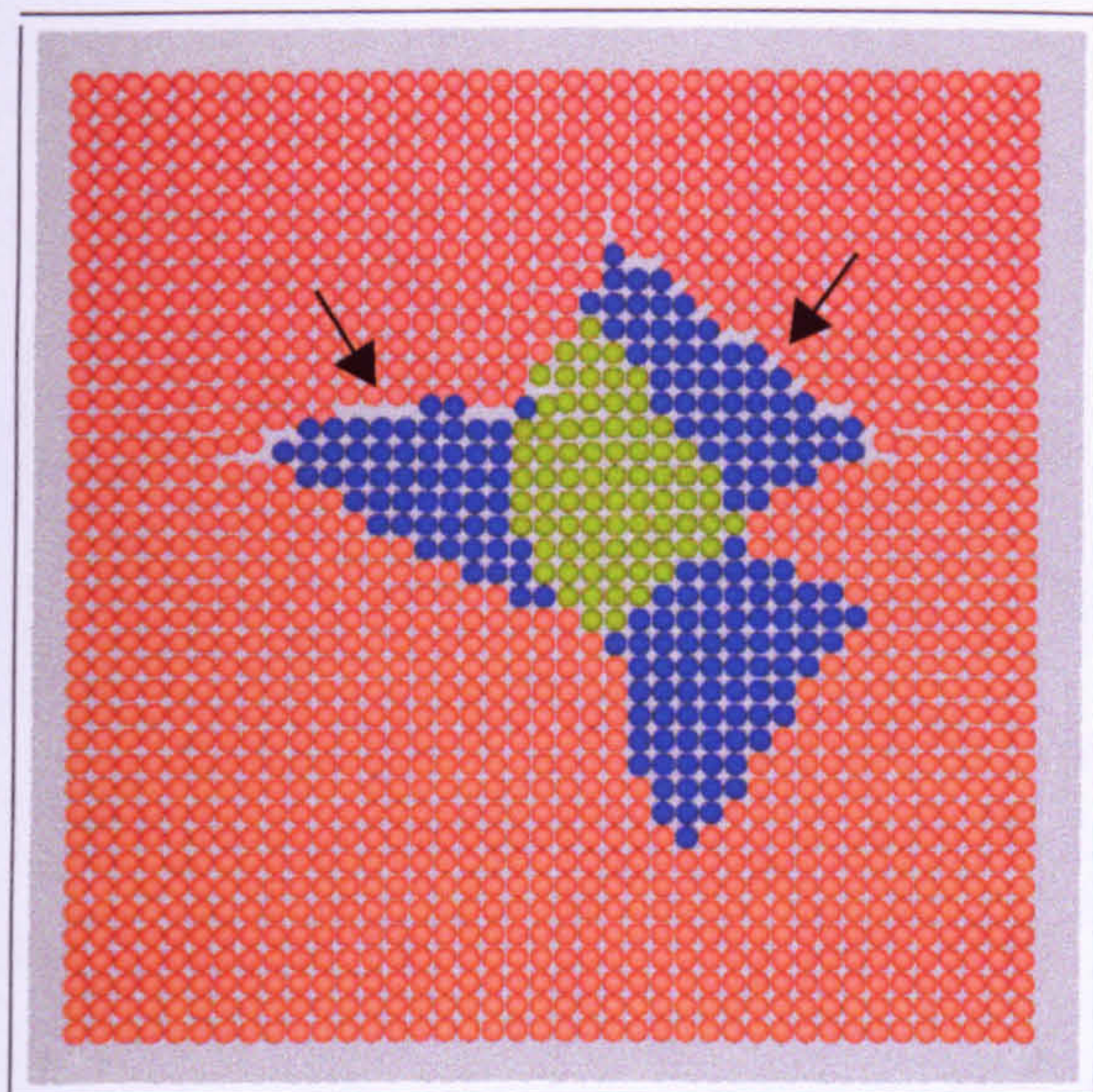


stage of the indentation process and proliferates with increased penetration depth. At the conclusion of the simulation with  $\phi = 0^\circ$ , there are 137 Fe atoms that have been displaced above the substrate surface. Fig. 5.5.7(c) shows that there is no piling-up of material along the side of the plastically deformed triangular region that lies parallel to the  $\langle 100 \rangle$  direction, but occurs along the remaining sides orientated close to the  $\langle 110 \rangle$  direction. The pile-up occurs here since the sides of the indenter displace the atoms closer to the nearest neighbour direction than the side parallel to the  $\langle 100 \rangle$  direction. Following indentation with  $\phi = 45^\circ$ , Fig. 5.5.7(d) shows that the pile-up of material occurs along each of the triangular sides of the plastically deformed region. However, the bulk of the pile-up occurs along the side of the deformed region that lies parallel to the  $\langle 110 \rangle$  direction. Analysing Fig. 5.5.7(c) and (d) shows that the yield of material pile-up is greatest when the substrate atoms are displaced along the  $\langle 110 \rangle$  direction, i.e. the nearest neighbour direction, and least along the  $\langle 100 \rangle$  direction. At the conclusion of the indentation process with  $\phi = 45^\circ$  there are 90 Fe atoms that have been displaced above the undisturbed substrate surface. Since the indenter is not axially symmetric, the rotation angle  $\phi$  clearly influences the abundance of atoms constituting the surface pile-up.

Structural analysis of the pile-up material around the plastically deformed triangular region shows it to be primarily arranged in crystalline bcc form with no vacancies or interstitials. The pile-up material on the surface of the substrate is mainly composed of 1<sup>st</sup> layer Fe atoms, with a sizeable fraction originating from the subsurface layers through the process of tip-induced plastic flow. Following indentation with  $\phi = 0^\circ$ , the surface pile-up has a maximum height of 6.4 Å (approximately 38% of the maximum penetration depth) and is configured from 80 1<sup>st</sup> layer atoms, 39 2<sup>nd</sup> layer atoms, 16 3<sup>rd</sup> layer atoms and 2 atoms from the 4<sup>th</sup> layer. For  $\phi = 45^\circ$ , the assemblage of Fe atoms on the crystal surface peaks at roughly 4.2 Å (approximately 25% of the maximum penetration depth) above the undisturbed surface and is configured from 81 1<sup>st</sup> layer atoms and only 9 atoms from the 2<sup>nd</sup> layer. Piling-up of the work material is also observed on the subsurface layers, showing similar distribution to those atoms on the surface of the substrate. After the 5<sup>th</sup> layer of the Fe sample, no significant piling-up is observed along the indenter sides.

At the end of the loading stage, the indenter just penetrated through the 13<sup>th</sup> layer in the Fe sample and so the images in Fig. 5.5.8 reveal the defects that occur in the





(a)



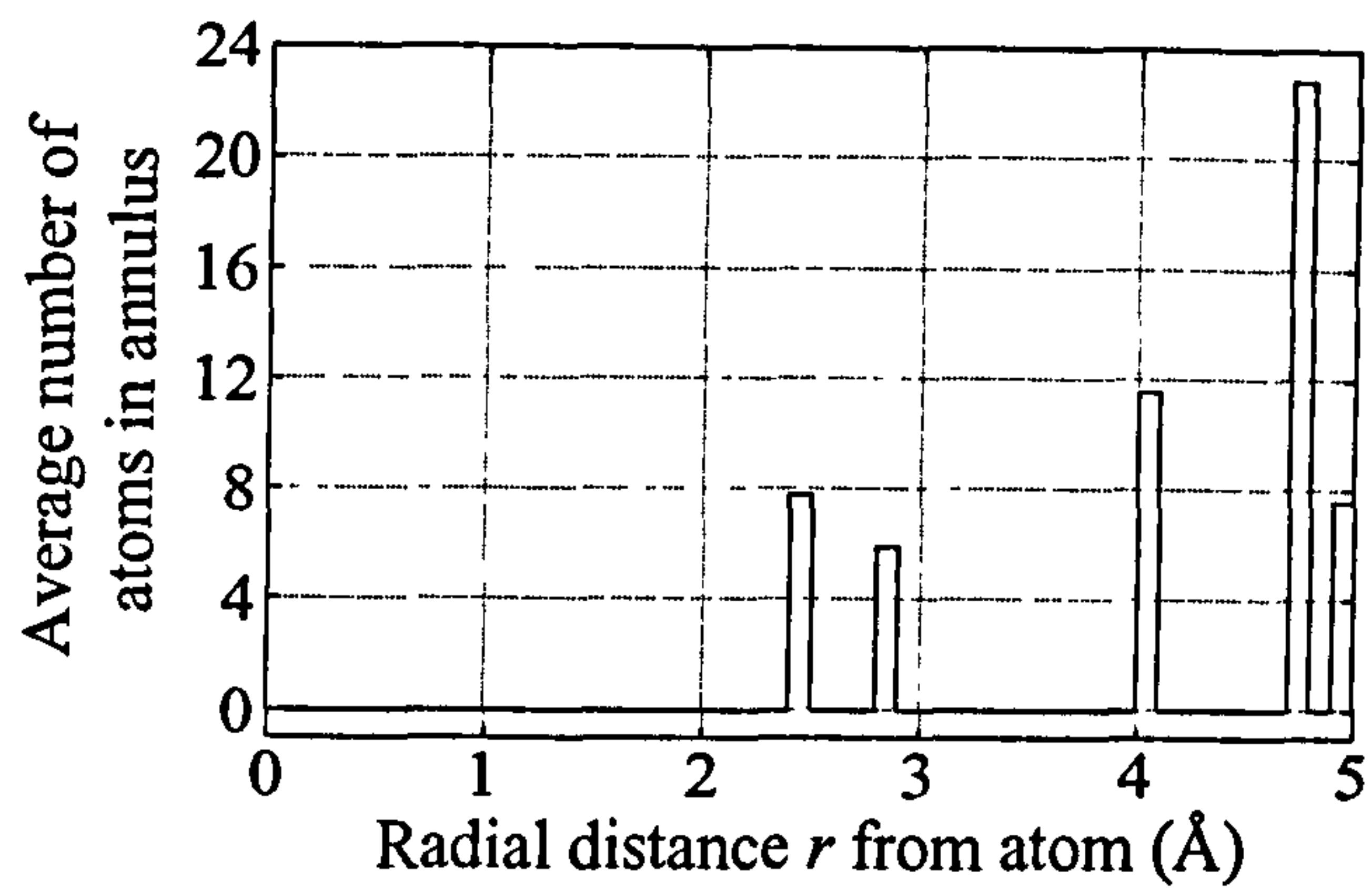
(b)

Fig. 5.5.8. Plan views of the Fe  $\{100\}$  substrate showing only the 15<sup>th</sup> layer at  $t = 150$  ps with: (a)  $\phi = 0^\circ$ ; (b)  $\phi = 45^\circ$ . The blue shaded atoms denote those atoms displaced from the 14<sup>th</sup> layer. The green shaded atoms represent those atoms displaced from layers preceding the 14<sup>th</sup> layer. The red shaded atoms represent atoms originating from the 15<sup>th</sup> layer. Note the minicracks along both the  $\langle 100 \rangle$  and  $\langle 110 \rangle$  directions as marked by the arrows.

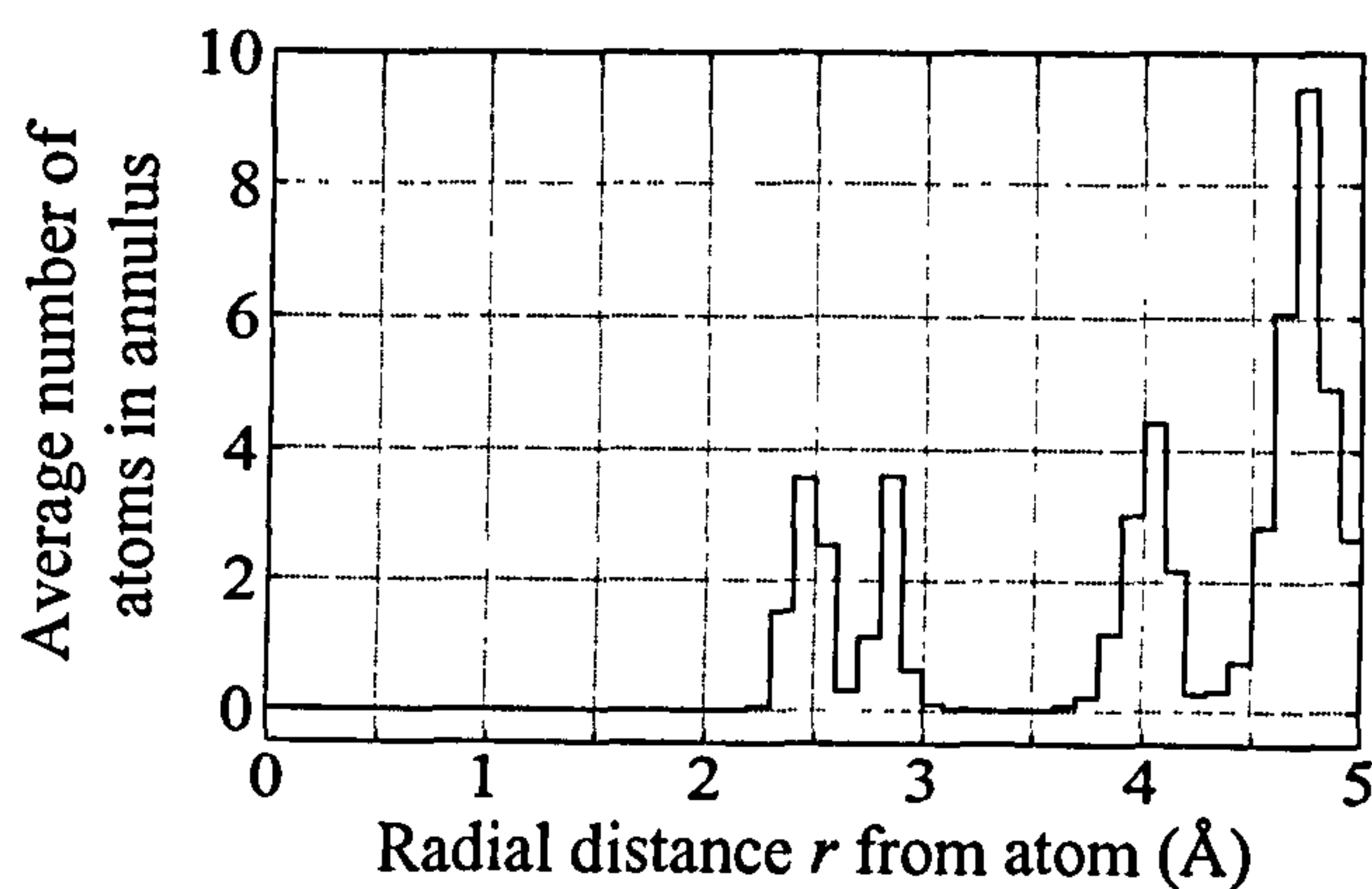
substrate layers underneath the tip at maximum indentation. Fig. 5.5.8 shows some atoms from preceding layers are permanently displaced to the 15<sup>th</sup> layer of the substrate and arranged in crystalline bcc form. This in turn causes some of the atoms from the 15<sup>th</sup> layer to be displaced to the succeeding layers. An animated movie shows that the displacement of atoms to succeeding layers occurs by the motion of point defects. Furthermore, as the indenter is extracted, some of the atoms from preceding layers are displaced back to their original layer. Both images in Fig. 5.5.8 show the displacement of atoms induces minicracks in crystal configuration, as marked by the arrows, which are observed along both  $\langle 100 \rangle$  and  $\langle 110 \rangle$  directions. This effect continues further down into the lattice and thus a deep crystal is required for the simulations. The range of plastic deformation exceeds more than twice the maximum indentation depth.

The compression of the Fe atoms during the indentation process has been examined by analysing the change in density of the substrate atoms. Radial distribution plots are presented in Fig. 5.5.9 at various stages of the indentation process with  $\phi = 0^\circ$

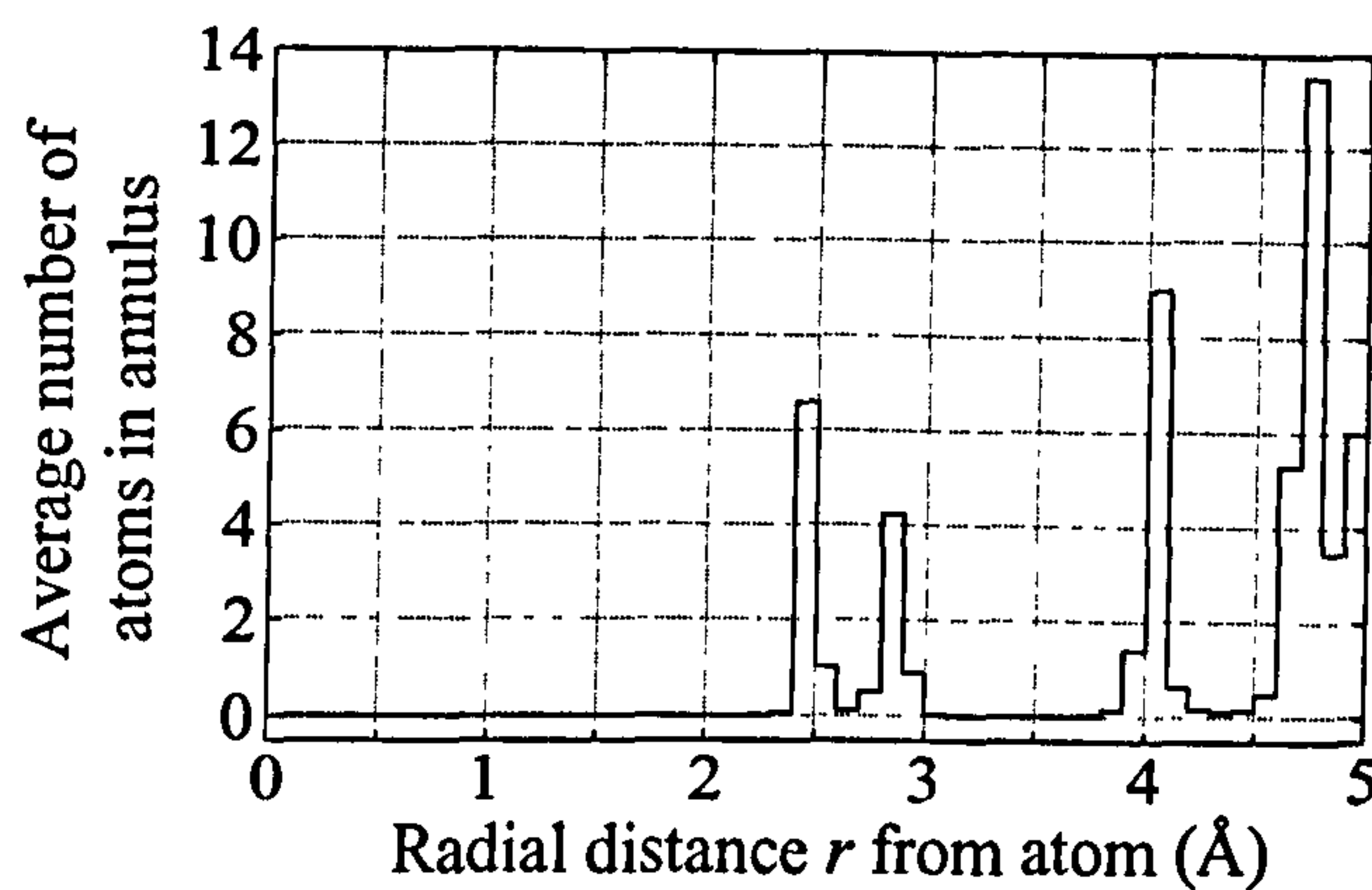




(a)



(b)



(c)

Fig. 5.5.9. Radial distribution plot of Fe density for indentation with  $\phi = 0^\circ$  at: (a)  $t = 0$  ps; (b)  $t = 75$  ps; (c)  $t = 150$  ps. For each atom,  $a_i$ , in a local area containing an initial 8,354 atoms around the local indentation region, the density of Fe atoms is evaluated in an annulus of width  $0.1 \text{ \AA}$  which is sited at a radial distance  $r \text{ \AA}$  from  $a_i$ .



and provide a helpful insight into the structural change of the work piece. The plot in Fig. 5.5.9(a) corresponds to indentation at  $t = 0$  ps and clearly reflects the crystalline configuration of the Fe substrate. The average number of neighbours for each Fe atom is slightly less than those in an effectively infinite system of bcc atoms, due to the inclusion of surface atoms. Fig. 5.5.9(b) shows the radial distribution of Fe density at the halfway stage of the indentation process. The spreading of the distribution shows how the contact region becomes disordered during the indentation. Clearly there is a limit in the compression of the Fe atoms. Detailed analysis reveals that the Fe atoms compressed to a minimum distance of 2.05 Å from each other. This corresponds to approximately 17 % compression in the nearest neighbour bond length. Fig. 5.5.9(c) shows the radial distribution of Fe density at the conclusion of the indentation process. As the compression in the work material relaxes, the plot shows the density of atoms in the substrate begins to return to its original distribution. However, the small discrepancy between Fig. 5.5.9(a) and (c) arises primarily from the plastic deformation of the substrate.

### Fe {100}{111} Grain Boundary Substrate

Shown in Fig. 5.5.10(a) is the force-depth curve for indentation into the Fe {100}{111} grain boundary substrate with  $\phi = 0^\circ$ . The peak force is approximately 170 eV/Å at a penetration depth of about 14 Å. Comparison with Fig. 5.5.3(a) shows that the maximum force is about 60% of that for the {100} substrate. Although the {111} surface is closer packed than {100}, the weaker bonding along the grain boundary accounts for the

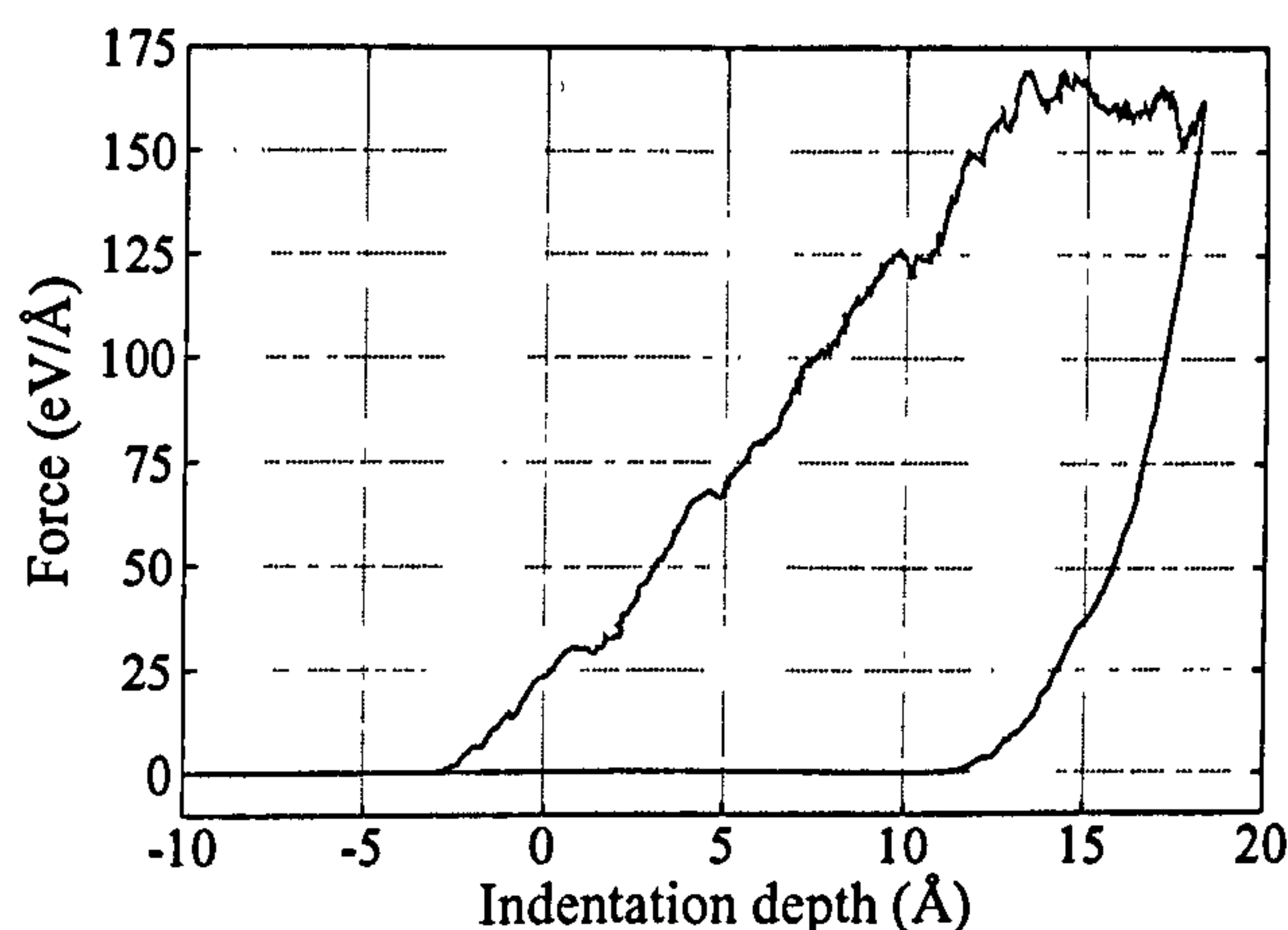


Fig. 5.5.10. Force-depth curve from the simulation of indentation into the Fe {100}{111} grain boundary substrate with  $\phi = 0^\circ$ .



lower force experienced by the indenter. The indenter reached a maximum penetration depth of approximately 18 Å and the tip compressed by 2 Å. Fig. 5.5.10 shows a plateau in the load-displacement curve during the loading stage, in the indentation region 13 Å - 18 Å. The indenter displaces more slowly near the peak penetration depth, and atoms relax to more favourable minimum energy configurations. The weaker bonding on the grain boundary assists this process and a number of substrate atoms are pushed up onto the surface near the halfway stage of the indentation. Therefore, the plateau in Fig. 5.5.10 stems from significant volume and density changes induced under the indenter tip in a short period of time. The rearrangement of atoms leading to a stationary value in the force curve is known as a ‘pop-in’ and has been observed experimentally for other metals [174], [184]-[185]. The same displacement discontinuity has also been observed for other materials, such as semiconductors [186]-[187]. Experimentally, ‘pop-ins’ are commonly attributed to the breakthrough of oxide layers. A displacement discontinuity in the unloading curve is known as a ‘pop-out’ and has also been observed

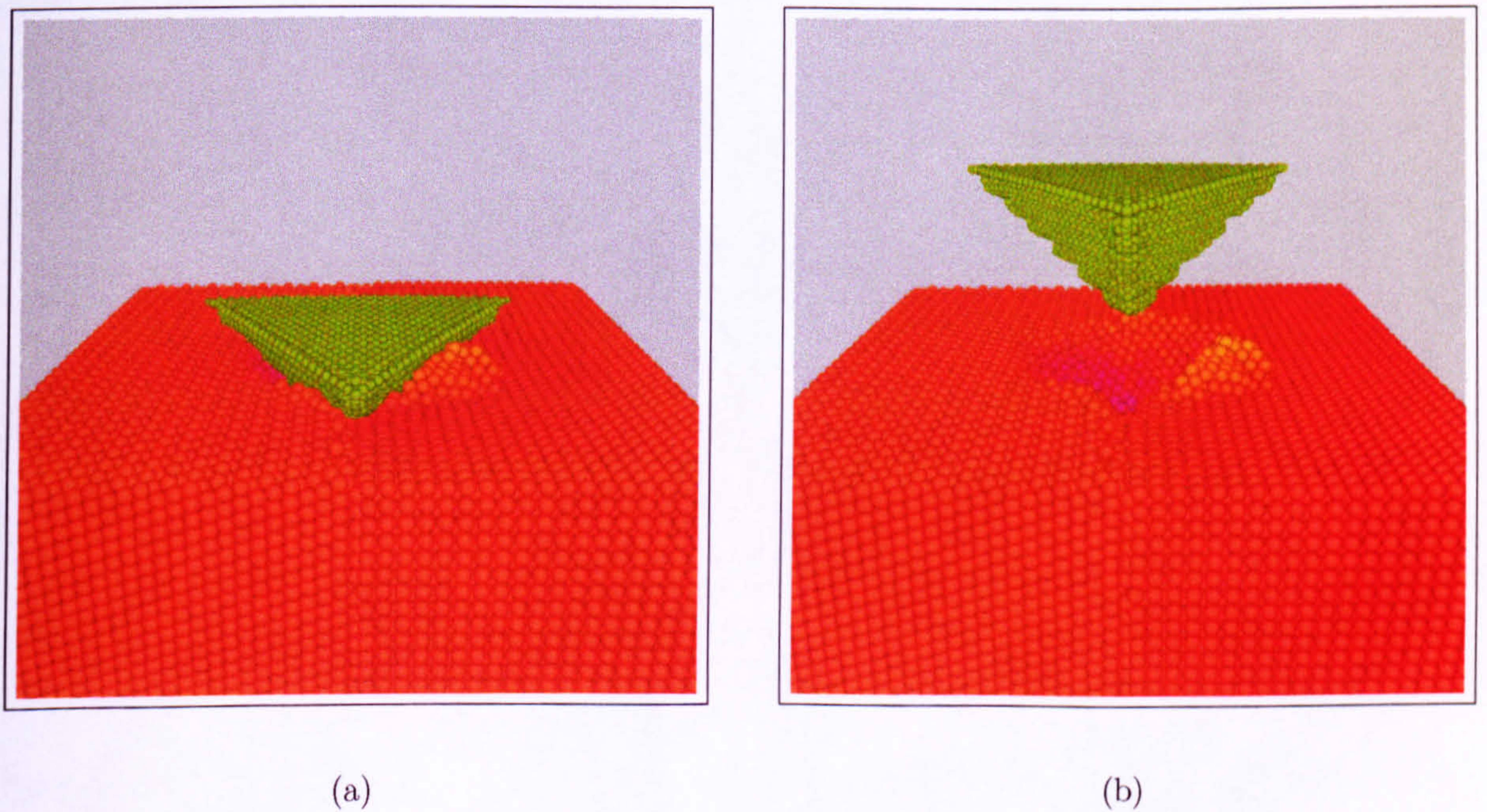


Fig. 5.5.11. Snapshots from the simulation of indentation into the Fe {100}{111} grain boundary crystal with  $\phi = 0^\circ$ . The grain boundary is aligned vertically along the middle of the substrate with the {111} grain on the left and the {100} grain on the right. (a) The halfway stage of the simulation at  $t = 75$  ps. Note the piling-up of substrate atoms occurs largely on the surface of the {100} grain. (b) Conclusion of the simulation at  $t = 150$  ps. Note the permanent impression of the indenter left in the substrate.



experimentally for some materials such as Si [188].

Snapshots from the simulation of indentation into the Fe  $\{100\}\{111\}$  grain boundary substrate are presented in Fig. 5.5.11<sup>1</sup>. The pile-up of material occurs primarily on the  $\{100\}$  grain of the substrate. There is no clear piling-up of material on the  $\{111\}$  facet. After full tip retraction, structural analysis reveals no voids across the grain boundary. Furthermore, a small amount of atom migration across the  $\{100\}\{111\}$  interface could be found in both grains. Fig. 5.5.12(a) shows the elastic deformation of substrate atoms around the plastically deformed triangular region. In the  $\{100\}$  grain, the substrate atoms displace more axisymmetrically, compared with the  $\{111\}$  grain. At the conclusion of the indentation process, 173 Fe atoms have been displaced above

<sup>1</sup>An animated movie of this is on the CD in the Appendix

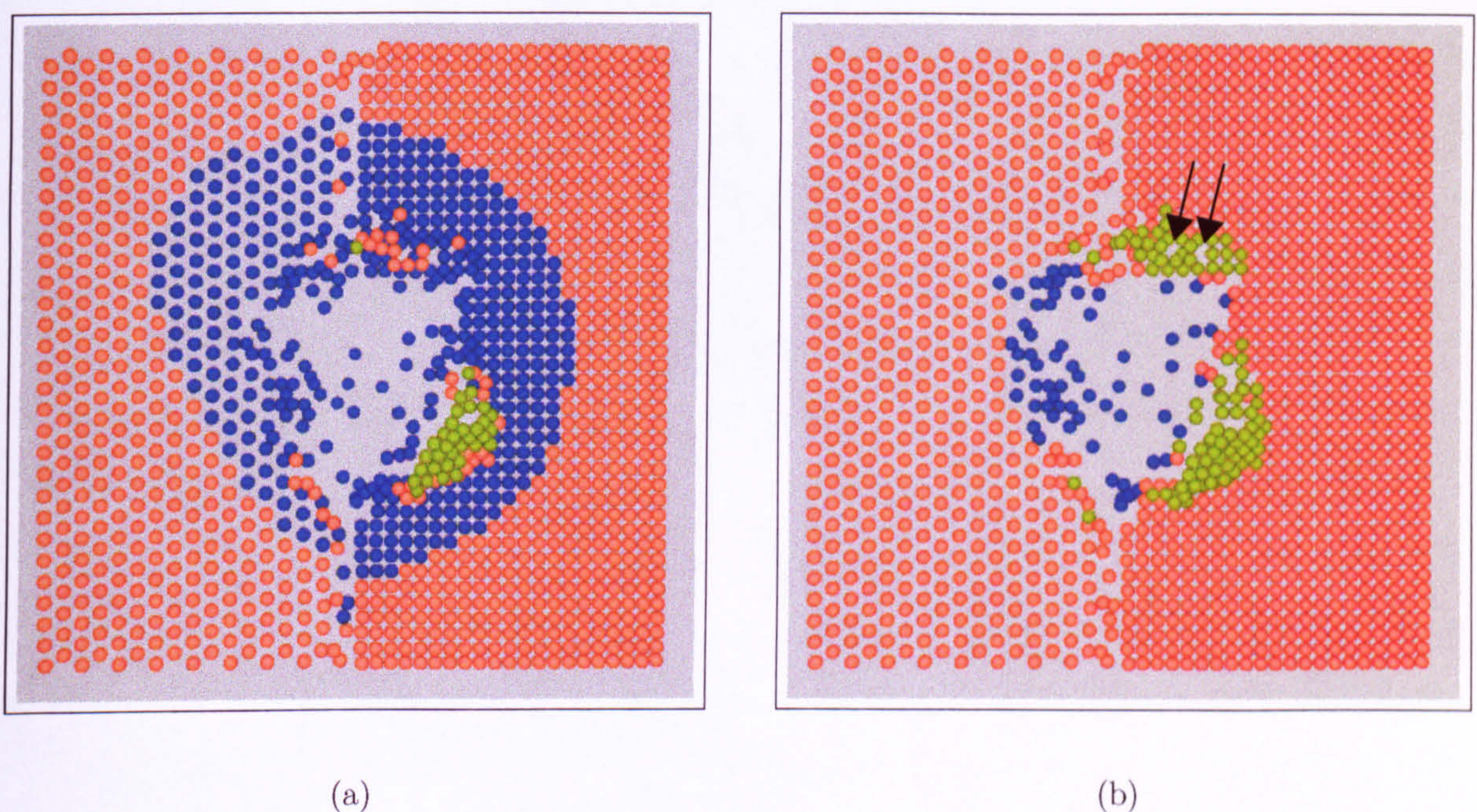


Fig. 5.5.12. Plan view of the plastically deformed triangular region in the Fe  $\{100\}\{111\}$  grain boundary substrate showing only 1<sup>st</sup> layer atoms at: (a)  $t = 75$  ps; (b)  $t = 150$  ps. The grain boundary is aligned vertically along the middle of the substrate with the  $\{111\}$  grain on the left and the  $\{100\}$  grain on the right. The green shaded atoms denote those atoms displaced above the layer by more than 1 Å and the blue shaded atoms represent those atoms displaced by more than 1 Å below the layer. The red atoms have not been displaced by more than 1 Å either above or below the layer. The arrows in (b) mark vacant lattice sites in the piled-up material.



the substrate surface by more than 1 Å on the {100} grain. Only four Fe atoms constituting the pile-up material are displaced above the {111} surface. The peak height of the piled-up material was approximately 8.2 Å (approximately 45% of the maximum penetration depth) above the surface with the {100} orientation. The difference in the pile-up yield for the {100} and {111} surface is discussed in more detail in Chapter 7. The piled-up material is primarily crystalline bcc and contains no interstitial sites, however there are two noticeable vacant lattice sites above the {100} grain as marked by the arrows in Fig. 5.5.12(b).

### 5.3.2 Face-centred-cubic Silver

From the load-displacement curves in Fig. 5.5.13, indentation with  $\phi = 0^\circ$  results in a peak force of 125 eV/Å acting on the indenter, which occurs just before the halfway stage of the indentation process at a penetration depth of approximately 17.5 Å. Indentation with  $\phi = 45^\circ$  results in a slightly lower peak force of 110 eV/Å, occurring at a penetration depth of about 18.5 Å. Comparing Fig. 5.5.3 with Fig. 5.5.13 shows that the maximum force acting on the indenter from the Ag sample is less than half that exerted by the Fe substrate, which clearly reflects the difference in nanohardness between the two samples. The diamond apex reached a maximum indentation depth of about 18 Å and 19.5 Å with  $\phi = 0^\circ$  and  $\phi = 45^\circ$  respectively. Indentation of the Fe {100} substrate results in greater compression of the diamond tip compared with the softer Ag work material. As the indenter is extracted from the Ag crystal, the elastic recovery of the substrate takes place over the penetration range of approximately 8 Å - 18 Å and 11 Å - 19.5 Å for indentation with  $\phi = 0^\circ$  and  $\phi = 45^\circ$  respectively. Fig. 5.5.3 and Fig. 5.5.13 show that the elastic recovery of both the Fe and Ag substrates during the unloading stage occurs over a range approximately equal to 35% - 40% of the maximum indentation depth. This is a much larger elastic recovery than experimentally observed due to the small penetration depths in the simulation model.

The halfway stage of the indentation process in Fig. 5.5.14(a) and (c) shows the substrates accommodating a large volume of the indenter, with piling-up of the work material along the indenter sides <sup>2</sup>. The primary mechanism leading to plastic-flow and material pile-up is the same as observed for Fe {100}. At the conclusion of the simula-

---

<sup>2</sup>An animated movie of this is on the CD in the Appendix



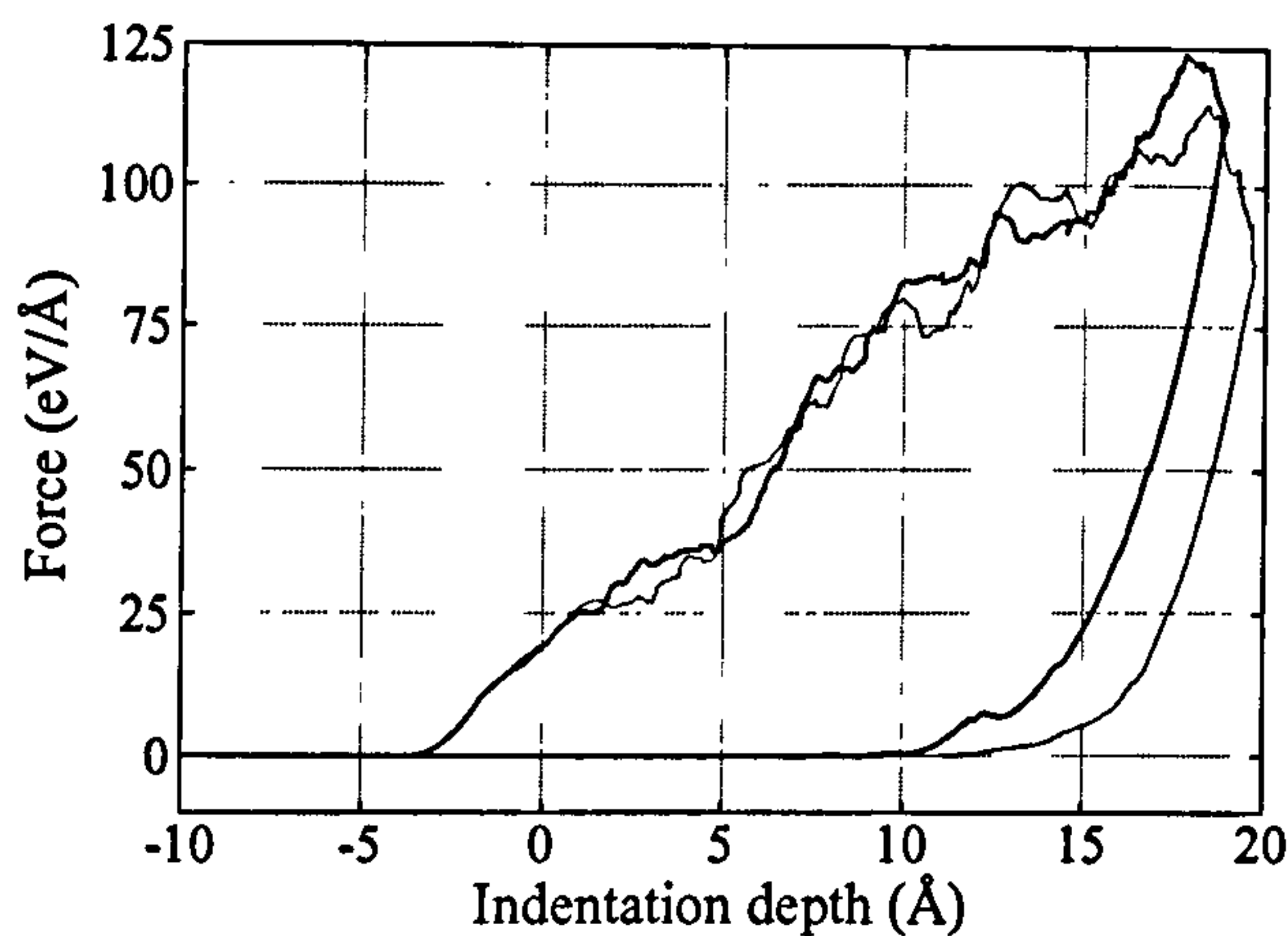


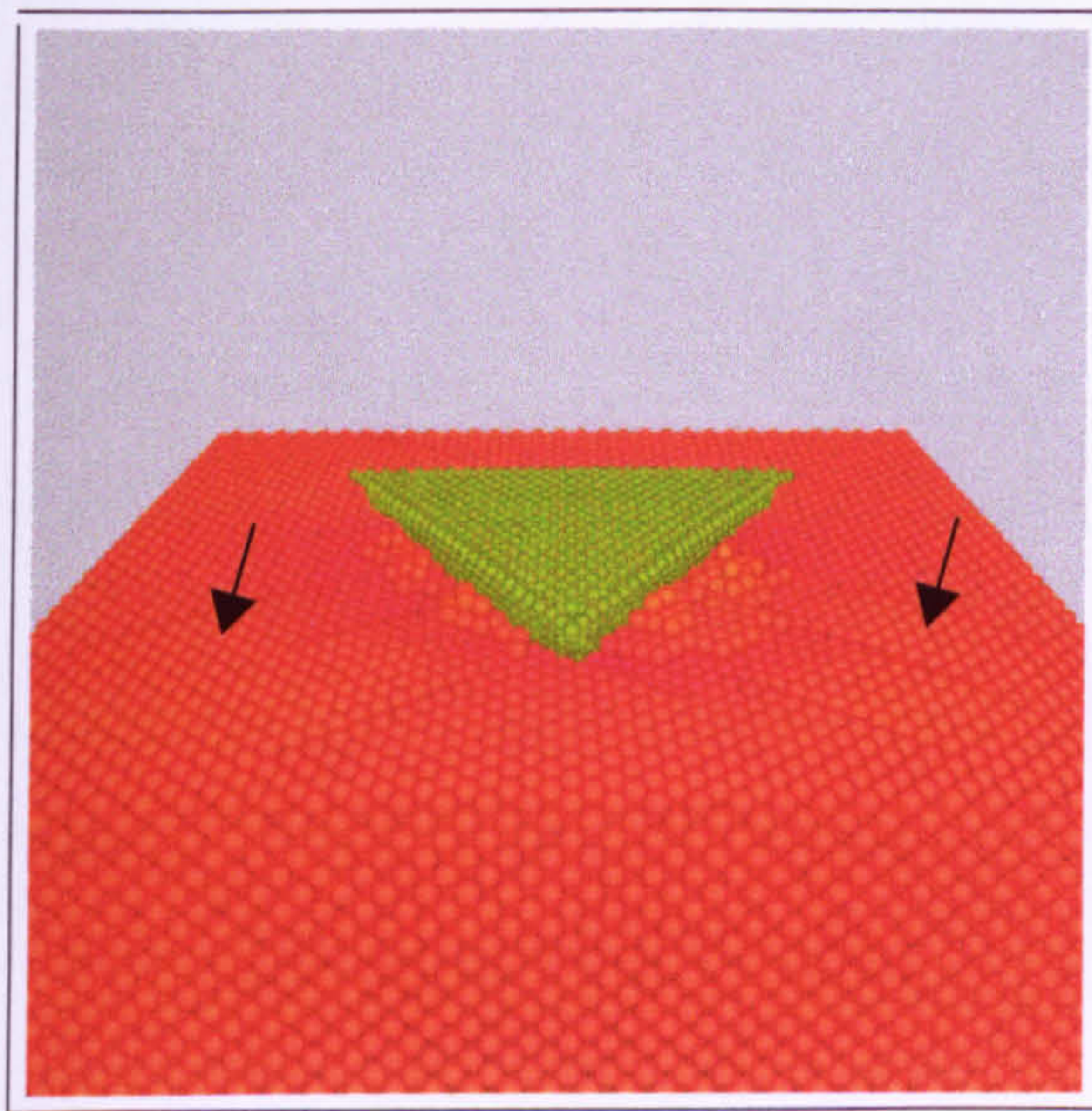
Fig. 5.5.13. Force-depth curves from the simulation of indentation into the Ag {100} crystal. The bold solid line corresponds to indentation with  $\phi = 0^\circ$  and the remaining line denotes indentation with  $\phi = 45^\circ$ .

tion, Fig. 5.5.14(b) and (d) show damage similar to that imparted to the Fe substrate, with a large permanent impression of the indenter left in the work material. The images in Fig. 5.5.14 also reveal 'slip markings' or 'slip bands' on the surface of the substrate (as marked by the arrows) and occur as planes of atoms glide over each other once a critical stress level has been surpassed. These crystallographic planes are called slip or glide planes. The direction of the slip is called a slip or glide direction. Hence, a slip system is a combination of the slip plane and slip direction. Crystallographic slip is a kind of dislocation, which in essence can be described as a lattice imperfection. For fcc crystals, the slip plane is typically the close packed {111} plane. The direction of slip in Fig. 5.5.14 is along the  $\langle 110 \rangle$  directions which agrees exactly with the literature [189]. A schematic representation of the slip system in the Ag work material is shown in Fig. 5.5.15. The slip direction is along  $\langle 110 \rangle$  since this is the direction where the {111} plane intercepts the {100} surface. The slip deformation behaviour of bcc metals is more complicated than fcc since slip can occur on a number of planes [190]-[191]. The deformation to the Ag crystal is both by piling-up of atoms along the indenter sides and by slip along glide planes.

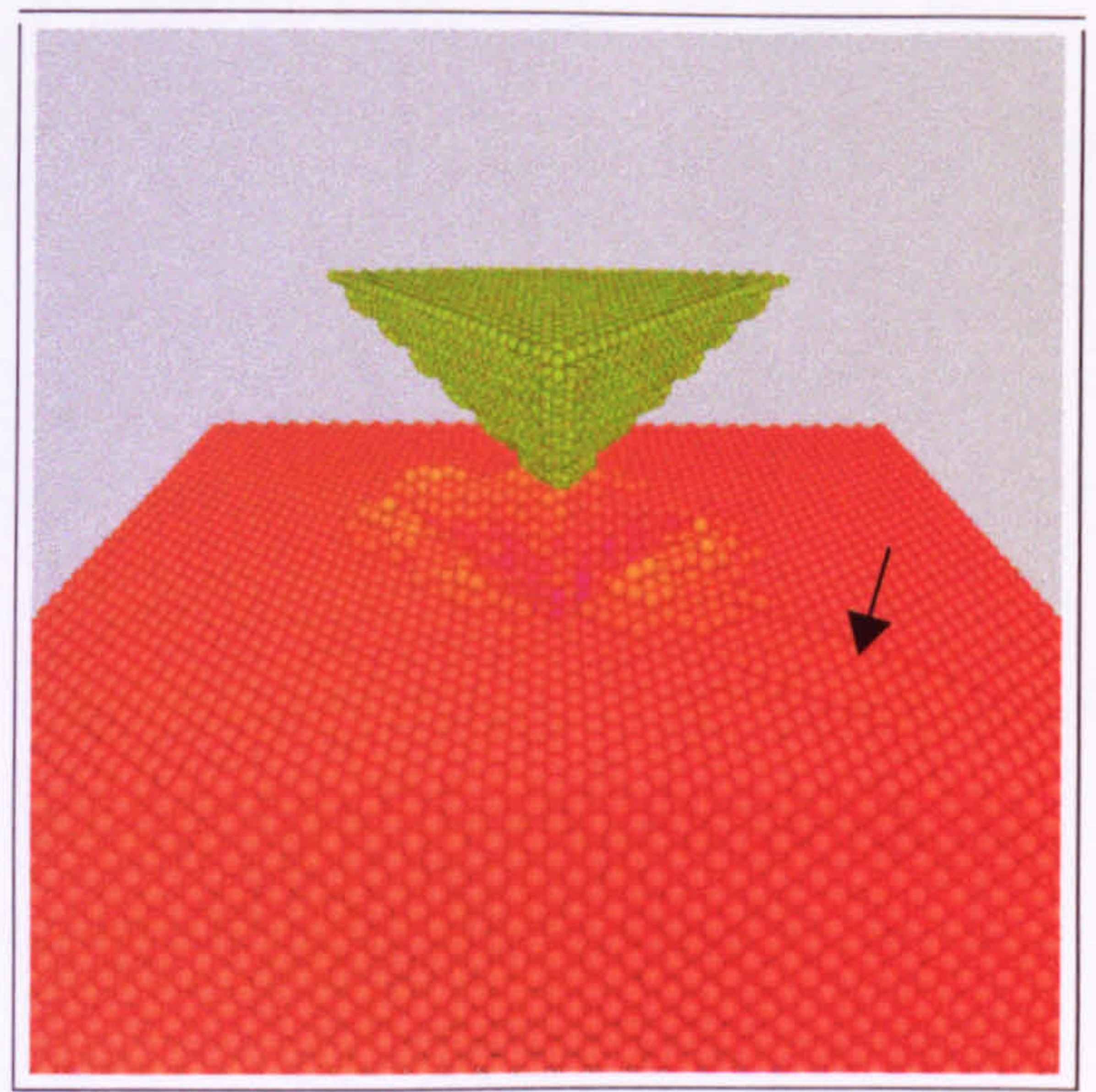
At the halfway stage of the simulation with  $\phi = 0^\circ$ , 69 Ag atoms have been displaced by more than 10 Å vertically into the material, compared with 43 atoms for  $\phi = 45^\circ$ . This is less than half the number of Fe atoms that displaced in the same manner during the simulations on the Fe {100} substrate. As the diamond apex reached peak penetration into the Ag crystal, the maximum vertical displacement of an Ag atom into the



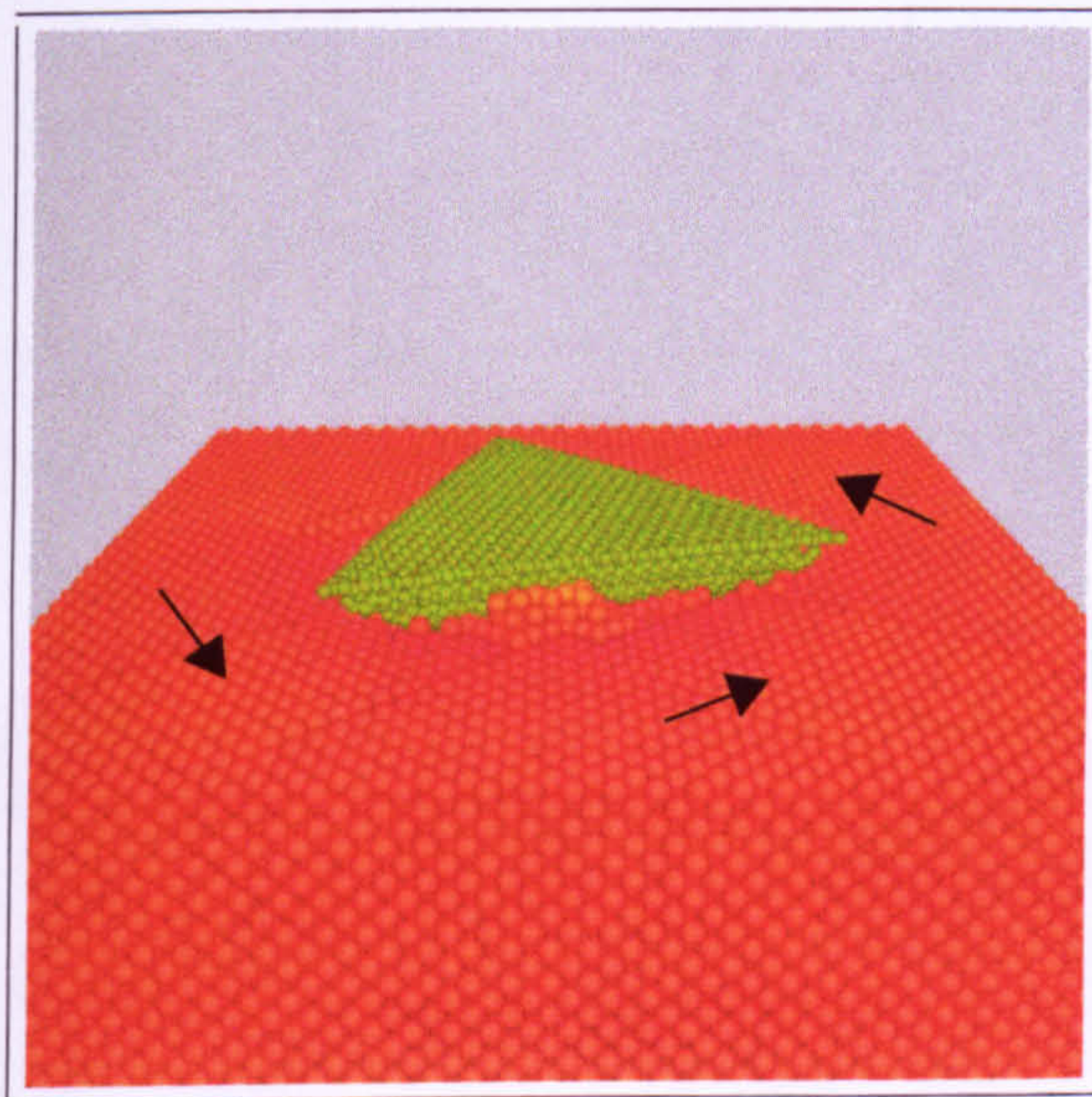
work material is 14.4 Å and 16.6 Å for indentation with  $\phi = 0^\circ$  and  $\phi = 45^\circ$  respectively. Fig. 5.5.16(a) and (b) clearly show a less axially symmetric elastic deformation



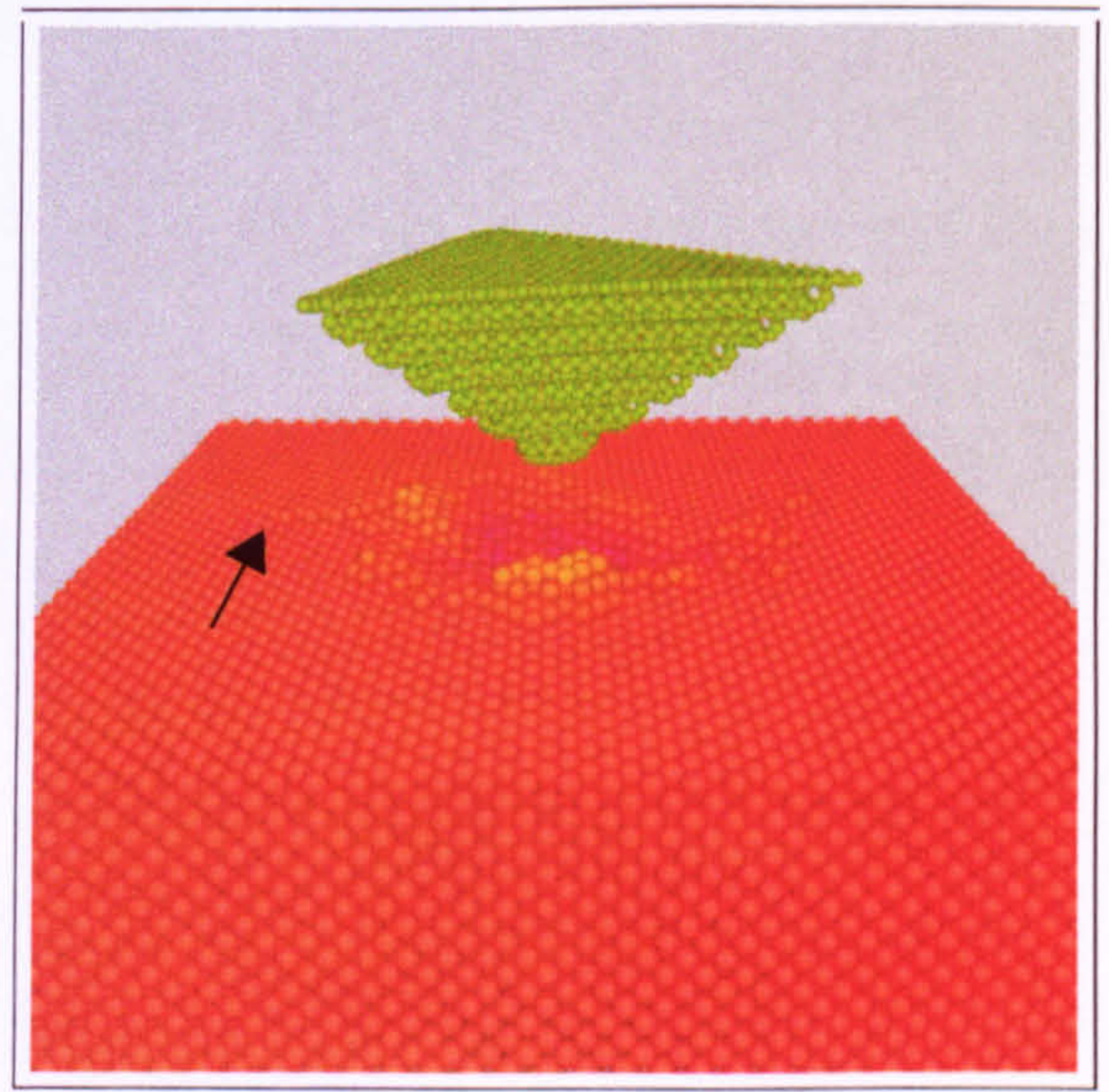
(a)



(b)



(c)



(d)

Fig. 5.5.14. Snapshots from the simulation of indentation into the Ag {100} crystal with: (a)  $\phi = 0^\circ$  at  $t = 75$  ps; (b)  $\phi = 0^\circ$  at  $t = 150$  ps; (c)  $\phi = 45^\circ$  at  $t = 75$  ps; (d)  $\phi = 45^\circ$  at  $t = 150$  ps. Note the large plastic deformation of the substrate and the piling-up of atoms along the sides of the plastically deformed triangular region. Also note the slip markings on the surface of the work material as marked by the arrows.



of surface atoms around the indenter compared with Fe. An interesting feature present in the surface of the work material during indentation with  $\phi = 0^\circ$ , is the minicrack marked by the arrow in Fig. 5.5.16(a). The feature measures approximately 25 Å in length and is also observed in subsurface layers, propagating along the  $\langle 110 \rangle$  direction. As the indenter is withdrawn from the work material the minicrack fully reconstructs.

The crystalline formation of slip bands in Fig. 5.5.16(a) and (b) propagated very quickly as a wave from the centre of the substrate surface along the  $\langle 110 \rangle$  directions (i.e. the out-of-plane  $\langle 111 \rangle$  directions) until they interacted with the boundaries. In reality, the slip markings would glide away from the indentation trace until they interact with defects in the crystal or collide with a grain boundary. The simulation cell employed here is much too small to observe such an effect. The transition from the slipped to the unslipped region is spread over several lattice distances. In the transition region, each atom is displaced further away from its initial lattice site. The highest point of the slip bands above the surface lay between 1 Å and 1.3 Å. The slip planes have not moved vertically by half a lattice constant and therefore the crystal continuity is not completely maintained. During indentation with  $\phi = 0^\circ$ , a parallel set of slip bands were observed propagating side-by-side. However, for indentation with  $\phi = 45^\circ$ , only single slip bands propagated along the  $\langle 110 \rangle$  directions. Although shallow, the slip bands were comparatively wide with peak measurements between 35 Å and 40 Å. At the conclusion of the indentation process, some of the slip bands have fully relaxed, while others are permanent deformations in the work material. The permanent slip markings do not

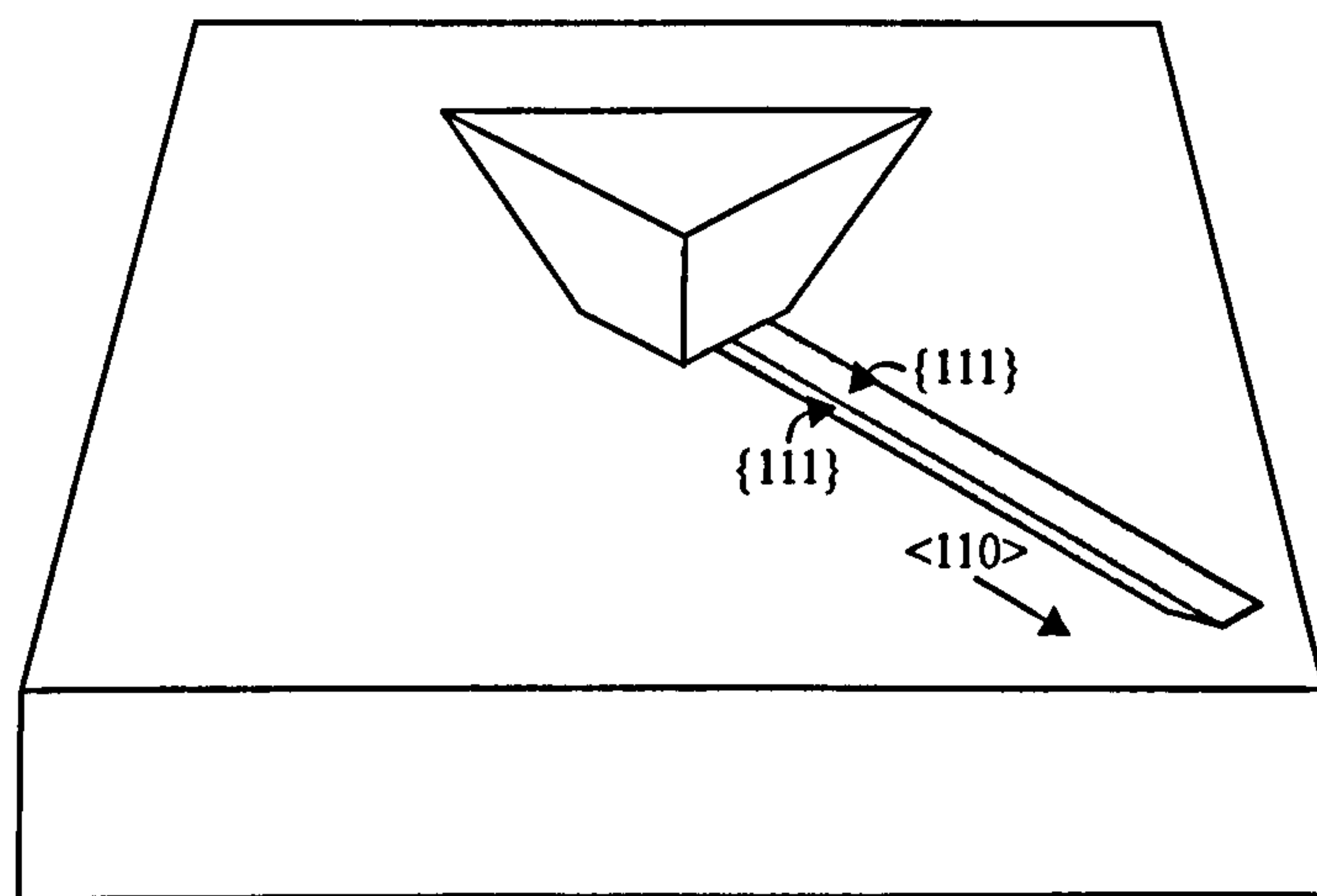


Fig. 5.5.15. Schematic representation of the slip system in the Ag  $\{100\}$  work material. Slip occurs in the  $\{111\}$  planes (shaded), along the compact  $\langle 110 \rangle$  directions.





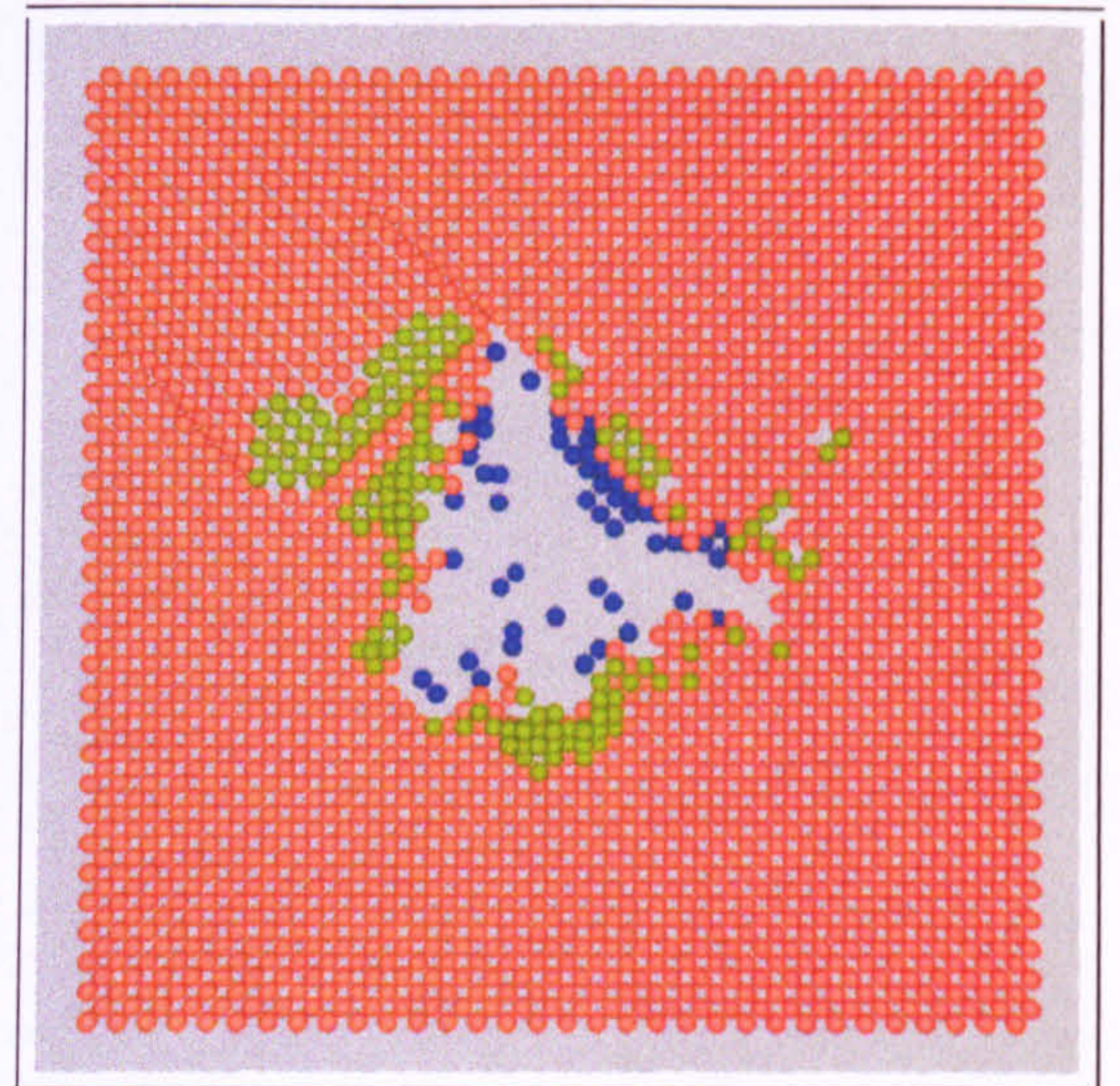
(a)



(b)



(c)



(d)

Fig. 5.5.16. Plan view of the 1<sup>st</sup> layer atoms in the Ag {100} substrate showing the plastically deformed triangular region with: (a)  $\phi = 0^\circ$  at  $t = 75$  ps; (b)  $\phi = 45^\circ$  at  $t = 75$  ps; (c)  $\phi = 0^\circ$  at  $t = 150$  ps; (d)  $\phi = 45^\circ$  at  $t = 150$  ps. The blue shaded atoms represent those atoms displaced by more than 1 Å below the surface. The green shaded atoms denote those atoms displaced above the surface by more than: (a),(b) 0.1 Å; (c),(d) 1 Å. The red atoms have not been displaced by more than 1 Å below the surface or by: (a),(b) 0.1 Å; (c),(d) 1 Å above the surface. Note the minicrack in (a) marked by the arrow.

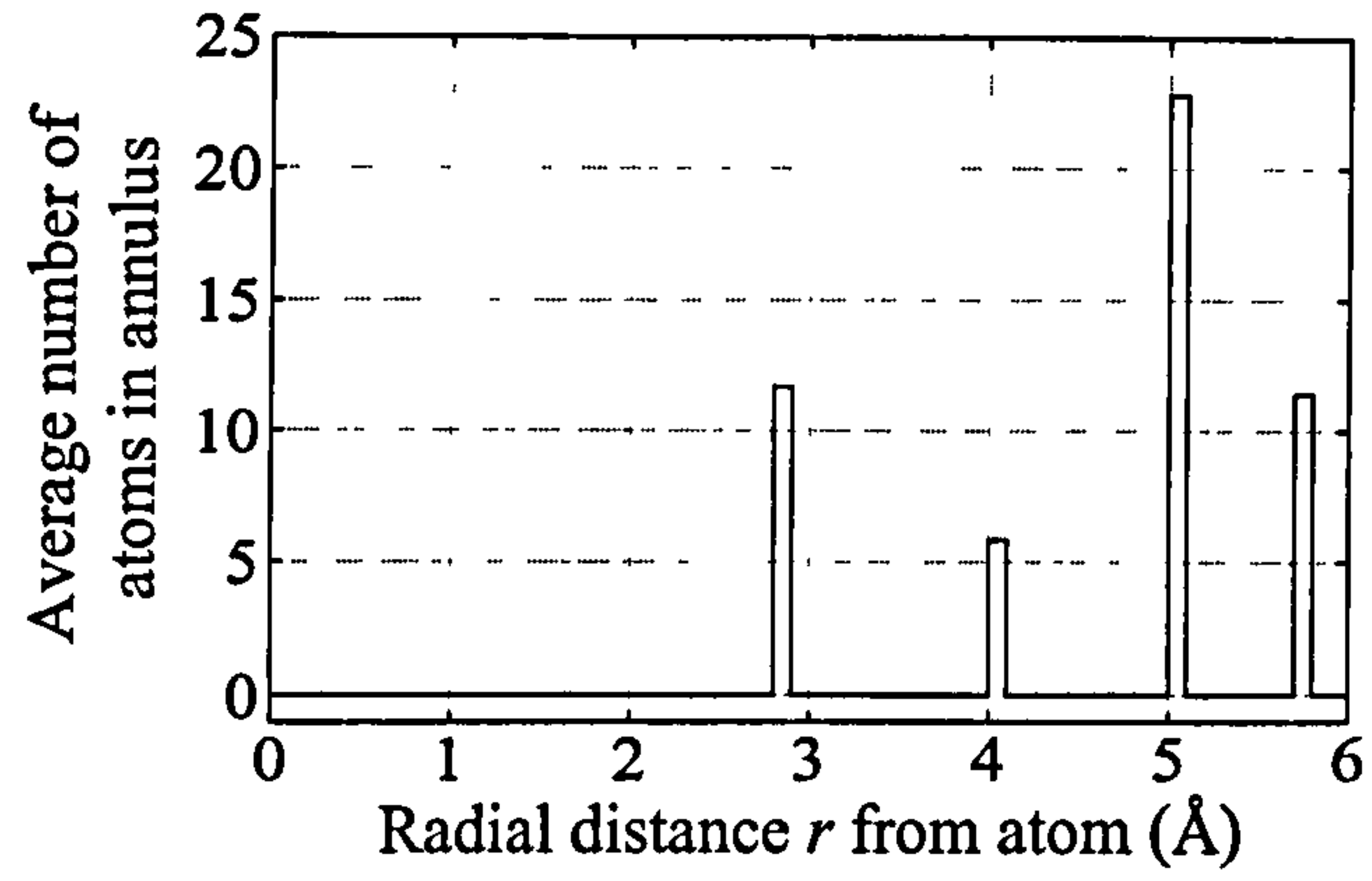


occur along each of the four possible compact directions in both simulations, which can be attributed to the asymmetry of the indenter. Additional simulations on Ag {100} established that a critical indentation depth of approximately 10Å needed to be reached for slip markings to appear on the substrate surface.

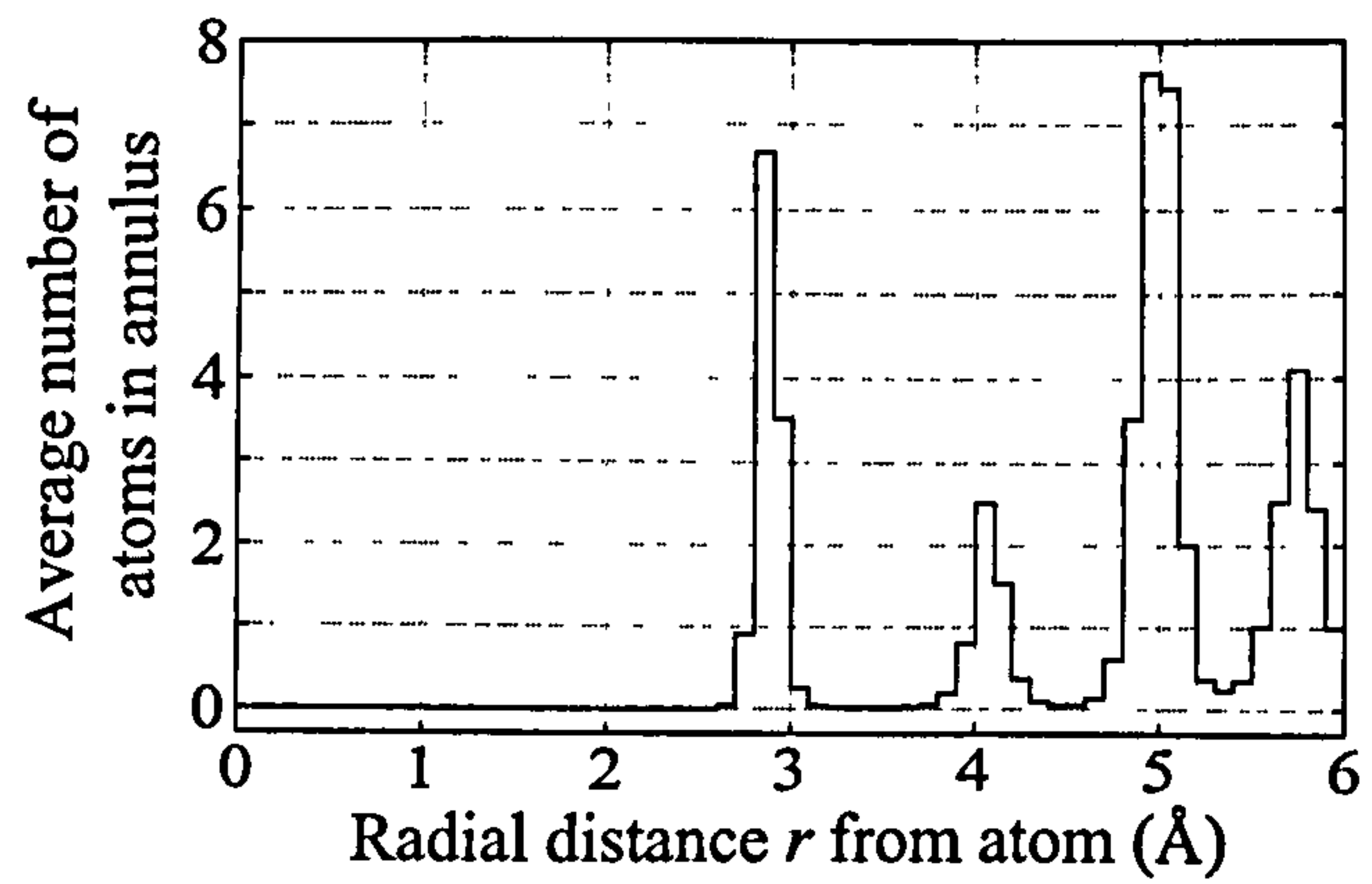
Comparison between Fig. 5.5.7(c),(d) and Fig. 5.5.16(c),(d) reveals that more substrate atoms are displaced above the surface of Ag than Fe. This would be expected since Ag is much softer than Fe and so pile-up can occur more easily. In Fig. 5.5.16(c) and (d), the distribution and yield of material pile-up is clearly influenced by the rotation of the indenter. Following indentation with  $\phi = 0^\circ$ , Fig. 5.5.16(c) shows a large accumulation of Ag atoms along the side of the plastically deformed triangular region parallel to  $\langle 100 \rangle$ . Here, the atoms appear to displace onto the surface along the  $\langle 110 \rangle$  direction. There is also a substantial assemblage of Ag atoms along the remaining sides of the deformed region. The side of the plastically deformed region that lies parallel to the  $\langle 110 \rangle$  direction in Fig. 5.5.16(d) shows few Ag atoms thrown up onto the surface. The remaining sides of the plastically deformed triangular region also show a small yield of displaced Ag atoms onto the surface compared with Fig. 5.5.16(c).

Structural analysis of the pile-up material on the surface of the Ag substrate shows the atoms to be primarily arranged in crystalline fcc form with no vacancies or interstitials. Following indentation with  $\phi = 0^\circ$ , the piled-up material reaches a peak height of 6.1 Å (approximately 34% of the maximum penetration depth) and is configured from 201 1<sup>st</sup> layer atoms and 28 2<sup>nd</sup> layer atoms. After indentation with  $\phi = 45^\circ$ , the pile-up material peaks at 5.9 Å (approximately 30% of the maximum penetration depth) above the undisturbed surface and is composed of 143 1<sup>st</sup> layer atoms, 21 2<sup>nd</sup> layer atoms and 2 3<sup>rd</sup> layer atoms. Permanent slip markings are also observed on the subsurface layers of the work material, forming similarly to those on the substrate surface, but with decreasing widths and lengths. Further analysis reveals that permanent slip markings are formed on each atomic layer to the maximum penetration depth. In each layer, these features are comparable to those in the preceding layer, but less substantial. Piling-up of material also occurs along the sides of the plastically deformed triangular region in the subsurface layers. However, after the 5<sup>th</sup> substrate layer, no significant piling-up of material occurs along the sides of the plastically deformed region. This is analogous to the observations of piled-up material on the subsurface layers in the Fe {100} substrate. Atoms in the Ag substrate near the peak penetration depth of the indenter behave in

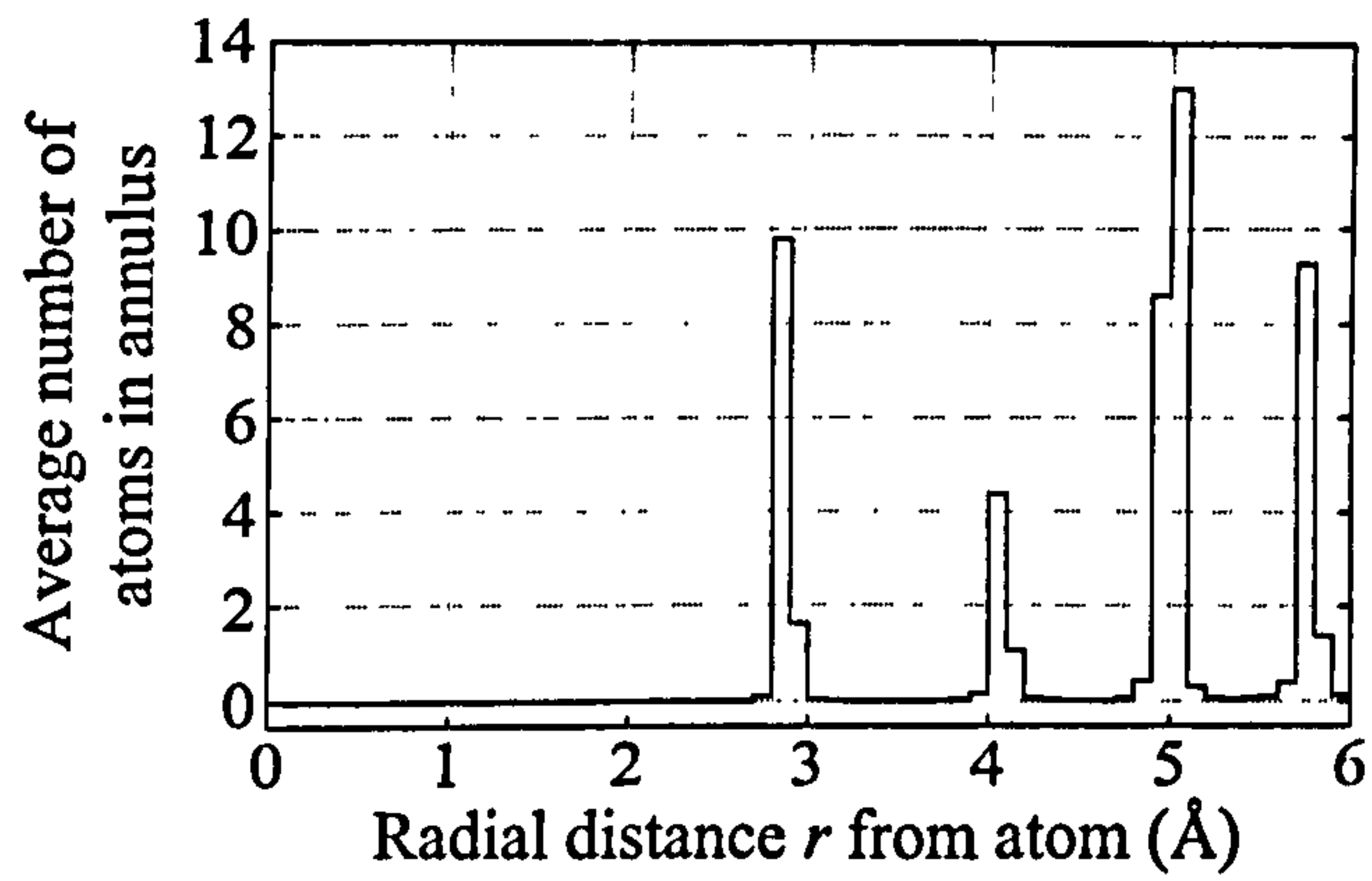




(a)



(b)



(c)

Fig. 5.5.17. Radial distribution plot of Ag density for indentation with  $\phi = 0^\circ$  at: (a)  $t = 0$  ps; (b)  $t = 75$  ps; (c)  $t = 150$  ps. For each atom,  $a_i$ , in a local area containing an initial 8,008 atoms around the local indentation region, the density of Ag atoms is evaluated in an annulus of width  $0.1 \text{ \AA}$  which is sited at a radial distance  $r \text{ \AA}$  from  $a_i$ .



a very similar manner to the atoms in the Fe substrate, where some layer atoms are displaced from preceding layers. As with Fe, the range of plastic deformation in Ag exceeds twice the peak indentation depth. The maximum kinetic energy of both the Fe and Ag substrates during the indentation was approximately 20 eV, which, if averaged across the substrate, corresponds to a peak temperature increase of about 5 °C.

The radial distribution of Ag density in the work material for indentation with  $\phi = 0^\circ$  is presented in Fig. 5.5.17 at different stages of the indentation process. Fig. 5.5.17(a) corresponds to the start of the indentation process at  $t = 0$  ps, and illustrates the crystalline structure of the Ag substrate. The radial distribution of Ag atoms at the halfway stage of the indentation process is presented in Fig. 5.5.17(b). As observed with Fe, the contact area becomes disordered during the indentation. Detailed analysis of the plot shows the limit in compression between two Ag atoms is approximately 2.55 Å. This corresponds approximately to 12% compression of the nearest neighbour bond length. Fig. 5.5.17(c) shows the radial distribution of Ag atoms at the conclusion of the indentation process.

## 5.4 Modification of Ackland's Ag Potential

In Ackland's EAM Ag potential, the energy of an atom,  $U_i$ , is determined by both a pair potential and a many body function, as discussed in Section 2.2.1, Chapter 2. The functions  $V(r_{ij})$  and  $\phi(r_{ij})$  (given in Chapter 2, by Eqn. 2.2.2.6 and Eqn. 2.2.2.7) are described by cubic splines fitted to various crystal properties. By denoting the atomic separation between atoms  $i$  and  $j$  as  $r$ , the functions  $V(r_{ij})$  and  $\phi(r_{ij})$  are written as

$$V(r) = \sum_{k=1}^6 a_k (r_k - r)^3 H(r_k - r) \quad (5.4.5.1)$$

$$\phi(r) = \sum_{k=1}^2 A_k (R_k - r)^3 H(R_k - r) \quad (5.4.5.2)$$

where  $r_k$  and  $R_k$  are chosen knot points such that  $r_1 > r_2 > r_3 > r_4 > r_5 > r_6$  and  $R_1 > R_2$ . The function  $H(x)$  is the Heaviside step function and is defined such that  $H(x) = 0$  for  $x \leq 0$  and  $H(x) = 1$  for  $x > 0$ . The coefficients  $a_k, A_k$  and  $r_k, R_k$  are given in Table 5.1. The coefficients  $r_1$  and  $R_1$  represent the cut-off radii of  $V(r)$  and  $\phi(r)$  respectively, which is equal to the separation distance between an atom and its third neighbours. In an infinite volume of an ideal fcc crystal, each atom  $i$  has 12 1<sup>st</sup>, 6 2<sup>nd</sup>



Table 5.1. Coefficients  $a_k$  and  $r_k$  in Ackland's Ag potential. The values are in units of the lattice constant (4.086 Å).

Coefficient	Value	Coefficient	Value
$a_1$	20.368494	$r_1$	1.2247449
$a_2$	-102.36075	$r_2$	1.1547054
$a_3$	94.31277	$r_3$	1.1180065
$a_4$	-6.220051	$r_4$	1.0000000
$a_5$	31.08088	$r_5$	0.8660254
$a_6$	175.56047	$r_6$	0.7071068
$A_1$	1.458761	$R_1$	1.2247449
$A_2$	42.946555	$R_2$	1.0000000

and 24 3<sup>rd</sup> neighbours which are situated at  $\frac{a}{\sqrt{2}}$ ,  $a$  and  $a\sqrt{\frac{3}{2}}$  respectively from  $i$ , where  $a$  denotes the lattice constant. The cut-off radii in Ackland's Ag potential is at the third neighbour spacing. This is not ideal for a MD simulation since the neighbour lists generated for each atom will be large due to the significant number of third neighbour atoms. By modifying the potential energy function such that the cut-off occurs just before the third neighbours, the size of the neighbour lists can therefore be reduced and hence, the computational efficiency for energy and force evaluations can be increased.

In the MD simulations, the neighbour lists have a skin radius equal to 5% of the potential cut-off. Therefore, by cutting Ackland's Ag potential off at 4.765 Å, the neighbour lists would have a new radius of 5.003 Å and will not include third neighbours. Fig. 5.5.18 shows the modification to the pair potential which was formed by truncating  $V(r)$  from the maximum at  $r/a \approx 1.084$ , and replacing it with a cubic spline which is smoothly cut-off at 4.765 Å. The modified potential  $V(r)$  is described as

$$V(r) = \begin{cases} \sum_{k=1}^6 a_k (r_k - r)^3 H(r_k - r) & \text{if } r < r_{tr} \\ \left[ t_1 (r - r_{tr})^3 + t_2 (r - r_{tr})^2 + t_3 \right] H(r_{ct} - r) & \text{if } r \geq r_{tr} \end{cases} \quad (5.4.5.3)$$

$$t_1 = 1.267566 \quad t_2 = -0.641271 \quad t_3 = 0.024315$$



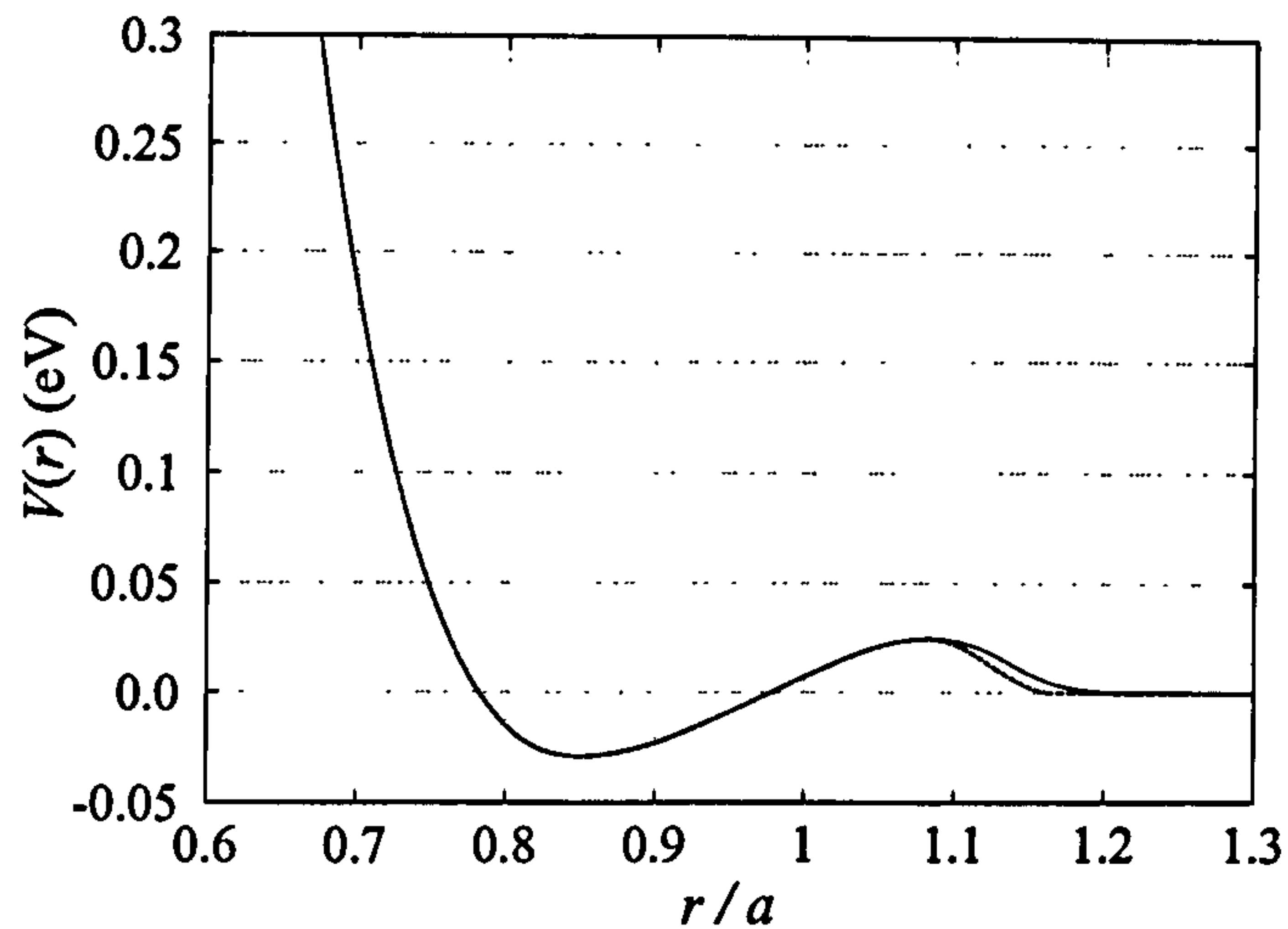


Fig. 5.5.18. The bold line represents Ackland's Ag pair potential  $V(r)$  plotted against  $r/a$ , where  $a$  is the lattice parameter and  $r$  is the atomic separation. The dashed line shows the modified part of the potential which is cut from the local maximum at  $r/a \approx 1.084$  Å and smoothly cut-off at  $r/a = 1.166$  Å.

where  $r_{tr} \approx 1.084$  and  $r_{ct} \approx 1.166$  in units of the lattice parameter. The function  $\phi(r)$  is also cut-off at 4.765 Å by adjusting the coefficient  $R_1$  in Table 5.1 to  $r_{ct}$ .

The load-displacement curves in Fig. 5.5.19 show a comparison between Ackland's original potential and the modified potential for indentation of Ag {100} with  $\phi = 0^\circ$ . Implementing the modified potential results in a peak force of approximately 95 eV/Å acting on the indenter at an indentation depth of about 19 Å. This corresponds to a

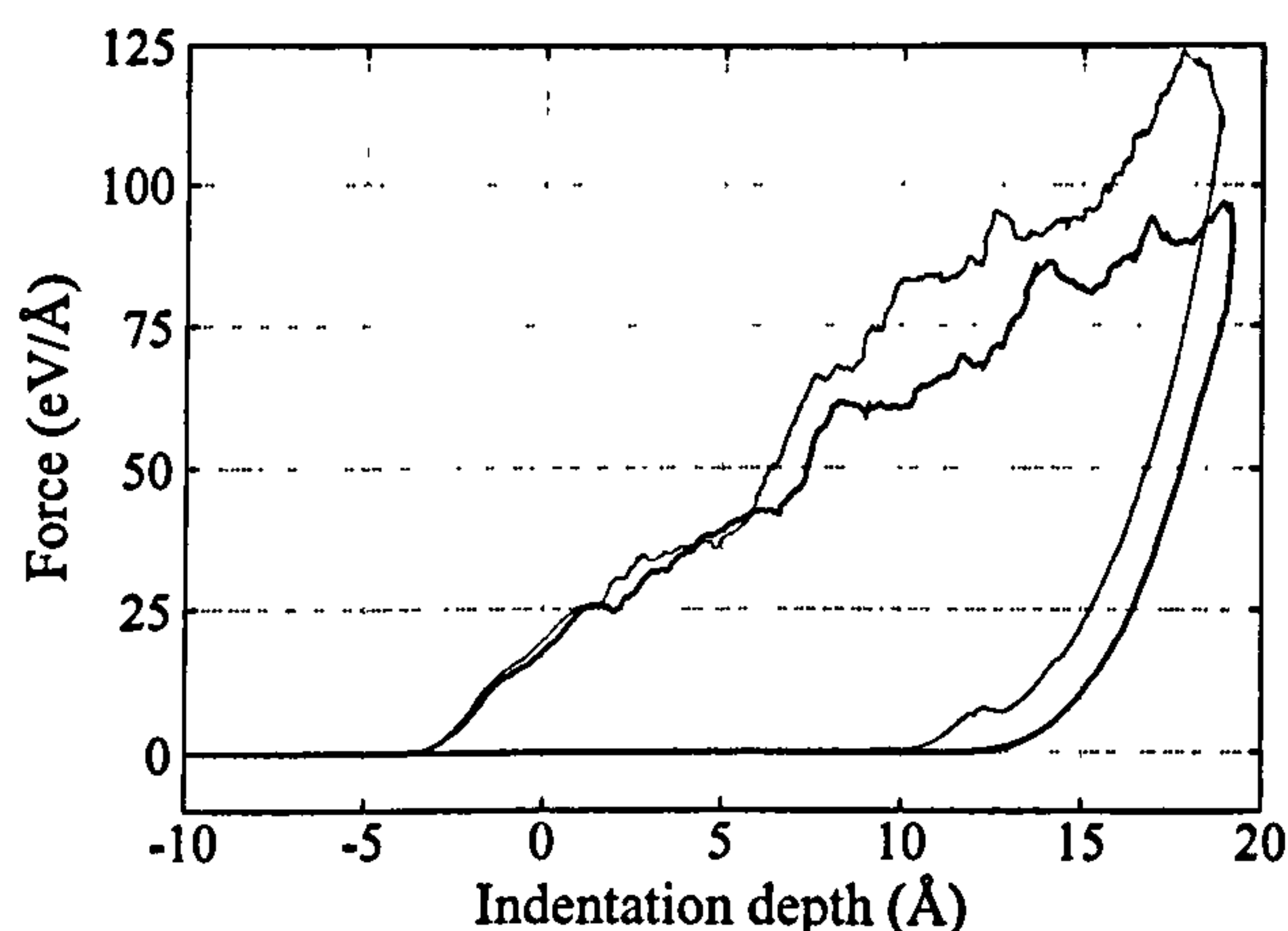


Fig. 5.5.19. Force-depth curves from the simulation of indentation into Ag {100} with  $\phi = 0^\circ$ . The bold line represents indentation with all Ag-Ag interactions described by the modified Ackland's Ag potential, which is smoothly cut-off at 4.765 Å. The remaining line corresponds to indentation where all Ag-Ag interactions are described by Ackland's original Ag potential, which is smoothly cut-off at 5.0044 Å.



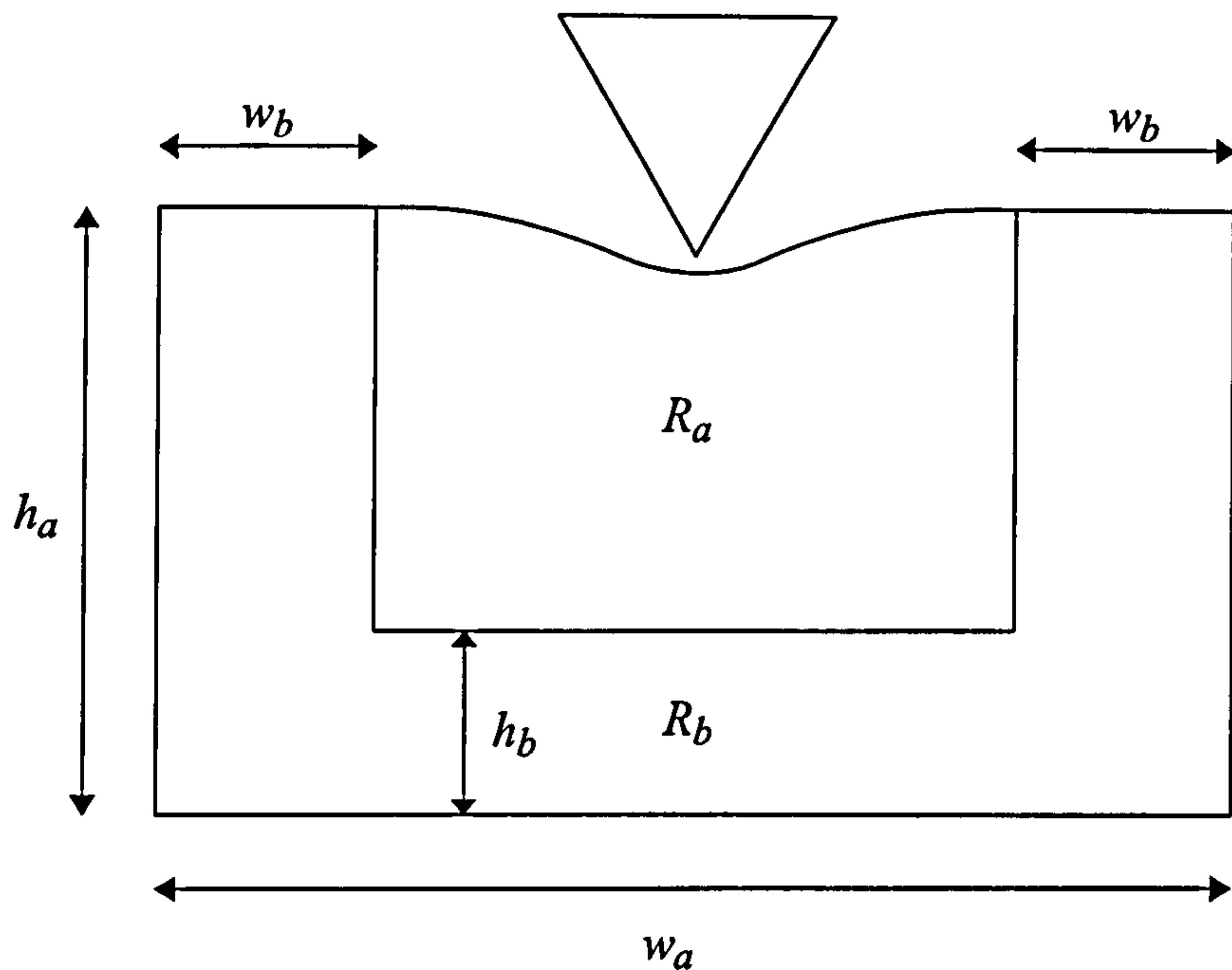


Fig. 5.5.20. Cross-section of a substrate employing the embedded original-modified Ackland Ag potential. The substrate has a height  $h_a$ , a width  $w_a$  and is split into regions  $R_a$  and  $R_b$ . Region  $R_a$  is constrained by vertical boundaries at a distance  $w_b$  from all sides of the substrate and a horizontal border positioned at a distance  $h_b$  from the underside of the substrate. Region  $R_b$  is then defined as the remaining volume in the substrate. In the embedded region  $R_a$ , Ackland's normal potential is implemented and in region  $R_b$ , the modified version of Ackland's potential is employed.

decrease of  $\approx 24\%$  in the maximum force of  $125 \text{ eV/\AA}$  observed when Ackland's original potential is employed. The two load-displacement curves compare well for low indentation depths. However, as the indenter tip displaces further into the work material, the discrepancy between the two curves becomes more significant. Furthermore, the elastic recovery of the work material is slightly less for indentation using the modified potential. The total CPU time for the simulation employing the modified potential was approximately 71.5 hours compared with 108.8 hours for the simulation utilising the original potential (times are based on the SUN workstation). Hence, by truncating the the potential just before the third neighbours, the total CPU time has been reduced by approximately 34% at a cost of significant inaccuracies describing the Ag-Ag interactions.

The discrepancies between the load-displacement curves in Fig. 5.5.19 occur since the modified potential only yields an accurate description of the silver work piece in an



ideal equilibrium state. The discrepancies in Fig. 5.5.19 can be reduced by employing both Ackland's potential and the modified potential, as illustrated in Fig. 5.5.20. By considering an embedded region of the substrate encompassing the local indentation region,  $R_a$ , the Ag-Ag interactions are described by Ackland's original potential and hence the correct mechanical behaviour of the work material should be closely maintained. In the region  $R_b$  outside the local indentation area, the Ag atoms are less dynamic than those sited around the local indentation region ( $R_a$ ) and hence, the atoms in region  $R_b$  can be described by the modified potential to increase the computational efficiency of the simulation.

Fig. 5.5.21 shows force-depth curves for indentation employing Ackland's original potential and the embedded original-modified potential. The force-depth curve compares very well to that produced from employment of Ackland's original potential. There is clearly less discrepancy between the two load-displacement curves compared with Fig. 5.5.19. With the embedded original-modified potential, indentation results in a maximum force of approximately 120 eV/Å acting on the indenter at an penetration depth of approximately 18 Å. The elastic recovery of the substrate compares very well between the two force-depth curves. This would be expected since the elastic recovery of the work material is centred around the local indentation region, where the Ag-Ag interactions were described by Ackland's original potential. The total CPU time was

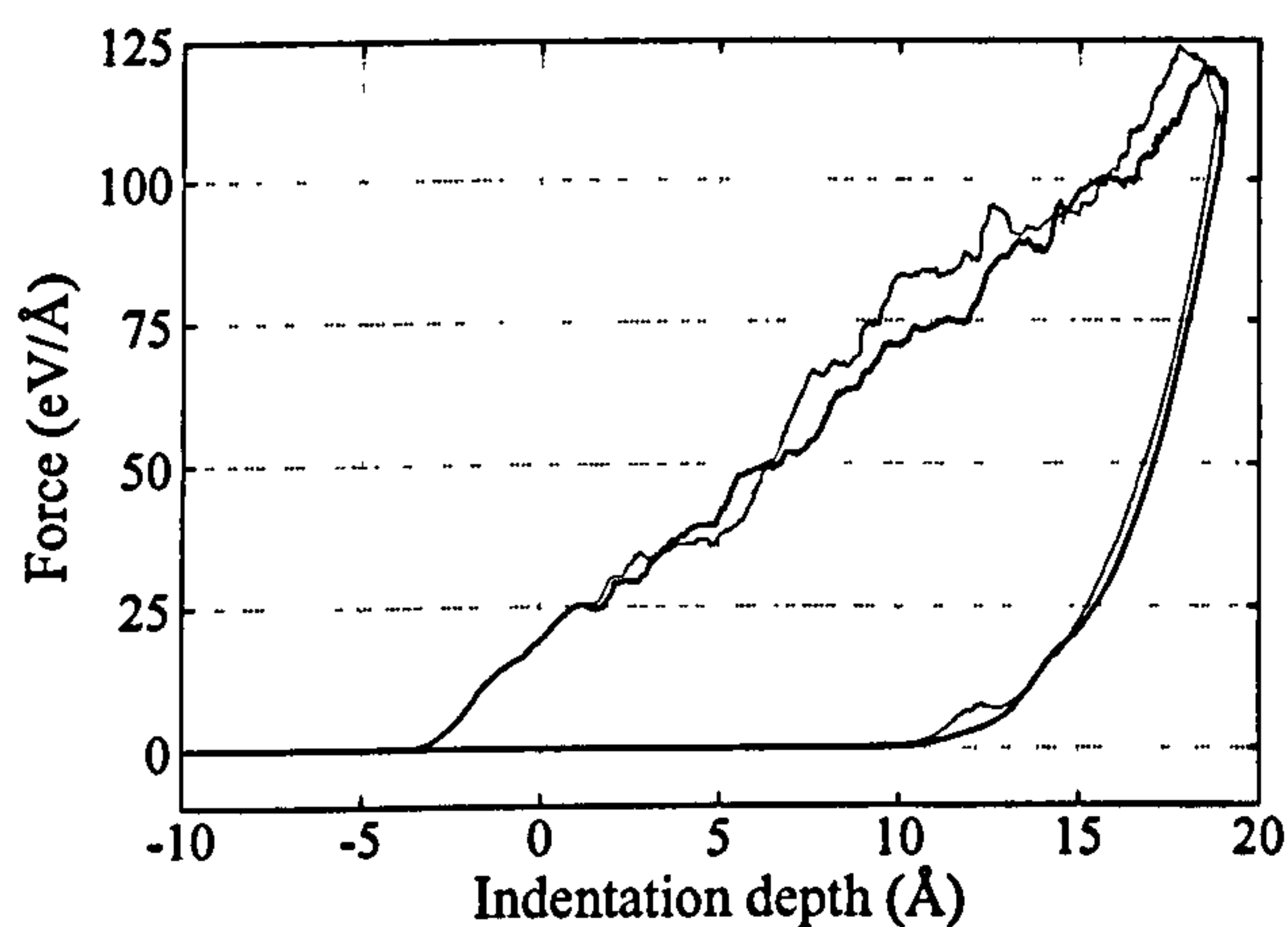


Fig. 5.5.21. Force-depth curves from the simulation of indentation into Ag {100} with  $\phi = 0^\circ$ . The bold line represents indentation implementing the embedded original-modified potential, where  $h_a \approx 40$  Å,  $h_b \approx 10$  Å,  $w_a \approx 130$  Å and  $w_b \approx 35$  Å. The remaining line corresponds to indentation where all Ag-Ag interactions are described by Ackland's original potential.



approximately 77.9 hours, which lies between the CPU time for indentation with the original potential (108.9 hours) and the modified potential (71.5 hours), as would be expected. Using the embedded original-modified potential maintains the development of slip bands on the Ag surface and also ensues in a similar distribution of tip-induced pile-up.

The embedded original-modified potential could be successfully applied to simulated phenomena where a large volume of the work piece is consistently in a near ideal equilibrium state. For example, during indentation of an Ag substrate configured from millions of atoms, there will be tens of thousands of atoms outside the local indentation region near the sides of the work material that will remain in a near equilibrium state. These atoms can be described by the modified potential, thus considerably decreasing the size of neighbour lists and increasing computational efficiency. However, the embedded original-modified potential presented here needs to be investigated further to examine any impairments of material properties and also the influence of the boundary separating regions  $R_a$  and  $R_b$ . For example, if the modification to Ackland's potential impairs the elastic properties, then indentation of the work material may ensue in discrepancies in the deformation behaviour across the  $R_a$  and  $R_b$  interface. The simulations using Ag in the preceding section used Ackland's original version of the potential.

## 5.5 Experimental Results and Discussion

### 5.5.1 Body-centred-cubic Iron

Nanoindentations were performed on ferrite grains between 5 and 30  $\mu\text{m}$ , in ordinary steel C 35 samples. Due to limitations in experimental resources, the crystal orientation of the ferrite grains could not be distinguished. A SFM image of the ferrite grains is presented in Fig. 5.5.22. The surface image shows different crystal orientations separated by grain boundaries. Multiple indentations were performed at various locations in the work piece with different loading forces and penetration depths. Nanoindentation into grain 1 with a force of 3 mN results in hillock growth along the left and right sides of the indented region. Along the uppermost edge, there is comparatively less piling-up of the work material. Two indentations were made in grain 2, where the large and small indented regions correspond to a maximum indentation force of 3 mN and 2 mN



respectively. Here, the hillock growth is distributed more symmetrically around the locality of the indentation. The difference between the indentation images in grain 1 and grain 2 clearly suggest a different orientation of the crystal structure of the substrate with respect to the indenter. Nanoindentation was also performed directly on the grain boundary between grains 1 and 2 in Fig. 5.5.22, with a force of 0.5 mN. To capture the mechanical properties of only the grain boundary, the indentation force has to be reduced otherwise the bulk behaviour of the adjacent grains will become too influential. The indentation image on the grain boundary in Fig. 5.5.22 clearly shows piling-up occurring preferentially in grain 2.

Fig. 5.5.23(a) shows a SFM image of indentations with a force of 1.5 mN in adjacent ferrite grains. The hillocks clearly form differently in each grain. The peak height of the piled-up material in the upper indent is approximately 17% of the maximum penetration depth. For the lower indent, the peak height of the hillocks is about 33% of the maximum indentation depth. A typical force-depth curve for Fe is shown in Fig. 5.5.23(b) with a peak indentation force of 1.5 mN, which results in a maximum penetration depth of approximately 160 nm. The elastic recovery of the ferrite work material is 14 nm,

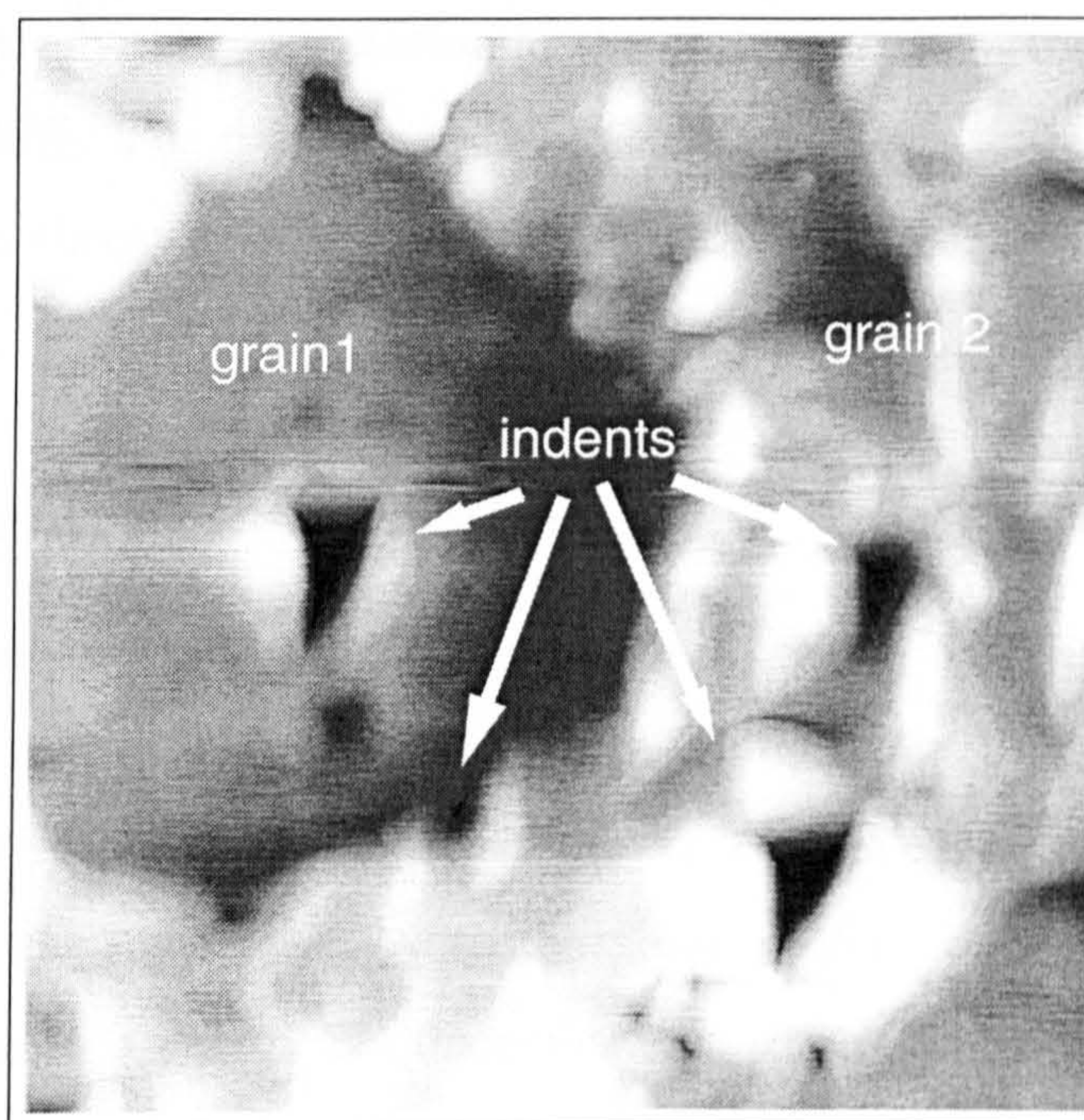
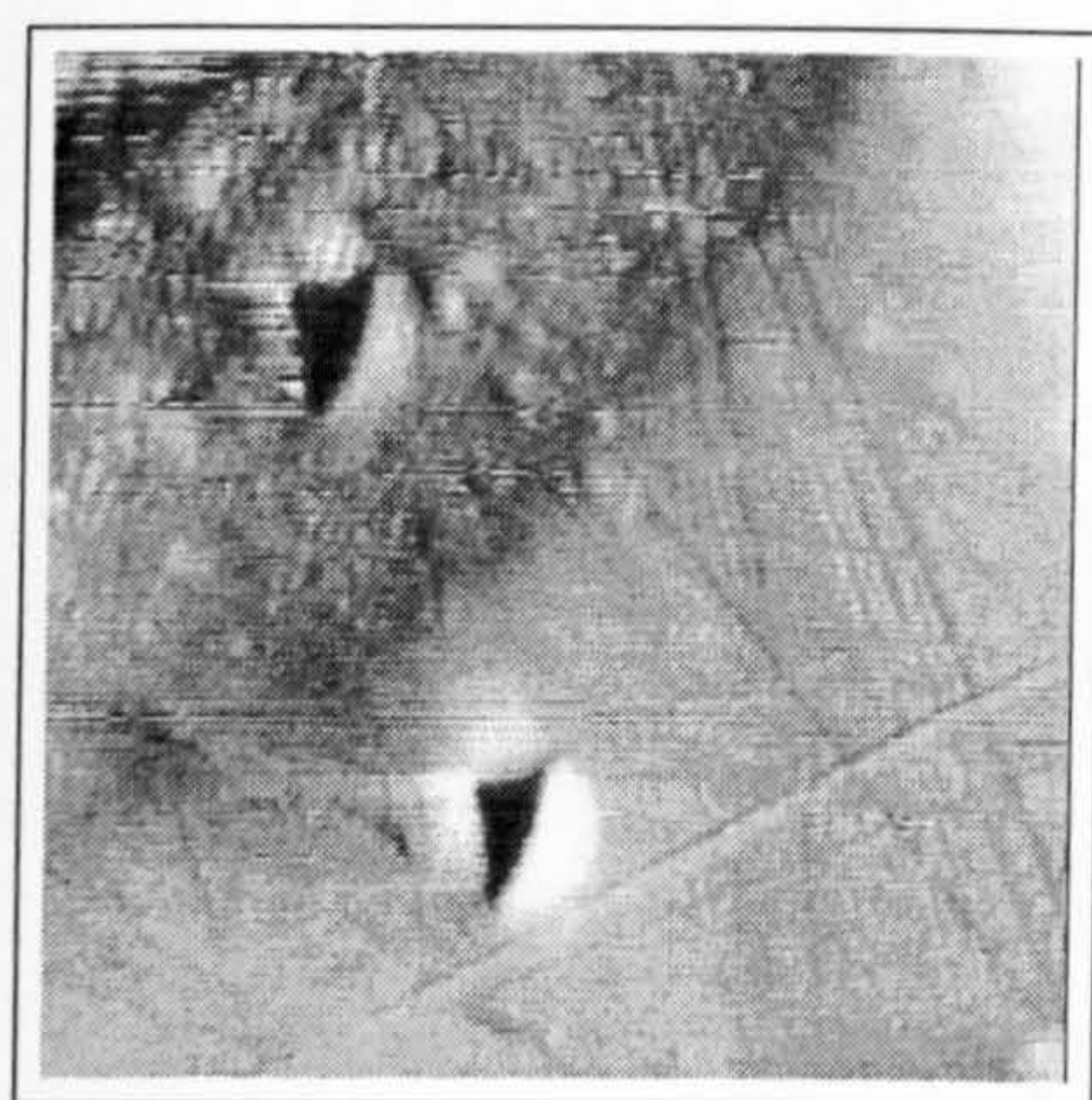
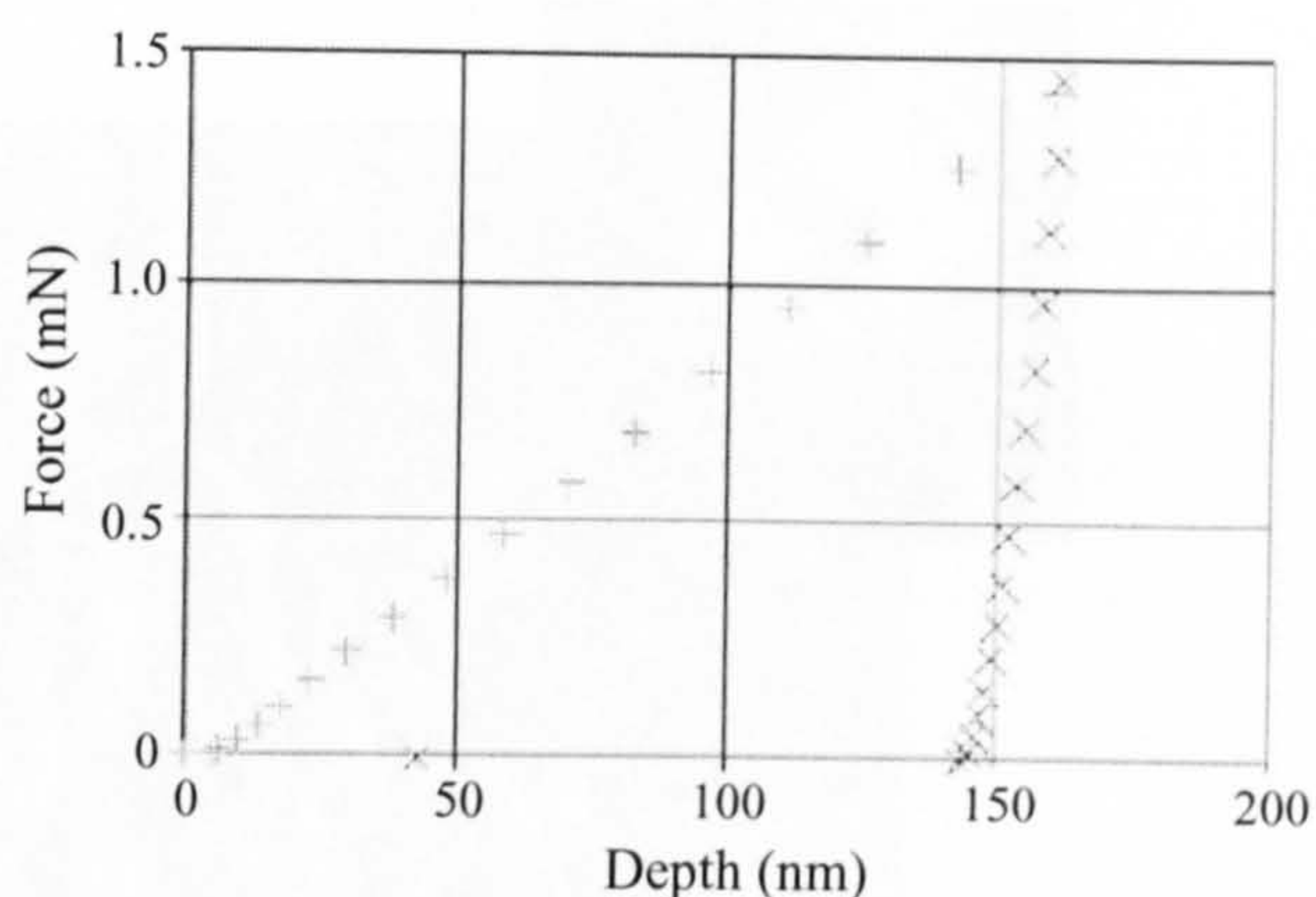


Fig. 5.5.22. SFM image of ferrite grains with several nanoindentations (as marked by the arrows) in grain 1 and grain 2 with a maximum force of 3 mN (large indents) away from the boundary and 0.5 mN at the boundary. There is another indent in grain 2 (smaller image) with an indentation force of 2 mN. Image size  $12\ \mu\text{m} \times 12\ \mu\text{m}$ .





(a)



(b)

Fig. 5.5.23. (a) SFM image of adjacent ferrite grains with indents in both grains showing pile-up of different forms. (b) corresponding force-depth curve for nanoindentation with a maximum indentation force of 1.5 mN: (+) increasing load curve; (x) decreasing load curve.

i.e. about 10% of the maximum indentation depth. For the 3 mN indentation images in Fig. 5.5.22, the plastic deformation of the work material is 87% and 89% for grain 1 and grain 2 respectively. For indentation at the grain boundary, the plastic deformation is approximately 86%. The nanohardness of the ferrite work material is  $1.9 \pm 0.1$  GPa and using Hertzian theory of contact (Section 3.4, Chapter 3), the Young's modulus is  $160 \pm 11$  GPa.

## 5.5.2 Face-centred-cubic Silver

The surface of a polycrystalline Ag sample is presented in Fig. 5.5.24. The three different grains A, B and C are separated by grain boundaries. In grains B and C, twin lamellas are clearly visible. The crystal orientation of each of the three grains could not be determined, for the same reason with the polycrystalline ferrite sample. Indentation into grain A results in a symmetric distribution of the piled-up material, whereas indentation of grains B and C ensues in hillocks formed predominantly along one side of the indentation region. Different crystal orientations of the grains result in the variation of the hillock distribution in the indentation images. In Fig. 5.5.25(a), the height profile line scan shows the hillocks formed around the 100 nm indentation in grain A have peak heights of 34 nm and 46 nm. From Fig. 5.5.25(b), the hillock formed around



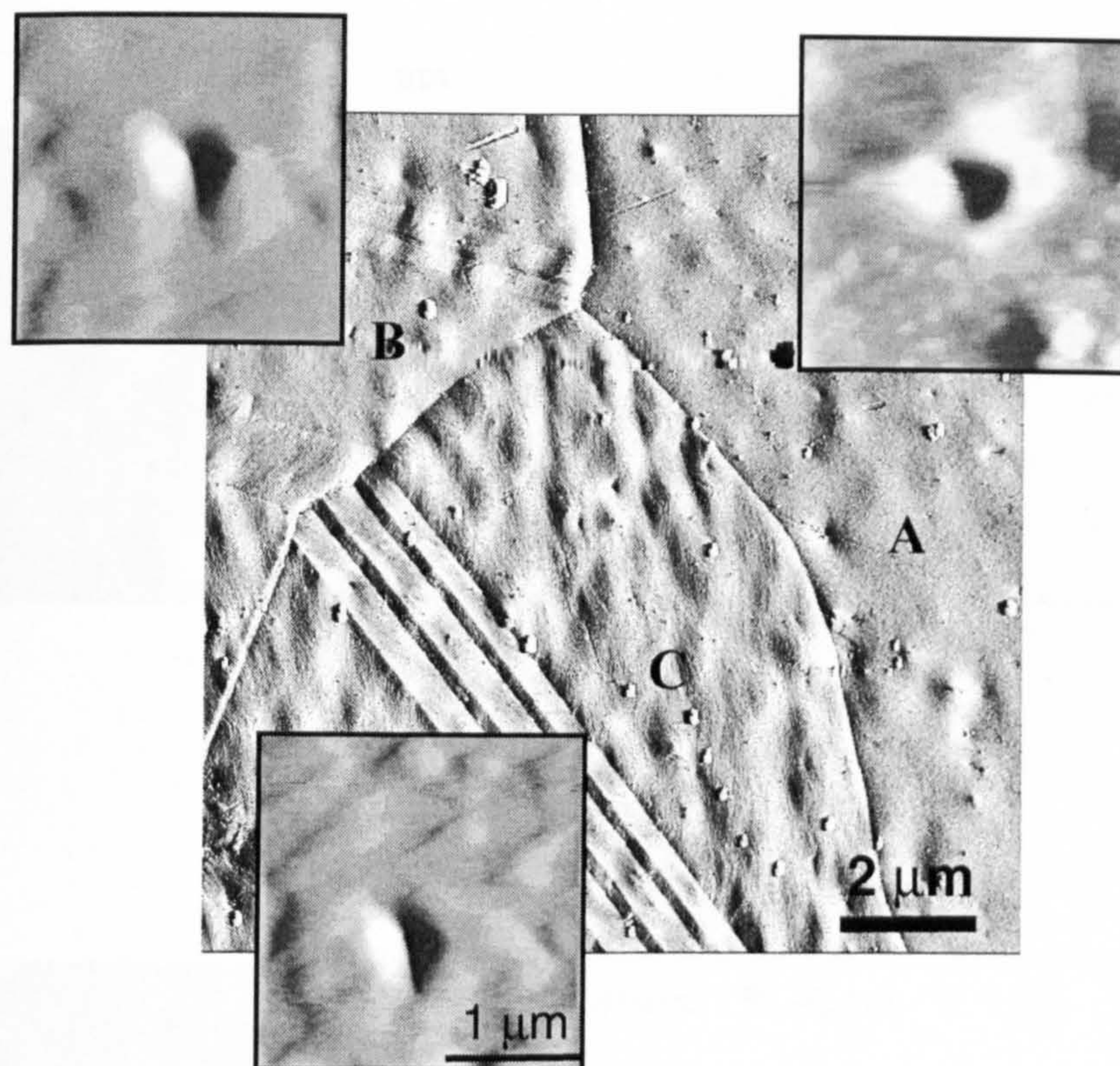


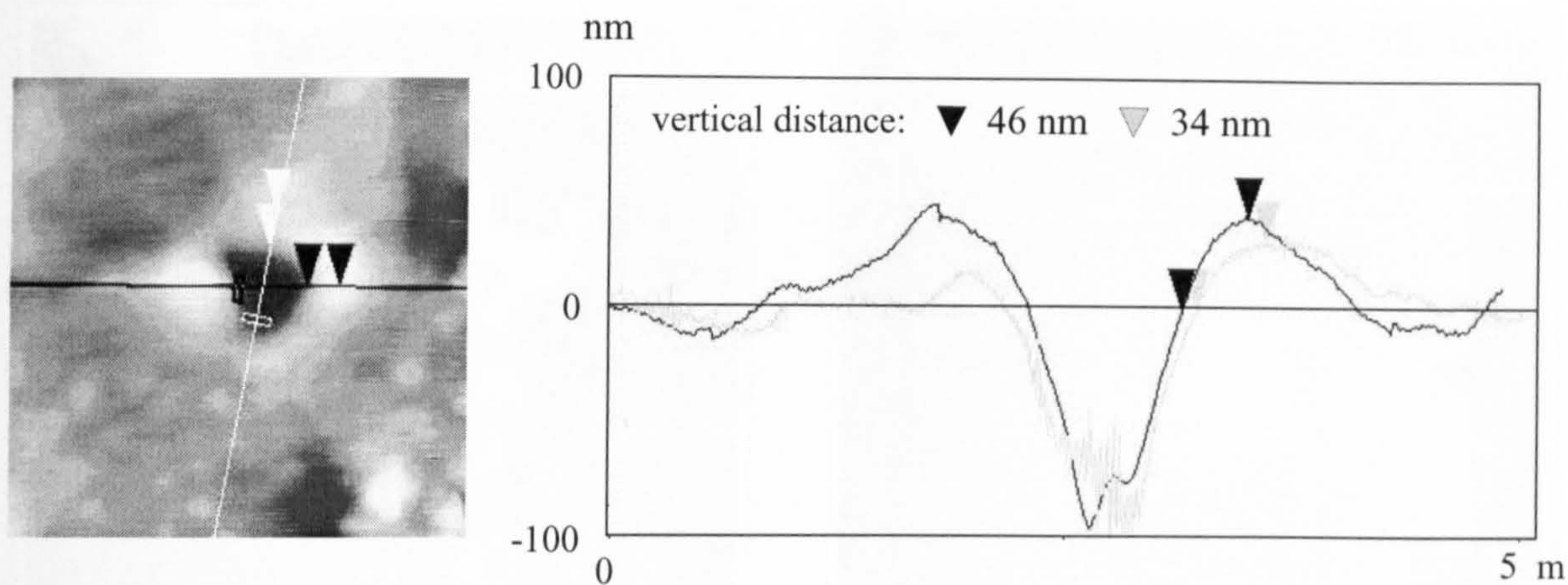
Fig. 5.5.24. SFM image of three adjacent Ag grains A, B and C showing grain boundaries and twin lamellas in B and C. The superimposed images correspond to indents in the grains with an a maximum indentation force of 0.5 mN.

the indentation in grain B is similar to those around the indentation in grain A, with a maximum height of 42 nm.

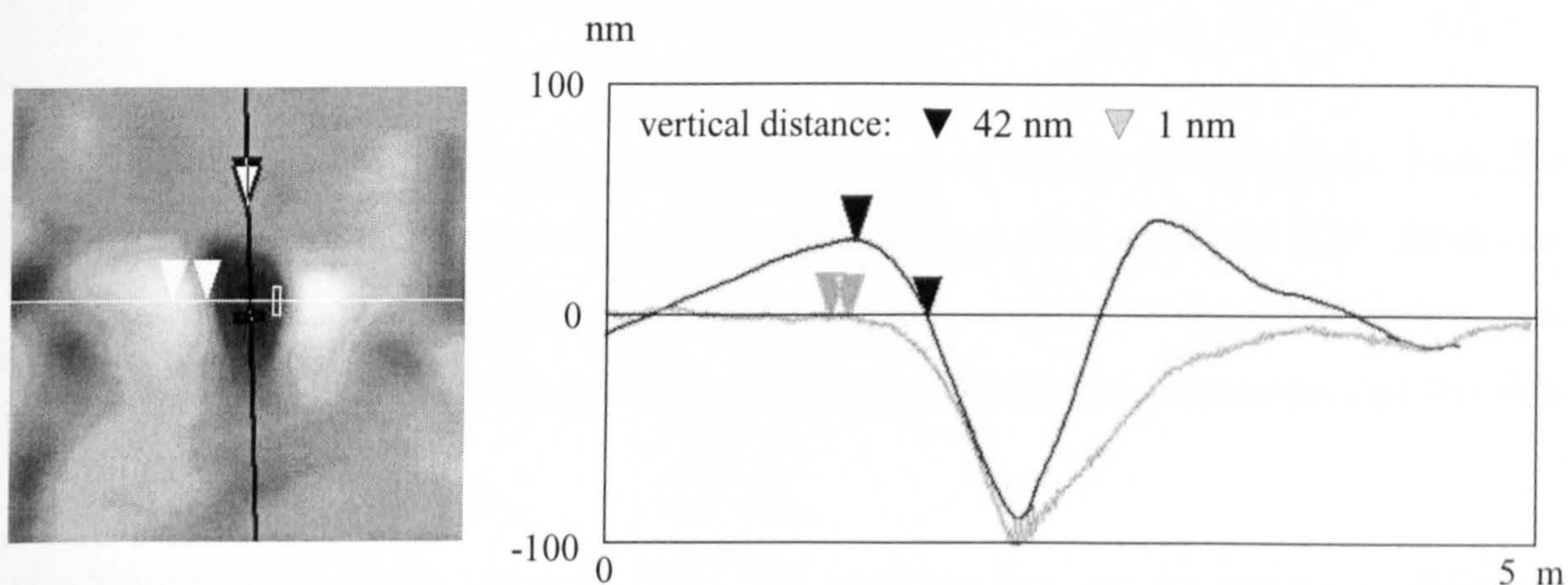
No slip markings are observed on the surface of the polycrystalline Ag sample following indentation, due to the limitation of the SFM instrument. However, a recent experimental study by Zimmerman *et al* [192] observed several slip markings following indentation of Au {100} with a tungsten indenter. Shown in Fig. 5.5.26(a) is an STM image by Zimmerman *et al* [192]<sup>3</sup> of two nanoindentations on the Au {100} surface. The image clearly shows pile-up around the indents together with slip markings along the  $\langle 110 \rangle$  direction, which were observed up to several hundred angstroms away from the indentation region. In a study by Gonzalez *et al* [193], slip markings observed on the Au {100} surface following indentation had an estimated height of 0.7 Å and widths up to 7 nm. Shown in Fig. 5.5.26(b) is a STM image obtained by Zimmerman *et al* [192] of a slip marking on Ag {100}, induced from ion-bombardment and annealing. The MD simulations on Ag presented in this chapter reproduce similar tip-induced slip markings

<sup>3</sup>With permission





(a)



(b)

Fig. 5.5.25. Nanoindentations in Ag with section analysis showing the piling-up of work material. Indents correspond to: (a) grain A and (b) grain B in Fig. 5.5.24. Note, the black and white arrows in the graph in (b) are the wrong way around.

on the  $\{100\}$  surface as observed on Au by Zimmerman *et al* [192].

A force-depth curve is presented in Fig. 5.5.27 for 1.5 mN indentation of the polycrystalline Ag work material, which results in an indentation depth of approximately 320 nm. Indentation of the ferrite grains with the same force resulted in half the maximum indentation depth observed with Ag. The elastic deformation for Ag is 18 nm, i.e. about 6% of the maximum indentation depth. The plastic deformation of the Ag material is therefore greater than the ferrite grain at 94%, as would be expected since Ag is softer than Fe. The nanohardness for Ag is calculated to be  $0.42 \pm 0.03$  GPa and



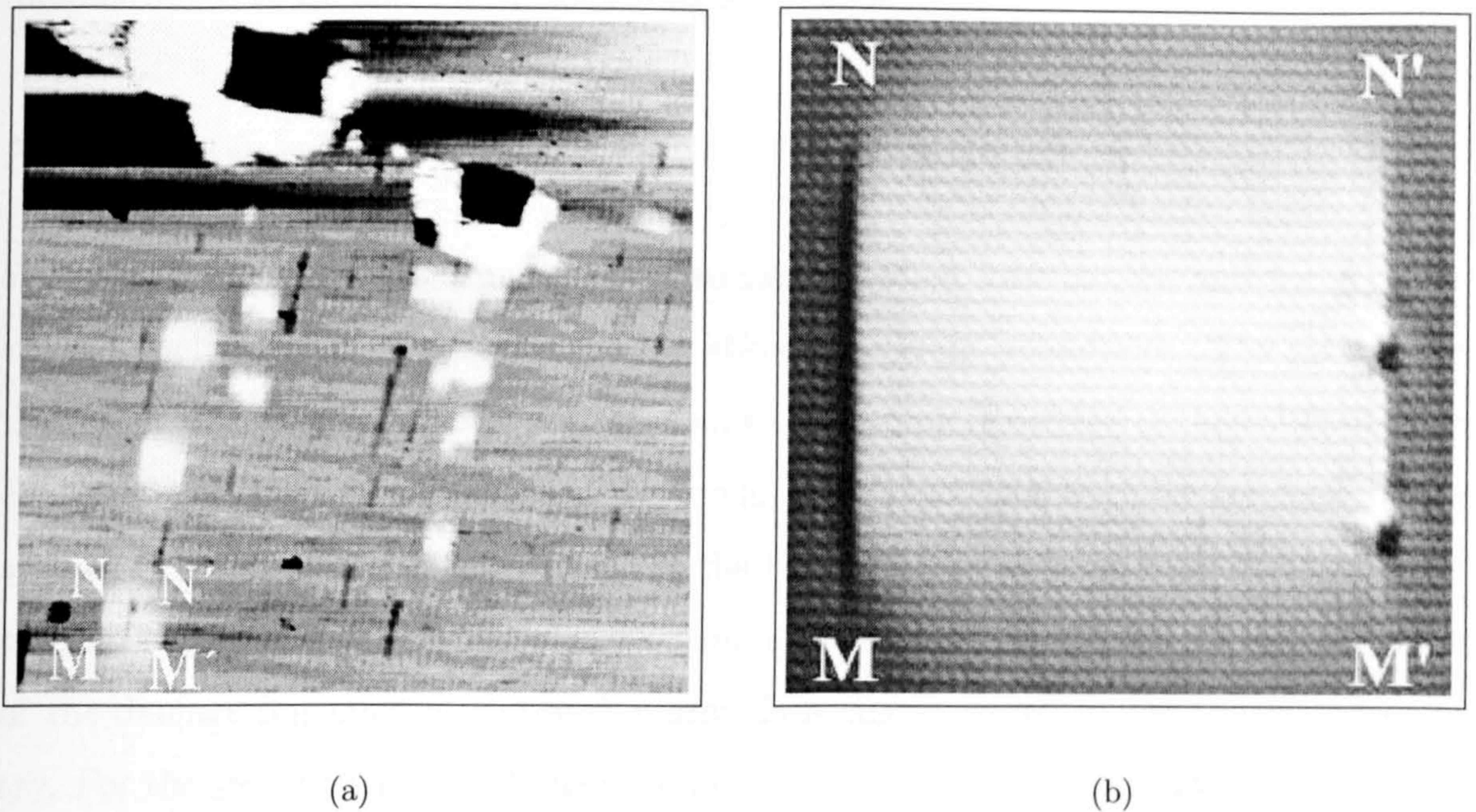


Fig. 5.5.26. (a) STM image of two nanoindentations in the Au {100} surface. Note the pile-up formed around the indents and the slip markings sited along the  $\langle 110 \rangle$  direction. Image size 98 nm  $\times$  98 nm. (b) STM image of a slip marking on Ag {100}. Image size 11.6 nm  $\times$  11.6 nm. Capital letters are used to compare the orientations of the slip markings in (a) and (b).

the Young's modulus is  $144 \pm 10$  GPa. For both the bcc and fcc materials, different crystal orientations were not reflected in the nanohardness and Young's modulus values since the variation lies within the experimental error. The experimental error in the

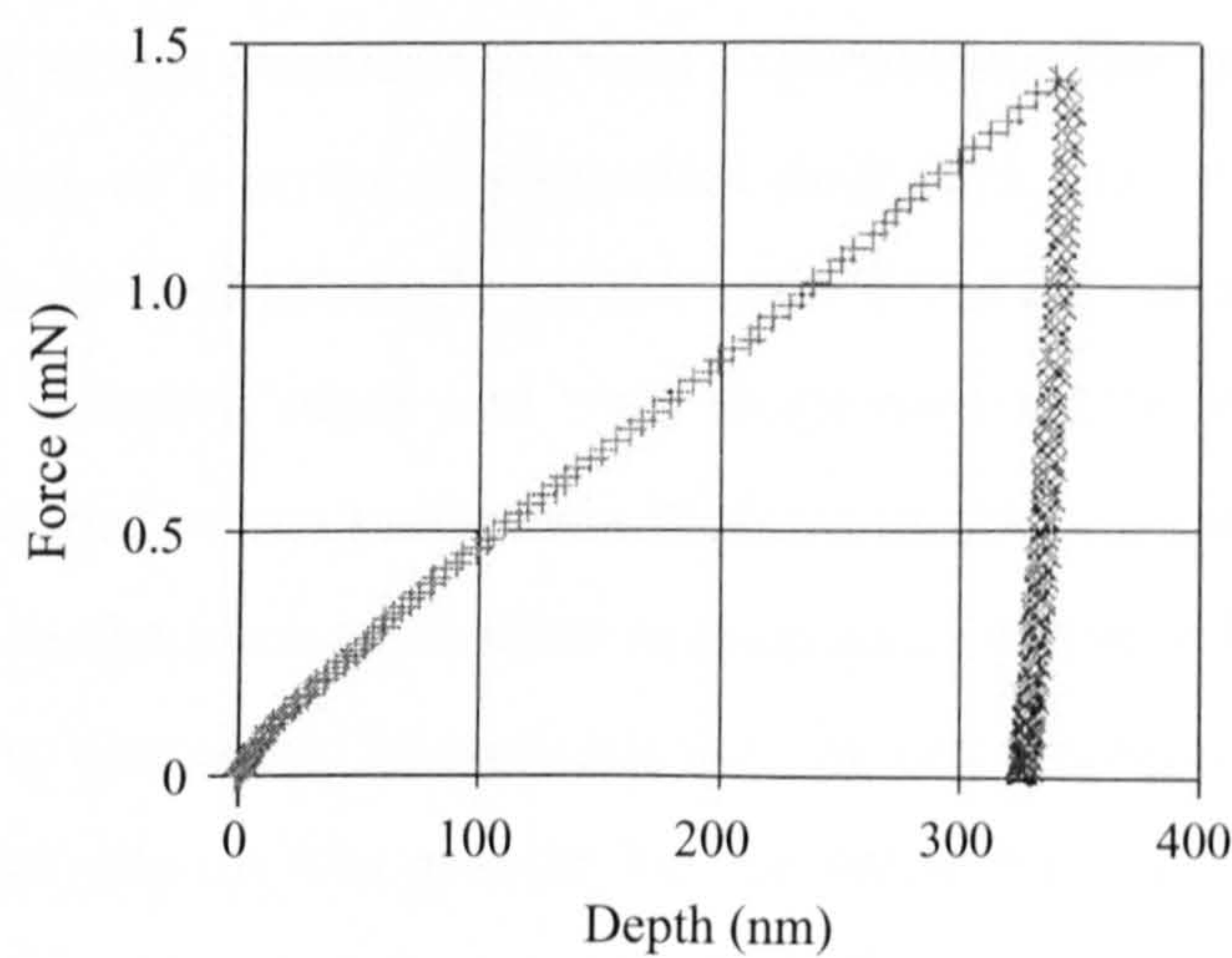


Fig. 5.5.27. Load-displacement curve for nanoindentation in Ag with a maximum indentation force of 1.5 mN: (+) increasing load curve; (x) decreasing load curve.



nanohardness is 5% and 7% in the Young's modulus.

## 5.6 Summary

We have performed MD simulations of nanoindentation into bcc Fe and fcc Ag substrates, including an investigation of the effect near grain boundaries. The rotation of the non-axisymmetric indenter with respect to the atomic structure of the substrate was considered to study the influence of the bcc and fcc crystal planes. The simulations give a good description of nanoindentation in the Fe and Ag substrates, supporting many of the experimental features. Visual inspection of the specimen's surface, shows the profile of the damage imparted to the work materials is characterised by the indenter geometry. For the softer fcc material, inelastic deformation is also characterised by numerous slip markings on the surface. Slip was only observed in the simulations propagating along the  $\langle 110 \rangle$  directions (i.e. the out-of-plane  $\langle 111 \rangle$  directions), which is in excellent agreement with experimental observations by Zimmerman *et al* [192]. The theoretical and experimental force-depth curves agree qualitatively, reflecting a harder bcc material compared with fcc. However, the MD simulations reflected a higher elastic deformation of the materials compared with experimental observations, due to the small indenter tip and penetration depths. For both work materials, the simulated load-displacement curves were not especially sensitive to the orientation of the indenter with respect to the crystal geometry of the substrate.

The MD simulations show that indentation ensues in tip-induced piling-up of substrate atoms, which agrees qualitatively with experiment. The pile-up does not occur as a viscous flow, but as a series of sequential displacements by the motion of point defects. The hillocks formed primarily on the surface and subsurface layers of the work material, along the indenter edges and were suppressed at the corners of the indent. The piling-up of material occurs preferentially along the close packed planes in the work material and forms in the same crystalline arrangement as the substrate. The piled-up material was found to contain no interstitials and, in some cases, a fraction of vacancies. The yield of material pile-up was greater for the softer fcc crystal structure than the harder bcc. Hillock growth was influenced by both the rotation of the indenter and the crystal orientation of the substrate, which agrees qualitatively with experiment where there is a definite observed orientation and crystallographic dependence. Analysis of



structural transformations around the indentation region were analysed by constructing radial distribution functions. Spreading of the distributions showed that the substrate contact region becomes disordered during indentation, but predominantly returns to its original crystallographic configuration as the indenter is withdrawn. Outside of the indentation region, all the material remained highly crystalline, deforming elastically in a broadly axisymmetric fashion. Indentation near a grain boundary showed a constant rearrangement of atoms occurs near the maximum indentation depth causes a ‘pop-in’ in the force-depth curve. Along the grain boundary the weaker bonding also reduced the nanohardness of the material with the maximum force about half that of the adjoining {100} grain for a given indentation depth.

It is difficult to compare the experimentally determined mechanical properties for the Fe and Ag materials with macroscopic values, since they were calculated using larger-scale materials. Only a comparison for the nanohardness of Ag with other experimentally measured values could be found in the literature which is in excellent agreement [172]. The mechanical properties calculations from the MD simulations show a relative difference in nanohardness compared to experimental values. For Fe, the calculated nanohardness from the simulated load-displacement curves was 7.4 GPa, approximately four times the experimental value. Using Hertzian theory of contact the Young’s modulus was 39 GPa, about one quarter of the experimental observation, indicating that greater indentation depths are required in the simulations for agreement with the continuum model. A similar discrepancy is found between the extracted values for Ag from simulation and experiment. Although there are discrepancies in the elastic properties of the Brenner potential, it is not so influential in this case, since diamond is so much harder than Fe and Ag.

The computational efficiency of Ackland’s Ag potential in the MD simulations has also been examined. By modifying Ackland’s potential such that it cuts-off before the third neighbours, the efficiency of the MD simulation code could therefore be improved. For simulations where all Ag-Ag interactions were described by the modified potential, the total CPU time was reduced by approximately 34%. However, it was found that both the indentation force and elastic recovery of the work piece was underestimated. An embedded original-modified potential was then employed, where Ag-Ag interactions in the local indentation region were described by Ackland’s original potential and Ag-Ag interactions outside the local indentation region were described by the



modified potential. This method closely reproduced the mechanical behaviour observed with indentation using just the original potential and reduced the total CPU time by approximately 28%.

Current simulations on the SUN workstations are constrained to simulations of a maximum of about 100,000 atoms. This limitation results in visible finite-size effects during the nanoindentation. For example, with the metals the range of plastic deformation exceeded the depth of the substrate and with Ag the tip-induced slip bands propagated until they interacted with the fixed edges. With graphite, waves of elastic deformation propagated until they intersected the rigid substrate sides. One way to partially alleviate such finite-size size effects is to employ a greater number of atoms by developing a *parallel* MD program for use with multiple processors.



# Chapter 6

## Parallel Molecular Dynamics

### 6.1 Introduction

There is a continual demand for high computational speed by data intensive applications in industry and research. For example, in computational materials science the evaluation of mass numerics heavily constrains feasible system size. To overcome this constraint, increases in computer power have to be achieved. Preliminary efforts to develop computer speed focussed on the fabrication of smaller and faster circuit elements. Although the performance of computers has grown exponentially, the fabrication of advanced processors is restricted by inherent physical limits. Furthermore, the cost of single processor computers increases more than their performance. Hence, increased computer performance cannot depend merely on the development of faster processors. An alternative approach to achieving boosted computational speed is through a *parallel computer*, which, by broad definition, consists of multiple processors which can operate on the same problem simultaneously. Implementing a set of processors to work co-operatively to solve a computational problem is known as *parallel processing*, and can be performed on a single machine containing multiple processors and/or on a series of interconnected computers. The latter approach has become a common method for building a ‘parallel environment’ on budget, where networks or clusters of workstations are referred to as a *Beowulf* machine [194]. For further information on parallel processing the reader may wish to proceed to the excellent book by Foster [195].

Parallel computers have evolved to become everyday tools of the computational scientist. Although parallel processing is more widespread with workstation clusters because of cost, massively parallel machines with up to hundreds of thousands of processors are



also implemented. In essence, the idea of parallel processing is that  $n$  CPUs provide up to  $n$  times the speed of a single CPU. Hence, the processing time should be  $\frac{1}{n}$ th of that obtained implementing a single CPU. In reality, this scenario is seldom achieved since the work load cannot be divided equally among the processors. Furthermore, surplus processing time is incurred by necessary data transfer and the synchronisation of computations. Despite this, substantial improvements in total processing time can be accomplished. The speedup therefore allows the use of larger-scale problems to be evaluated by parallel processing in a reasonable amount of time, or for smaller-sized problems to be computed in a shorter amount of time.

Significant implementation of parallel computers occurred approximately two decades ago. Typical parallel computers consisted of multiple processors connected to a globally addressable memory, see Fig. 6.6.1(a). Numerous parallel languages have been developed for parallel processing with shared memory. Probably the most widely utilised is OpenMP [196], which has evolved as a standard for shared memory programming environments. The modern day trend with shared memory parallel computers is to utilise a small number of very fast processors. However, as the number of CPUs on shared memory computers increases, performance improvements are limited. To overcome this constraint, parallel computers implemented distributed memory, as illustrated in Fig. 6.6.1(b). Here, each CPU has local memory which is only addressable from the CPU to which it is associated with. Hence, this provides a scalable architecture since additional memory is attainable for additional CPUs. Since there is no shared memory in this case,

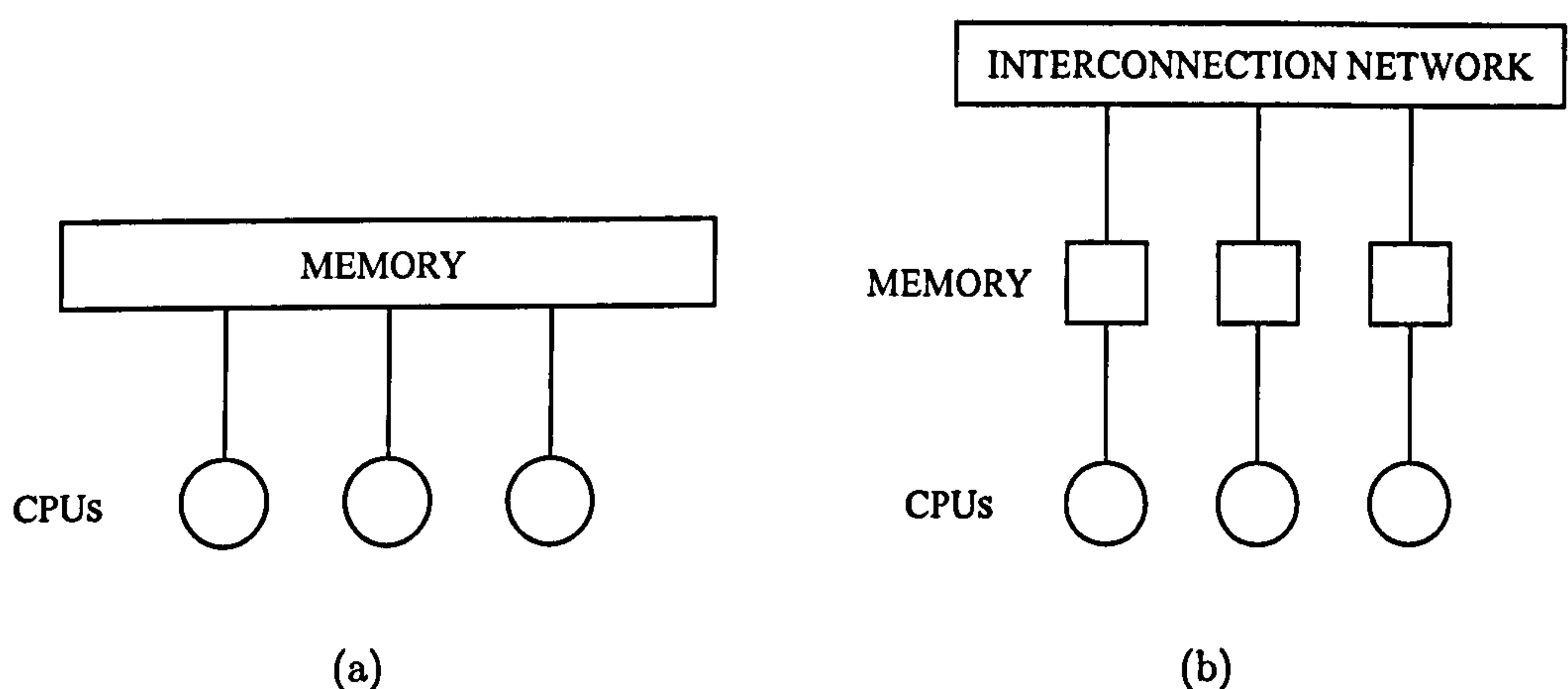


Fig. 6.6.1. Schematic representation of: (a) shared memory model; (b) distributed memory model.



parallel processing explicitly involves passing information (or messages) from one CPU to another. In a distributed memory architecture this is achievable since the processors are interconnected in a communications network.

In general, parallel processing with the message passing model creates a fixed number of multiple tasks across selected processors. Each task executes the same program, but operates on different data. The operated data can be accessed by other processors through message passing. Hence, communications serve to avoid duplicate work being processed. A variety parallel languages have evolved for message passing, such as Parallel Virtual Machine (PVM) [197] and the Message Passing Interface (MPI) [198]-[199]. First developed in 1993-1994, MPI has evolved as a standard in message passing, as defined by the MPI forum [198]-[199]. In essence, MPI is a library of functions and macros (not a language) that enables message passing and supports numerous programming languages such as Fortran, C and C++. MPI also provides the portability which allows applications developed on one platform to be run on another, without requirements of redevelopment.

In MD, the computational goal for parallelisation is to perform each timestep as quickly as possible. This permits larger atom numbers to be utilised or longer simulation times. Furthermore, parallelisation allows the possibility of using more complex interatomic potentials. At present, optimum parallel MD simulations on typical multiprocessor machines involve systems of around 10-100 million atoms. The use of massively parallel machines allows systems of around one billion atoms to be employed. Many implementations of parallel MD having been developed [80], [200]-[201] to obtain better cost effectiveness. Bachlechner *et al* [200] performed MD simulations using approximately 2.1 million atoms to study dislocation emission at the Si/Si<sub>3</sub>Ni<sub>4</sub> interface. In a recent study by Walsh *et al* [201], MD simulations with up to 100 million atoms were carried out to study nanostructured materials.

This chapter discusses the development of a parallel MD code using MPI. With the increasing availability of multiprocessor computers, developing problems in a form compliant for parallel solution is critical for effective computation. In principle, parallelisation of a MD simulation on a parallel machine with  $n_p$  processors consists of decomposing the system of atoms into  $n_p$  smaller systems. Parallelisation is achieved by loop splitting, where the work done in a loop is split over processors. For example, consider the following loop:



```

DO I=1,N
    A(I) = B(I) + C(I)
ENDDO

```

By implementing parallel processing, this loop can be executed upon by a group of processors simultaneously. If  $N$  processors are available then one processor could execute  $A(1) = B(1) + C(1)$  and another processor  $A(2) = B(2) + C(2)$  and so forth. Hence, loop splitting provides a method for rapidly increasing the total execution time of a program. In MD there are many opportunities for parallelisation since numerous calculations are independent, such as energy and force evaluation. Therefore, they can be computed in parallel in any order and any grouping. In addition to describing the parallelisation of the serial MD code, the basic performance characteristics are determined and evaluated for conjecturing scalability to larger physical systems and larger parallel machines.

## 6.2 Program Development

Parallelising serial programs for use with a distributed parallel computer is not an easy task to perform. Parallelisation increases the complexity of software because of the extra degrees of freedom it introduces. The extended complexity stems from many difficulties, such as:

- What program revisions are required to facilitate parallelism and reduce communications overhead?
- What kind of parallelisation scheme should be adopted such that the resources of the target architecture are effectively used?
- What is the impact on performance by varying system size and the number of processors?

Hence, the transition from traditional sequential computation generally requires a comprehensive reformation of the basic strategies to develop optimised parallel code. Reformulating serial code into a form compliant for parallelisation is a type of *functional decomposition*.



### 6.2.1 Revision to Fortran 90

Since the existing MD code was developed under the Fortran 77 standard, the preliminary reformation was focussed on a thorough revision to the Fortran 90 standard [202]. Fortran 90 is better suited to more modern computing than its predecessor and offers many features that facilitate functional decomposition. The most useful properties which have been implemented are *modules* and *dynamic* array allocation.

Modules, which are perhaps the most important quality of Fortran 90, are varieties of a program unit like subroutines and functions. They offer extremely powerful functionality since they control accessibility of the entities declared within to other program units. Thus, the essence of modular design is to reduce program complexity and furthermore, to facilitate code reuse. A module has the general form

```
MODULE module name

  Declaration statements.

CONTAINS

  Definitions of module procedures.

END MODULE module name
```

Contained within a module are different procedures which all have local data access. Therefore, procedures which are interrelated and require access to the same data are usually grouped together within a module. The accessibility of the procedures outside the module can be controlled through private and public declarations. Such declarations further allow modules to manage the practicability of data. Thus, modules can provide global data access, therefore making the need for common blocks and the passing of information via arguments redundant. Since modules involve declarations, they are implemented at the beginning of a program or other modules via a *USE module name* statement. Therefore, entities made employable by this statement are accessed by *use-association*.

A great disadvantage with Fortran 77 is the requirement for static array allocation. However, in many scientific programs the exact size of an array is not known until numerous computations have been performed or some data inputted. Therefore, programmers have to guess the size of the array prior to execution, which can lead to obvious problems. This issue is rectified in Fortran 90 by allowing dynamic array allocation through the *ALLOCATABLE* statement. Here, the compiler defers the allocation of



space to an array until it is allocated dynamically in the execution through the `ALLOCATE` statement. In programs where storage needs to be efficiently controlled, dynamic arrays can be deallocated by the use of `DEALLOCATE`. The ability to deallocate an array is also useful where the size of an array repeatedly changes, since the array can be resized after deallocation.

## 6.2.2 Profile of Serial MD Code

Profiling is the process of determining how much each part of the code contributes to the total execution time. Thus, profiling the serial MD code will conclude which portions of the code will return the largest performance gains when parallelised. The compliancy of the identified portions for parallelisation can then be assessed, and functional decomposition applied if required. The preliminary parallelisation issues were focussed on constituents of the MD core, namely the routine calculations incurred every timestep. The essence of the MD core consists of the calculation of the force on each atom and the integration of the equations of motion, where coordinates and velocities are updated (see Fig. 2.2.3, Chapter 2). This is also coupled with the periodic recalculation of the cell lists and neighbour lists. The total expense of cell and neighbour list construction together with force evaluation and integration is illustrated in Table 6.1, as a percentage of the elapsed time during a typical simulation.

Table 6.1. Expense of force evaluation and integration together with cell/neighbour list construction following indentation of Fe {100}, as percentage of total elapsed time. The whole system was configured from 48,856 atoms and the simulation run for 150 ps.

Constituent of MD core	Expense as % of total elapsed time <sup>a</sup>
Cell list construction	0.04
Integration	3.1
Neighbour list construction	4.7
Force evaluation	91.5

<sup>a</sup>The remaining percentage of runtime stems from system initialisation/termination and data output in the non-core.



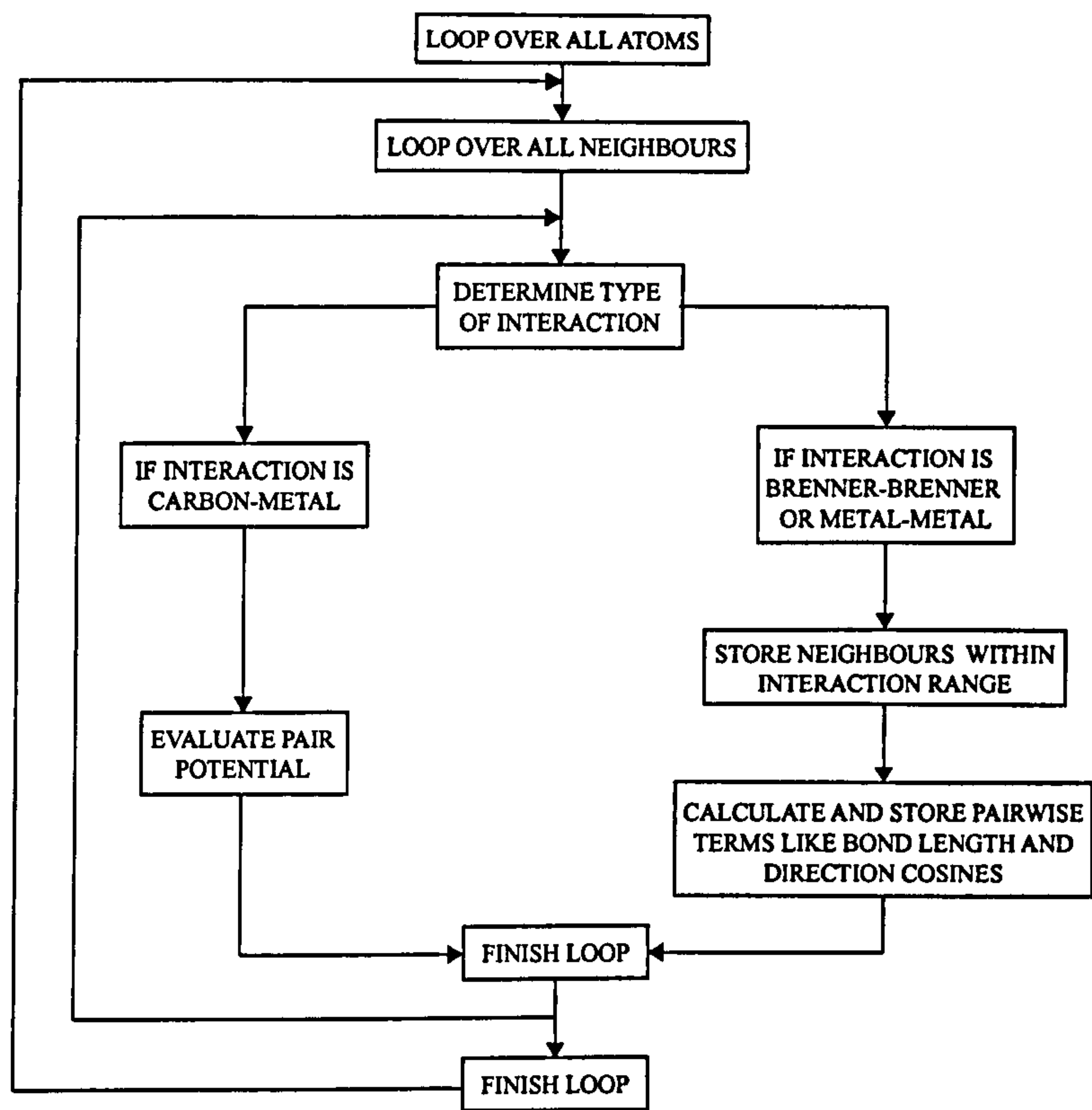
Clearly the most computationally intensive constituent of the MD core is the force evaluations ( $\approx 90\%$  of the total runtime). By comparison, the time incurred during integration and construction of the cell/neighbour lists accounts for an almost inconsequential amount. Parallelising the non-core will yield an insignificant payoff since the contribution to total execution time is negligible. Although neighbour list updates incur far less time than force evaluations, they are the next largest contributor to total runtime. Hence, preliminary parallelisation efforts are concentrated on the force evaluations and construction of the neighbour lists. Thus, only selected parts of the MD core will run in parallel with the remainder effectively running as serial. Indeed it is possible that the MD core could become inefficient if the remaining core constituents are parallelised since the algorithm may become communication bound. To develop a highly optimised and efficient code, the cost of recomputation always has to be weighed against the cost of communicating the same result between processors.

### 6.2.3 Functional Decomposition

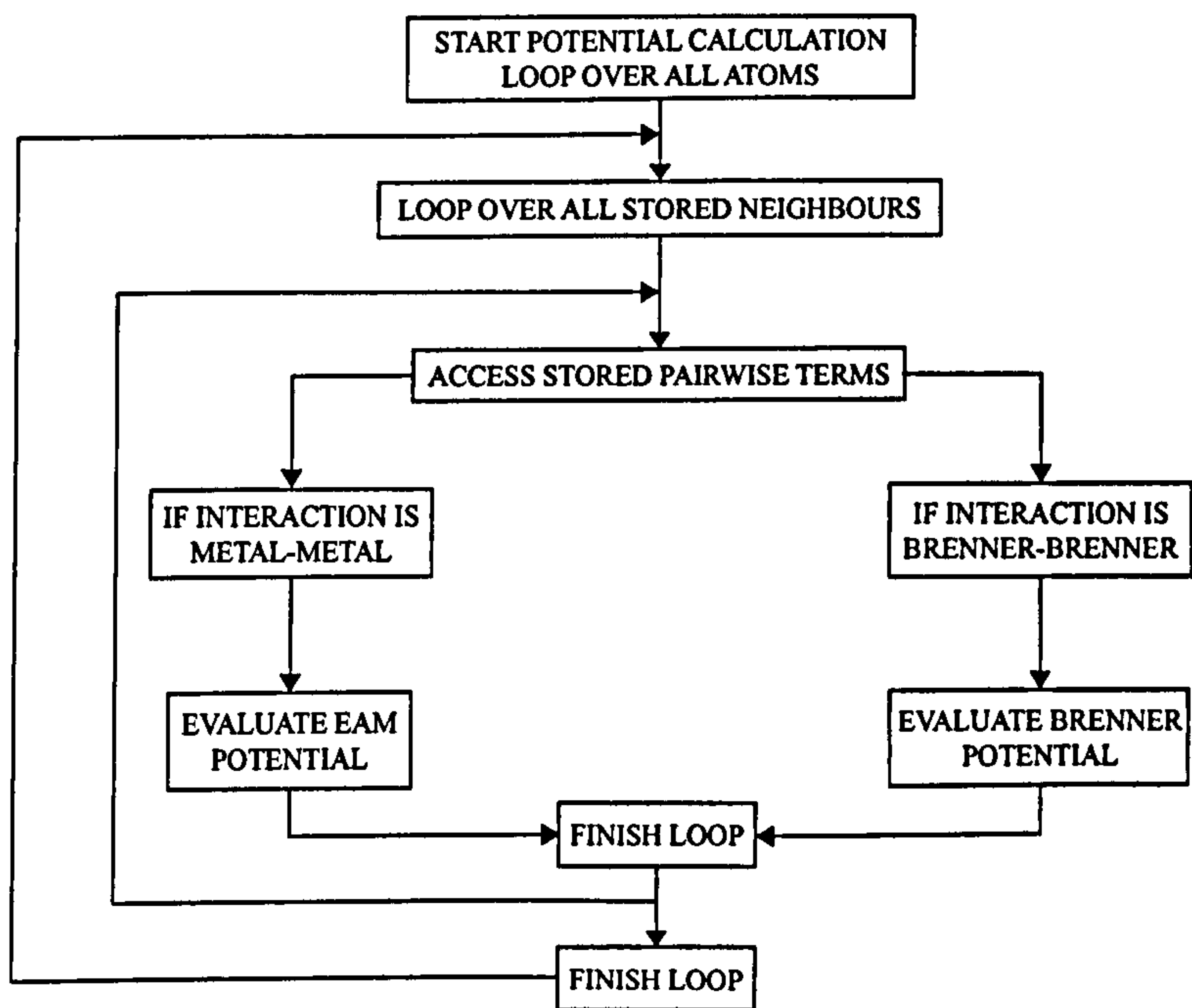
#### Energy and Force Evaluation

The existing serial version of the code uses a tri-component potential for C/Si/H systems [203]. Of the tri-component description, only the Brenner hydrocarbon potential is implemented in the simulations presented in this thesis. The general format of the subroutine used in the potential evaluation is shown in Fig. 6.6.2. The energy and force calculations are split into two different parts. In the first component (Fig. 6.6.2(a)), information from the neighbour list is extracted. Each atom and its neighbours are examined to determine the type of interaction. If the interaction is of Brenner-metal type, then the repulsive ZBL pair potential is evaluated. If the interaction is of Brenner-Brenner or metal-metal type, then the neighbours are stored in an array if they are within the interaction range. This array is effectively the same as the neighbour list, minus those atoms that reside in the skin. Atoms that lie outside the interaction range are simply neglected. Furthermore, pairwise terms such as bond length, direction cosines and both cut-off functions and derivatives are calculated and stored. Since the neighbours of an atom and the corresponding pairwise terms are entailed many times during energy evaluation, the storage is done to improve computational efficiency since it saves time recalculating. The second part of the energy evaluation (Fig. 6.6.2(b)) consists of the





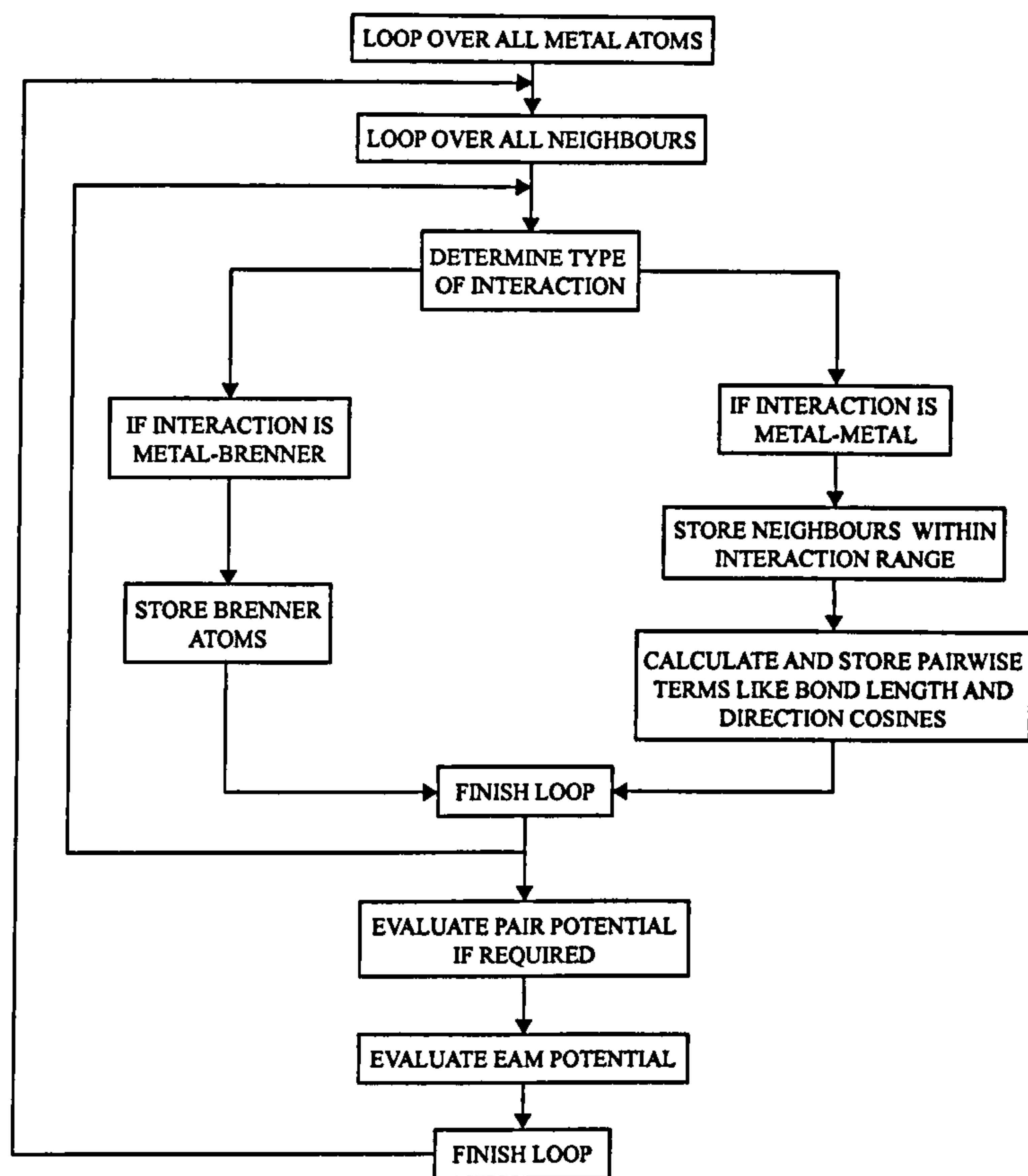
(a)



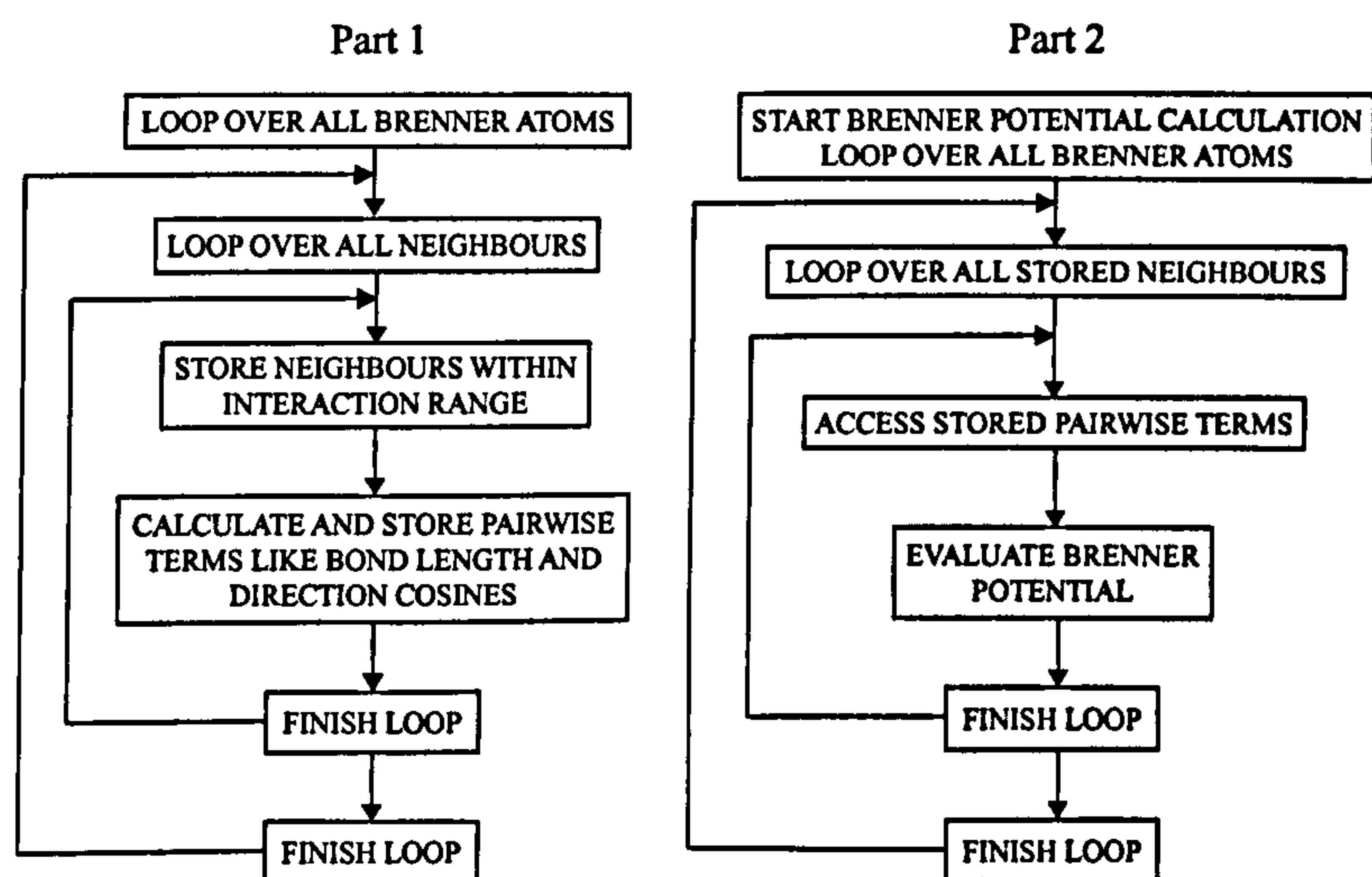
(b)

Fig. 6.6.2. Flowchart of the energy and force subroutine in the serial MD code. The subroutine is split into: (a) Pair potential evaluation for Brenner-Metal interactions and storage of pairwise terms; (b) Many-body calculations for EAM and Brenner potentials.





(a)



(b)

Fig. 6.6.3. Flowchart of the energy and force evaluation in the serial MD code following functional decomposition. For metal atoms, the potential calculation is executed in one loop over atoms and their neighbours. For Brenner atoms, the evaluation is separated into parts 1 and 2 for the pairwise terms and many-body calculations respectively.



many-body calculations. For each atom, the pairwise interactions are extracted from the temporary neighbour list. The stored pairwise terms are also accessed for use in the many-body calculations. The EAM or Brenner potential is then evaluated depending on the type of interaction.

The function of the energy and force subroutine depicted in Fig. 6.6.2 is five-fold, with the pairwise storage for metal and Brenner atoms and the evaluation of three different potentials. The first consideration was to reduce the complexity and improve the readability of the code by splitting the EAM and Brenner potentials into separate subroutines, together with the calculation and storage of the pairwise terms. The revised format of the energy and force subroutine is shown in Fig. 6.6.3. In each subroutine only the metal or Brenner atoms have to be looped over, which facilitates better the parallelisation of the potential loops. The reformation shown in Fig. 6.6.3 also imposes a simple constraint that all atoms must be grouped together by their potential type, since it is easier to loop over consecutive numbers of atoms.

In the Brenner potential the force acting on the bond  $i - j$  in Fig. 6.6.4 is dependent on the first and second neighbours of atoms  $i$  and  $j$ . Hence, the storage of pairwise terms for *all* Brenner atoms is required before the respective potential is evaluated. However, the most significant problem with the subroutine illustrated in Fig. 6.6.2(a) is the storage of pairwise terms for each metal atom. For the metal potentials, only the pairwise terms associated with atom  $i$  are required. Therefore, the global storage of pairwise terms in Fig. 6.6.2 incurs excess memory. This is remedied in the revision of the energy and force subroutine in Fig. 6.6.3, by calculating the pairwise terms and evaluating the potential

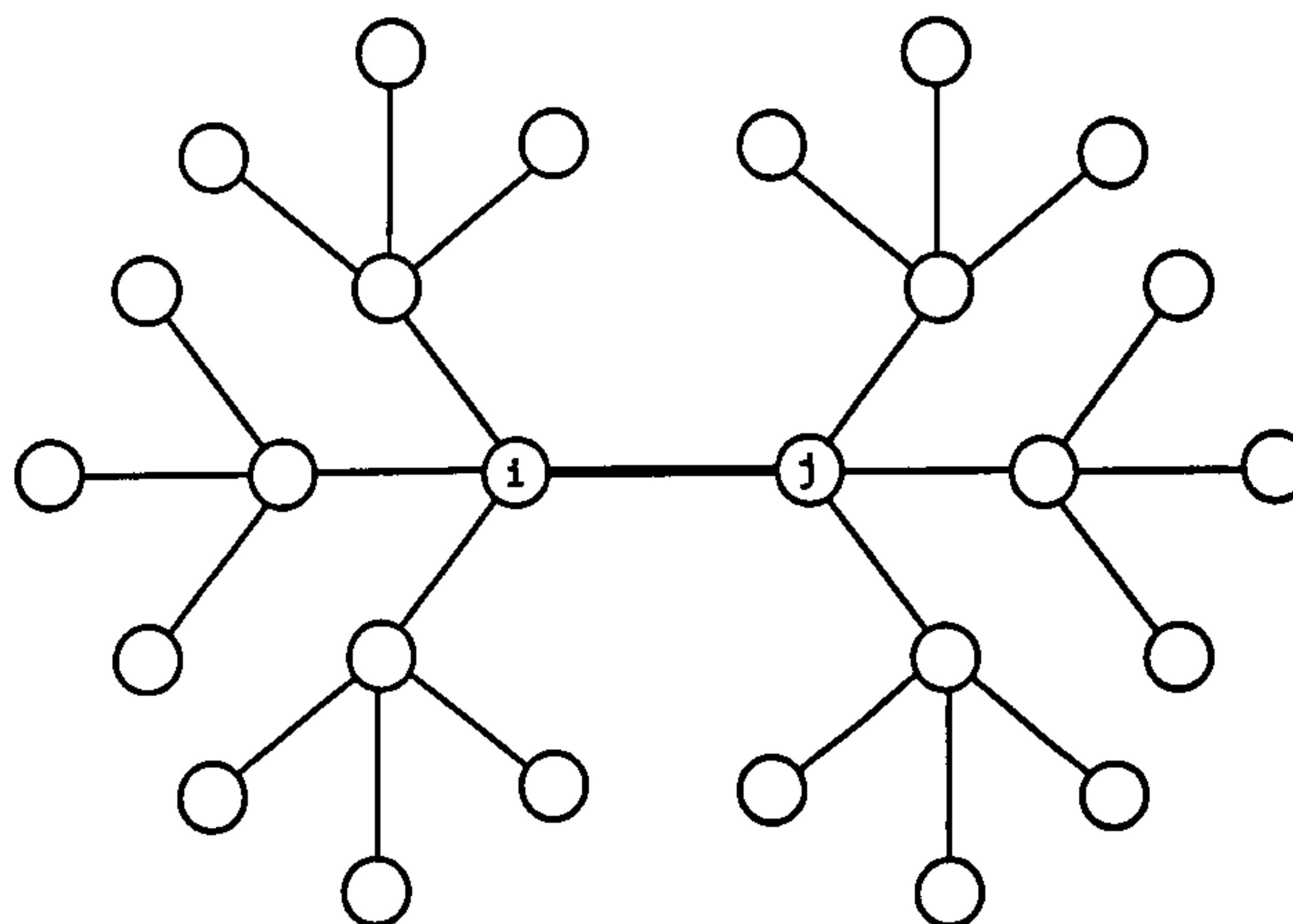


Fig. 6.6.4. The energy of the bond  $i - j$  in the Brenner potential is dependent on the positions of  $i$  and  $j$  and the positions of all the 1<sup>st</sup> and 2<sup>nd</sup> neighbours of  $i$  and  $j$ .



in the same loop. The pairwise terms stored for each atom are overwritten by the next iteration and so memory storage of the pairwise terms is minimal, regardless of system size. Also computed in the loop over metal atoms is the pair potential for Brenner-metal interactions. It makes no difference if the pair potential is calculated in the loop over the Brenner atoms other than the order of computation is reversed.

## Neighbour List Construction

The existing serial MD code utilises the cell index method [107] (as discussed in Section 2.2.4, Chapter 2) to build the neighbour lists. For each atom, the neighbour list is constructed employing a linked list approach [7]. The essence of linked lists is summarised in Fig. 6.6.5, showing a two-dimensional representation of cells. To construct a neighbour list for atom  $i$  in cell number 5, only the host cell and half of the neighbouring cells (shaded region) are considered. When the neighbour list of atom  $i$  is constructed, any atoms that are located in cells in the unshaded region, say atom  $j$ , will not be included. The idea is that when the neighbour list of atom  $j$  is constructed it will consider all atoms in cells 4, 5, 6, 7 and 8. Therefore, if atom  $i$  is within interaction range, it will add  $i$  to the neighbour list of  $j$ , but it will also add  $j$  to the neighbour list of  $i$  using the linked list approach. Thus, the significance of using linked lists is to save computation time, since it reduces the number of cell evaluations required to construct the neighbour list of each atom. The general format of the serial MD code used to generate the neighbour list for each atom is shown in Fig. 6.6.6. The cells are first looped over and the primary atom in the cell identified. The atoms in the host cell and half neighbouring cells are then looped over and added to each others neighbour lists if the pair interact and have not been previously considered.

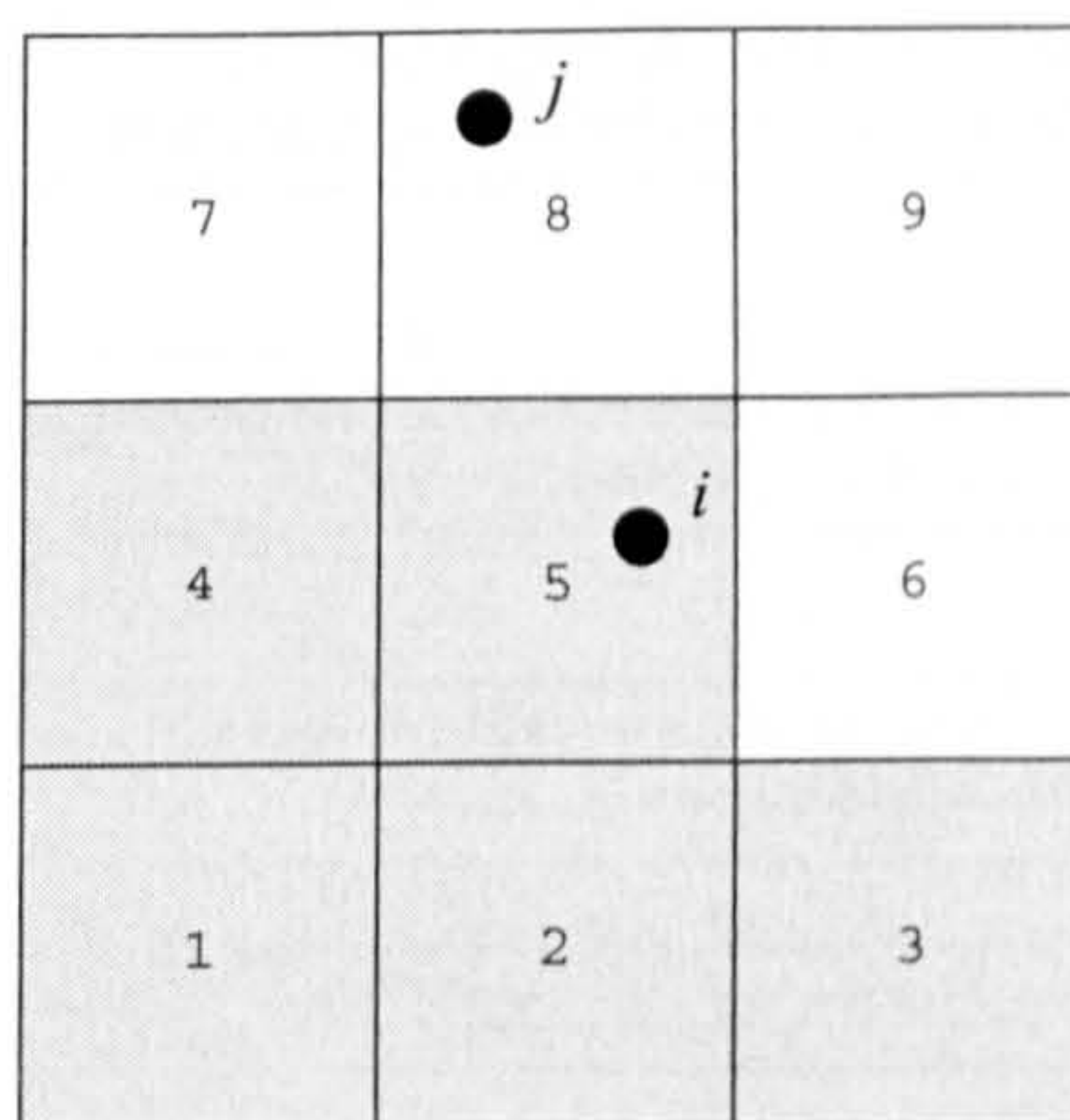


Fig. 6.6.5. Two-dimensional representation of cells used in the linked list algorithm.



However, the linked list method cannot be used with relative ease if the neighbour list routine is to be parallelised. Consider again the two-dimensional cell depiction in Fig. 6.6.5. If the construction of neighbour lists is partitioned across multiple processes, then the neighbour list for atoms  $i$  and  $j$  may reside on different processes. Clearly this introduces coding complexity if atoms located on different processors are to be added to each others neighbour lists. As a preliminary solution, the construction of neighbour lists was modified to include the evaluation of all neighbouring cells and the employment of linked lists was made redundant. The existing format of the neighbour list routine also had to be changed to allow easier parallelisation. This was achieved by first looping over all the atoms in the system, followed by only the host and neighbouring cells. Thus, the parallelisation is accomplished by splitting the loop over the atoms across the processors. This approach leads to simplification in neighbour list pointers and determining efficient load balancing. In addition to the structural change of the

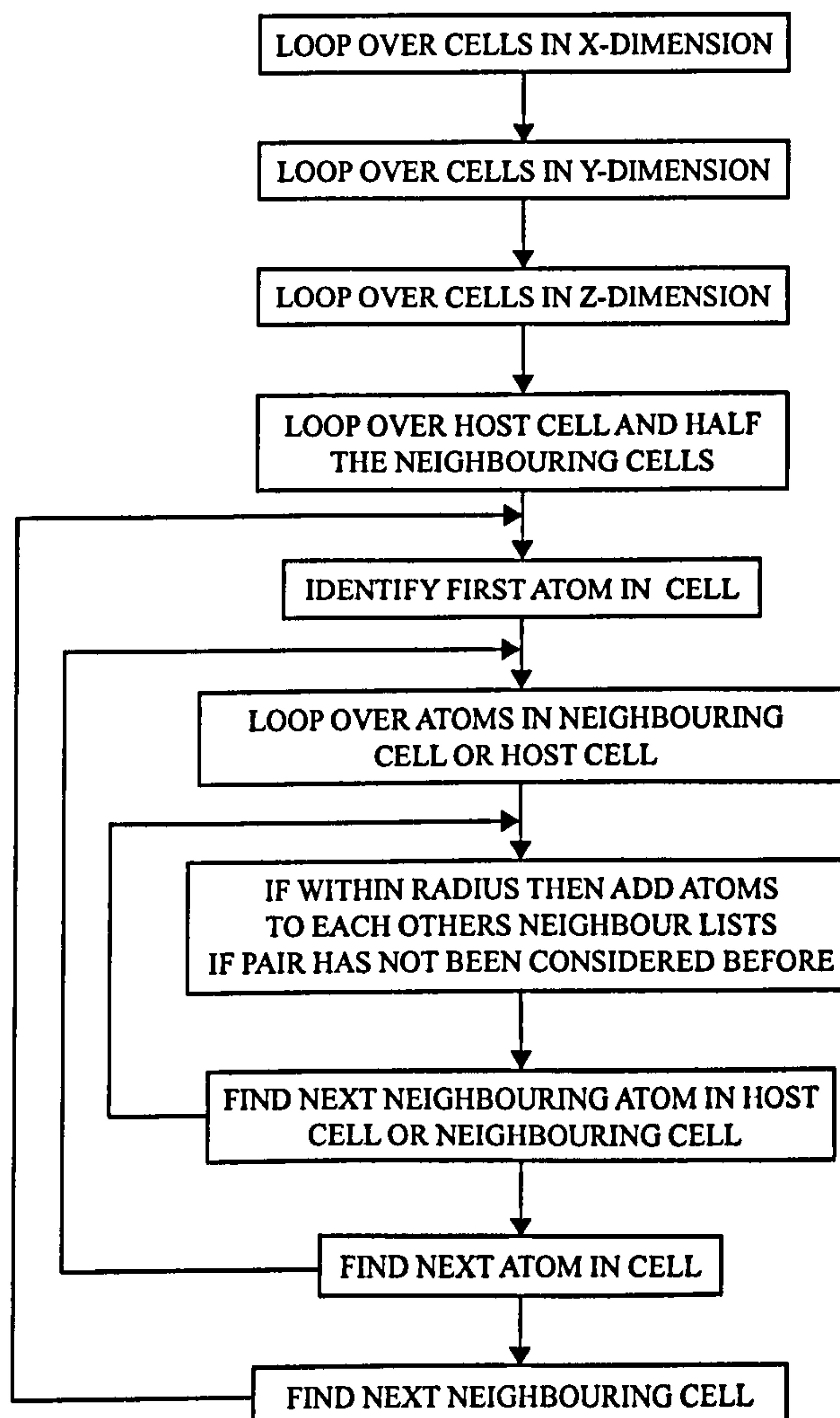


Fig. 6.6.6. Flowchart of the neighbour list construction algorithm in the serial MD code.



neighbour list, a further modification was also made as a result of the fact that the pair potential for metal-Brenner interactions is performed in the loop over the metal atoms (see Fig. 6.6.3(a)). The neighbour lists for Brenner atoms have been amended to ignore any metal atoms within interaction range. The format of the new neighbour list routine is shown in Fig. 6.6.7.

The modified neighbour list routine creates two arrays, NEBPNT() and NEBOUR(). The NEBPNT array stores the number of neighbours each atom has within the interaction range and the additional skin thickness. For a system of  $N$  atoms, the NEBPNT array is dimensioned  $N+1$ . The first element of the array NEBPNT is assigned a dummy value of one. The second array element is then assigned the number of neighbours associated with atom number one, summed with the preceding element value. This process is then repeated for all remaining atoms in the system. Thus, the number of neighbours for any atom  $i$  is simply obtained by  $\text{NEBPNT}(i+1) - \text{NEBPNT}(i)$ . If the neighbour list routine was parallelised with respect to the original loop over cells, then an additional pointer array would be required since element  $i$  in NEBPNT may not necessarily correspond to atom  $i$ , but the  $i$ th atom encountered during cell evaluation. This is the principle reason for parallelising the neighbour list routine with respect to the loop over atoms. The

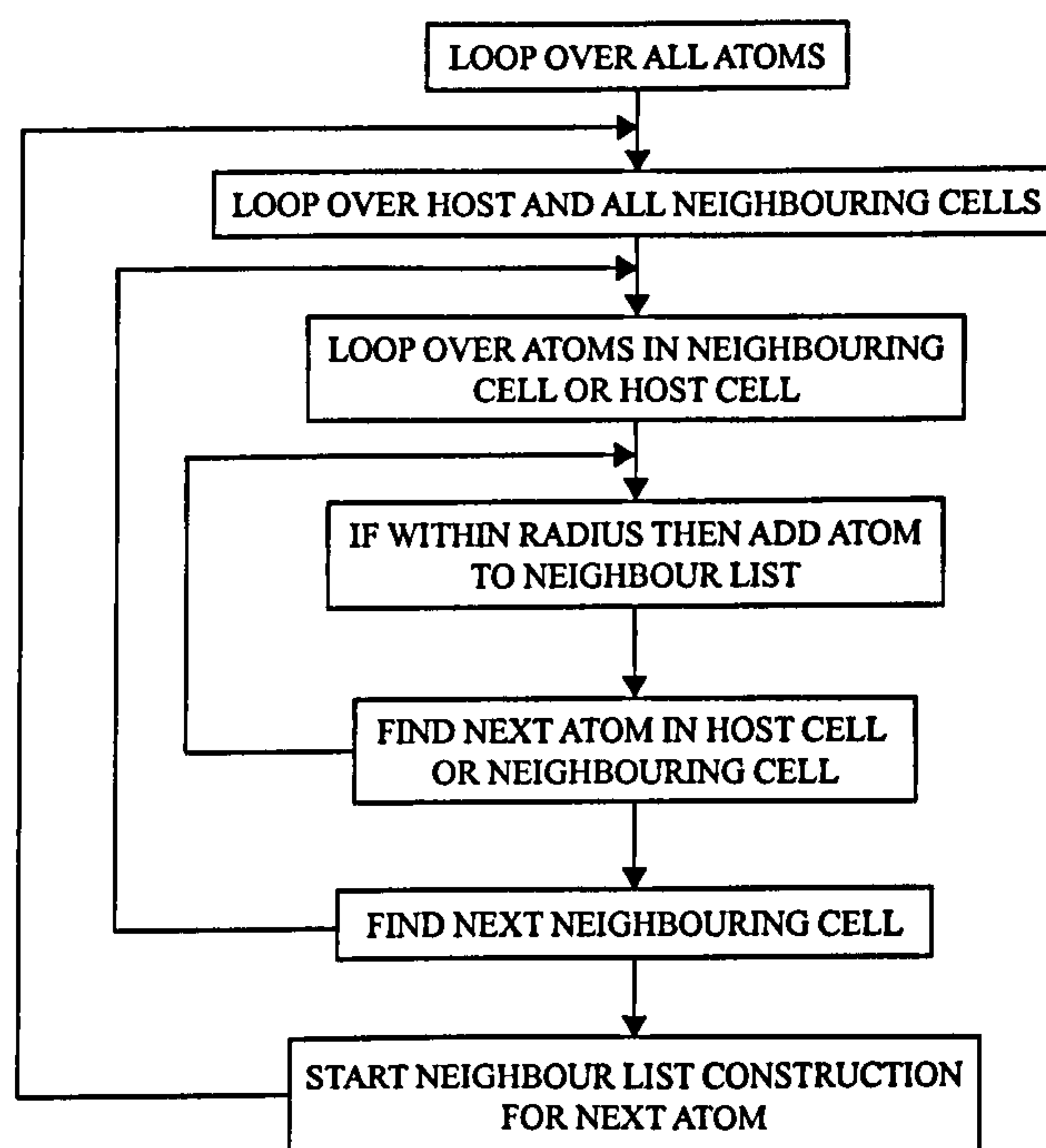


Fig. 6.6.7. Flowchart of the neighbour list construction algorithm in the serial MD code following functional decomposition.



NEBOUR array stores the neighbours for each atom. The dimension of NEBOUR is given as

$$\sum_1^{N_{\text{specie}}} \text{NATM}_{\text{specie}} \times \text{SPECIE}_{\text{avneb}} \quad (6.2.6.1)$$

where  $N_{\text{specie}}$  is the number of atom species in the system,  $\text{NATM}_{\text{specie}}$  is the total number of atoms for a given specie and  $\text{SPECIE}_{\text{avneb}}$  is the average number of neighbours per atom for the corresponding specie. The NEBPNT array serves as a pointer to the NEBOUR array. Hence, the neighbours of atom  $i$  can be accessed by looping over NEBOUR from element  $\text{NEBPNT}(i)$  to  $\text{NEBPNT}(i+1)-1$ .

## 6.3 General MPI Programs and Basic Concepts

There are a few essential integral parts that are common to every MPI program. The program and each subprogram must include the `mpif.h` file which contains the underlying macros and definitions. Each call to a MPI function contains a list of arguments. In a Fortran program, each MPI function call contains the argument `IERROR` in its last argument, which lists the error code. The error code returns either `MPI_SUCCESS` or an implementation-defined error. To establish the MPI environment, the function `MPI_INIT` is called. This must be done before any other calls to MPI functions can be made and only called once. Associated with all MPI communication is a *communicator*. In essence, communication is concerned with the flow of information between *processes* or *tasks* (the executable on a processor). The default communicator is `MPI_COMM_WORLD` which describes all the processes. Communicators can also be formed to contain specific groups of processes and therefore used for local communication. Any call to a MPI routine imposes a barrier which synchronises all of the processes. The general layout of a standard MPI program is given in the following code segment.

```
PROGRAM name
```

```
  Variable definitions.
```

```
  "mpif.h"
```

```
  Establish MPI environment.
```

```
  CALL MPI_INIT(IERROR)
```

```
  Find out number of processes executing program
```

```
  and assign rank value.
```

```
  CALL MPI_COMM_RANK(MPI_COMM_WORLD, RANK, IERROR)
```



```
CALL MPI_COMM_SIZE(MPI_COMM_WORLD, NPROC, IERROR)
```

```
    Main body of code.
```

```
Terminate MPI environment.
```

```
CALL MPI_FINALIZE(IERROR)
```

```
END PROGRAM name
```

Each process is identifiable by a rank value, which is determined by the MPI function `MPI_COMM_RANK`. For a group of  $n$  processes, rank values are assigned from 0 to  $n-1$  and returned in the argument `RANK`. The number of processes is obtainable by the MPI function `MPI_COMM_SIZE`, which returns the value to the argument `NPROC`. Before the program finishes, the MPI environment must be finalised. This is achieved by the MPI routine `MPI_FINALIZE` which in essence completes any ‘unfinished business’ left within the MPI environment. Each process must call `MPI_FINALIZE`, after which no MPI calls are permitted.

## 6.4 Message-Passing Operations

### 6.4.1 Send and Receive Operations

The most basic message-passing functions in MPI are the *send* and *receive* operations. When data transfer is required between two processes, one process executes a *send* operation and the second process executes a *receive* operation. To communicate successfully the data, information about the message must be given. The Fortran binding for send and receive operations are

```
MPI_SEND(SBUFFER, COUNT, DATATYPE, DEST, TAG, COMM, IERROR)
```

and

```
MPI_RECV(RBUFFER, COUNT, DATATYPE, SOURCE, TAG, COMM, STATUS, IERROR)
```

The processes which are involved in the message-passing must both be constituents of the communicator `COMM`. The data in buffer `SBUFFER` of size `COUNT` and data type `DATATYPE` is sent to the process with rank `DEST`. The data is then received in the buffer `RBUFFER` from the process with rank `SOURCE`. The `TAG` is a user-specified integer which is used to differentiate between messages received from a single process. The argument `STATUS` returns information on the data that was received. An operation that involves all the processes in a communicator is known as a *collective operation*, which can be separated



into *data movement* and *reduction operations*.

## 6.4.2 Data Movement

In data movement, data is rearranged across the processes. Simple examples are the need to broadcast, gather or scatter data. In the preliminary development of the parallel MD code, only the broadcast and gather data movement operations are utilised. The routine for broadcasting data is `MPI_BCAST`, which is illustrated in Fig. 6.6.8. The process from which the data is being broadcast is called the *root* or *master* process. The root process can be defined as any of the processes in the group, although it is typically defined by a rank value of 0. To use the `MPI_BCAST` routine, the size of data and data type must be specified, together with the communicator and the root process. All processes, including the root process, call the broadcast routine. The Fortran binding for the `MPI_BCAST` routine is

```
MPI_BCAST(BUFFER, COUNT, DATATYPE, ROOT, COMM, IERROR)
```

The routine will broadcast the data in `BUFFER` of size `COUNT` and data type `DATATYPE` on the root process `ROOT` to all processes in the communicator `COMM`.

The gather operation has the opposite effect of a scatter operation, and is illustrated in Fig. 6.6.9. The essence of a gather routine is to send data from the *i*th process to the *i*th data location on the specified root process. The Fortran binding for the gather operation is

```
MPI_GATHER(INBUFF, COUNT, DATATYPE, OUTBUFF, RECVCOUNT, RECVDATATYPE,  
ROOT, COMM, IERROR)
```

The gather operation sends the data of data type `DATATYPE` and size `COUNT` on each

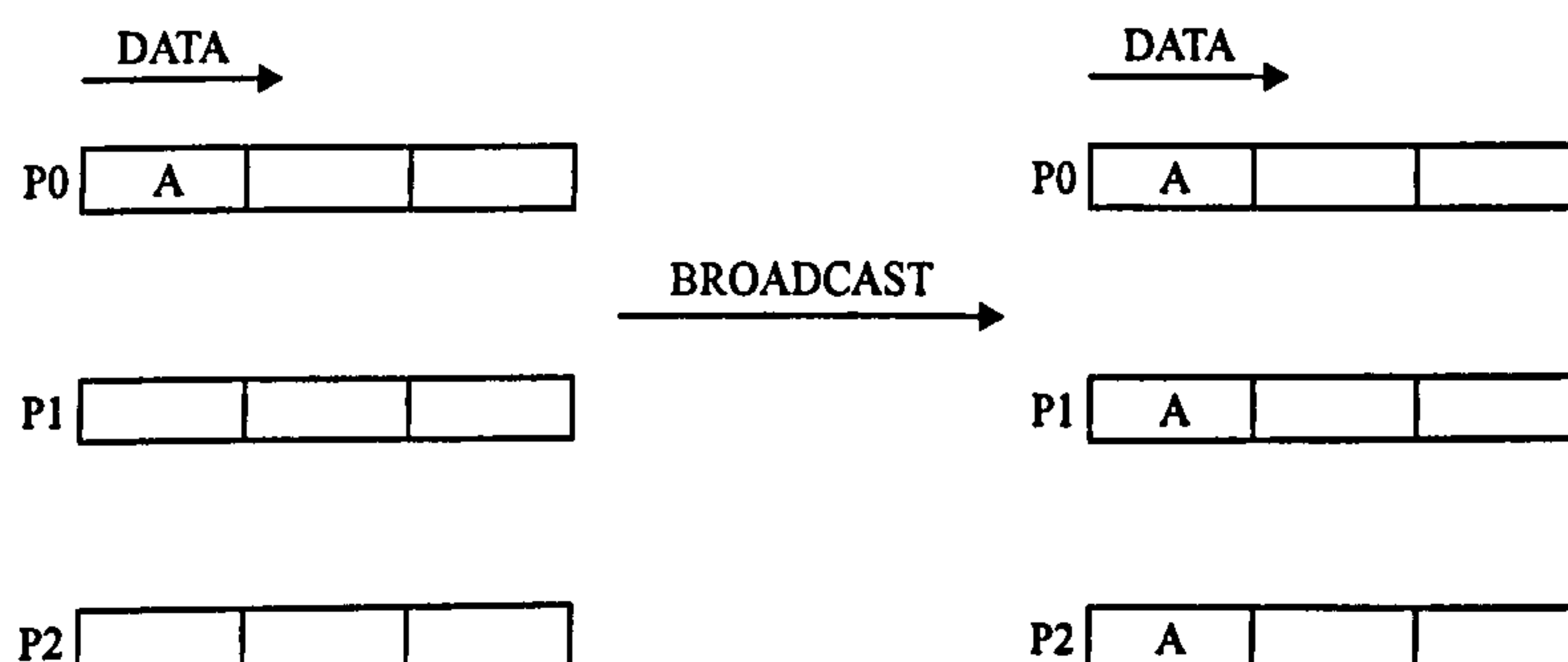


Fig. 6.6.8. Data motion for the `MPI_BCAST` routine with process P0 as root. Initially the data A is located on the root process. After the broadcast command, data A is replicated on all the processes.



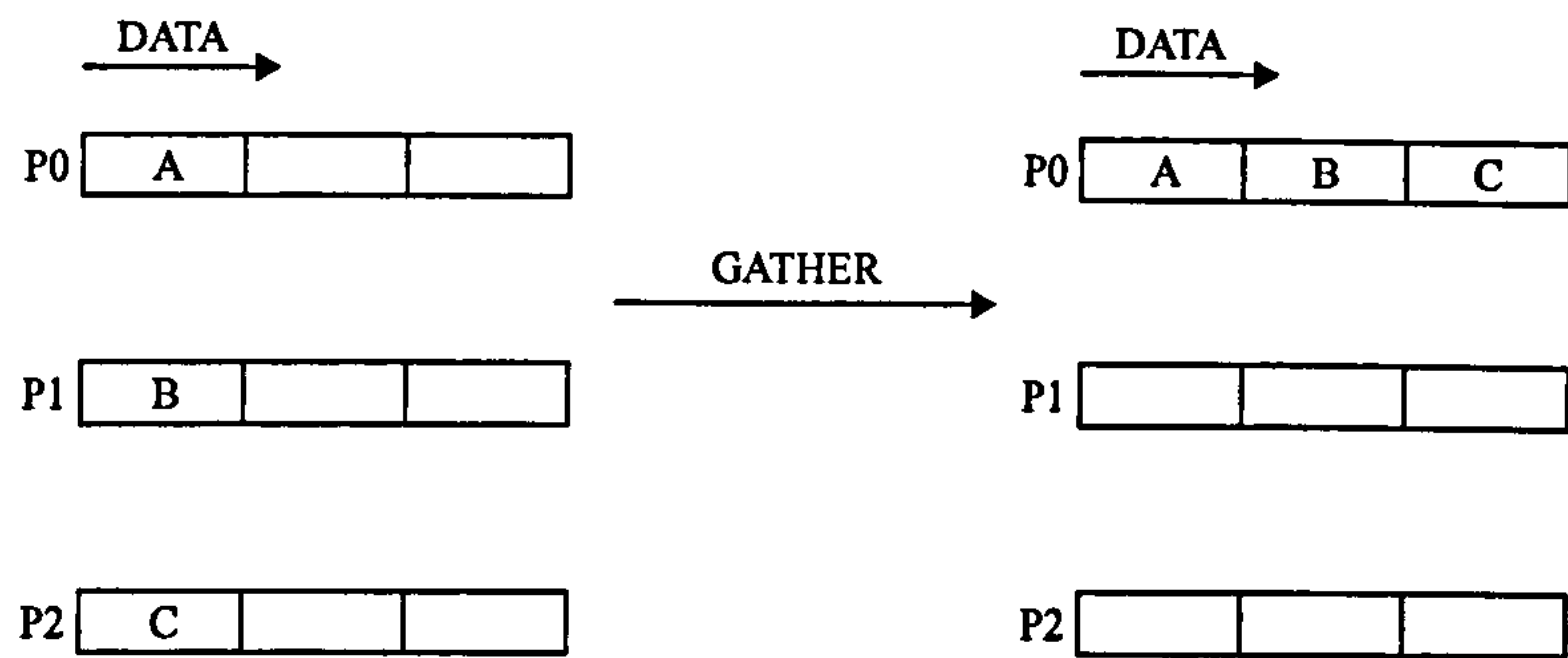


Fig. 6.6.9. Data motion for the MPI\_GATHER routine with process P0 as root. After data movement the data from each process is assembled together on the root process, in sequential non-overlapping locations.

process in the input buffer INBUFF to the output buffer OUTBUFF of the root process ROOT. The data is received as data type RECVDATATYPE and of size RECVCOUNT. The data is placed in non-overlapping locations in OUTBUFF, where the data from process  $i$  precedes the data from process  $i+1$ . The gather routine requires that *all* processes send the same size of data (usually  $COUNT = REVCOUNT$  and  $DATATYPE = RECVDATATYPE$ ). If the data gathered on the root process is required globally, then the broadcast routine could be implemented. However, MPI also provides a variant of the MPI\_GATHER routine, called MPI\_ALLGATHER, which effectively combines a gather and broadcast routine into one. For  $n$  processes its effect is also the same as if there were  $n$  calls to MPI\_GATHER with a different root process each time.

A common scenario is for the size of data to be gathered from each process to differ in size. For such instances MPI provides another gather variant, MPI\_ALLGATHERV, whose

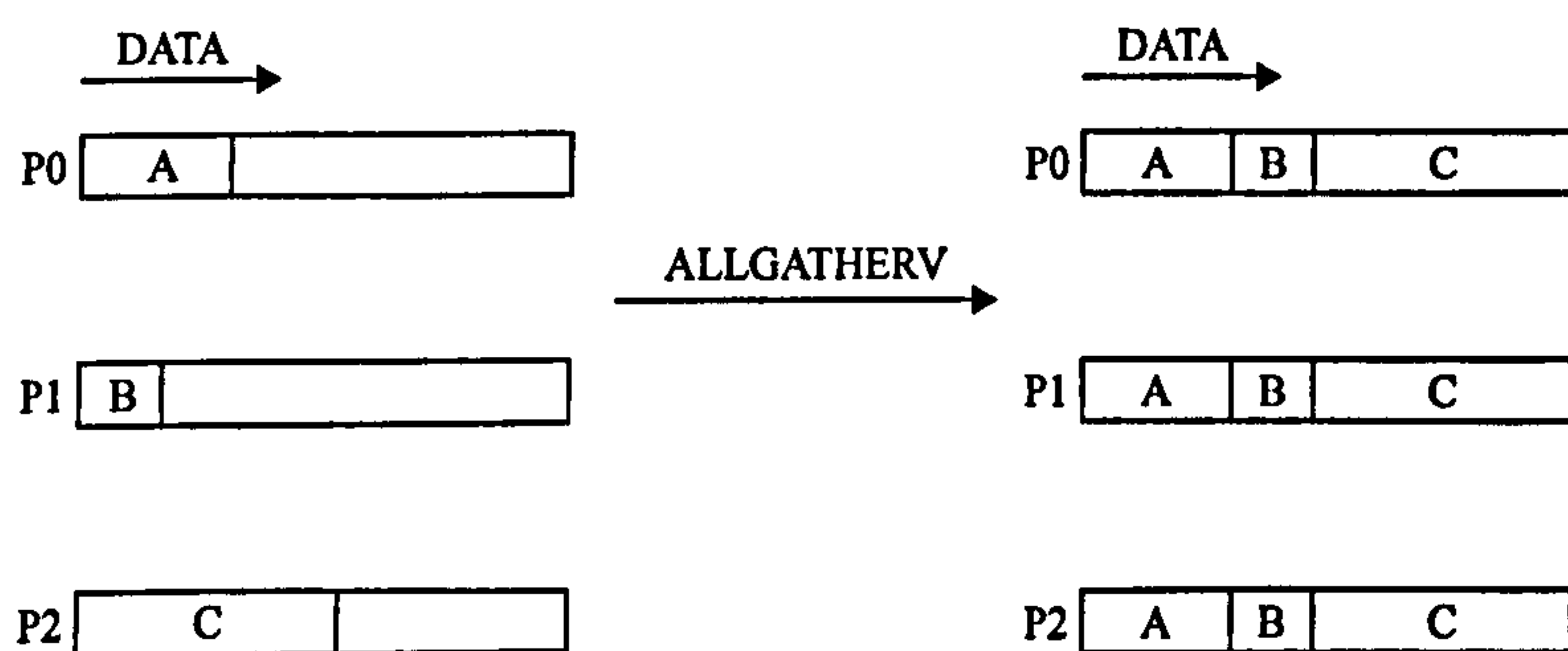


Fig. 6.6.10. Data motion for the MPI\_ALLGATHERV routine. Data on each process, which varies in size, is assembled together on all processes. The DISP array would have 0, A and A+B as its elements. Therefore, it offsets data A in the receive buffer by 0, data B by A and data C by A+B.



Fortran binding is

```
MPI_ALLGATHERV(INBUFF, COUNT, DATATYPE, OUTBUFF, RECVCOUNT, DISP,  
RECVDATATYPE, ROOT, COMM, IERROR)
```

The size of the data on each process is used to construct the array `DISP`, which contains the displacement of the data relative to the receive buffer on the root process. The gather routine then locates the data from the  $i$ th process and positions it in the receive buffer of the root process, where the location is given by the displacement in the  $i$ th element of `DISP`. The operation of the `MPI_ALLGATHERV` routine is illustrated in Fig. 6.6.10.

### 6.4.3 Reduction Operations

In reductive operations, data across all of the processes is collected together on a single process. The reduction operation is illustrated in Fig. 6.6.11. The Fortran binding for a reduction operation is

```
MPI_REDUCE(INBUFF, OUTBUFF, COUNT, DATATYPE, OP, ROOT,  
COMM, ERROR)
```

The reduction operation `MPI_REDUCE` combines data values of data type `DATATYPE` and size `COUNT` in the input buffer `INBUFF` of each process with a specified operation `OP`. Typical operations are summation (`MPI_SUM`), product (`MPI_PROD`), minimum (`MPI_MIN`) and maximum (`MPI_MAX`). The combined values are then returned to the output buffer `OUTBUFF` of the root process `ROOT`. There is also a reduction variant, `MPI_ALLREDUCE`, which effectively combines together a broadcast statement and `MPI_REDUCE` routine. Using this reduction variant, the combined values on the output buffer on the root process are sent to the output buffer on every other process.

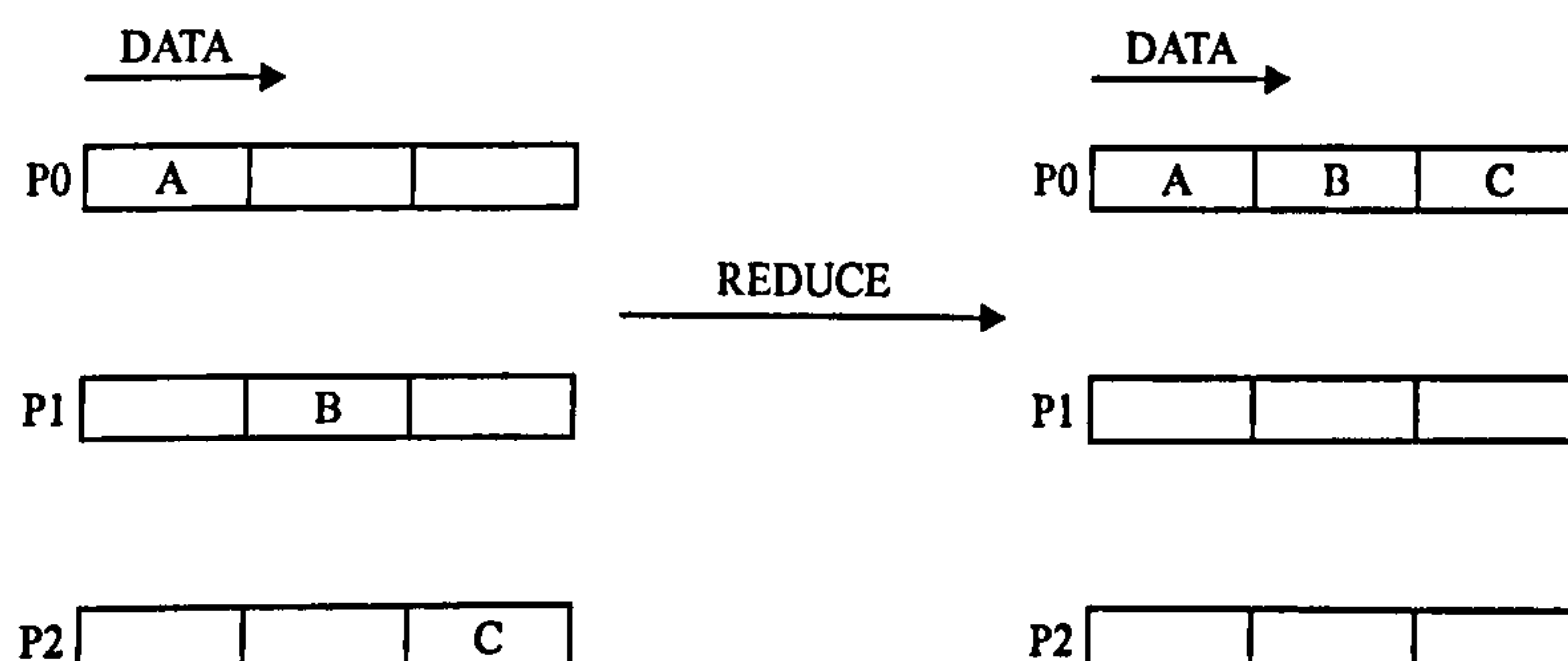


Fig. 6.6.11. Data motion for the `MPI_REDUCE` routine with process `P0` as root. Initially data is declared on each process at different data locations. After reduction, the data on each process is combined together on the root process.



## 6.5 Decomposition Methods

Partitioning the atoms across the processes is known as a *decomposition*. A number of conventional decomposition methods exist for parallel MD. The type of decomposition method utilised determines the form of communication used in the message passing (the two most common forms of communication are local and global). One decomposition approach is *atom* decomposition, where a partition of atoms is assigned to each process. This is a commonly used technique in MD simulations, see for example Plimpton [204]. For a system of  $n_{\text{atm}}$  atoms and  $n_p$  processors (assume  $n_{\text{atm}}$  is a multiple integer of  $n_p$ ), the most basic atom decomposition is to allocate  $n_{\text{atm}} / n_p$  atoms to each processor. The atoms allocated to each process need not be spatially related. Each process then operates on the atoms that have been assigned to it, no matter where they are (or displace to) in the simulation domain. Clearly, the atom decomposition method is advantageous by its simplicity, but it suffers from the requirement to perform global communications of atom coordinates. This requirement is imperative since information of spatially neighbouring atoms may not necessarily reside on nearby processors. Thus, the atom decomposition method produces a *replicated* data model since each process requires access to the dynamics of all the atoms in the system. Therefore, atom decomposition can heavily constrain system size if available memory is limited.

An alternative method is to assign a partition of physical space to the processors, which is known as *spatial* or *domain* decomposition. This approach has been utilised by numerous groups, for example see Nyland *et al* [205] or Srinivasan *et al* [206], and references therein. For  $n_p$  processors the computational box is simply divided into  $n_p$  domains (usually box shaped) and the atoms that reside in each domain are allocated to different processors. The spatial decomposition method is advantageous since it requires only local communication of coordinates for atoms that interact across the domain interfaces. Furthermore, the communication overhead decreases as the number of processors increases, since the surface area of each domain becomes smaller. This type of decomposition scheme generates a *non-replicated* data model, where memory is significantly reduced because each processor only stores data for a subset of the simulation volume. Thus, spatial decomposition is especially advantageous in situations where memory availability heavily constrains system size. However, this method is much more complicated to implement compared with atom decomposition. For example, in an in-



homogenous system, or where the system is irregular in shape, the decomposition may not be obvious. Furthermore, there is a continuous need to move atoms to different processors when atoms migrate across a domain and to resize the spatial domains to avoid imbalance due to high fluctuations in density. Thus, in the preliminary development of the parallel MD code for simulating nanoindentation, an atom decomposition scheme is used because it is simpler.

## 6.6 Parallelisation Scheme

The parallel MD code is written so that it can be run both in serial or in parallel. The flowchart in Fig. 6.6.12 illustrates the functioning of the code for parallel execution. All code associated with data input is buffered in a conditional statement such that at the beginning of the simulation only the root process reads in data. The inputted data is then broadcast to all other processes using the `MPI_BCAST` routine. Similarly, only the root process performs data output. The parallelisation of the force and energy calculations, together with the neighbour list routine and the load balancing method is discussed in the succeeding subsections.

### 6.6.1 Adaptive Load Balancing

In essence, the approach adopted for parallelisation is to distribute the work load in an equal fashion over the processors. This process is called *load balancing*. Efficient load balancing can make the difference between modest and maximum performance gains. Ideally, all processes will have an equal work load, as illustrated in Fig. 6.6.13(a). Since the load balance is equal on all processes, the execution time of  $t_1$  is the minimum possible. However, this scenario is rarely achievable since the work load cannot always be split evenly over the processes. If there is a load imbalance then some of the processes may finish operating on their set of data before others, and therefore they will become idle. This leads to a synchronisation cost, since surplus time will be spent waiting for remaining ‘overloaded’ processes to finish their operations before communications can be performed. A representation of load imbalance is given in Fig. 6.6.13(b). Here, the load on process 0 exceeds the ideal by a certain quantity, while the load on process 3 is below the ideal by the same quantity. Hence, there is a synchronisation cost of  $\Delta t$  due to the imbalance. In reality, load distribution is determined in such a way to minimise



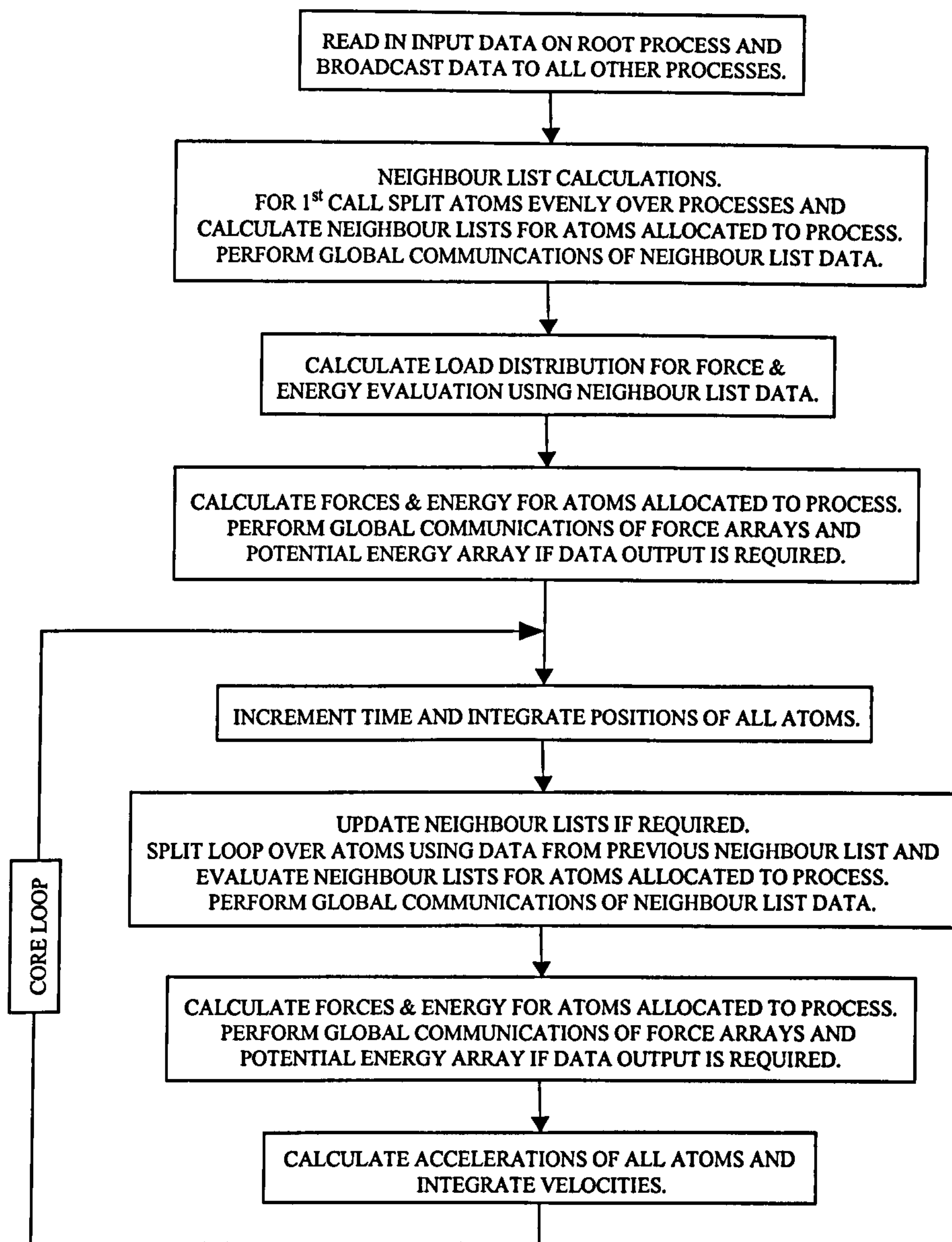


Fig. 6.6.12. Flowchart illustrating the functioning of the parallel MD program.

$\Delta t$ .

The decomposition of atoms could distribute equal numbers of atoms to each process. However, the work load associated with the energy and force evaluations can be quantified in terms of the total number of neighbours. Hence, with a equal division of atoms each process may have different work load. Therefore, in the parallel MD code the number of neighbours of each atom is used to determine how to distribute the labour among the processes. The parallelisation of the energy and force calculations is achieved by splitting each loop over the atoms. If the loops start at point `ATMSTRT` and finish at `ATMFNSH` then the ideal load on each process is given by

$$\frac{\text{NEBPNT}(\text{ATMFNSH}+1) - \text{NEBPNT}(\text{ATMSTRT})}{\text{NPROC}} \quad (6.6.6.1)$$



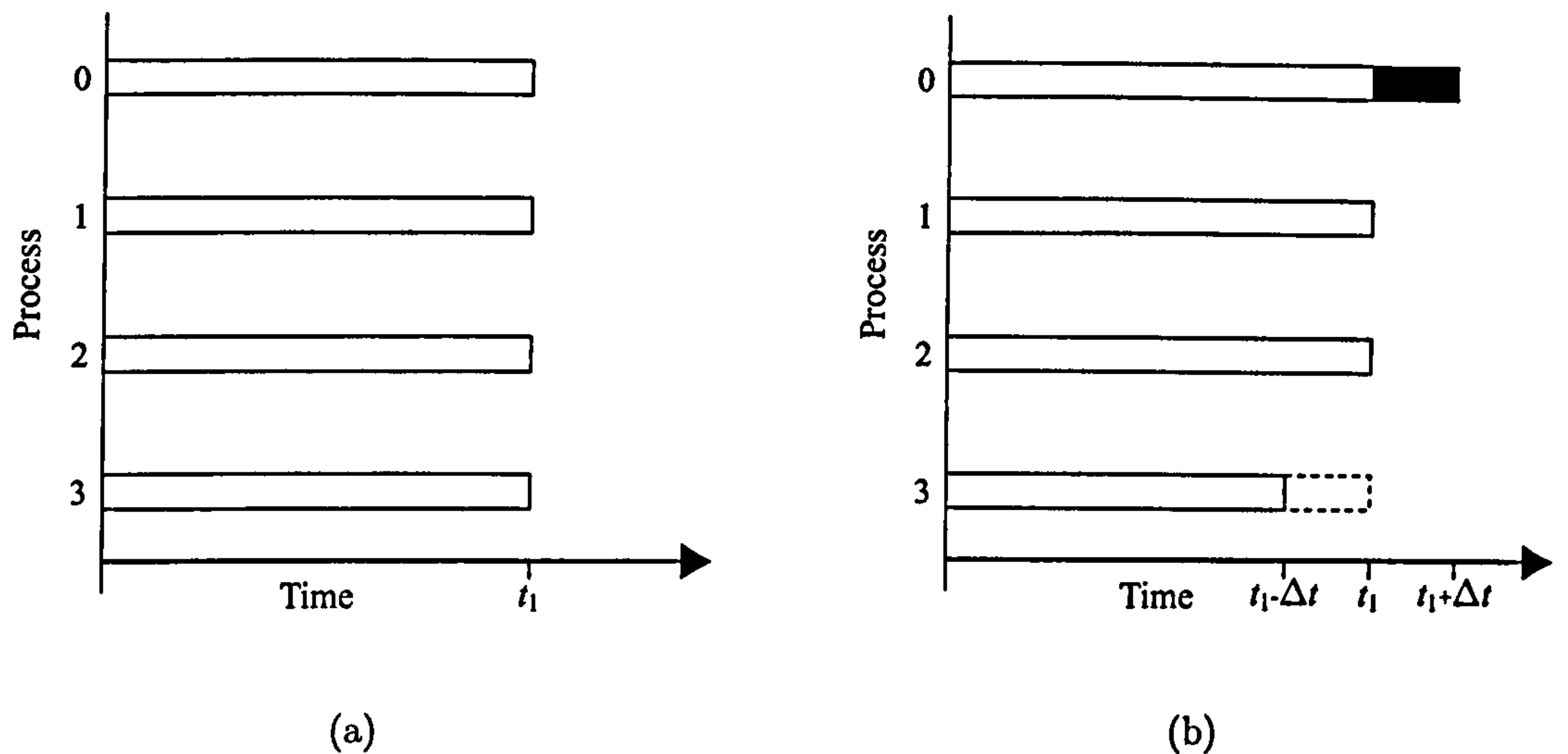


Fig. 6.6.13. (a) Ideal load balancing where the execution time  $t_1$  is the minimum possible. (b) Imperfect load balancing which leads to a synchronisation cost of  $\Delta t$  on the minimum execution time  $t_1$  due to the 'overloaded' process.

where  $NPROC$  is the number of processes. To determine the most efficient load distribution, the range of atoms having a total neighbour sum approximately equal to Eqn. 6.6.6.1 is computed using the neighbour list data. Since the neighbour list is ordered by atom number, nothing is known about the spatial locality of the decomposition. However, since the substrate and indenter are generated from algorithms where atoms are constructed in an ordered fashion, most neighbouring atoms will reside on the same process. Using NEBPNT the array elements are looped over from  $ATMSTRT$  to  $ATMFNSH$ . When the neighbour sum is equal to or exceeds the value determined from Eqn. 6.6.6.1, the atom number incurred determines the load distribution for the first process. The process is then repeated to establish the load distribution for the next process and so forth, by nesting the loop over NEBPNT in a loop over the number of processes. The methodology for determining the load distribution for the energy and force calculations is summarised by the following code segment.

Determine ideal load on processes.

```
IDEAL_LOAD = INT( (NEBPNT(ATMFNSH+1) - NEBPNT(ATMSTRT)) / NPROC)
```

Initialise limiting value in NEBPNT to find or surpass.

```
NEBVALUE = IDEAL_LOAD + NEBPNT(ATMSTRT)
```

Initialise loop over NEBPNT to start from ATMSTRT.

```
LOOPSTRT = ATMSTRT
```



Loop over number of processes.

DO I = 1,NPROC

Loop over NEBPNT.

DO J = LOOPSTRT,ATMFNSH

Check when total number of neighbours up to atom J is greater than  
or equal to limiting value.

IF( NEBPNT(J) .GE. NEBVALUE )EXIT

ENDDO

Store atom number where total neighbours is equal to or greater than  
limiting value.

NATPROC(I) = J-1

Determine new limiting value in NEBPNT to find or surpass.

NEBVALUE = NEBPNT(J) + IDEAL\_LOAD

Start loop over NEBPNT from last value of J.

LOOPSTRT = J

ENDDO

The work load of a specific computation is not always known prior to execution and so the division of labour cannot be performed statically (i.e. fixed at compile time). For example, the work load of the neighbour list generator cannot be determined since the number of neighbours of each atom is initially unknown. Therefore, the division of labour has to be performed dynamically during process execution. For MD simulations with long-range forces, say the computation of the electrostatic energy for  $N$  charged atoms, load balancing is simple to achieve since atoms interact with all other atoms. However, simulations with short-range potentials, as used in this thesis, can develop load imbalance due to density variations and therefore ensue in performance degradation.

At the beginning of each nanoindentation simulation, the tip and substrate are in a near equilibrium state and so neighbour list updates are minimal. After mechanical contact is made, the density of atoms will fluctuate and therefore the frequency of neighbour list updates increases with continued penetration. Clearly, as the neighbours of an atom change, the work load associated with that atom can also change. For example, during indentation an atom under compression will have an increased number of neighbours and thus a larger associated work load. If the work load distribution is only determined once, at the start of computation, then an inequality in the distribution will occur. It



is therefore important to implement an adaptive load balancing scheme to account for changes in work load as the simulation progresses. To accomplish this, the partition of atoms over the processes must be automatically performed during the simulation.

Load balancing at every timestep would be wasteful since it would divert the computer resources away from the computation. Since the load balance is only subject to change when the neighbour lists have been updated, the load imbalance does not have to be checked every timestep. Therefore, whenever the neighbour lists are updated the load distribution is performed again. However, there is an overhead cost incurred with any load balancing scheme, due to the periodic calculations required to repartition the work load among the processes. Despite this, significant improvements in processor efficiency can be achieved. A recent parallel MD study using spatial decomposition by Srinivasen *et al* [206] reported up to a 50% reduction in total computation time with dynamic load balancing.

### 6.6.2 Energy and Force Evaluation

Since the pairwise terms for all pair interactions are required in the Brenner potential, global communication of the arrays storing the pairwise terms could be made. However, preliminary results showed this was an inefficient approach, with the communications taking longer than the actual calculation and storage of the pairwise terms. To avoid global communications of the pairwise storage arrays, each process must ensure that it has access to all pairwise terms associated with the atoms allocated to it. If for each process the loop over the Brenner atoms in the potential calculation starts at BRENSTRT and finishes at BRENFNH, then a list of atoms (BRENSTR) containing the 1<sup>st</sup> and 2<sup>nd</sup> neighbours of each atom from BRENSTRT to BRENFNH can be produced. To avoid duplicate pairs being evaluated by the same process, the BRENSTR list preliminary contains each atom from BRENSTRT to BRENFNH. Each atom from BRENSTRT to BRENFNH is then looped over and the 1<sup>st</sup> and 2<sup>nd</sup> neighbours computed. If any neighbours reside on a different process, then they are added to the BRENSTR list if they have not yet been considered. Although this method renders a redundant need for global communications of pairwise terms, duplicate work will be incurred since some of the same pairwise terms will be required by different processes. Furthermore, there may be a risk of an imbalance across the processes for evaluation of the Brenner pairwise terms since the number of 2<sup>nd</sup> neighbours is not considered in the load distribution scheme.



Before computation of the energy and forces, the respective array elements are all set to zero. Each process then loops over all the atoms assigned to it during the load balancing. Therefore, all processes only operate on the array elements corresponding to the assigned atoms and their neighbours. After the energy and force evaluations have been performed, global summing of the force arrays is made using the MPI reduction operation `MPI_ALLREDUCE`. Each process then has access to the force on every atom and it can therefore integrate the equations of motion for all atoms. Since data output is only performed by the root process, the reduction operation `MPI_REDUCE` is used to sum the potential energy arrays across all processes together onto the root, whenever data output is required.

### 6.6.3 Neighbour List Construction

To construct the neighbour list for each atom, all atoms in the host and neighbouring cells are evaluated. Hence, the work load associated with the neighbour list generator can be defined by the total number of cell evaluations performed. Therefore, an array `NCELLEVAL` is introduced to store the number of cell evaluations associated with the neighbour list construction of each atom. For a system of  $N$  atoms, the `NCELLEVAL` array is dimensioned  $N+1$ . The first element of the array `NCELLEVAL` is assigned a dummy value of one. The second array element is then assigned the number cell evaluations associated with atom number one, summed with the preceding element value. This process is then repeated for all remaining atoms in the system. Thus, the number of cell evaluations for any atom  $i$  is simply obtained by `NCELLEVAL(i+1) - NCELLEVAL(i)`.

Load balancing the loop over the atoms in the neighbour list generator with respect to the work load requires the data from the `NCELLEVAL` array, which is only known after all the neighbour lists have been computed. Therefore, for the first call to the neighbour list routine the atoms are distributed equally among the processes. For subsequent calls, load balancing is performed in the same fashion as for the energy and force calculations, except using the data from the `NCELLEVAL` array generated during the preceding neighbour list construction. Although the loop over atoms is split using the old neighbour list data, it will still give a good decomposition since the difference between successive neighbour list updates is typically very small.

After the neighbour list has been constructed, global communications are required. Since the `NCELLEVAL` array is only required to determine the load distribution for the



NEBPNT ELEMENT:	1	2	3	4	5	6	7	8	9	10
PROC 0:	1	5	9	15	0	0	0	0	0	0
PROC 1:	0	0	0	1	4	10	17	0	0	0
PROC 2:	0	0	0	0	0	0	1	5	10	18

(a)

NEBPNT ELEMENT:	1	2	3	4	5	6	7	8	9	10
PROC 0:	1	5	9	14	14	14	14	14	14	14
PROC 1:	0	0	0	1	4	10	16	16	16	16
PROC 2:	0	0	0	0	0	0	1	5	10	18

(b)

Fig. 6.6.14. The NEBPNT array formed by three processes operating on three separate decompositions: (a) Before pre-processing; (b) After pre-processing.

subsequent neighbour list construction, it is more efficient to reduce the array onto the root process only. The root process can then determine the load distribution and broadcast it to the other processes. For  $N$  atoms and  $NPROC$  processes, this saves broadcasting  $(NPROC - 1) \times (N + 1)$  at the expense of  $\approx NRPOC^2$ . Since the number of neighbours on each process is unknown before the construction of the neighbour lists, a pointer to the element in the NEBOUR array where each process should start, cannot be used. Hence, each process starts at the first element in the NEBOUR array. To collect together the NEBOUR array the MPI gather variant routine `MPI_ALLGATHERV` is utilised, as illustrated in Fig. 6.6.10. Before the NEBPNT array can be collected together using the reduction operation `MPI_ALLREDUCE`, some pre-processing is required. Consider the NEBPNT array shown in Fig. 6.6.14(a). Here, each process operates on the atoms allocated to it to produce the NEBPNT array. For each process (apart from the process which is assigned the last decomposition of atoms) the last element operated on coincides with the start of the decomposition of the next process. Therefore, one must be subtracted from this element and duplicated to all remaining elements hereafter, as shown in Fig. 6.6.14(b).



## 6.7 Performance Evaluation

With the execution of serial code, performance can be determined by checking the numerics of data output. However, with parallel code there is an additional requirement to analyse the speed of execution. The efficiency of parallel applications is a function of both load balancing and scalability. Scalability can be defined as an estimation of how the computation of a particular problem varies with changes in both system size and the number of processes. A simple measure of how the computation will change with an increasing number of processes is *speedup*, which can be determined from timing profiles. For a fixed system size implementing  $n$  processes, a speedup factor ( $S_p$ ) can be defined as

$$S_p = \frac{\text{Execution time with 1 process}}{\text{Execution time with } n \text{ processes}} \quad (6.7.6.1)$$

In addition to analysing the performance of the program as a whole, timing profiles allow the efficiency of individual computations to be examined. This therefore allows specific areas of the code to be targeted with the need for further development. In the

Table 6.2. Timing profile (in seconds) of the parallel MD code following a 1 ps simulation with approximately 1.2 million atoms.

	Number of Processors					
	2	4	8	16	32	64
Finnis Potential <sup>a</sup>	12232.3	6095.6	3190.3	1543.2	806.0	411.7
Brenner Pairwise Storage	35.3	16.7	9.5	4.6	2.8	1.6
Brenner Potential	467.9	231.0	114.3	56.0	27.9	14.4
Energy and Force	396.1	630.7	978.1	1450.6	2191.6	2936.8
Comms.						
Neighbour List	387.8	194.2	104.7	66.7	40.7	21.5
Neighbour List Comms.	67.5	76.9	98.7	118.6	146.9	163.8
Average time per timestep	14.6	8.1	5.9	4.5	5.0	7.2
Speedup over 1 processor	1.85	3.33	4.58	6.00	5.40	3.75

<sup>a</sup>This timing also includes evaluating Fe-C interactions.



parallel MD code, the efficiency of each parallelised subroutine is analysed by timing the computation using the UNIX operating system timing mechanism `dtime()`. This routine simply returns the time since the last call to `dtime()` was made. Hence, the time interval for execution of the parallelised subroutines can be determined by calling `dtime()` before and after each subroutine call. This profiling approach is limited in that it only provides information on where the program is spending time. Although it is not necessarily highly accurate, it is implemented at a very low cost and is sufficient enough to allow a suitable estimation of scalability. When more detailed profiling is required, MPI can be instrumented with logging routines which allow the sequence of events to be visually studied with time.

Since parallel computers are typically used to solve problems with a small fixed size faster, or to permit the use of larger system sizes, it is crucial to analyse how the parallel MD code scales under both scenarios. The performance of the parallel MD code was primarily tested on a fixed system size with a Fe substrate. The indenter was configured from 30,369 atoms, and the substrate from 1,183,964 atoms. Simulations were run for 1 ps using at first 1 processor (as serial) and then 2, 4, 8, 16, 32 and 64 processors. Although the simulation time is small, it is sufficient to determine the performance of each parallelised subroutine and the extent of the communications overhead. A timing profile illustrating the performance of the parallel MD code is given in Table 6.2.

In all simulations the load-balancing is excellent, with the load on each process being between 98% - 102% of the ideal load. Furthermore, the load balancing is not costly to implement and only takes a fraction of the total CPU time. From Table 6.2 the execution time of the parallelised subroutines approximately halves as the number of processes doubles. For ideal speedup with a fixed system size, the execution time is assumed to halve as the number of processors doubles. However, this is seldom achieved due to the difficulty in equally distributing work loads and the need for communications. The speedup over 2 and 4 processes is quite good, but deteriorates thereafter. There is no performance gain after 16 processes. As the number of processes increases, the execution time incurred during global communications also increases. At around 16 processors, the global communication time dominates and is greater than the time to execute the potentials/neighbour lists. However, it is the global communication of the force and potential energy arrays that is solely responsible for the impairment in performance, since this is incurred every timestep. Using 64 processors, the time to communicate the



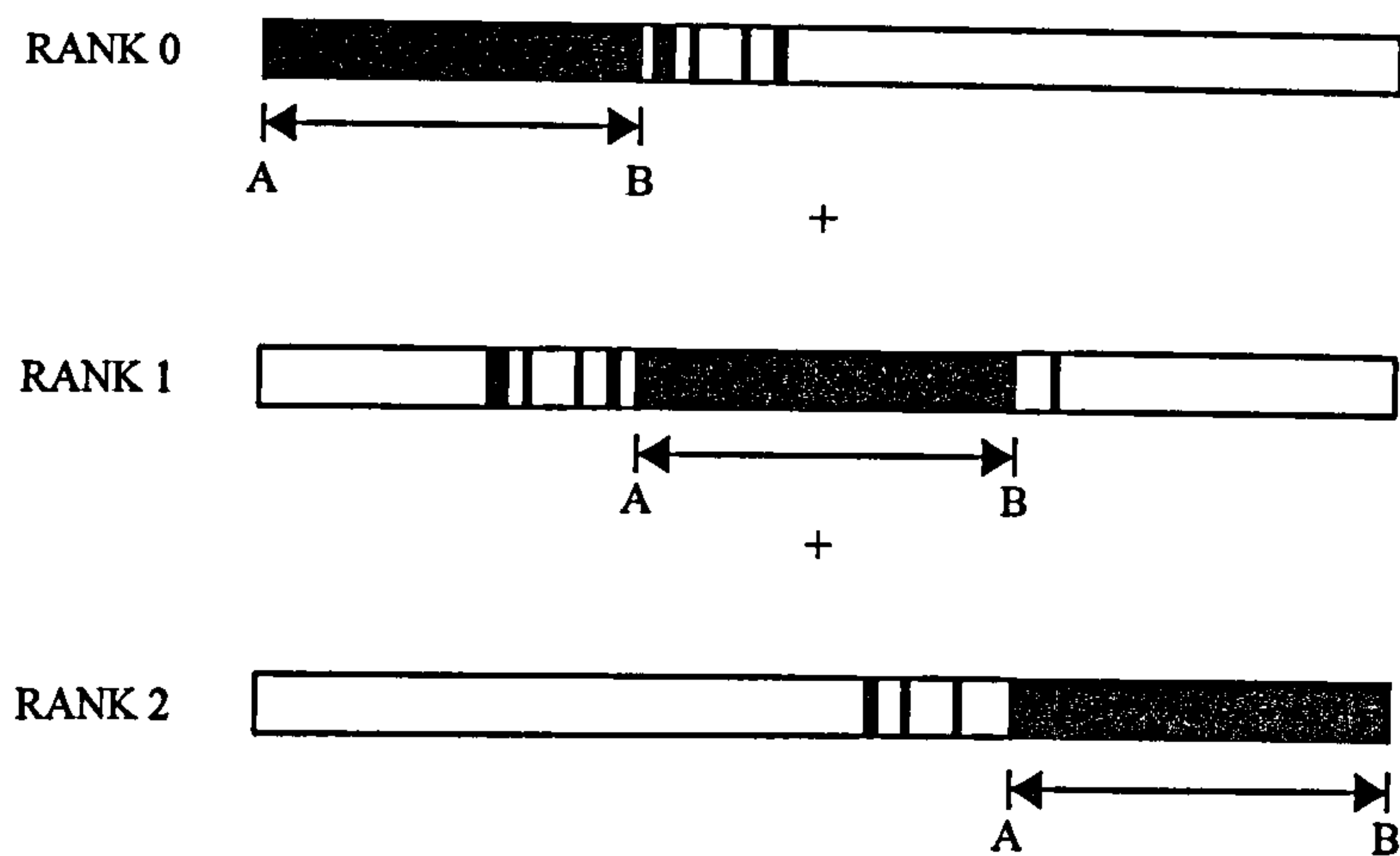


Fig. 6.6.15. Global summing of a force/energy array operated upon by three different processes. The shaded region between A and B represent the atoms allocated to the host process. The remaining shaded regions denote atoms that are neighbours of some of the atoms between A and B and reside on a different process. The unshaded regions represent atoms which are not operated on by the host process, but are still involved in global summing.

force and potential energy arrays is more than seven times that for the calculation of the potentials.

The reason the scaling is poor for increasing number of processes is that the code becomes communication bound. Since each process only operates on selected atoms, there are some atoms that are not evaluated but still involved in global summing, as depicted in Fig. 6.6.15. As the number of processes increases, the fraction of atoms on each process that remain unoperated on also increases. Thus, a large percentage of the communication time involves summing and broadcasting the forces and potential energy of atoms that are not evaluated by a process in the potential calculations. To improve the scalability of the parallel MD code, the communications overhead incurred by the potential energy and force arrays needs to be considerably reduced.

## 6.8 Performance Tuning

When the neighbour list is updated and the load balancing is determined, the atoms allocated to each process remain the same until the neighbour list becomes updated. Therefore, each process only needs to acquire the total force acting on the atoms allocated to it, and any of their neighbours that reside on a different process. However, the



root process requires the total force acting on every atom in order to provide global data output. Thus, if each non-root process creates a list storing all the atoms allocated to it and any neighbours that may reside on another process, then these can be summed onto the root process and redistributed using *send* and *recv* MPI operations.

If there are  $N$  atoms allocated to each non-root process then the first  $N$  elements of the stored atom list will correspond to the  $N$  atoms allocated to the process. The subsequent elements will correspond to atoms that are neighbours of some of the  $N$  atoms but reside on a different process. Before the forces for the stored atoms are sent to the root process, they are packed into an array. This is achieved using the MPI routine `MPI_TYPE_INDEXED`, whose Fortran binding is

```
MPI_TYPE_INDEXED(NUMBER_OF_BLOCKS, ARRAY_OF_BLOCKLENGTHS,  
ARRAY_OF_DISPLACEMENTS, OLDTYPE, NEWTYPE, IERROR)
```

The data in the packed array is sent to the root process as a series of blocks. Since the first  $N$  elements of the packed array correspond to sequential atoms, they can be sent as just one block of length  $N$  (it is less costly to send one block of length  $N$  than  $N$  unit blocks). The remaining elements of the packed array will not *all* correspond to consecutive atom numbers and therefore have to be sent as a collection of varying blocks lengths. Once the root process has received the forces of the atoms on non-root processes, it has to unpack the array in the receive buffer before the summation. The first two arguments of `MPI_TYPE_INDEXED` routine are the number of blocks to be sent and an array giving the length of each block. The third argument is an array containing the displacement of each block relative to the first element in the force arrays. The fourth and fifth arguments are the type of data to move and the new data type relating to the packed array, respectively. The code to sum all the forces onto the root process can be summarised by the following code segment.

```
IF(RANK .EQ. 0) THEN.
```

```
  Loop over all other processes.
```

```
  DO I=2,NPROC
```

```
    Receive force on stored atoms from non-root processes using MPI_RECV.
```

```
    Loop over stored list of atoms on non-root process.
```

```
    DO J = ATOMSTORE(I-1),ATOMSTORE(I)-1
```

```
      Unpack received force array.
```

```
      Sum force on root atom to force on received atom.
```



```

        ENDDO
    ENDDO
ELSE
    Create packed array of forces for stored atoms with MPI_TYPE_INDEXED.
    Send array of forces for atoms in stored list to root using MPI_SEND.
ENDIF

```

The potential energy is summed together onto the root process in the same fashion as for the force arrays, whenever data output is required. Once the root process has summed all the forces, it needs to send back the forces for all atoms required by the non-root processes. This is because each non-root process only needs to integrate the equations of motion for the atoms stored in its list. The non-root processes do not need to unpack the forces received from the root, since the packed array in the receive buffer can be implemented in the integration algorithm. The root process integrates the equations of motion for all atoms to ensure it can perform global data output when required. Although this creates an imbalance across the processes, it will cause a negligible impairment to performance since the integration routine accounts for an inconsequential amount of the total CPU time. After summation on the root process, the potential energy does not need to be sent back to non-root processes since it is only required for data output. The code to send the forces back from the root to the non-root processes is essentially the reverse of the previous code segment and can be summarised by the following code segment.

```

IF(RANK .EQ. 0) THEN.
    Loop over all other processes.
    DO I=2,NPROC
        Create packed array of forces for stored
        atoms on non-root process with MPI_TYPE_INDEXED.
        Send total force on stored atoms back to non-root
        processes using MPI_SEND.
    ENDDO
ELSE
    Receive total force on stored atoms from root using MPI_RECV.
ENDIF

```

The flowchart in Fig. 6.6.16 illustrates the functioning of the MD core for parallel



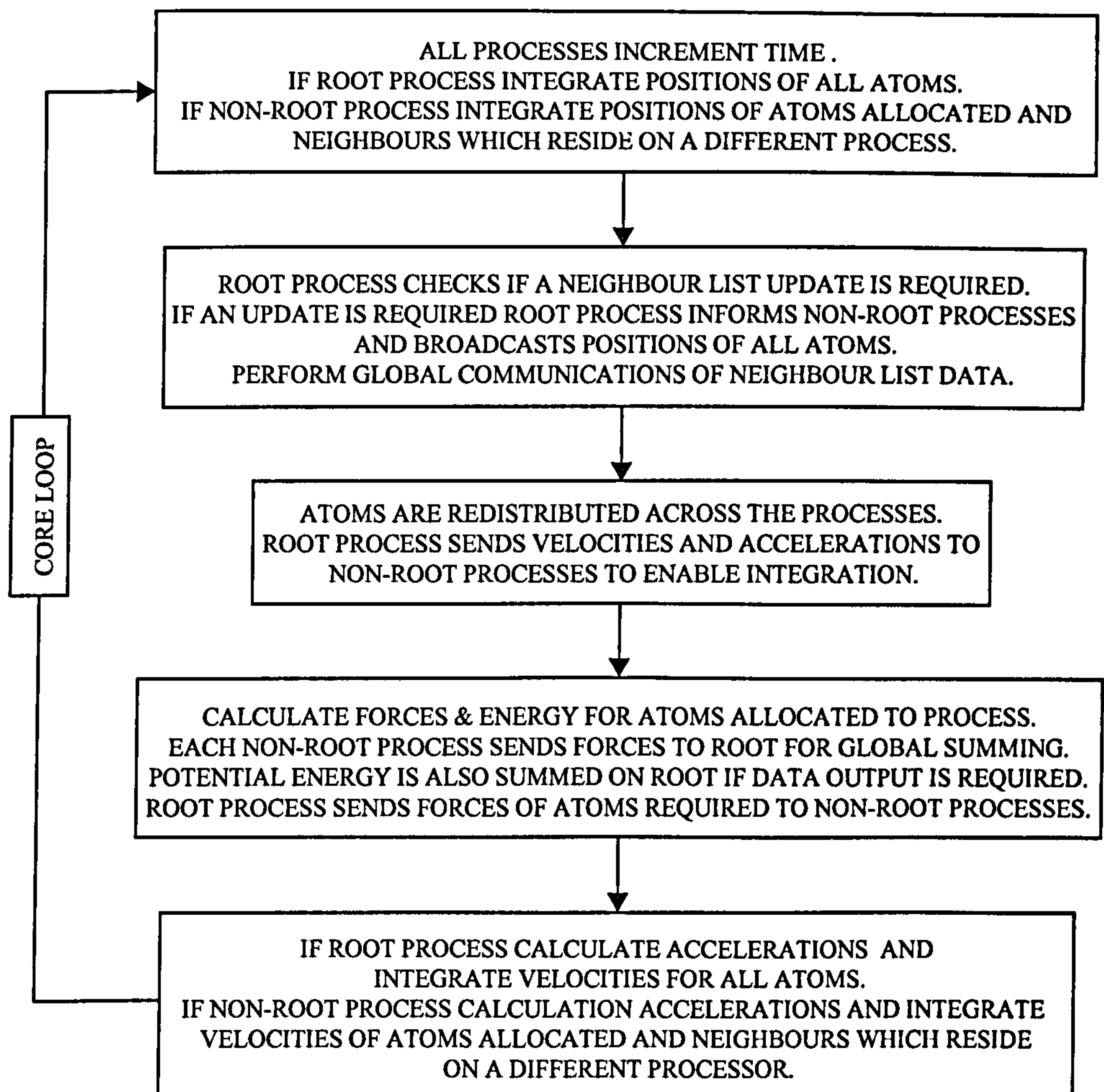


Fig. 6.6.16. Flowchart illustrating the functioning of the parallel MD program following the performance tuning.

execution following the performance tuning. Since only the root process integrates the equations of motion for all the atoms, only the root process checks the validity of the neighbour lists. If an update is required, it informs the non-root processes and broadcasts the positions of all atoms. When the atoms have been redistributed across the processes, the root process sends the velocity and acceleration of the atoms that are required by the non-root processes in the integration algorithm. This is done in the same way the root process sends the forces back to the non-root processes in the previous code segment.

A timing profile illustrating the performance of the parallel MD code following tuning is given in Table 6.3. There is a significant performance gain compared with the timings in Table 6.2, since the communications overhead for the force and potential energy arrays has been considerably reduced. The time to sum the forces and potential energy onto the root is approximately just as costly as the send/receive communications.



Table 6.3. Timing profile (in seconds) of the tuned parallel MD code following a 1 ps simulation with approximately 1.2 million atoms.

	Number of Processors					
	2	4	8	16	32	64
Finnis Potential <sup>a</sup>	11336.5	5685.2	2854.9	1445.2	731.7	376.5
Brenner Pairwise Storage	31.1	15.8	8.0	4.2	2.1	1.2
Brenner Potential	454.6	224.6	110.6	54.6	27.0	14.0
Energy and Force	92.0	132.4	175.8	274.8	305.8	492.0
send/recv Comms.						
Energy and Force	95.9	150.0	188.5	248.3	325.1	491.5
summation to root						
Neighbour List	374.2	190.1	106.3	60.7	32.6	18.1
Neighbour List Comms.	62.1	77.4	95.7	115.4	140.4	156.7
Average time per timestep	13.5	7.6	4.7	3.6	2.7	2.4
Speedup over 1 processor	2.00	3.55	5.74	7.50	10.00	11.25

<sup>a</sup>This timing also includes evaluating Fe-C interactions.

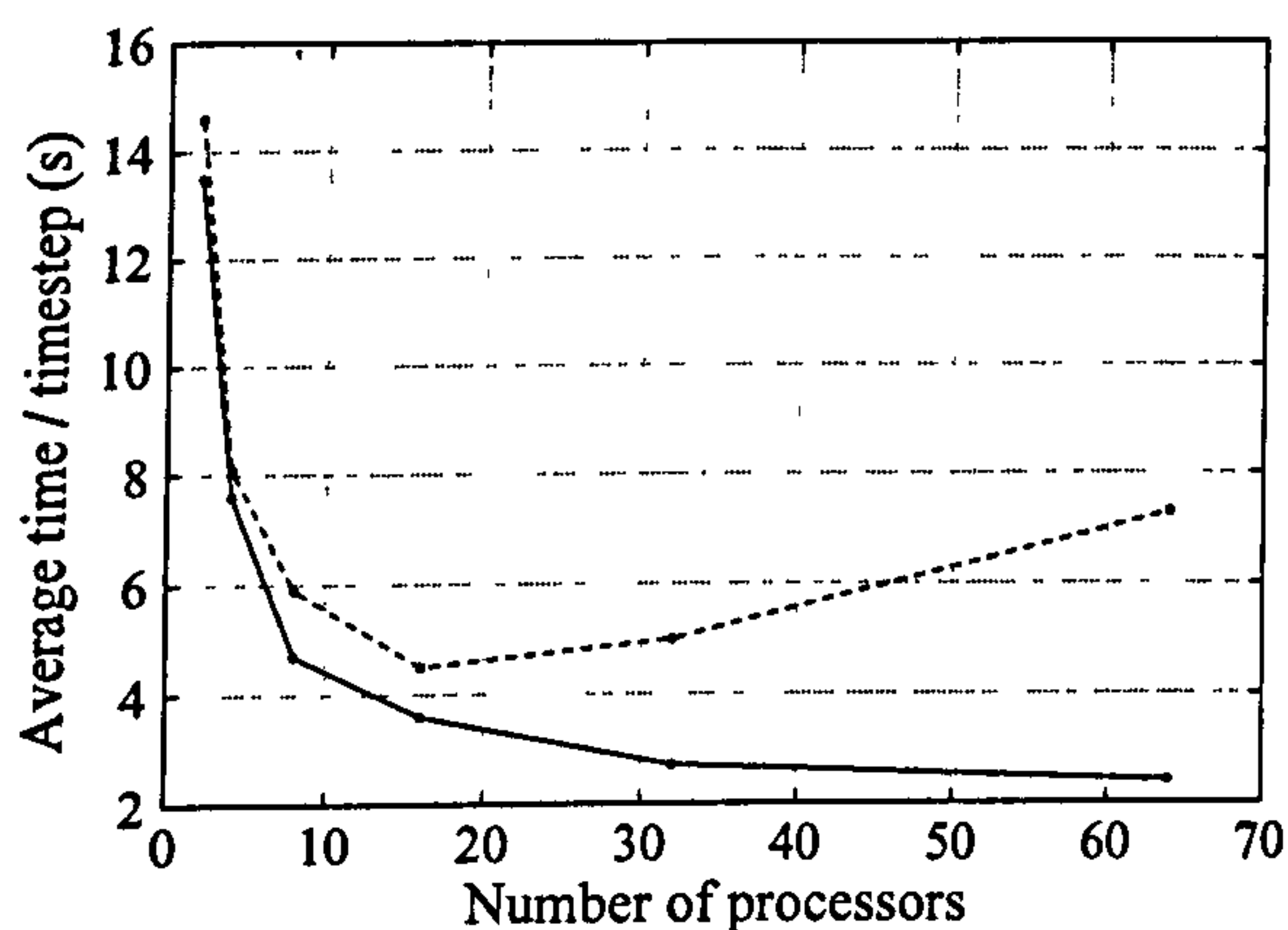
The communication time of the forces and potential energy arrays begins to dominate at around 32 processors when it becomes longer than the evaluation of the potentials. The scaling of the tuned code compared with the preliminary development is shown in Fig. 6.6.17. There is a performance gain with the tuned code in all cases. However, this decreases significantly with increasing processors. The performance gain at 64 processors compared with 32 processors is not of significant benefit in terms of the cost in CPU hours.

Simulations of 1 ps were also performed with varying system size to determine scalability to larger number of atoms. An indenter with 30,369 atoms was used and varying substrate sizes to double the total system of approximately 0.125 million atoms on 4 processors to 2.0 million atoms on 64 processors. The scalings obtained from these simulations are given in Fig. 6.6.18 and show that the average time per timestep increases as both the system size and number of processors double. For ideal performance, the average time per timestep should be approximately the same as the system size doubles

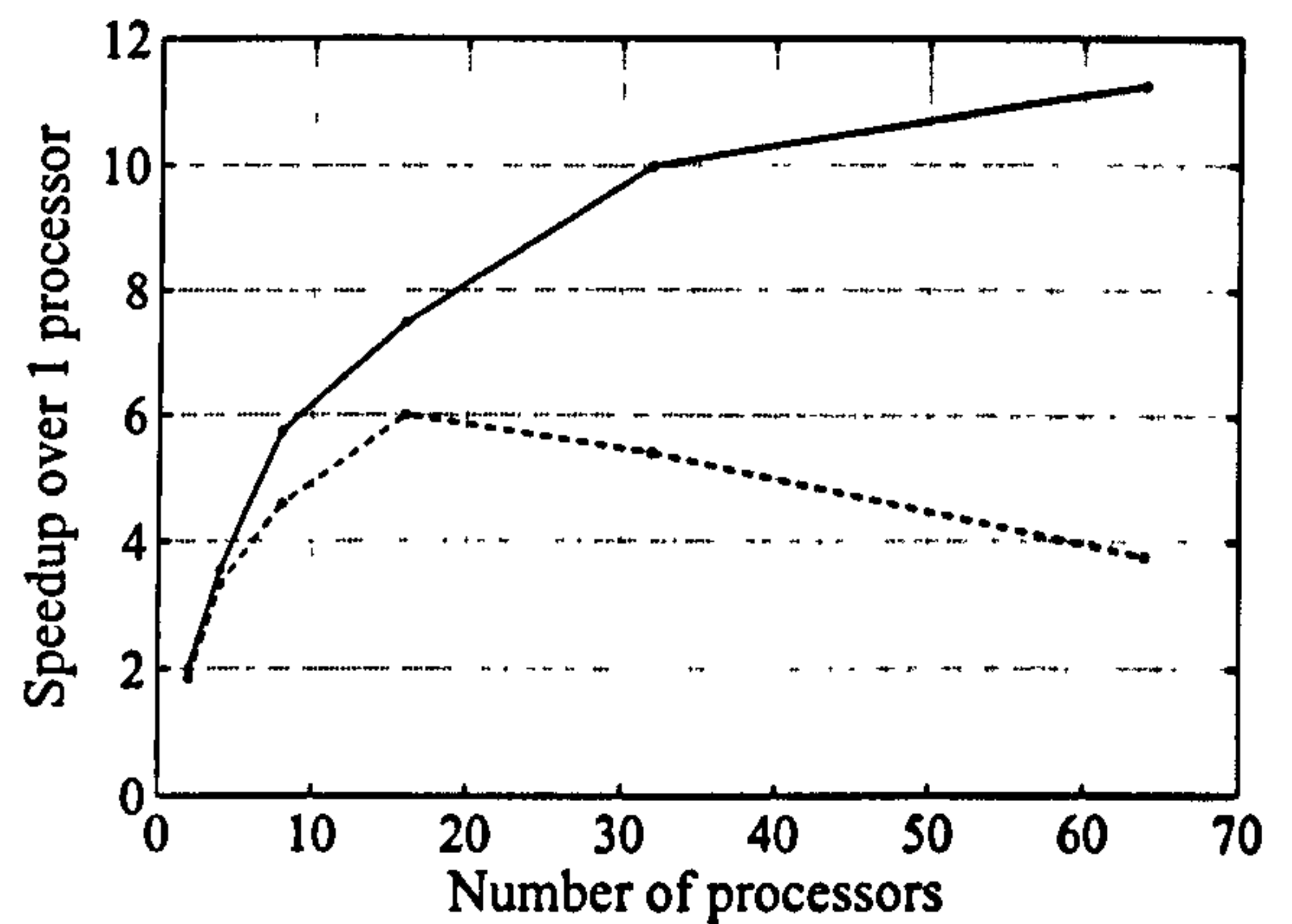


with the number of processors. The discrepancy in Fig. 6.6.18 arises from the increase in the communications overhead for the force and potential energy arrays as the number of processors increases.

Since the send and receive messages for the force and energy communications are only sent/received one at a time, this causes some processes to be temporarily idle and sit in a queue. This queue obviously becomes larger as the number of processes increases and this causes a bottleneck in the communications. Another contributor to the communications overhead is the amount of extra data sent and received to/from the root to avoid global summing the forces on all processes. Consider the spatial locality of substrate atoms following atom decomposition at  $t = 0$  ps depicted in Fig. 6.6.19. The atoms are numbered such that the decomposition corresponds to horizontal slabs. Since the potential energy and force for neighbours of a decomposition that reside on a different process are also evaluated by the host process, the number of these neighbours (say  $N_{\text{extra}}$ ) heavily influences the communications overhead. If a process is allocated  $N$  atoms, then the percentage of  $N_{\text{extra}}$  relative to  $N$  can be as small as 5 % for large  $N$ . However, as the number of processes increases,  $N$  decreases and the percentage of  $N_{\text{extra}}$  relative to  $N$  can exceed 100 %. Thus, the initial surface area of the decomposi-



(a)



(b)

Fig. 6.6.17. (a) The change in the average time per timestep as the numbers of processors increases. (b) The speedup over one processor as the number of processors increases. The solid line corresponds to the parallel MD code after performance tuning. The dashed line denotes the preliminary parallel MD code. The results are from 1 ps simulations with approximately 1.2 million atoms.



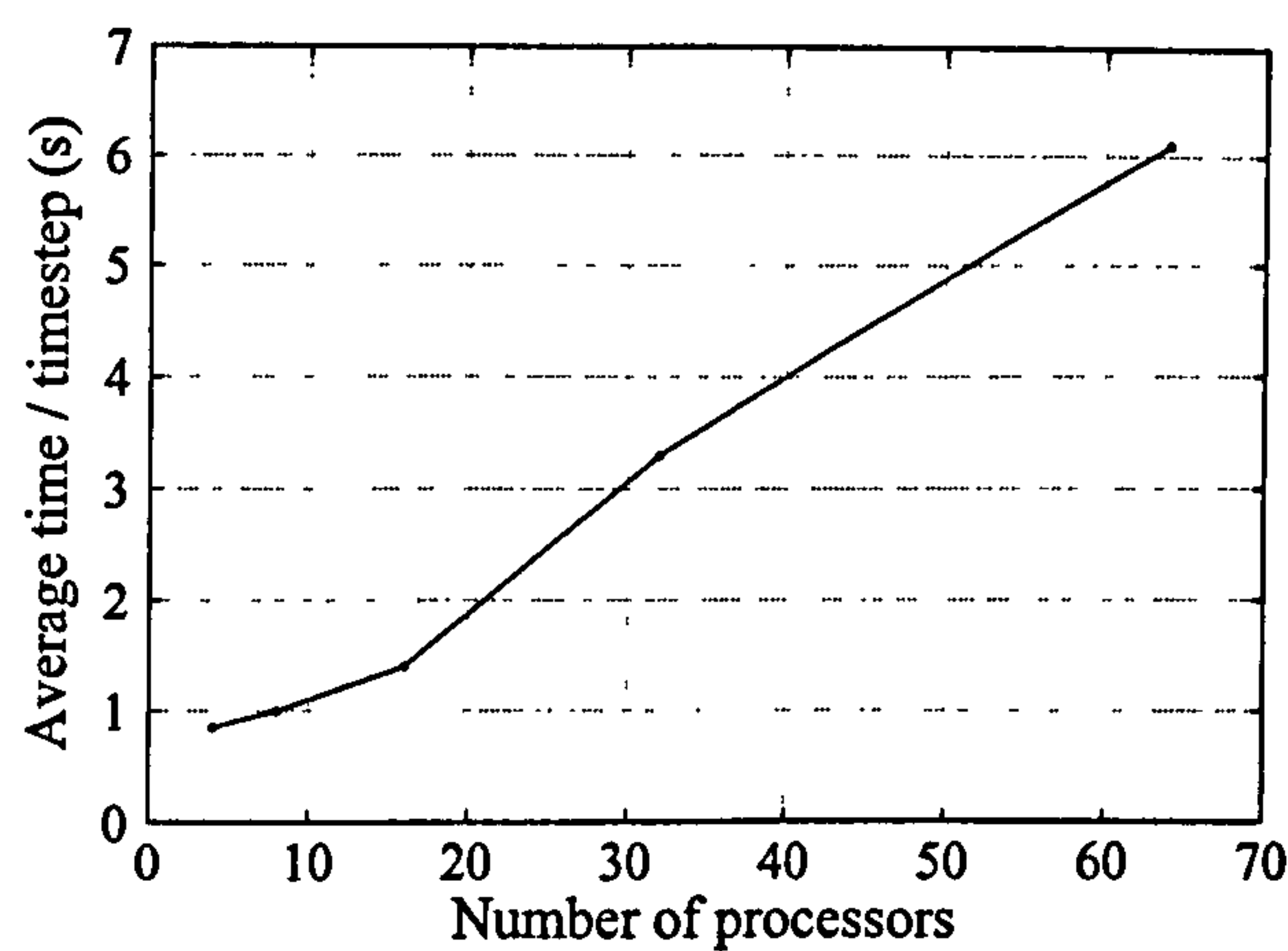


Fig. 6.6.18. The change in the average time per timestep as both the system size and number of processors doubles from approximately 0.125 million atoms on 4 processors to 2.0 million atoms on 64 processors.

tion will have a significant impact on the communications overhead. As the indentation progresses, the spatial locality of the decomposition in Fig. 6.6.19 will become highly disordered and the cost of evaluating neighbours that are not on the host process will increase. However, this could be quickly overcome in part by applying pre-processing to form vertical slabs. Here, assuming each process has a large workload, the decompo-

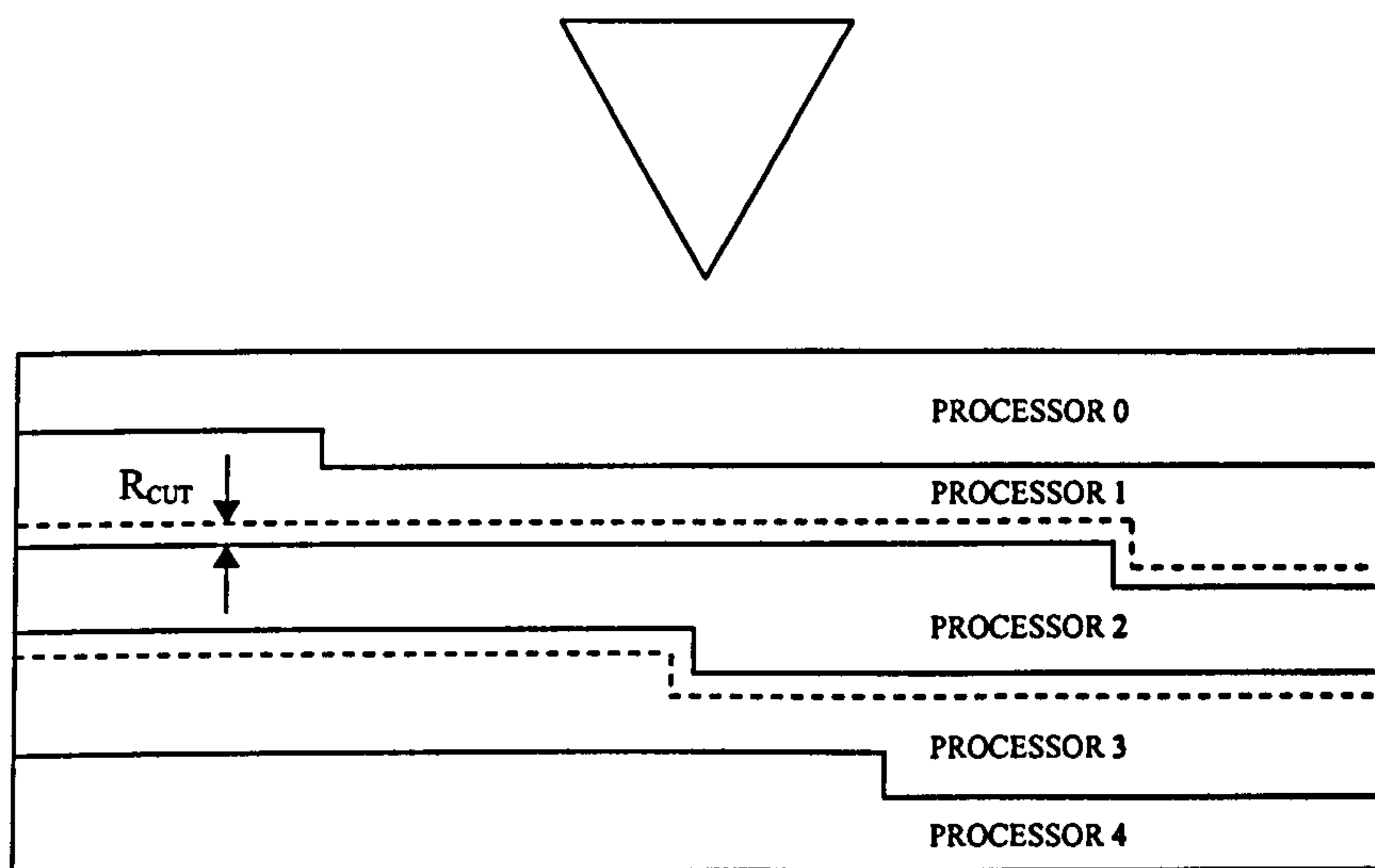


Fig. 6.6.19. Hypothetical spatial locality of substrate atoms following atom decomposition at  $t = 0$  ps. The potential energy and force for atoms within the distance  $R_{\text{CUT}}$  from the edges of the decomposition are also determined by the same process. The thickness of  $R_{\text{CUT}}$  is usually equal to the cut-off distance of the interatomic potential (for C atoms described by the Brenner potential, the thickness must also account for 2<sup>nd</sup> neighbours of the atoms interacting across the domain interfaces).



sition will maintain most of its spatial locality throughout the indentation.

Current simulations with the parallel MD code are constrained to systems of a few million atoms, using an optimum of approximately 16 processors (considering the speedup and cost in CPU hours). The speedup on 16 processors is reasonable, but it is still far from values for ideal scaling. This constraint will be primarily relaxed with improved scaling using a spatial decomposition scheme, where communication is local and not global. Simulating one million metal atoms with the EAM potential requires approximately 400 MB per processor. As the number of atoms pushes towards tens of millions then memory becomes a crucial factor and the replicated data model is insufficient. This constraint will also be relaxed with spatial decomposition since data only needs to be local and not global, i.e. each process only needs to store data for the atoms which it operates on.

## 6.9 Summary

A parallel MD program has been developed using the MPI paradigm to allow the simulation of greater atom numbers in a feasible time scale. A thorough revision of the sequential code to the Fortran 90 standard was made, incorporating many new features. A functional decomposition of the code was performed to produce a format suitable for parallelisation. Profiling the code identified potential energy and force evaluation, together with the construction of the neighbour lists as the areas which would return the largest performance gains when parallelised. The parallelisation scheme was based on atom decomposition, incorporating a dynamic load balancing algorithm that adaptively repartitioned the work load across the processes during the simulation.

Performance evaluation showed that the parallel MD code scaled poorly as the number of processes increased, since the communications overhead for the force and potential energy arrays became too dominant. This was attributed to globally summing *all* atoms that resided on a process, when only a fraction were operated on. As the number of processes increased, this fraction became smaller and smaller. Performance tuning was performed by only communicating the forces and potential energy to the root process for atoms that resided on the non-root processes and their neighbours. This resulted in better scaling to larger numbers of processors, enabling cost-effective simulations of over one million Fe atoms to be performed on 16 processors. However, scaling results showed



that the performance gain is limited as the number of processors increases since the code becomes communication bound. This was primarily attributed to the idle status of non-root processes whilst queuing to send/receive their data to/from the root. The performance of the parallel MD code has not been analysed for an all Brenner system, however, it would be expected to scale slightly better since the number of neighbours (including 2<sup>nd</sup>) is less compared with metals. Hence, the amount of data communicated to the root process will be less. Furthermore, the Brenner potential is more costly to implement than the EAM potential and therefore, the time to perform the force and energy communications with respect to the total execution time of the Brenner potential will be less.



# Chapter 7

## Million Atom Simulations of Fe Nanoindentation

### 7.1 Introduction

In recent years, low cost parallel computers have revolutionised computational materials science by permitting significant improvements in cost effectiveness. Although a multitude of million atom MD simulations have been reported on in the literature, there have only been a small number of million atom MD studies of nanoindentation [207]-[208]. In a recent investigation, Walsh *et al* [207] reported on 10 million atom simulations of nanoindentation of  $\text{Si}_3\text{Ni}_4$ . Indentations up to 100 Å were made, which resulted in the formation of cracks, voids and local pressure-induced amorphization under the indenter apex. Using thousands of processors on massively parallel machines, Vashishta *et al* [208] performed nanoindentation simulations using semiconductor materials configured from up to one billion atoms.

This chapter presents parallel MD simulations of single crystal Fe indentation, employing three different surfaces and over one million atoms. Mechanisms of material transport and indentation-induced dislocations are studied, together with the preferred crystallographic directions for pile-up. Comparisons are made with experimental results from single crystals, presented in two companion papers [209]-[210]. A small number of other research groups have examined pile-up formation and dislocation emission for metals by MD. For example, during indentation of Au {111} Kelchner *et al* [211] and Zimmerman *et al* [212] observed complex dislocations that evolved to intercept the surface. Experimentally, dislocations have also been studied in detail for Au [213], Cu



[214] and Ni [215]. However, there are few direct comparisons in the literature between simulation and experiment for single metal crystals. The simulation results in this chapter highly reproduce experimental observations for pile-up formation in the bcc work material. The simulations were run on dual processor Macs and multi-processor SGI machines in Sydney, Australia and also at Manchester University.

## 7.2 Adding Curvature to the Indenter Tip

The ability to simulate over one million atoms in an efficient way allows the use of a much larger indenter to penetrate to increased depths. To generate a more realistic indenter, the tip can be computationally rounded to give a defined radius of curvature. Consider a cube-cornered pyramid surrounded by a hemisphere as illustrated in Fig. 7.7.1(a). The pyramid is positioned in the centre of the hemisphere such that the three corners intersect the hemisphere at a certain radial distance. The radius of the hemisphere ( $r_{\text{hem}}$ ) is given by  $\frac{a_0}{\sqrt{3}}$ , where  $a_0$  is the pyramidal edge side length. The height of the indenter ( $h_{\text{ind}}$ ) is given by  $\frac{a_0}{\sqrt{6}}$  and therefore the sphere completely encompasses the pyramid. Fig. 7.7.1(b) illustrates a vertical cross-section through the pyramid, denoted by AB in Fig. 7.7.1(a). The angle of the edge AC with the horizontal plane is denoted by  $\phi_1$ , which is equal to  $\arctan\left(\frac{1}{\sqrt{2}}\right)$ . Now consider positioning a sphere with radius  $r_{\text{curv}}$  and centre  $o$ , such that the vertex of two adjacent pyramidal planes (i.e. AC in Fig. 7.7.1(b)) is tangential to the sphere. This imposes a constraint such that the maximum radius of curvature is  $a_0$ . The surface of the tip is illustrated by the path  $p_1$  to  $p_2$ . The distances  $h_1$  and  $h_2$  are computed from

$$h_1 = r_{\text{curv}} \cos(\phi_2) \tan(\phi_1) \quad (7.2.7.1)$$

$$h_2 = r_{\text{curv}} \sin(\phi_2) \quad (7.2.7.2)$$

and together, define the height at which the sphere must be positioned for tangential intersection with the adjoining pyramidal planes. Furthermore,  $h_1$  denotes the critical cut-off distance below which surface is described by the equation of the sphere.

To generate a rounded pyramidal tip with a radius of curvature  $r_{\text{curv}}$  the indenter is first constructed as detailed in Section 4.2, Chapter 4. The values  $h_1$  and  $h_2$  are computed from Eqn. 7.2.7.1 and Eqn. 7.2.7.2 respectively, to position the sphere for



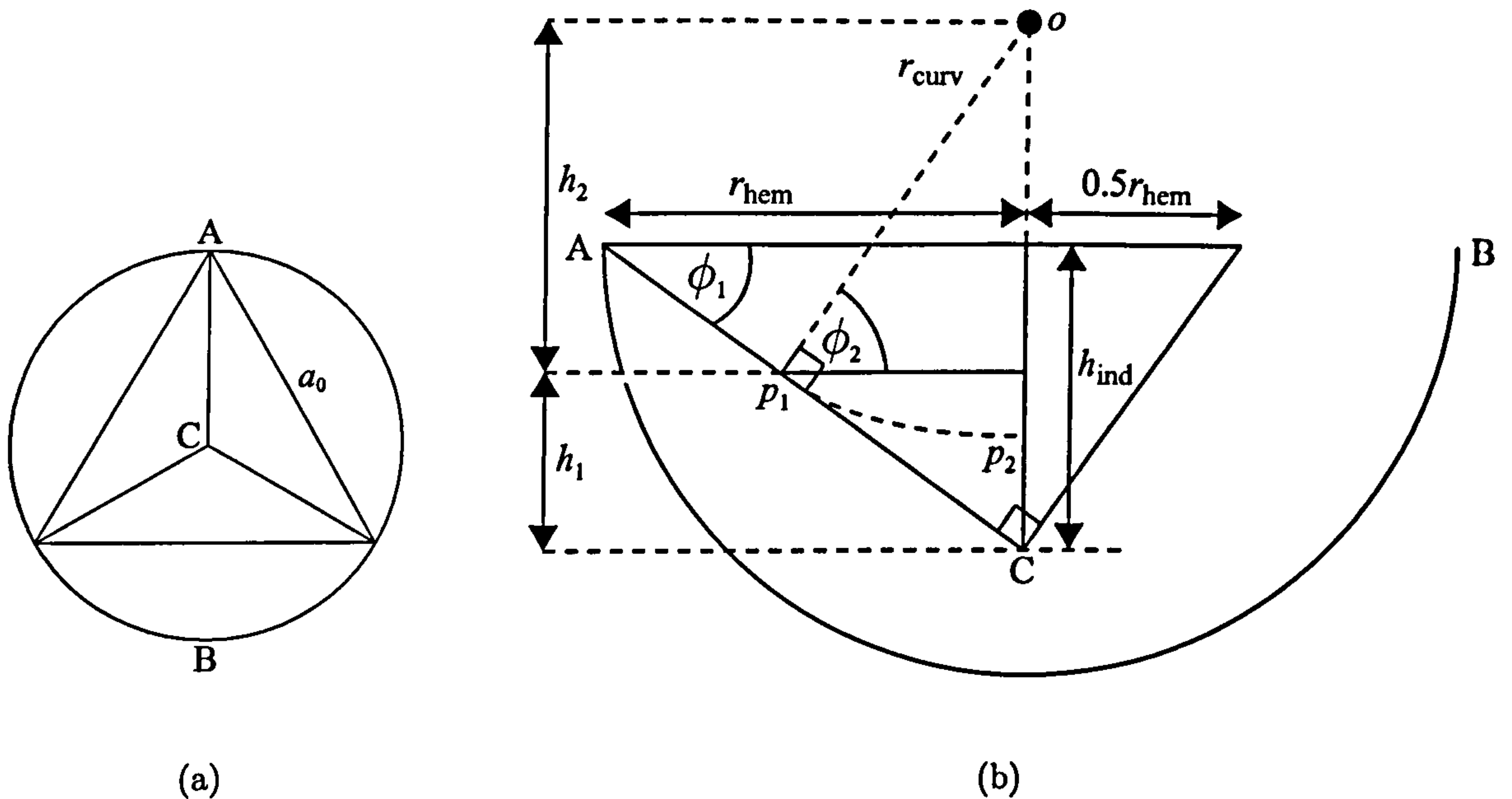


Fig. 7.7.1. (a) Plan view of a sphere encompassing a cube-cornered pyramid of side length  $a_0$  with tip positioned at C. (b) Schematic representation of a vertical cross-section of the pyramid along a vertex of two adjacent planes, illustrating the method for applying curvature to the apex.

a given radius of curvature. Any atoms that are located within a distance  $h_1$  from the apex and reside outside the region encompassed by the sphere are then physically removed. Following the addition of tip curvature, the indenter is equilibrated in the same manner as before.

### 7.3 Simulation Details

A pyramidal indenter with a radius of curvature  $\approx 100$  Å is used, as illustrated in Fig. 7.7.2. The structure has a height of approximately  $h = 63$  Å with an edge side length of  $a = 162$  Å, and is configured from 64,373 atoms, with 5,184 atoms forming the fixed top layers. Each substrate has approximate dimensions  $300$  Å  $\times$   $300$  Å  $\times$   $150$  Å and is generated from just over 1.1 million atoms. The  $\{110\}$ ,  $\{100\}$  and  $\{111\}$  substrates are configured from 74, 106 and 183 atomic layers respectively. The vertical edges and bottom two layers of the substrate are held fixed, while all remaining atoms are damped. At the beginning of each simulation, the indenter apex is sited 4 Å above the middle of the substrate surface and the maximum displacement of the constrained indenter atoms,



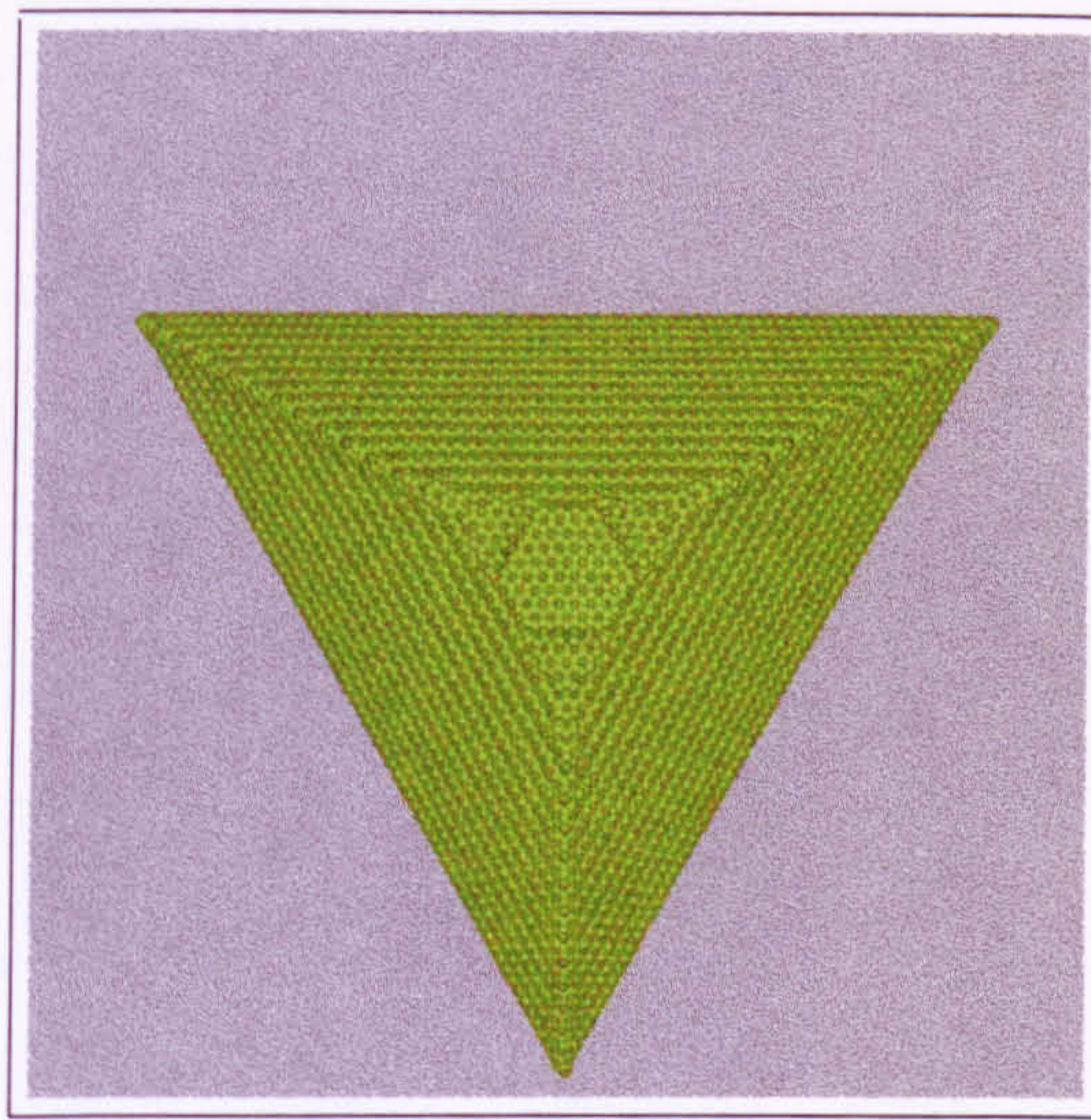


Fig. 7.7.2. Plan view of the large indenter used in the million atom Fe simulations, with a radius of curvature of 100 Å.

$r_{\max}$ , is set to 44 Å. Tests with different indentation periods were performed and the speed reduced until very similar force-depth curves were produced. This resulted in a period of 90 ps being used, giving an average indentation speed of 98 ms<sup>-1</sup>. The classical

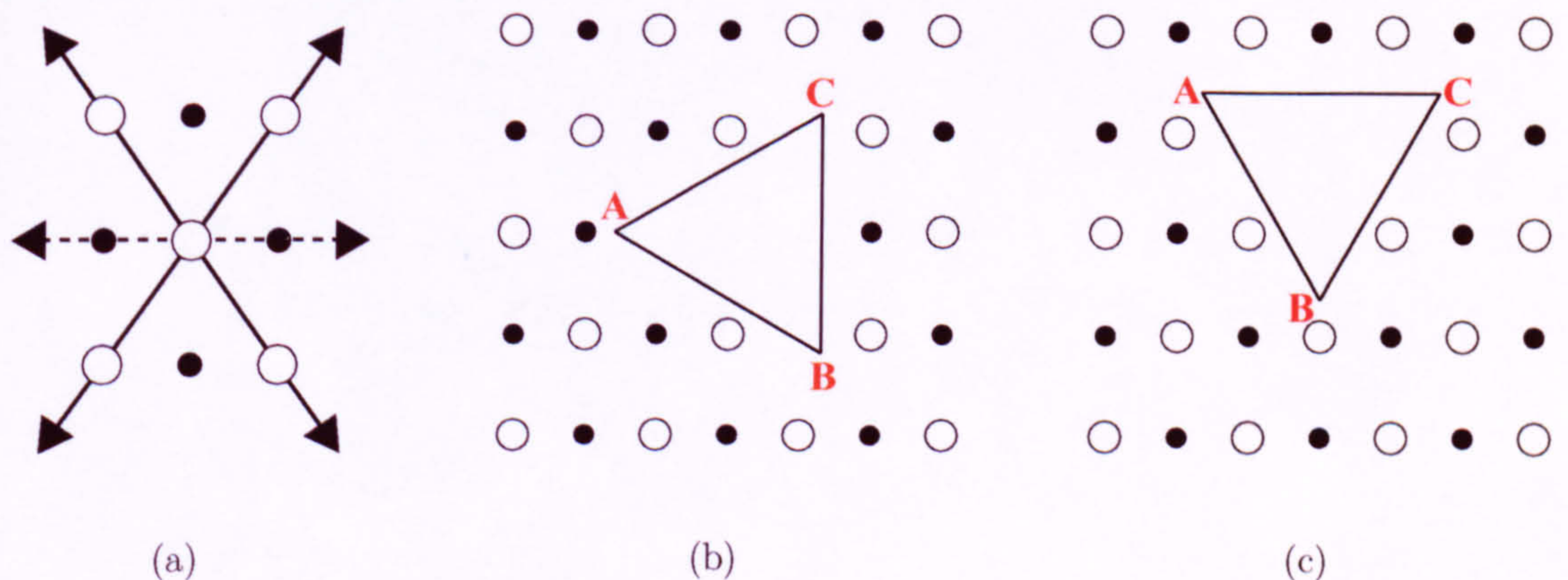


Fig. 7.7.3. Nearest neighbour directions in the {110} plane. The solid arrows represent the in-plane  $\langle 111 \rangle$  directions and the dashed arrows denote the out-of-plane  $\langle 111 \rangle$  directions. (b),(c) Plan views of the indenter rotation with respect to the atomic structure of the {110} substrate for: (b)  $\phi = 0^\circ$ ; (c)  $\phi = 30^\circ$ . Unshaded and shaded circles denote 1<sup>st</sup> and 2<sup>nd</sup> layer atoms respectively. In (b) the indenter side BC is adjacent to the out-of-plane  $\langle 111 \rangle$  direction, with the normal to the remaining sides aligned by  $5.26^\circ$  from the in-plane  $\langle 111 \rangle$  direction. In (c) the normal to the indenter side AC is aligned by  $35.26^\circ$  from the in-plane  $\langle 111 \rangle$  direction with the remaining sides aligned from  $24.74^\circ$ .



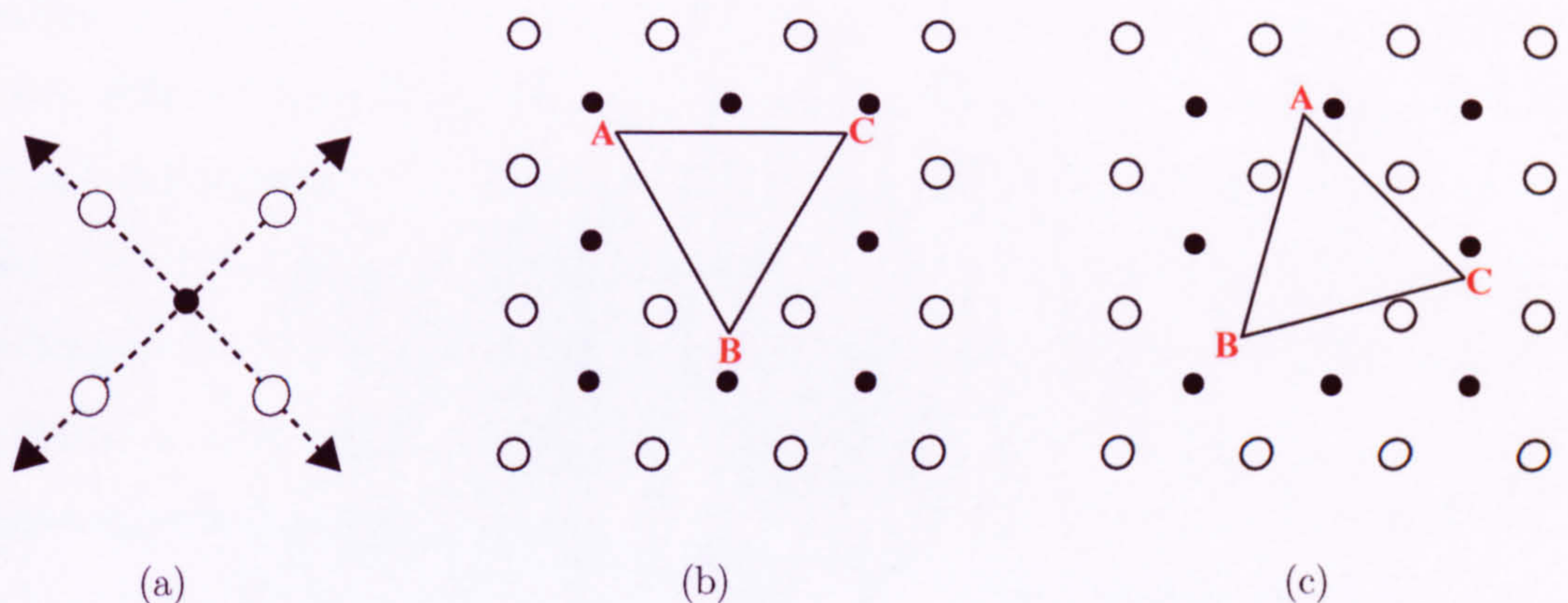


Fig. 7.7.4. (a) Nearest neighbour directions in the  $\{100\}$  plane. The dashed arrows denote the out-of-plane  $\langle 111 \rangle$  directions. (b),(c) Plan views of the indenter rotation with respect to the atomic structure of the  $\{100\}$  substrate for: (b)  $\phi = 0^\circ$ ; (c)  $\phi = 45^\circ$ . Unshaded and shaded circles denote 1<sup>st</sup> and 2<sup>nd</sup> layer atoms respectively. In (b) the indenter side AC is parallel to  $\langle 100 \rangle$  with the normal to the remaining sides aligned  $15^\circ$  from the out-of-plane  $\langle 111 \rangle$  direction. In (c) the indenter side AC is adjacent to the out-of-plane  $\langle 111 \rangle$  direction with the normal to the remaining sides aligned  $30^\circ$  from the out-of-plane  $\langle 111 \rangle$  direction.

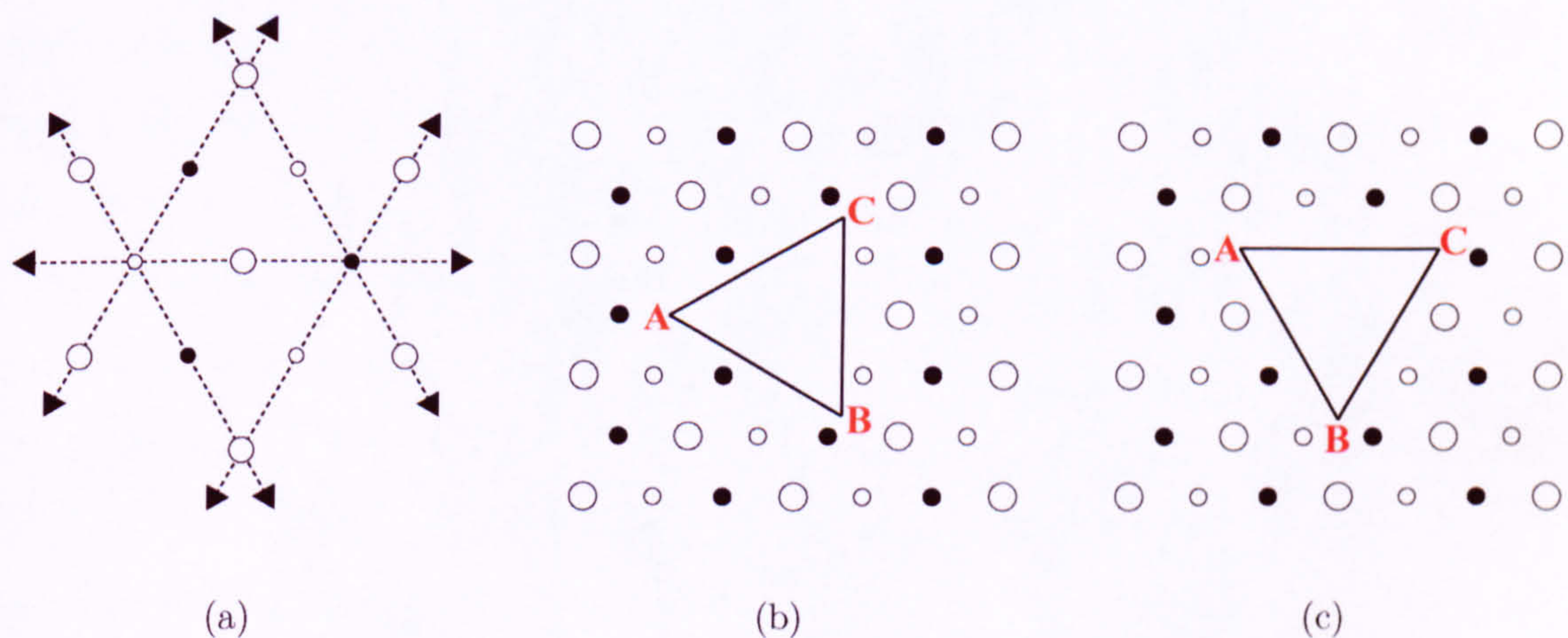


Fig. 7.7.5. (a) Nearest neighbour directions in the  $\{111\}$  plane. The dashed arrows denote the out-of-plane  $\langle 111 \rangle$  directions. (b),(c) Plan views of the indenter rotation with respect to the atomic structure of the  $\{111\}$  substrate for: (b)  $\phi = 0^\circ$ ; (c)  $\phi = 30^\circ$ . Large and small unshaded circles denote 1<sup>st</sup> and 3<sup>rd</sup> layer atoms respectively, while shaded circles represent 2<sup>nd</sup> layer atoms. The normal of each indenter side is aligned to out-of-plane  $\langle 111 \rangle$  directions in (b) and mis-aligned by  $30^\circ$  in (c).



equations of motion for all atoms are integrated with a constant timestep of 1.0 fs.

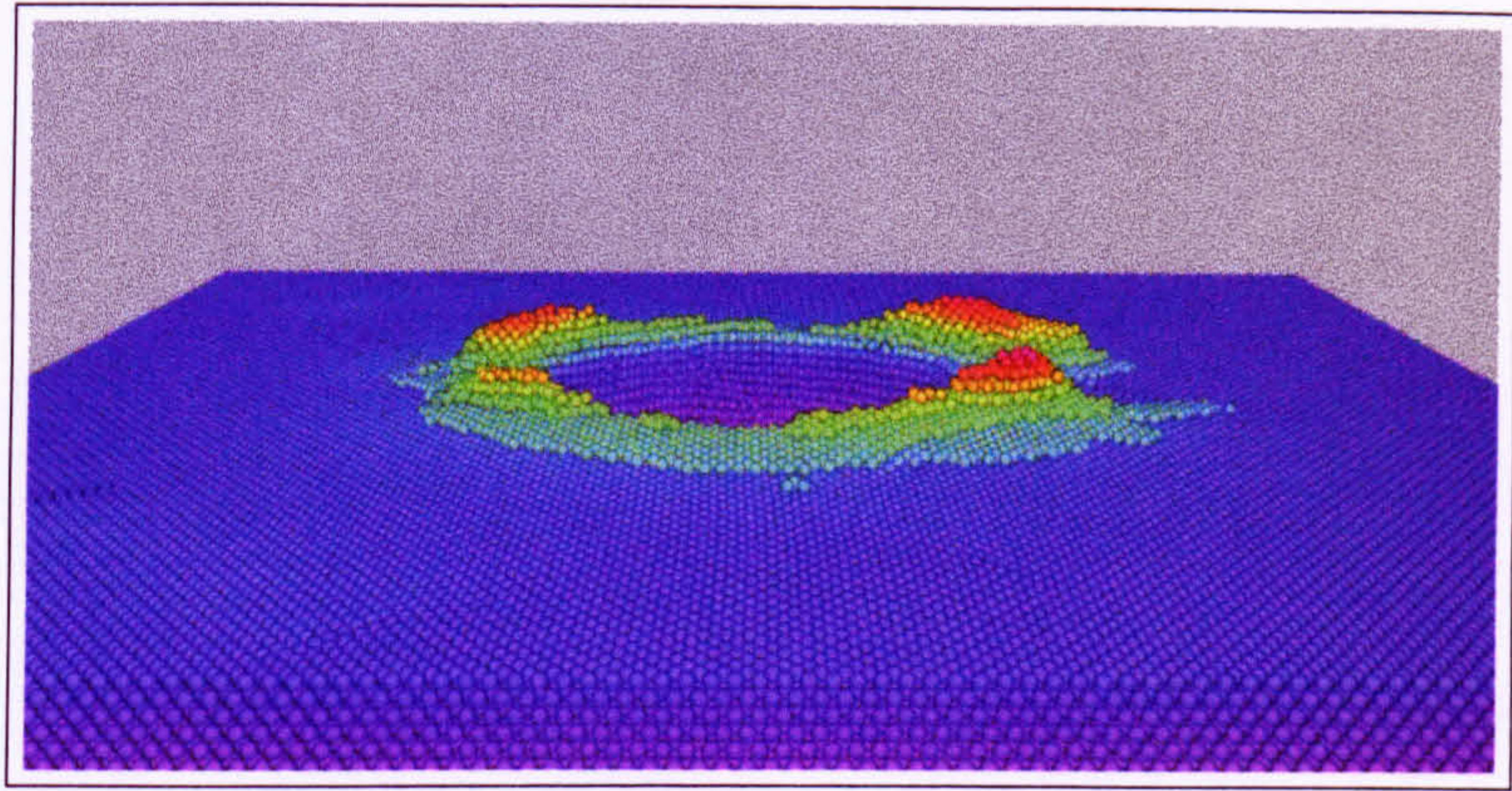
Two different rotations of the indenter are considered for all three substrates to reflect the crystal symmetry of the substrate with respect to the three-fold symmetry of the indenter. The rotations are defined by  $\phi$ , as shown in Fig. 7.7.3 - Fig. 7.7.5 together with the compact  $\langle 111 \rangle$  directions for the three crystal surfaces studied. Only the  $\{110\}$  surface contains *both* in-plane and out-of-plane  $\langle 111 \rangle$  directions. Neither the  $\{100\}$  or  $\{111\}$  surfaces contain in-plane  $\langle 111 \rangle$  directions. For comparison with experimental results for conical indentation in one of the companion papers [209], an additional simulation with Fe  $\{110\}$  is performed with the paraboloidal interface (as described in Chapter 3), where a radius of curvature of 25 Å is used. Since the deformation that occurs in metal crystals is anisotropic, deformation induced with the axisymmetric paraboloid interface should reflect the substrate crystal structure.

## 7.4 Simulation Results and Discussion

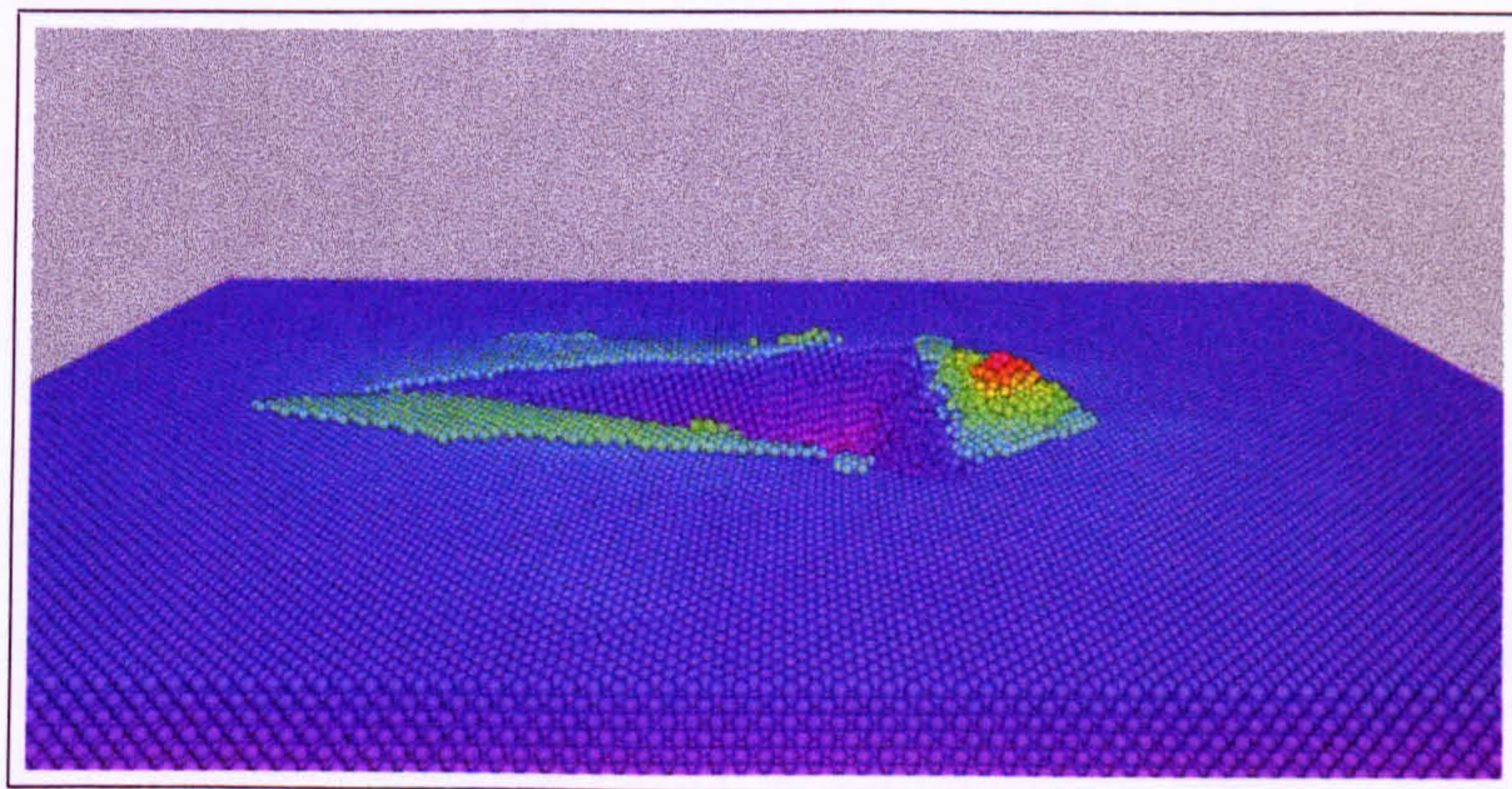
### 7.4.1 Fe $\{110\}$ Substrate

The surface image in Fig. 7.7.6(a) clearly reflects the two-fold crystal symmetry of the work material. For small indentation depths, the pile-up is observed to occur preferentially along the four in-plane  $\langle 111 \rangle$  directions. As the pile-up increases, the hillocks merge together along the out-of-plane  $\langle 111 \rangle$  direction. Thus, for larger indentation depths the pile-up will appear as two separate hillocks, extending along the out-of-plane  $\langle 111 \rangle$  directions. For indentation with the pyramidal indenter in Fig. 7.7.6(b) and (c), the indenter asymmetry is reflected. In Fig. 7.7.6(b) the pile-up is greatest along the side of the indent adjacent to the out-of-plane  $\langle 111 \rangle$  directions (i.e. side BC in Fig. 7.7.3(b)), where it extends to 5-6 layers in height. Here, the normal to the side of the indent is in the direction of the nearest neighbours and so pile-up occurs preferentially. Along the remaining sides of the indent the pile-up is considerably less at only 1-2 layers. This is because the normal of the indent sides is mis-aligned from the nearest neighbour directions. The image in Fig. 7.7.6(c) clearly shows preferential pile-up of 3 layers along the sides left and right of the indent (i.e. sides AB and BC in Fig. 7.7.3(c)). The remaining side of the indent is parallel with the out-of-plane  $\langle 111 \rangle$  directions and shows a much smaller pile-up yield of only 1 layer. This occurs since the normal of the indent

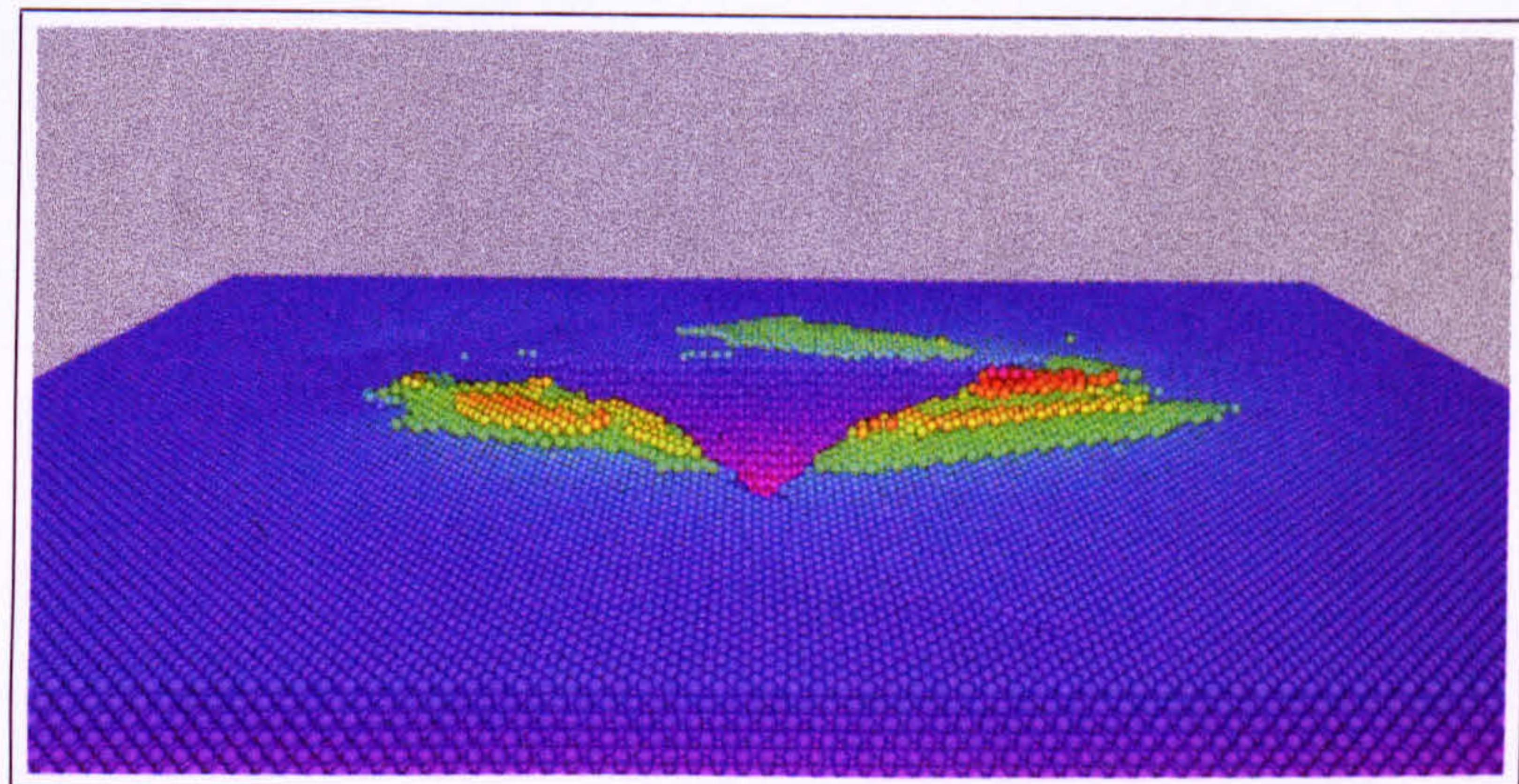




(a)



(b)



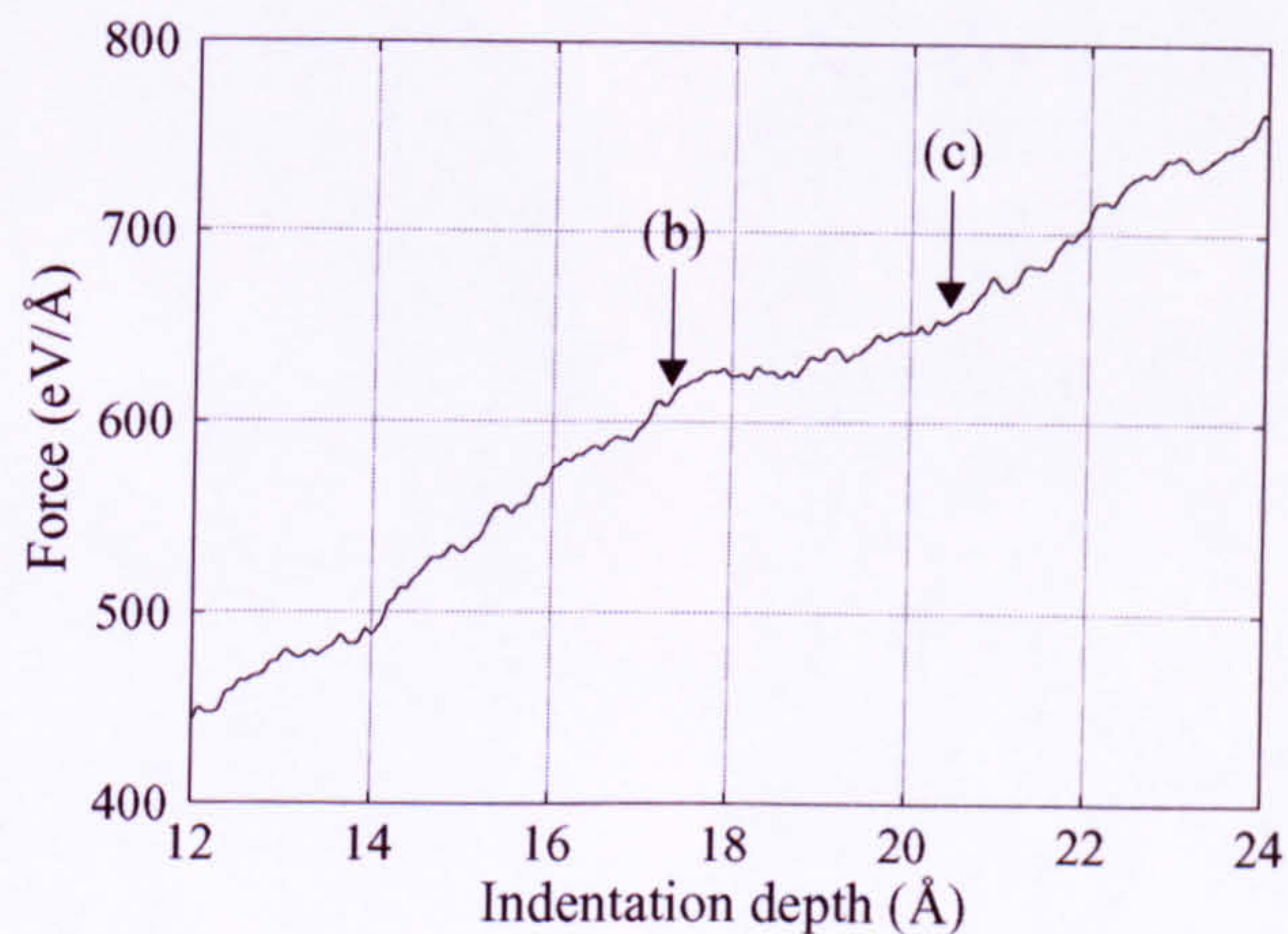
(c)

Fig. 7.7.6. The surface of the Fe {110} substrate following indentation by: (a) Paraboloid interface; (b) Pyramidal tip with  $\phi = 0^\circ$ ; (c) Pyramidal tip with  $\phi = 30^\circ$ . Atoms are coloured according to their vertical position from the undisturbed surface.

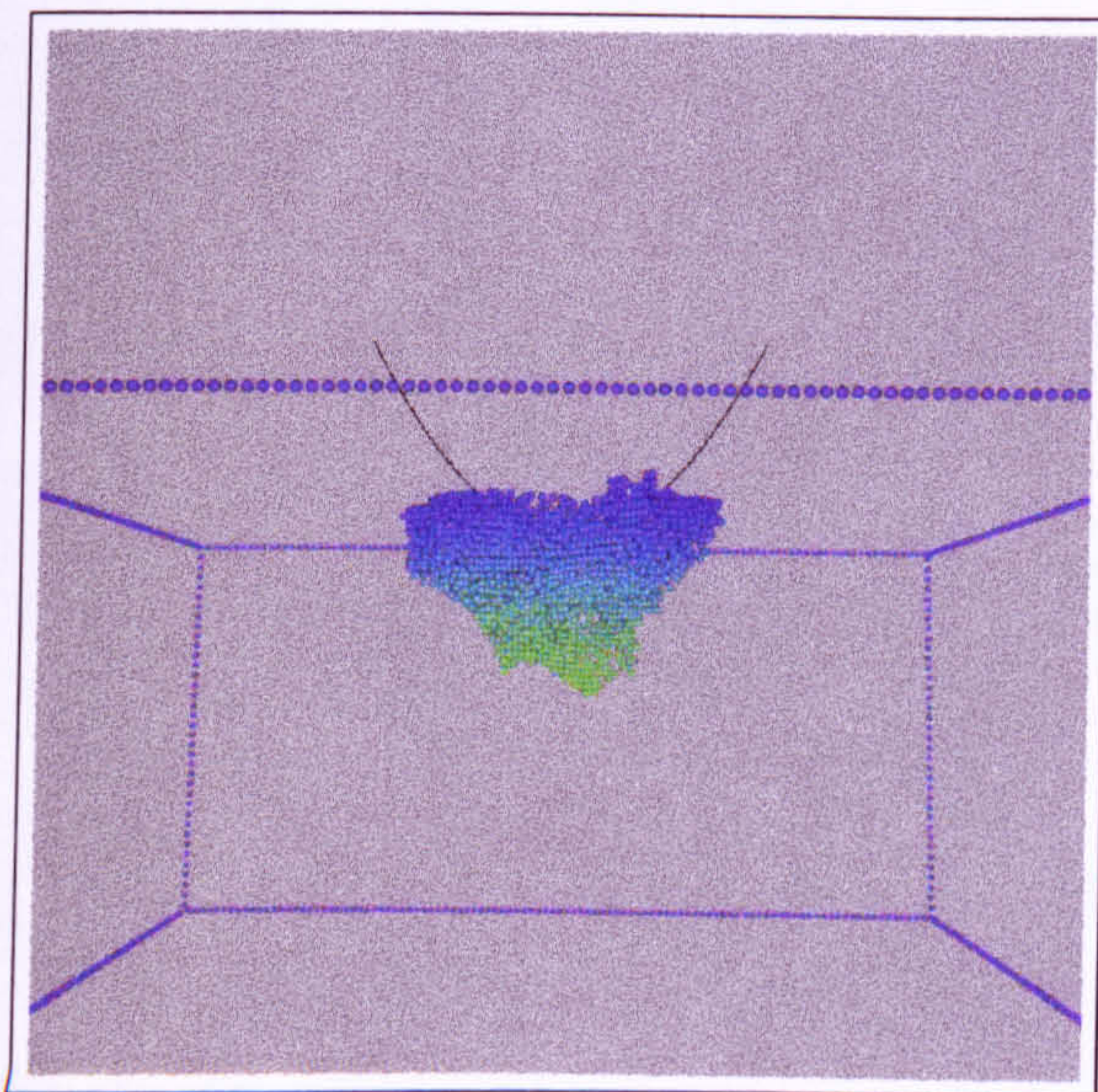


sides AB and BC in Fig. 7.7.3(c) is closer to the nearest neighbour directions compared with the normal to side AC.

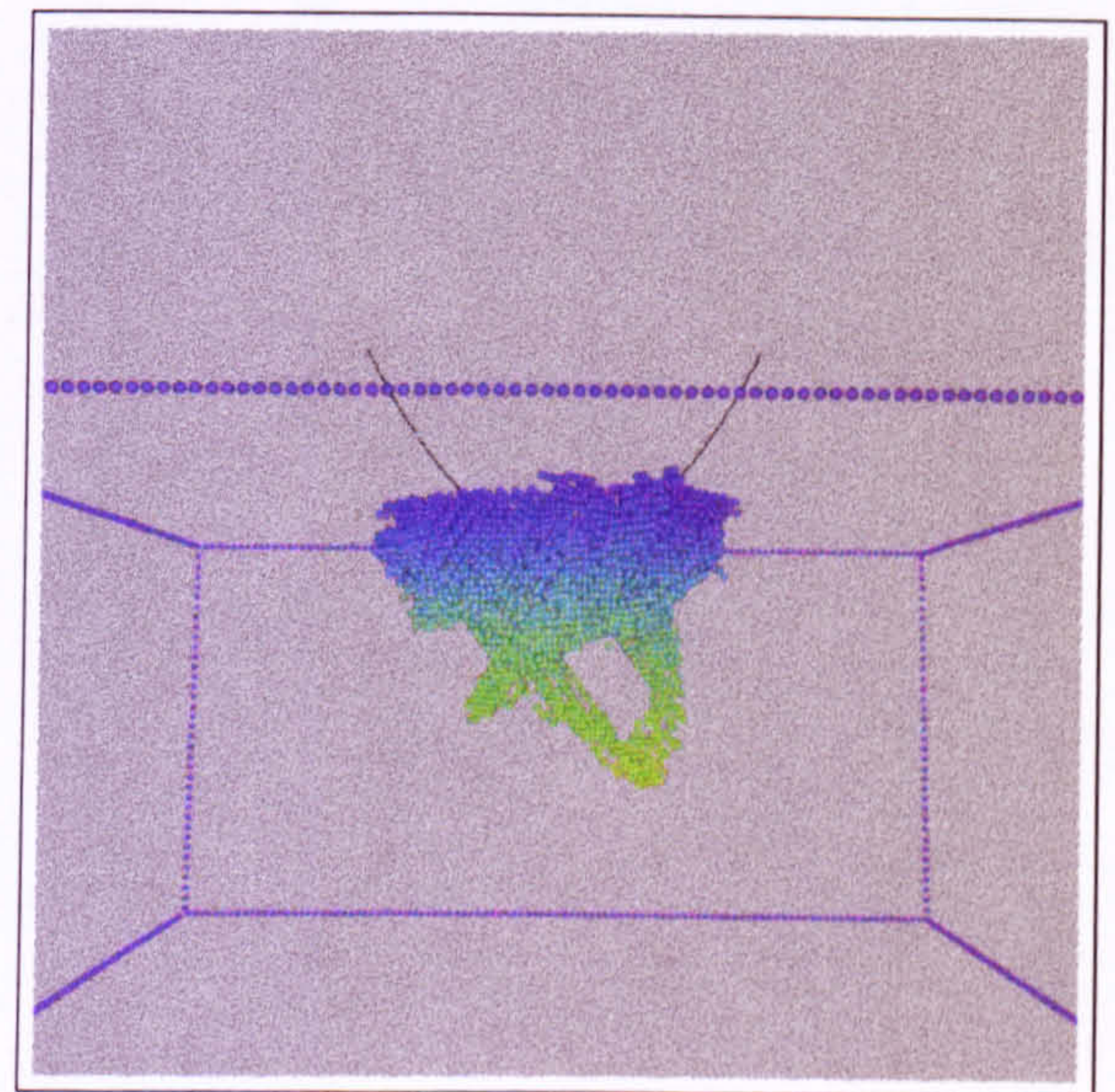
A 'pop-in' is shown close-up in the force-depth curve in Fig. 7.7.7(a) over the inden-



(a)



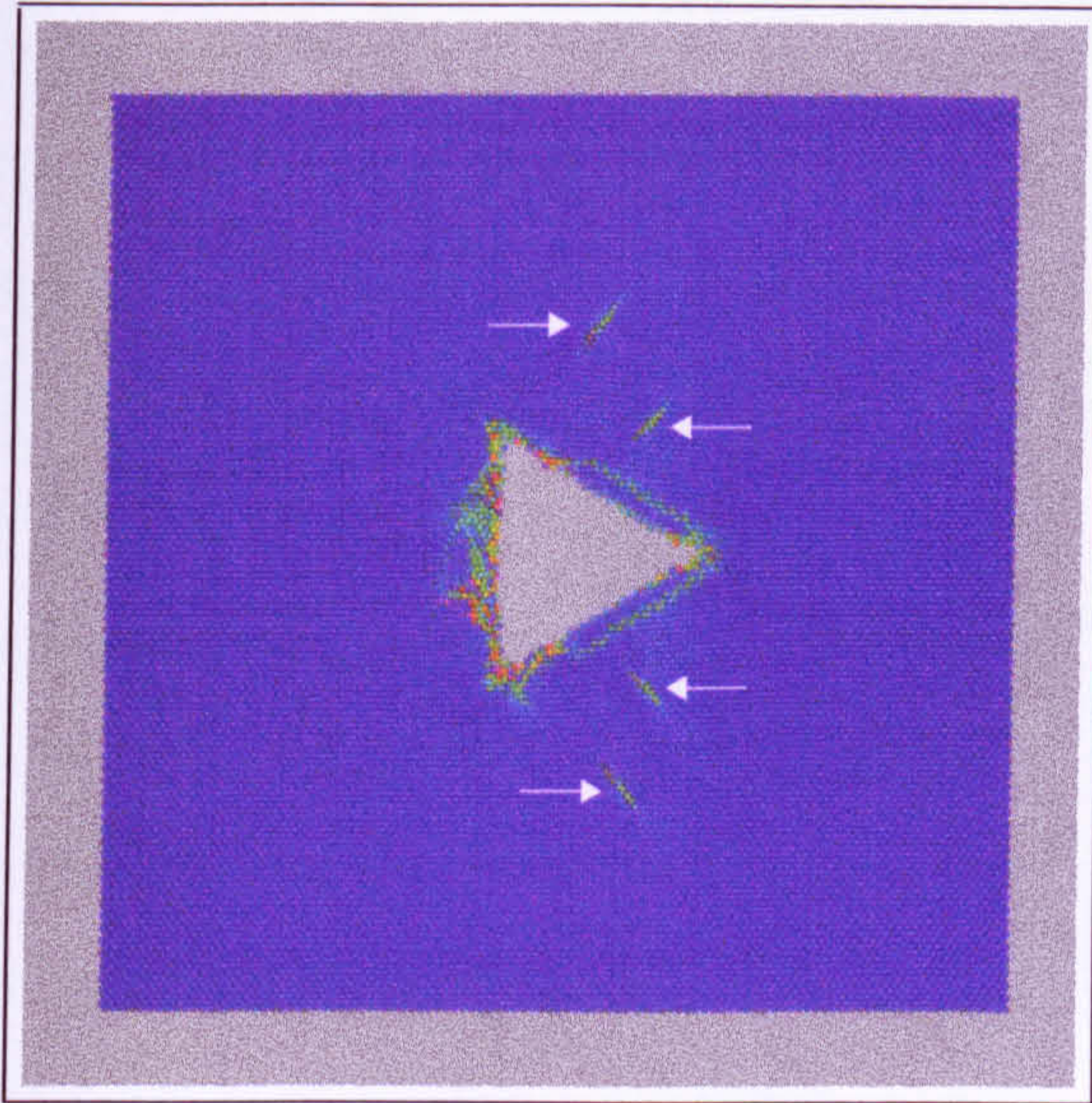
(b)



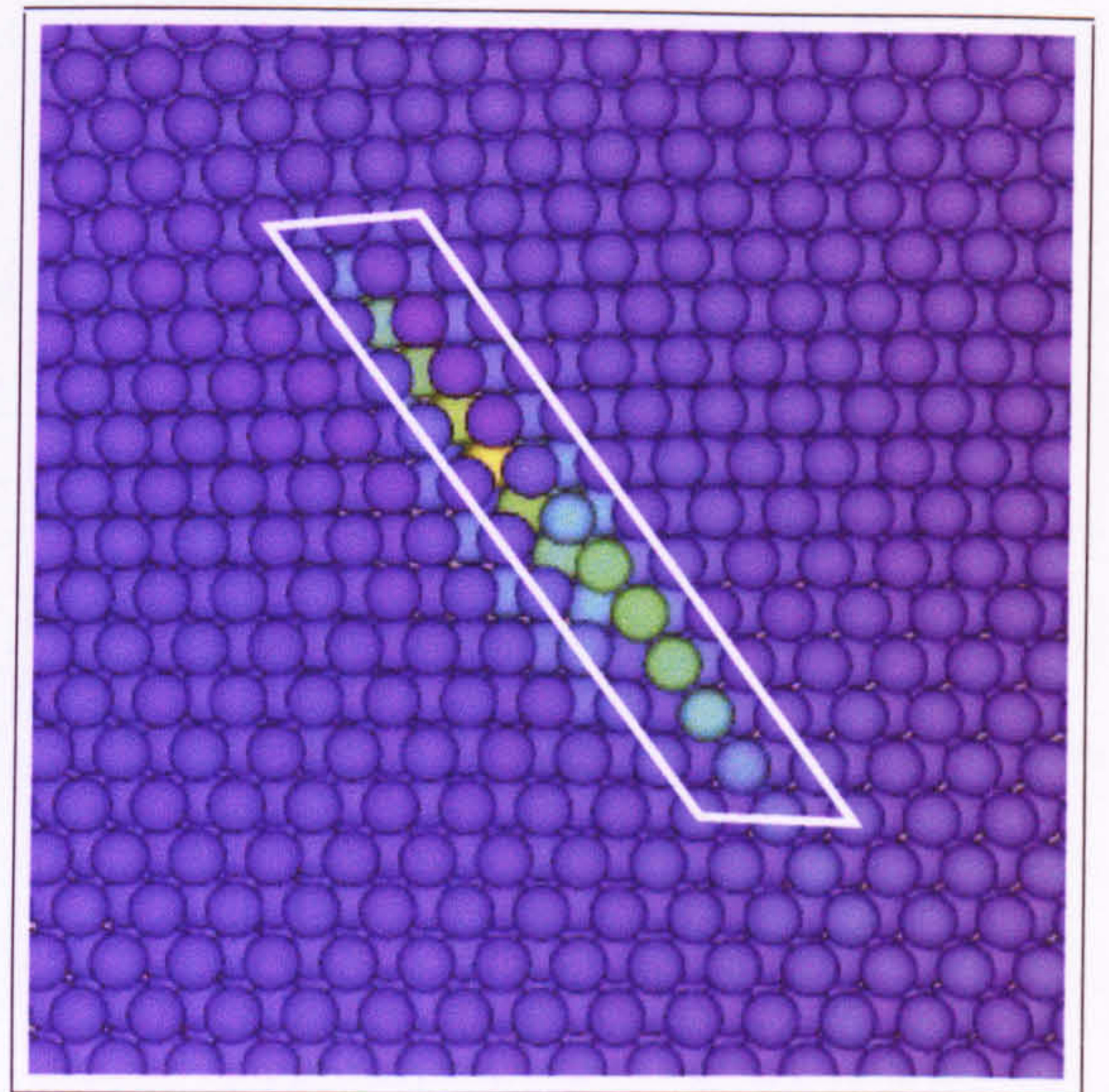
(c)

Fig. 7.7.7. Region of the force-depth curve from indentation of Fe {110} with the paraboloid interface showing a 'pop-in' over the approximate depth range 17.5 Å - 19.0 Å. Substrate atoms and the interface profile before (b) and after (c) the emission of a dislocation loop in the  $\langle 111 \rangle$  direction, corresponding to the arrows in (a). Atoms are shown in the energy range -4.0 eV to -4.2 eV (93 % - 98 % of the Fe cohesive energy) and shaded on their vertical position from the undisturbed surface. The outermost blue shaded atoms simply denote the edge of the substrate.

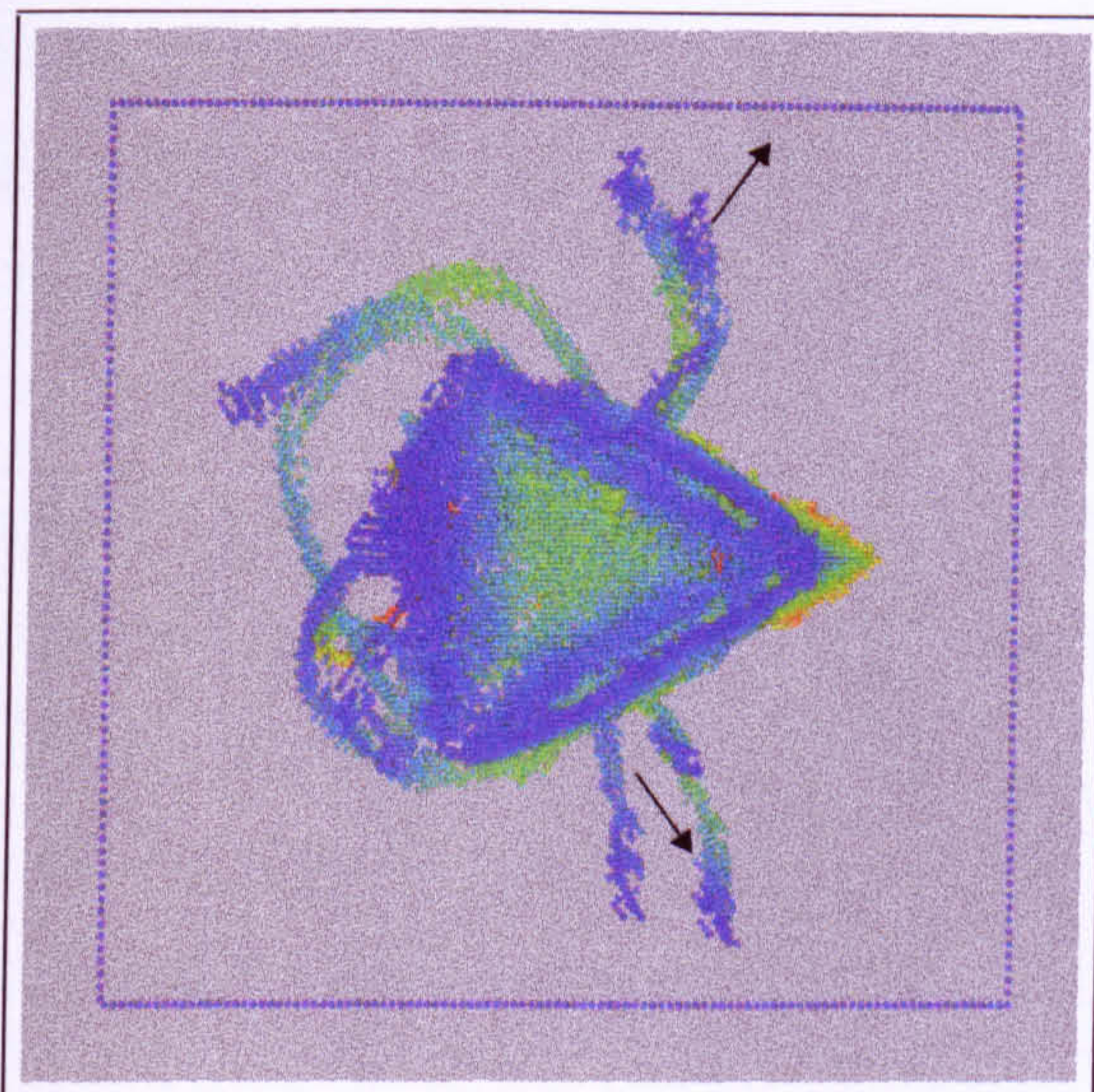




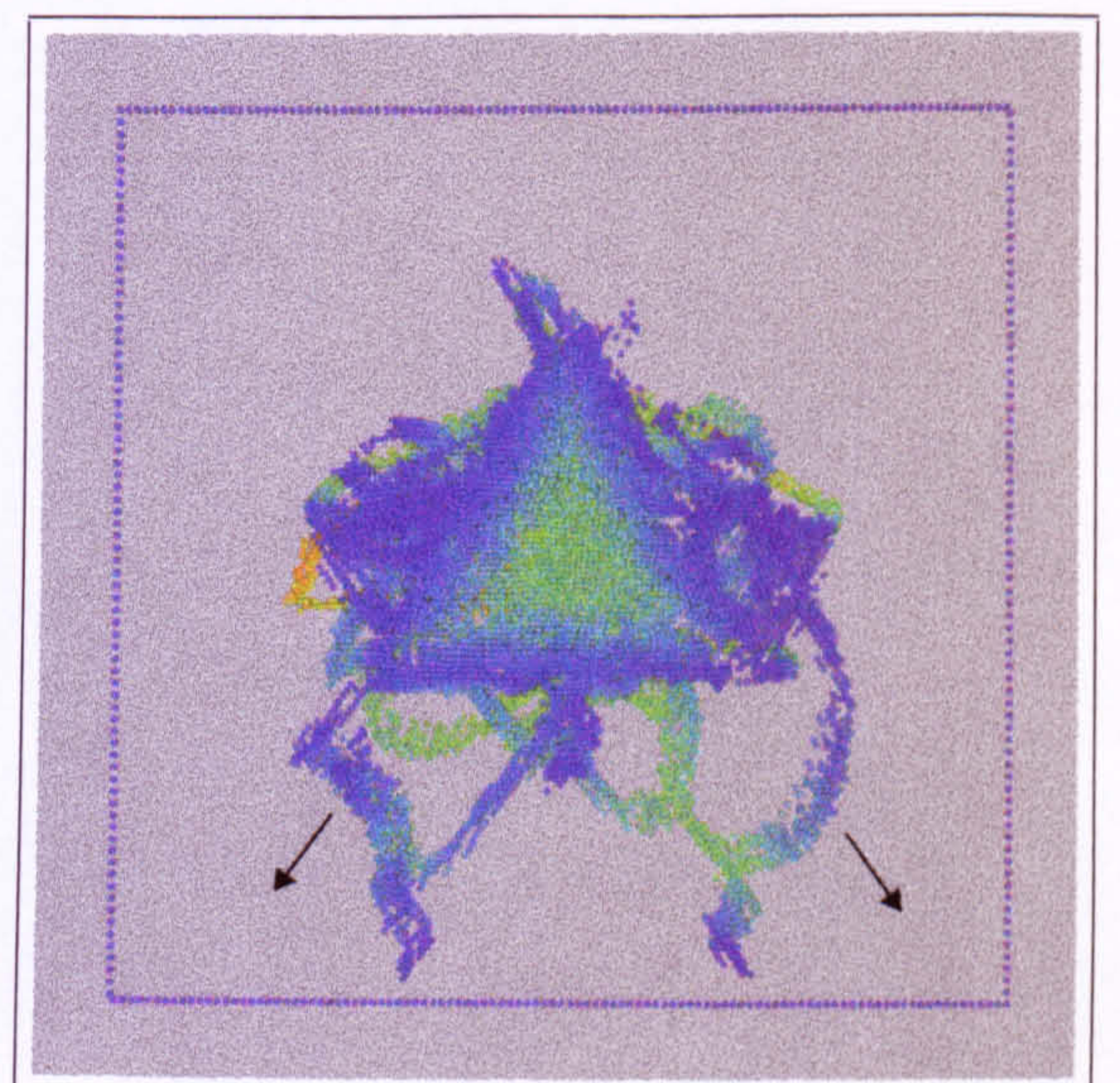
(a)



(b)



(c)



(d)

Fig. 7.7.8. Dislocations in Fe {110} at: (a),(b)  $t = 18$  ps with  $\phi = 0^\circ$ ; (c)  $t = 45$  ps with  $\phi = 30^\circ$ ; (d)  $t = 45$  ps with  $\phi = 30^\circ$ . In (a) and (b) the atoms are shaded on energy. For (c) and (d) atoms are shown in the energy range -4.0 eV to -4.2 eV (93 % - 98 % of the Fe cohesive energy) and shaded on their vertical position from the undisturbed surface. In (a), arrows mark the intersection of dislocation loops with the surface. In (c) and (d), arrows mark the direction of motion for the dislocation loops along the in-plane  $\langle 111 \rangle$  directions. The outermost blue shaded atoms simply denote the substrate edge.



tation range  $\approx 17.5 \text{ \AA} - 19.0 \text{ \AA}$  for indentation with the paraboloid interface. The images in Fig. 7.7.7(b) and (c) show that this coincides with the emission of a dislocation loop from underneath the tip <sup>1</sup>. To study the structures of dislocations, the potential energy of atoms between 93% - 98% of the Fe cohesive energy is filtered. However, this method is somewhat limited in that it may also include regions of elastically deformed material in addition to defects. As the indentation progresses, more dislocation loops are emitted. These are shown in Fig. 7.7.8 and Fig. 7.7.9 for indentation with the pyramidal indenter. Some of the dislocation loops emitted intersect the surface, as marked by the arrows in Fig. 7.7.8(a), and transport material away from the indent along the in-plane  $\langle 111 \rangle$  directions. The intersection with the surface introduces a stacking fault, as shown in the encompassed region in Fig. 7.7.8(b), and appears as a 'bump'. Plan views of the dislocation loops are shown in Fig. 7.7.8(c) and (d), where the arrows denote the direction of motion for the loops <sup>2</sup>. Interestingly, there is broad reflection symmetry for the dislocation loops occurring about the out-of-plane  $\langle 111 \rangle$  directions for  $\phi = 0^\circ$  and adjacent to the out-of-plane  $\langle 111 \rangle$  directions for  $\phi = 30^\circ$ . For the  $\{111\}$  and  $\{100\}$  faces, dislocations will not be observed propagating across the surface, since the  $\langle 111 \rangle$  directions are only out-of-plane and not in-plane.

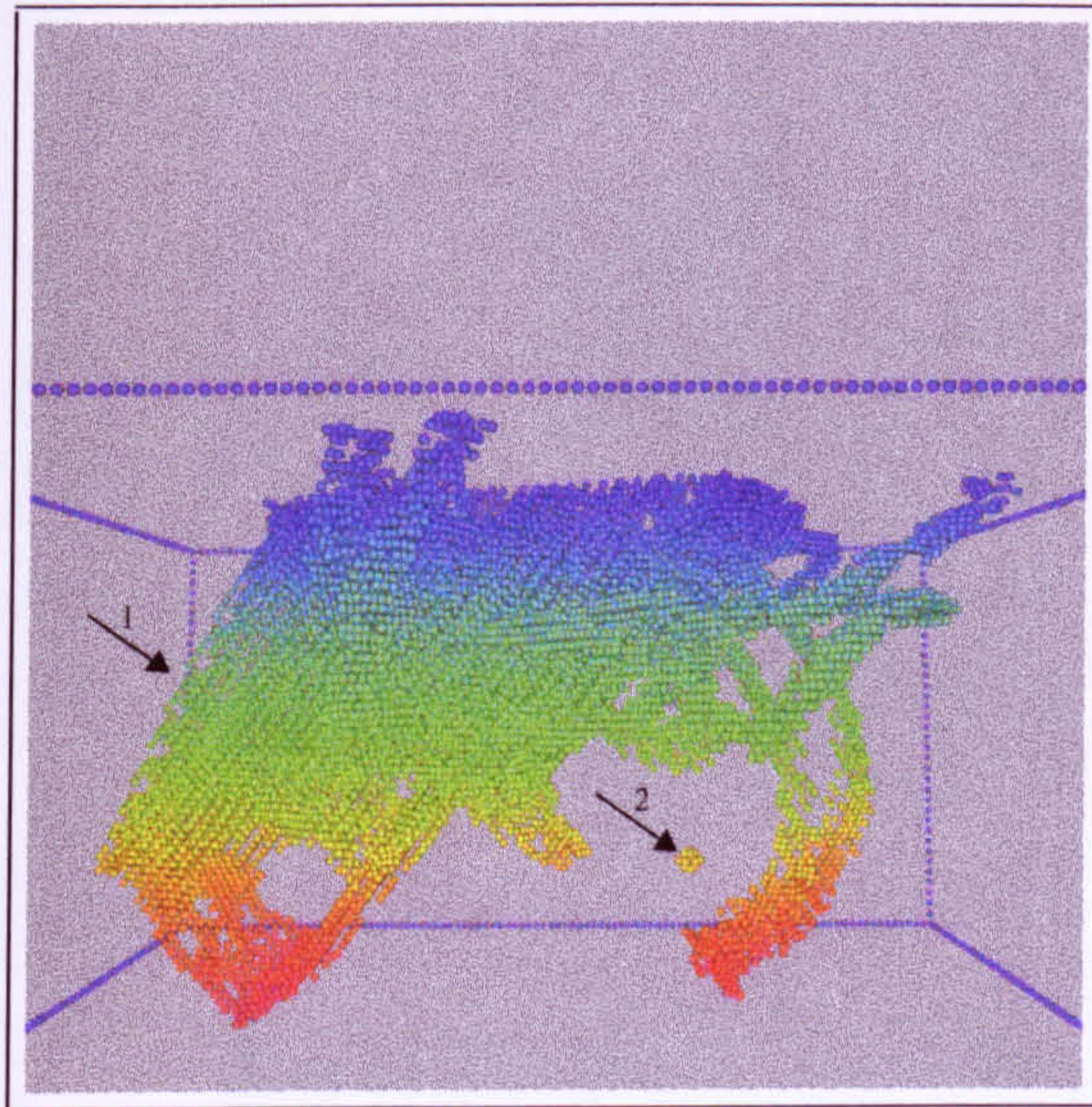
Side views of the dislocations in the work material are shown in Fig. 7.7.9, at the maximum indentation depth. Arrow 1 in Fig. 7.7.9(a) shows a large slip occurs in the close packed out-of-plane  $\{111\}$  direction. Note that this only occurs with  $\phi = 0^\circ$ , where one side of the indenter is adjacent to the out-of-plane  $\langle 111 \rangle$  directions. Arrow 2 shows a cluster of atoms surrounding a lattice vacancy induced by plastic deformation. As the indentation depth increases, the dislocation loops propagate far away from the indent. Some of the loops intersect the fixed underside layers of the work piece and become 'buckled', as marked by the arrow in Fig. 7.7.9(b). In reality when dislocations intersect a grain boundary or defect they may continue to propagate in different directions. In addition to the in-plane  $\langle 111 \rangle$  directions, dislocation loops also propagate along the out-of-plane  $\langle 111 \rangle$  directions. The dislocations moving in the out-of-plane  $\langle 111 \rangle$  directions can cross-slip, when the  $(110)$  planes intersect along the  $\langle 111 \rangle$  directions. When the stress in the work material is relaxed as the tip is withdrawn, the dislocation loops retract, as shown by the images in Fig. 7.7.9(c) and (d). As the dislocation loops along

---

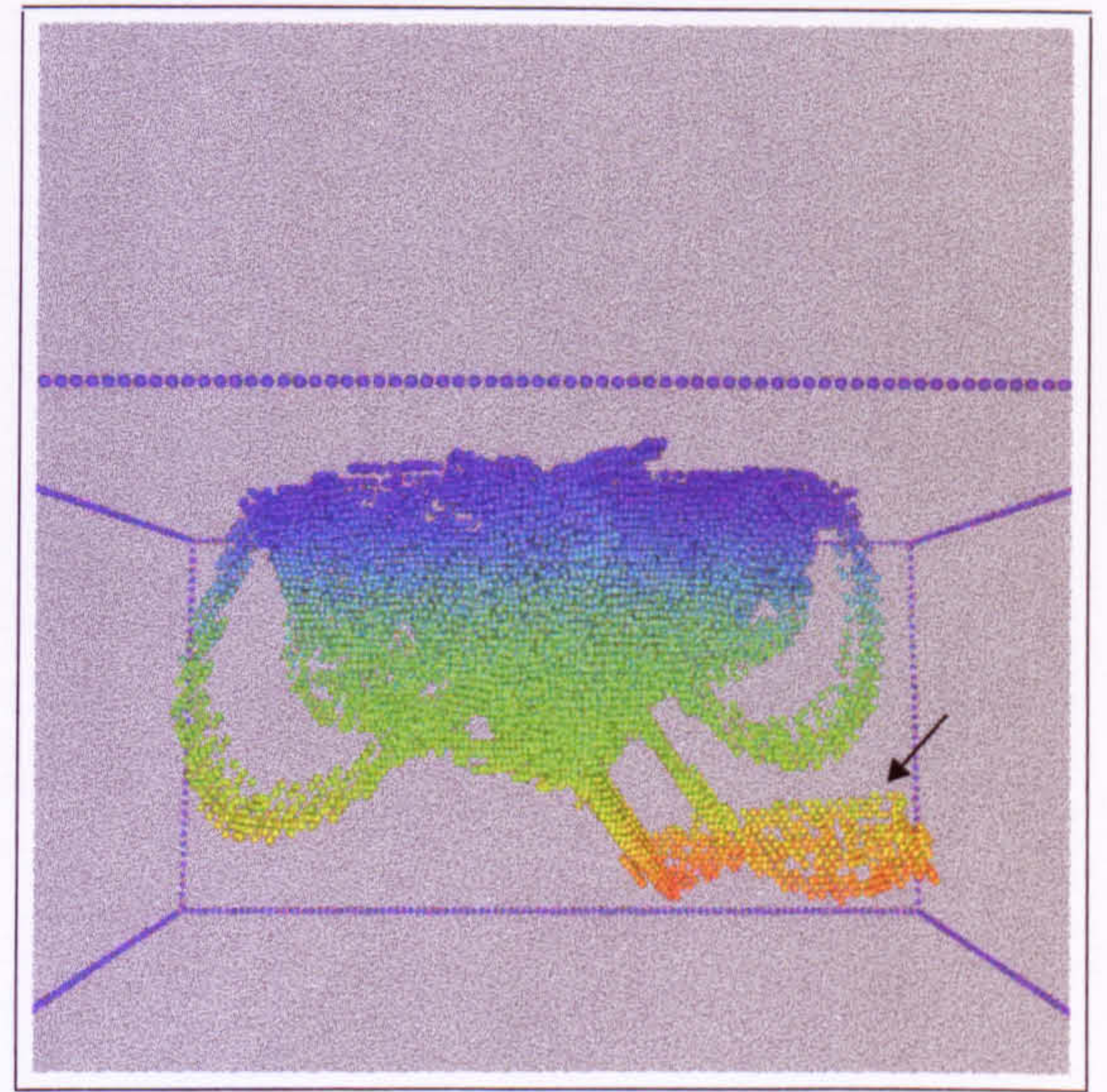
<sup>1</sup>An animated movie of this is on the CD in the Appendix

<sup>2</sup>An animated movie of this is on the CD in the Appendix

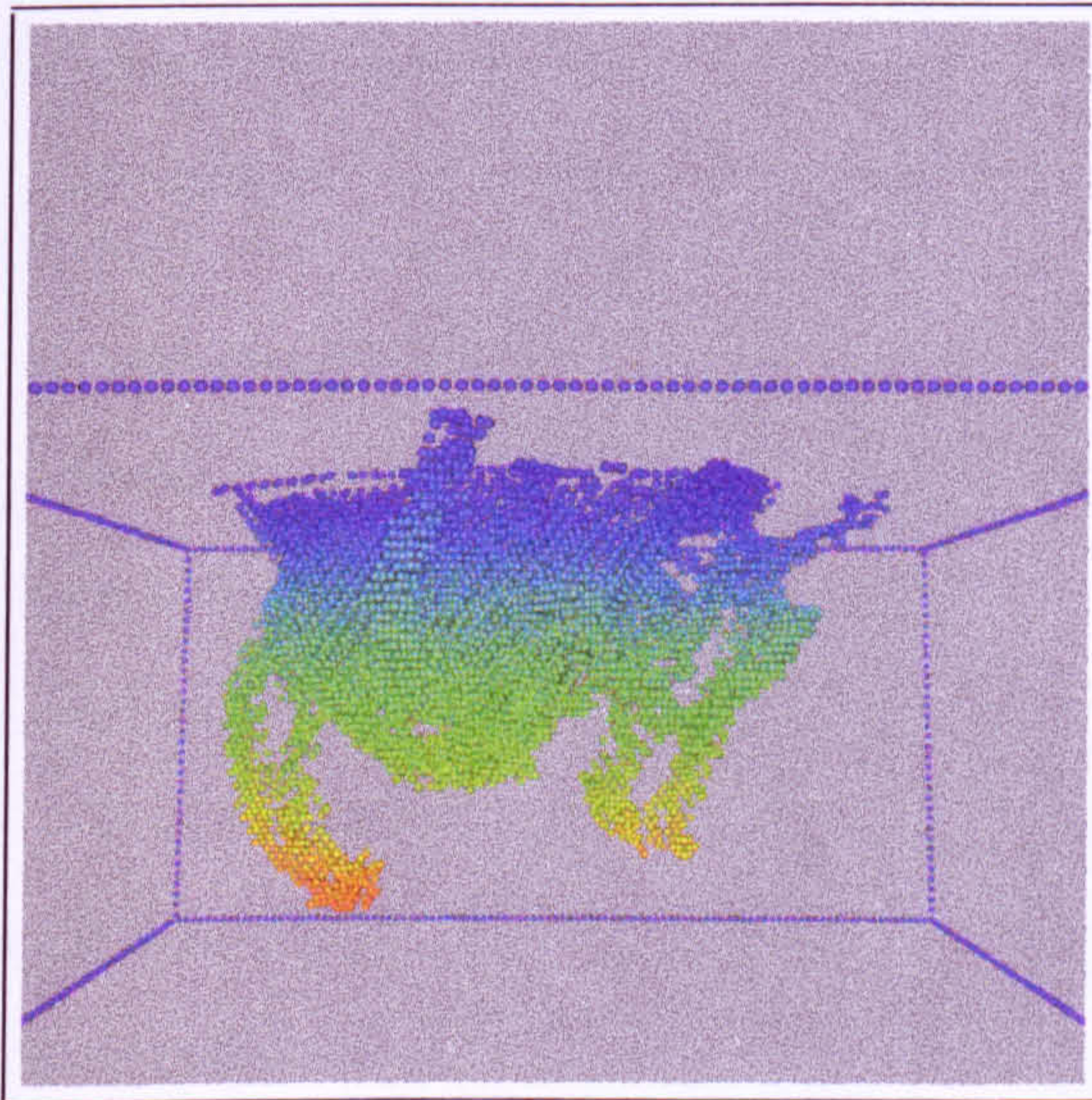




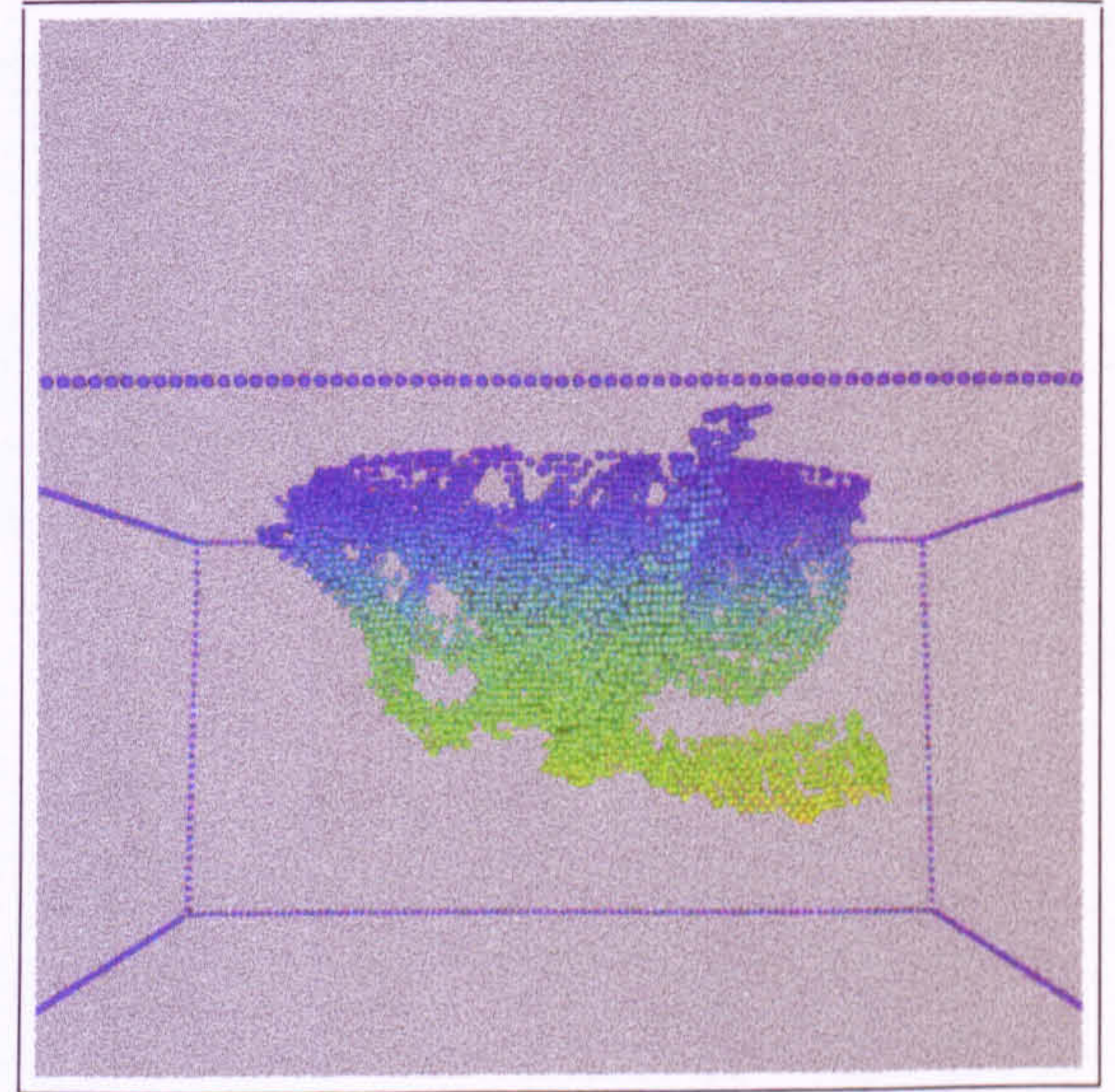
(a)



(b)



(c)



(d)

Fig. 7.7.9. Dislocations in the Fe {110} crystal for: (a)  $\phi = 0^\circ$  at  $t = 45$  ps; (b)  $\phi = 30^\circ$  at  $t = 45$  ps; (c)  $\phi = 0^\circ$  at  $t = 90$  ps; (d)  $\phi = 30^\circ$  at  $t = 90$  ps. Atoms are shown in the energy range -4.0 eV to -4.2 eV (93 % - 98 % of the Fe cohesive energy) and shaded on their vertical position from the undisturbed surface. The outermost blue shaded atoms simply denote the edge of the substrate. Arrows 1 and 2 in (a) mark a region of slip and a deformation induced lattice vacancy, respectively. The arrow in (b) marks the 'buckling' of a dislocation loop after intersecting the fixed underside layers of the substrate.



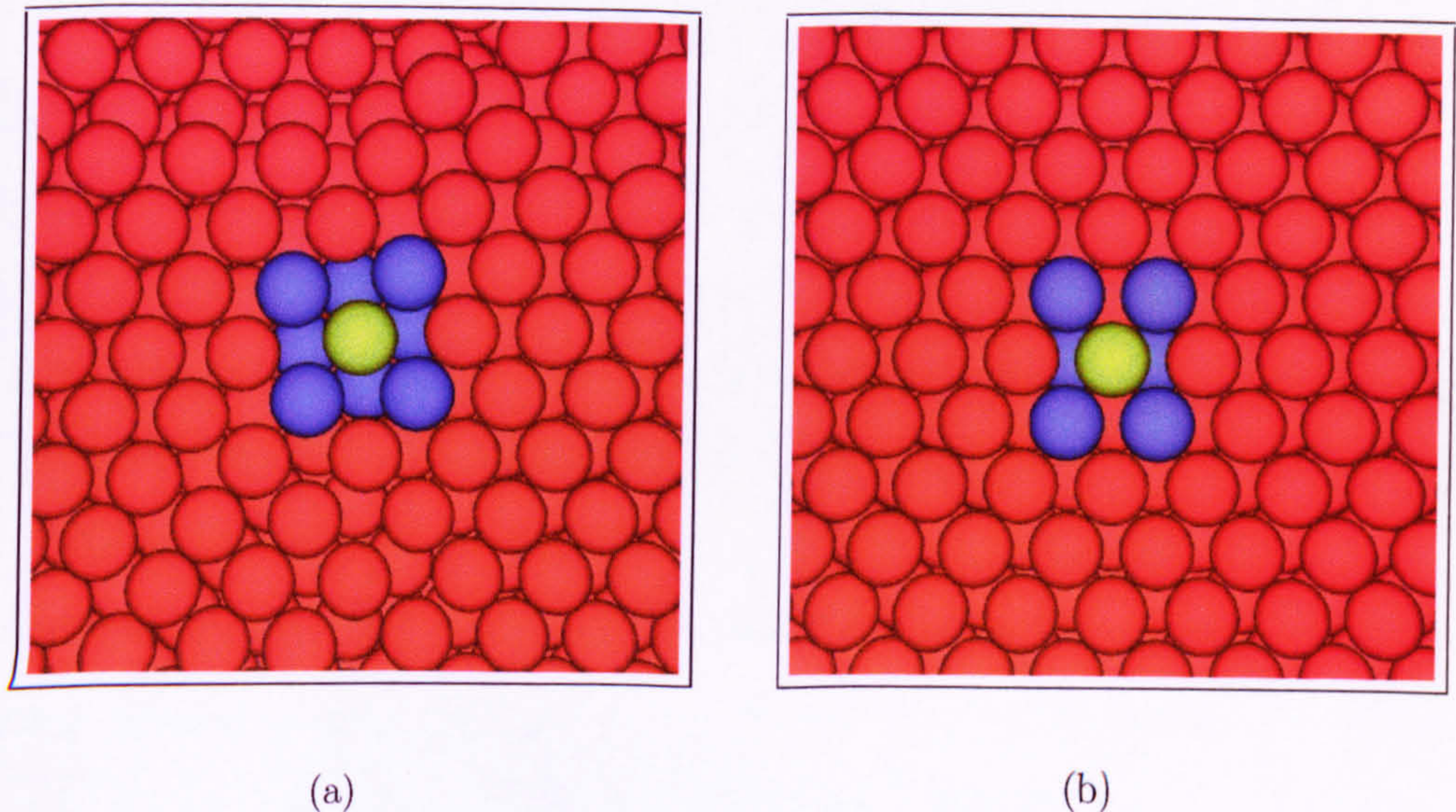


Fig. 7.7.10. The coordination of an Fe atom (shaded green) in a densified region around the indent for  $\{110\}$  at: (a) 45 ps; (b) 90 ps. The nearest neighbours of the green atom are coloured blue, and all other atoms shaded red. Note that at the halfway stage in (a) the green shaded atom and its nearest neighbours tend towards a fcc configuration. In all images, the nearest neighbour cut-off distance is assumed to be 2.60 Å.

the out-of-plane  $\langle 111 \rangle$  directions move back towards the indent, the cross-slip forces material up onto the surface, causing most of the pile-up to occur during the unloading stage rather than the loading stage. This occurs as a series of sequential displacements rather than as a continuous flow.

It is well known that indentation can induce phase transformations within a material specimen [216]. To determine the extent of any phase transformations, the change in the coordination of the Fe atoms during the indentation was analysed. As the indenter penetrates the work piece, atoms are compressed which ensues in increased coordination and densification around the indentation region. Atoms with a high coordination number of 12 at the halfway stage were examined to determine if a phase change occurs in the densified regions. Fig. 7.7.10(a) shows that some of the atoms tend towards a fcc configuration. However, this is only a temporary change as the atoms are arranged in a bcc configuration at the conclusion of the indentation, as shown in Fig. 7.7.10(b). For larger indentation depths, the greater compression may induce permanent phase transformations in a fcc configuration. For further information on crystallographic phase transformations in metals, the reader is referred to Porter [216].

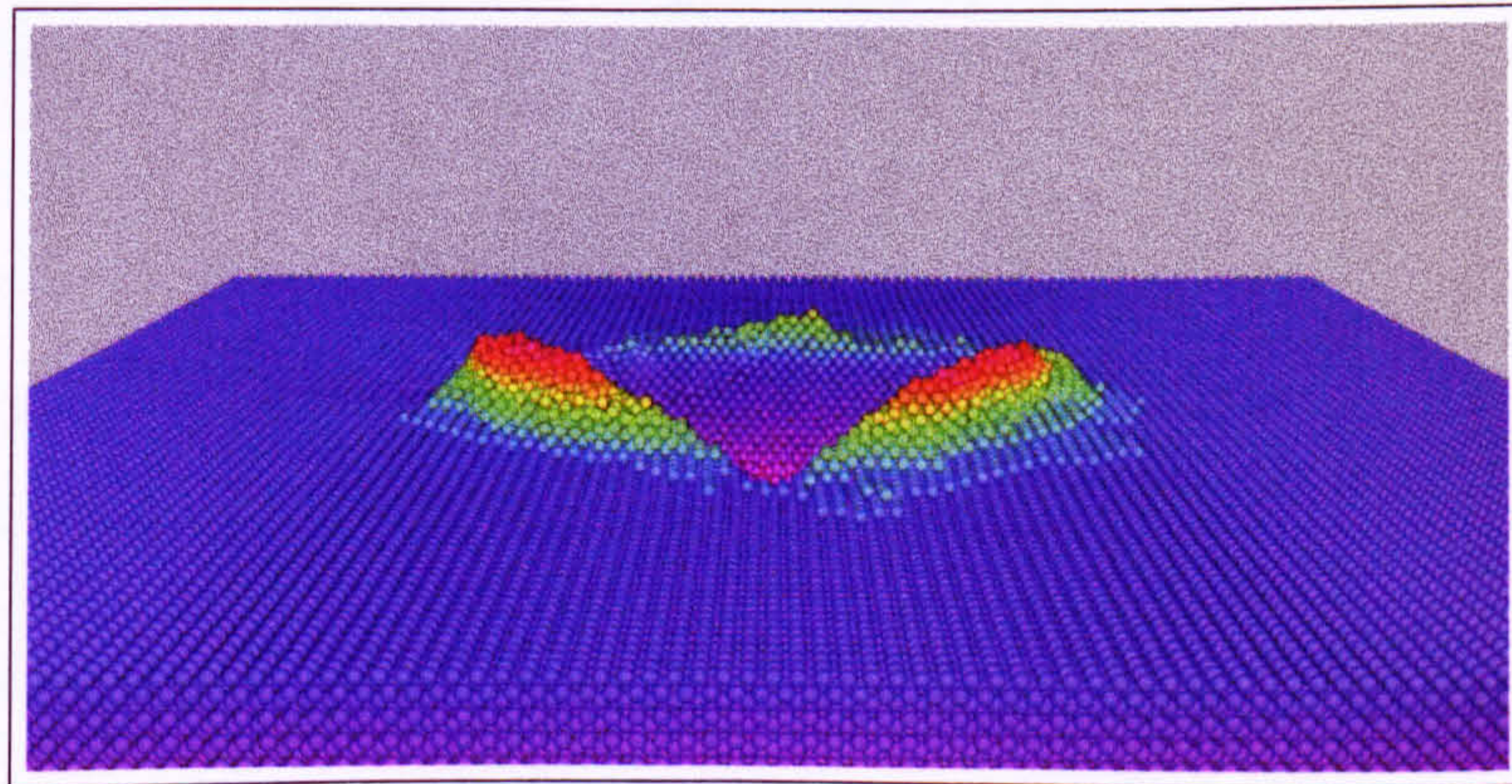


### 7.4.2 Fe {100} Substrate

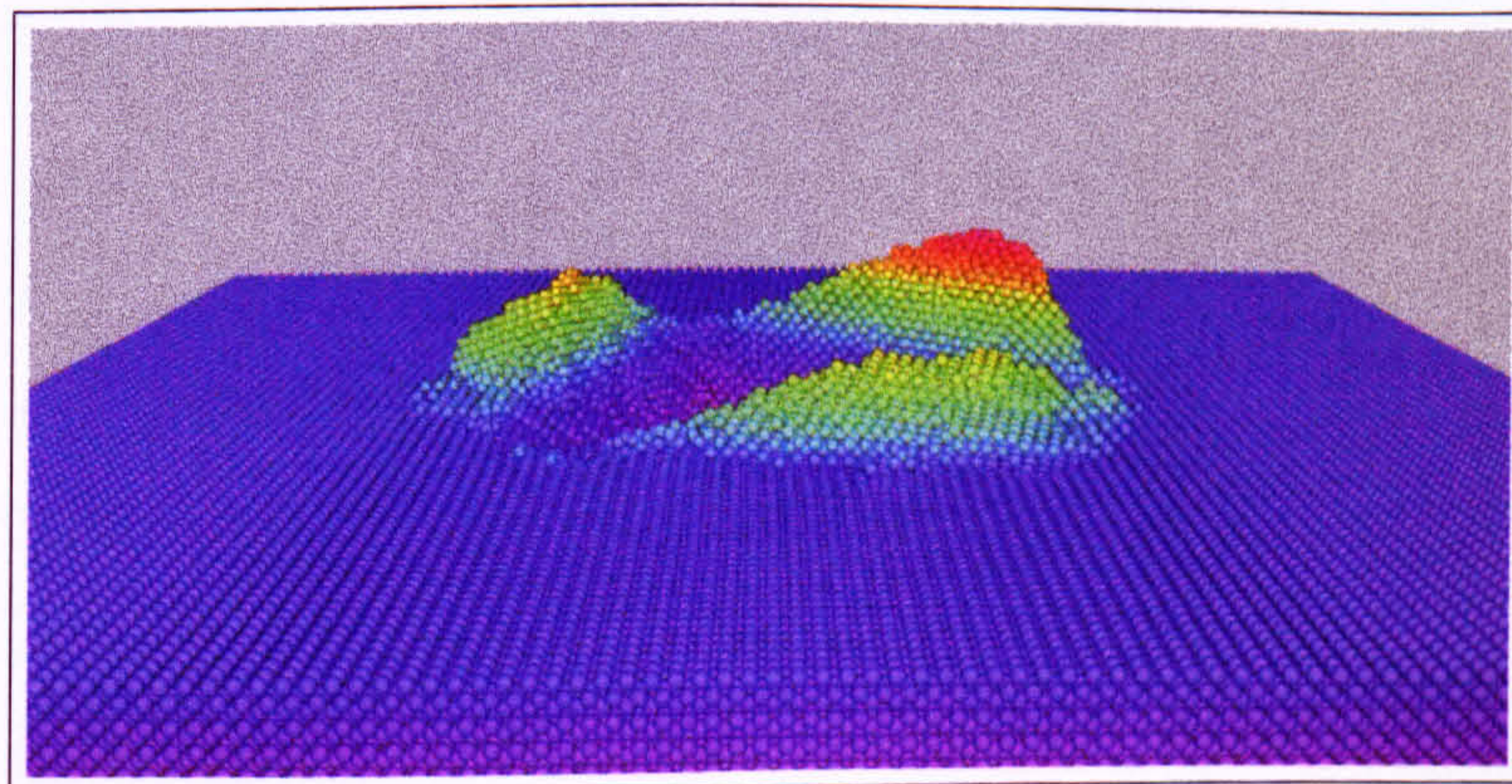
For the {100} surface, preferential pile-up should occur along the in-plane  $\langle 110 \rangle$  azimuths (i.e. the out-of-plane  $\langle 111 \rangle$  directions). The surface topography for Fe {100} is shown in Fig. 7.7.11<sup>3</sup>. Following indentation with  $\phi = 0^\circ$ , Fig. 7.7.11(a) shows preferential pile-up occurs along the sides left and right of the indent, with peak heights of 13.2 Å and 15.8 Å respectively. The normal to these sides is mis-aligned from the  $\langle 110 \rangle$  azimuths by  $15^\circ$ . Along the uppermost edge there is very little pile-up since the mis-alignment of the normal to the close packed  $\langle 110 \rangle$  azimuths is much larger at  $45^\circ$ . Following indentation with  $\phi = 45^\circ$ , Fig. 7.7.11(b) clearly shows preferential pile-up along the

---

<sup>3</sup>Animated movies of this are on the CD in the Appendix



(a)



(b)

Fig. 7.7.11. The surface of the Fe {100} substrate following pyramidal indentation with: (a)  $\phi = 0^\circ$ ; (b)  $\phi = 45^\circ$ . Atoms are coloured according to their vertical position from the undisturbed surface.



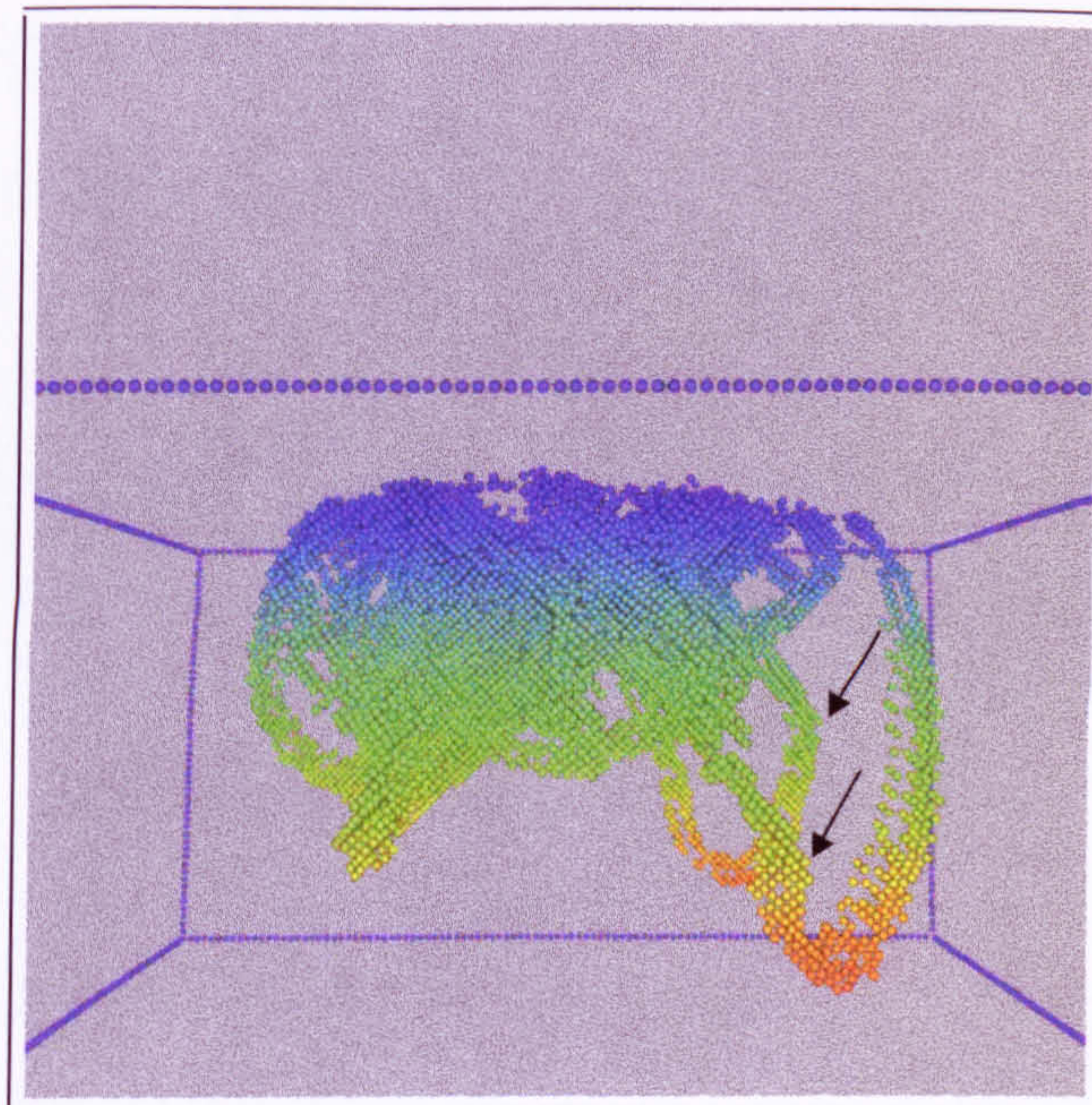


Fig. 7.7.12. Dislocations in the Fe  $\{100\}$  crystal for  $\phi = 0^\circ$  at  $t = 33.75$  ps. Atoms are shown in the energy range  $-4.0$  eV to  $-4.2$  eV (93 % - 98 % of the Fe cohesive energy) and shaded on their vertical position from the undisturbed surface. The outermost blue shaded atoms simply denote the edge of the substrate. The arrows mark dislocation loops which have cross-slipped.

side of the indent whose normal is aligned exactly along the  $\langle 110 \rangle$  azimuth. Here, the pile-up height is much larger compared with  $\phi = 0^\circ$  at  $24.9$  Å. There is also significant pile-up along the remaining two sides where the normal to the sides is mis-aligned from  $\langle 110 \rangle$  azimuths by  $30^\circ$ .

The dislocation loops formed in the Fe  $\{100\}$  work material propagate in the out-of-plane  $\langle 111 \rangle$  directions. All of the tip-induced dislocation loops can contribute to the piling-up of material. The high symmetry of the out-of-plane  $\langle 111 \rangle$  directions in the  $\{100\}$  surface means that it is easier for cross-slip to occur and so the pile-up yield is considerably larger compared with  $\{110\}$  (approximately three times larger). Furthermore, for the  $\{110\}$  surface the in-plane  $\langle 111 \rangle$  directions transport material away from the indent, which further reduces the pile-up yield. For  $\{100\}$  the cross-slip occurs readily during both loading and unloading of the indenter, with most of the pile-up forming during the loading stage. Fig. 7.7.12 shows where cross-slip for two dislocation loops has occurred, since the atoms do not lie in a plane.

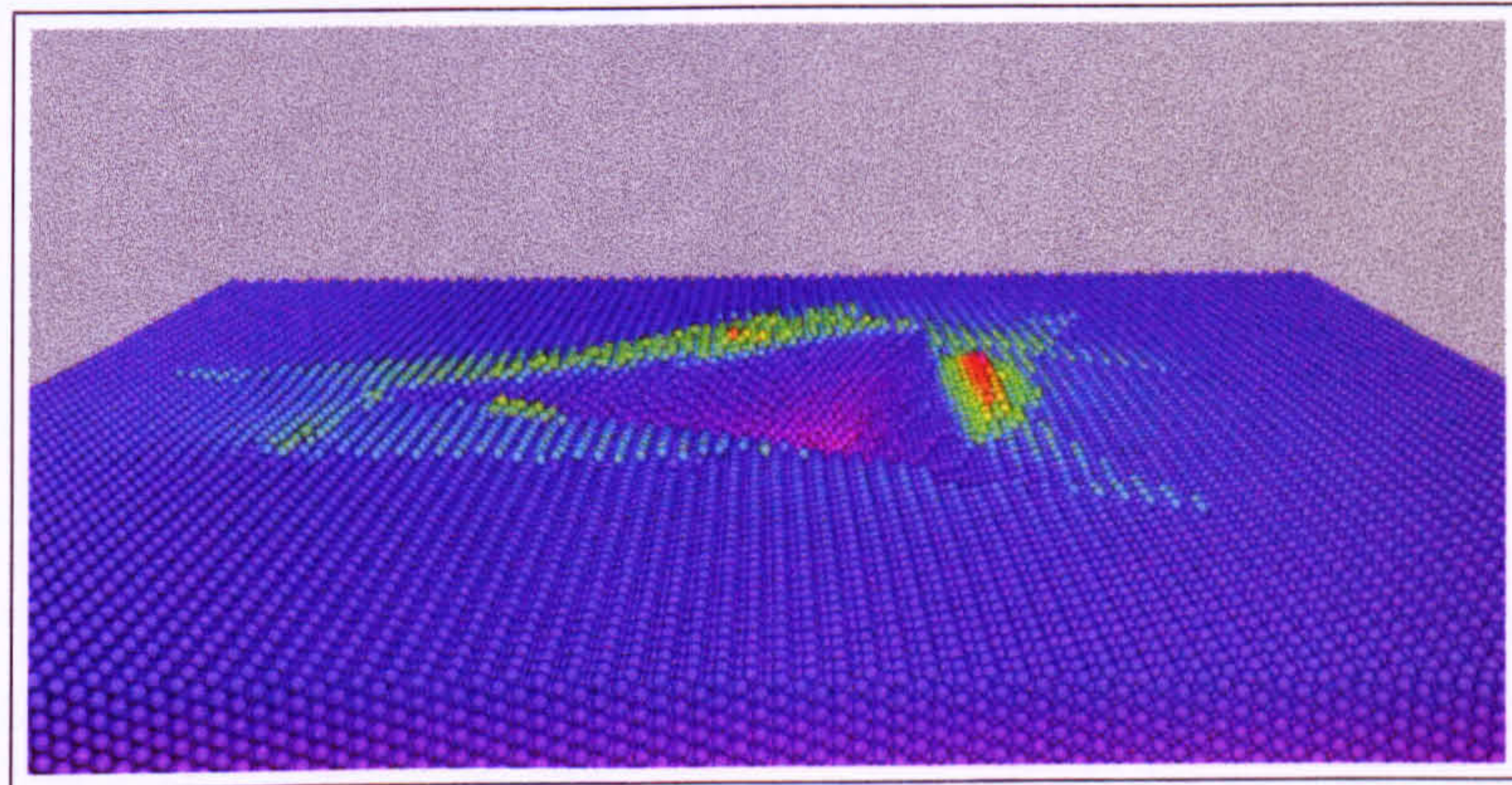


### 7.4.3 Fe {111} Substrate

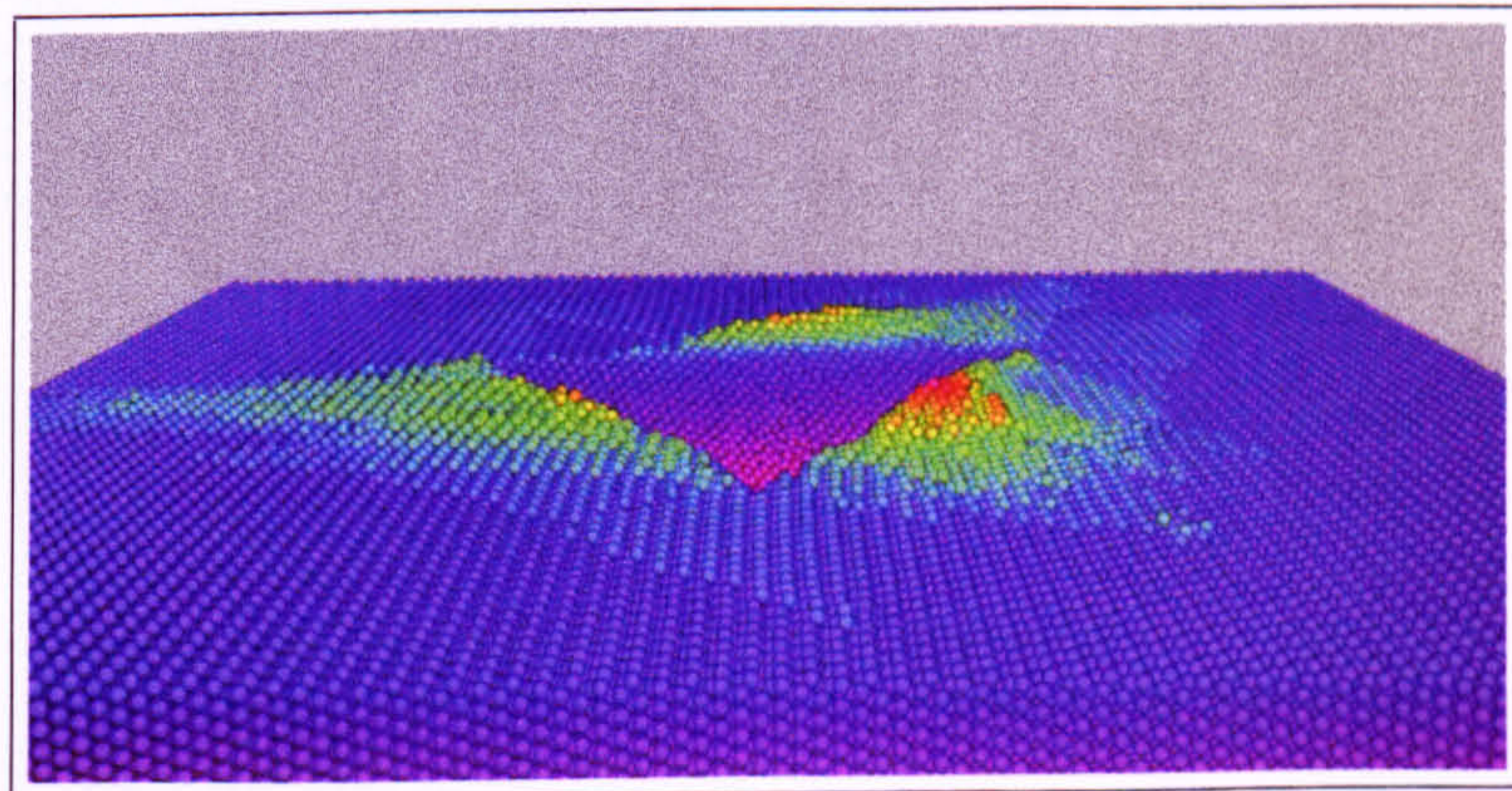
The hexagonal arrangement of the Fe {111} surface exhibits three-fold symmetry such that for each rotation of the indenter, the normal to each indent side is aligned along the same crystallographic direction. Therefore, for each rotation the pile-up distribution along the indent sides should be more symmetric than for the other surfaces studied. For indentation with  $\phi = 0^\circ$ , the normal to each side of the indent is aligned exactly along the out-of-plane {111} direction. However, the surface topography shown in Fig. 7.7.13(a) and (b) shows a larger pile-up along one side of the indent compared with the remaining sides <sup>4</sup>. This appears to be purely statistical behaviour and for larger

---

<sup>4</sup>An animated movie of this is on the CD in the Appendix



(a)



(b)

Fig. 7.7.13. The surface of the Fe {111} substrate following pyramidal indentation with: (a)  $\phi = 0^\circ$ ; (b)  $\phi = 30^\circ$ . Atoms are coloured according to their vertical position from the undisturbed surface.



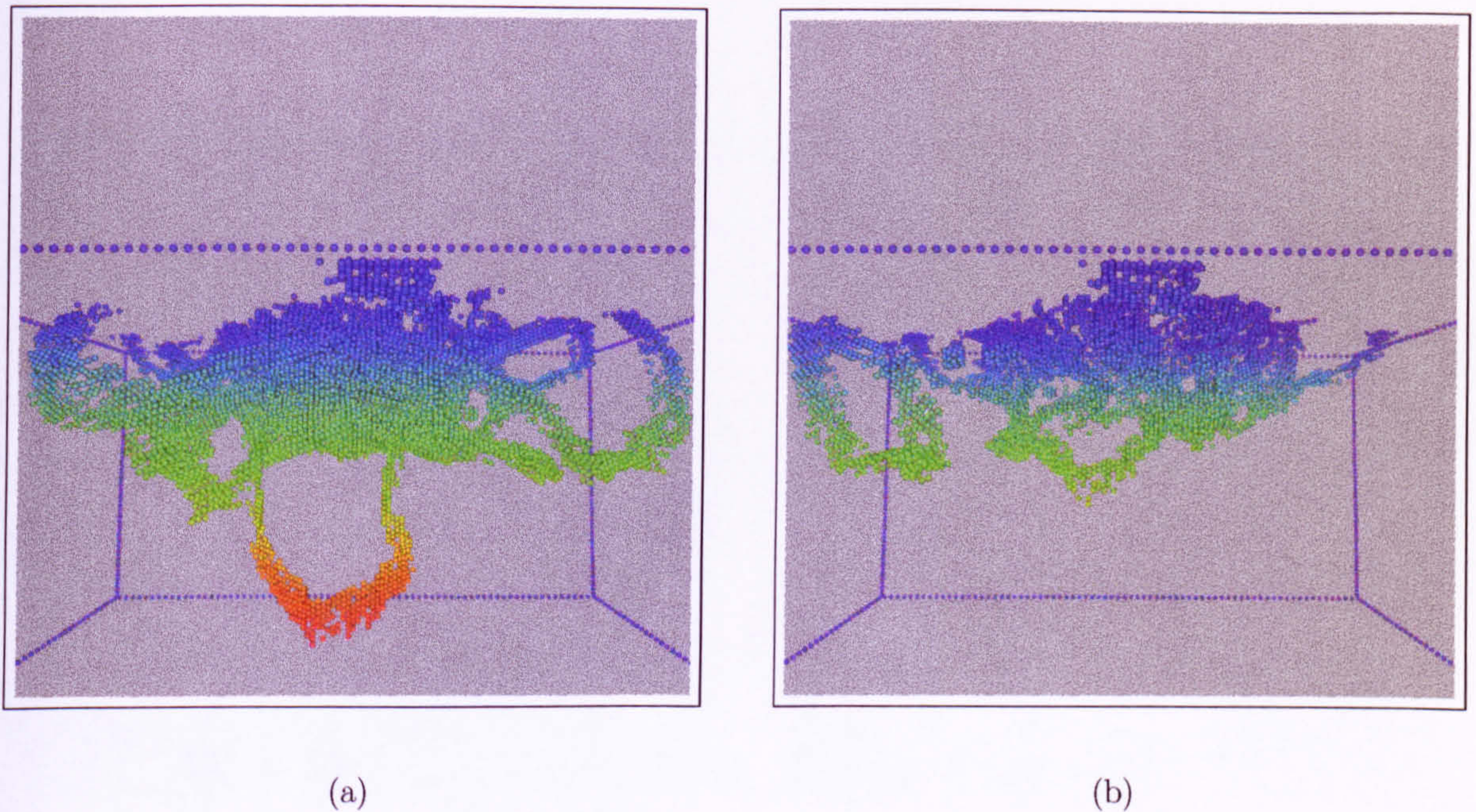


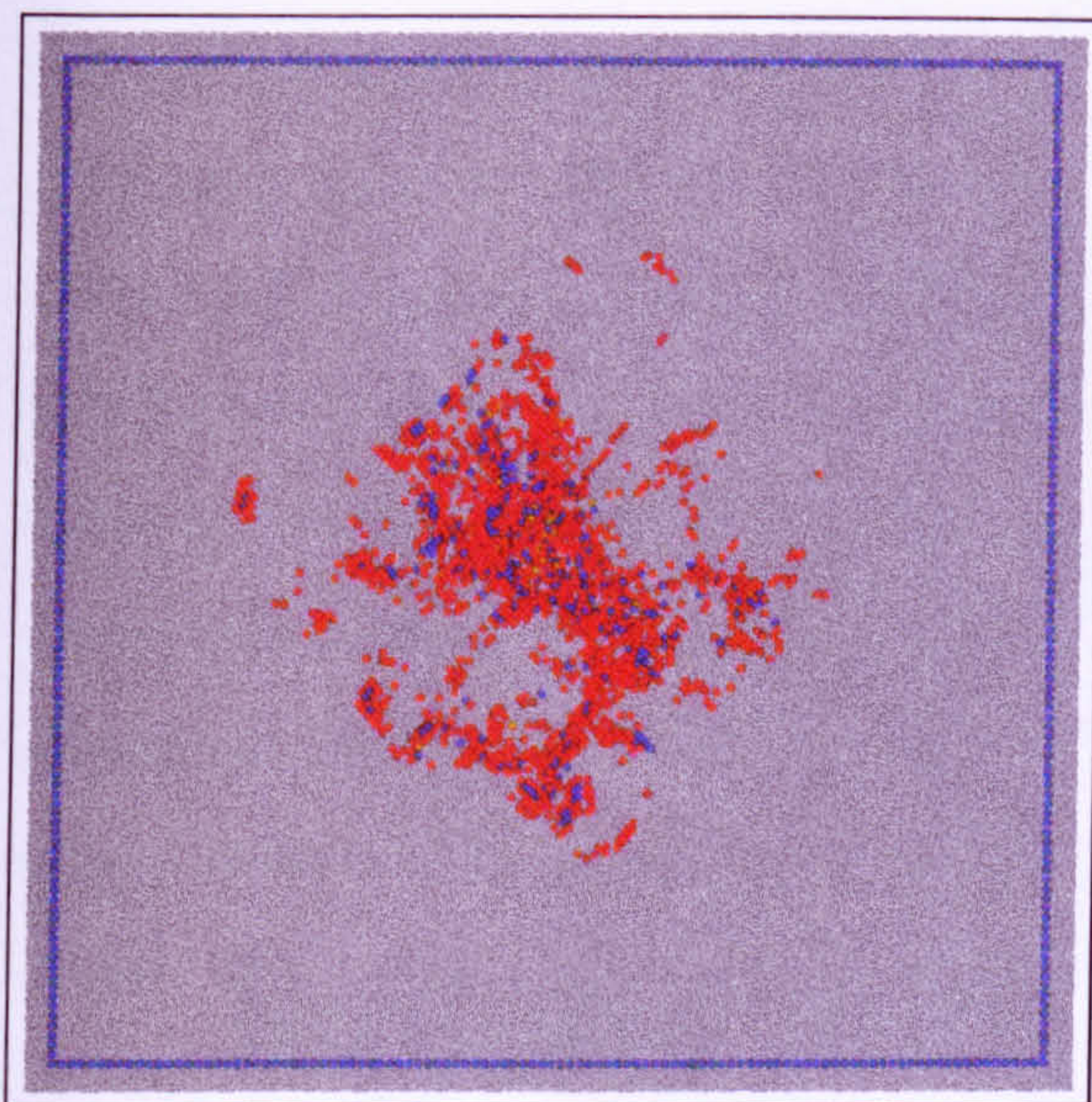
Fig. 7.7.14. Dislocations in the Fe  $\{111\}$  crystal with  $\phi = 30^\circ$  at: (a)  $t = 45$  ps; (b)  $t = 90$  ps. Atoms are shown in the energy range  $-4.0$  eV to  $-4.2$  eV (93 % - 98 % of the Fe cohesive energy) and shaded on their vertical position from the undisturbed surface. The outermost blue shaded atoms simply denote the edge of the substrate.

indentation depths, the pile-up should appear more symmetric. An obvious difference compared with  $\{110\}$  and  $\{100\}$  is that for  $\{111\}$  the pile-up is much more spread out over the surface. Following indentation with  $\phi = 30^\circ$ , Fig. 7.7.13(b) shows the pile-up is even more spread out over the surface compared with Fig. 7.7.13(a). Tip-induced dislocation loops are shown in Fig. 7.7.14 for indentation with  $\phi = 30^\circ$ . Like the pile-up on the surface, the dislocation loops are also spread further out around the indent

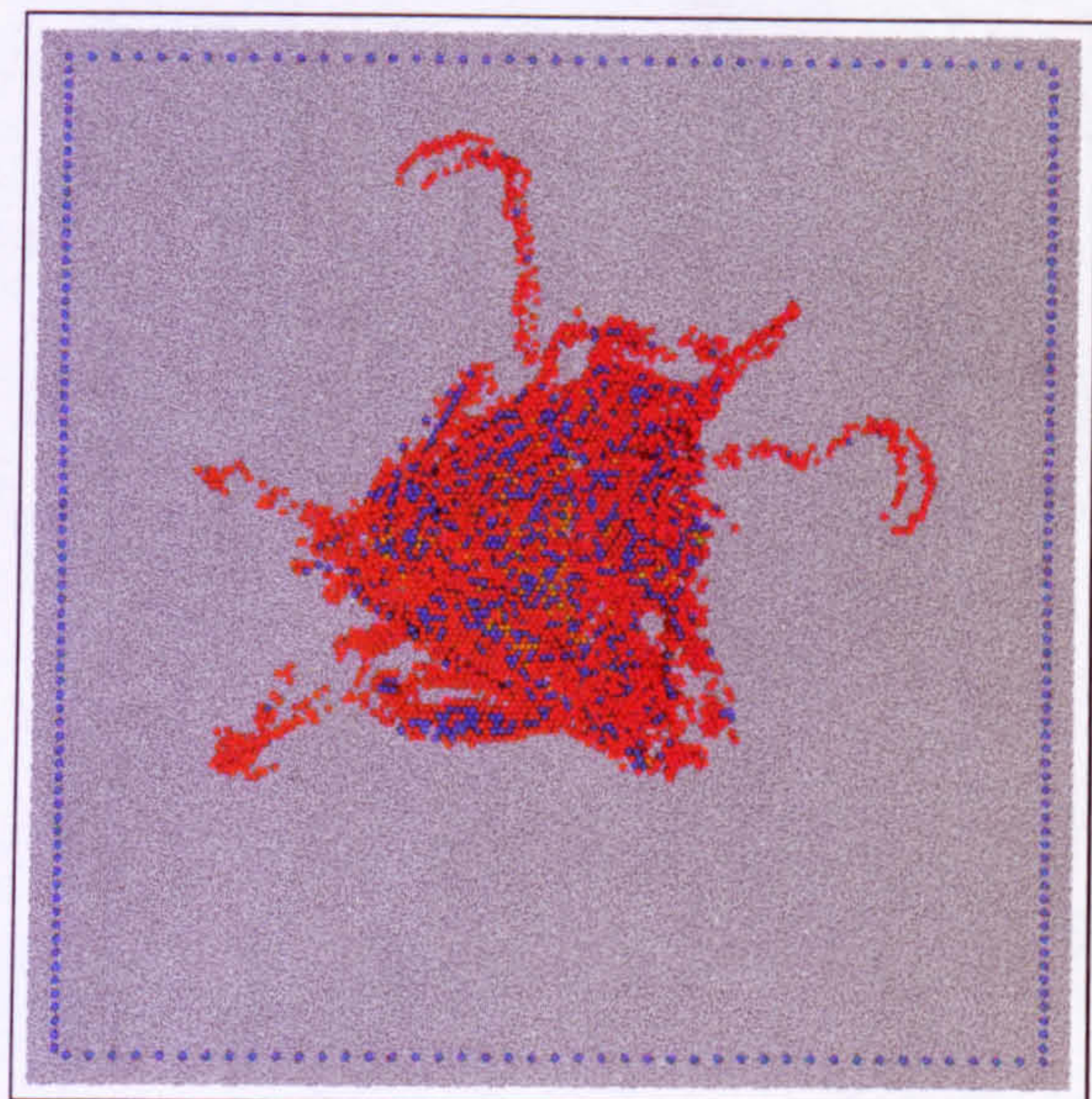
Table 7.1. Nearest neighbour in layer distances and layer spacing for the three studied surfaces of Fe, where  $a$  is the lattice constant.

	Surface Orientation		
	$\{100\}$	$\{110\}$	$\{111\}$
Nearest Neighbour in Layer	$a$	$\frac{\sqrt{3}a}{2}$	$\sqrt{2}a$
Layer Separation	$\frac{a}{2}$	$\frac{a}{\sqrt{2}}$	$\frac{a}{2\sqrt{3}}$

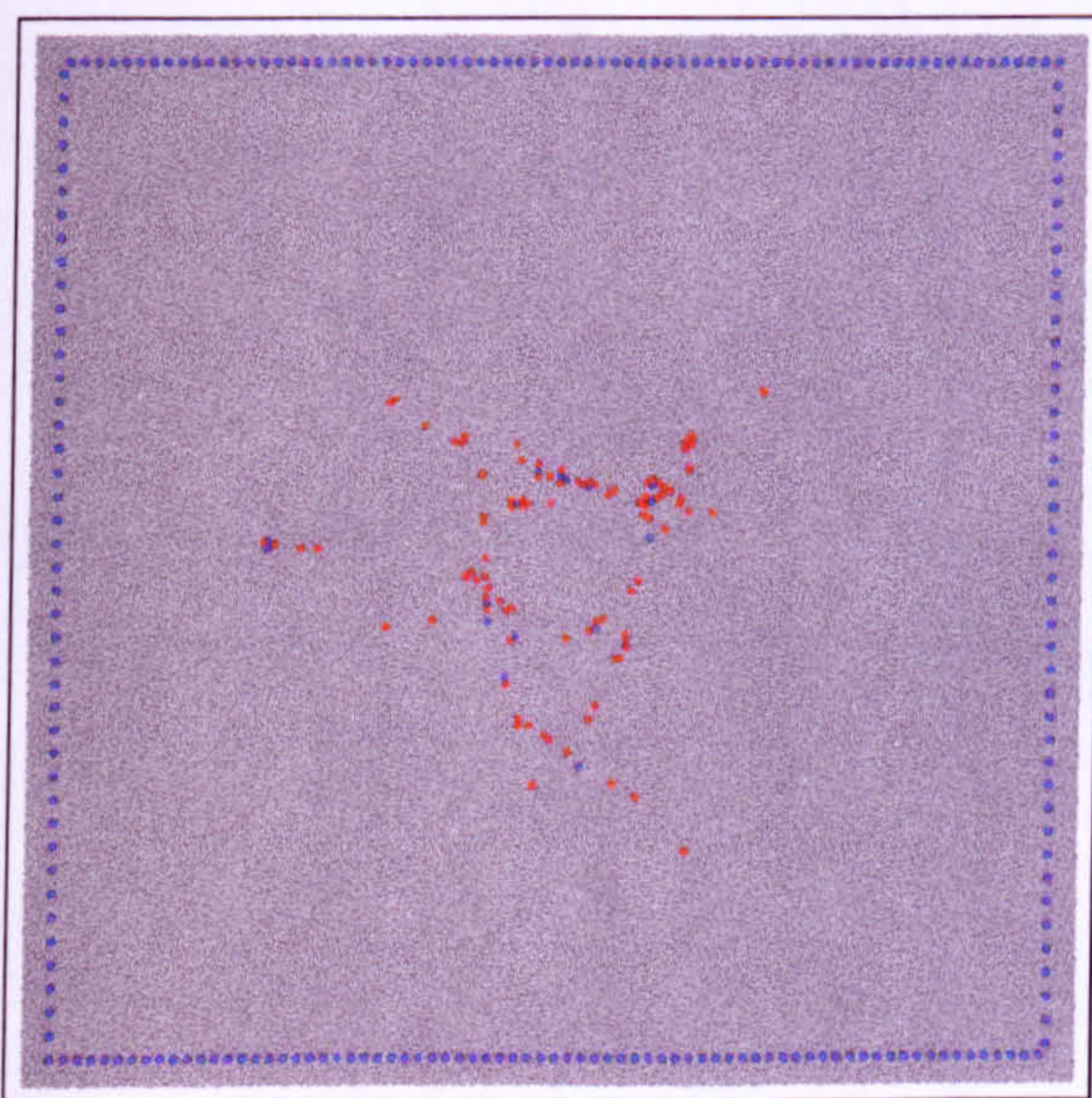




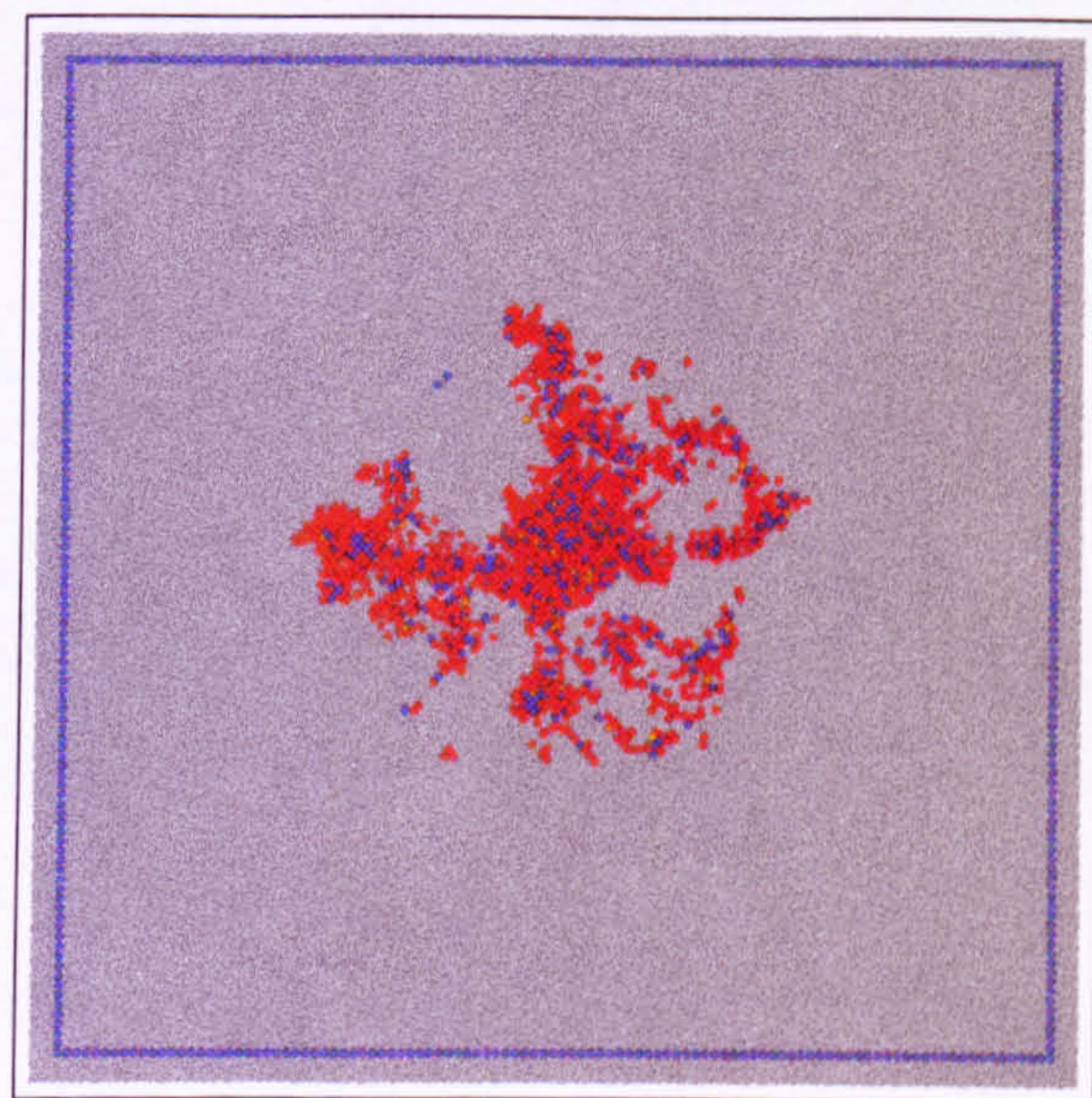
(a)



(b)



(c)



(d)

Fig. 7.7.15. The coordination of Fe atoms during indentation for: (a) Fe {100} with  $\phi = 45^\circ$  at  $t = 45$  ps; (b) Fe {111} with  $\phi = 0^\circ$  at  $t = 45$  ps; (c) Fe {100} with  $\phi = 45^\circ$  at  $t = 90$  ps; (d) Fe {111} with  $\phi = 0^\circ$  at  $t = 90$  ps. The red shaded atoms have a coordination of 9, blue shaded atoms a coordination of 10, yellow shaded atoms a coordination of 11 and the green shaded atoms a coordination of 12. The outermost blue shaded atoms simply denote the edge of the substrate. In all images, the nearest neighbour cut-off distance is assumed to be  $2.60 \text{ \AA}$ .



compared with the  $\{110\}$  and  $\{100\}$  surfaces.

Table 7.1 shows that the  $\{111\}$  surface is the most closely packed in the vertical direction, compared with  $\{100\}$  and  $\{110\}$ . Also, the  $\{111\}$  surface has the largest nearest neighbour spacing within the layer. Fig. 7.7.15 shows the densification of the  $\{100\}$  and the  $\{111\}$  substrates during indentation process. In Fig. 7.7.15(a) indentation of the  $\{100\}$  surface induces a high pile-up yield, with relatively little densification around the indent at maximum indentation. By contrast in Fig. 7.7.15(b), indentation of the  $\{111\}$  surface produces high densification around the indent, with comparatively little pile-up. Therefore, for the  $\{111\}$  surface the close packing of layers in the indentation direction, causes atoms to be preferentially displaced within the layer where the atom spacing is larger. This gives a much smaller pile-up yield compared with the  $\{100\}$  surface. As the indenter is withdrawn from the  $\{100\}$  work material, Fig. 7.7.15(c) shows there is no significant density change induced by the indentation as the compression of atoms relax and the coordination reduces. However, with the  $\{111\}$  substrate, the extraction of the tip in Fig. 7.7.15(d) shows there is substantial permanent densification around the indent.

#### 7.4.4 Force-depth Curve Analysis

The force-depth curves following indentation of Fe  $\{110\}$  with  $\phi = 0^\circ$  and  $\phi = 30^\circ$  are shown in Fig. 7.7.16 and are independent of indenter orientation. Indentation with the paraboloid interface resulted in a similar force-depth curve, except that the maxi-

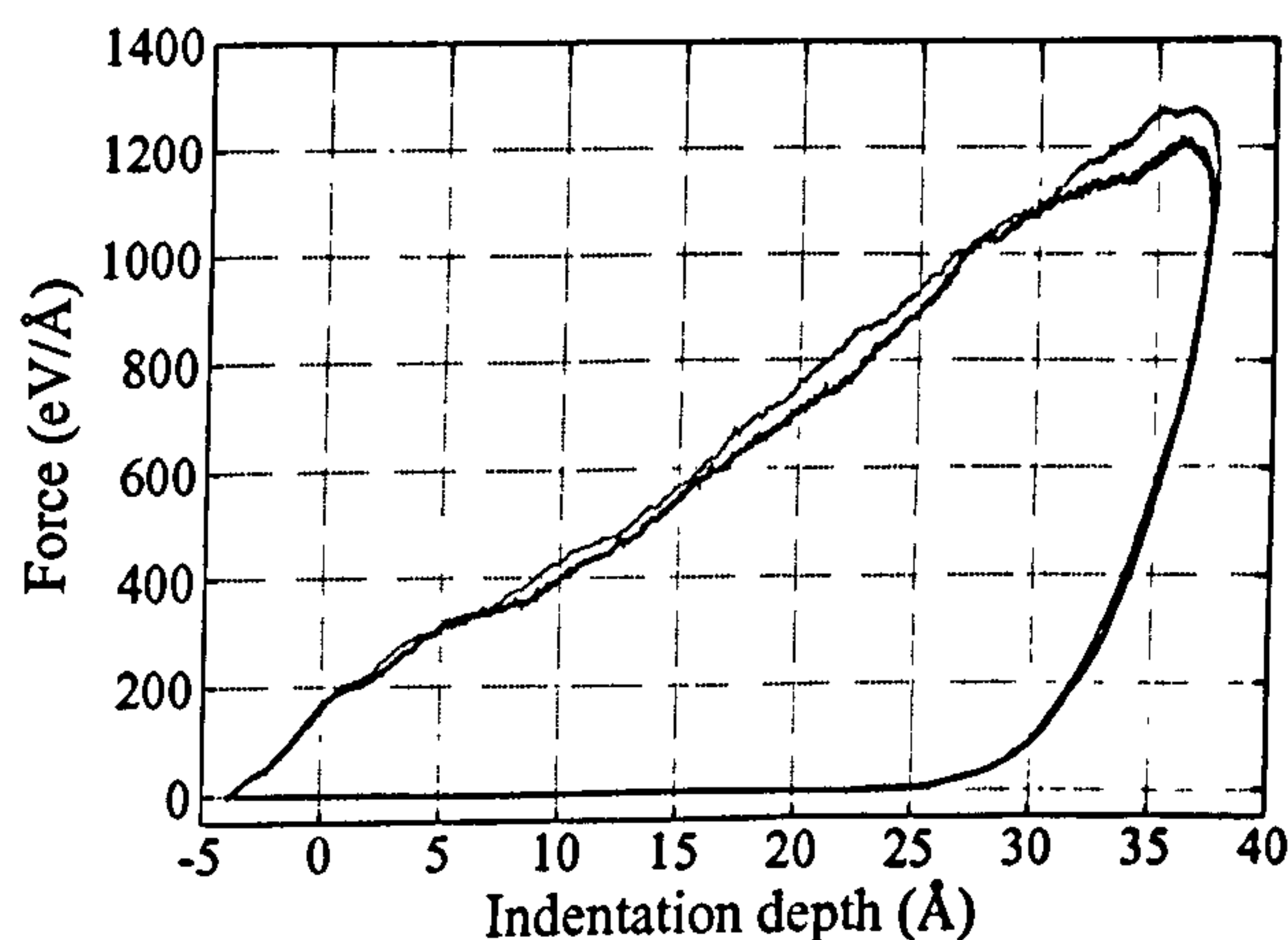


Fig. 7.7.16. Force-depth curves from the simulations of indentation into the Fe  $\{110\}$  crystal. The bold solid line corresponds to indentation with  $\phi = 0^\circ$  and the remaining line denotes indentation with  $\phi = 30^\circ$ .



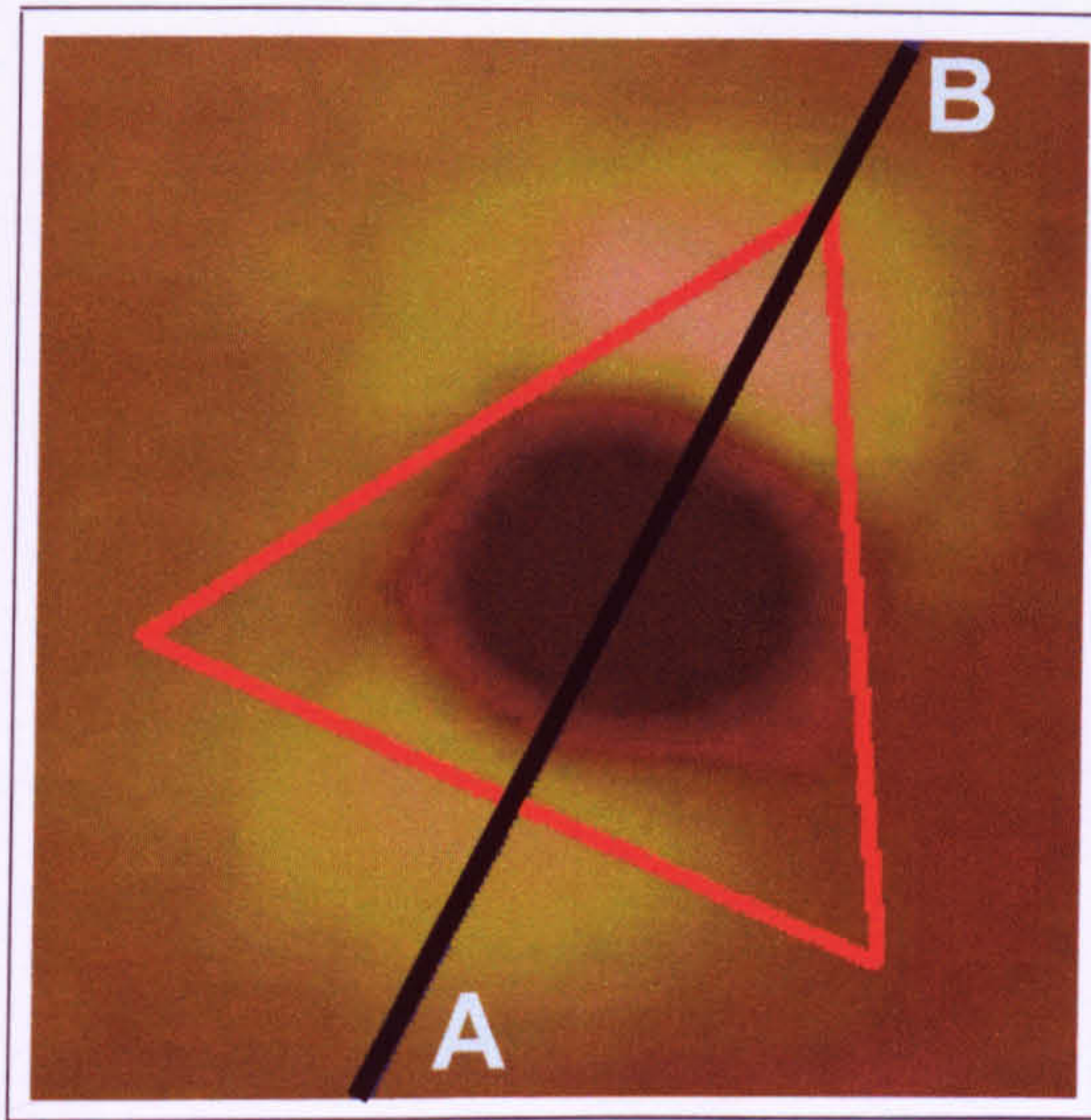
imum indentation depth was slightly greater due to tip compression with the pyramidal indenter. Very similar curves are obtained for the  $\{100\}$  and  $\{111\}$  surfaces using the cube-cornered indenter. The maximum force exerted on the atomistic tip was 1331 eV/Å for  $\{100\}$ , 1313 eV/Å for  $\{111\}$  and 1274 eV/Å for  $\{110\}$ . The employment of over one million atoms using the parallel MD code should allow for a more realistic determination of mechanical properties, compared with the system sizes for Fe and Ag in Chapter 5, since the finite-size effects have been partially alleviated. The nanohardness of the work pieces is calculated to be 3.25 GPa, 3.23 GPa and 3.14 GPa for  $\{100\}$ ,  $\{111\}$  and  $\{110\}$  respectively. Therefore, the small indentation depths used here reflect only a very small difference in nanohardness across the three different surfaces. The calculated Young's modulus is around 50% higher than in experiments (see next section), however, this is subject to large errors due to the difficulty in determining the gradient of the unloading force-depth curve.

## 7.5 Experimental Results and Discussion

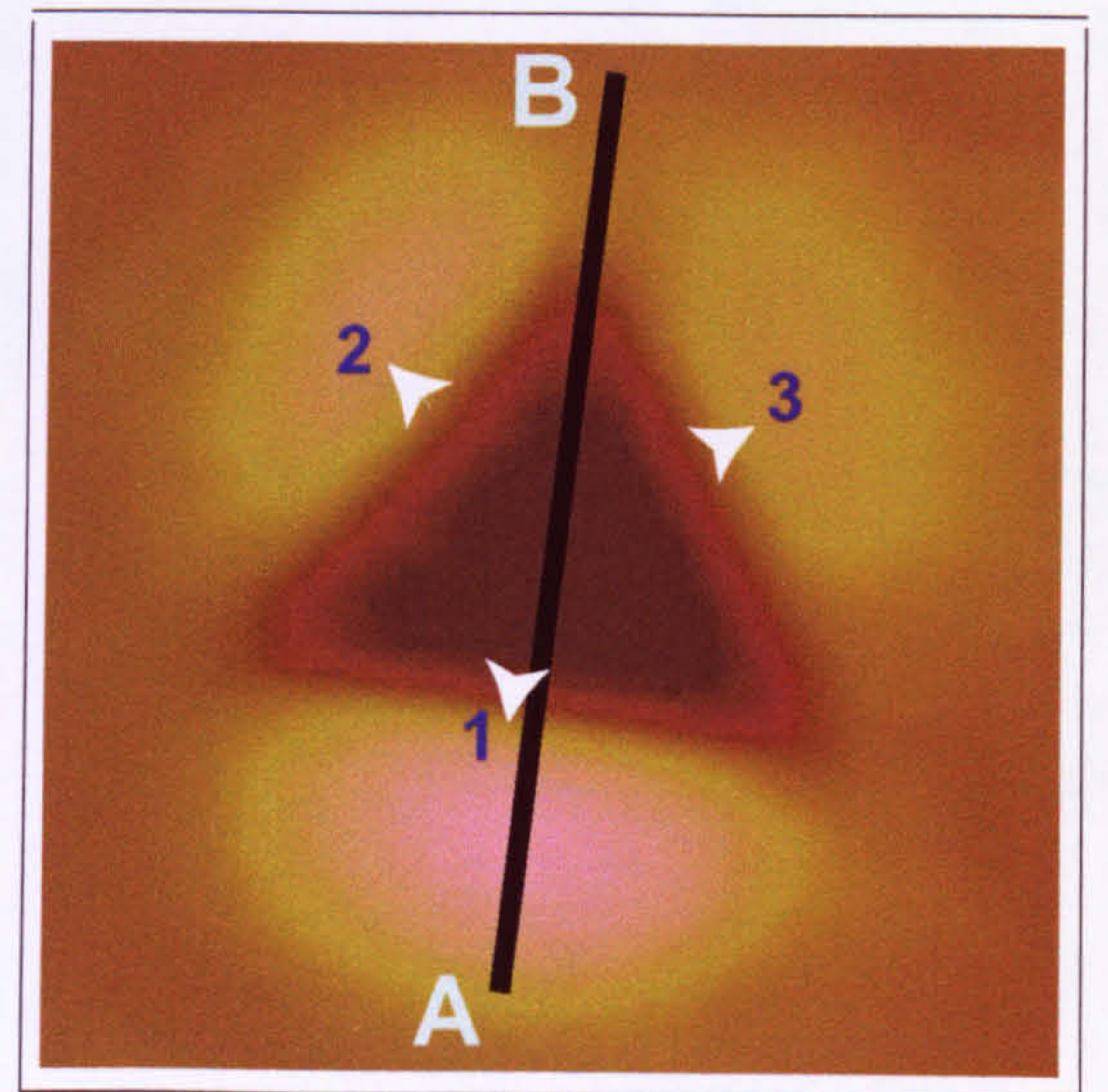
### 7.5.1 Fe $\{110\}$ Substrate

All experiments were performed using the Hysitron Nanoindenter Triboscope [152]. The sample preparation for the single crystals is discussed in the companion papers [209]-[210]. Experiments were performed on single crystal Fe  $\{110\}$  using both a spherocone (cone of 90° apex angle ending in a spherical cap of approximately 400 nm radius) and a cube-cornered indenter (with a radius of curvature of 120 nm). Fig. 7.7.17(a) presents a SFM image of the sample following indentation with the spherocone and clearly exhibits two-fold symmetry. The line AB is aligned parallel to the out-of-plane  $\langle 111 \rangle$  directions, as depicted in Fig. 7.7.3(a), and dissects the centre of the two pile-ups. This is in good agreement with the simulation image in Fig. 7.7.6(a), which shows pile-ups along the in-plane  $\langle 111 \rangle$  directions merge together for larger depths to give the appearance of two single hillocks propagating along the out-of-plane  $\langle 111 \rangle$  directions. The cube-cornered indenter is then aligned along the line AB, as shown by the red triangle in Fig. 7.7.17(a). The image in Fig. 7.7.17(b) shows the indented area following indentation with the pyramidal indenter using this orientation. Reflection symmetry is found about the line AB, with preferential piling-up occurring along the side of the triangle perpendicular to

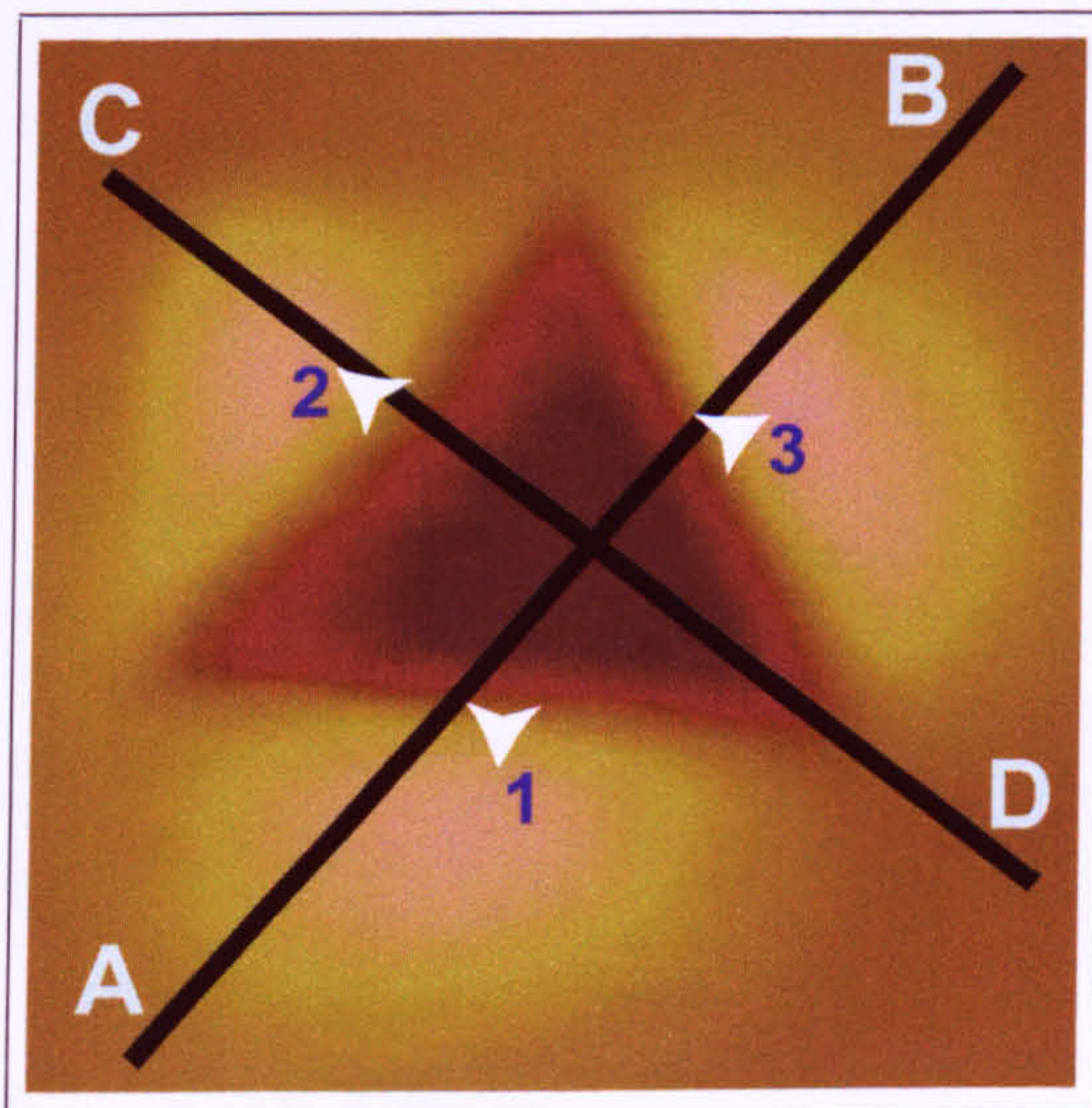




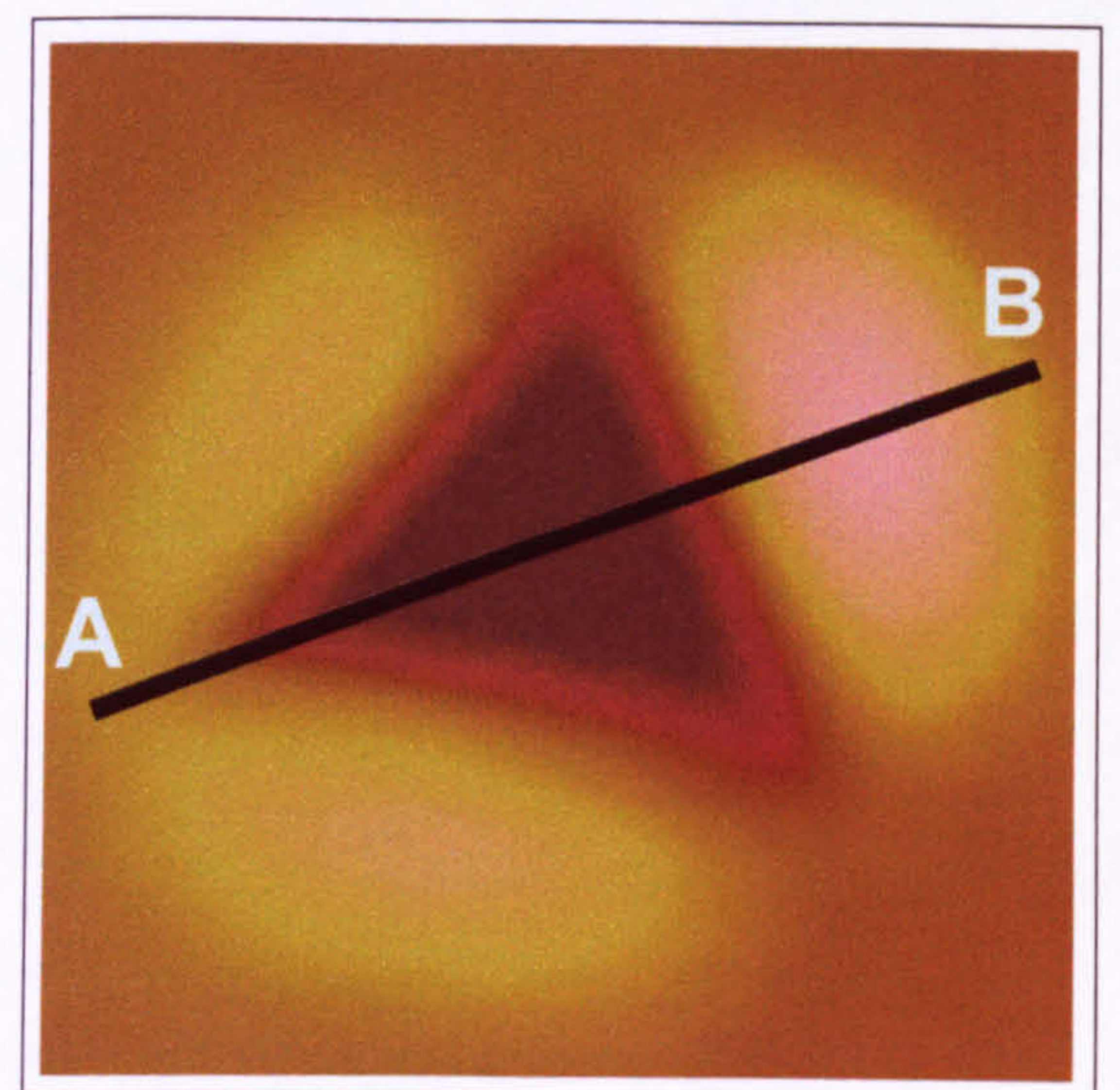
(a)



(b)



(c)



(d)

Fig. 7.7.17. SFM images of the indented area in the Fe  $\{110\}$  sample. All images are  $1\ \mu\text{m} \times 1\ \mu\text{m}$  in size. The directions of maximum stress are marked by the arrows. The line AB is aligned along the out-of-plane  $\langle 111 \rangle$  directions and the line CD is perpendicular to AB. The dark regions correspond to the indentation hole and the light regions represent the induced pile-up. (a) Indentation with a spherocone showing two symmetric pile-ups; (b) The asymmetric pile-up in the case of a pyramidal indenter with reflection symmetry about the line AB; (c) Rotation of the crystal by  $30^\circ$  showing reflection symmetry about CD; (d) Rotation of the crystal by  $60^\circ$  showing the same nanotopography as in (b).



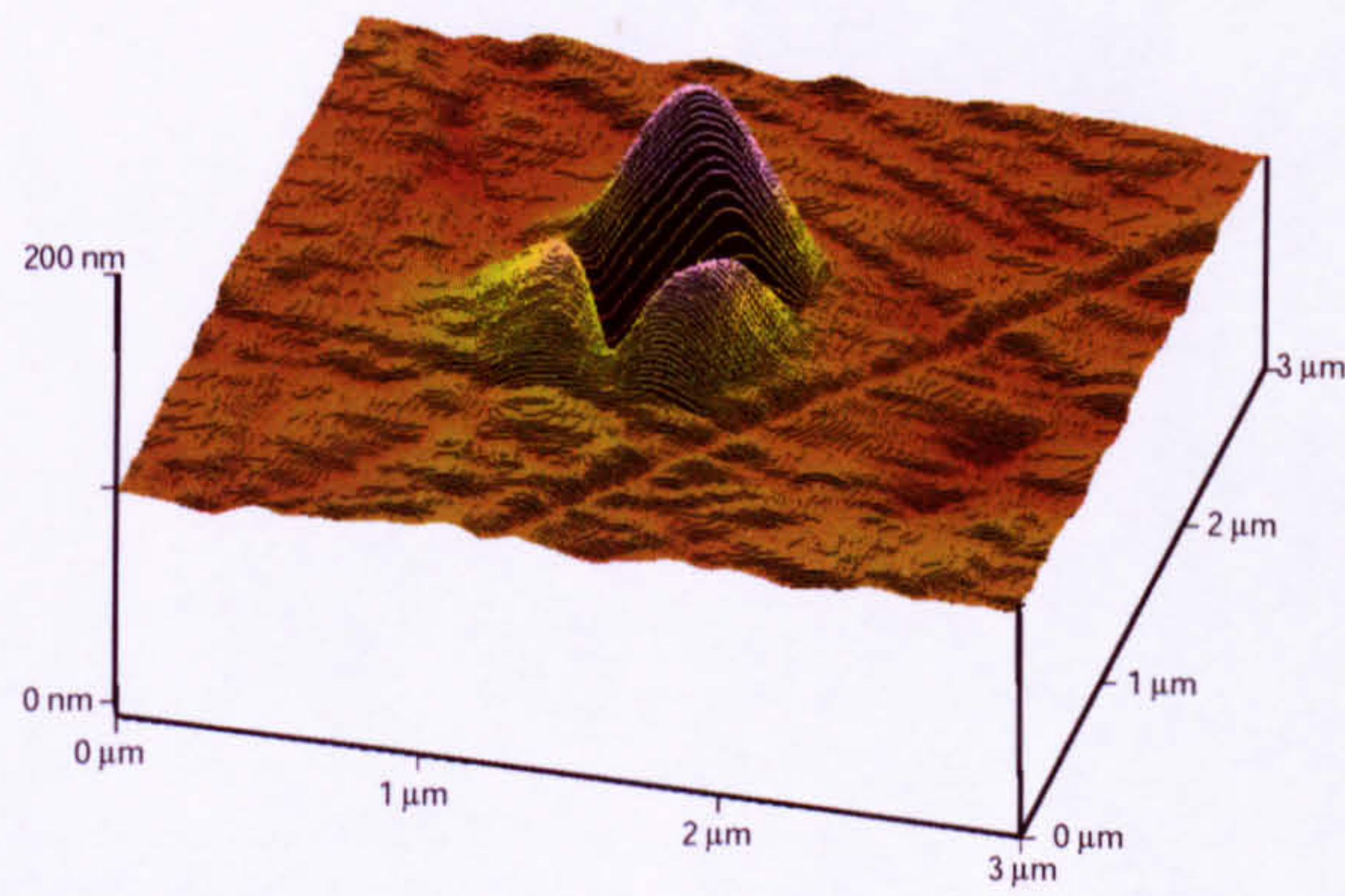


Fig. 7.7.18. Three-dimensional representation of the Fe {110} surface in Fig. 7.7.17(b), showing the difference in pile-up height along the three sides of the indent.

AB (side 1) which corresponds to the two pile-ups in Fig. 7.7.17(a). This orientation corresponds to Fig. 7.7.6(b) in the simulations and compares favourably. The direction of maximum stress is perpendicular to the indenter side, as marked by the arrows in Fig. 7.7.17(b)-(c). The volume of the pile-ups aligned along sides 2 and 3 of the indent in Fig. 7.7.17(b) are measured to be the same as the hillock along side 1. The height of the hillock along side 1 is 82 nm, whereas along the remaining sides the pile-up height is much less at 39 nm and 43 nm.

By rotating the sample by  $30^\circ$  and using a higher force than in Fig. 7.7.17(b), Fig. 7.7.17(c) shows reflection symmetry about the line CD. Side 2 of the indent is aligned parallel to AB and shows a smaller hillock compared with those along sides 1 and 3. This compares to Fig. 7.7.6(c) where pile-up is smallest along the side of the indent parallel to the out-of-plane  $\langle 111 \rangle$  directions and occurs preferentially along the two remaining sides. The height of the hillock along side 3 is approximately 102 nm, compared with 91 nm and 86 nm for side 1 and side 2 respectively. When the sample is rotated by  $60^\circ$  in Fig. 7.7.17(d) the same nanotopography behaviour is observed as in Fig. 7.7.17(b). A three-dimensional representation of the hillocks in Fig. 7.7.17(b) is shown in Fig. 7.7.18, illustrating the difference if the pile-up height along each side of the indent.

Fig. 7.7.19 shows how the pile-up changes with increasing load. For very small loads up to 0.1 mN, no pile-ups can be imaged using the SFM, and the indenter cross-section is almost axially symmetric. As the load increases to 0.2 mN Fig. 7.7.19(b) shows two symmetric pile-ups occur depicting the surface crystal structure, as observed with the spherocone in Fig. 7.7.17(a). In Fig. 7.7.19(c) at a load of 0.4 mN, the pyramidal



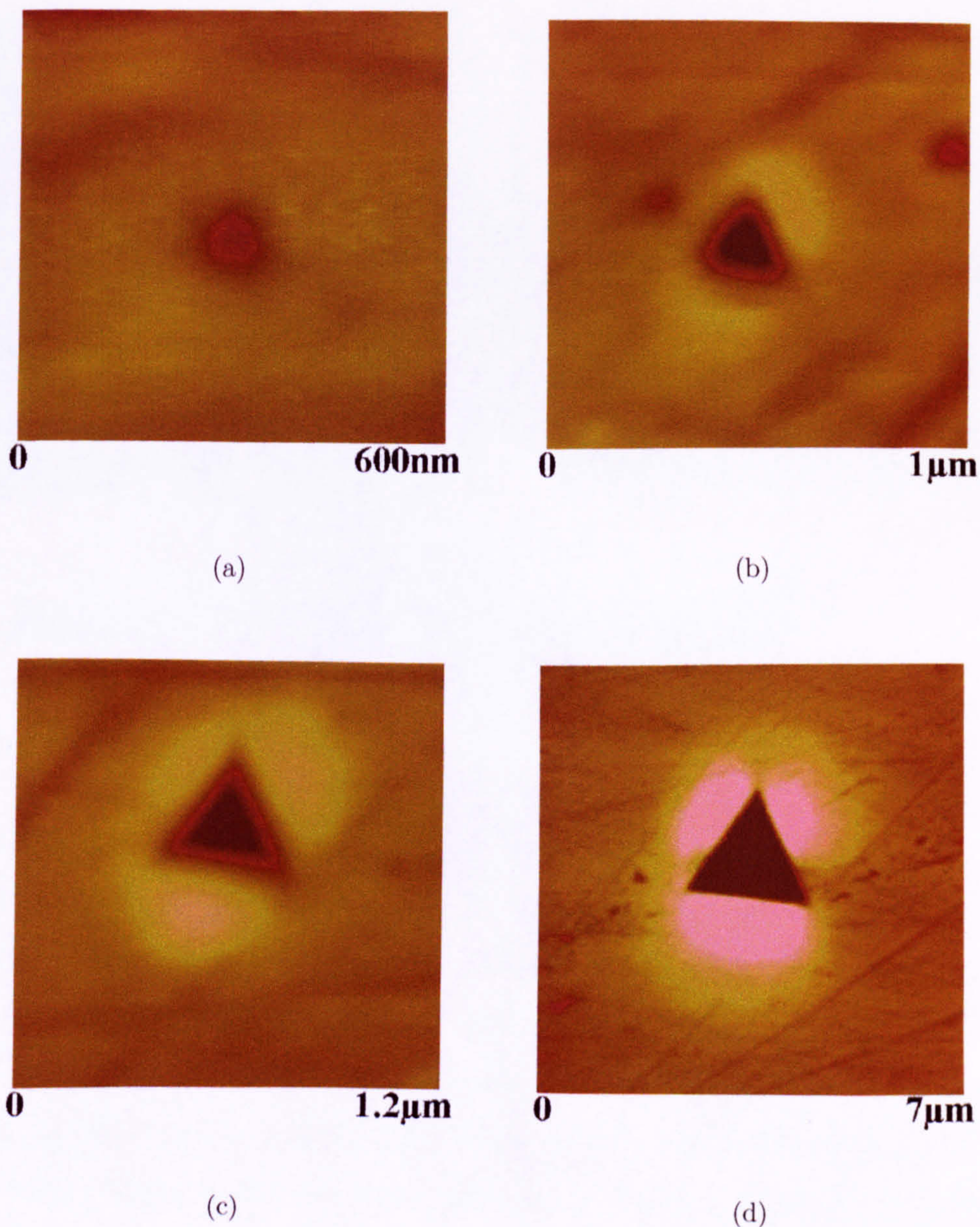


Fig. 7.7.19. SFM images showing the change in pile-up with increasing load for Fe {110}. (a) 0.1mN; (b) 0.2 mN; (c) 0.4 mN; (d) 6 mN. Note that in (a) no pile-ups are observable and the indenter cross-section is almost axially symmetric.

structure of the indenter becomes apparent and asymmetries begin to appear. With an increased load of 6 mN in Fig. 7.7.19(d) the full characteristic asymmetric pyramidal form is again seen.

### 7.5.2 Fe {100} Substrate

SFM images of indents into the {100} face of Fe are shown in Fig. 7.7.20. There are two large pile-ups in Fig. 7.7.20(a), with much less pile-up occurring along the remaining side



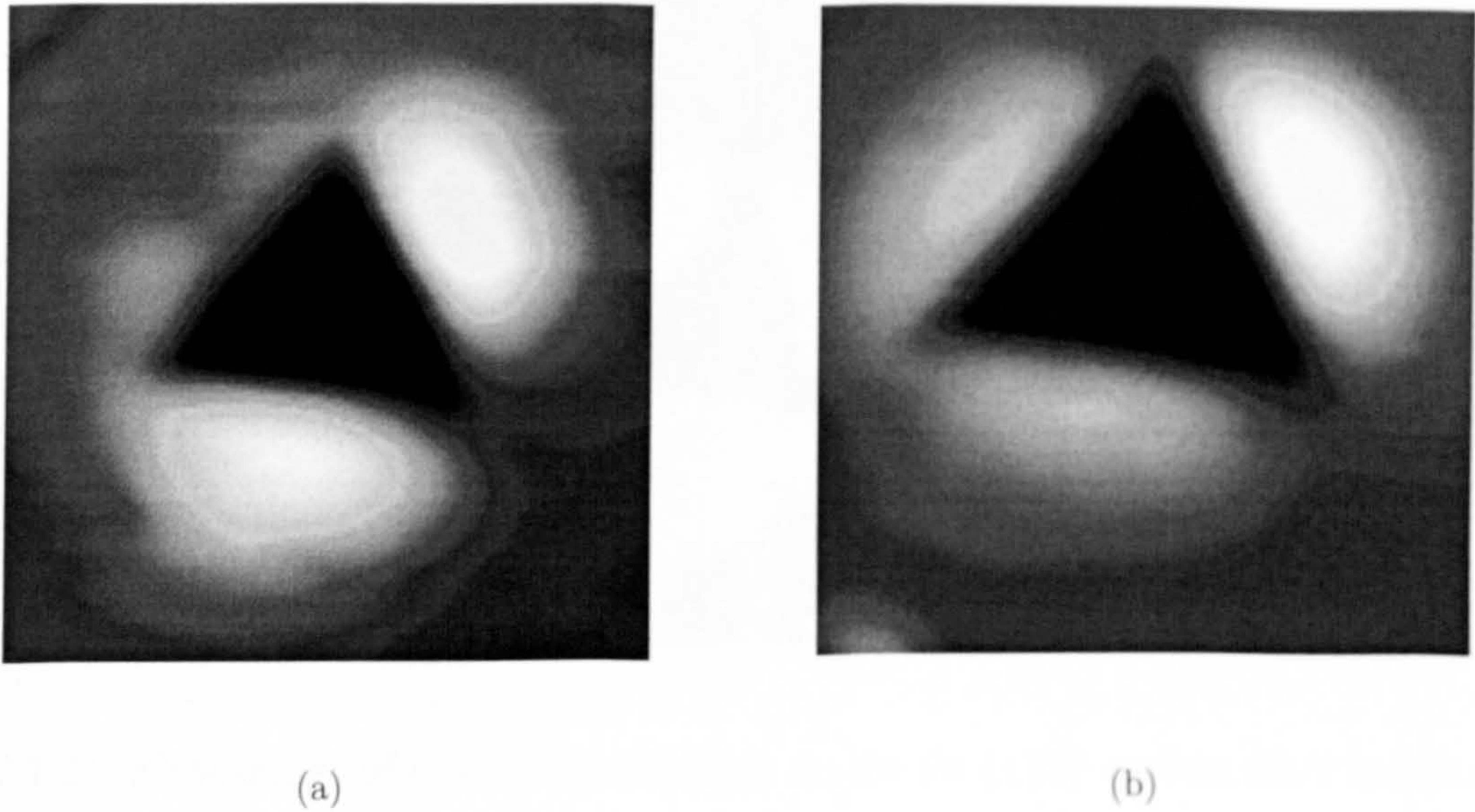


Fig. 7.7.20. SFM images of pile-up distribution on the Fe  $\{100\}$  surface after indentation with a maximum force of 1 mN. Image size: (a)  $1\mu\text{m} \times 1\mu\text{m}$ ; (b)  $1.25\mu\text{m} \times 1.25\mu\text{m}$ .

of the indent. Hence, the normal to the two sides with large pile-ups will be very close to the  $\langle 110 \rangle$  azimuth. There will be a large mis-alignment between the  $\langle 110 \rangle$  azimuth and the normal to the side with little pile-up. The two large hillocks have heights of 44 nm and 35 nm, whilst the smallest hillock is only 5 nm in height. The pile-up distribution is very similar to the simulation results for Fe  $\{100\}$  in Fig. 7.7.11(a). When the sample is rotated by  $45^\circ$ , there is a significant change in the pile-up distribution, as shown in Fig. 7.7.20(b). There is now one large hillock along one side of the indent with a height of 49 nm, with two smaller hillocks of height 22 nm and 26 nm occurring along the remaining sides. This pile-up distribution is analogous to that in the simulation image in Fig. 7.7.11(b).

### 7.5.3 Fe $\{111\}$ Substrate

A SFM image of the  $\{111\}$  face of Fe is shown in Fig. 7.7.21 following indentation with a force of 2mN (note this force is much larger than that used with the  $\{110\}$  or  $\{100\}$  samples). The pile-up is more symmetric compared with the  $\{110\}$  and  $\{100\}$  surfaces. The height of the pile-up around the three sides of the indent was 55 nm, 25nm and 38 nm. The hillocks are therefore similar in height to those for  $\{100\}$ , but were induced with twice the indenter force used with the  $\{100\}$  work piece. Furthermore, the pile-up



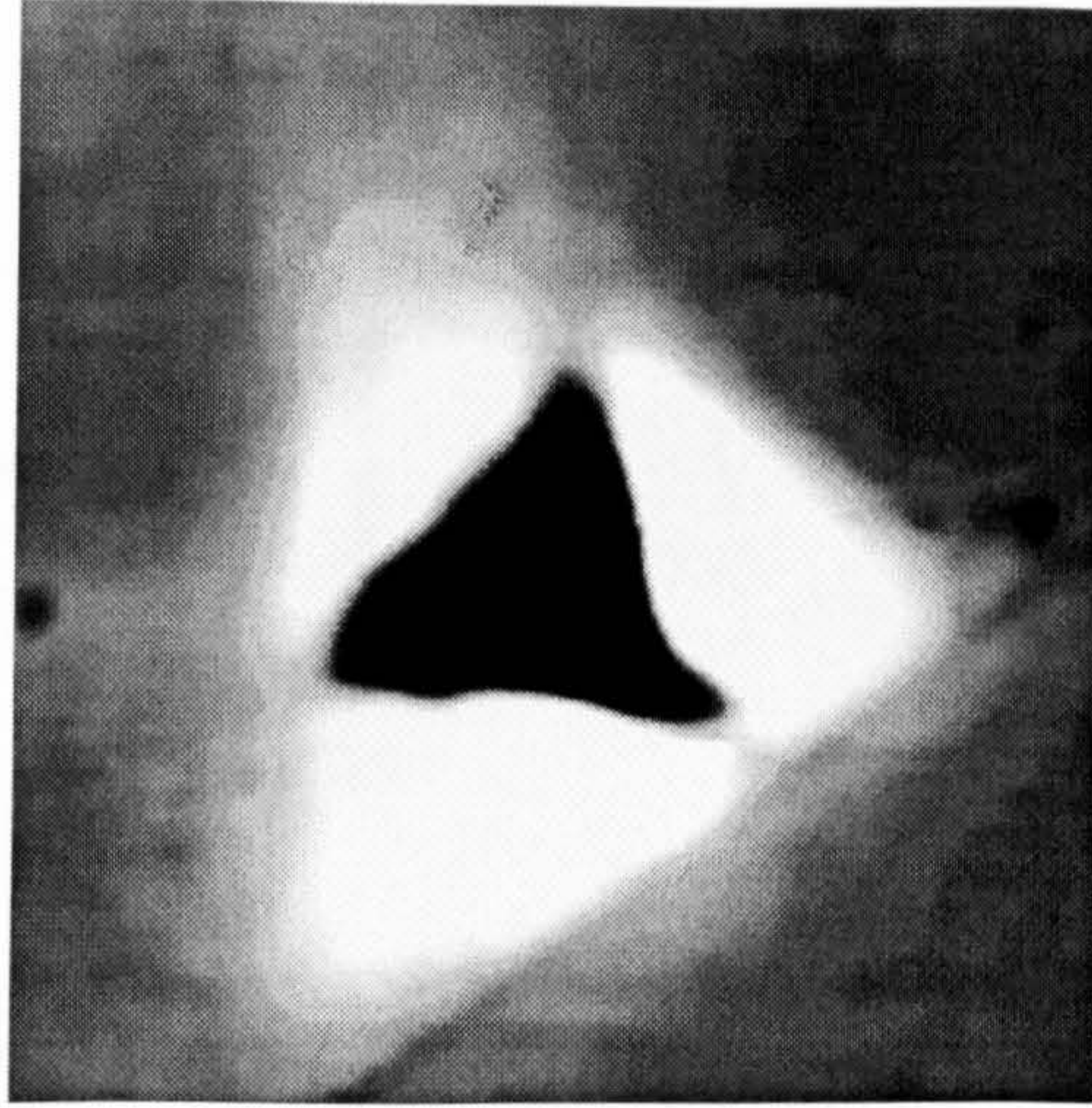


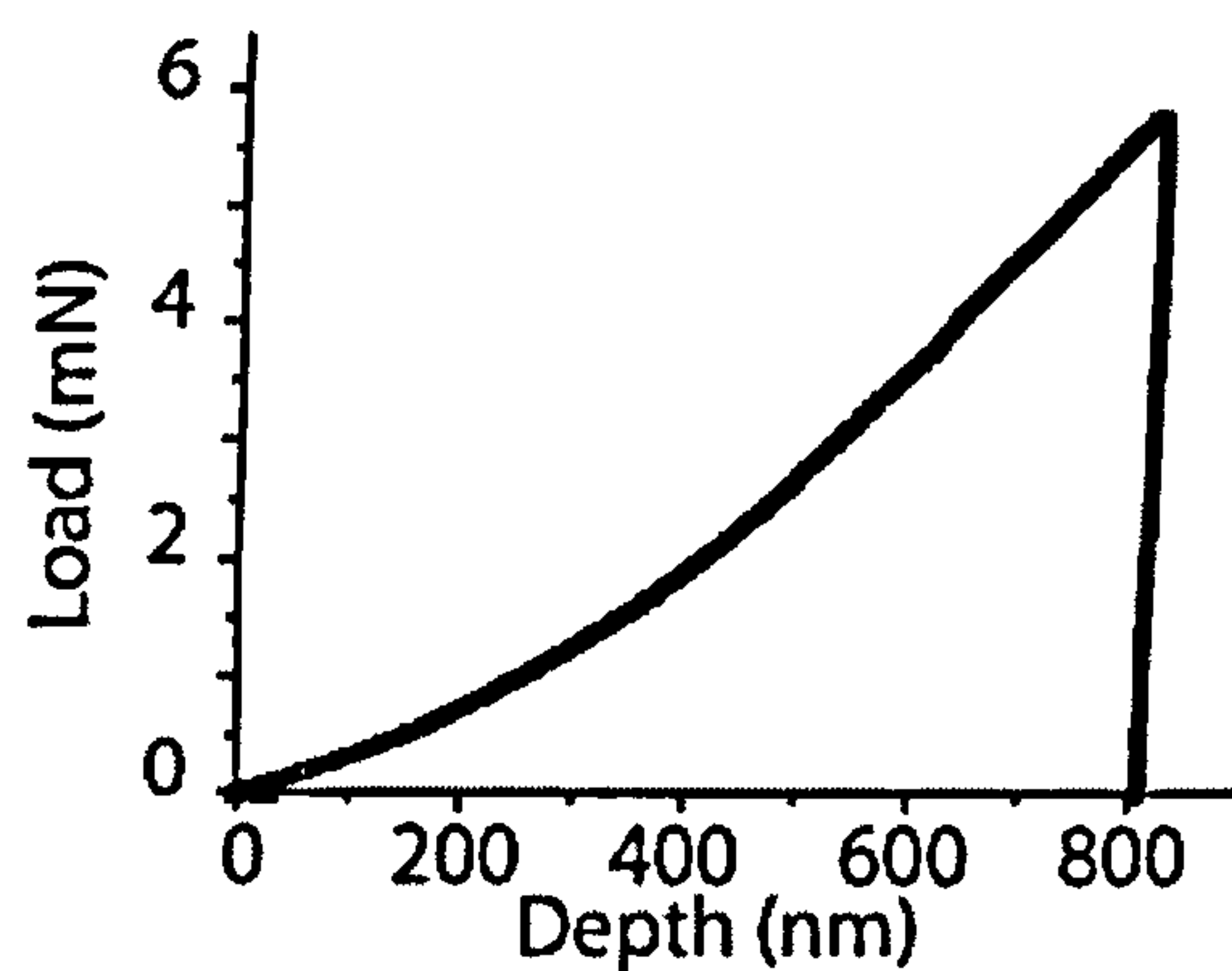
Fig. 7.7.21. SFM image of pile-up distribution on the Fe {111} surface after indentation with a maximum force of 2 mN. Image size  $3\mu\text{m} \times 3\mu\text{m}$ .

is much more spread out compared with the other surfaces, which agrees qualitatively with the simulations. Other nanoindentations performed on the {111} surface show that the pile-up adjacent to the indenter sides appears very similar irrespective of the orientation.

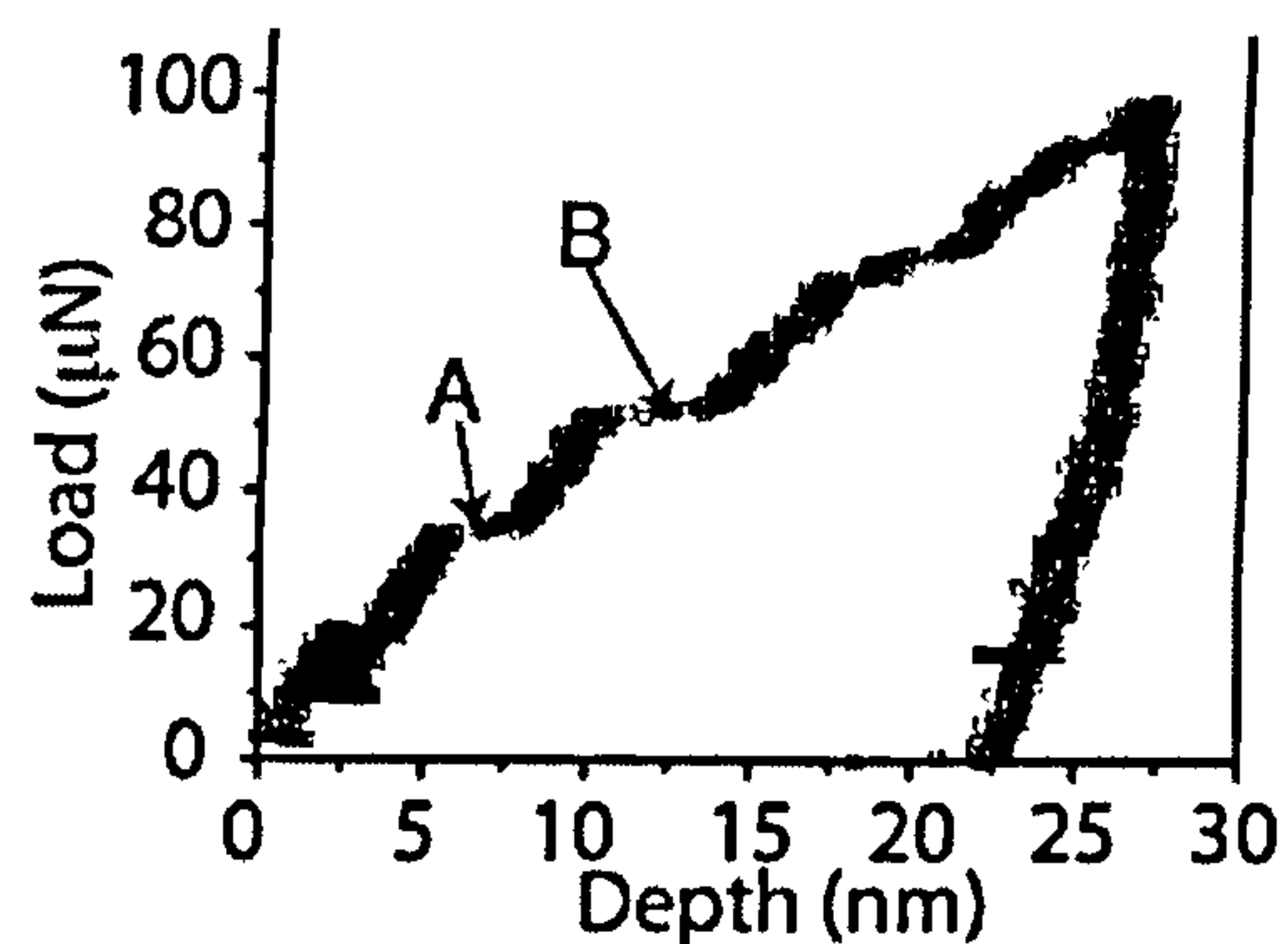
#### 7.5.4 Force-depth Curve Analysis

The force-depth curve from indentation of the Fe {110} crystal with a loading force of 6 mN is shown in Fig. 7.7.22(a). When the loading force is reduced to 0.1 mN, Fig. 7.7.22(b) shows the curve is not smooth and exhibits multiple ‘pop-ins’ marked by the letters A and B in the diagram, where the force remains constant with increased indentation depth. The calculated nanohardness from the force-depth curves is  $\approx 4.75$  GPa for Fig. 7.7.17(a) and 2.25 GPa for Fig. 7.7.17(b). The Young’s modulus increases from around 220 GPa to 300 GPa. The variation in nanohardness as a function of indentation depth is shown in Fig. 7.7.22(c) for Fe {110} and Fe {100}. For small contact depths (less than 200 nm) the nanohardness is similar between the two faces and decreases with increased contact. After a contact depth of around 200 nm, the nanohardness starts to reach a constant value, and the difference in nanohardness between the two samples becomes apparent. The nanohardness extracted from the simulated force-depth curves are smaller than experimental values of between 6 GPa - 8 GPa for small indentation depths ( $< 50$  nm), and are more similar to values for deeper indentation depths.

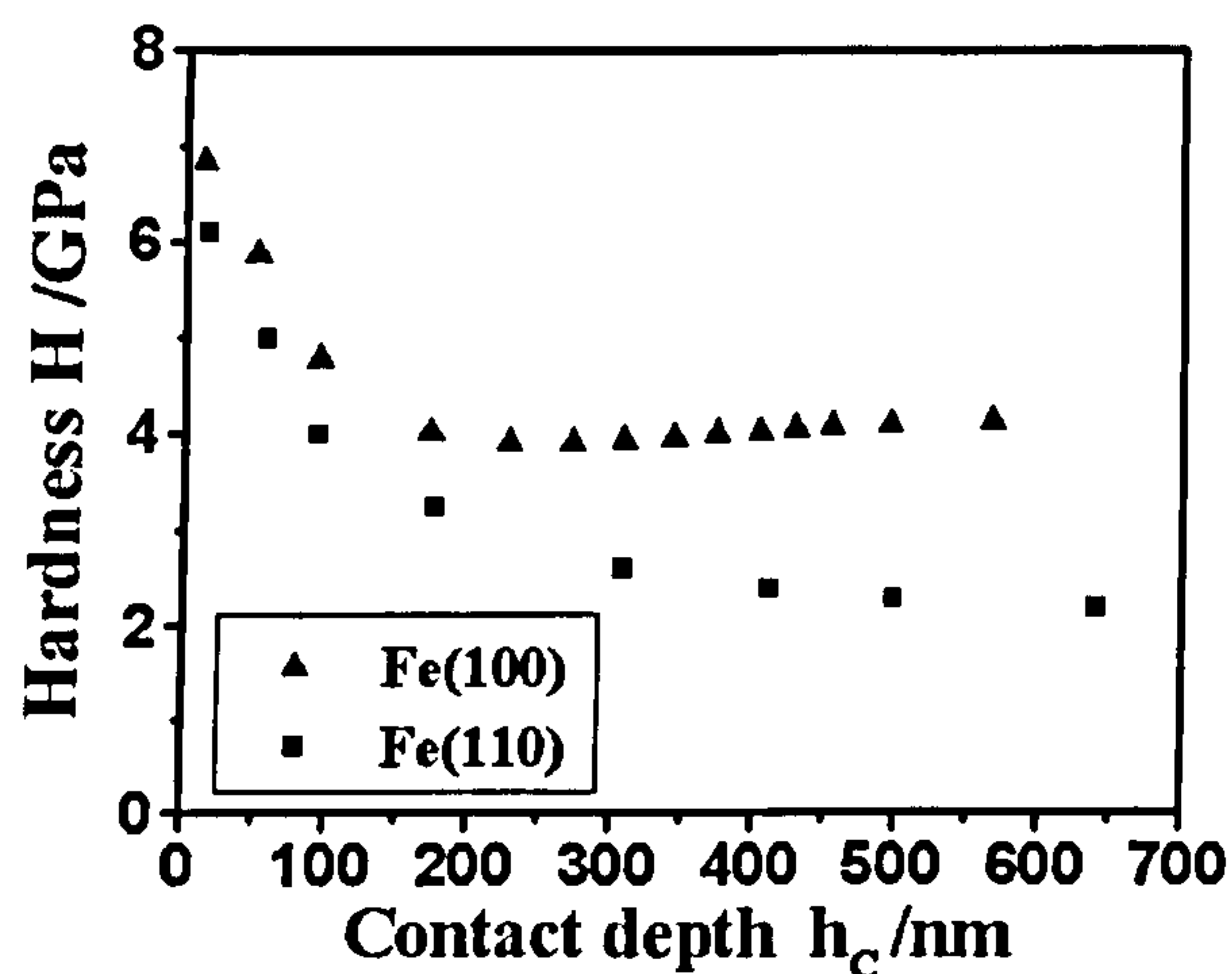




(a)



(b)



(c)

Fig. 7.7.22. (a),(b) Experimental force-depth curves for; (a) 6 mN loading force and (b) 0.1 mN loading force. (c) Experimental curves showing the variation in nanohardness as a function of the indentation depth for Fe {110} and Fe {100}.

## 7.6 Summary

Million atom parallel MD simulations have been performed on the {110}, {100} and {111} surface of bcc Fe to study dislocation mechanisms and preferred crystallographic directions for hillock formation. The three different crystal orientations studied show a diverse distribution of the tip-induced nanotopography. Thus, the nanoindentation technique could be used for orientation mapping. This is particularly important for polycrystals, where the surface orientation of individual grains is not known. In both simulations and experiment, the pile-up reflected the crystal symmetry of the surface.



In each case, the pile-up is greatest when the normal of an indenter side is adjacent to the compact  $\langle 111 \rangle$  directions. When the normal of an indenter side is mis-aligned from the  $\langle 111 \rangle$  direction the pile-up yield decreases. In all cases, the pile-up is greatest along the middle of the indent side, where the maximum stress occurs. Along the corners of the indent, the pile-up is suppressed.

In the simulations, indentation of the  $\{111\}$  surface yielded the smallest pile-up, since the atoms are close packed in the vertical direction, and atoms are preferentially displaced within the layer where the atomic spacing is generous. This leads to a sizeable volume of permanent densification surrounding the indent. The simulation and experimental images show that the pile-up is more spread out over the  $\{111\}$  surface. Indentation of the  $\{110\}$  and  $\{100\}$  surfaces produces more asymmetry in the pile-up compared with  $\{111\}$ , showing distinct preferred crystallographic directions for hillock formation. It is argued [210] that dislocation loops propagating along the out-of-plane  $\langle 111 \rangle$  directions can cross-slip and this can cause piling-up. Since the  $\{100\}$  surface is more symmetric compared with  $\{110\}$  (it contains more out-of-plane  $\langle 111 \rangle$  directions), cross-slip can occur more easily on the  $\{100\}$  surface. Furthermore, the  $\{110\}$  surface contains four in-plane  $\langle 111 \rangle$  directions which transport material away from the indent. These factors combined give a larger pile-up yield on  $\{100\}$  compared with the  $\{110\}$  surface.

The simulations showed that ‘pop-ins’ in the force-depth curves coincide with the emission of dislocation loops around the indent, which propagated along the close packed directions. Each of the three different surfaces show unique dislocations due to the alignment of the slip planes relative to the surface. On intersection with the surface the dislocation loops can produce a stacking fault and give the appearance of a ‘bump’ on the surface. The experimental force-depth curves also revealed ‘pop-ins’, when the indentation force was reduced to the order of tenths of mN. Simulations with  $\{110\}$  also showed how the compression of atoms around the indent can impart phase transformations tending towards a fcc configuration. This was only a temporary change, as the compression relaxed during tip extraction and the atoms returned to a bcc configuration.

In the simulations, the different crystal structures were not generally reflected in the force-depth curves or nanohardness values. Only a 3% variation in nanohardness was observed across the three faces, suggesting that each surface exhibits similar me-



chanical properties over small indentation depths. The extracted nanohardness values compared favourably to experimental values for large contact depths ( $> 200$  nm). However, the experimental results showed the nanohardness increased as the contact depth was reduced. At contact depths of less than 50nm the nanohardness was similar, regardless of the surface orientation. When the contact depth increased, the difference in nanohardness between the surfaces became apparent. The Young's modulus extracted from the simulated force-depth curves was about 50% higher than experimental values, which stems from the difficulty in estimating the gradient of the unloading curve and the small indentation depth.

The million atom simulations have helped to partially alleviate the finite-size effects. Comparisons with the simulations using Fe in Chapter 5 with approximately 40,000 atoms show less edge effects occur. However, in the simulations presented in this chapter, the indentation to the maximum depth (approximately 27% of the substrate thickness) still ensues in interactions with the fixed underside layers of the substrate. Ideally, the experimental rule of thumb should be used, where indentation is performed up to about one tenth of the film thickness to minimise the influence of the underlying substrate. The use of over one million atoms has permitted increased indentation depths, which is crucial to generate a significant pile-up yield to conclude preferential crystallographic directions for hillock formation. For example, the maximum pile-up yield for Fe {100} in the million atom simulation is 5508, compared with only 137 in the 40,000 atom simulation. The use of over one million atoms also yields different values for nanohardness. In the preliminary 40,000 atom simulation, the nanohardness for the {100} face was calculated to be 7.4 GPa compared with 3.25 GPa in the million atom simulation.



# Chapter 8

## Conclusions and Future Work

Classical MD simulations have been performed to study the elastic-plastic deformation behaviour of carbon materials and both bcc Fe and fcc Ag during nanometre-sized indentations. The indenter was preliminary described by a non-deformable interface with pyramidal and axisymmetric geometries. An atomistic description of a 90° pyramidal indenter was also used to study deformation of the tip, adhesive tip-substrate interactions and atom transfer, together with damage after adhesive rupture and mechanisms of tip-induced structural transformations and surface nanotopography. The MD simulations showed interesting yielding phenomena over the range of work materials and surface orientations studied. Diverse deformation behaviour ranged from simple elastic behaviour with graphite, to complex plastic deformation with metals where dislocations and pile-up propagate along certain crystallographic planes. The limiting factor in comparison between the MD simulations and experimental observations is the length scales accessible to each. Despite this, the MD simulations correlated well with experiment by qualitatively modelling the deformation behaviour of the test specimens. Thus, in conclusion MD simulations combined with experiment provide a unique insight into nanoindentation.

Quantitative agreement between experimental results and the preliminary MD simulations could not be found. This stemmed primarily from the finite-size effects in the simulation model, which were imposed by constraints in available computer power. The use of parallel computers, simulating over one million atoms helped to alleviate the finite-size effects and produced results that agreed even better with experiment. The Brenner potential used to describe the interactions within the indenter was not fitted to the elastic constants and will therefore contribute partially to quantitative discrepan-



cies. There are other factors in the MD simulations that limit the physically meaningful interpretation of the numerics. For example, with the exception of  $\alpha$ -C, the substrates are modelled as ‘ideal’ solids, i.e. defect-free and atomically flat. In reality surfaces are seldom atomically flat, containing a multitude of impurities, like oxides, and therefore contact occurs at many asperities. The time scales used in the simulations may have averted some kinetic processes from occurring. Furthermore, the simulations were performed at zero temperature which may have precluded thermally-activated processes developing. A recent theoretical study by Lu *et al* [217] reported on the nanoindentation of Al at different temperatures and found dislocation motion was heavily influenced by the temperature. In addition, experiments with quasi crystals have shown that temperature can heavily influence nanohardness [218]-[219].

The parallel MD code developed for simulating nanoindentation has recently been adapted to investigate friction on the atomic scale. First simulations of scratching the Ag {100} surface with a diamond indenter have been performed [220]. The method of displacing the tip during both indentation and scratching has been developed using

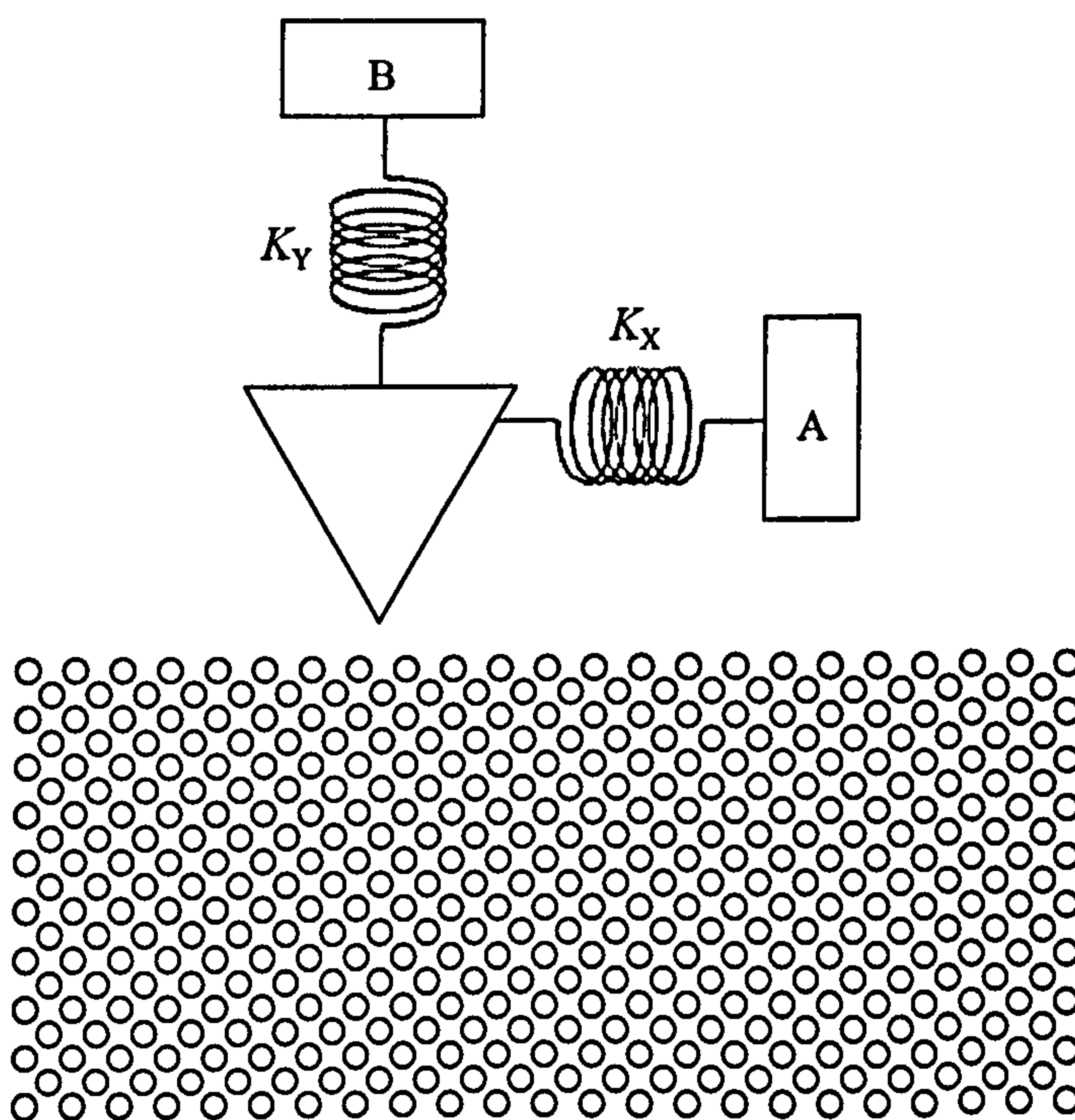


Fig. 8.8.1. Schematic representation of the spring indenter displacement. The indenter is attached to two springs in the vertical (indentation) and horizontal (scratching) directions. The springs are attached to support blocks A and B, and have spring constants  $K_X$  and  $K_Y$  respectively.



the method implemented by Shimuzu *et al* [87] and is illustrated in Fig. 8.8.1. This proposed model allows the influence of the spring constant used experimentally in the cantilever to be considered. Springs with constants  $K_X$  and  $K_Y$  are attached from the indenter to the supports A and B respectively, in both the indentation and scratching directions. During indentation, support B moves at a constant speed and support A moves with respect to the indenter, and vice versa for scratching. The incorporation of the spring and support A during scratching allows the stick-slip phenomena to be investigated [86]-[87]. Since the elastic energy is stored during indentation, this model combined with the parallel MD code may allow the catastrophic breaking of graphite layers to be simulated. This is of particular interest since this large-scale deformation phenomena has been observed experimentally by Richter *et al* [124], but has yet to be modelled by MD.

The parallel MD code is currently being developed using a spatial domain decomposition. By implementing a spatial decomposition, the scalability of the parallel MD

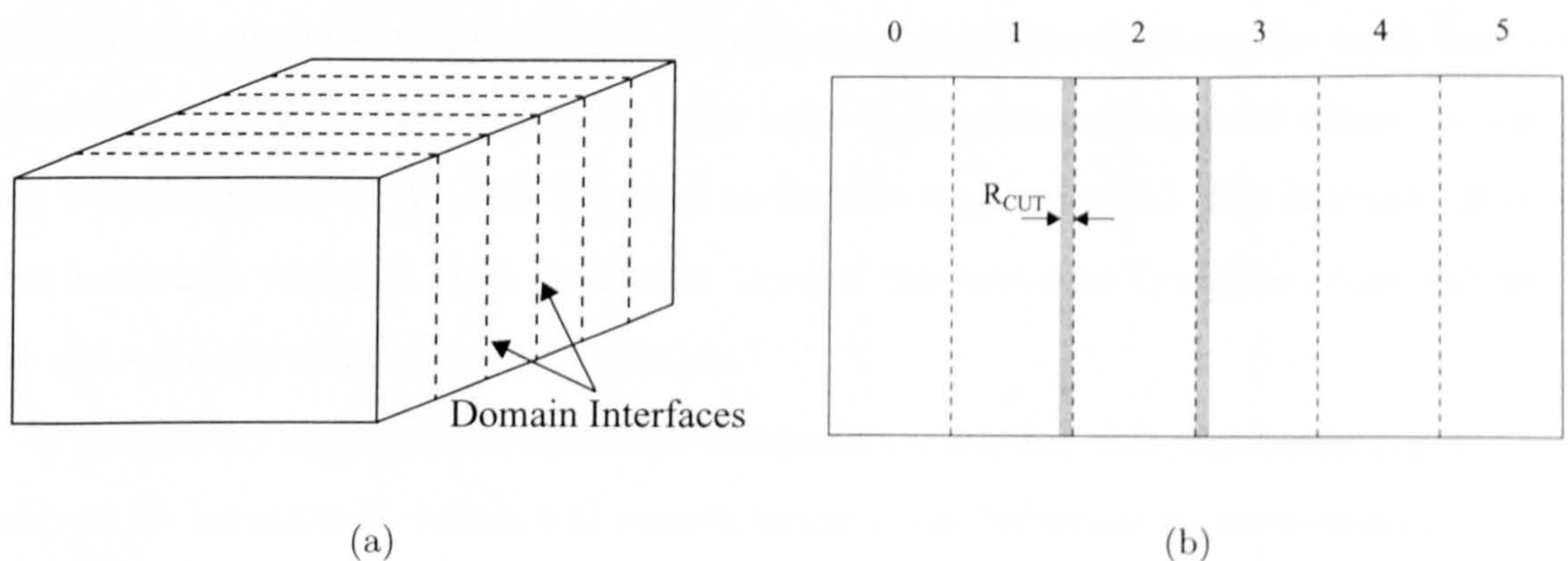


Fig. 8.8.2. (a) Schematic representation of a simple spatial decomposition of the computational box where domains formed from vertical slabs are assigned to different processors. (b) The communication of interactions across neighbouring domains. Processor 2 requires the positions of the atoms in the shaded regions (on neighbouring domains), which interact with atoms in the host domain. Therefore, processors 1 and 3 send the forces acting on these atoms to processor 2. The thickness  $R_{CUT}$  is usually equal to the cut-off distance of the interatomic potential and the skin thickness (for C atoms described by the Brenner potential, the thickness must also account for 2<sup>nd</sup> neighbours of the atoms interacting across the domain interfaces). The same communication process is applied to all the remaining domains.



code can be improved because the communications overhead and memory usage are rapidly reduced since only local communication and local data storage is required. Data arrays for positions, velocities, forces etc., are made local together with the neighbour lists. Consider the simple spatial decomposition depicted in Fig. 8.8.2(a), where the computational box is divided into vertical slabs, and each domain is assigned to a different processor. The communication scheme is illustrated in Fig. 8.8.2(b), where each processor only communicates interactions across the neighbouring domains. When an atom migrates across the domain interface it needs to be removed from the list of atoms in the source domain and added to the list of atoms in the new domain. Therefore, there is a frequent need to check which domain an atom resides within. In the parallel MD code, a cubic spatial decomposition scheme has been implemented, where each processor has 26 domain boundaries. Since the indenter is irregular in shape, the cubic spatial decomposition will produce a load imbalance. Therefore, the interface model of the indenter has been preliminary utilised. For the substrate, load balancing has initially been neglected since it is not trivial to perform. Such a scheme will inevitably be complex and so performance could be maximised by redistributing the work load only when the efficiency of any processor falls below a minimum threshold value. In the future, parallelisation of the MD non-core could also be considered. For example, if online visualisation is required then execution time of the non-core becomes more significant and non-core parallelisation is justifiable.

Improved scaling with the spatial decomposition scheme will allow even greater atom numbers to be utilised, which will enable larger-scale indentation phenomena, like fracture for example, to be studied. Also, the indentation size effect could be addressed by employing greater indentation depths to provide further insight into this phenomena. With the emergence of computers with higher processing capability and memory, billion atom simulations will soon become feasible. Advances with massively parallel machines may enable trillion atom simulations to be performed [221]. Coupled with more realistic interatomic potentials, MD simulations will allow for more favourable comparison with experimental observations and also analytical models derived from classical continuum theory. As parallel architectures become more available and more powerful, the use of ab-initio simulations, and other quantum mechanical methods, will also be inevitably applied to larger and larger systems.

There is now a wealth of experimental nanoindentation information, encompassing



a wide range of materials. Since only covalent and metallic materials have been investigated in this thesis, many other materials, such as ionic crystals and ceramics, need to be examined by MD to provide increased insight. Different crystal structures and surface grains also remain to be probed since crystal orientation and geometry can exhibit diverse deformation behaviour. Metallic materials with hexagonal-close-packed (hcp) crystal structure exhibit dominant slip planes [222] and will provide an interesting comparison to the dislocation and pile-up behaviour of bcc and fcc metals. Future work with metals could also include an attractive term in the potential describing the tip-substrate interactions to study aspects interfacial bonding, such as ‘jump-to-contact’ and ‘connective neck’ formation and rupture, and the influence they have on mechanisms of deformation. In the immediate future, million atom simulations with low index faces of Ag are planned, to compare with the results presented in the preceding chapter with bcc Fe.

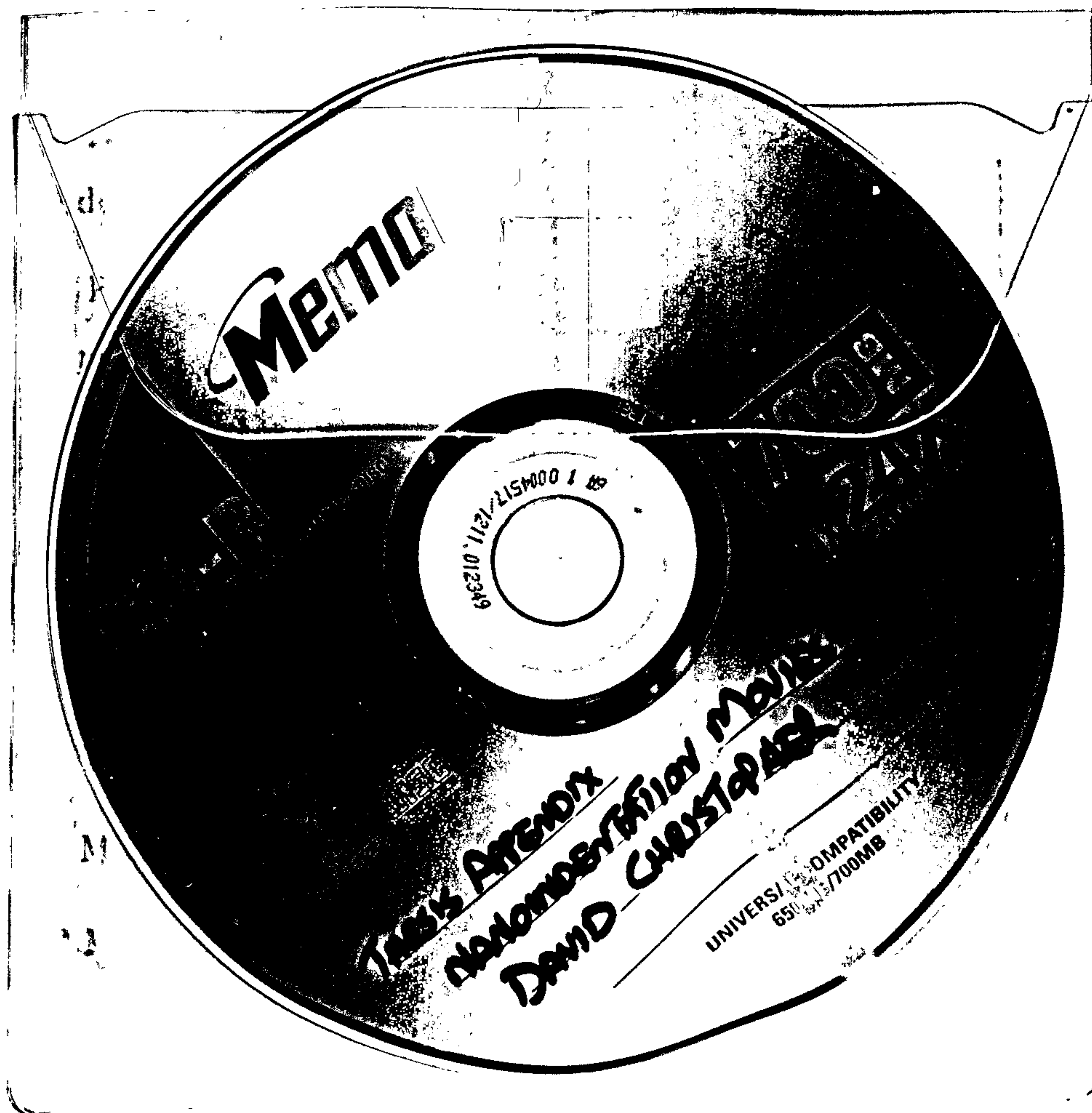
In addition to friction, there are numerous other areas of nanotribology that the nanoindentation model could be developed for and applied to. For example, experimentalists sometimes use repeated indentation in order to remove adsorbates present on the surface of a specimen [223]. Furthermore, in many micromachines repetitive contact between interfaces occurs. Hence, the nanoindentation model could be extended to investigate wear properties of materials through repetitive contact and how deformation from cyclic loading may differ from that induced from single indentations. Another area of nanotribology is the fabrication of nanometre tolerance components [224]. Simulations could therefore use the diamond tip to ‘cut’ the substrate and investigate wear properties.



# Appendix A

## Animated Movies

The CD contains selected animated movies of the nanoindentation process.





# Bibliography

- [1] M M Woolfson and G J Pert. *An Introduction to Computer Simulation*. Oxford University Press, 1999.
- [2] G Ciccotti, D Frenkel, and I R McDonald. *Simulation of Liquids and Solids: Molecular Dynamics and Monte Carlo Methods in Statistical Mechanics*. North-Holland, Amsterdam, 1987.
- [3] D Raabe. *Computational Materials Science*. Wiley-VCH, 1998.
- [4] P E Lewis and J P Ward. *The Finite Element Method: principles and applications*. Addison-Wesley, 1991.
- [5] D Frenkel and B Smit. *Understanding Molecular Simulation: From Algorithms to Applications*. Academic Press, 1996.
- [6] R Smith. *Atom and Ion Collisions in Solids and at Surfaces*. C.U.P, Cambridge, UK, 1997.
- [7] M P Allen and D J Tildesley. *Computer Simulation of Liquids*. Oxford University Press, 1987.
- [8] A L Leach. *Molecular Modelling. Principles and Applications*. Longman, 1996.
- [9] C M Goringe, D R Bowler, and E Hernández. *Rep, Prog. Phys.*, 60(12):1447, 1997.
- [10] N Metropolis, A W Rosenbluth, M N Rosenbluth, A N Teller, and E Teller. *J. Chem. Phys.*, 21:1087, 1953.
- [11] M T Robinson. *Sputtering by Particle Bombardment 1*. Springer, Berlin, 1981.
- [12] B J Alder and T E Wainwright. *Molecular dynamics by electronic computers*. In I. Prigogine, editor, *Proc. of the Int. Symp. on statistical mechanical theory of transport processes (Brussels, 1956)*. Interscience, Wiley, New York, 1958.



- [13] J B Gibson, A N Goland, M Milgrim, and G H Vineyard. *Phys. Rev.*, 120:1229, 1960.
- [14] A Rahman. *Phys. Rev.*, 136:A405, 1964.
- [15] J R Beeler. *Radiation Effects - Computer Experiments*. North Holland, 1983.
- [16] D E Harrison Jr. *CRC Crit. Rev. Solid St. Mater Sci.*, 14:1299, 1988.
- [17] J R Brown, R Earnshaw, M Jern, and J A Vince. *Visualization: Using Computer Graphics to Explore Data and Present Information*. Wiley and Sons, 1995.
- [18] R J Roe. *Computer Simulation of Polymers*. Prentice-Hall, NJ, 1990.
- [19] The Materials Information Society. *Hardness Testing*. ASM International, 1999.
- [20] D Tabor. *The Hardness of Solids*. Oxford University Press, 1951.
- [21] G A Hankins. *Proc. Instn. Mech. Engrs*, 1:423, 1923.
- [22] H O'Neill. *Carnegie Schol. Memoirs, Iron & Steel Inst.*, 17:109, 1928.
- [23] E G Herbert. *Engineer*, 135:390, 1923.
- [24] A Wahlberg. *J. Iron & Steel Inst.*, 59:243, 1901.
- [25] E Meyer. *Zeits. d. Vereines Deutsch. Ingenieure*, 52:645, 1908.
- [26] P Ludwik. *Die Kegelprobe*. J. Springer, Berlin, 1908.
- [27] R Smith and G Sandland. *Proc. Instn. Mech. Engrs.*, 1:623, 1922.
- [28] H O'Neill. *Hardness Measurement of Metals and Alloys*. Chapman and Hall, 1967.
- [29] F Knoop, C G Peters, and W B Emerson. *Nat. Bureau of Standards*, 23:39, 1939.
- [30] E S Berkovich. *Ind. Diamond Rev.*, 11:129, 1951.
- [31] G Chow and K E Gonsalves. *Nanotechnology: molecularly designed materials*. American Chemical Soc., 1996.
- [32] G L Timp. *Nanotechnology*. Springer-Verlag New York, 1999.
- [33] W D Nix. *Mat. Sci. Eng. A*, 234:37, 1997.



- [34] R Hasunuma, T Komeda, and H Tokumoto. *Jpn. J. Appld. Phys.*, 36:3827, 1997.
- [35] L Xiaodong, D Dongfeng, and B Bhushan. *Acta Mater.*, 45(11):4453, 1997.
- [36] A B Mann and J B Pethica. *Phil. Mag. A*, 79(3):577, 1998.
- [37] J E Bradby, S O Kucheyev, J S Wiliams, J Wong-Leung, M V Swain, P Munroe, G Li, and M R Philips. *Appl. Phys. Lett.*, 80(3):383, 2002.
- [38] W C Oliver and G M Pharr. *J. Mater. Res.*, 7(6):1564, 1992.
- [39] W D Nix. *J. Mater. Sci. Eng. A*, 234:234, 1997.
- [40] C Deus, B Wolf, and P Paufler. *Phil. Mag. A*, 75:1171, 1997.
- [41] B Wolf, S Baunack, and P Paufler. *Phys. Stat. Sol. A*, 172:317, 1999.
- [42] J Woirgard, C Tromas, J C Girard, and V Audurier. *J. European Ceramic Soc.*, 18(15):2297, 1998.
- [43] A Krell and S Schadlich. *J. Mater. Sci. Eng. A*, 307:172, 2001.
- [44] A Gouldstone, H J Koh, K Y Zeng, A E Giannakopoulos, and S Suresh. *Acta Mater.*, 48(9):2277, 2000.
- [45] J Caro, J Fraxedas, P Gorostiza, and F Sanz. *J. Vac. Sci. Tech. A*, 19(4):1825, 2001.
- [46] M Heuberger, G Dietler, and L Schlapbach. *J. Vac. Sci. Tech. B*, 14:1250, 1996.
- [47] A Folch, P Gorostiza, J Servat, J Tejada, and F Sanz. *Surf. Sci.*, 380:427, 1997.
- [48] B D Beake and G J Leggett. *Polymer*, 43:319, 2002.
- [49] A Hodzic, J K Kim, and Z H Starhurski. *Polymer*, 41:6895, 2001.
- [50] H J Butt, A Doppenschmidt, G Huttli, E Muller, and O I Vinogradova. *J. Chem. Phys.*, 113(3):1194, 2000.
- [51] M Erikson and S Jacobson. *Tribol. Int.*, 33(12):817, 2000.
- [52] G Willems, J P Celis, P Lambrechts, M Braem, and G Vanherle. *J. Biomed. Mater. Res.*, 27:747, 1993.



- [53] S Habelitz, S J Marshall, G W Marshall, and M Balooch. *Archives of Oral Biology*, 46(2):173, 2001.
- [54] J Y Rho, M E Roy, T Y Tsui, and G M Pharr. *J. Biomed. Mater. Res.*, 45(1):48, 1999.
- [55] Y Y Lim and M M Chaudhri. *Phil. Mag. A*, 79(12):2979, 1999.
- [56] M Goken, M Kempf, and W D Nix. *Acta Mater.*, 49:903, 2001.
- [57] T W Scharf, H Deng, and J A Barnard. *J. Vac. Sci. Tech. A*, 15(3):963, 1997.
- [58] X D Li and B Bhushan. *Thin Solid Films*, 315:214, 1998.
- [59] W R LaFontaine, B Yost, and C Li. *J. Mater. Res.*, 5(4):776, 1990.
- [60] Y Y Lim and M M Chaudhri. *J. Phys. D*, 34:70, 2001.
- [61] T Chudoba, N Schwarzer, F Richter, and U Beck. *Thin Solid Films*, 377:366, 2000.
- [62] J G Swadener, B Taljat, and G M Pharr. *J. Mater. Res.*, 16(7):2091, 2001.
- [63] R Erlandsson and V Yakimov. *Phys. Rev. B*, 62(20):13680, 2000.
- [64] S Sridhar, A E Giannakopoulos, and S Suresh. *J. Appl. Phys.*, 87(12):8451, 2000.
- [65] L Riester, R Bridge, and K Breder. *Mat. Res. Soc. Symp. Proc*, 522:45, 1998.
- [66] K Sangwal, P Gorostiza, and F Sanz. *Surf. Sci.*, 446:314, 2000.
- [67] B Wei and K Komvopoulos. *J. Tribol.*, 118(2):431, 1996.
- [68] M A Lantz, S J O'Shea, and M E Welland. *Phys. Rev. B*, 56(23):15345, 1997.
- [69] J D Kiely, R Q Hwang, and J E Houston. *Phys. Rev. Lett.*, 81(20):4424, 1998.
- [70] S Akita, H Nishijima, T Kishida, and Y Nakayama. *Jap. J. Appl. Phys.*, 39:7086, 2000.
- [71] G Cross, A Schirmeisen, A Stadler, P Grutter, M Tschudy, and M Durig. *Phys. Rev. Lett.*, 80(21):4685, 1998.
- [72] A B Mann and J B Pethica. *Langmuir*, 12:40583, 1996.



- [73] B D Beake and G J Leggett. *Polymer*, 43:319, 2002.
- [74] F J Baltá Calleja. *Adv. Polym. Sci.*, 66:117, 1985.
- [75] A K Bhattacharya and W D Nix. *Int. J. Solids. Struct.*, 24(9):881, 1988.
- [76] D E Vlachos, Y P Markopoulos, and V Kostopoulos. *Comp. Mech.*, 27:138, 2001.
- [77] G S Smith, E B Tadmor, N Bernstein, and E Kaxiras. *Acta Mater.*, 49:4089, 2001.
- [78] R Pérez, M C Payne, and A D Simpson. *Phys. Rev. Lett.*, 75(26):4748, 1995.
- [79] S H Ke, T Uda, R Pérez, I Štich, and K Terakura. *Phys. Rev. B*, 60(16):11631, 1999.
- [80] G Eisenhauer and K Schwan. *J. Parallel & Dist. Comp.*, 35:76, 1996.
- [81] B Bhushan (ed.). *Handbook of Micro/Nano Tribology*. CRC Press, 1999.
- [82] J A Harrison, C T White, R J Colton, and D W Brenner. *Mater. Res. Soc. Bull.*, 18:50, 1993.
- [83] R Komanduri, N Chandrasekaran, and L M Raff. *WEAR*, 240:113, 2000.
- [84] T Fang and C Weng. *Nanotechnology*, 11:148, 2000.
- [85] R Komanduri, N Chandrasekaran, and L M Raff. *WEAR*, 242:60, 2000.
- [86] U Landman, W D Luedtke, and W M Ribarsky. *J. Vac. Sci. Tech. A*, 7:2829–2839, 1989.
- [87] J Shimizu, H Eda, M Yoritsune, and E Ohmura. *Nanotechnology*, 9:118, 1998.
- [88] W G Hoover, A J De Groot, C G Hoover, I F Stowers, T Kawai, B L Holian, T Boku, S Ihara, and J Belak. *Phys. Rev. A*, 42(10):5844, 1990.
- [89] I L Singer and H M Pollock (eds.). *Fundamentals of Friction: Macroscopic and Microscopic Processes*. MIT press, 1992.
- [90] M Lupkowski and J F Maguire. *Phys. Rev. B*, 45(23):13733, 1992.
- [91] M Born and J E Mayer. *Zeitschrift fur Physik*, 75:1, 1932.
- [92] J E Lennard-Jones. *Proc. Roy. Soc. A*, 106:441, 1924.



- [93] L A Girifalco and V G Weitzer. *Phys. Rev.*, 114:687, 1959.
- [94] J Tersoff. *Phys. Rev. Lett.*, 56:632, 1988.
- [95] J Tersoff. *Phys. Rev. B*, 39:5566, 1989.
- [96] D Brenner. *Phys. Rev. B.*, 42(15):9458, 1990.
- [97] D Brenner. *Phys. Rev. B.*, 46:1948, 1992.
- [98] M S Daw and M I Baskes. *Phys. Rev. B*, 29(12):6443, 1984.
- [99] H Hohenberg and W Kohn. *Phys. Rev.*, 136:864, 1964.
- [100] R A Johnson. *Phys. Rev. B*, 37(8):3924, 1988.
- [101] H Berendsen and W Van Gunsteren. *Soc. Italiana di Fisica*, page 43, 1985.
- [102] R W Hockney. *Meth. in Comp. Phys.*, 9:136, 1970.
- [103] M C Swope, H C Anderson, P H Berens, and K R Wilson. *J. Chem. Phys.*, 76:637, 1982.
- [104] D Beeman. *J. Comp. Phys.*, 20:130, 1976.
- [105] W G Hoover. *Molecular Dynamics*. Springer-Verlag, Berlin, 1986.
- [106] L Verlet. *Phys. Rev.*, 159:98, 1967.
- [107] R W Hockney and J W Eastwood. *Computer Simulation Using Particles*. McGraw-Hill, New York, 1981.
- [108] W D Eckstein. *Computer Simulation of Ion-Solid Interactions*. Springer, Berlin, 1991.
- [109] K M Beardmore. *Ph.D. Thesis*. Loughborough University, 1995.
- [110] C E Kolb. *Rayshade User's Guide and Reference Manual*. 1992.
- [111] C Kittel. *Introduction to Solid State Physics*. Wiley, London, 1996.
- [112] J Lindhard, M Scharff, H E Schiott, and K Dan Vidensk. *Selsk. Mat. Fys. Medd.*, 33, 1963.



- [113] D G Pettifor and A M Cottrell (eds.). *Electron Theory in Alloy Design*. Institute of Materials, London, 1992.
- [114] H O Pierson. *Handbook of Carbon, Graphite, Diamond and Fullerenes*. Noyes, 1993.
- [115] B Bhushan (ed.). *Modern Tribology Handbook, Vol II*. CRC Press, 2001.
- [116] J A Harrison, R J Colton, C T White, and D W Brenner. *Mat. Res. Soc. Symp. Proc.*, 239:573, 1992.
- [117] J A Harrison, R J Colton, C T White, and D W Brenner. *Surf. Sci.*, 271:57, 1992.
- [118] A Garg, J Han, and S B Sinnott. *Phys. Rev. Lett.*, 81(11):2260, 1998.
- [119] A Garg and S B Sinnott. *Phys. Rev. B*, 60(19):13786–13791, 1999.
- [120] F N Dzegilenko, D Srivastava, and S Saini. *Nanotechnology*, 10:253, 1999.
- [121] J N Glosli, M R Philpott, and J Belak. *Mater. Res. Soc. Symp. Proc.*, 383:431, 1995.
- [122] S B Sinnott, R J Colton, C T White, O A Shenderova, D W Brenner, and J A Harrison. *J. Vac. Sci. Tech. A*, 15(3):936, 1997.
- [123] S Umemura, Y Andoh, S Hirono, T Miyamoto, and R Kaneko. *Phil. Mag. A*, 74(5):1143, 1996.
- [124] A Richter, R Ries, R Smith, M Henkel, and B Wolf. *Diamond and Related Materials*, 9:170, 2000.
- [125] E Martinez, J L Andujar, M C Polo, J Esteve, J Robertson, and W I Milne. *Jpn. J. Appl. Phys.*, 10(2):145, 2001.
- [126] X D Li, D F Diao, and B Bhushan. *Acta Mater.*, 45(11):4453, 1997.
- [127] S Akita, H Nishijima, T Kishida, and Y Nakayama. *Jpn. J. Appl. Phys.*, 39(12B):7086, 2000.
- [128] R Smith and K Beardmore. *Thin Solid Films*, 272(2):255, 1996.



- [129] J P Biersack, J Ziegler, and U Littmack. *The Stopping and Range of Ions in Solids*. Pergamon, 1985.
- [130] M J Henkel. *M.Phil Thesis*. Loughborough University, 2000.
- [131] V V Pokropivny, VV Skorokhod, and A V Pokropivny. *Modelling Simul. Mater. Sci. Eng.*, 5:579, 1997.
- [132] W N Reynolds. *Physical Properties of Graphite*. Elsevier, 1968.
- [133] C L Mantell. *Carbon and Graphite Handbook*. Interscience, 1968.
- [134] R Berman. *Physical Properties of Diamond*. Oxford University Press, 1965.
- [135] H Hertz and J Reine Angew. *Mathematik*, 92:156, 1882.
- [136] K L Johnson. *Contact Mechanics*. C.U.P, Cambridge, 1985.
- [137] D W Brenner O A Shenderova, J A Harrison, S J Stuart, B Ni, and S B Sinnott. *J. Phys.: Condens. Matter*, 14:783, 2002.
- [138] M F Doerner and W D Nix. *J. Mater. Res.*, 1:601, 1986.
- [139] G V Samsanov (ed.). *Handbook of Hardness Data*. Israel Program for Scientific Translations, Jerusalem, 1971.
- [140] J H Westbrook and H Conrad (eds.). *The Science of Hardness Testing and Its Research Applications*. American Society for Metals, Metals Park, OH, 1973.
- [141] D Christopher, R Smith, and A Richter. *Nucl. Instr. and Meth. in Phys. Res. B*, 180:117, 2001.
- [142] B Wolf, M Swain, M Kempf, and P Paufler. *J. Mater. Sci.*, 35:723, 2000.
- [143] S Ciraci, A Baratoff, and Inder P Batra. *Phys. Rev. B*, 41(5):2763, 1989.
- [144] R Astala, M Kaukonen, R M Nieminen, and T Heine. *Phys. Rev. B*, 61(4):2973, 2000.
- [145] A Hirsch. *The Chemistry of the Fullerenes*. Thieme, 1994.
- [146] X D Li, D F Diao, and B Bhushan. *J. Mater. Res.*, 8:3019, 1993.



- [147] L S Pan and D R Kania. *Diamond: Electronic Properties and Applications*. Kluwer, Dordrecht, Netherlands, 1995.
- [148] T Koehler, T Frauenheim, and G Jungnickel. *Phys. Rev. B*, 52(11):11837, 1995.
- [149] F Rossi, B Andre, A Van Veen, P E Mijnaerends, H Schut, W Gissler, J Haupt, G Lucazeau, and L Abello. *J. Appl. Phys.*, 75(6):3121, 1994.
- [150] H U Jäger and K Albe. *J. Appl. Phys.*, 88(2):1129, 2000.
- [151] K Nordlund, J Keinonen, and T Mattila. *Phys. Rev. Lett.*, 77(4):699, 1996.
- [152] Triboscope Nanomechanical Test Instruments. *Hysitron Handbook*. 1997.
- [153] R Wiesendanger and H-J Güntherodt (Eds.). *Scanning Tunneling Microscopy II*. Springer-Verlag, Berlin, 1995.
- [154] J S Field. *The Properties of Diamond*. Academic Press, London, 1979.
- [155] V D Blank, S G Buga, N R Serebryanaya, G A Dubitsky, R H Bagramov, M Y Popov, V M Prokhorov, and S A Sulyanov. *Appl. Phys. A*, 64:247, 1997.
- [156] V D Blank, V N Denisov, A N Ivlev, B N Mavrin, N R Serebryanaya, G A Dubitsky, S N Sulyanov, M Y Popov, N A Lvova, S G Buga, and G N Kremkova. *Carbon*, 36:1263, 1998.
- [157] A Richter and R Ries. *SPIE*, 94:3725, 1999.
- [158] B K Gupta, B Bhushan, C Capp, and J V Coe. *J. Mater. Res.*, 9:2823, 1994.
- [159] H Coufal, K Meyer, R K Grygier, M de Vries, D Jenrich, and P Hess. *Appl. Phys. A*, 59:83, 1994.
- [160] W Zhao, J Tang, A Puri, R L Sweany, Y Li, and L Chen. *J. Mater. Res.*, 11:2749, 1996.
- [161] M M Chaudhri and M Winter. *J. Phys. D: Appl. Phys.*, 21:370, 1988.
- [162] N Gane and F P Bowden. *J. Appl. Phys.*, 39:1432, 1968.
- [163] U Landman, W D Luedtke, N A Burnham, and R J Colton. *Science*, 248:454, 1990.



- [164] U Landman and W D Luedtke. *J. Vac. Sci. Tech. B*, 9:414, 1991.
- [165] U Landman, W D Luedtke, and E M Ringer. *WEAR*, 153:3, 1992.
- [166] A Buldum, S Ciraci, and I P Batra. *Phys. Rev. B*, 57(4):2468, 1997.
- [167] O Tomangnini, F Ercolessi, and E Tosatti. *Surf. Sci.*, 287:1041, 1993.
- [168] J Belak, D B Boercker, and I Stowers. *MRS Bull.*, page 55, 1993.
- [169] A Bolshakov, W C Oliver, and G M Pharr. *J. Mater. Res.*, 11(3):760, 1996.
- [170] L Kuipers and J W M Frenken. *Phys. Rev. Lett.*, 70(25):3907, 1993.
- [171] M Brandbyge, J Schiøtz, M R Sørensen, P Stolze, K W Jacobsen, J K Nørskov, L Olesen, E Laegsgaard, I Stensgaard, and F Besenbacher. *Phys. Rev. B.*, 52(11):8499, 1995.
- [172] G M Pharr and W C Oliver. *J. Mater. Res.*, 4(1):94, 1988.
- [173] Y Liu and A H W Ngan. *Scripta Mater.*, 44:237, 2001.
- [174] S G Corcoran, R J Colton, E T Lilleodden, and W W Gerberich. *Phys. Rev. B*, 55(24):16057, 1997.
- [175] G E Abrosimova, A S Aronin, Yu V Kir'janov, T F Gloriant, and A L Greer. *NanoStruct. Mater.*, 12:617, 1999.
- [176] Y Huang, M J Aziz, J W Hutchinson, A G Evans, R Saha, and W D Nix. *Acta Mater.*, 49:2853, 2001.
- [177] W Bollman. *Crystal Defects and Crystalline Interfaces*. Springer-Verlag, New York, 1970.
- [178] G A Bruggeman R J Harrison and G A Bishop. *Grain Boundary Structure and Properties*. Academic Press, New York, 1976.
- [179] P J Goodhew. *Grain Boundary Structure and Kinetics*. ASM, Metals Park OH, 1980.
- [180] D Christopher, R Smith, and A Richter. *Nanotechnology*, 12:372, 2001.



- [181] M W Finnis and J E Sinclair. *Philos. Mag. A*, 50:45, 1984.
- [182] G J Ackland, G Tichy, V Vitek, and M W Finnis. *Philos. Mag. A*, 56(6):735, 1987.
- [183] A C Damask and G J Dienes. *Point Defects in Metals*. Gordon and Breach, 1963.
- [184] M Goken, M Kempf, M Bordenet, and H Verhoff. *Surface and Interface Analysis*, 27:302, 1999.
- [185] T Ohmura, S Matsuoka, K Tanaka, and T Yoshida. *Thin Solid Films*, 385:198, 2001.
- [186] G. Patriarche and E Le Bourhis. *Phil. Mag. A*, 80(12):2899, 2000.
- [187] H S Leipner, D Lorenz, A Zeckzer, H Lei, and P Grau. *Physica B*, 308:446, 2001.
- [188] V Domnich, Y Gogotsi, and M Trenary. *Mat. Res. Soc. Symp. Proc.*, 649, 2001.
- [189] R W K Honeycombe. *The Plastic Deformation of Metals*. Edward Arnold, London, 1984.
- [190] G I Taylor and C F Elam. *Proc. R. Soc. A*, 112:337, 1926.
- [191] G I Taylor and C F Elam. *Proc. R. Soc. A*, 153:273, 1936.
- [192] O Rodríguez de la Fuente, J A Zimmerman, M A González, J de la Figuera, J C Hamilton, W W Pai, and J M Rojo. *Phys. Rev. Lett.*, 88(3):036101, 2002.
- [193] O Rodríguez de la Fuente, J A Zimmerman, M A González, and J M Rojo. *Mat. Res. Soc. Symp. Proc.*, 640, 2001.
- [194] T L Sterling, J Salmon, D J Becker, and D F Savarese. *How to Build a Beowulf*. MIT press, 1999.
- [195] I Foster. *Designing and Building Parallel Programs*. Addison-Wesley, 1995.
- [196] L Dagum and R Menon. *IEEE Computational Science and Engineering*, 5:46, 1998.
- [197] A Geist. *PVM3 User's Guide and Reference Manual*. 1994.



- [198] Message Passing Interface Forum. *MPI: A Message-Passing Interface Standard*. 1994.
- [199] Message Passing Interface Forum. *MPI-2: Extensions to the Message-Passing Interface*. 1997.
- [200] M E Bachlechner, A Omeltchenko, A Nakano, R K Kalia, P Vashishta, I Ebbsjö, and A Madhukar. *Phys. Rev. Lett.*, 84(2):322, 2000.
- [201] P Vashishta, M E Bachlechner, T Campbell, R K Kalia, H Kikuchi, S Kodiyalam, A Nakano, S Ogata, F Shimojo, and P Walsh. *Progress of Theoretical Physics Supplement*, 138:175, 2000.
- [202] I M Smith. *Programming in Fortran 90*. John Wiley & Sons, 1995.
- [203] K Beardmore and R Smith. *Phil. Mag. A*, 74(6):1439, 1996.
- [204] S Plimpton. *J. Comput. Phys.*, 117:1, 1995.
- [205] L Nyland, J Prins, R Yun, J Hermans, H Kum, and L Wang. *J. Parallel & Dist. Comp.*, 47:125, 1997.
- [206] S G Srinivasan, I Ashok, H Jönsson, G Kalonji, and J Zahorjan. *Comput. Phys. Commun.*, 102:44, 1997.
- [207] P Walsh, R K Kalia, A Nakano, P Vashishta, and S Saini. *Appl. Phys. Lett.*, 77(26):4332, 2000.
- [208] P Vashishta, M Bachlechner, A Nakano, T J Campbell, R K Kalia, S Kodiyalam, S Ogata, F Shimojo, and P Walsh. *Appl. Surf. Sci.*, 182:258, 2001.
- [209] D Christopher, S D Kenny, R Smith, B Wolf, R Ries, A Richter, and B King. *Phys. Rev. Lett.*, 2002. Submitted.
- [210] R Smith, D Christopher, S D Kenny, A Richter, and B Wolf. *Phys. Rev. B*, 2002. Submitted.
- [211] C L Kelchner, S J Plimpton, and J C Hamilton. *Phys. Rev. B*, 58(17):11085, 1998.
- [212] J A Zimmerman, C L Kelchner, P A Klein, J C Hamilton, and S M Foiles. *Phys. Rev. Lett.*, 97(16):165507, 2001.



- [213] J. de la Figuera, M A González, R Garecía-Martínez, J M Rojo, O S Hernán, A L Vázquez de Parga, and R Miranda. *Phys. Rev. B*, 58:1169, 1998.
- [214] A Samsavar, E S Hirschorn, T Miller, F M Leibsle, J A Eades, and T C Chiang. *Phys. Rev. Lett.*, 65:1607, 1990.
- [215] J Jacobsen, L Pleath Nielsen, F Besenbacher, I Stensgaard, E Laegsgaard, T Rasmussen, K W Jacobsen, and J K Nørskov. *Phys. Rev. Lett.*, 75:489, 1995.
- [216] D A Porter and K E Easterling. *Phase Transformations in Metals and Alloys*. London: Chapman and Hall, 1992.
- [217] H Yu, J B Adams, and L G Hector Jr. *Modelling Simul. Mater. Sci. Eng.*, 10:319, 2002.
- [218] B Wolf and P Paufler. *Phys. Stat. Solid. A*, 172(2):341, 1999.
- [219] B Wolf, K O Bambauer, and P Paufler. *J. Mater. Sci. Eng. A*, 298:284, 2001.
- [220] D Mulliah, D Christopher, S D Kenny, and R Smith. *Nucl. Instr. and Meth. in Phys. Res. B*, 2002. Submitted.
- [221] A Nakano, M Bachlechner, P Branicio, T J Campbell, I Ebbsjo, R K Kalia, A Madhukar, S Ogata, A Omeltchenko, J P Rino, F Shimojo, P Walsh, and P Vashishta. *IEE Transaction on Electronic Devices*, 47:1804, 2000.
- [222] D J Bacon. *The Structure and Properties of Crystal Defects*. Elsevier, Amsterdam, 1984.
- [223] G Rubio, N Agraït, and S Viera. *Phys. Rev. Lett.*, 76(13):2302, 1996.
- [224] J Li, D Stein, C McMullan, D Branton, M J Aziz, and J A Golovchenko. *Nature*, 412:166, 2001.